

C10027  
21288



VERVALLEN

P1149  
1138

BIBLIOTHEEK TU Delft  
P 1149 1138



C

272128

FUNDAMENTAL INVESTIGATION ON  
INTERACTION FORCES IN  
BUBBLE SWARMS AND ITS  
APPLICATION TO THE DESIGN  
OF CENTRIFUGAL SEPARATORS

PROEFSCHRIFT

TER VERKRIJGING VAN DE GRAAD VAN DOCTOR IN  
DE TECHNISCHE WETENSCHAPPEN AAN DE TECHNISCHE  
HOGESCHOOL DELFT, OP GEZAG VAN DE RECTOR  
MAGNIFICUS PROF. DR. IR. F.J. KIEVITS, VOOR EEN  
COMMISSIE AANGEWENZEN DOOR HET COLLEGE  
VAN DEKANEN TE VERDEDIGEN OP WOENSDAG  
2 MEI 1979 DES MIDDAGS OM 14.00 UUR

DOOR

ROBERT WISMAN

werktuigkundig ingenieur

geboren te Amsterdam



Dit proefschrift is goedgekeurd door  
de promotor PROF. IR. D.G.H. LATZKO  
en de copromotor PROF. IR. J.O. HINZE

Straks komt een wijzer, die 't wegredeneert

*P.A. de Génestet: Waar en Hoe*

☆☆

*Leekedichtjens (1860)*

## CONTENTS

LIST OF SYMBOLS	9
ABSTRACT	15
1. INTRODUCTION	17
1.1 Statement of the problem	17
1.2 Scope of the investigation	19
2. GAS-LIQUID INTERACTION FORCES IN BUBBLE SWARMS	20
2.1 Introduction	20
2.2 One-dimensional model for gas-liquid flow	22
2.21 Conservation laws	22
2.211 Mass balances	22
2.212 Momentum balance for the gas phase	23
2.213 Momentum balance for the liquid phase	24
2.214 Momentum balance for the mixture	25
2.22 Phase interaction	25
2.221 Drag force	26
2.2211 Single solid particle	26
2.2212 Single bubble	27
2.2213 Swarms of solid particles	30
2.2214 Swarms of bubbles	35
2.222 Virtual mass	38
2.23 Supporting analyses	41
2.231 Frictional pressure drop	41
2.232 Bubble diameter	47
2.24 Two-dimensional effects	54
2.3 Experimental data	59
2.31 Air-water experiments	60
2.311 Outline of the method	60
2.3111 Drag force coefficient	60
2.3112 Virtual mass coefficient	61
2.312 Range of variables	62
2.313 Description of the test facility	62
2.3131 Air-water loop	62
2.3132 Test section geometries	64
2.314 Instrumentation and data acquisition	65
2.3141 Flow measurements	65
2.3142 Void fraction measurements	67
2.3143 Pressure measurements	72
2.3144 Temperature measurements	74
2.3145 Data handling	74
2.315 Data processing	75
2.316 Results	78
2.3161 Pressure, void fraction and velocity distribution	78
2.31611 Axial pressure profiles	78
2.31612 Axial void fraction profiles	79
2.31613 Radial void fraction profiles	92
2.31614 Axial velocity profiles	92
2.3162 Interaction force coefficients	94
2.31621 Drag force coefficient	94
2.31622 Virtual mass coefficient	96
2.32 Steam-water experiments	99
2.321 Outline of the method	99

2.3211	Drag force coefficient	100
2.3212	Virtual mass coefficient	101
2.322	Range of variables	104
2.323	Description of the test facility	106
2.3231	Steam-water loop and major components	106
2.3232	Test section geometries	109
2.324	Instrumentation	110
2.3241	Loop instrumentation	110
2.3242	Test instrumentation and data acquisition	112
2.32421	Flow measurements	112
2.32422	Pressure measurements	114
2.32423	Temperature measurements	116
2.32424	Data handling	117
2.325	Data processing	117
2.326	Results	118
2.3261	Pressure, void fraction and velocity distributions	118
2.32611	Axial pressure profiles	118
2.32612	Void fraction profiles	119
2.32613	Velocity profiles	119
2.3262	Interaction force coefficients	132
2.32621	Drag force coefficient	132
2.32622	Virtual mass coefficient	134
2.4	Interaction force correlations	136
2.41	Drag force	136
2.411	Analysis	136
2.4111	Cluster formation	137
2.4112	Momentum transfer	138
2.412	Extension to mist flow	141
2.42	Virtual mass	144
2.421	Analysis	144
2.422	Extension to mist flow	145
3.	NUMERICAL PROCEDURES FOR DESCRIBING ROTATING TWO-PHASE FLOW	147
3.1	Introduction	147
3.2	Model for rotation-symmetric flow	147
3.21	Conservation laws	148
3.211	Mass balances	148
3.212	Momentum balances	148
3.2121	Momentum balances in a free flow field	148
3.2122	Tangential momentum balances between guide vanes	150
3.22	Additional equations	151
3.221	Interaction forces	151
3.222	Artificial viscosity terms	153
3.223	Boundary conditions	155
3.3	Solution methods	158
3.31	Introduction	158
3.32	Explicit scheme	159
3.321	Outline of the method	159
3.322	Initial value computation	160
3.323	Program sequence	162
3.324	Computation of velocity and pressure fields	164
3.3241	Axial velocities	164
3.3242	Radial velocities	166
3.3243	Tangential velocities	167
3.3244	Pressure distribution	169
3.325	Extension to computed void fraction distribution	171

3.33	Alternating direction implicit method	172
3.331	Outline of the method	172
3.332	Criteria for stability	176
3.3321	Necessary condition	176
3.3322	Sufficient condition	180
3.333	Evaluation of the ADI procedure	181
3.3331	Determination of the integration interval	182
3.3332	Computation time	184
3.334	Conclusion	186
3.4	Application of the explicit scheme to separator analysis	187
3.41	Comparison with experimental results	188
3.411	Impression of local values for all flow parameters	189
3.412	Wall pressures	193
3.42	Evaluation and further development	198
4.	GAS-LIQUID SEPARATION	200
4.1	Introduction	200
4.2	Steam-water separation in boiling water nuclear reactors	200
4.21	BWR steam supply system	200
4.22	Types of mechanical separator	201
4.23	Separator performance evaluation	204
4.231	Economics of the separating effect	207
4.232	Pressure loss evaluation	208
4.3	Selection of separator type	209
4.4	Introductory air-water experiments	210
4.41	Objectives	210
4.42	Test facility	210
4.421	Test loop	210
4.422	Test section geometries	211
4.43	Scope of experiments	212
4.431	Range of flow parameters	212
4.432	Measured data	213
4.433	Application of the ANALEST procedure	214
4.44	Results	214
4.441	Axial and radial pressure profiles	215
4.442	Axial and radial void fraction profiles	217
4.443	Axial velocity profiles	232
4.444	Tangential velocity	233
4.45	Analyses of separating performance	233
4.451	Separation length	234
4.452	Gas core diameter	234
4.453	Gas core stability	235
4.454	Liquid carry-over and gas carry-under	238
4.455	Compound efficiency of the separating effect	241
4.456	Pressure loss	242
4.46	Discussion	243
4.5	Air-water separator test	246
4.51	Introduction	246
4.52	Test facility	246
4.53	Separator geometry	248
4.531	Channel shape	248
4.532	Vortex finder	249
4.533	Blade profile	249
4.54	Data acquisition	250
4.55	Scope of the separator tests	251
4.56	Results	253

4.561	Radial void fraction profiles	253
4.562	Axial pressure profile	254
4.563	Separator performance	255
4.57	Discussion	259
4.571	Air-water separator	259
4.572	Extension to steam-water separators	260
4.573	Size extrapolation	261
5.	CONCLUSIONS	263
	ACKNOWLEDGEMENTS	265
	REFERENCES	267
	SAMENVATTING	279
	APPENDICES	
2-A	Error in momentum balance due to change of phase	281
2-B	Effect of radially non-uniform flow in the drift flux model	283
2-C	Increase of momentum due to peaks in the liquid velocity	290
2-D	Dissipation of mechanical energy in two-phase flow	292
2-E	Instrument listing for the atmospheric air-water test facility	294
2-F	Computation of radial void fraction distribution	295
2-G	Error estimation for the drag force coefficient $C_D$	297
2-H	Second two-dimensional effect on the $C_D$ - $\alpha$ correlation	299
2-I	Analysis of the velocity peak around a bubble	302
2-J	Derivation of a correlation for the virtual mass coefficient B	307
2-K	Expression for the derivative $\frac{d\alpha}{dz}$ for steam-water mixtures in a straight test section	311
2-L	Instrument listing for the high pressure steam-water test facility	313
2-M	Computation of the heat loss $Q_R$	316
2-N	Momentum exchange in the wake of a bubble	317
2-O	Droplet diameter in mist flow	320
2-P	Peak velocity ratio of a Rankine body	323
2-Q	Equations for vertical one-dimensional two-phase flow	326
3-A	Viscosity terms in turbulent two-phase flow momentum balances	330
3-B	Tangential velocity component between blades	334
3-C	Selection of the proper root from the quadratic axial velocity equations	336
3-D	Dynamic pressure	337
4-A	Cost effects of separator performance	344
4-B	Measurement procedure for separator gas exit flows	348

LIST OF SYMBOLS

A	area	$m^2$
	constant	
	matrix	
B	virtual mass coefficient	
b	peak width	m
C	coefficient	
	matrix	
$\Delta C$	cost variation	
c	concentration by volume	
	sonic velocity	m/s
D	channel diameter	m
	determinant	
	matrix	
d	bubble diameter	m
E	energy	W
F	volume force	$N/m^3$
$F^*$	(= $F/u^2$ ) specific volume force	$Ns^2/m^5$
f	force	N
	frequency	
$\Delta f$	cost variation	
g	gravitational constant	$m/s^2$
h	height	m
	enthalpy	J/kg
	radial grid number	
I	radiation intensity	photons/ $m^2s$
	unity matrix	
Im	imaginary part of complex number	
i	$\sqrt{-1}$	
	interest	%
j	volumetric flux	m/s
K	constant	
k	axial grid number	
	overall heat transfer coefficient	$J/m^2s^0K$
L	length	m
l	length	m
M	momentum flux	$kg/ms^2$
	stability matrix	
	measured value	

m	power	
n	power and reciprocal power number order	
O	channel periphery order of magnitude	m
P	predicted value	
p	pressure reciprocal power	$N/m^2$
$\Delta p$	pressure difference	$N/m^2$
Q	heat loss volumetric flow rate from/to source/sink	W $m^3/s$
q	reciprocal power	
R	channel radius under relaxation factor	m
$R_{ij}$	coefficient of second-order velocity-correlation tensor	
Re	real part of complex number	
r	coordinate radius power interest	m m  %
S	contour	$m^2$
s	slip integration route	
T	time absolute temperature	s $^{\circ}K$
t	time coordinate thickness	s m
u	velocity	m/s
$\underline{u}$	vector of flow parameters (cf. expressions (3-70) and (3-71))	
V	volume	$m^3$
v	coefficient of Fourier series	
W	volume mass force	$N/m^3$
$\underline{w}$	vector of non differential terms from mass and momentum balances	
x	coordinate quality	m

y	coordinate	m
z	coordinate	m

### Greek symbols

$\alpha$	void fraction	
	film heat transfer coefficient	$\text{J/m}^2\text{s}^0\text{K}$
$\beta$	volumetric quality	
	constant	
	number in Fourier series expansion	
$\gamma$	angle	
	number in Fourier series expansion	
$\delta$	angle	
	deviation	
	finite difference operator	
$\delta_{ij}$	Kronecker delta	
$\Delta$	difference	
$\epsilon$	turbulence viscosity	$\text{m}^2/\text{s}$
	specific energy dissipation	$\text{m}^2/\text{s}^3$
	deviation	
$\zeta$	finite difference function (cf. expression (3-89))	
	pressure loss coefficient	
$\zeta_b$	blade correction factor	
$\eta$	dynamic viscosity	$\text{Ns/m}^2$
	fraction	
	efficiency	
$\theta$	temperature	$^{\circ}\text{C}$
$\kappa$	half an integration step	
$\lambda$	friction factor	
	eigen value	
	thermal conductivity	$\text{J/ms}^0\text{K}$
$\mu$	photon absorption coefficient	$-\text{/m}$
	finite difference function (cf. expression (3-89))	
$\nu$	kinematic viscosity	$\text{m}^2/\text{s}$
$\xi$	additional term (generally $\xi \ll 1$ )	
$\rho$	density	$\text{kg/m}^3$
	spectral radius	
$\sigma$	surface tension	$\text{N/m}$
	standard deviation	

$\tau$	shear stress	$N/m^2$
$\phi_m$	mass flow rate	kg/s
$\phi_v$	volume flow rate	$m^3/s$
$\phi'_{lg}$	volumetric evaporation mass flow rate	kg/s $m^3$
$\varphi$	specific evaporation mass flow rate	kg/s m
$\Psi$	scatterband	

### Subscripts

A	acceleration	P	present
B	Bankoff	p	particle, pressure, peak, positive, chord number
b	bubble, barometer, blade	R	riser
c	continuous, correction, cold, compound, core	r	relative, radial, real
co	carry-over	S	Sauter diameter
cr	critical, cross section	s	superficial, solid, system, separator
cu	carry-under	sat	saturation
D	drag, downcomer	ss	stainless steel
d	droplet, dynamic, discontinuous, dryer	t	turbulence, total, resultant, tangential
E	energy, gas exit	tp	two-phase
e	effective	ts	test section
f	fluid, flow meter	v	virtual mass, viscosity, volumetric
fr	friction	W	Weber number
fw	feed water	w	wall, wake
g	gas	ZF	Zuber and Findlay
h	radial grid number	z	axial
i	interaction, number, inside, coordinate direction	$\tau$	shear stress
j	coordinate direction	$\varphi$	tangential
k	axial grid number, chord, coordinate direction, phase	$\zeta$	center line
l	liquid	o	initial
lg	liquid evaporating to gas	80,50	cumulative fraction
M	mixer	$\infty$	infinity
m	momentum, mass, mixture, measured, mechanical		
N	Newton's region		
n	order, negative, natural, normal		
o	outside		

## Superscripts

n	iteration step number	☆	without physical meaning, scaled parameters
T	transformed	⊕	peak (cf. figure 2-46))
'	turbulence velocity	∞	single bubble/particle
★	shear stress velocity, reduced	α	bubble/particle swarm

## Definitions

< > cross-sectional average:  $\langle x \rangle = \frac{1}{A} \int_A x dA$

— time average, one dimensional average

u true phase velocity; in one-dimensional model:

$$u_g = \bar{u}_g = \frac{\langle \alpha u_g \rangle}{\langle \alpha \rangle} \quad u_l = \bar{u}_l = \frac{\langle (1-\alpha) u_l \rangle}{\langle 1-\alpha \rangle}$$

u<sub>s</sub> superficial velocity:

$$u_{sg} = \langle \alpha u_g \rangle = \frac{\phi v_g}{A} \quad u_{sl} = \langle (1-\alpha) u_l \rangle = \frac{\phi v_l}{A}$$

Fr Froude number  $\frac{u^2}{gh}$

Nu Nusselt number  $\frac{\alpha D}{\lambda}$

Re Reynolds number  $\frac{\rho u d}{\eta}$

We Weber number  $\frac{\rho u^2 d}{\sigma}$

## ABSTRACT

The present investigation deals with two aspects of gas-liquid flows, viz. interaction forces between the phases in bubble swarms and numerical description of rotating gas-liquid flows. The insight obtained was applied to the development of axial gas-liquid cyclones, as used i.a. as primary separators in nuclear boiling water reactors.

The investigation on interaction forces in bubble swarms has led to correlations for the drag force coefficient  $C_D$  and the virtual mass coefficient  $B$ , occurring in the gas and liquid momentum balances. The experimental verification took place in both atmospheric air-water mixtures and in steam-water mixtures at pressures between 5 and 7 MN/m<sup>2</sup>. Test sections with constant and variable cross section were used in both cases in order to study both steady and accelerating mixture flows. In all test sections the superficial water velocity was varied between 0.9 and 2.5 m/s, while the gas volume fraction was varied between 0.2 and 0.75. In the atmospheric air-water experiments the gas volume fraction was measured in addition to the axial pressure profile. These measurements were carried out for 10 channel cross sections by means of photon absorption, permitting the two coefficients to be obtained directly from the one-dimensional momentum balances. No such gas volume fraction measurements were possible for the high pressure steam-water mixtures, requiring the development of special procedures for computing the drag force and virtual mass coefficients from the pressure profiles of the straight and converging test section, respectively.

Computation of the two coefficients from the momentum balances required the development of auxiliary correlations for two-phase frictional pressure drop and for the bubble diameter. In addition the one-dimensional momentum balances were corrected for two-dimensional effects by means of a numerical analyses, although these effects were found to be of minor importance. The drag force coefficient could be represented by a function of the gas volume fraction  $\alpha$  only. In order to explain the considerable discrepancy between this correlation and those applicable to solid-particle-liquid flows a qualitative analyses was performed, based on the interaction of bubbles and particles with the wakes of other bubbles or particles. Correlation of the virtual mass coefficient required the introduction of a new parameter in addition to the gas volume fraction. The relationship with this parameter, called the peak velocity ratio and based on the relative velocities in the neighbourhood of a bubble, was established by experiment and verified by analyses based on potential flow. Dependence on the gas volume fraction agrees with analytical correlations from the existing literature.

The before mentioned correlations were subsequently utilized in the numerical description of the two-dimensional (rotation-symmetric) flow. This numerical description required the solution of the system of eight coupled partial differential equations consisting of the mass balances and the axial, radial and tangential momentum balances of the two phases. Two different numerical solution methods were investigated. The "alternating direction implicit" (ADI) method separately solves a main system of six equations and a secondary system of the two tangential momentum balances. This uncoupling is desirable from the view point of limiting computer time and acceptable because of the weak link between the tangential momentum balances and the remaining balances. Much attention was paid during the realisation of this solution method to the numerical stability of the process. The computing time required, however, turned out to be excessive. After establishing that the reasons were inherent to the combination of the method and the type of flow to which it was applied a second solution method was developed and implemented

in the computer program ANALEST. In this solution method all the balances are uncoupled and solved sequentially, each balance giving the solution for one of the unknowns. This sequential solution procedure is repeated until the values for the eight flow parameters remain constant. The ANALEST version discussed in chapter 3, however, computes only seven parameters, viz. the pressure and six velocities, while the spatial distribution of the gas volume fraction is provided as input. The necessary steps for further development of the procedure to the point where all eight flow parameters are computed are also discussed in chapter 3.

The results of the afore mentioned work have subsequently been applied to the development of a venturi separator for nuclear boiling water reactors. After a series of introductory experiments a venturi separator was designed and tested with atmospheric air-water mixtures, the superficial water velocities and volumetric qualities of which were derived from data on part load operation of a BWR. The separating efficiencies and pressure drop of this separator have been compared to the requirements defined by reactor manufacturers, taking into account economic aspects. Indications are given concerning the further development of this venturi separator, taking into account the transition from air-water to steam-water mixtures and the rules for geometrical upscaling.

## 1. INTRODUCTION

### 1.1. Statement of the problem

The ultimate purpose of the present investigation is to contribute to the development of a so called venturi separator (cf. figure 1-1) for application to steam-water mixtures of nuclear boiling water reactors (BWR). In the mid sixties PRINS [1] started an investigation in the Laboratory for Thermal Power Engineering at Delft University of Technology on various aspects of steam-water separation in nuclear steam supply systems, resulting - among other things - in the proposal for a venturi shaped centrifugal separator for BWR's. Although his first separator tests yielded a rather poor separating performance, it was subsequently decided in view of the possible advantages of the venturi separator to continue its development in said laboratory under responsibility of the present author.

A modern BWR power plant is a single loop system (cf. figure 4-1) with forced circulation through the nuclear core where partial evaporation takes place. The steam-water mixture passes through the primary separators on top of the core whence the water is returned to the downcomer for recirculation whilst the steam is led to the turbine by way of the secondary impingement dryers. The primary separation - for which the

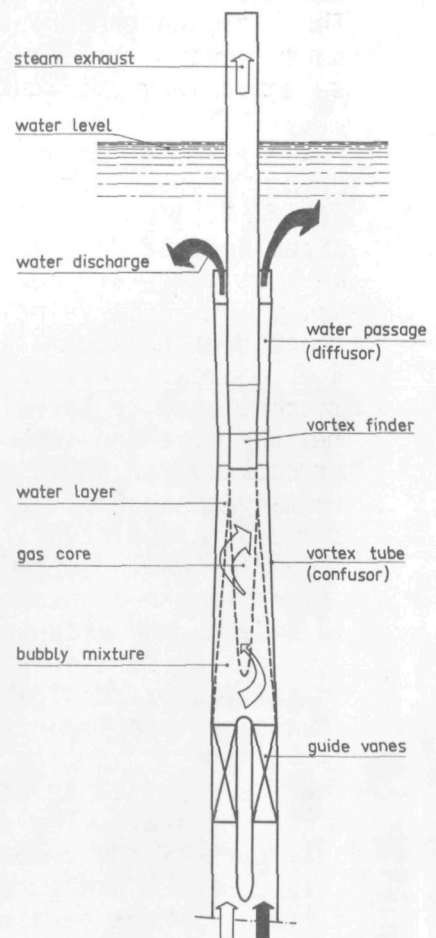


FIGURE 1-1

*Venturi separator*

venturi separator is intended - deals with inlet mixtures containing up to 15% steam by weight. This limit derives i.a. from the neutron moderating function of the water; for safety reasons the reactor has to be under-moderated, i.e. the thermal power output of the nuclear core decreases with decreasing moderator-to-fuel ratio. At the steam exit water carry-over may not exceed 20% by weight in order to prevent malfunction of the secondary dryers resulting in

- loss of thermodynamic efficiency of the turbine cycle due to
  - denting of turbine blades by erosion
  - scale deposits on the turbine blades
- long term radioactive contamination of the turbine and condenser

The carry-under of steam into the downcomer has to be minimized as far as possible because it causes

- decreased subcooling at the core inlet, resulting in
  - reduction of thermal power output
  - reduced stability margin
  - lower critical heat flux ratio
- danger for cavitation of the circulation pump
- reduced attenuating capability of the downcomer resulting in increased fast neutron exposure for the reactor vessel's beltline region

Contrary to fossil-fired circulation boilers where separation takes place in a steam drum, the BWR separators and dryers are located on top of the reactor core, i.e. the available area is determined by the reactor vessel diameter.

Thus, though the problem of phase separation is essentially the same in both types of boiler, the requirements are much more stringent and the solution more difficult in BWR's.

The history of steam-water separation in BWR's, extensively reviewed by Prins, started with gravity separation in the early small sized BWR (< 100 MWe) plants. Its application is restricted to such small reactor sizes because the velocity of the steam leaving the free surface has to be kept below around 0.4 m/s in order to prevent excessive liquid carry-over. This exit velocity increases with increasing power output because the amount of steam raised is proportional to the volume of the core, i.e. approximately to the diameter cubed, while the free surface increases proportional to the diameter squared, resulting in proportionality between reactor size and steam velocity. Therefore mechanical separation was introduced for BWR's with increasing power output. Several designs of primary separators have been developed (cf. subsection 4.2.2.), all of the centrifugal type. Most of them are located on top of the core and therefore called upcomer cyclones, in contrast to downcomer cyclones placed in the downcomer next to the core. After considering the advantages and disadvantages of both types Prins selected the upcomer cyclone for further study and development, which subsequently focussed on the venturi design. The compactness of this design represents an advantage, the importance of which increases with reactor power as explained by Prins (cf. section 4.3.). Further advantages are its simple geometry and the expected relatively low pressure loss due to its converging-diverging shape. The converging section increases the rotation, hence only part of the rotation has to be generated by the guide vanes, which should reduce pressure losses. Additional gain was expected from the diffuser where part of the kinetic energy is transformed into static pressure.

## 1.2. Scope of the investigation

Being an university research project, the present investigation not only aims at an improved separator, but also at improved understanding of gas-liquid flows and the possibility to apply this insight for design purposes other than steam-water separators. In the course of the investigation its emphasis increasingly shifted towards this second, more general objective.

This increasing emphasis on general applicability is reflected in the development of a computer program based on the differential mass and momentum balances for dispersed gas-liquid flow, used here to predict the flow in the cyclone but applicable to a wide variety of other two-phase flows.

Apart from the effort to develop a mathematical procedure for the solution of the set of governing partial differential equations, a great deal of effort was directed at completion of the phase momentum balances. Notwithstanding the efforts of PRINS [1] and many others, no rigorous description and correlations for interaction forces between the two phases are available from literature, therefore the development of correlations for the drag force and virtual mass of bubble swarms was included in the present investigation.

Thus the work reported here consists of three distinct main parts, viz.

- an investigation on the drag force and virtual mass of bubble swarms
- the development of a numerical procedure to solve the set of eight coupled partial differential equations, defining the phase mass and momentum balances
- experiments for the development of the venturi separator

The investigation on the interaction forces, discussed in chapter 2, is based on experiments with atmospheric air-water mixtures as well as high pressure (up to  $7 \text{ MN/m}^2$ ) steam-water mixtures. These experiments cover the entire range of superficial water velocities - from 1.3 up to 2.5 m/s - and void fractions - from 0.2 up to 0.8 - of interest for the venturi separator. Straight, converging and diverging test sections were applied in order to study the effects of acceleration and deceleration.

Chapter 3 describes the development of two numerical procedures for solving the set of mass and momentum balances for rotating gas-liquid flows. One of the methods failed but is included in the discussion to show the reasons for its failure. The results of the successful method in its present <sup>\*</sup>) state, i.e. not yet fully completed, are compared with measurements for separator flows.

Chapter 4 goes into the primary separation in BWR's. The experimental part consists of introductory experiments with rotating atmospheric air-water mixtures. The directly measured data obtained from these experiments are then combined with detailed information from application of the numerical procedure and used to design a venturi separator. Preliminary air-water tests on this separator are reported next. Because these tests were performed on a downscaled version of the separator, this chapter concludes with a discussion on the consequences of upscaling and application to high pressure steam-water mixtures.

---

<sup>\*</sup>) "present" indicates the time of completion of this report.

## 2. GAS-LIQUID INTERACTION FORCES IN BUBBLE SWARMS

### 2.1. Introduction

Apart from pure science for the sake of science, history of two-phase flow studies starts - as is widely known and mentioned by PRINS [1] - with the development of formulae and criteria for use in engineering practice, which were meant above all for the design of hardware and include only very little physical aspects.

An excellent example of these "black box" correlations are the graphs given by MARTINELLI and NELSON [2] for the determination of the frictional and acceleration pressure drop - in case of forced circulation boiling of water - in which the pressure and exit quality form the only parameters in addition to the mass flow.

These graphs were in turn based upon local frictional pressure drop data obtained by LOCKHART and MARTINELLI [3] through extrapolation from single-phase flow data. This technique of extrapolation from single-phase correlations has long remained at the base of the majority of two-phase flow analyses for engineering applications and is still used at the present time.

An improvement in two-phase flow analyses was achieved by the introduction of simple analytical models such as e.g. the variable density single fluid model proposed by BANKOFF [4] for predicting the average slip between the phases at a given cross section in channel flow.

Subsequent analytical models based on two-phase flow characteristics - e.g. the drift-flux model from WALLIS [7] - have led to better physical understanding and correlations of increasing sophistication. However, for engineering problems such as the centrifugal separation process treated in this investigation, the number of relevant variables far exceeds the capabilities of such simple analytical models, leading to the continued need for empirical correlations of limited validity, generally obtained from full scale experiments ([27], [28], [29], [30]).

The increasing availability of large, high-speed computers opened the possibility for fundamental analyses based on the conservation laws for mass and momentum. The latter is described by the Navier-Stokes equations which for the case of single-phase steady state turbulent flow, neglecting body forces, may be written as follows:

$$u_j \frac{\partial u_i}{\partial x_j} = - \frac{1}{\rho} \frac{\partial p}{\partial x_i} + \nu \frac{\partial^2 u_i}{\partial x_j \partial x_j} - \overline{\frac{\partial u_i u_j}{\partial x_j}} \quad (2-1)$$

These equations are solved by introduction of supporting equations for the Reynolds stresses  $-\rho \overline{u_i u_j}$ . A review of these supporting equations and their applications in engineering computations given by ROTTA [5] shows these equations to be partly analytical and partly empirical. In two-phase flow solution of the Navier-Stokes equations becomes extremely difficult, mainly because of the necessary discretization of all the bubbles and the introduction of their moving boundaries, including coalescence and breaking up. Such discretization is only practicable if the flow equations are greatly simplified. An example of this approach is given by JOHANSSON, CLIFT and GRACE [6] for fluidized beds. The simplifications they made - in using potential flow and doublets for the representation of the bubbles and in very simple assumptions for bubble rising velocity and coalescence of bubbles - are so extensive that the rather good agreement with experiments is surprising. Nevertheless it is unlikely that such simplifications can give good results for two-phase flow computations in general.

A much more generalized approach for solving the Navier-Stokes equations is given by the well-known stochastic model. Most important in this model is the elimination of discrete bubbles by the introduction of the void fraction  $\alpha$  defined as a time average by:

$$\alpha = \frac{\int_0^T c \, dt}{\int_0^T dt} \quad (2-2)$$

in which the concentration  $c$  equals one if the phase at the point of interest is gas and zero if this point is in the liquid phase. It should be noticed that the properties of the gas phase such as velocity, bubble diameter, etc. remain unchanged by the introduction of this void fraction and are part of the model.

The vectors of the gas and liquid velocities are defined in the same way as:

$$\bar{u}_g = \frac{\int_0^T c \, u_g \, dt}{\int_0^T c \, dt} \quad (2-3)$$

and

$$\bar{u}_l = \frac{\int_0^T (1-c) \, u_l \, dt}{\int_0^T (1-c) \, dt} \quad (2-4)$$

from which the superscribed dashes at the left hand sides - indicating the time average - are always omitted because these velocities are the only one known in the model.

An obvious analogy exists between these definitions and the square of the turbulent velocity defining the Reynolds stresses:

$$\overline{u_i' u_i'} = \frac{\int_0^T u_i' u_i' \, dt}{\int_0^T dt} \quad (2-5)$$

which has been successfully used for computations of turbulent flow without discretization of the turbulent velocity  $u_i'$  itself. It should be stressed at this point, that this model for two-phase flow is not an extrapolation of single-phase flow, but is based on a stochastic description of the flow valid for both turbulent single-phase and two-phase flow.

In two-phase flow analyses the fluctuations in liquid velocity caused by flowing around the bubbles are eliminated by the introduction of the time average velocity. As a consequence the pressure distribution around the bubbles is also eliminated. Hence the resulting drag force and virtual mass have to be introduced as body forces in the Navier-Stokes equations for the time average velocities and pressure. The applicability of the stochastic model for numerical approximations is thus predicated upon the availability of correlations for these two interaction forces.

Experimental evidence on the magnitude of these interaction forces is scanty for the case of bubble swarms relevant for this investigation, as borne out by a fairly recent interpretive review by PRINS [1]. As will

be evident from the foregoing, such quantitative data on the interaction forces are prerequisite to numerical analysis of venturi separator flow. The present chapter is therefore entirely devoted to the analytical and experimental development of correlations for these interaction forces. A second reason for the great attention paid to this subject stems from its importance for future applications of the stochastic model to numerical analysis of two-phase flow, analogous to the present day numerical approach for turbulent single-phase flow. The potential for thus raising the state-of-art of two-phase flow analysis to that presently achieved for single-phase flow indicates increased future interest in the stochastic model and thus in interaction force correlations extending far beyond the scope of the present investigation.

## 2.2. One-dimensional model for gas-liquid flow

For the sake of simplicity the experiments reported in this chapter are analyzed on the basis of a one-dimensional model. This simplification appears justified because the flows under consideration are bubbly - and froth flows for the higher void fractions - having a rather uniform cross-sectional void distribution. Moreover a numerical evaluation of the two-dimensional effects in these axial symmetric flows is subsequently carried out (see subsection 2.2.4.) in order to reduce any error due to the one-dimensional assumption.

This assumption also implies that - apart from subsection 2.2.4. - no difference is made between the spatial average and local values at a cross section, hence the superscribed dashes indicating average values are henceforth omitted for the sake of simplicity.

### 2.2.1. Conservation laws

The steady state equations given below have been derived before by PRINS [1] and are to be found in all pertinent handbooks e.g. WALLIS [7]. The main purpose of the following description is therefore to evaluate the physical interpretation of the interaction forces, which may differ slightly from previous derivations. In this discussion the interaction forces are only discussed as general body forces  $F_D$  and  $F_A$ ; their detailed form will be discussed in subsection 2.2.2..

#### 2.2.1.1. Mass balances

The total mass in the control volume of the one-dimensional cross section shown in figure 2-1 remains constant, yielding:

$$\frac{d}{dz} \phi_t = 0 \quad (2-6)$$

However, due to change of phase the evaporating (or condensing) mass has to be considered as a mass source or sink respectively, giving for the gas phase:

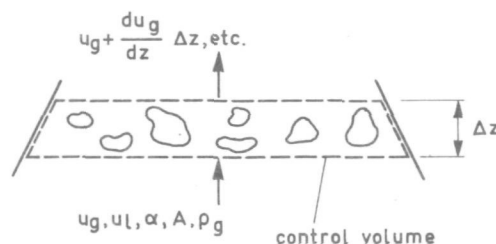


FIGURE 2-1

*Control volume for total mass considerations*

$$\frac{d}{dz} \phi_g = \varphi_{lg} \quad (2-7)$$

where  $\varphi_{lg}$  is the evaporating mass flow per unit length.  
For one-dimensional flow the gas mass flow may be written as:

$$\frac{d}{dz} (\rho_g \alpha A u_g) = \varphi_{lg} \quad (2-8)$$

In the same way the mass balance for the liquid phase is derived as:

$$\frac{d}{dz} (\rho_l (1-\alpha) A u_l) = - \varphi_{lg} \quad (2-9)$$

For the present experiments  $\varphi_{lg}$  serves as a correction. In case of atmospheric air-water experiments the change of phase is related to the humidity of the saturated air and may be taken zero without any significant loss of accuracy. For the high-pressure steam-water experiments there is some flashing due to the pressure drop in the test section and a little condensation due to heat leakage from the test section; both corrections are of little significance.

#### 2.2.1.2. Momentum balance for the gas phase

For a complete derivation including extensive discussion of the various steps is referred to PRINS [1]. The discussion in these subsections will be limited to the essentials and additions to or deviation from this reference.

As shown by Prins two types of interaction force have to be introduced to represent the eliminated pressure distribution around a bubble, viz.

- the dragforce  $f_D$ ,  
caused by the relative motion between the phases, and
- the acceleration force  $f_A$ ,  
required to accelerate the fluid flow around the bubble, which is represented by a virtual mass added to the mass of the bubble.

As the present model, based on the void fraction, does not distinguish single bubbles, the forces  $f_D$  and  $f_A$  have to be transformed to volume forces  $F_D$  and  $F_A$  acting on the control volume. Introduction of  $n$  as the number of bubbles per unit volume i.e.:

$$n = \alpha / \frac{\pi}{6} d^3 \quad (2-10)$$

yields

$$F_D = \alpha f_D / \frac{\pi}{6} d^3 \quad (2-11)$$

and

$$F_A = \alpha f_A / \frac{\pi}{6} d^3 \quad (2-12)$$

Incorporation of these volume forces in the force balance for the control volume of figure 2-2 yields:

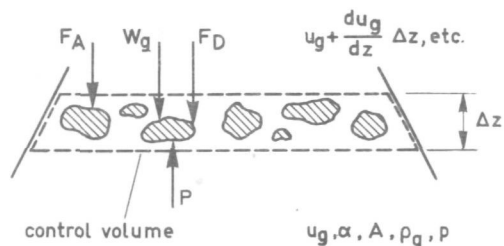
$$- \frac{d}{dz} (\alpha A \rho_g u_g^2) \Delta z + P A \Delta z - W_g A \Delta z - F_D A \Delta z - F_A A \Delta z = 0 \quad (2-13)$$

with:

$$P = -\alpha \frac{dp}{dz} \quad (2-14)$$

FIGURE 2-2

Control volume for momentum considerations of gas phase



and:

$$W_g = \alpha \rho_g g \quad (2-15)$$

Substitution of equations (2-14) and (2-15) in (2-13) gives the momentum balance for the gas phase:

$$\frac{d}{dz} (\alpha A \rho_g u_g^2) + F_A A = -\alpha A \frac{dp}{dz} - \alpha A \rho_g g - F_D A \quad (2-16)$$

The viscosity forces inside the dispersed bubbles result in a shear stress at the bubble surfaces which is incorporated in the drag force  $F_D$ ; therefore no distinct viscosity forces appear in this momentum balance. An effect only roughly discussed by Prins concerns change of phase, which is not properly taken into account in this momentum balance. This is shown very clearly by subtracting  $u_g$  times the mass balance (2-8) from the momentum balance (2-16) yielding:

$$\alpha A \rho_g u_g \frac{du_g}{dz} + \varphi_{1g} u_g + F_A A = -\alpha A \frac{dp}{dz} - \alpha A \rho_g g - F_D A \quad (2-17)$$

where the term  $\varphi_{1g} u_g$  represents the momentum of newly formed gas in case of evaporation. The error made in the above momentum balances is the omission of the initial momentum of the mass  $\varphi_{1g}$  at the moment of evaporation, viz.  $\varphi_{1g} u_1$  resulting in the term  $\varphi_{1g}(u_g - u_1)$  instead of  $\varphi_{1g} u_g$  to the momentum balance for the gas phase.

However, it is not clear how this force should be distributed over the gas and liquid phase. WALLIS [7] has introduced a fraction  $\eta$  resulting in an additional momentum of  $\eta \varphi_{1g}(u_g - u_1)$  for the gas flow and of  $(1-\eta)\varphi_{1g}(u_g - u_1)$  for the liquid flow. The factor  $\eta$  depends mostly on the process - evaporation or condensation - and on the interaction forces. The resulting error in the gas balance  $\varphi_{1g}\{(1-\eta)u_g + \eta u_1\}$  has been estimated for the present steam-water experiments in Appendix 2-A, based on flashing due to pressure drop. The result:

$$|\varphi_{1g}\{(1-\eta)u_g + \eta u_1\}| \leq |0.01 \alpha A \frac{dp}{dz}| \quad (2-18)$$

indicates that this error is minor compared to the error in the measured value of  $\alpha A \frac{dp}{dz}$  itself. For this reason use of the above improper representation of the effects of phase change appears acceptable.

### 2.2.1.3. Momentum balance for the liquid phase

Again referring to Prins and to figure 2-3 the following equation is derived for the liquid:

$$\rho_l \frac{d}{dz} ((1-\alpha)A u_l^2) = - (1-\alpha)A \frac{dp}{dz} - (1-\alpha)A \rho_l g + F_D A - \left(\frac{dp}{dz}\right)_{fr} A \quad (2-19)$$

where the frictional pressure drop - commonly used in engineering practice -

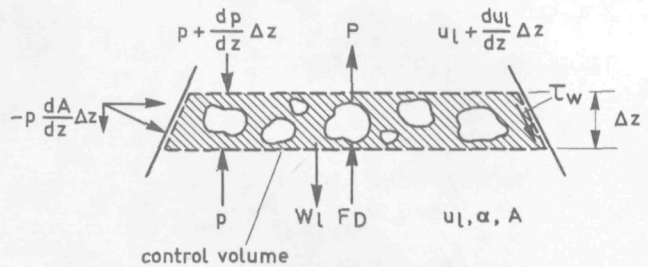


FIGURE 2-3

Control volume for momentum considerations of liquid phase

is related to the wall shear stress  $\tau_w$  by:

$$\left(\frac{dp}{dz}\right)_{fr} A \Delta z = \tau_w \Delta z \quad (2-20)$$

and  $\rho_l$  is supposed to be constant.

Most striking in this equation is the absence of the virtual mass force, apparently violating Newton's third law which is used for all other forces both here and in the gas balance. In discussing this point Prins has followed the reasoning presented by HINZE [9] for a single solid particle, concluding that Newton's third law is satisfied by the presence of the force  $f_A$  at the external boundaries of the total mixture.

As a consequence of the above the force  $F_A$  does exist in the momentum balance of the mixture, influencing the pressure drop of the mixture. As shown by PRINS [10] this approach is supported by the experimental data of ROSE and GRIFFITH [11], who measured the force exerted by an air-water mixture on a turning Tee, deflecting the flow at right angles from its original direction.

The question appears in order why the drag force  $F_D$  is treated differently from the virtual mass force by including it in equation 2-19. As a matter of fact HINZE [9] concluded that it should not appear in the liquid momentum balance. However, his theoretical analysis is based on a velocity defect in the liquid velocity profile behind the particle or bubble, while in case of swarms of bubbles (and particles) this velocity defect may be assumed to be smoothed out rather quickly by the turbulence of the flow itself. It thus appears plausible that the velocity wakes will not affect the velocity profiles at the external boundaries of the liquid control volume and only have to be taken into account at the internal boundaries. However, as stated by WISMAN [12] and discussed in subsection 2.2.3.1.

the frictional pressure drop  $\left(\frac{dp}{dz}\right)_{fr}$  contains a term  $\lambda_i F_D$ , which implies that a fraction  $\lambda_i$  of the drag force  $F_D$  does "reach" the wall, which forms part of the external boundaries. If the fraction  $\lambda_i$  - which depend on geometrical and flow parameters - equals one the result is conform the theoretical analysis of HINZE [9].

#### 2.2.1.4. Momentum balance for the mixture

The momentum balance for the mixture is found by adding equations (2-16) and (2-19):

$$\begin{aligned} \frac{d}{dz} (\alpha A \rho_g u_g^2) + \rho_l \frac{d}{dz} ((1-\alpha) A u_l^2) + A F_A = \\ = -A \frac{dp}{dz} - A(\alpha \rho_g + (1-\alpha) \rho_l) g - A \left(\frac{dp}{dz}\right)_{fr} \end{aligned} \quad (2-21)$$

#### 2.2.2. Phase interaction

In this subsection the mathematical formulation of the interaction forces  $F_D$  and  $F_A$  will be derived with respect to single bubbles.

In addition a short review will be given of experimental and analytical correlations for these interaction forces, for a more extended review

see PRINS [ 1 ] .

#### 2.2.2.1. Drag force

In engineering practice the drag force of a submerged body is usually presented as:

$$f_D = C_D A_b \frac{1}{2} \rho u_r^2 \quad (2-22)$$

In order to give the drag force the same sign and direction as the relative velocity  $u_r$  the momentum flux is written as  $\rho u_r |u_r|$ , while in case of spheres the cross section  $A_b$  equals  $\frac{\pi}{4} d^2$ , yielding for the present:

$$f_D = C_D \frac{\pi}{4} d^2 \frac{1}{2} \rho_1 u_r |u_r| \quad (2-23)$$

Substitution of  $f_D$  in equation (2-11) yields:

$$F_D = \frac{3}{4} \alpha \frac{C_D}{d} \rho_1 u_r |u_r| \quad (2-24)$$

It should be noticed that this formula is only valid for one-dimensional flow. For multi-dimensional flow a more extensive analysis is required with respect to the representation of the momentum flux; this will be discussed in subsection 3.1.1.2..

For practical use of the momentum equations a correlation for the ratio  $\frac{C_D}{d}$  is needed, as for example investigated by PRINS [ 1 ] . Referring the discussion on correlations for the bubble diameter to subsection 2.2.3.2., the attention will be focussed to the drag force coefficient  $C_D$ .

An extensive review of literature data for both single bubbles and bubble swarms was given by PRINS [ 1 ] .

In addition to updating this information the present text intends to put it into a wider perspective by considering drag force coefficients for four forms of two-phase flow, viz.

- single solid particle
- single bubble
- swarm of solid particles
- swarm of bubbles

This extension of the data results from the present author's view that no significant discontinuities between these four flow forms are to be expected. Apart from the difference in density (compare table tennis ball versus solid ball) the only differences between bubbles and solid particles are the presence of internal circulation and deformation in the former case, while the main differences between single particles or bubbles and swarms - apart from variations in bubble diameters due to coalescence, to be discussed later - consists of wake effects exerted by particles or bubbles on their downstream followers. None of these differences is connected with abrupt changes; hence it seems logical to expect continuous transitions between the four flow forms and to compare them with each other.

##### 2.2.2.1.1. Single solid particle

From experiments with single solid spheres in infinite fluids SCHLICHTING [ 13 ] constructed the "standard" drag curve shown in figure 2-4. From this curve it appears that the proportionality with the momentum flux inferred by equation (2-22) holds only in the region  $700 < Re_p < 2.10^5$ , for which Newton found the value  $C_D = 0.44$ . While the inertia effect

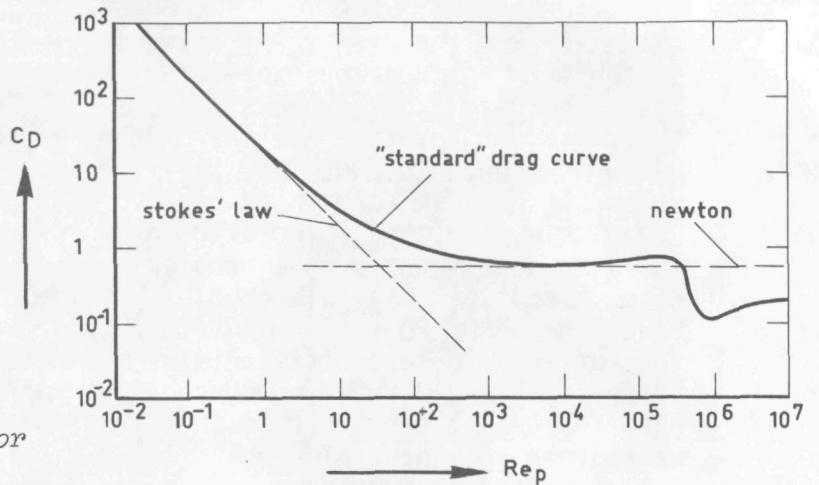


FIGURE 2-4

Standard drag curve for single solid spheres

dominates this region it can be completely neglected in comparison to the shear forces at the particle surface for  $Re_p < 1$ . For this latter region the drag force is proportional to the relative velocity only, resulting in a drag force coefficient - in equation (2-22) - given by Stokes' law as

$$C_D = \frac{24}{Re_p}$$

In consequence of the smooth transition zone between these two regions, the drag force coefficient can be approximated reasonably well - for all regions - by:

$$C_D = 0.44 + \frac{24}{Re_p} \quad \text{for } Re_p < 2.10^5 \quad (2-25)$$

More complex correlations are reviewed by S00 [14], but the possible gain in accuracy afforded by their use appears irrelevant for the present study in view of the effects discussed in the following subsections.

#### 2.2.2.1.2. Single bubble

For experiments and analyses on single bubbles in stagnant liquid the reader is referred - for the sake of brevity - to the extensive reviews given by PRINS [1] and S00 [14] and the resultant figure 2-5. For low

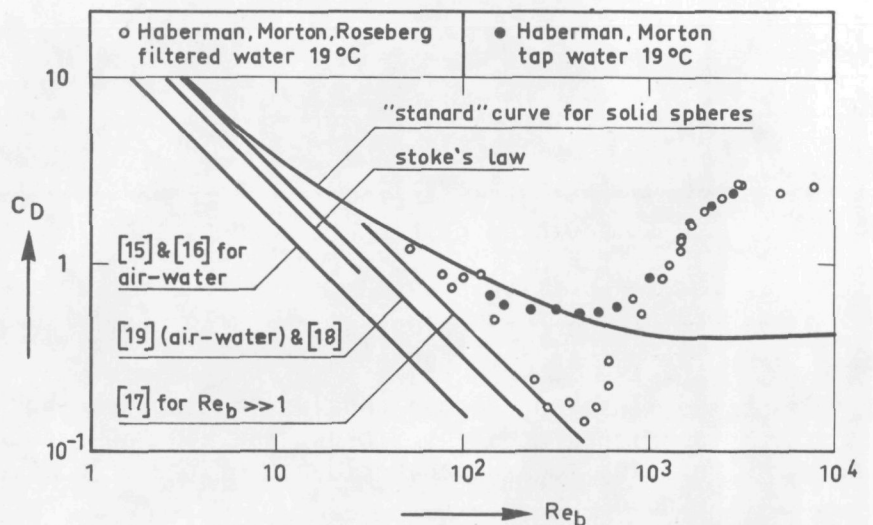


FIGURE 2-5

Drag force coefficient for air bubbles in stagnant water as a function of their Reynolds number

values of  $Re_b$  the drag coefficient is seen to follow Stokes' law, while it tends to reach a constant value (Newton flow) for very high  $Re_b$  values ( $Re_b > 5000$ ).

The region of interest for the present investigation is roughly delimited by  $1000 < Re_b < 10,000$ , i.e. the region where the bubbles are flattened to an ellipsoidal form which becomes mushroom-shaped with increasing Reynolds number, while the drag force is increasingly dominated by vortex shedding downstream of the bubbles.

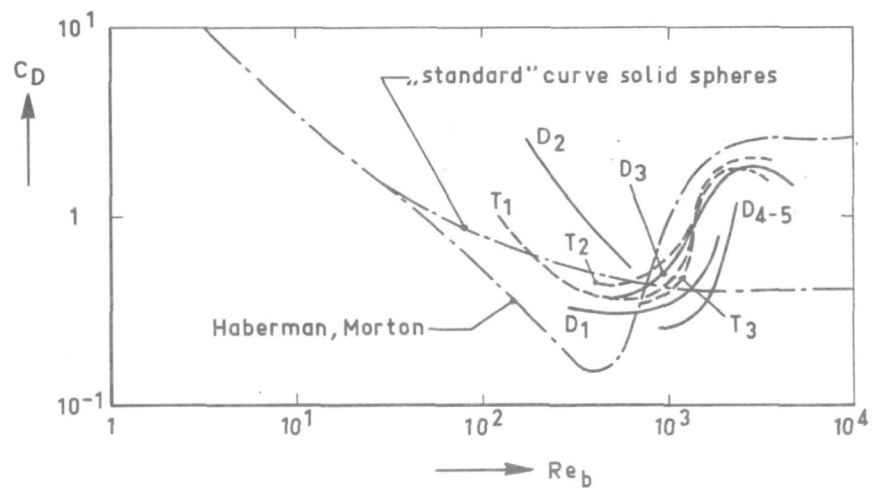
Rise velocities of single bubbles in flowing water have been studied by BAKER and CHAO [25]. In figure 2-6 their results are presented in the form of drag force coefficients as a function of the bubble Reynolds number with the Reynolds number of the main stream as parameter.

Unfortunately the scatter in the experimental results is very large warranting only general conclusions on the drag force coefficient. The following conclusions have been drawn by the authors:

FIGURE 2-6

*Drag coefficient for air bubbles in flowing water as a function of their Reynolds number*

system Reynolds numbers	
demineralized water	$t_{ap}$ water
D <sub>1</sub> 51,500	T <sub>1</sub> 48,600
D <sub>2</sub> 94,100	T <sub>2</sub> 86,650
D <sub>3</sub> 131,000	T <sub>3</sub> 124,600
D <sub>4</sub> 299,000	
D <sub>5</sub> 386,000	



- ★ the minima in the curves occur at higher values of the bubble Reynolds number compared to experiments in stagnant water,
- ★ the drag coefficients tend to merge with increasing bubble Reynolds numbers,
- ★ the peak values of the drag coefficients for  $Re_b > 3000$  are lower than in stagnant water.

The first and second conclusions together indicate that the main stream turbulence modifies Stokes' law, but does not affect the Newton region, pointing towards an influence of the effective viscosity in the bubble Reynolds number.

Replacing the liquid viscosity  $\eta_l$  in the bubble Reynolds number by the turbulence viscosity

$$\eta_t = \eta_l \left(1 + \frac{\epsilon}{\nu}\right) \quad (2-26)$$

makes the bubble Reynolds number decrease by a factor  $(1 + \frac{\epsilon}{\nu})$  and reshifts the curves in figure 2-6 to the left. Computation of the kinematic turbulence viscosity at the centerline by Reichardt's formula [26 ]:

$$\left(\frac{\epsilon}{\nu}\right)_c = 0.03335 \text{Re}_s^* \quad (2-27)$$

where

$$\text{Re}_s^* = \frac{\rho_1 u_1^* D}{\eta_1} \quad (2-28)$$

and

$$u_1^* = \sqrt{\frac{\tau_w}{\rho_1}} \quad (2-29)$$

results in a value for  $(1 + \frac{\epsilon}{\nu})$  of about 200 which is much too large for the actual experiments.

It appears more logical, however, to assume that the turbulence in the neighbourhood of the bubble is determined only by eddies smaller than the bubble itself, and hence to characterize this turbulence by the bubble diameter rather than by the channel diameter. This leads to the insertion of a modified Reynolds number:

$$\text{Re}_b^* = \frac{\rho_1 u_1^* d}{\eta_1} \quad (2-30)$$

in correlation (2-27); resulting in a reduced value for the factor  $(1 + \frac{\epsilon}{\nu})$  of about 1 up to 4, which is the right magnitude for the correction of the bubble Reynolds number. However, insufficient analytical or experimental evidence is available to support the above assumption, hence no correlation for the dependency of the main stream turbulence in the Stokes' region can be proposed at present.

The third conclusion of Baker and Chao indicated a small dependency of the drag coefficient in the Newton region on the turbulence, which is caused by the shape of the bubbles. Use of the effective bubble diameter

$$d_e = \sqrt[3]{\frac{6}{\pi} V_b} \quad (2-31)$$

- as done in all the referenced publications - introduces a dependency on the shape of the bubble defined by:

$$C_{D_e} = \frac{d^2}{d_e^2} C_D \quad (2-32)$$

where  $d$  is the diameter of the projected bubble area in the direction of flow.

The more spherical shape found by Baker and Chao compared to the results reported in [20 ] and [21 ] for stagnant water - most probably caused by the inertia forces from the turbulence velocity acting randomly all over the bubble surface - results in a decrease in projected area and thus in a lower apparent drag coefficient.

For stagnant water the value  $C_{D_e} = 2.6$  derived from figure 2-5, together with the ratio:

$$\frac{d}{d_e} = 2.3 \quad (2-33)$$

found by DAVIES and TAYLOR [ 22 ] for mushroom-shaped bubbles, result in a drag force coefficient:

$$C_D = 0.49 \quad (2-34)$$

In view of the possible measurement errors the agreement between this value and Newton's value of 0.44 may be considered good. It is hence to be expected that for very high turbulence the drag coefficient will again approach the value of 0.44 holding for single bubbles in the Newton region.

### 2.2.2.1.3. Swarms of solid particles

Several authors have investigated the relative velocity of swarms of particles in fluidization and sedimentation. In order to provide a framework for evaluation of the relevant experimental data we shall first derive an analytical expression - based on the velocity ratio

$\frac{u_r^\alpha}{u_r^\infty}$  - for the ratio  $\frac{C_D^\alpha}{C_D^\infty}$  between the drag force coefficient of particles in

swarms to that of a single particle moving in an "infinite" fluid. For non-accelerating flow the left hand sides of the momentum balances (2-16) and (2-19) are zero. Elimination of  $\frac{dp}{dz}$  from these equations and substitution of equation (2-24) yields for particle-liquid flow ( $\rho_g \rightarrow \rho_p$ )

$$F_D = \frac{3}{4} \alpha \frac{C_D^\alpha}{d} \rho_l u_r^\alpha |u_r^\alpha| = \alpha(1-\alpha)(\rho_l - \rho_p)g + \alpha \left(\frac{dp}{dz}\right)_{fr} \quad (2-35)$$

For the present analytical purpose the term  $\alpha \left(\frac{dp}{dz}\right)_{fr}$  will be omitted, implying the omission of the effects of diameter ratio  $\frac{d}{D}$  and Froude number  $\frac{u_l^2}{gD}$ .

Application of formula (2-35) to a single particle of the same diameter yields:

$$\frac{3}{4} \frac{C_D^\infty}{d} \rho_l u_r^\infty |u_r^\infty| = (\rho_l - \rho_p)g \quad (2-36)$$

where  $C_D^\infty$  and  $u_r^\infty$  are the values pertaining to the single particle in an infinite fluid.

Dividing equations (2-35) and (2-36) yields:

$$\frac{C_D^\alpha}{C_D^\infty} = (1-\alpha) \left(\frac{u_r^\alpha}{u_r^\infty}\right)^2 \quad (2-37)$$

Notwithstanding the general validity of the above correlation it is tacitly assumed that the drag coefficient for any given value of  $\alpha$  is independent of the velocity, which assumption is only valid in the Newton region. Although, as mentioned in 2.2.2.1.2., this is the only region of interest for the present investigations, the considerations will now be extended to the Stokes' region in order to show that a common physical basis can be established for the interpretation of experimental results

extending over the entire range of  $Re_p$  numbers.

In this region the drag coefficient is always dependent on the relative velocity as appears from Stokes' law:

$$C_D = \frac{K}{Re_p} \quad (2-38)$$

Distinction of this effect from the influence of the particle fraction on the drag coefficient is obtained by transformation of equation (2-37) to

$$\frac{K^\alpha}{K^\infty} = \frac{Re_p^\alpha}{Re_p^\infty} (1-\alpha) \left( \frac{u_r^\infty}{u_r^\alpha} \right)^2 \quad (2-39)$$

where:

$$Re_p^\infty = \frac{\rho_l u_r^\infty d}{\eta_l} \quad (2-40)$$

In fluidization the Reynolds number for a swarm of particles  $Re_p^\alpha$  can be derived from the definition valid for single particles:

$$Re_p^\alpha \sim \frac{\text{momentum}}{\text{shear stress}} = \frac{(1-\alpha)\rho_l u_r^{\alpha 2}}{\eta_t \frac{\partial u_r^\alpha}{\partial r}} \quad (2-41)$$

Incorporation of the turbulence viscosity by substituting equation (2-26) and replacing  $\frac{\partial u_r^\alpha}{\partial r}$  by  $\frac{u_r^\alpha}{d}$  as usual, yields:

$$Re_p^\alpha = \frac{(1-\alpha)\rho_l u_r^\alpha d}{\eta_l \left(1 + \frac{\epsilon}{\nu}\right)} \quad (2-42)$$

and thus:

$$\frac{K^\alpha}{K^\infty} = \frac{1}{\left(1 + \frac{\epsilon}{\nu}\right)} (1-\alpha)^2 \frac{u_r^\infty}{u_r^\alpha} \quad (2-43)$$

Although it should be possible with a reasonable effort to involve a model for the turbulence viscosity  $\epsilon$  for two-phase flow from the considerations presented in subsections 2.2.2.1.2., 2.2.3.1. and 2.2.3.2., such an effort would far exceed the scope of the present investigations. It is possible, however, to fulfill the aim of providing a common basis of understanding for experimental results extending over the entire range of particle Reynolds numbers by limiting the attention at low  $Re_p$  values to the region where  $Re_p^\infty \ll 1$ , where the turbulence viscosity  $\epsilon$  vanishes because of low velocity and/or small particle diameter. The two equations (2-37) and (2-43) obtained by analysis shall now be supplemented by experimental velocity ratio data - for both fluidization and sedimentation - published by RICHARDSON and ZAKI [31] and extending over the range  $0.03 \leq Re_p^\infty \leq 10^4$ . They presented their results in the form of the correlation:

$$\frac{u_s}{u_r^\infty} = (1-\alpha)^n \quad (2-44)$$

where  $u_s$  is the superficial velocity, thus:

$$u_r^\alpha = \frac{u_s}{(1-\alpha)} \quad (2-45)$$

and

$$\frac{u_r^\alpha}{u_r^\infty} = (1-\alpha)^{n-1} \quad (2-46)$$

The power  $n$  was found to be dependent on  $Re_p^\infty$  and  $\frac{d}{D}$ .

For the sake of comparison of these experimental results with correlations (2-37) and (2-43), derived with the implicit omission of the effects of diameter ratio and Froude number, the power  $n_0$  valid for  $\frac{d}{D}$  approaching zero shall be used here.

A plot of the  $n_0$  data is given in figure 2-7, from which it appears that  $n_0$  equals 2.39 and 4.65 in the Newton and Stokes' region respectively.

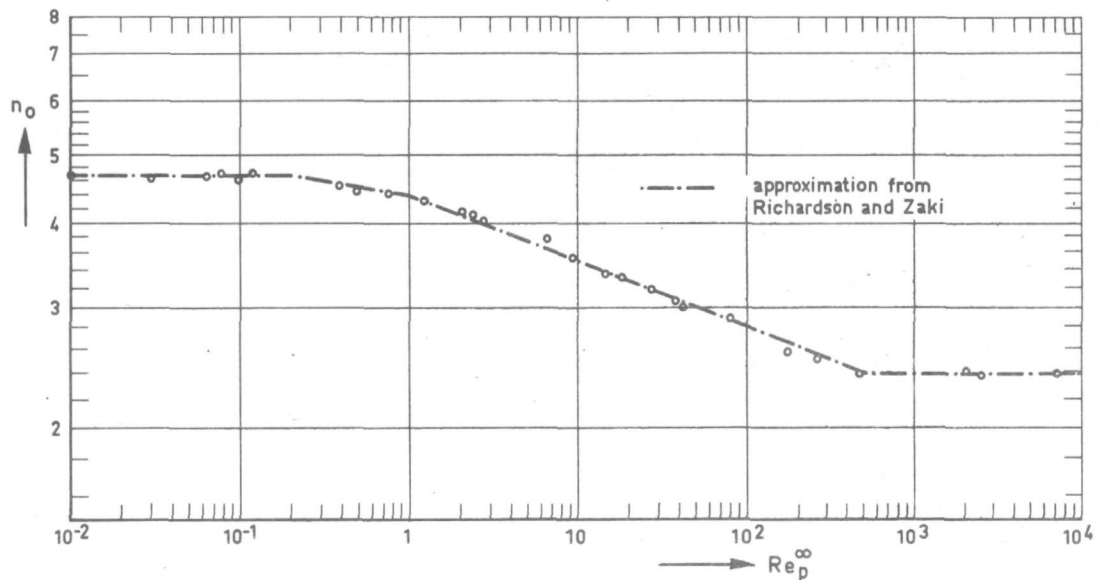


FIGURE 2-7

Power  $n_0$  from [31] as a function of the Reynolds number

Substitution of these values in equation (2-46) and use of  $\frac{u_r^\alpha}{u_r^\infty}$  in equations (2-43) and (2-37) yields:

- for the Newton region:

$$\left( \frac{C_D^\alpha}{C_D^\infty} \right)_N = (1-\alpha)^{-1.78} \quad (2-48)$$

- for the Stokes' region:

$$\frac{K^\alpha}{K^\infty} = \frac{1}{(1 + \frac{\epsilon}{v})} (1-\alpha)^{-1.65} \quad (2-49)$$

For these specific fluidization and sedimentation experiments the particle diameters and velocities in the Stokes' region are so low that the Reynolds number  $Re_p^*$  - as defined in equation (2-30) - vanishes and thus  $\frac{\epsilon}{v} = 0$ . Considering the similarity between the two above formulae and the limited accuracy of the  $n_0$  data from RICHARDSON and ZAKI [31] it appears justified to represent the effect of particle volume fraction on the drag force coefficient by one single correlation:

$$\frac{C_D^\alpha}{C_{DN}^\infty} = \frac{K^\alpha}{K^\infty} = (1-\alpha)^{-1.7} \quad (2-50)$$

which modifies equation (2-25) for a single particle to the general formula:

$$C_D = (0.44 + \frac{24}{Re_p})(1-\alpha)^{-1.7} \quad (2-51)$$

where  $Re_p$  is defined in equation (2-42).

From the above it appears evident that the transition of  $n_0$  from 4.65 to 2.39 coincides with the transition from the Stokes' region to the Newton region, which would correspond to a transition from equation (2-37) to equation (2-43). While this cannot be proved exactly in the absence of a correlation for the factor  $(1 + \frac{\epsilon}{v})$ , the smooth transition of  $n_0$  and the coincidence of this transition zone with the transition zone of the "standard" drag curve convinces the author of the general validity of correlation (2-51). In addition it should be noticed that the factor  $(1 + \frac{\epsilon}{v})$  is only relevant in the region where  $Re_p$  is not very large ( $Re_p < 500$ ). Hence the value of Reynolds number  $Re_p^*$  - defined by equation (2-30) - determining the factor  $(1 + \frac{\epsilon}{v})$  will also be fairly small, leading to a maximum estimated value of only 3 for  $(1 + \frac{\epsilon}{v})$ .

This value is borne out by comparison of the values obtained from equation (2-51) to drag force coefficients derived by SOO [14] on the basis of the pressure drop correlation for fluidized beds obtained from ERGUN [32].

For the region  $\frac{(1-\alpha)\rho_1 u_r d}{\eta_1} < 100$  this comparison shows that the present

values can be made to coincide with those of Soo for  $(1 + \frac{\epsilon}{v})$  values between 1 and 2.5, which may be regarded as a justification of the above mentioned upper limit for the factor  $(1 + \frac{\epsilon}{v})$ .

As stated previously the influence of diameter ratio  $\frac{d}{D}$  and Froude number  $\frac{u_1^2}{gD}$  is neglected up until now by omitting the last term of equation (2-35).

This last term - being positive while the left hand side (due to the sign of  $u_r^\alpha$ ) and the first term of the right hand side are negative - decreases the absolute value of the relative velocity  $u_r^\alpha$  as RICHARDSON and ZAKI [31] expressed by the rise of the value for  $n$  in correlation (2-44) on

account of  $\frac{d}{D}$ . However, this does not affect the general validity of  $C_D$  of correlation (2-51), because the effect of change of the velocity ratio  $\frac{u_r^\alpha}{u_r^\infty}$  in the correlations (2-37) and (2-39) is eliminated by the addition of the term emanating from the last term of equation (2-35). A further verification of the validity of correlation (2-50) may be obtained by comparison with the semi-analytical approach of MERTES and RHODES [33] who take into account the reduction of free area for the flow around the particles with increasing particle volume fraction. On the basis of the average free area in cell with a cubic particle arrangement they find:

$$\frac{u_r^\alpha}{u_r^\infty} = \frac{(1-\alpha)}{(1-\alpha) + 1.209\alpha^{2/3}} \quad (2-52)$$

Substitution of this ratio in equation (2-37) yields:

$$\frac{C_D^\alpha}{C_D^\infty} = \frac{\{(1-\alpha) + 1.209\alpha^{2/3}\}^2}{(1-\alpha)} \quad (2-53)$$

Figure 2-8 shows reasonable agreement between this correlation, correlation (2-50) and some experimental data for particle fractions up to 0.6. The deviation of correlation (2-53) for higher particle fractions is most probably caused by the increasing improbability of a cubic arrangement for these particle fractions, while the discrepancy between the experiments and correlation (2-50) is probably caused by the  $\frac{d}{D}$  and Froude effects mentioned before.

It shall be noted, however, that substitution of the velocity ratio from (2-52) into equation (2-43) valid for the Stokes' region results in poor agreement with the experiments. No explanation has been found for this fact. However, the striking coincidence of the experimental data from the Stokes' and Newton region - as appears in figure 2-8 - justifies the validity of correlation (2-51).

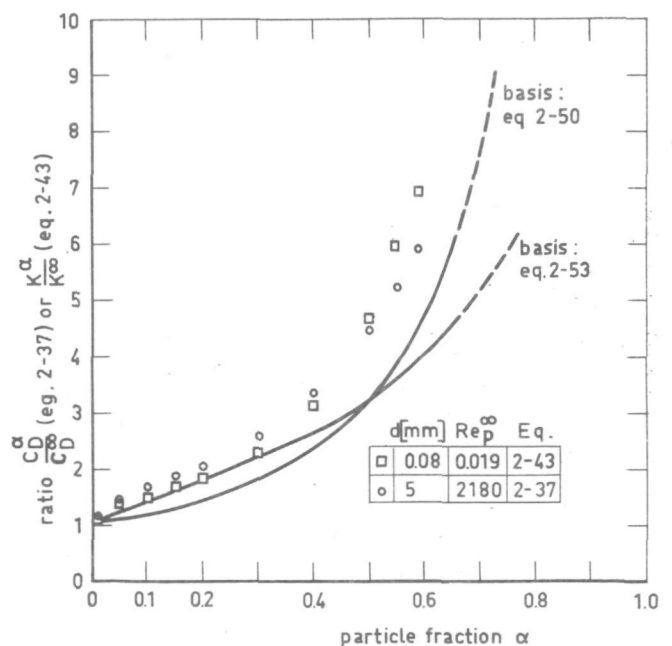


FIGURE 2-8

*Effect of neighbouring particles on the drag coefficient*

2.2.2.1.4. Swarms of bubbles

Investigation of the drag coefficient ratio  $\frac{C_D^\alpha}{C_D^\infty}$  for bubble flow is more

complex than for particle flow, because of complex physical effects such as changes in shape (flattening), coalescence and internal circulation. Of these the latter appears of minor relevance for the present investigation, while the two former shall be combined into the influence of the bubble diameter. For variable bubble diameter equation (2-37) changes into

$$\frac{C_D^\alpha}{C_D^\infty} = \frac{d^\alpha}{d^\infty} (1-\alpha) \left( \frac{u_r^\infty}{u_r^\alpha} \right)^2 \tag{2-54}$$

where it should be noticed that in the Stokes' region  $C_D$  in turn depends on the bubble diameter.

The influence of the bubble diameter clearly appears in the experiments reported by ZUBER and HENCH [ 34 ], on the movement through stagnant water of bubbles formed by air entrainment through perforated plates with various orifice diameters. In figure 2-9A the air throughput - and hence the superficial and relative velocities - are seen to be dependent of the orifice diameter, which undoubtedly influences in the bubble diameter. For orifice diameters of 4.06 and 1.52 mm and a relative velocity exceeding about 0.4 m/s approximation of the bubble diameter as being a few times greater than the orifice diameter leads to Reynolds numbers of a few thousands, i.e. just within the Newton region. Thus for these two cases the drag coefficient can be assumed to satisfy the correlation:

$$C_D^\alpha = C_D^\infty f(\alpha) \tag{2-55}$$

where  $C_D^\infty$  is the same for both cases.

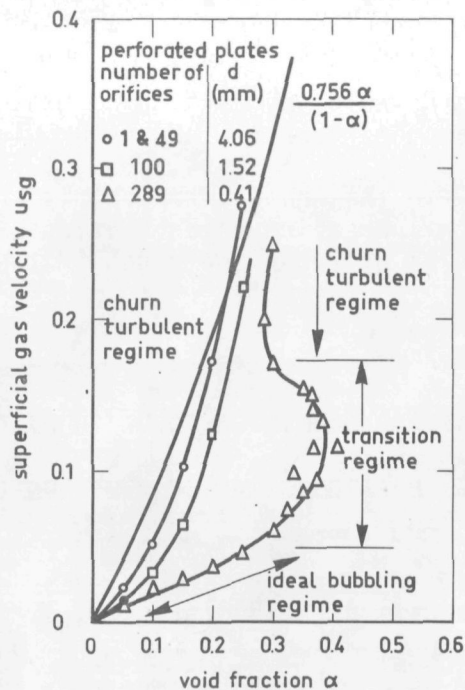


FIGURE 2-9A

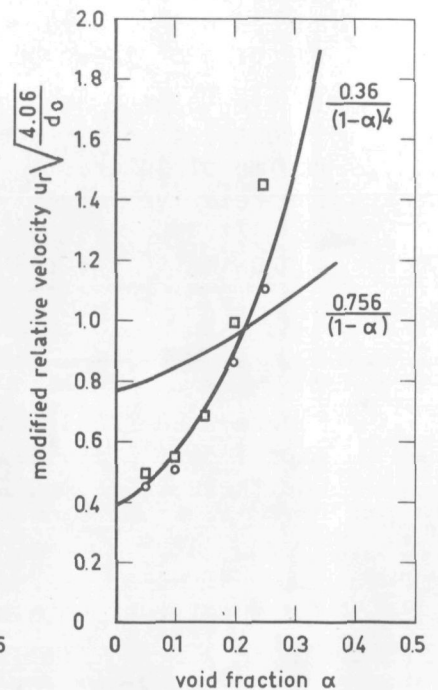


FIGURE 2-9B

Gas velocities in stagnant water (data of ZUBER and HENCH [ 34 ])

Application of equation (2-35) to these cases of bubble flow in stagnant water -  $\rho_p \rightarrow \rho_g$  and  $(\frac{dp}{dz})_{fr} = 0$  - leads for equal void fraction in both cases to:

$$\frac{3}{4}\alpha\left\{\frac{C_D^\alpha}{d^\alpha} \rho_l u_r^\alpha |u_r^\alpha|\right\}_1 = \frac{3}{4}\alpha\left\{\frac{C_D^\alpha}{d^\alpha} \rho_l u_r^\alpha |u_r^\alpha|\right\}_2 = \alpha(1-\alpha)(\rho_l - \rho_g)g \quad (2-56)$$

where the subscripts 1 and 2 indicate the test with orifice diameters of 4.06 and 1.52 mm respectively. Substitution of equation (2-55) yields:

$$u_{r_2}^\alpha \sqrt{\frac{d_1^\alpha}{d_2^\alpha}} = u_{r_1}^\alpha \quad (2-57)$$

The assumption of proportionality between bubble diameters and orifice diameters results in an almost exact agreement with equation (2-57) for the aforementioned orifices as shown in figure 2-9B.

This good agreement is in great contrast with the experiments with 0.41 mm orifice diameter. The disagreement in this latter case can be explained by the much smaller bubble diameter and the resulting lower relative velocity, which jointly caused a decrease of the bubble Reynolds number to about 100, i.e. the bubbles are in the Stokes' region and rise uniformly and steadily. Zuber and Hench found a transition from this "ideal bubbly flow" when the void fraction reaches a value of 0.3 (see figure 2-9A). It is the present author's opinion that at this point coalescence of the bubbles becomes significant, resulting in a shift to the Newton region and thus to relative velocities of the same magnitude as in the tests with larger orifice diameter. This opinion is confirmed by figure 2-9A.

The description of this latter flow regime - called churn-turbulent by Zuber and Hench - as agitated and unsteady with significant agglomeration, agrees with the large turbulence in the Newton region caused by vortex shedding of the bubbles in this region.

In view of the bubble Reynolds numbers to be expected in the present investigation on separator flows the churn-turbulent flow regime is the regime of interest.

The relative velocity in the churn-turbulent is known (see e.g. WALLIS [7]) to increase with increasing void fraction. HENCH and JOHNSTON [35] approximated the results of Zuber and Hench in the churn-turbulent regime by:

$$u_{sg} = \frac{0.756 \alpha}{(1-\alpha)} \quad (2-58)$$

Figure 2-9A shows this approximation to be in fair agreement with the experimental results.

For these experiments in stagnant water equation (2-58) can be written as:

$$u_g = u_r = \frac{0.756}{(1-\alpha)} \quad (2-59)$$

and substitution in equation (2-35) leads to:

$$\frac{C_D}{d} = 54.9 (1-\alpha)^3 \quad (2-60)$$

PRINS [1] adopts the factor  $(1-\alpha)^3$  but found for his experiments - with superficial water velocities from 2 up to 3 m/s - a constant value of 30

instead of 54.9.

A more careful examination of Zuber and Hench's relative velocity data according to figure 2-9B indicates, however, that:

$$u_r = \frac{0.36}{(1-\alpha)^4} \quad (2-61)$$

is a much better approximation (omitting the relatively minor influence of the bubble diameter postulated in (2-57)) leading to:

$$\frac{C_D}{d} = 26.2 (1-\alpha)^9 \quad (2-62)$$

The steep increase of relative velocity and corresponding decrease of the drag coefficient with increasing void fraction is confirmed by the experiments of SMISSAERT [36] for flowing water. However, despite the rather low water flow rates of these experiments, including even a series in stagnant water, increase of the relative velocity shown in figure 2-10 is less steep than found by Zuber and Hench.

A first approximation shows a dependency of the relative velocity on void fraction varying from  $(1-\alpha)^{-1.8}$  for stagnant water up to  $(1-\alpha)^{-2.5}$  for a superficial water velocity of 0.244 m/s. Although it would obviously be desirable to have at one's disposal measurements made at higher superficial water velocities, the present data appear adequate for confirming the influence of the superficial liquid velocity on the exponent of correlations like (2-61).

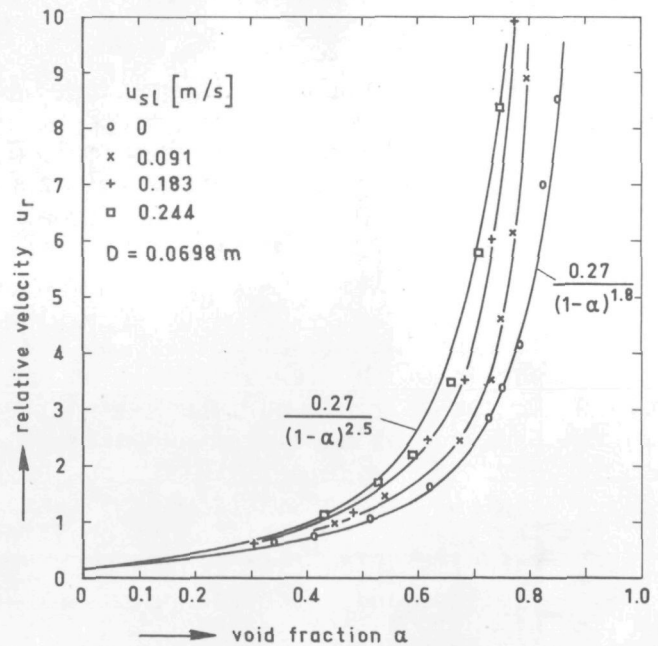


FIGURE 2-10

Relative velocity as a function of void fraction and superficial liquid velocity (data of SMISSAERT [36])

WALLIS [7] stated part of the void fraction dependency and the dependency of the superficial water velocity in channel flow to be an effect of nonuniform flow and found by analysis that the true relative velocity - in the experiments of Smissaert - varies only with a factor  $(1-\alpha)^{-1.0}$  and is independent of the superficial water velocity. This analysis, however, is based on the model of ZUBER and FINDLAY [37] for two-dimensional effects. As proved in appendix 2-B and discussed in subsection 2.2.4. this model of Zuber and Findlay is incorrect for predicting the two-dimensional effects, making the result of Wallis doubtful.

This doubt is increased when considering - as mentioned before - that the water velocity must have some influence on the relative velocity in channel flow via the frictional pressure drop and bubble diameter. Notwithstanding quantitative uncertainties the above review does show a large decrease of  $\frac{C_D}{d}$  with increasing void fraction while for particle flows an increase appears. This contrast between these two types of two-phase flow can hardly be explained by differences such as internal circulation and deformation in the case of bubbles. While no simple explanation for this difference is to be found in literature up till now a tentative in this direction will be made in subsection 2.4. on the basis of the experimental results of the present investigation.

In order to eliminate all additional effects as thoroughly as possible supporting analyses will be carried out with reference to:

- the wall shear stress, in order to eliminate the influence of the frictional pressure drop on the relative velocity
- the bubble diameter, in order to be able to study the drag coefficient proper
- the effects of nonuniformities in channel flow.

The experiments will be performed at water velocities and void fractions characteristic for separator flow in order to maximize the relevance of the results for the purpose of the present investigation, while the void fraction will be varied over a wide range in order to determine the dependency on this most important parameter as thoroughly as possible.

#### 2.2.2.2. Virtual mass

The virtual added mass mentioned in subsection 2.2.1.2. causing the additional acceleration force  $F_A$  in equation (2-13) has been incorporated in fluid dynamics analyses for a long time (see e.g. LAMB [39]). Although - as shown below - it appears as an increase of the particle mass and is hence named "virtual added mass" it has nothing to do with the momentum of the particle, as is indicated clearly by Kelvin (see LAMB [39]) who named this additional term impulse. In fact it is a resultant force from the pressure on the particle surface caused by the inertia of the surrounding fluid: in case of change of the relative velocity of the particle the flow around it becomes unsteady and the pressure distribution on the particle surface will differ from that of the initial steady flow. Thus for an accelerating particle a component resulting from the unsteady part of the velocity distribution around the bubble is added to the pressure distribution of the steady situation which constitutes the particle drag. The analysis of this additional force is always based on frictionless potential flow (see e.g. MILNE-THOMSON [40]), where the particle drag vanishes and the pressure distribution on the particle surface results directly in the additional acceleration force. HINZE [9] made such an analysis for a single sphere with velocity  $u_s(t)$  in an infinite fluid with velocity  $u_{f\infty}(t)$  at infinity,  $u_{f\infty}(t)$  and  $u_s(t)$  having both the same direction. After computation of the pressure distribution Hinze derived the following momentum (and force) balance for the sphere (written in Lagrange notation):

$$\frac{\pi}{6} d^3 \left[ -\left(\frac{dp}{dx}\right)_{\infty} \right] = \frac{\pi}{6} d^3 \rho_s \frac{du_s}{dt_s} + \frac{\pi}{12} d^3 \rho_f \left( \frac{du_s}{dt_s} - \frac{du_{f\infty}}{dt_s} \right) \quad (2-63)$$

The left hand side of this equation represents the pressure gradient force, while the first term of the right hand side is the acceleration force of

the sphere itself. The second term is the additional force  $f_A$  due to the "virtual added mass": it appears as if the mass of the particle - with respect to the relative motion - were increased by an amount equal to half the liquid displaced. This value of one half is only valid for a sphere and will change for different shapes of the submerged body: the more streamlined the body the smaller the "virtual added mass" and vice versa. Therefore the additional force is written as:

$$f_A^\infty = \frac{\pi}{6} d^3 B \rho_f \left( \frac{du_s}{dt_s} - \frac{du_{f^\infty}}{dt_s} \right) \quad (2-64)$$

where the virtual mass coefficient B depends on the shape of the body and the direction of the flow to the body.

Values for B for ellipsoids with various axis ratios and various angles of attack are given in [ 39 ] and [ 41 ].

Writing equation (2-64) in Euler notation for stationary motion and extending it to a homogeneous distribution of n particles per unit volume through the use of equation (2-12) leads to:

$$F_A^A = \alpha \frac{f_A}{\frac{\pi}{6} d^3} A = \alpha A \rho_f u_s \frac{\partial}{\partial x} B (u_s - u_{f^\infty}) \quad (2-65)$$

In this expression the virtual mass coefficient B is part of the differential quotient because this quotient stems from the differentiation of the velocity potential in which the effects of neighbouring particles on the velocity distribution and hence on the virtual mass coefficient are incorporated.

For gas-liquid flows the additional force in the momentum balance for the gas phase (2-16) should thus be written as:

$$F_A^A = \rho_l \frac{d}{dz} (\alpha A B u_g (u_g - u_l)) \quad (2-66)$$

as derived by PRINS [ 1 ].

An attempt to quantify the postulated dependency of the virtual mass coefficient B on the void fraction was made by ZUBER [ 42 ], who used the well-known (see e.g. MILNE-THOMSON [ 40 ]) virtual mass of a sphere placed in the center of a second sphere filled with liquid. Assuming the diameter ratio of the spheres equal to  $\alpha^{1/3}$  the virtual mass for this type of flow yields:

$$B = \frac{1}{2} \frac{(1+2\alpha)}{(1-\alpha)} \quad (2-67)$$

A more profound analysis was performed by VAN WIJNGAARDEN [ 43 ], who investigated the virtual added mass of randomly distributed spheres using the virtual added mass of pairs of spheres with centerlines either parallel or perpendicular to the velocity of the liquid. For low "void fractions" the result is:

$$B = \frac{1}{2}(1 + 2.78\alpha) + O(\alpha^2) \quad (2-68)$$

which should be considered an improvement over correlation (2-67) approximated as  $B = \frac{1}{2}(1 + 3\alpha) + O(\alpha^2)$  for low values of the void fraction. These analytical results, indicating increasing virtual mass coefficient B with increasing void fraction, are contradictory to the analysis by PRINS [ 10 ] of the experiments of ROSE and GRIFFITH [ 11 ] with air-water mixtures in a turning Tee, which show a marked decrease of the virtual mass coefficient B with increasing void fraction. The same trend appears

in the experiments of PRINS [1] for air-water mixtures in a converging channel, which he correlated by:

$$B = 3.155 (1-\alpha)^{10.85} \quad (2-69)$$

While granting possible inaccuracies due to the admittedly difficult data reduction from experimental flow parameters to values for B, the trend of decreasing virtual mass coefficient found by Prins is far too pronounced to leave room for doubt. It is moreover to be expected because of the decreasing amount of liquid flowing around the bubbles.

In order to find a reasonable explanation for this discrepancy between analytical and experimental results VAN WIJNGAARDEN [43] made a second approach to the problem by studying the momentum flux of a bubble-liquid mixture in a given control volume. This approach differs from the model described before by taking into account the momentum caused by the inhomogeneities in the liquid velocity in the neighbourhood of a bubble/particle, whereas the present model deals only with the time average velocities (cf. equations (2-3) and (2-4)) and incorporates local effects in the neighbourhood of the bubbles/particles in the interaction forces  $F_D$  and  $F_A$ .

In appendix 2-C it is shown that inclusion of the liquid velocity peaks at the bubble boundary always results in an increase of the momentum flux proportional to the square of the peak value, which is consistent with the result given by Van Wijngaarden:

$$M = (1-\alpha)\rho_l u_l^2 + \frac{1}{5} \alpha \rho_l (u_g - u_l)^2 \quad (2-70)$$

where for the sake of simplicity the mass of the bubbles is set to zero. The proportionality of the additional term with  $(u_g - u_l)^2$  instead of  $u_g(u_g - u_l)$  as appears in expression (2-66) is used by Van Wijngaarden to explain the discrepancy between analyses and experiments. Writing the additional term  $\frac{1}{5} \alpha \rho_l (u_g - u_l)^2$  of expression (2-70) in the more general form of a virtual mass term  $\alpha B' \rho_l (u_g - u_l)^2$  and equating it to the virtual mass term  $\alpha B \rho_l u_g (u_g - u_l)$  of expression (2-66) leads to the equation

$$B = B' \frac{u_g - u_l}{u_g} \quad (2-71)$$

The velocity ratio  $\frac{u_g - u_l}{u_g}$  in this expression was evaluated by Van Wijngaarden - on the basis of his result for the bubble velocity in a mixture instantaneously accelerated from the stagnant state - and found to depend on the void fraction as<sup>\*)</sup>

\*) It should be stressed that this result refers to an instantaneously accelerated mixture, while in the present investigation stationary vertical gas-liquid flows are studied. The discrepancy, for example, between the slip after acceleration - expressed in equation (2-72) - written as  $s = \frac{1}{K_1 + K_2 \alpha}$  and the well-established formulae of BANKOFF [4]  $s = \frac{1-\alpha}{K-\alpha}$  for the ever existing slip in the case of vertical flow, points to the questionable applicability of Van Wijngaarden's second approach to the flows studied by Prins and in this investigation.

$$\frac{u_g - u_l}{u_g} \sim (1 - 0.93\alpha) \quad (2-72)$$

This offers the possibility of a decreasing coefficient B with void fraction and hence is a possible explanation for the inconsistency between the decrease of B found experimentally in [1] and [10] and the increase to be expected from the analytical approach described above.

While this may reconcile the two descriptions it is impossible - at the present stage of knowledge - to decide which of the two is preferable and/or correct. This is due to the uncertainty about the definition and representation of the local pressure fluctuations in the neighbourhood of the bubbles/particles in Van Wijngaarden's second approach.

For historical reasons the author has retained the classical description of equation (2-66) for the present investigation. In addition, however, the experimental results will be examined too - in subsection

2.3.1.6.2.2. - for proportionality with the factor  $\frac{u_g - u_l}{u_g}$  in order to investigate the validity of equation (2-71).

### 2.2.3. Supporting analyses

Before the momentum balances (2-16) and (2-19) can be utilized to obtain experimental values for the interaction forces  $F_D$  and  $F_A$  the following three flow variables - which will not be measured in the experiments - have to be known:

- the frictional pressure drop  $(\frac{dp}{dz})_{fr}$ , in order to complete the liquid momentum balance
- the bubble diameter  $d$ , in order to separate  $C_D$  from the quotient  $\frac{C_D}{d}$  defining the drag force  $F_D$
- the two-dimensional effects due to the non-uniform velocities and void fraction in the channel flows of these experiments, in order to incorporate the local variations in a cross-section.

The physical background and resulting correlations for these variables will be discussed in the following subsections.

#### 2.2.3.1. Frictional pressure drop

In the present investigation the frictional pressure drop - or wall shear stress - as it appears in the liquid momentum balance reaches values up to the same magnitude as the interaction forces, hence an accurate pressure drop correlation is prerequisite for an accurate determination of the interaction forces. For this purpose the author proposed a new pressure drop correlation having a better accuracy than existing correlations [12]\*). This correlation was derived with the following considerations in mind:

- any correlation proper for two-phase flow should retain its validity for single-phase flow, which is an extreme case of two-phase flow.
- the drag force of the discontinuous phase, in addition to being represented by the  $F_D$  term in the momentum balance, will also

\* ) *The present text covers only the analytical background and essential steps of the derivation; for a more extensive description the reader is referred to the original paper.*

influence the wall shear stress through the phenomena of wake formation adjacent to the bubbles (or particles).

- the Reynolds number - determining the turbulence - should be based on the actual flow conditions.

Elaboration of the second principle leads to the general description of the frictional pressure drop:

$$\left(\frac{dp}{dz}\right)_{fr} = \frac{\lambda_m}{D} \frac{1}{2} M_{tp} + \lambda_i F_D \quad (2-73)$$

where  $\lambda_m$  and  $\lambda_i$  are the friction factors for the momentum flux and volumetric drag force respectively, and the momentum flux for two-phase flow is defined by<sup>\*</sup>):

$$M_{tp} = (1-\alpha)\rho_l u_l^2 + \alpha\rho_g u_g^2 \quad (2-74)$$

The drag force  $F_D$  for non-accelerating flow was given in subsection 2.2.2.1.3. as:

$$F_D = \alpha(1-\alpha)(\rho_l - \rho_g)g + \alpha\left(\frac{dp}{dz}\right)_{fr} \quad (2-35)$$

Substitution of expressions (2-74) and (2-35) in equation (2-73) yields:

$$\begin{aligned} \left(\frac{dp}{dz}\right)_{fr} = & \frac{\lambda_m}{(1-\alpha\lambda_i)D} \frac{1}{2}(1-\alpha)\rho_l u_l^2 \times \\ & \times \left[ 1 + \frac{\alpha}{(1-\alpha)} \frac{\rho_g}{\rho_l} \left(\frac{u_g}{u_l}\right)^2 + 2 \frac{\lambda_i}{\lambda_m} \alpha \frac{\rho_l - \rho_g}{\rho_l} \frac{gD}{u_l^2} \right] \end{aligned} \quad (2-75)$$

The Reynolds number is defined as the ratio of the inertia and viscosity forces. The inertia force is represented by the momentum flux, given for two-phase flow by expression (2-74).

The viscosity force for wall friction must of course be related to the situation at the wall. For adiabatic vertical two-phase flow there is always a boundary layer of pure liquid. Hence the viscosity force is represented by:

$$f_v = \eta_l \frac{du_l}{dr} \quad (2-76)$$

In single-phase flow the differential quotient  $\frac{du_l}{dr}$  is well characterized by the quotient of the mean velocity and the channel diameter, yielding the well-known Reynolds number. In case of two-phase flow it will be clear that, whereas the numerator of the quotient can again be characterized by the true liquid velocity only, the denominator cannot be characterized by the channel diameter. This last fact is particularly evident for annular flow, where the thickness of the liquid layer is much more characteristic for the liquid flow at the wall than the channel diameter. A simple computation of this liquid layer thickness in case of annular flow yields:

$$2t = (1-\sqrt{\alpha})D \quad (2-77)$$

<sup>\*</sup>) The effects of non-uniformity in channel flow are not taken into account in order to be consistent with single-phase flow practice where the same effects exist but are always omitted.

Use of this annular flow model yields for the Reynolds number for two-phase flow:

$$\begin{aligned} Re_{tp} &= \frac{(1-\alpha)\rho_l u_l^2 + \alpha\rho_g u_g^2}{\eta_l \frac{u_l}{(1-\sqrt{\alpha})D}} = \\ &= \frac{(1-\alpha)\rho_l u_l D}{\eta_l} (1-\sqrt{\alpha}) \left[ 1 + \frac{\alpha}{1-\alpha} \frac{\rho_g}{\rho_l} \left( \frac{u_g}{u_l} \right)^2 \right] \end{aligned} \quad (2-78)$$

For vanishing void fraction the definitions of frictional pressure drop and Reynolds number for two-phase flow - given by equations (2-75) and (2-78) respectively - change into the normal definitions for single-phase liquid flow. In view of the first consideration for two-phase flow  $\lambda_m$  will hence have to equal the friction factor  $\lambda$  for single-phase flow. The present correlation states that this equality is not only true for vanishing void fraction but holds for all void fractions, yielding:

$$\lambda_m = 0.00560 + \frac{0.500}{Re_{tp}^{0.32}} \quad (2.10^3 < Re_{tp} < 2.10^5) \quad (2-79)$$

which correlation originates from the values for smooth pipes in the Moody diagram [44] for single-phase flow, as used by DUKLER et al [45].

The only remaining parameter to be determined from experimental data is the friction factor  $\lambda_i$  for the interaction force. For this purpose only those published wall shear stress data which were obtained directly from the force acting on a loose sleeve in the test section have been utilized, in order to obtain maximum accuracy. A total of 236 measurements has been gleaned from the investigations of MALNES [46], CRAVAROLO [47] and NIESE [48] after further screening based on the systematic error in their experiments.

The range of relevant flow parameters for the selected measurements tabulated in table 2-11, is seen to cover the entire range of interest for the present investigation. Because of the selection of the annular flow model as the basis for the two-phase flow Reynolds number it is essential to investigate the validity of the correlation for other flow patterns. For this purpose all 236 measurements have been plotted in a flow pattern map - see figure 2-12 - in order to assess whether the range of flow parameters is sufficiently wide to be representative for the various two-phase flow regimes. This flow pattern map based upon the superficial gas and liquid velocities, has been verified by HEWITT and ROBERTS [49] for a wide range of density ratios  $\rho_g/\rho_l$ , including those of the present measurements. As can be seen from figure 2-12 all flow patterns are represented by the selected data, thereby confirming their

TABLE 2-11

*Range of flow parameters of the frictional pressure drop data*

parameter	range or values
void fraction [-]	0 - 0.91
liquid velocity [m/s]	0.6 - 6.2
gas velocity [m/s]	0.0 - 29.3
density ratio [-]	0.001 - 0.046
liquid viscosity [Ns/m <sup>2</sup> ]	0.0010 and 0.0012
diameter [m]	0.0250 and 0.1143
Reynolds number for two-phase flow [-]	$1 \times 10^3 - 2.5 \times 10^5$

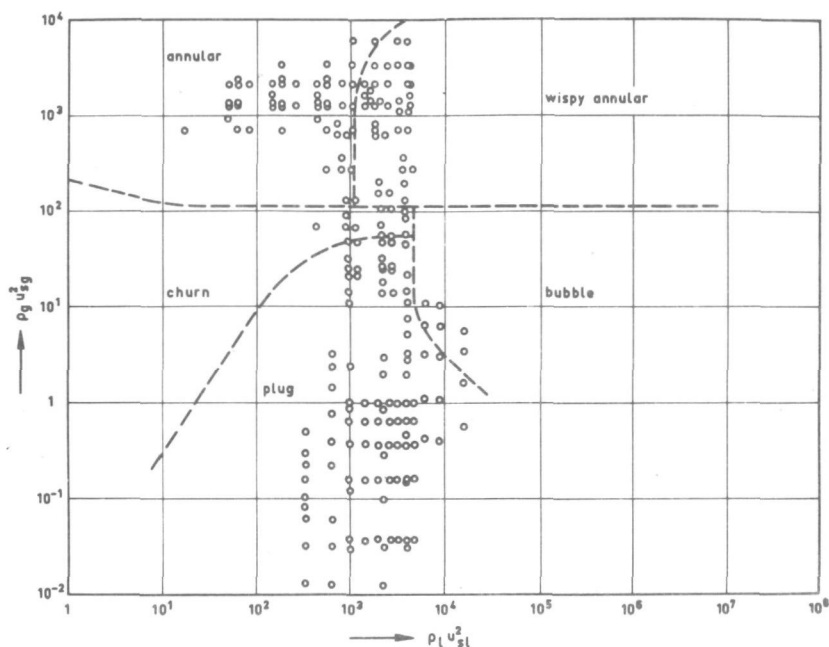


FIGURE 2-12

Flowpattern of all 236 data for the frictional pressure drop

suitability for establishing a correlation aiming at general validity.

Both for determination of the interaction force friction factor  $\lambda_i$  and for evaluation of the final pressure drop correlation three statistical parameters have been computed viz. the arithmetic mean deviation  $\bar{\delta}$ , the standard deviation  $\sigma$  and the scatterband  $\psi$  defined as the fractional deviation with respect to  $\bar{\delta}$  including 68% of the measurements. These three parameters are all based upon the fractional deviation  $\delta$  between calculated and measured values, defined by:

$$\delta_i = \frac{P_i - M_i}{M_i} \times 100\% \quad (2-80)$$

where  $M_i$  and  $P_i$  are the measured and predicted values for the  $i$ -th measurement. Hence

$$\bar{\delta} = \frac{1}{n} \sum_{i=1}^n \delta_i \quad (2-81)$$

and

$$\sigma = \sqrt{\left( \sum_{i=1}^n (\delta_i - \bar{\delta})^2 \right) / (n-1)} \quad (2-82)$$

The scatterband  $\psi$  is derived by hand from the frequency distribution of the deviation. The introduction of this additional statistical variable has been proposed by DUKLER et al [45] because the frequency distribution of the deviation  $\delta$  is not symmetric - in which case  $\psi$  would equal  $\sigma$  - due to the fact that the deviation  $\delta$  can vary only from -100% to +∞%.

A first computation of individual friction factors  $\lambda_i$  for each measurement indicates that the drag force has only a weak influence on the frictional pressure drop,  $\lambda_i$  being of the same magnitude as the friction factor for momentum  $\lambda_m$ .

This small contribution to the frictional pressure drop results in a wide

scatter for the individual friction factors  $\lambda_i$ . Physical considerations indicate that  $\lambda_i$  should decrease with increasing turbulence because the velocity wakes of the bubbles in the center region of the channel are smoothed out by turbulence before they "reach" the wall and thus cannot effect the wall shear stress. In view of this trend - being the same as for  $\lambda_m$  - and the abovementioned equal magnitude of the two friction factors, the proposed correlation for the friction factor  $\lambda_i$  is simplified to  $\lambda_i = K\lambda_m$ ; the generally existing dependency of K on one or more flow parameters is ignored and K is assumed to be a constant.

For the full set of 236 measurements the value  $K = 0.3$  was found to result in zero mean deviation. On the other hand additional computation limited to a subset of 39 measurements for which the Froude number  $\frac{u_i^2}{gD}$  was smaller than 4, so as to obtain a relatively large contribution of the drag force term in correlation (2-75) yielded  $K = 1.65$  as the best value. In view of the weak influence of  $\lambda_i$  on the pressure drop predicted by the proposed correlation (2-75), it appears to be sufficiently accurate for the present investigation\*) to choose  $\lambda_i$  - rather arbitrarily - as:

$$\lambda_i = 0.5 \lambda_m \quad (2-83)$$

This is borne out by an evaluation of the accuracy of pressure drop correlation (2-75) in comparison with the accuracy of two other correlations viz. those of DUKLER (case 2) [45] - which was the most accurate existing correlation - and of LOCKHART-MARTINELLI [3], which is the most widely used correlation in engineering practice.

The results of these computations - based on the correlations (2-75) and (2-79) - are represented in table 2-13, both for all 236 measurements taken together and for separate groups of measurements divided according to parameter range and source. In addition to the three statistical parameters mentioned above, the value  $|\bar{\delta}| + \psi$  has also been tabulated. As stated by DUKLER et al [45] this value gives the best measurement of the spread; hence the selection for the best correlation is based on these values. For each separate group of measurements the best correlation thus defined is marked with an asterisk\*.

\*) Further analyses on  $\lambda_i$  in [50] result in the correlation:

$$\lambda_i = \left[ 1 + \frac{Re_{tp}}{30} \sqrt{\frac{\lambda_m}{8} \left[ 1 + \frac{\alpha}{1-\alpha} \frac{\rho_g}{\rho_l} \left( \frac{u_g}{u_l} \right)^2 \right]} \right]^{-0.735}$$

which gives a significant improvement in accuracy for the 182 measurements with water as liquid phase. However, the decrease of accuracy for the 54 measurements with alcohol as liquid phase indicates that this correlation has no general validity. Further extension of the set of experimental data in [51] using measurements from [52], [53] and [54] and analysis of this total set of 482 measurements confirm the lack of general validity of the above correlation for  $\lambda_i$ . The final conclusion of [51] is that the Reynolds number for two-phase flow (expression (2-78)) should be changed to:

$$Re_{tp} = \frac{(1-\alpha)\rho_l u_l D}{\eta_l} \left[ 1 + \frac{\alpha}{1-\alpha} \frac{\rho_g}{\rho_l} \left( \frac{u_g}{u_l} \right)^2 \right]$$

to improve the accuracy of  $\lambda_i$  beyond that of the present correlation which, however, is sufficient for the present purpose.

flow parameter or source	num- ber	correlation												
		Dukler (case 2)				Lockhart-Martinelli				present correlation				
		$\bar{\delta}$	$\sigma$	$\psi$	$ \bar{\delta} +\psi$	$\bar{\delta}$	$\sigma$	$\psi$	$ \bar{\delta} +\psi$	$\bar{\delta}$	$\sigma$	$\psi$	$ \bar{\delta} +\psi$	
all measurements	236	2.9	31.2	30.0	32.9	49.7	81.0	74.5	124.2	1.7	27.8	26.5	28.2 <sup>±</sup>	
void fraction $\alpha=0.0-0.2$	50	-11.6	13.7	12.9	24.5	-11.4	13.5	13.0	24.4	-9.2	12.7	12.0	21.2 <sup>±</sup>	
	$\alpha=0.2-0.4$	61	-5.9	25.2	31.5	37.4	8.6	53.2	50.5	59.1	-5.1	23.0	25.9	31.0 <sup>±</sup>
	$\alpha=0.4-0.6$	53	9.3	32.1	34.5	43.8	66.7	83.9	95.0	161.7	0.8	24.7	23.5	24.3 <sup>±</sup>
	$\alpha=0.6-0.8$	47	26.8	35.3	40.0	66.8	139.9	70.6	79.2	219.1	15.5	31.7	32.3	47.8 <sup>±</sup>
	$\alpha=0.8-1.0$	25	-4.8	31.6	27.5	31.3 <sup>±</sup>	66.5	55.1	50.0	116.5	15.7	41.1	37.5	53.2 <sup>±</sup>
density ratio $\rho_g/\rho_l \approx 0.001$	110	-12.4	18.8	23.6	36.0	-16.6	18.5	22.3	38.9	-10.8	17.4	20.8	31.6 <sup>±</sup>	
	$\rho_g/\rho_l = 0.018-0.028$	46	1.0	23.1	21.9	22.9	68.0	38.6	43.8	111.8	-0.8	20.6	22.0	22.8 <sup>±</sup>
	$\rho_g/\rho_l = 0.036-0.046$	80	25.1	35.8	39.8	64.9	130.4	72.7	102.5	232.9	20.2	32.6	32.9	53.1 <sup>±</sup>
liquid viscosity $\eta_l \approx 0.0010$	182	-11.2	17.8	35.0	46.2	10.7	43.7	47.0	57.7	-10.7	14.9	15.0	25.7 <sup>±</sup>	
	$\eta_l = 0.0012$	54	48.5	22.3	21.0	69.5	172.7	50.2	55.0	227.7	43.4	18.6	14.6	58.0 <sup>±</sup>
diameter	$D=0.0250$	195	5.3	33.4	38.3	43.6	62.4	83.6	70.0	132.4	3.5	29.8	34.2	37.7 <sup>±</sup>
	$D=0.1143$	41	-8.5	11.3	11.7	20.2	-8.7	18.4	11.8	20.5	-7.1	11.3	9.9	17.0 <sup>±</sup>
Cravarolo	126	16.3	33.7	38.5	54.8	107.6	69.2	75.0	182.6	12.5	30.5	30.7	43.2 <sup>±</sup>	
Niese	41	-8.5	11.3	11.7	20.2	-8.7	18.4	11.8	20.5	-7.1	11.3	9.9	17.0 <sup>±</sup>	
Malnes	69	-14.7	21.8	25.0	39.7	-20.1	21.3	24.6	44.7	-13.0	19.9	22.4	35.4 <sup>±</sup>	

TABLE 2-13

Comparison of various pressure drop correlations (values in percent)

It appears clearly from table 2-13 that the present correlation compares favourably with the other two correlations for each group except that for  $\alpha_g = 0.8 - 1.0$ , while even for this latter group the mean deviation and spread are not unduly large. The small disadvantage for this group is probably caused by the fact that in this case the wall shear stress is not dominated by a water layer, the high void fraction pointing towards a mist flow pattern with only a very thin liquid layer at the wall where the shear stress is determined by the gas flow. However, this flow pattern is of no direct interest for the purpose of the present investigation. Table 2-13 confirms the well-known fact that the Lockhart-Martinelli correlation yields large deviations. This is particularly conspicuous for high density ratios, where the correlation has been improved for steam-water mixtures by that of MARTINELLI and NELSON [2], which, however, is not suitable for other mixtures as used in the present evaluation. Comparing the present correlation to that of DUKLER (case 2) [45] the improvement is seen to be rather small - 0-10% for  $|\bar{\delta}| + \psi$  in general - but very consistent throughout the entire range of two-phase flow conditions. In addition the present correlation has the great advantage of being firmly based on a two-phase model rather than on extensive mathematical curve fitting. The curve fitting technique used for Dukler's correlation results in a complex polynomial of the fourth degree for the logarithm of the volumetric quality. By contrast the present correlation results in a simple computation of the frictional pressure drop, with possibilities for further simplification for many types of two-phase flow, as discussed in [12].

Notwithstanding the fact that an annular flow model lies at the basis of the present correlation, no indications are found that the validity is restricted to this flow regime (except for the mist flow region mentioned above). It may be freely used for other flow regimes including the churn turbulent flow regime which is predominant in the present experiments on the interaction forces.

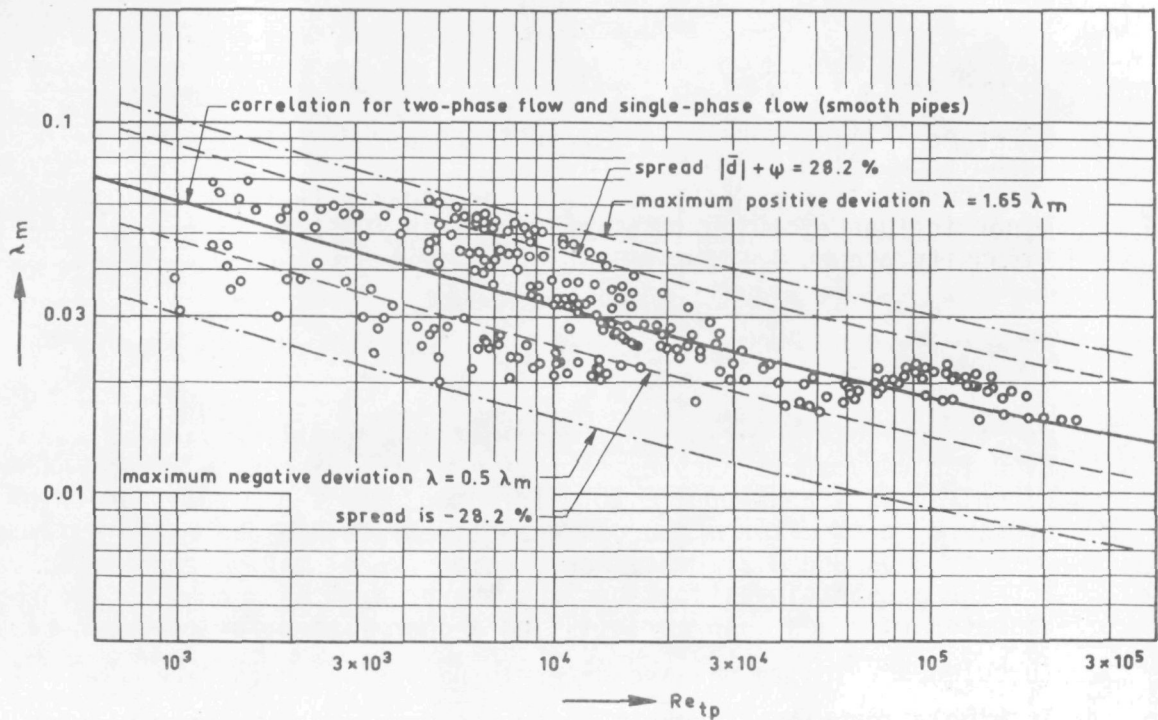


FIGURE 2-14

Friction factor  $\lambda_m$  as a function of the Reynolds number for two-phase flow  $Re_{tp}$

Due to the proportionality of  $\lambda_i$  to  $\lambda_m$  postulated by correlation (2-83) the friction factor  $\lambda_m$  is the only remaining parameter determining the predicted pressure drop. The values needed for the friction factor  $\lambda_m$  to fit the measured frictional pressure drops are plotted in figure 2-14 against the Reynolds number for two-phase flow. The results show a random spread on both sides of the line representing equation (2-79), while none of the measurements shows a deviation above 65%.

For application in the present investigation it should be noticed that use of expression (2-75) for experiments with accelerating flows will of course require the addition of acceleration terms to the last term, which is derived above from equation (2-35) for non-accelerating flow.

### 2.2.3.2. Bubble diameter

As mentioned in the introduction of subsection 2.2.3. the reason for developing a correlation for bubble diameters is to separate the drag

force coefficient  $C_D$  from the quotient  $\frac{C_D}{d}$  - appearing in the expression for drag force  $F_D$  - in order to compare the  $C_D$  values proper for bubble swarms with those of particle swarms and single bubbles.

The bubble size is likely to be determined by the balance between the surface tension and fluid stresses, i.e., by a suitably defined Weber number. The definition of the Weber number usually found in literature, where the fluid stresses are based upon the relative velocity, does not present a suitable basis for such a correlation, as found by PRINS [1]. However, HINZE [55] stated that the fluid stress causing the breakup of bubbles/drops is determined by the dynamic pressure forces of the turbulent motion; resulting in the following critical Weber number:

$$We_{cr} = \frac{\rho_c \overline{u'^2} d}{\sigma} \quad (2-84)$$

where  $\rho_c$  is the density of the continuous phase and  $\overline{u'^2}$  is the mean square turbulence velocity.

This correlation is only valid if the shear stress due to viscosity is of minor influence, which is stated by HINZE [55] to be the case if the viscosity group:

$$\frac{\eta_d}{\sqrt{\rho_d \sigma d}} \ll 1 \quad (2-85)$$

and the viscosity ratio  $\eta_d/\eta_c$  does not reach extreme values. Even for very small bubbles ( $d = 10^{-4}$  m) the viscosity group reaches values of only  $6 \cdot 10^{-2}$  and about  $2 \cdot 10^{-3}$  for atmospheric air-water and high pressure steam-water mixtures respectively, while the ratio  $\eta_d/\eta_c$  varies between 0.02 and 0.2. Hence correlation (2-84) may be considered valid for the present investigations and the problem of computing the bubble diameter resolves into establishing a correlation for the mean square turbulence velocity  $\overline{u'^2}$  and determining the value for  $We_{cr}$ .

In highly turbulent flows the energy spectrum can be approximated by Kolmogoroff's energy distribution law leading to a mean square turbulence velocity  $\overline{u'^2}$  which is independent of viscosity and solely dependent on the energy dissipation per unit mass and time  $\epsilon$  [ $m^2/s^3$ ] according to the relation

$$\overline{u'^2} = 2.0(\epsilon d)^{2/3} \quad (2-86)$$

where the constant 2.0 has been proposed by BATCHELOR [57].

The specific energy dissipation  $\epsilon$  is, in appendix 2-D, derived from the mechanical energy balance as<sup>\*</sup>):

$$\epsilon = \frac{3}{4} \frac{\alpha}{1-\alpha} \frac{C_D}{d} u_r^2 |u_r| [1 + \epsilon_E] \quad (2-87)$$

Substitution of this expression in (2-86) yields for the mean square turbulence velocity:

$$\overline{u'^2} = 2.0 \left( \frac{3}{4} \frac{\alpha}{1-\alpha} C_D [1 + \epsilon_E] \right)^{2/3} u_r^2 \quad (2-88)$$

while substitution of this result in definition (2-84) for the Weber number yields:

<sup>\*</sup>) The main contribution of the energy dissipation stems from the relative motion of the bubbles through the liquid, yielding that:

$$\epsilon_E = \frac{2}{3} \frac{1-\alpha}{\alpha} \frac{\lambda_m d}{C_D D} \frac{u_l^2 |u_l|}{u_r^2 |u_r|} \cdot \frac{1 + \epsilon_p}{1 - \alpha \lambda_i}$$

and

$$\epsilon_p = \frac{\alpha}{1-\alpha} \frac{\rho_g}{\rho_l} \left( \frac{u_g}{u_l} \right)^2 + 2 \frac{\lambda_i}{\lambda_m} \alpha \frac{\rho_l^{-\rho} g}{\rho_l} \frac{gD}{u_l |u_l|}$$

are mostly negligibly small compared to unity.

$$We = 2.0 \frac{\rho_c u_r^2 d^{5/3}}{\sigma} \left( \frac{3}{4} \frac{\alpha}{1-\alpha} \frac{C_D}{d} [1 + \xi_E] \right)^{2/3} \quad (2-89)$$

For the Reynolds stresses  $\rho_c \overline{u^2}$  acting on the bubble surface HINZE [58] derived the expression  $(1-\alpha)\rho_l u_l^2 u_l^2$ , which indicates that  $\rho_c = (1-\alpha)\rho_l$ . This is reasonable if a specific bubble is considered surrounded by a bubbly mixture having a liquid mass - and thus momentum - proportional to  $(1-\alpha)\rho_l$ . Taking into account this effect the Weber number reads as:

$$We = 2.0 \frac{(1-\alpha)\rho_l u_r^2 d^{5/3}}{\sigma} \left( \frac{3}{4} \frac{\alpha}{1-\alpha} \frac{C_D}{d} [1 + \xi_E] \right)^{2/3} \quad (2-90)$$

The determination of the critical value for the Weber number will be based upon the model of SEVIK and PARK [56]. This decision appears justified by the verification by Sevik and Park of their model for two series of experiments referring to different types of two-phase flow, viz.

- their own experiments with a single air bubble in a circular free water jet, where they found experimental and predicted values for the critical Weber number of 2.52 and 2.48 respectively
- measurements of CLAY [59] with droplets in a liquid for small droplet fraction, for which HINZE [55] determined a value of  $We_{cr} = 1.18$  and the model predicts - for  $\rho_d \approx \rho_c$  - a value of 1.0.

This model of Sevik and Park is based upon the assumption - stated without further explanation - that one of the natural frequencies of the bubble is equal to a frequency existing in the flow and that breakup of a bubble as occurring in actual practice will be due to resonance between these two frequencies.

According to LAMB [39], the natural frequency of the n-th order mode of a spherical bubble/drop is given by:

$$(2\pi f_n)^2 = \frac{(n-1)n(n+1)(n+2)}{n\rho_c + (n+1)\rho_d} \frac{\sigma}{\left(\frac{d}{2}\right)^3} \quad (n \geq 2) \quad (2-91)$$

while Sevik and Park propose for the flow-induced frequency:

$$f = \frac{\sqrt{u^2}}{l} \quad (2-92)$$

where the characteristic length  $l$  is taken equal to the diameter of the bubble. In the present author's opinion this latter choice can be justified by the fact that the flow-induced frequency is determined by the eddies passing by the bubble: small eddies do not contain enough energy to affect the bubble, while eddies larger than the bubble only entrain the bubble in their flow field, leaving the eddies with sizes approaching the bubble diameter to affect the deformation of the bubble.

The statement of Sevik and Park that  $f^2 = f_n^2$ , yields:

$$\frac{\overline{u^2} d}{\sigma} = \frac{2}{\pi^2} \frac{(n-1)n(n+1)(n+2)}{n\rho_c + (n+1)\rho_d} \quad (2-93)$$

This correlation shows that the higher order natural frequencies affect bubbles of larger diameters. Thus the process of coalescence of small bubbles to a larger bubble is limited by breakup of this latter as it reaches the size where its lowest natural frequency equals the flow-induced frequency, while a larger bubble - generated by accident - breaks up immediately by resonance at one of the higher order frequencies. The lowest natural frequency of order  $n=2$  is thus seen to define the maximum

bubble size.

In accordance with the approach taken for the Weber number of expression (2-90) the natural frequency of a particular bubble is supposed to be defined by the density of the surrounding mixture yielding  $\rho_c = (1-\alpha)\rho_l + \alpha\rho_g$ , while of course  $\rho_d = \rho_g$ .

Together with the substitution of  $n=2$  in expression (2-93) this yields:

$$\frac{(1-\alpha)\rho_l \overline{u'^2} d}{\sigma} = \frac{2.43}{1 + \frac{1.5+\alpha}{1-\alpha} \frac{\rho_g}{\rho_l}} \quad (2-94)$$

With introduction of:

$$\xi_W = \frac{1.5+\alpha}{1-\alpha} \frac{\rho_g}{\rho_l} \quad (2-95)$$

which is mostly small compared to unity for gas-liquid flows and considering the earlier reasoning that  $\rho_c = (1-\alpha)\rho_l$ , equation (2-94) reads as:

$$We_{cr} = \frac{2.43}{1+\xi_W} \quad (2-96)$$

Substitution of expression (2-90) for the Weber number in correlation (2-96) yields the correlation for the bubble diameter:

$$d = \left( \frac{1.22}{1+\xi_W} \frac{\sigma}{\rho_l u_r^2} \right)^{3/5} \left( \frac{3}{4} \alpha \sqrt{1-\alpha} \frac{C_D}{d} [1+\xi_E] \right)^{-2/5} \quad (2-97)$$

From this result it appears that the quotient  $\frac{C_D}{d}$  has to be known to compute the bubble diameter\*).

This quotient can be obtained from the momentum balances (2-16) and (2-19).

For practical application it appears more convenient to incorporate the  $\frac{C_D}{d}$  ratio in the drag force  $F_D$  according to equation (2-24), resulting in the following expression for the bubble diameter:

$$d = \left\{ \frac{1.22}{1+\xi_W} \left( \frac{\sigma}{(1-\alpha)\rho_l u_r^2} \right)^{1/3} \right\}^{3/5} \left\{ \frac{\sigma}{F_D \frac{u_r}{|u_r|} [1+\xi_E]} \right\}^{2/5} \quad (2-98)$$

where  $\xi_E$  now has to be computed as:

$$\xi_E = \frac{\left( \frac{dp}{dz} \right)_{fr} \frac{u_l}{u_r}}{F_D} \quad (2-99)$$

\* ) The explicit correlation for the bubble diameter yields:

$$d = \frac{1.22}{1+\xi_W} \frac{\sigma}{\rho_l u_r^2} \left( \frac{3}{4} \alpha \sqrt{1-\alpha} C_D [1+\xi_E] \right)^{-2/3}$$

which, however, in general as well as for the present investigation cannot be applied because it requires an explicit correlation for the drag force coefficient  $C_D$ .

while  $\epsilon_W$  remains unchanged<sup>\*</sup>).

Experimental verification for this correlation is obtained by comparison of the resulting diameters with the bubble diameters measured by PETRICK [38] for 12 upward and 12 downward atmospheric air-water flows with void fractions up to 0.35.

The measured bubble diameters appear, of course, as bubble size distributions. Physical analyses (see e.g. KOTTLER [60]) lead to the log-normal distribution<sup>\*\*</sup>), which, however, does not take into account the limitation of a maximum existing diameter. The upper limit distribution proposed by MUGELE and EVANS [62], does take this limitation into account and gives a good approximation of the log-normal distribution for the smaller bubble diameters. The cumulative fraction<sup>\*\*\*</sup>) for measurement 2-R (cf. table 2-16) - which is representative for all of Petrick's measurements - is plotted in figure 2-15 against the bubble radius and shows good agreement for the experimental values with the upper limit distribution, and thus with the log-normal distribution as far as the smaller bubbles are concerned. This good agreement appears for all of Petrick's experiments for which the characteristic parameters are tabulated in table 2-16.

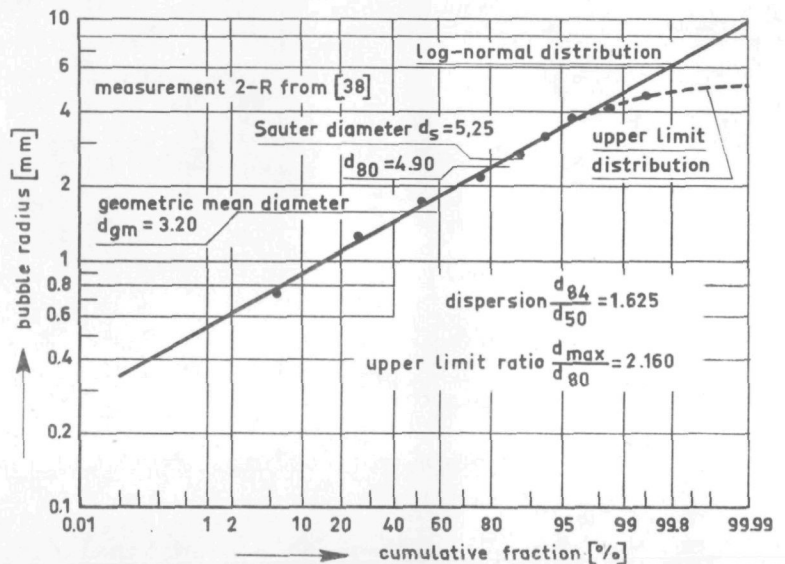


FIGURE 2-15

Representative example  
of the measurements  
from PETRICK [38]

<sup>\*</sup>) After completion of the above derivation the author became aware of the derivation by NAGEL and KÜRTEEN [86] of a similar correlation for bubble diameters also based on Kolmogoroff's law (i.e. expression (2-86)). However, rather than deriving the specific energy dissipation from the mechanical energy balance they obtained this parameter from measured pressure losses. The most significant difference is the use of Sevik's and Park's model in the present correlation yielding the critical Weber number, whereas Nagel and Kürteen give only an estimation of the magnitude based on data for particle cohesion given by RUMPF [87]. Lack of time has prevented the inclusion of a comparison between Nagel and Kürteen's results and those obtained by the present author.

<sup>\*\*</sup>) In the log-normal distribution the frequency distribution for the logarithm of the bubble diameters equals a normal Gaussian distribution (see e.g. MASTERS [61] for formulae and description).

<sup>\*\*\*</sup>) The cumulative fraction  $x\%$  is defined as the fraction with diameters less than  $d_x$ . The cumulative fraction of a log-normal distribution is represented by a straight line on probability paper.

code number	flow parameters			distribution parameters		diameter $d_{80}$	
	$u_{s1}$	$\alpha$	$\times 10^3$	$\frac{d_{84}}{d_{50}}$	$\frac{d_{max}}{d_{80}}$	experi-mental	present model
UPWARD FLOW							
1R	0.46	0.0637	0.20				5.93
2R	0.46	0.170	0.61	1.625	2.16	4.90	4.20
3R	0.46	0.303	1.53	1.600	2.47	3.03	3.10
4R	0.46	0.346	2.01	1.465	2.29	3.76	2.84
5R	0.66	0.0770	0.20	1.680	2.16	5.30	5.58
6R	0.66	0.188	0.62	1.493	2.34	3.75	3.85
7R	0.66	0.316	1.52	1.700	2.76	2.75	2.81
8R	0.66	0.351	1.96	1.598	2.02	3.23	2.55
9R	0.84	0.0763	0.20	1.950	1.91	5.10	5.02
10R	0.84	0.176	0.61	1.740	2.72	3.24	3.41
11R	0.84	0.307	1.50				2.54
12R	0.84	0.335	2.00	1.503	2.17	2.56	2.22
DOWNWARD FLOW							
1D	0.28	0.0899	0.0142	1.903	1.56	8.80	8.15
2D	0.28	0.137	0.0164	1.575	2.16	6.67	6.67
3D	0.28	0.177	0.0228	1.600	2.52	6.30	5.98
4D	0.28	0.184	0.0260	1.608	1.75	6.48	5.91
5D	0.40	0.1060	0.0366	1.761	1.64	7.78	6.90
6D	0.40	0.155	0.0574	1.643	1.85	6.54	5.85
7D	0.40	0.199	0.0796	1.525	2.15	5.74	5.28
8D	0.40	0.230	0.0983				4.99
9D	0.49	0.1110	0.0579	1.563	2.00	5.60	6.55
10D	0.49	0.165	0.0830	1.575	2.07	4.68	5.40
11D	0.49	0.216	0.1060	1.740	2.78	4.00	4.74
12D	0.49	0.246	0.1160				4.44

TABLE 2-16

Experimental values of PETRICK [ 38 ] and predicted bubble diameter

The existence of a bubble diameter distribution instead of a single bubble diameter implies that the diameter predicted by the correlation may differ from the value to be used in the  $\frac{C_D}{d}$  ratio. The following reasoning may help clarify this point.

From the physical background of the correlation - which assumes that the bubbles coalesce until the critical size is reached - it might at first be inclined to expect that the predicted diameter equals the maximum diameter. However, the fact that some bubbles - just below the critical size - will coalesce to bubbles larger than the critical diameter and exist for a while before breaking up, makes it clear that a small fraction of the bubbles has a diameter larger than the predicted diameter. For the present this fraction is assumed to be 20% (i.e. that the predicted diameter is  $d_{80}$ ) which assumption will be varified.

As indicated by equations (2-10), (2-11) and (2-23) the diameter in the quotient  $\frac{C_D}{d}$  stems from the summation of the individual drag forces  $f_D$  to the volumetric drag force  $F_D^*$ , i.e.:

\* ) The existence of different relative velocities for each individual bubble is omitted from this analysis.

$$F_D = \sum_{i=1}^n f_{D_i} = C_D \frac{\pi}{4} \sum_{i=1}^n d_i^2 \frac{1}{2} \rho_l |u_r| u_r \quad (2-100)$$

and the transformation of  $\sum_{i=1}^n d_i$  to  $\frac{6}{\pi} \frac{\alpha}{d}$  by means of the equation:

$$\alpha = \frac{\pi}{6} \sum_{i=1}^n d_i^3 \quad (2-101)$$

Thus the diameter in the quotient  $\frac{C_D}{d}$  is defined by:

$$d = \frac{\sum_{i=1}^n d_i^3}{\sum_{i=1}^n d_i^2} \quad (2-102)$$

which is known in literature as the Sauter or volume-surface diameter (see e.g. MASTERS [61]).

For the size distribution of measurement 2-R - mentioned before as representative for Petrick's measurements - this Sauter diameter is computed as  $d_S = 5.25$  mm, while the predicted diameter appears to be  $d_{80} = 4.90$  mm from figure 2-15. In view of the inaccuracy in the derivation of equation (2-102) caused by the variation in relative velocity  $u_r$  for each individual bubble this difference of 7% between  $d_S$  and  $d_{80}$  can be ignored and the Sauter diameter in the quotient  $\frac{C_D}{d}$  may therefore be represented by  $d_{80}$ .

The resulting diameters computed<sup>\*</sup>) with the correlation are compared to the measured values for  $d_{80}$  in figure 2-17. The agreement is surprisingly

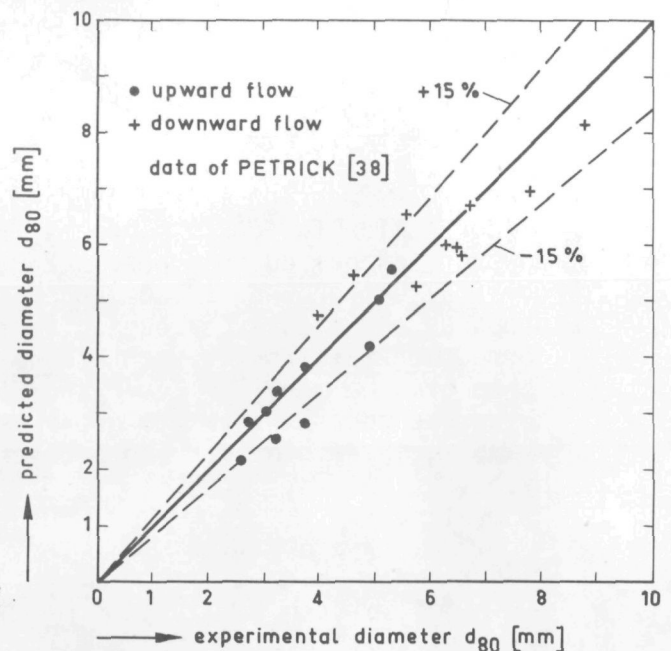


FIGURE 2-17

Comparison of experimental and predicted bubble diameters

<sup>\*</sup>) Due to the fact that PETRICK [38] has only tabulated the void fraction, quality and superficial water velocity an estimate has to be made for the air density in order to determine the slip and relative velocity. From the lay out of the test loop the local pressure is estimated as 1.4 bar yielding  $\rho_g = 1.75$ .

good, having a scatterband of only 15%, while the validity of the present model is firmly supported by the fact that the model gives a good agreement for both upward and downward flows.

This result of predicting  $d_{80}$  - and thus a good approximation of the Sauter diameter - from the size distribution makes the correlation directly applicable for computing the drag force coefficients  $C_D$  from the experimental values  $\frac{C_D}{d}$ .

#### 2.2.4. Two-dimensional effects

The cross-sectional variations in velocity and void fraction known to exist in channel flow were not taken into account in the derivation of the momentum balances (2-16) and (2-19) where the flow was assumed to be one-dimensional. Considering, for example, the first term of the momentum balance for the gas phase  $\frac{d}{dz} (\alpha A \rho_g u_g^2)$  this term has to be written as  $\frac{d}{dz} \int_A \alpha \rho_g u_g^2 dA$  in case of nonuniform channel flow. Instead of this cross-sectional average  $\frac{d}{dz} \langle \alpha \rho_g u_g^2 \rangle A$  the one-dimensional approach deals with the product of cross-sectional averages for each individual flow parameter,  $\frac{d}{dz} \langle \alpha \rangle A \langle \rho_g \rangle \langle u_g \rangle^2$ , which two expressions are well-known to differ. For two-phase flow the cross-sectional averages for the gas and liquid velocities  $\langle u_g \rangle$  and  $\langle u_l \rangle$  may be meaningless and even misleading for steep radial void fraction profiles. Hence the computations are always based on:

$$\bar{u}_g = \frac{\langle \alpha u_g \rangle}{\langle \alpha \rangle} = \frac{u_{sg}}{\langle \alpha \rangle} \quad (2-103)$$

and:

$$\bar{u}_l = \frac{\langle (1-\alpha) u_l \rangle}{\langle 1-\alpha \rangle} = \frac{u_{sl}}{\langle 1-\alpha \rangle} \quad (2-104)$$

These two-dimensional effects can be taken into account by the introduction of correction factors as appears from the model of ZUBER and FINDLAY [37]. However, as proved in appendix 2-B this model is based on an incorrect physical background and interpretation of experimental data. Moreover it proposes one single correction factor instead of a set of individual correction factors for each of the terms of the momentum balances. Therefore the model of Zuber and Findlay is not used and the present author proposes instead to use a set of correction factors of which, for example, the factor for the acceleration term of the gas phase is defined by:

$$K_1 = \frac{\langle \alpha \rho_g u_g^2 \rangle}{\bar{\alpha} \bar{\rho}_g \left( \frac{u_{sg}}{\bar{\alpha}} \right)^2} \quad (2-105)$$

where for the sake of simplicity  $\bar{\alpha}$  and  $\bar{\rho}_g$  are defined as  $\bar{\alpha} = \langle \alpha \rangle$  and  $\bar{\rho}_g = \langle \rho_g \rangle$ .

Although these correction factors may vary along the axial coordinate due

\*) A cross-sectional average, further to be denoted by brackets  $\langle \rangle$ , is defined as  $\langle x \rangle = \frac{1}{A} \int_A x dA$ .

to flow profile changes, this effect is assumed to be negligible<sup>\*</sup>) and thus the momentum balances are based on constant correction factors. Substitution of the expressions (2-24) and (2-66), for the drag force and impulse respectively, in the momentum balances (2-16) and (2-19) yields:

- for the gas phase:

$$K_1 \frac{d}{dz} (\alpha A \rho_g u_g^2) + K_{21} \rho_l \frac{d}{dz} (B \alpha A u_g^2) - K_{22} \rho_l \frac{d}{dz} (B \alpha A u_g u_l^2) =$$

$$-K_3 \alpha A \frac{dp}{dz} - K_4 \alpha A \rho_g g - \frac{3}{4} \alpha A \frac{C_D}{d} \rho_l (K_{51} u_g^2 + K_{52} u_l^2 - 2K_{53} u_g u_l) \quad (2-106)$$

- for the liquid phase:

$$K_6 \rho_l \frac{d}{dz} ((1-\alpha) A u_l) = -K_7 (1-\alpha) A \frac{dp}{dz} - K_8 (1-\alpha) A \rho_l g +$$

$$+ \frac{3}{4} \alpha A \frac{C_D}{d} \rho_l (K_{51} u_g^2 + K_{52} u_l^2 - K_{53} u_g u_l) - \left(\frac{dp}{dz}\right)_{fr} A \quad (2-107)$$

where the superscribed dashes - indicating cross-sectional averages - have been omitted.

The terms for the interaction forces  $F_A$  and  $F_D$  are seen to split into two and three terms respectively, concerning the gas and liquid velocity instead of the relative velocity; this is done because the correction factors  $K_2$  and  $K_5$  would be indefinite in case of zero relative velocity. The values for this set of correction factors -  $K_1$  up to  $K_8$  - defined in table 2-21 shall be obtained by using estimated radial distribution functions for the velocities and void fraction. The velocity distributions are assumed to follow the power law known from single-phase turbulent flow, viz.

$$\frac{u_l}{u_{l\epsilon}} = \left(1 - \frac{r}{R}\right)^{1/p} \quad (2-108)$$

and

$$\frac{u_g}{u_{g\epsilon}} = \left(1 - \frac{r}{R}\right)^{1/q} \quad (2-109)$$

In single-phase flow the radial velocity distribution is known (see e.g. [63]) to be dependent of convergence and divergence of the channel. Assuming this to hold also for two-phase flow, it is necessary to distinguish the following four geometries corresponding to the test sections used in the present investigation (cf. subsections 2.3.1.3.2. and 2.3.2.2.2.):

- a straight pipe
- two converging test sections with a half angle of convergence of 2°12' and 3°40' respectively
- a diverging part of a test section with a half angle of divergence of 7°30'.

In the absence of firm evidence to the contrary it seems reasonable to

<sup>\*</sup>) The practical justification for this assumption even for converging and diverging channel is given by the values of table 2-21.

start from values of p for the straight pipe lying on either side of the single-phase value p=7, i.e. to assume p=6, 7, 8 for the straight pipe. Various qualitative considerations such as the increasing uniformity of the flow distribution for converging channels and the increased uncertainty for the distribution of the gas velocity then lead to the chosen power values shown in table 2-18.

Although radial distribution functions for the void fraction can be obtained from the measurements on atmospheric air-water mixtures reported in subsection 2.3.1.4.2., the polynomial approximation of these distributions are too complex to be suitable for the present analysis. Therefore the void fraction distribution is also chosen as<sup>\*</sup>):

$$\frac{\alpha}{\alpha_{\xi}} = \left(1 - \frac{r}{R}\right)^{1/n} \quad (2-110)$$

where the range for n given in table 2-18 is wide enough to cover all relevant geometries. As indicated in table 2-21, a fourth parameter,  $\bar{\alpha}$ , is required in addition to the local phase velocities and void fractions in order to obtain quantitative values for the various correction factors. This stems from the fact that - in contrast to the local velocities and void fraction - the local "liquid fraction"  $(1-\alpha)$  is not strictly proportional to its mean value  $(1-\bar{\alpha})$ . Correction factors containing the "liquid fraction" - either directly or via the mean liquid velocity  $\bar{u}_l = \frac{u_{sl}}{1-\alpha}$  - may therefore be expected to show a dependency on the mean "liquid fraction". As shown in table 2-18 the mean void fraction  $\bar{\alpha}$  is

velocity distribution: liquid phase $\frac{u_l}{u_{l\xi}} = \left(1 - \frac{r}{R}\right)^{1/p}$		
gas phase $\frac{u_g}{u_{g\xi}} = \left(1 - \frac{r}{R}\right)^{1/q}$		
geometry	power p	power q
diverging 7°30'	4 5 6 7	4 5 6 7
straight	6 7 8	5 6 7 8 9
converging 2°12'	7 8 9 10	7 8 9 10 12 14
converging 3°40'	9 10 12 14 16 18 20	9 10 12 14 16 18 20
void fraction distribution: $\frac{\alpha}{\alpha_{\xi}} = \left(1 - \frac{r}{R}\right)^{1/n}$		
all geometries	power n: 3 4 5 6 7 8 9 10 12 14	
cross-sectional average $\bar{\alpha}$ :	0.1 0.2 0.3 0.4 0.5 0.6 0.7	

TABLE 2-18

Powers for distribution functions

<sup>\*</sup>) The difference in correction factors resulting from the use of the "camel back" void fraction profile, having a maximum near the wall - as measured in [1], [64] and [65] - was found too small to warrant its selection in addition to equation (2-110) all the more so, because such "camel back" void fraction distributions were not found in the present author's experiments.

varied from 0.1 up to 0.7, such being the range of interest for the present investigation.

Combination of the chosen values for the four parameters  $p$ ,  $q$ ,  $n$  and  $\bar{\alpha}$  yields for each of the correction factors a number of values ranging from 1050 for the straight test section up to 3430 for the converging test section with the largest angle of convergence. These values were first evaluated by means of histograms, typified by those shown in figure 2-19 for the factor  $K_6$ . From these histograms it was concluded that:

- ★ all the correction factors differ from unity in the positive sense, justifying the use of correction factors greater than unity as an improvement over the value 1 of the one-dimensional model
- ★ the variation of the mean values due to the geometry is significant.

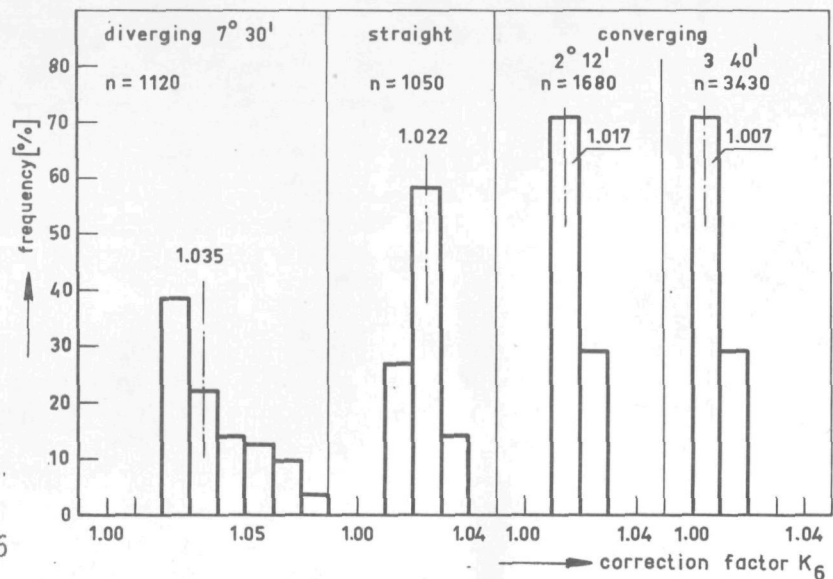


FIGURE 2-19

Histograms for the two-dimensional correction factor  $K_6$

Subsequently the origin of the extreme values of the correction factors was investigated by consecutive variation of each of the distribution parameters while keeping the other three at constant representative values. As an example of these analyses the four graphs for the correction factor  $K_6$  are shown in figure 2-20. These analyses lead to the conclusion that:

- ★ extreme values for the correction factors occur only if one or more of the distribution parameters are extreme, i.e. if the powers  $p$ ,  $q$  and/or  $n$  are less than 4 and/or the mean void fraction greater than 0.6.

Special attention was paid to the correction factors  $K_3$  and  $K_7$  involving the pressure gradient  $\frac{dp}{dz}$ . In case of converging and diverging channels the pressure varies over each cross-section and hence the corresponding correction factors deviate from unity. In [66] an analytical correlation relating the cross-sectional average of the pressure gradient to the pressure gradient at the wall  $(\frac{dp}{dz})_w$  was derived.  $K_3$  and  $K_7$  were found to depend on the second derivative of the pressure at the wall  $(\frac{d^2p}{dz^2})_w$  and on the local channel diameter  $D$  in addition to the angle of convergence/divergence. The deviation from unity, however, was found to be so small

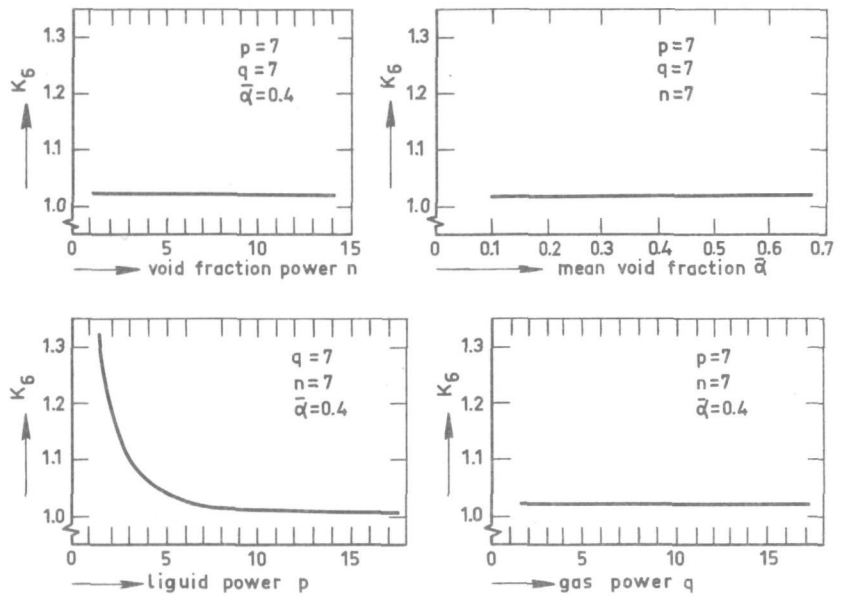


FIGURE 2-20

Dependency of correction factor  $K_6$  on the four distribution parameters

for practical conditions - about 0.002 - that the correction factor  $K_3$  and  $K_7$  will be taken equal to unity. For practical reasons the same is done for the factor  $K_4$  representing the variation of the gas density in a cross-section.

Table 2-21, in addition to giving the definitions for the correction factor, lists their mean values and standard deviations for each of the four geometries. From this table it appears that the two-dimensional effect can be described by four correction factors. Furthermore it appears that three of these correction factors - including the two with the greatest deviation from unity - refer to the relative velocity as it appears in the interaction forces  $F_A$  and  $F_D$ , leading to the conclusion that the two-dimensional effects almost exclusively affect the relative velocity. Taking for example a close look at the results for a straight pipe it is found that:

$$\langle \alpha u_g (u_g - u_l) \rangle = 1.009 \bar{\alpha} \bar{u}_g (1.009 \bar{u}_g - 1.047 \bar{u}_l) \quad (2-111)$$

and

$$\langle \alpha (u_g - u_l)^2 \rangle = \bar{\alpha} (1.009 \bar{u}_g - 1.045 \bar{u}_l)^2 \quad (2-112)$$

The deviation relative to  $\bar{\alpha} \bar{u}_g (\bar{u}_g - \bar{u}_l)$  and  $\bar{\alpha} (\bar{u}_g - \bar{u}_l)^2$  respectively is seen to be largest for small slip ratios  $s = \frac{\bar{u}_g}{\bar{u}_l}$ : in case of  $s = 1.2$  this

relative deviation is 10% and 35% respectively, indicating on one hand that the two-dimensional effect has to be taken into account, but on the other hand that the rather rough estimation described above is sufficiently accurate for the present investigation.

factor	definition	channel geometry			
		diverging 7°30'	straight	converging 2°12'	3°40'
K <sub>1</sub>	$\frac{\langle \alpha \rho_g u_g^2 \rangle}{\bar{\alpha} \rho_g \left(\frac{u_{sg}}{\bar{\alpha}}\right)^2}$	1.027 ± 0.014	1.019 ± 0.008	1.009 ± 0.007	1.006 ± 0.004
K <sub>21</sub>	equal to K <sub>1</sub>				
K <sub>22</sub>	$\frac{\langle \alpha u_g u_1 \rangle}{\bar{\alpha} \frac{u_{sg}}{\bar{\alpha}} \frac{u_{s1}}{1-\bar{\alpha}}}$	1.079 ± 0.040	1.057 ± 0.040	1.037 ± 0.035	1.028 ± 0.019
K <sub>3</sub>	$\frac{\langle \alpha \frac{dp}{dz} \rangle}{\bar{\alpha} \left(\frac{dp}{dz}\right)_w}$	1.000 ± 0.003	1.000	1.000 ± 0.001	1.000 ± 0.002
K <sub>4</sub>	$\frac{\langle \alpha \rho_g \rangle}{\bar{\alpha} \rho_g}$	equal to K <sub>3</sub>			
K <sub>51</sub>	equal to K <sub>1</sub>				
K <sub>52</sub>	$\frac{\langle \alpha u_1^2 \rangle}{\bar{\alpha} \left(\frac{u_{s1}}{1-\bar{\alpha}}\right)^2}$	1.127 ± 0.060	1.092 ± 0.050	1.079 ± 0.050	1.042 ± 0.035
K <sub>53</sub>	equal to K <sub>22</sub>				
K <sub>6</sub>	$\frac{\langle (1-\alpha) u_1^2 \rangle}{(1-\bar{\alpha}) \left(\frac{u_{s1}}{1-\bar{\alpha}}\right)^2}$	1.035 ± 0.014	1.022 ± 0.008	1.017 ± 0.006	1.007 ± 0.006
K <sub>7</sub>	$\frac{\langle (1-\alpha) \frac{dp}{dz} \rangle}{(1-\bar{\alpha}) \left(\frac{dp}{dz}\right)_w}$	equal to K <sub>3</sub>			
K <sub>8</sub>	$\frac{\langle (1-\alpha) \rho_g \rangle}{(1-\bar{\alpha}) \bar{\rho}_g}$	equal to K <sub>3</sub>			

TABLE 2-21

*Two-dimensional effect correction factors and their standard deviation*

### 2.3. Experimental data

The aim of this part of the investigation is to develop correlations for the drag force coefficient  $C_D$  and virtual mass coefficient  $B$ , primarily for use in computations of venturi separators under boiling water nuclear reactor conditions i.e. for steam-water mixtures at a pressure of 7 MN/m<sup>2</sup> and (saturation) temperature of 286°C. However, in view of the difficulty to achieve highly accurate measurements under these conditions, introductory atmospheric air-water experiments were included in order to determine as accurately as possible the physical aspects relevant for the interaction force coefficients and to develop correlations based on this physical background.

These correlations were subsequently verified and extended by means of steam-water experiments under reactor conditions and at 5 MN/m<sup>2</sup> (saturated).

In view of the differences between the air-water and steam-water experiments they will be discussed separately.

### 2.3.1. Air-water experiments

These experiments were carried out in three test sections (cf. subsection 2.3.1.3.2.): a straight tube, a converging and a venturi-shaped test section. The latter two were included in order to create accelerating and decelerating flows required for virtual mass studies and to observe the influence of acceleration/deceleration on the drag force coefficient  $C_D$  first determined in the straight tube.

#### 2.3.1.1. Outline of the method

##### 2.3.1.1.1. Drag force coefficient

Both for the straight tube and the converging/diverging test sections the drag force coefficient  $C_D$  is computed from the liquid phase momentum balance for pseudo one-dimensional flow (2-107), yielding<sup>\*</sup>):

$$\frac{C_D}{d} = \frac{K_6 \rho_l \frac{d}{dz} ((1-\alpha) A u_l^2) + K_7 (1-\alpha) A \frac{dp}{dz} + K_8 (1-\alpha) A \rho_l g + A \left( \frac{dp}{dz} \right)_{fr}}{\frac{3}{4} \alpha A \rho_l (K_{51} u_g^2 + K_{52} u_l^2 - K_{53} u_g u_l) \frac{|\sqrt{K_{51}} u_g - \sqrt{K_{52}} u_l|}{\sqrt{K_{51}} u_g - \sqrt{K_{52}} u_l}} \quad (2-113)$$

The drag force coefficient  $C_D$  is subsequently obtained by multiplying the quotient  $\frac{C_D}{d}$  by the bubble diameter  $d$  computed according to correlation (2-98).

The right hand side of expression (2-113) is computed from measurements for

- the void fraction  $\alpha$  (cf. subsection 2.3.1.4.2.), measured at ten levels along the test section from which the derivative  $\frac{d\alpha}{dz}$  is computed by means of a least square approximation for a Chebyshev polynomial.
- the pressure distribution along the test section (cf. subsection 2.3.1.4.3.), yielding the pressure gradient  $\frac{dp}{dz}$  from a polynomial approximation based on the spline method.
- the water mass flow  $\phi_{ml}$  (cf. subsection 2.3.1.4.1.), yielding the liquid velocity:  $u_l = \frac{\phi_{ml}}{(1-\alpha)\rho_l A}$
- the air mass flow  $\phi_{mg}$  (cf. subsection 2.3.1.4.1.), yielding the air velocity:  $u_g = \frac{\phi_{mg}}{\alpha \rho_g A}$

The cross-sectional area  $A$  and its derivative  $\frac{dA}{dz}$  are of course known for each test section geometry, while the frictional pressure drop  $\left(\frac{dp}{dz}\right)_{fr}$  and the two-dimensional correction factors  $K$  are established according to the correlation and analyses of subsections 2.2.3.1. and 2.2.4. respectively.

<sup>\*</sup>) The last term of the denominator stems from  $\frac{|u_r|}{u_r}$  - giving the drag force the same direction as the corrected relative velocity - introduced before in expression (2-23) and omitted temporarily in subsection 2.2.4. for sake of simplicity.

The liquid phase momentum balance is the obvious choice for computation of the drag force coefficient because of the absence of the virtual mass term in this balance. Nevertheless a weak influence of the virtual mass still remains: the frictional pressure drop and bubble diameter correlation contain the drag force  $F_D$ , which contains in turn acceleration terms and thus impulse - additional to expression (2-35) for non-accelerating flow - as mentioned before at the end of subsection 2.2.3.1.

Therefore the drag force and virtual mass coefficient are computed simultaneously in case of the converging and venturi-shaped test section, whereas for the straight test section the very small contribution of the virtual mass term is eliminated by taking the virtual mass coefficient  $B$  equal to zero.

### 2.3.1.1.2. Virtual mass coefficient

The virtual mass coefficient  $B$  is obtained from experiments in the converging and venturi-shaped test sections only, because in the straight test section the impulse is too small compared to the other terms of the momentum balance: the acceleration being due to expansion of the air only.

The virtual mass coefficient  $B$  is computed from the mixture momentum balance because the drag force  $F_D$  does not exist in this balance. Differentiating the virtual mass term for reasons explained in subsection 2.3.1.6.2.2., this balance results in a first order differential equation for  $B$ :

$$\begin{aligned} B\rho_l \frac{d}{dz} (\alpha A(K_{21}u_g^2 - K_{22}u_g u_l)) + \alpha A\rho_l (K_{21}u_g^2 - K_{22}u_g u_l) \frac{dB}{dz} = \\ = -K_1 \frac{d}{dz} (\alpha A\rho_g u_g^2) - K_6 \rho_l \frac{d}{dz} ((1-\alpha)Au_l^2) - K_3 \alpha A \frac{dp}{dz} + \\ + K_7(1-\alpha)A \frac{dp}{dz} - K_4 \alpha A\rho_g g - K_8(1-\alpha)A\rho_l g - A\left(\frac{dp}{dz}\right)_{fr} \quad (2-114) \end{aligned}$$

This differential equation is integrated numerically - from bottom to top of the test section - with a fourth order predictor/corrector method, described in most handbooks on numerical analysis (e.g. [67]).

The four distinct function values  $B$  and  $\frac{dB}{dz}$  needed at the bottom of the test section to start the predictor/corrector method are derived by a central difference approximation for the three values  $B_{-1}$ ,  $B_0$ ,  $B_1$  - at the coordinates  $z-\Delta z$ ,  $z$  and  $z+\Delta z$  respectively - yielding a set of three coupled algebraic equations derived from equation (2-114) from which  $B_0$  and  $\left(\frac{dB}{dz}\right)_0$  are computed. These values are the input for the Runge-Kutta method which is chosen to achieve the first four values required for more accurate fourth order predictor/corrector method in use for further integration along the test section.

The flow parameters to be measured are the same as mentioned above for the drag force coefficient  $C_D$ . Experience showed that for relative velocities  $|u_r| < 0.4$  m/s - occurring in the venturi-shaped test section, where the relative velocity in the diffuser part changes from positive to negative - the impulse becomes too small to compute the virtual mass coefficient with reasonable accuracy. Therefore the numerical integration is terminated if the relative velocity decreases to 0.4 m/s and restarted - in the same way as described above - at the coordinate where the value  $u_r = -0.4$  m/s is reached.

### 2.3.1.2. Range of variables

In addition to the classification into accelerating, steady and decelerating flow for the three test sections mentioned before, a wide range of flow velocities for each of the phases is desirable for the present investigation, where for a proper description of the two-phase flow mixtures the air velocity should be defined in terms of void fraction.

Within the upper limit of  $\alpha = 0.75$  imposed by the limited air supply to the test section and a lower limit of  $\alpha = 0.25$  selected from the viewpoint of relevance for this investigation, five nominal void fractions were selected viz. 0.25, 0.38, 0.50, 0.63 and 0.75 in order to restrict the total amount of experiment work.

The upper limit for the water velocity is related to the superficial velocity to be expected in the steam-water separator, viz. about 2 m/s. In the absence of a meaningful lower limit five superficial water velocities decreasing by fixed intervals were selected: 0.9, 1.3, 1.7, 2.1 and 2.5 m/s (in combination with the selected void fractions this results in superficial air velocities ranging from 0.4 up to 15 m/s). A number of 25 mixture adjustments is thus obtained for each test section.

The above flow values refer to the inlet of the test sections.

The water mass flows follow from the superficial water velocities and test section inlet areas. The superficial air velocities needed for the desired void fractions are computed using the results of ROUMY [68]. The air mass flows are then obtained with a simple correction for density changes due to variations in test section shape and water velocity.

The  $3 \times 5 \times 5 = 75$  measurements are coded by a number consisting of three figures:

- the first figure refers to the test section;  
0 (which is often omitted) indicates the straight test section,  
1 means the converging test section (one cone),  
2 means the venturi-shaped test section (two cones).
- the second number refers to the superficial water velocity;  
1 stands for the lowest velocity (0.9 m/s) and 5 for the highest velocity (2.5 m/s).
- the third number refers to the nominal void fraction;  
1 stands for the lowest (0.25) and 5 for the highest nominal void fraction (0.75).

So, for example, measurement 142 means the experiment in the converging test section with the fourth superficial water velocity, viz. 2.1 m/s, and the second nominal void fraction, viz. 0.38.

### 2.3.1.3. Description of the test facility

#### 2.3.1.3.1. Air-water loop

Water is circulated by a centrifugal pump, whereas the air is blown once through the test section, as indicated in the schematical flow sheet of figure 2-22.

The water discharged from the pump passes through a venturi-type flow-meter and enters the air-water mixer. After the mixer a flow-straightener and a straight mixing length of about 3 meter is available for establishing fully developed two-phase flow before entering the test section.

The air leaving the test section is separated from the water in a centrifugal separator tank.

From the separator tank the water flows to a settling tank where any carry-under air is separated by gravity from the water returning to the pump. This Delta centrifugal pump has a maximum capacity of 40 kg/s at a head of 23 m,

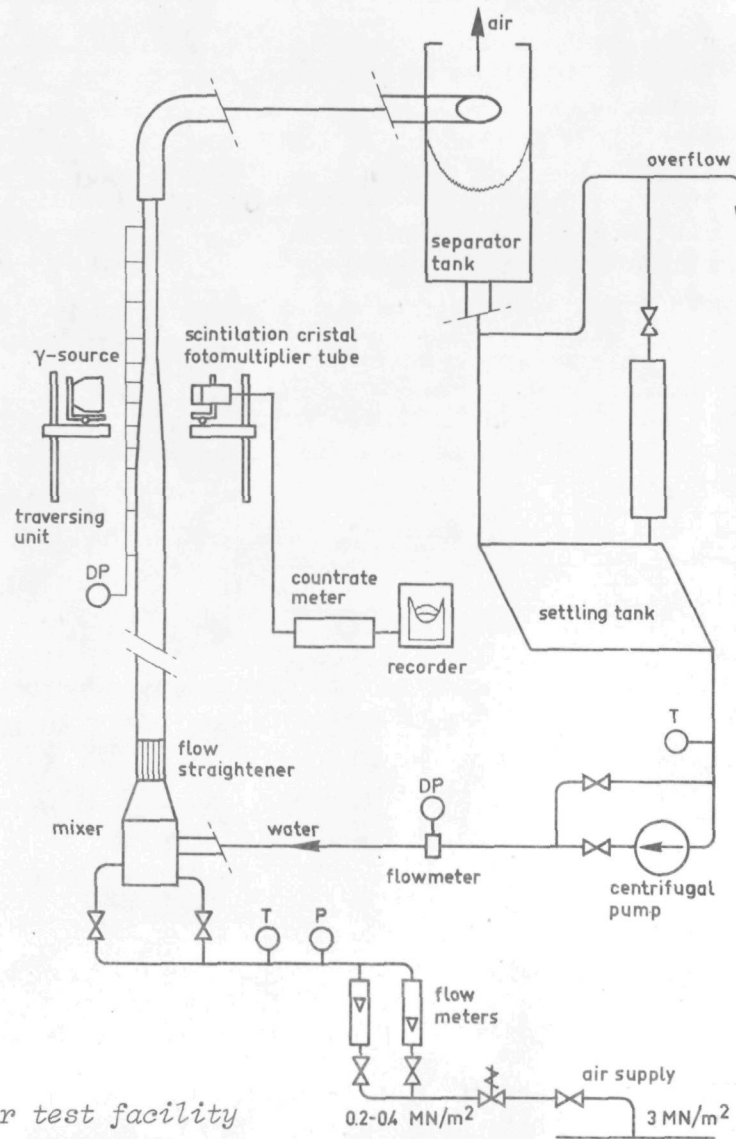


FIGURE 2-22

Atmospheric air-water test facility

the flow through the circuit being adjustable by means of a bypass around the pump .

The air is taken from the 3 MN/m<sup>2</sup> utility net in the laboratory and throttled to 0.2-0.4 MN/m<sup>2</sup>. After passing through a flowmeter and being mixed in the air-water mixer it flows through the test section, is separated from the water and discharged to the laboratory hall.

The air-water mixer is schematically presented in figure 2-23. It consists mainly of 585 pipes with a bore of 4 mm each through which the air enters the mixer. These pipes are divided into two groups of 195 and 390 pipes respectively. The first group is used for the lower void fractions (0.25 and 0.38); the second group serves for the medium void fractions (0.50 and 0.63), while the use of the two groups together results in a direct approximation of the largest void fraction (0.75). For each group the air enters from two sides to homogenize the distribution across the cross section. Distribution of the water, which flows around the pipes, is achieved by built-in flow resistances, while in addition the cone at the top of the mixer causes a further homogeneization of the mixture.

The tanks and mixer are made of stainless steel and the piping of plastic (P.V.C.) to avoid rust in the circulating flow, while the parts between the

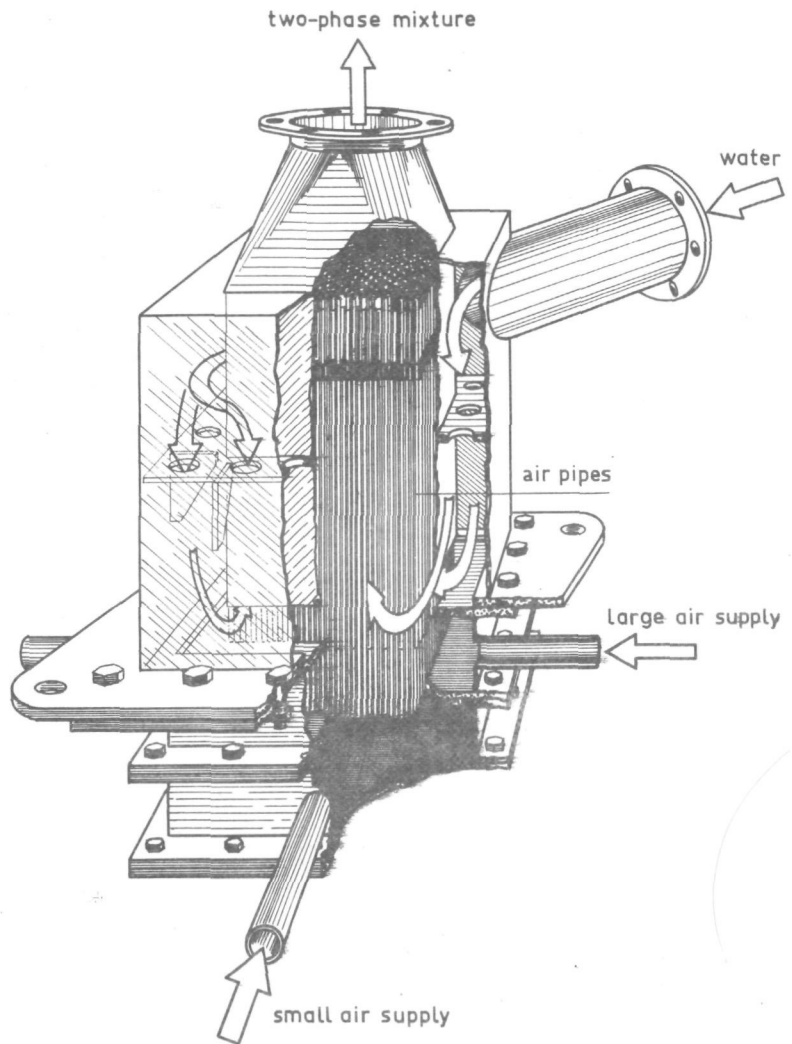


FIGURE 2-23

*Air-water mixer*

mixer and separator tank are made of clear perspex for direct observation of the two-phase flow.

#### 2.3.1.3.2. Test section geometries

As shown in figure 2-24 the three test sections are each 1.725 m long so as to make them interchangeable in the loop and contain 11 pressure taps, making a total of 13 pressure measurements including the two pressure taps of the common inlet section.

Void fraction measurements are carried out for the cross-sections corresponding to the ten lowest pressure taps of each test section. The pressure taps and measurement levels are numbered from bottom to top: e.g. tap 5 is connected with measurement level 3', tap 7 with level 5', etc.

In the straight test section the measurement levels are distributed equidistantly, while in the converging test section six of the ten measurement levels are placed in the cone where the velocity increases by about a factor of two from inlet to outlet. In the venturi-shaped test section attention is focussed on the region just ahead of the throat - where the acceleration is greatest - and the diverging part of the test section. It should be noticed that in both converging parts of the test sections the acceleration increases from bottom to top and thus a wide range of accelerations is covered by the use of only two test sections.

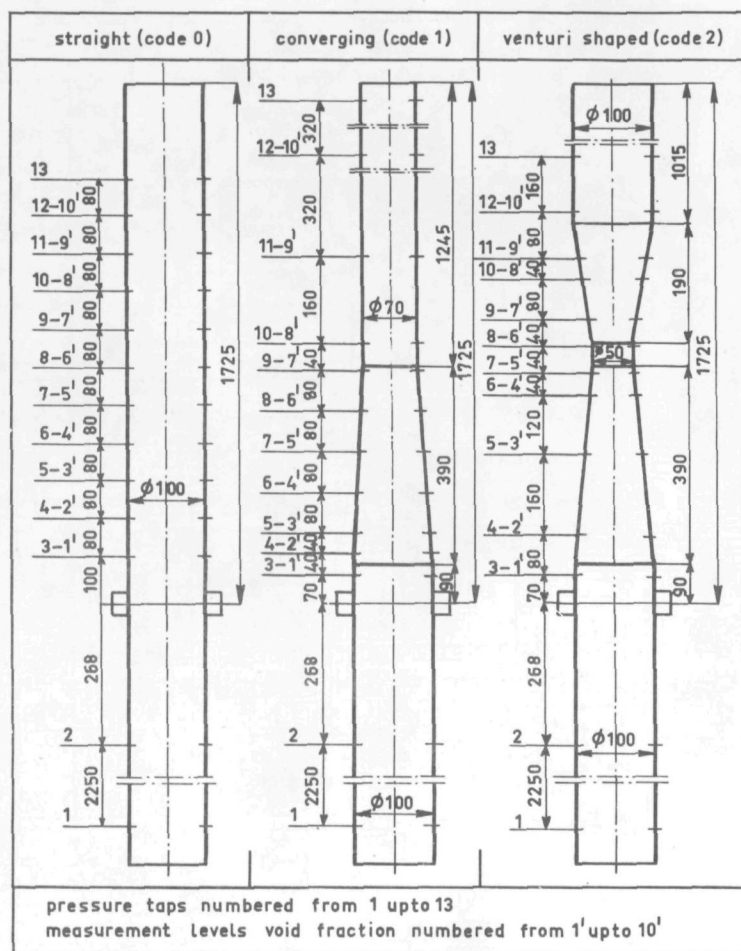


FIGURE 2-24  
Test section geometries

#### 2.3.1.4. Instrumentation and data acquisition

The instrumentation is schematically presented in figure 2-25, while the details are listed in appendix 2-E. The present subsection describes the measuring techniques and the formulae to compute the flow quantities from the measured values. In addition an error estimation is given for these flow quantities.

##### 2.3.1.4.1. Flow measurements

The water flow venturi-type flowmeter mentioned earlier was made of brass to DIN 1952 [69] standards resulting in in- and outlet diameters of 99.4 mm and a throat diameter of 73.715 mm.

The formula for the computation of the mass flow is:

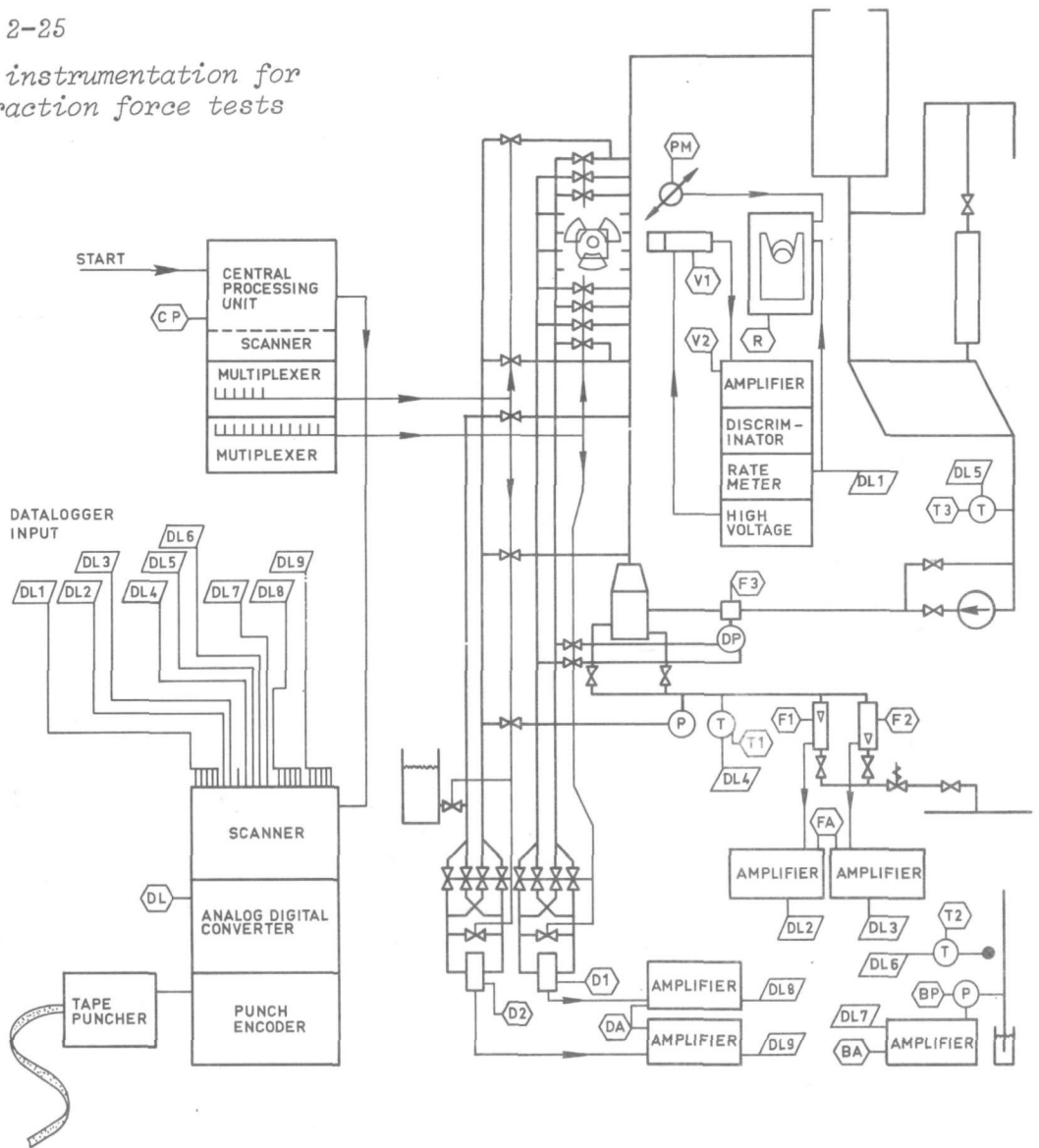
$$\phi_{m1} = \beta A_0 \sqrt{2\rho_1 \Delta p} \quad (2-115)$$

where

- $\beta$  and  $A_0$  are constants, derived from [69] for the abovementioned dimensions
- $\rho_1$  is the water density computed on the basis of a second order polynomial for the water temperature
- $\Delta p$  is the pressure difference, measured and computed as described in subsection 2.3.1.4.3.

FIGURE 2-25

Loop instrumentation for interaction force tests



The accuracy of this measurement is determined by:

- the possible error in the product  $\beta A_0$  for the prevailing manufacturing tolerances given in [ 69 ] as  $\pm 1.9\%$ .
- the error in the differential pressure consisting of an error of 1% in the measuring pressure difference cell and a standards deviation of about 0.75% due to fluctuations in the measured signal itself, yielding a total error of

$$\sqrt{1.9^2 + \frac{1}{2}(1^2 + 0.75^2)} = \pm 2.1\%$$

The air mass flow  $\phi_{mf}$ , measured with rotameter flowmeters, has to be corrected for density deviations from the design conditions, viz.

$$\phi_{mg} = \phi_{mf} \sqrt{\frac{P_f}{1.3} \frac{T_f}{293}} \quad (2-116)$$

where

- $\phi_{mf}$  is the flow indicated by the flowmeter (which gives an electric output signal by transforming the displacement of the float into a change of impedance of a coil).
- $p_f$  and  $T_f$  are the pressure (in bars) and absolute temperature down-

stream of the flowmeters. The pressure is obtained by adding the measured barometric pressure to the pressure differential between atmosphere and flowmeter outlet.

The mass flow through the flowmeter thus obtained is further corrected for moisture taken up by the almost dry air upon entering the mixer and test section. The mass flow of saturated wet air in the test section is:

$$\phi_{mgts} = \phi_{mg} \frac{1+x}{1.0002} \quad (2-117)$$

where

- x is the quality of saturated air
- the factor 1.0002 is an estimation of the quality at the flowmeter:  $x_f = 0.0002$  (air supply from compressed air mains with an estimated relative humidity of 5%).

The quality of saturated air is given (cf. e.g. BAEHR [70]) by:

$$x = 0.6220 \frac{p_{sat}}{p_{ts} - p_{sat}} \quad (2-118)$$

where  $p_{ts}$  is the actual pressure in the test section and  $p_{sat}$  the partial pressure of the water vapour, which is computed from the measured temperature on the basis of a second order polynomial.

The density of the wet air - required for computation of the volumetric air flow and air velocity - is accordingly obtained from [70]:

$$\rho_g = (348.3 p_{ts} \cdot 10^{-5} - 131.6 p_{sat} \cdot 10^{-5}) / T_{ts} \quad (2-119)$$

The possible error in the mass flow  $\phi_{mgts}$  stems from:

- flowmeter inaccuracy, given by the manufacturer as 3%;
- the standard deviation of the fluctuating flowmeter output signal, which is less than 0.1%;
- the error in the flowmeter pressure due to inaccuracy of the pressure difference cell and the standard deviation of the measured signal, yielding a total of  $\sqrt{1^2 + 0.75^2} = \pm 1.25\%$ ;
- the relative error in the absolute temperature: 0.3%,

while the error in the quality x can be ignored because of the small effect of this correction. Thus a total error is derived of:

$$\sqrt{3^2 + 0.1^2 + \frac{1}{2}(1.25^2 + 0.3^2)} = \pm 3.2$$

for the air mass flow.

The error in the volumetric air flow and superficial velocity is in addition increased by the error in the test section pressure  $p_{ts}$  which also equals 1.25%, resulting in an overall error of:

$$\sqrt{3.2^2 + 1.25^2} = \pm 3.4\%$$

for the computed gas velocities.

#### 2.3.1.4.2. Void fraction measurements

The void fraction is measured by the  $\gamma$ -ray technique, already mentioned as standard for two-phase flow investigations by PRINS [1].

The great advantage of this method is its high accuracy in the absence of obstructions in the flow channel, which is in contrast with electric resistance or impedance void gauges, hot wire anemometry and isokinetic

sampling<sup>\*</sup>).

As detailed below the average void fraction over a chord in the test section is measured by the absorption of a collimated photon beam directed along the chord through the flowing mixture, where the reduction in radiation intensity is a measure of the amount of material encountered by the beam. Two additionally measured attenuation signals from the air- and water-filled test sections serve as references for this signal from the mixture. The measurement of these attenuation signals requires that the reduced intensity of the photon beam be measured in such a way that only those photons are counted which have had no interaction with the attenuating material, i.e. that scattering effects be eliminated.

The distinction between photons which did not interact with the material and those that did, can be based on:

- direction: starting with a photon beam containing only parallel photons, only those photons which did not interact will still have the same direction after passing through the material,
- energy: using a  $\gamma$ -source with mono-energetic photons only those photons which did not interact will still have the same energy after passing through the material.

For the production of a beam of parallel photons from a point source a semi-infinite channel is theoretically needed. The same theoretical requirement applies for the detection channel which must separate the photons with the original beam direction from the others.

Because of the finite channel dimensions and the absence of a mono-energetic  $\gamma$ -source a combination of both approaches is used. The lead shielding placed in front of the photon counter contains a channel with a rather large length/diameter ratio (length: 70 mm, inner diameter 2.3 mm). The channel in the source holder is rather short and ends in an expanding cone to facilitate alignment of the source and detector; this expanding cone does not affect the collimation because the source is perceived by the measuring area at the photon counter as a point source with a very small angle, while the lead shielding prevents photons from outside this small angle from reaching the detector, so that the photons which are counted are nearly parallel. In addition to this distinction in the direction of the photons, only photons within a very narrow energy spectrum are measured. This is made possible by the use of a 0.5 Curie  $\text{Cs}^{137}$  source. Cesium has a 662 keV peak in its photon spectrum and emits almost no higher energy photons (photon absorption by pair production is thus eliminated because it requires a photon energy exceeding 1020 keV). By measuring only photons in a small "window" around this peak the measurement with mono-energetic photons is approximated, while in addition the effect of back-scattered photons in the counter is eliminated.

This "window" is adjusted on the count rate meter (cf. schematical figure 2-25) where a pulse height analyser discriminates the photons within the desired narrow span of energy. The photons are detected by a scintillation counter consisting of a NaJ crystal and a photomultiplier tube, the latter being connected to the high voltage supply adjusted at a voltage of about 1000 Volts. In this configuration the maximum count rate is  $1.8 \times 10^4$  photons/s, which is chosen close to the maximum limit of  $2 \times 10^4$  photons/s of the detector, in order to minimize the statistical error in the amount of photons delivered by the source.

---

<sup>\*</sup>) Another more recent measuring technique showing the same advantage is the Laser Doppler technique, which however until now can only be used for low void fractions.

As mentioned above the photon beam coincides with a chord of the cross section under investigation, hence only the mean void fraction of each chord can be measured. By measuring a large number of these chordal void fractions, the mean void fraction for the cross section can be computed. For this purpose a sidewise translation in the plane of the cross section is imparted to the source and counter. In principle no translation should occur during each chord measurement, which consists of 5 discrete scans - at intervals of 0.25 second - of the continuous intensity signal: the purpose of this discretization is to eliminate stochastic effects. However the practical realization of such a discontinuous motion would require highly complex mechanisms; therefore a very slow continuous translation is used instead as an approximation. Two electric motors cause a displacement of 115 mm in 420 seconds, during which time the intensities of 84 chords are measured, and there after return the installation to the initial position in 60 seconds (the scan command for each chord is controlled by a cam mounted on one of the two electric drive motors). Each of the 84 periods of 5 seconds of the measuring stroke consists of 4 seconds pure translation and 1 second of combined translation and scanning. The translation velocity - being 0.274 mm/s - thus yields a displacement of only 0.274 mm during each series of 5 recordings, which is small with respect to the diameter of the photon beam, viz. 2.3 mm, and the nominal chord spacing of  $115/84 = 1.4$  mm. Moreover this low translation velocity causes a slow variation of the intensity signal required for a proper measurement: the continuous signal of the count rate meter is obtained by integration of the counted discrete photons requiring an integration time of about 1 second to reach the proper value. The small remaining error is eliminated in the further computation of the mean chordal void fraction, as the errors are about the same for the mixture and air- and water-filled attenuation signals because of their identical starting position and therefore cancelled out. The positions of the 84 chords are identical for each of the three signals due to the precision of the initial position of the cam - controlling the scan command - at the start of each measurement traverse. Prior to computation of the mean chordal void fractions chords located beyond the inner tube diameter are eliminated by using the photon intensity signals measured on the empty (air-filled) test section. These intensities show a dip at each side of the test section where the inner boundary is reached, because the wall thickness across the measuring chord is highest at that point. The exact location of the inner boundary is established by interpolation between this lowest intensity and the values for two adjacent chords, assuming that the intensity curve is symmetrical with respect to the dip, which assumption is borne out by practice (cf. figure 2-26). The mean void fractions for the remaining chords are obtained by comparing the three intensity signals for the test section filled with the flowing two-phase mixture, pure liquid and pure gas respectively, using the attenuation law for radiation:

$$I_t = I_0 e^{-\mu t} \quad (2-120)$$

where

- $\mu$  is the absorption coefficient
- $t$  is the thickness of absorbing material traversed by the beam
- $I_0$  is the initial beam intensity
- $I_t$  is the intensity of the beam after attenuation by the absorbing material.

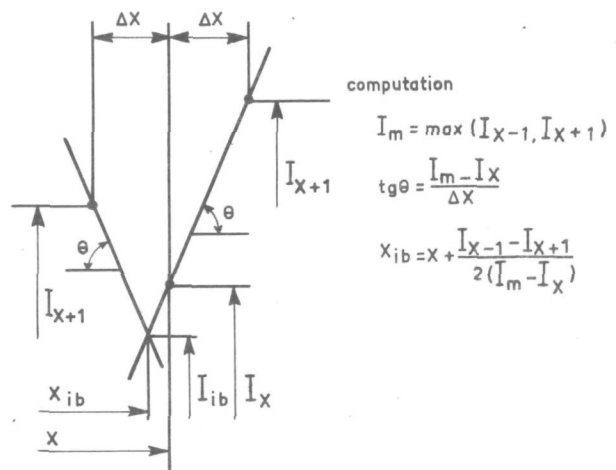


FIGURE 2-26

Computation of the inner boundary coordinate

Successive attenuation by the various absorbing material yields for

- the gas signal:

$$I_g = I_0 e^{-\mu_g L_k} \cdot e^{-\mu_t t} \quad (2-121)$$

- the liquid signal:

$$I_l = I_0 e^{-\mu_l L_k} \cdot e^{-\mu_t t} \quad (2-122)$$

where

- $L_k$  is the chord length
- $t$  is the total wall thickness along the beam
- $\mu_g$ ,  $\mu_l$  and  $\mu_t$  are the absorption coefficients for the gas, liquid and test section material respectively.

From the review of the method given by SCHROCK [71] it follows that under normal conditions the mixture can be assumed to give an attenuation equal to the combination of a liquid layer with thickness  $(1-\langle\alpha\rangle_k)L_k$  and a gas layer with thickness  $\langle\alpha\rangle_k L_k$ , yielding for the mixture signal:

$$I_m = I_0 e^{-(1-\langle\alpha\rangle_k) \mu_l L_k} \cdot e^{-\langle\alpha\rangle_k \mu_g L_k} \cdot e^{-\mu_t t} \quad (2-123)$$

Combination of the various formulae yields:

$$\frac{I_m}{I_l} = e^{-(\mu_g - \mu_l) \langle\alpha\rangle_k L_k} \quad (2-124)$$

and

$$\frac{I_g}{I_l} = e^{-(\mu_g - \mu_l) L_k} \quad (2-125)$$

yielding for the mean chordal void fraction:

$$\langle \alpha \rangle_k = \frac{\ln \frac{I_m}{I_l}}{\ln \frac{I_g}{I_l}} \quad (2-126)$$

In order to standardize the computation of the mean cross-sectional void fraction irrespective of test section shape the original set of mean chordal void fractions is transformed to a fixed number of 41 equidistant chords per cross section. The coordinates of the chords are expressed in relative radii, between -0.95 and 0.95. To avoid singularity problems at the test section walls - where the void fraction equals zero - the chords coinciding with the wall (-1.00 and 1.00) are replaced by chords with coordinates - 0.99 and 0.99.

The void fractions on these 41 standard chords are approximated by a Chebyshev polynomial of order 12 (13 terms) computed from the set of measured void fractions by the method of least squares. This approximation results in a further smoothing of the void fraction measurement errors. For computation of the mean cross-sectional void fraction<sup>\*</sup>) the chordal void fraction is considered to represent the mean void fraction for a small area adjacent to the actual chord, yielding for the mean cross-sectional void fraction:

$$\langle \alpha \rangle_{cr} = \frac{1}{A_t} \sum_{n=1}^{41} \langle \alpha \rangle_{kn} A_n \quad (2-127)$$

In order to determine the error in the mean cross-sectional void fraction, the errors in the mean chordal void fraction are first analyzed, after correcting for the dead time of the counter and for background radiation. Such errors are due to:

- imperfect collimation of the photons
- spread in photon energy i.e. deviation from the ideal mono-energetic beam
- the stochastic character of the measured intensities due to both the stochastic photon emission from the Cs<sup>137</sup> source and the stochastic character of the two-phase flow itself. Insertion of the standard deviation of the signals in formula (2-126) results in an error of  $\Delta \langle \alpha \rangle_k = 0.003$
- the change in the absorption coefficient  $\mu_g$  due to variation in the gas density from about 1.3 kg/m<sup>3</sup> during measurement of the gas signal up to a maximum of about 3 kg/m<sup>3</sup> during measurement of the mixture signal (occurring for maximum flow in the converging test section). This error is established at less than 0.75% in [72].
- inaccurate chord location due to errors in the determination of the inner boundaries of the test section and to vibration of the test section and translation unit.

An exact analysis of the combination of these errors is almost impossible. Therefore the error analysis is based upon the actual measurements: the deviations between the measured mean chordal void fractions and the more or less smoothed values obtained by least square approximation for the computation of the void fractions at the 41 standard chords are assumed to be

<sup>\*</sup>) The radial void fraction distribution - which becomes of special interest in the separator experiments discussed in sections 4.2. and 4.3. - is computed from the same set of 41 standard chord void fractions by a method discussed in appendix 2-F.

characteristic for the error in the former set of values. These deviations appear to be independent from the actual mixture composition and show a rather consistent radial distribution from about 0.015 for the chords in the middle of the cross section up to about 0.06 for the 2 or 3 chords closest to the test section walls. In view of the small contribution of these outside chords to the mean cross-sectional void fraction - as evident from formula (2-127) - a uniform value of 0.02 is assumed for this deviation.

It is evident that the true measurement error in the mean chordal void fractions will be larger than 0.02 due to the imperfect smoothing of the 12th order Chebyshev polynomial. In the absence of an analytical formulation for this remaining error in the void fractions of the standard set of 41 chords, it is also estimated at 0.02.

The error in the mean cross-sectional void fraction caused by this chordal error can be approximated from formula (2-127) as  $\Delta\langle\alpha\rangle_{cr} = \frac{0.02}{\sqrt{41}} \approx 0.003$ , resulting in a relative error varying from 1.2% to 0.4% for the range of void fractions between 0.25 and 0.75.

#### 2.3.1.4.3. Pressure measurements

All pressure measurements in this investigation are pressure difference measurements, except for an additional measurement of the atmospheric pressure - by means of a barometer - in use for the computation of the absolute pressures in the test section.

The pressure differences measured are:

- the twelve differences between the thirteen taps (always two adjacent taps)
- the difference between the lowest tap (number 1) and atmosphere
- the difference between atmosphere and the highest tap (number 13)
- the difference between atmosphere and the air pressure after the flowmeters
- the static pressure difference across the venturi flowmeter for water

These 16 differences are measured with two different differential pressure cells actuated by the displacement of an elastic membrane. This displacement is measured by two induction coils in the cell forming a Wheatstone bridge together with two resistances in the carrier frequency amplifier.

The cells' original maximum pressure ranges are reduced from 0.1 MN/m<sup>2</sup> to 0.01 and from 1 MN/m<sup>2</sup> to 0.2 MN/m<sup>2</sup> respectively by adjusting the amplifier in order to improve the accuracy: the 5 largest differences are measured with the highest range cell and the other 11 with the lowest range cell. In view of the stochastic character of the two-phase flow each pressure difference is measured 5 times at 0.25 second intervals by connecting the amplifier output to 5 subsequent channels of the data logger. The most probable measurement value and its standard deviation are derived from these measurements in the way discussed in subsection 2.3.1.5.

The accuracy was further improved by eliminating the drift - which was found to amount to a few percent of the maximum range, most probably due to temperature effects - by measuring a "positive" and "negative" pressure difference. This is done by interchanging the connections of the pressure taps to the cell between each two measurements and averaging the two resulting absolute values thus eliminating any zero error.

The interchange of the tap connections to the cells is done by electronic switching of magnetic valves, controlled by the same central processing unit - designed and built at the author's laboratory - which also controls the switching of the entire magnetic valve system used for subsequent connection of the different taps to the differential pressure cells.

The barometer measuring the atmospheric pressure has an electric output and was built at the author's laboratory. A wire of high electric resistance (material: kanthal) extends through and above the usual mercury column; due to the low resistance of the mercury column the resistance of this wire depends solely on the length of wire extending above the column. This resistance is measured using an amplifier of the type employed for strain gauge measurements.

The formula in use for the barometric pressure is:

$$p_b = K_1 + K_2 h + K_3 \theta + K_4 \frac{1+K_5 \theta}{1+K_6 h} \quad (2-128)$$

where  $h$  and  $\theta$  are the measured height of the column and the ambient temperature respectively, while the last two terms represent corrections for the temperature dependency of the specific resistance of the kanthal wire and for the small amount of air enclosed above the column.

The six constants  $K$  are obtained by calibration yielding a standard deviation of 3 millibar.

The computation of all differential pressures consists of three consecutive steps, viz.

- correction of the sign of the measured value: due to the measurement of "positive" and "negative" pressure differences half the measured values are assigned the opposite sign.
- computation of the measured differential pressure at the measuring cell, i.e. converting millivolts to  $N/m^2$
- incorporation of the hydrostatic pressure differences due to the water-filled connections between taps and cells.

The resulting formula combining these three steps reads:

$$\Delta p_n = \pm [K \text{ mV}]_n + \rho_l g \Delta h_n \quad (2-129)$$

where

- $\Delta p_n$  is the resulting  $n$ -th pressure difference
- $[K \text{ mV}]_n$  is the measured millivolt value, obtained from "positive" and "negative" measurements
- $K$  is the gauge value of the differential pressure cell
- $\Delta h_n$  is the difference in height between the taps of the  $n$ -th pressure difference.

The standard deviation is obtained by combining the standard deviations of the sets of "positive" and "negative" values:

$$\sigma_t = \sqrt{\frac{1}{2}(\sigma_p^2 + \sigma_n^2)}$$

The deviation between the two total pressure differences obtained by summation of the 12 individual differences  $\Delta p_i (i=2 \dots 13)$  and by subtraction of the overpressures at the bottom  $\Delta p_1$  and the top  $\Delta p_{14}$  of the test section respectively, viz.

$$\epsilon = (\Delta p_1 - \Delta p_{14}) - \sum_{i=2}^{13} \Delta p_i \quad (2-130)$$

is combined with the set of 14 standard deviations in order to provide ultimate corrections for the pressure differences as follows:

$$\Delta p_{C_i} = \Delta p_i + \frac{\sigma_i}{\sum_{i=1}^{14} \sigma_i} \epsilon \quad (2-131)$$

From these corrected differential pressures the absolute pressures subsequently used for computing the pressure gradients  $\frac{dp}{dz}$  are obtained by addition:

$$p_j = \sum_{i=1}^j \Delta p_{c_i} + p_b \quad (2-132)$$

where  $p_b$  is the atmospheric pressure.

The error in these pressure gradients can be derived from the measurement error  $\epsilon$  defined by (2-130) which was found to have a standard deviation less than 0.8% of the total pressure difference across the test section  $\Delta p_T$ . The correction described above will decrease this error. By contrast the polynomial approximation used to obtain the gradients  $\frac{dp}{dz}$  from the absolute pressures will introduce some inaccuracy increasing the error in the gradient. Hence the final error in the pressure gradients is estimated to be 0.8%.

#### 2.3.1.4.4. Temperature measurements

Three temperatures are measured, viz.

- the temperature of the water, required for computation of the air and water densities in the test section
- the temperature of the air downstream of the flowmeters, required for correction of the measured air flow
- the ambient temperature, required for correction of the barometer pressure.

These temperatures are measured with standard chromel-alumel thermocouples, with their cold junctions held at  $50 \pm 0.05^\circ\text{C}$  by a transostat. Hence the absolute temperatures follow from:

$$T = (273+50) + K [mV_T] \quad (2-133)$$

where the constant  $K$  is given by the manufacturer.

Because of the weak influences of the temperature on the resulting flow variables the thermocouples are not calibrated: the accuracy is estimated at  $\pm 1^\circ\text{C}$ .

#### 2.3.1.4.5. Data handling

The analog signals received by the data logger are converted in a digital voltmeter. This voltmeter includes a scanner which sends the digital signals to a punch encoder, whence they are transmitted to a paper tape puncher: an 8-hole adjusted ASKI-code is used on the paper tape.

Of the 100 available data logger channels only 22 are in use. The associated transducers and thermocouples are:

- channels 0 through 4: photon intensity ratemeter
- channel 5: 0.006 to 0.06 kg/s air flowmeter
- channel 6: 0.03 to 0.3 kg/s air flowmeter
- channel 7: reserved for a third air flowmeter in use with the separator tests reported in subsection 4.3.
- channel 8: thermocouple downstream of the air flowmeters
- channel 9: ambient temperature thermocouple
- channel 10: water flow thermocouple
- channel 11: amplifier for barometric pressure
- channel 12 through 16: 0.01 MN/m<sup>2</sup> pressure difference cell
- channel 17 through 21: 0.2 MN/m<sup>2</sup> pressure difference cell.

During measurement of the photon intensities only the first 5 channels are connected to the digital voltmeter.

During measurement of the pressure differences all 22 channels are successively connected with the digital voltmeter, with the first 5 channels giving only dummy values. This cycle is repeated 24 times by the central processing unit, corresponding to the "positive" and "negative" measurements of the 12 pressure differences measured with the low range pressure difference cell (the high range cell is in use for only 6 pressure differences).

For each channel the polarity, 5 digits and a blank are punched at a rate of 4 channels per second.

Prior to computation of the flow variables from the measured millivolt values, the punched data are reordered and the most probable value for each measured quantity is derived from its stochastic set of values, as discussed in the next subsection.

#### 2.3.1.5. Data processing

As already discussed above for the void fraction and differential pressures, the stochastic character of two-phase flow is taken into account by measuring the signals for all relevant parameters several times. The present subsection deals with the acquisition of these data sets, and the computation of the most probable value for each set.

In order to provide a better understanding of the data acquisition the sequence of measurements and of punched tape processing will be exposed. Table 2-27 specifies the measured values and their measuring frequencies. The measurement sequence is repeated for each of the ten measurement levels along the test section under investigation. Such a level measurement consists of the void fraction measurements at the concerning level and the measurement of all pressures, flows and temperatures.

In order to minimize the number of air and water reference photon intensities these reference values are measured only once for each level prior to the complete measurement for three mixture adjustments<sup>\*</sup>). The mixture measurements at each level start with the measurement of the photon intensity consisting of 84 chordal measurements of 5 values each.

The intensity measurement is followed by the measurements of the pressure differences, flows and temperatures as shown in table 2-27. This cycle is repeated 12 times because there are 12 pressure differences (including 1 zero) to measure. Each cycle consists of a "positive" and "negative" measurement (cf. 2.3.1.4.3.), yielding a total of 24 scans. As stated in subsection 2.3.1.4.3. each value is measured 5 times, hence this procedure results in 2 sets of 5 values for each pressure difference including that of the venturi water flow meter. Simultaneously a set of 24 values for each of the signals of the air flowmeter, temperatures and barometric pressure device is obtained.

The resulting paper tape, consisting of the ten level measurements for the three mixture adjustments considered, is rearranged by the computer to yield measurement sets of 5, 2x5 or 24 values per level for each of the measured parameters. From each of these sets the most probable value and its standard deviation is derived.

Despite the availability of numerous subroutines for the analysis of stochastic signals, none of these was found satisfactory for eliminating

---

<sup>\*</sup>) *In order to ensure a proper read out of the punched tape the mixture measurements are separated on the tape by the adjustment code number (cf. subsection 2.3.1.2.) and the level number, while in addition the complete measurement for a measurement level is predicted by its level number.*

measurementlevel 1	
reference measurements for the void fraction	
- air-reference 84 chords (5 measured values each chord)	420
- water-reference idem	420
mixture adjustment A	
void fraction measurement	
- 84 chords (5 measured values each chord)	420
1st pressure differences (and flows, temperatures, etc.)	
"positive" measurement	22
- 5 dummy values	
- low range airflowmeter	
- high range airflowmeter	
- 1 dummy value	
- thermocouple aircsupply	
- thermocouple surrounding	
- thermocouple watercircuit	
- barometric pressure device	
- pressure difference cell 1 (5 measured values for one pressure difference)	
- pressure difference cell 2 idem	
"negative" measurement	22
idem	
2nd pressure differences (and flows, temperatures, etc.)	
idem	22 + 22
up to and including the 12th pressure differences	
	10 (22 + 22)
mixture adjustment B	
idem	$420 + 12 (22 + 22) = 948$
mixture adjustment C	
idem	$420 + 12 (22 + 22) = 948$
up to and including measurementlevel 10	
	$9(2 \times 420 + 3 \times 948) =$
	$9 \times 3684 = 33156$
	total number $10 \times 3684 = 36840$

TABLE 2-27

Sequence and number of  
the measured values

extreme values from the present experiments in such a way as to obviate the need for manual checks for punching errors and extreme values on the 12,000 numbers per series, i.e. a total of some  $12,000 \times 3$  (test sections)  $\times 25$  (mixture adjustments) = 900,000 numbers. Hence a special subroutine was developed which eliminates the extreme values as well as computing the most probable value from the remainder.

As can be seen in the flow sheet of this subroutine PROBMEAN in figure 2-28 the determination of extreme values starts with the computation of the mean value and its standard deviation of the entire set under consideration. Any value deviating from this mean value by more than 1.3 times the

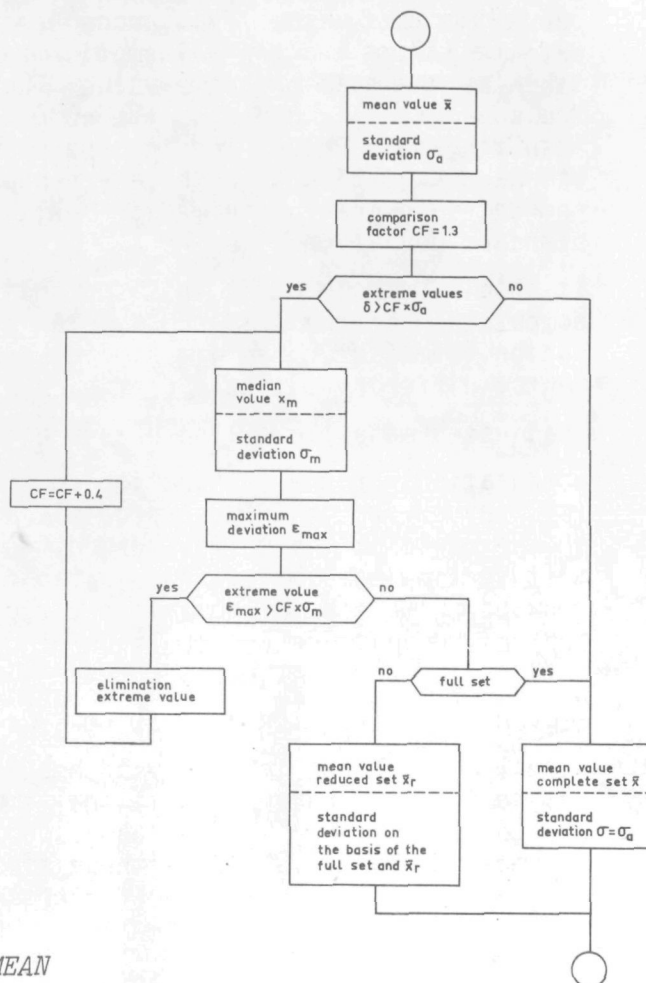


FIGURE 2-28

Flowsheet of subroutine PROBMEAN

standard deviation is supposed to be an extreme value<sup>\*</sup>): if no such deviation exists the mean value of entire set represents the most probable value.

The existence of one or more extreme values implies that the previously computed mean value should not be used for further computations: instead of this mean value the median value from the set will be used as a yardstick for defining extreme values together with a new standard deviation computed on the basis of this median value.

A new check for extreme values is subsequently carried out with reference to this median value. This recheck is necessary both because the new standard deviation is greater than that previously computed on the basis of the mean value and because the maximum deviation itself also changes. If the greatest deviation in this recheck is found to be an extreme value the corresponding value is removed and the same procedure is repeated with the median and standard deviation of the reduced set. However, to prevent elimination of too many measured values on behalf of the reduced standard

<sup>\*</sup>) The factor 1.3 stems from the sets consisting of 5 values; according to the Gaussian-distribution - which is assumed to be valid for these stochastic signals - only 19.4% of the values has a deviation exceeding 1.3 times the standard deviation. Hence the existence of such a deviation for 20% - equivalent to one value - of the set yields an overrepresentation of extreme values which should be eliminated.

deviation the comparison factor 1.3 is then adapted by an increase of 0.4 per eliminated value. This procedure is continued until there are no more extreme values and the arithmetic mean value of the final reduced set is taken as the most probable value. The standard deviation resulting from the subroutine is based on the complete initial set of values and the resulting mean value. The incorporation of possible extreme values in the standard deviation is necessary because the existence of extreme values indicates an inaccurate measurement, which should be manifested in a large standard deviation.

It should be noted that this subroutine PROBMEAN is used too for the computation of the most probable axial pressure distribution which distribution is measured ten times, i.e. once for each of the ten level measurements, differing a little from each other due to small deviations in the readjusted mass flows. The pressure gradient  $\frac{dp}{dz}$  - required for the computations of the interaction forces as described in subsection 2.3.1.1. - is obtained from this most probable distribution by a polynomial approximation on the basis of the spline method. In this method the total length of the test section is divided in a suitable number of intervals each having their own approximation polynomial (see e.g. [73]). For the present investigation the polynomials are chosen to be of degree three, while the total approximation is taken continuous for the function value  $p$  and its first derivative  $\frac{dp}{dz}$ . The void fraction derivative  $\frac{d\alpha}{dz}$  is obtained from the data of the individual measurement levels by a Chebyshev polynomial approximation. This polynomial will have an additional smoothing effect on the small deviations due to fluctuations in the readjusted air and water flow, while in addition the most probable values of these flows are used in the final computations of the interaction force coefficients.

#### 2.3.1.6. Results

Prior to deriving the interaction force coefficients the direct results, viz. pressure, void fraction and phase velocities, will be discussed in order to give an impression of the character of the investigated flows and of the accuracy of the measurements.

##### 2.3.1.6.1. Pressure, void fraction and velocity distribution

From the total set of 75 measurements 5 measurements with constant void fraction and 5 measurements with constant superficial water velocity have been selected for each of the three test sections in order to show the influences of these two basic parameters.

In view of the region of interest for the present separator investigation a void fraction of 0.63 and a superficial water velocity of 2.1 m/s have been selected for this purpose, i.e. the measurements carrying a 4 as last and penultimate figure respectively, according to the code of subsection 2.3.1.2..

Measurements 245 and 254 were not carried out because the combination of high pressure ( $p > 260 \text{ kN/m}^2$ ) and high volumetric quality requires an extremely large air mass flow which was not available for this investigation.

##### 2.3.1.6.1.1. Axial pressure profiles

These distributions are presented in the figures 2-29 through 2-31 for each of the three test sections.

The pressure gradient in the straight test section (figure 2-29) appears to be almost constant and dominated by the hydrostatic pressure gradient: in the "row" for constant superficial velocity the gradient  $\frac{dp}{dz}$  decreases

with increasing void fraction due to the proportionality with the hydrostatic pressure gradient  $\{(1-\alpha)\rho_l + \alpha\rho_g\}g$ . For high void fractions 0.63 and 0.75 this decrease is terminated due to the increase of the frictional pressure drop which is proportional to the square of the real water velocity. In general the frictional pressure drop is of minor influence as can be seen in the "column" for constant void fraction, where the pressure gradient remains almost constant notwithstanding the variation in superficial and real water velocity.

For the converging test section (figure 2-30) the domination of the acceleration pressure drop - proportional to the square of the real water velocity - appears clearly for both constant void fraction and superficial water velocity. The total pressure drop reaches a level up to  $100 \text{ kN/m}^2$  - where expansion of the air becomes significant as will be discussed in the next subsection. In the tail end of the test section - having an inner diameter of 0.07 m - the pressure gradient is mostly determined by the frictional pressure drop due to the increased real water velocities and decreased diameter. The almost constant pressure gradient downstream of pressure tap 11 (measurement level 9) point towards a fully developed flow only 0.2 m (equivalent to 3D) after leaving the converging cone.

The measurements in the venturi-shaped test section (figure 2-31) show a larger acceleration pressure drop in the converging part due to the greater area reduction. Pressure recovery in the diffuser takes place at low efficiency and depends on the void fraction, which is in agreement with the experiments and analysis of KORSTANJE [74]. From the continuing pressure increase at the last pressure tap - 0.18 m downstream of the diffuser - it appears that the diffuser is probably too short causing separation of the flow from the wall. The most significant feature of the flow downstream of the throat is the huge void fraction caused by expansion of the air, and its different radial distribution discussed below.

From figure 2-31 it is obvious that the steep gradient at the throat typical for the venturi pressure profile requires a highly sophisticated approximation technique for computation of the gradient  $\frac{dp}{dz}$ : this was found by a polynomial approximation based on the spline method (see e.g. [73]) where pressure profile and test section geometry can be taken into account by the choice of the splines. Measurement 244 may serve as a typical example: the standard deviation is  $0.41 \text{ kN/m}^2$  and the maximum deviation  $0.96 \text{ kN/m}^2$ , which is an extremely good approximation in view of the total pressure drop of  $260 \text{ kN/m}^2$ .

The very steep pressure gradient of measurement 244 - a pressure drop of  $150 \text{ kN/m}^2$  over a distance of only 0.08 m - points to the possibility of a shock wave due to reaching the critical mass flow. This point will be discussed in subsection 2.3.1.6.1.4..

#### 2.3.1.6.1.2. Axial void fraction profiles

For the straight test section (figure 2-32) the small void fraction gradient caused by expansion of the air is small enough -  $\frac{d\alpha}{dz} < 0.03$  - to justify omission of the virtual mass term as described in subsection 2.3.1.1.. In case of the converging test section (figure 2-33) the void fraction decreases in the lower part of the cone where the acceleration of the air exceeds that of the water. At the end of the cone the pressure drop reaches a magnitude where expansion of the air becomes sufficiently important to yield increasing void fractions. It is obvious that these effects are proportional to the pressure gradients and hence depend on the superficial water velocity and the void fraction itself, determining the real water velocity.

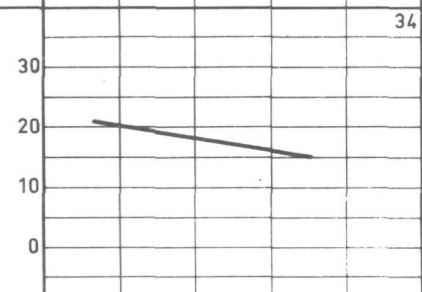
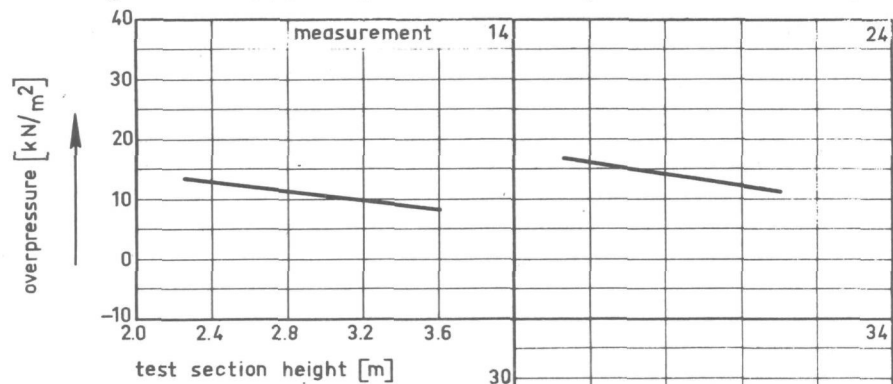
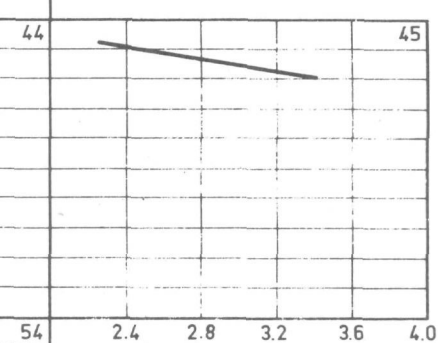
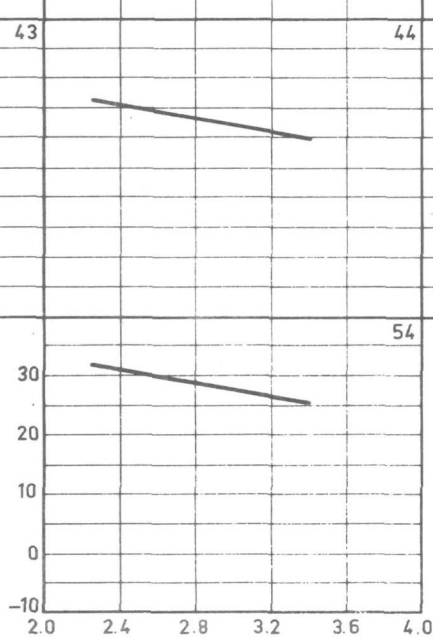
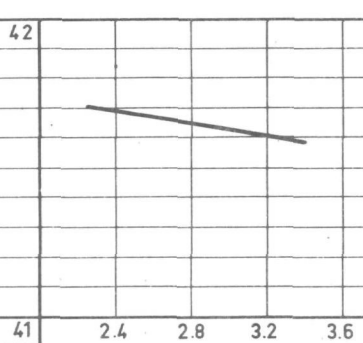
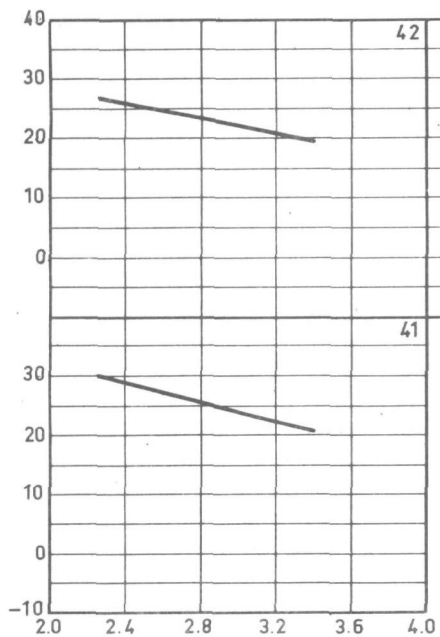


FIGURE 2-29

*Axial distribution of the overpressure in the straight test section*



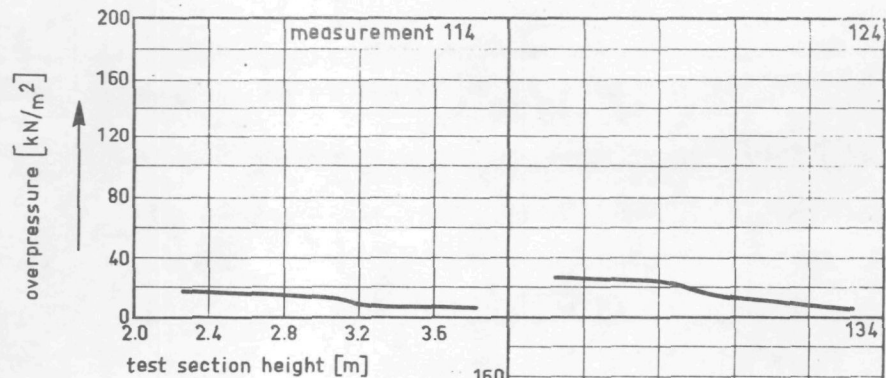
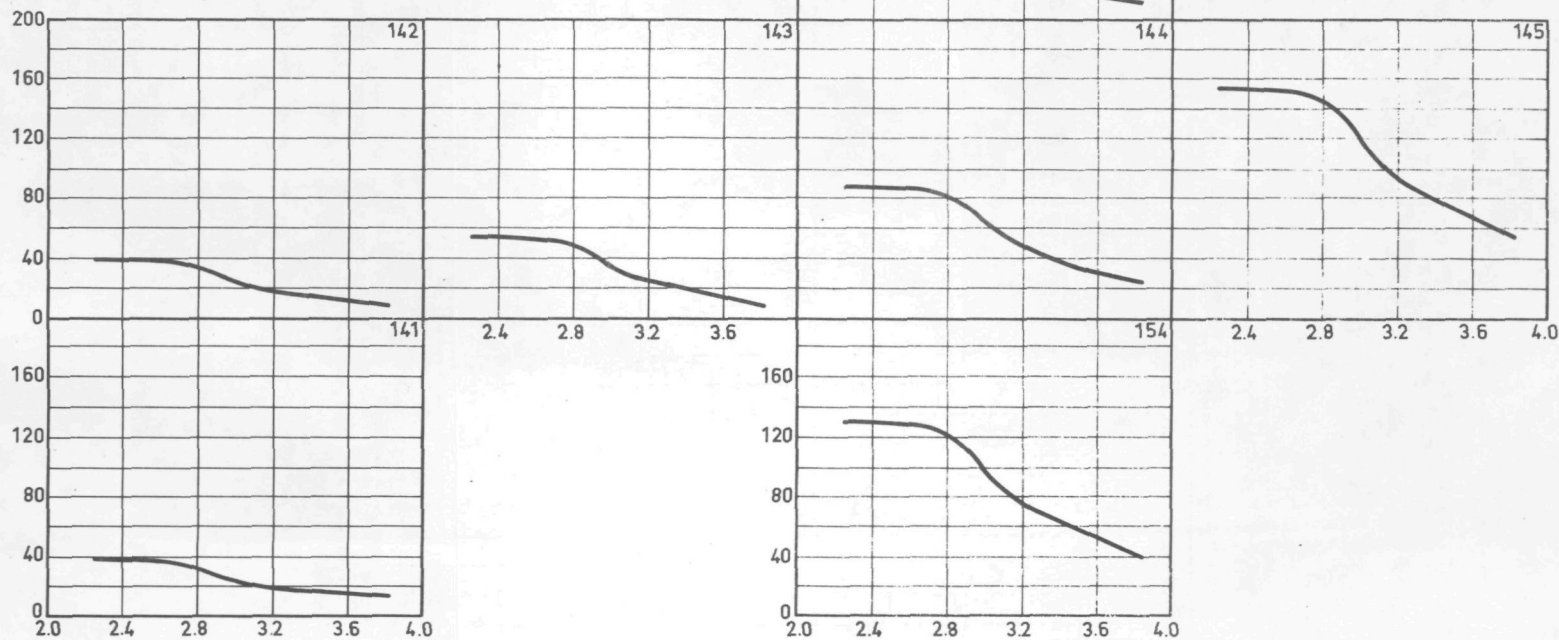


FIGURE 2-30

*Axial distribution of the overpressure in the converging test section*



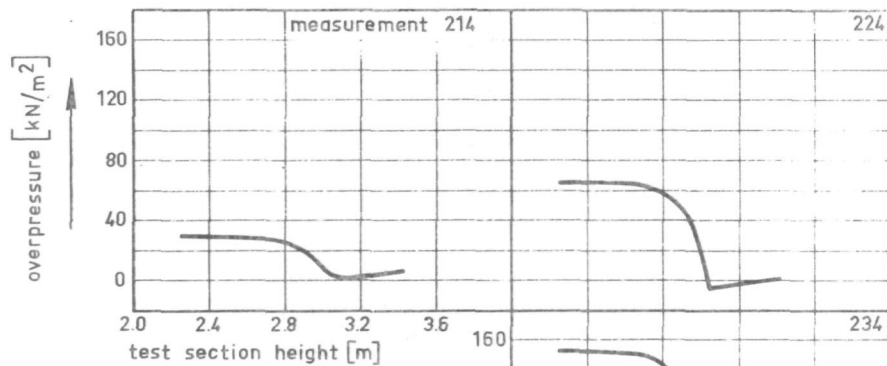
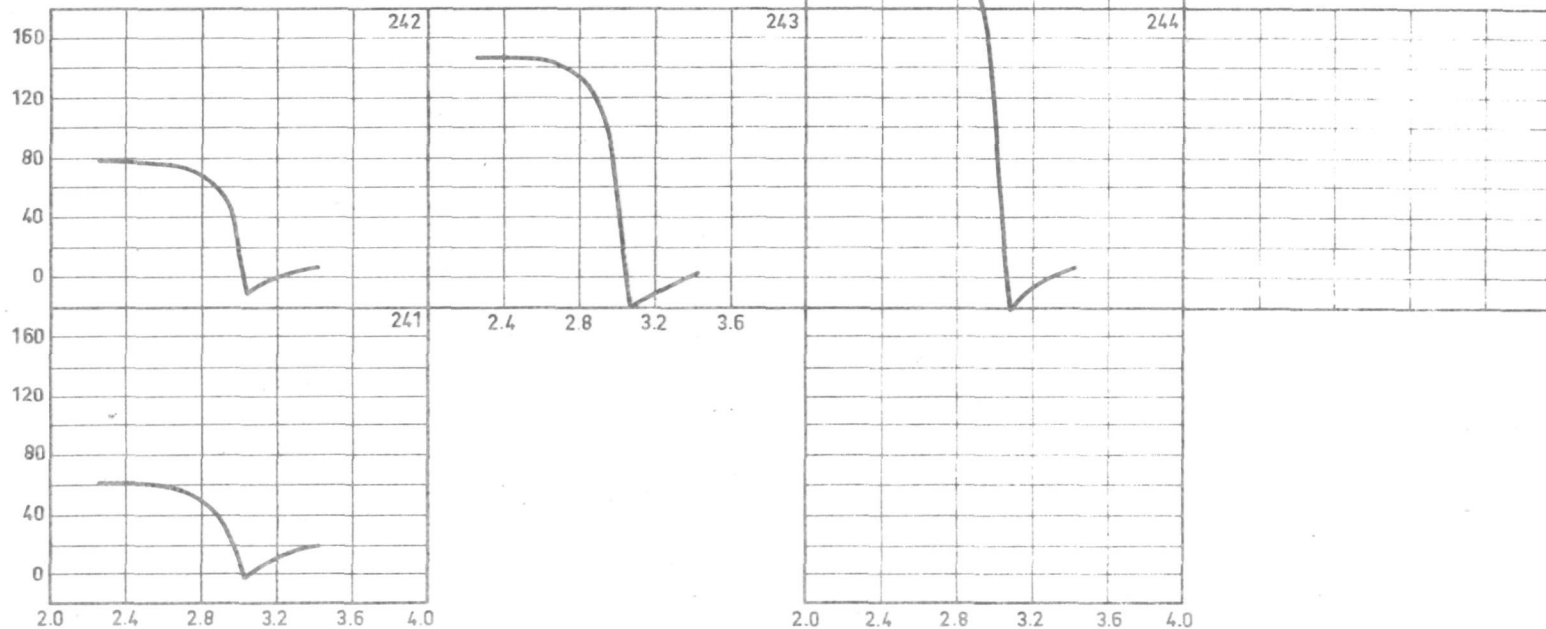


FIGURE 2-31

*Axial distribution of the overpressure in the venturi-shaped test section*



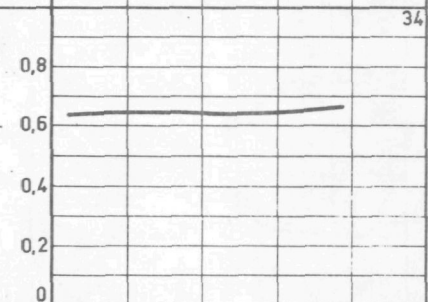
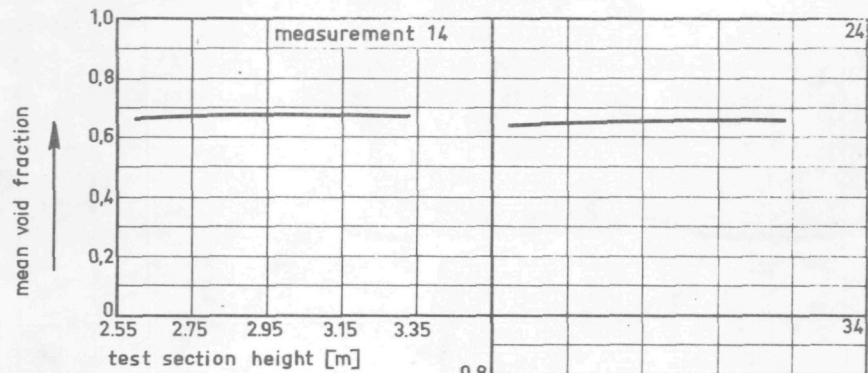
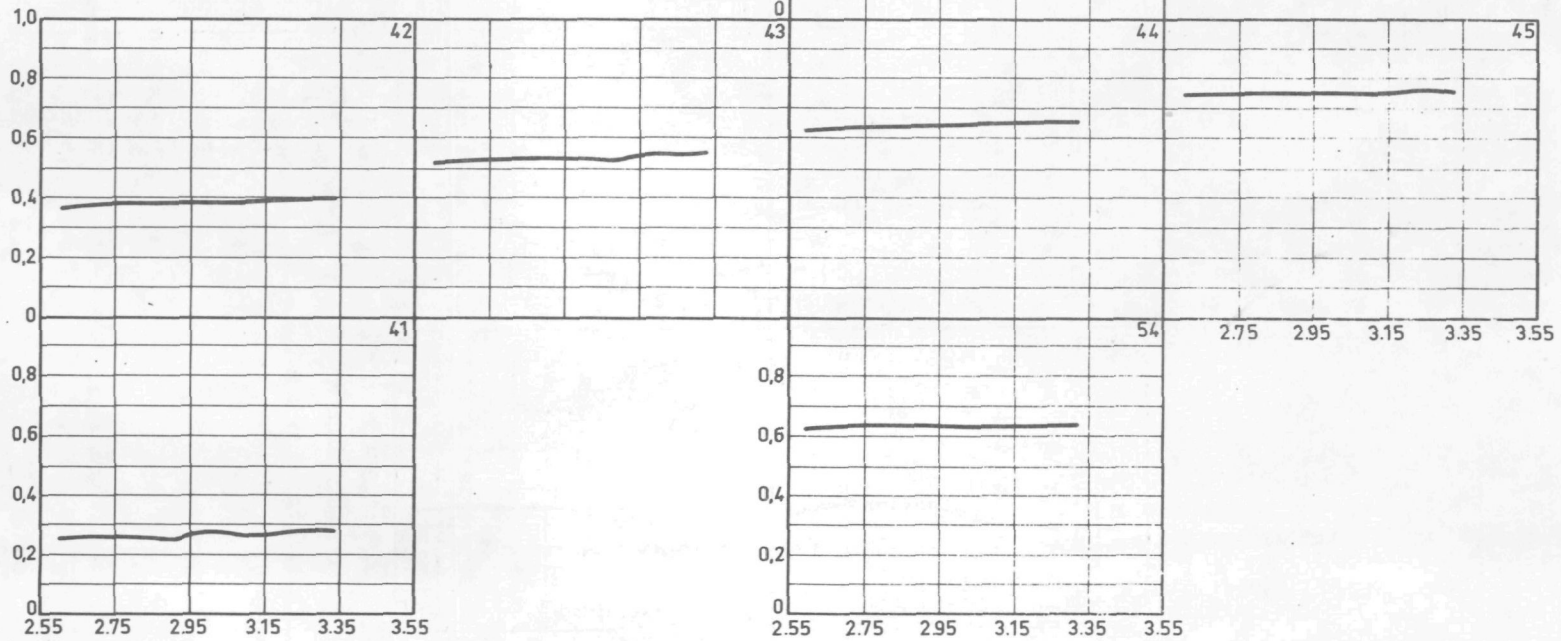


FIGURE 2-32

*Axial distribution of the mean void fraction in the straight test section*



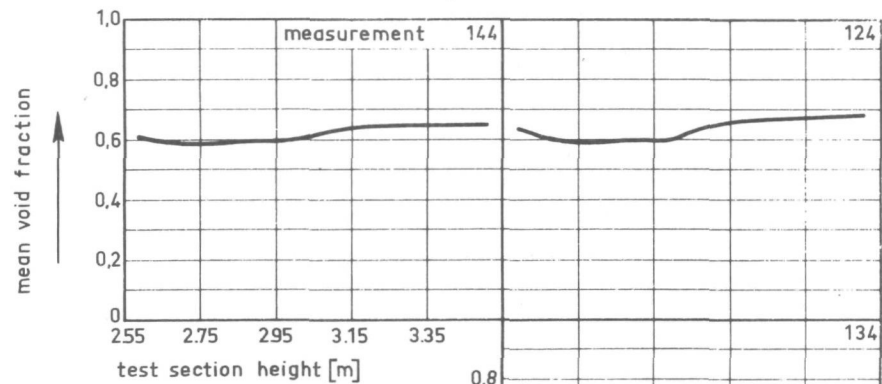
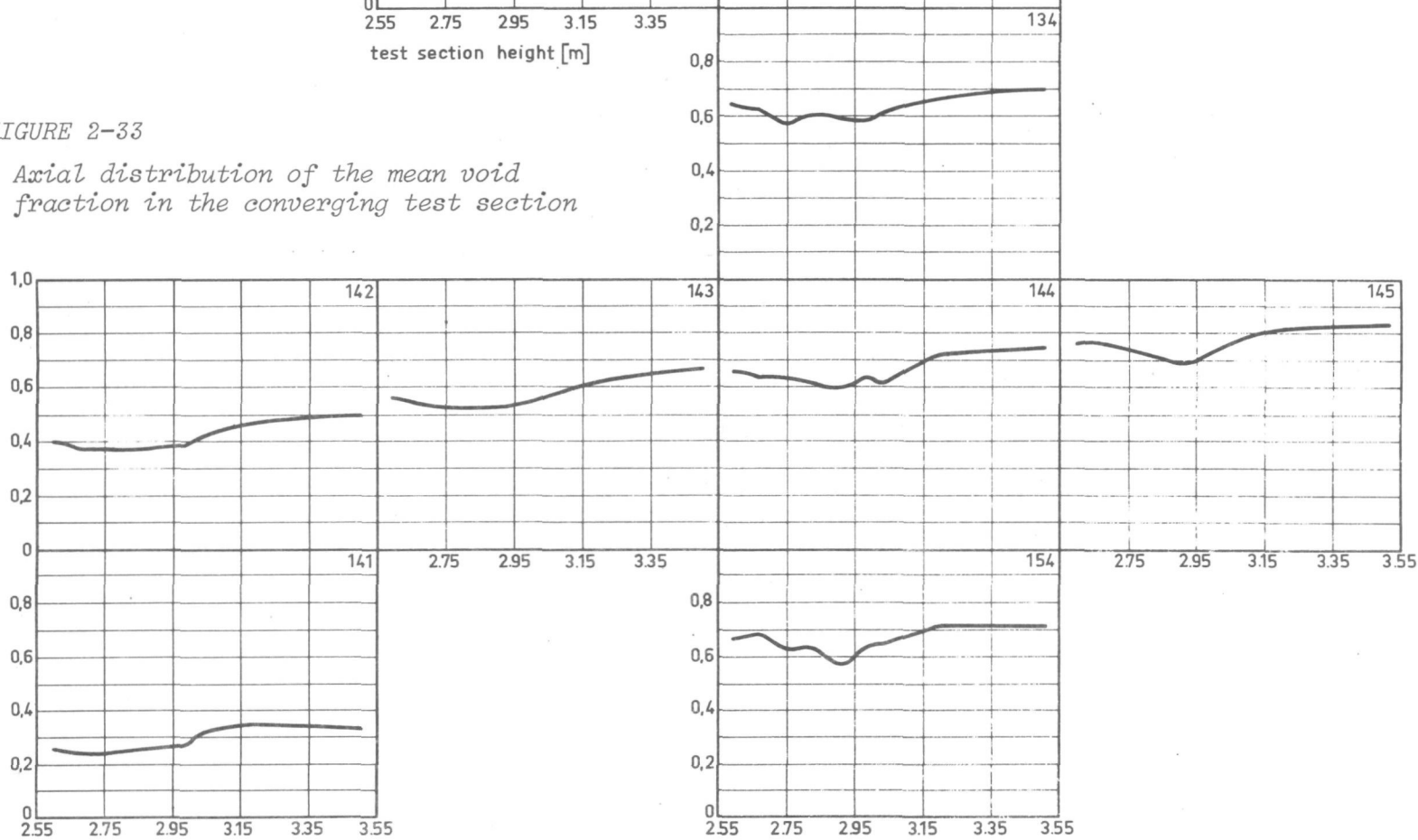


FIGURE 2-33

*Axial distribution of the mean void fraction in the converging test section*



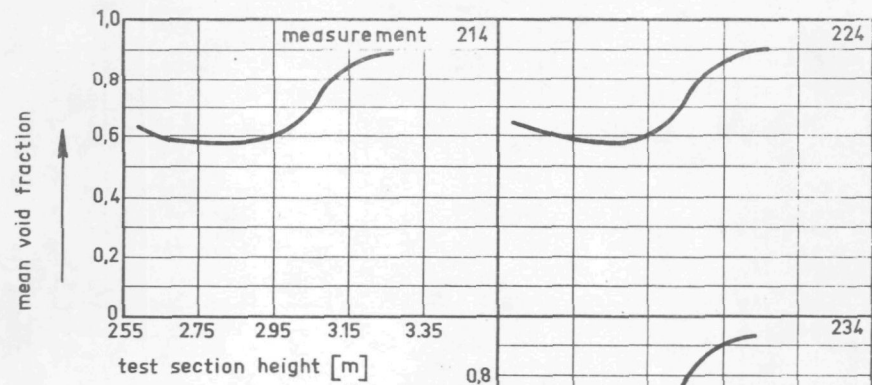
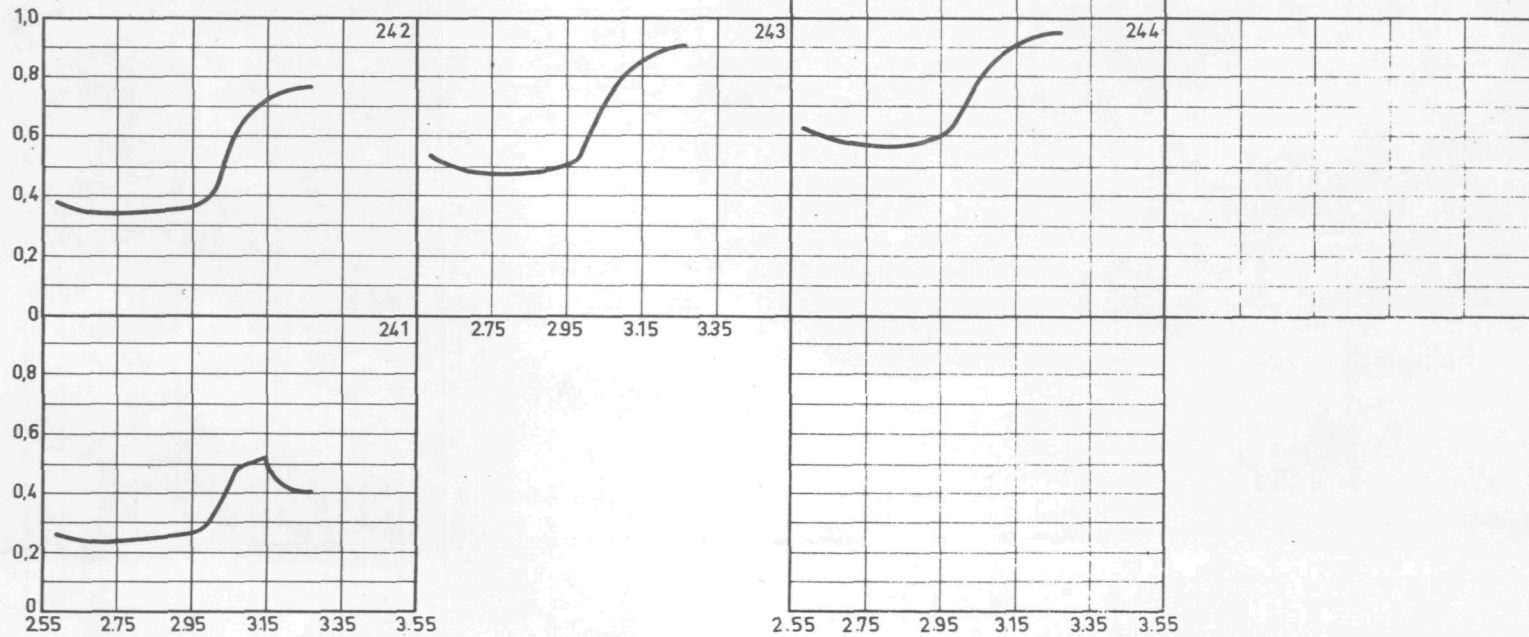


FIGURE 2-34

*Axial distribution of the mean void fraction in the venturi-shaped test section*



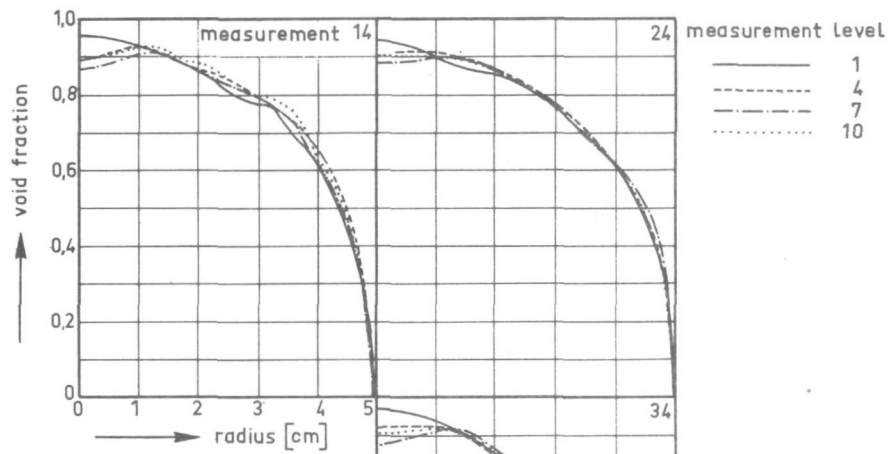
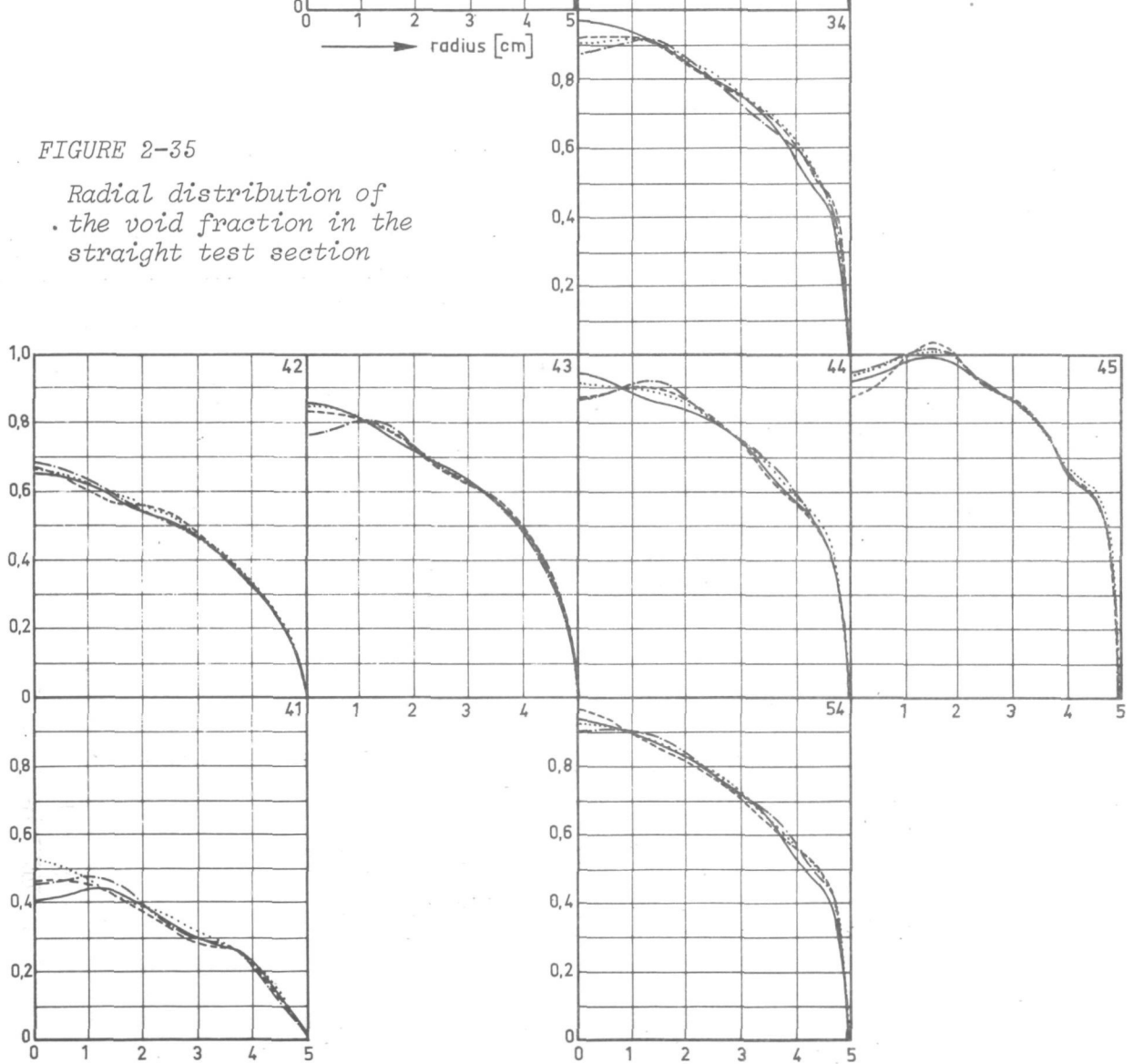


FIGURE 2-35

*Radial distribution of  
the void fraction in the  
straight test section*



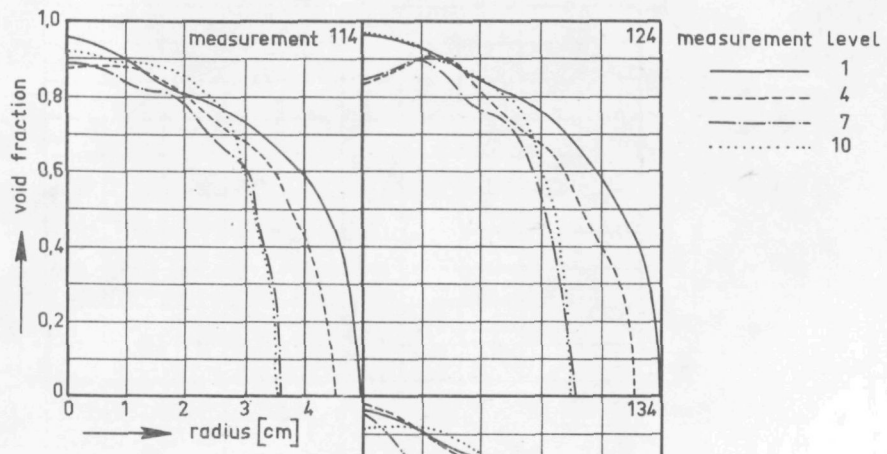
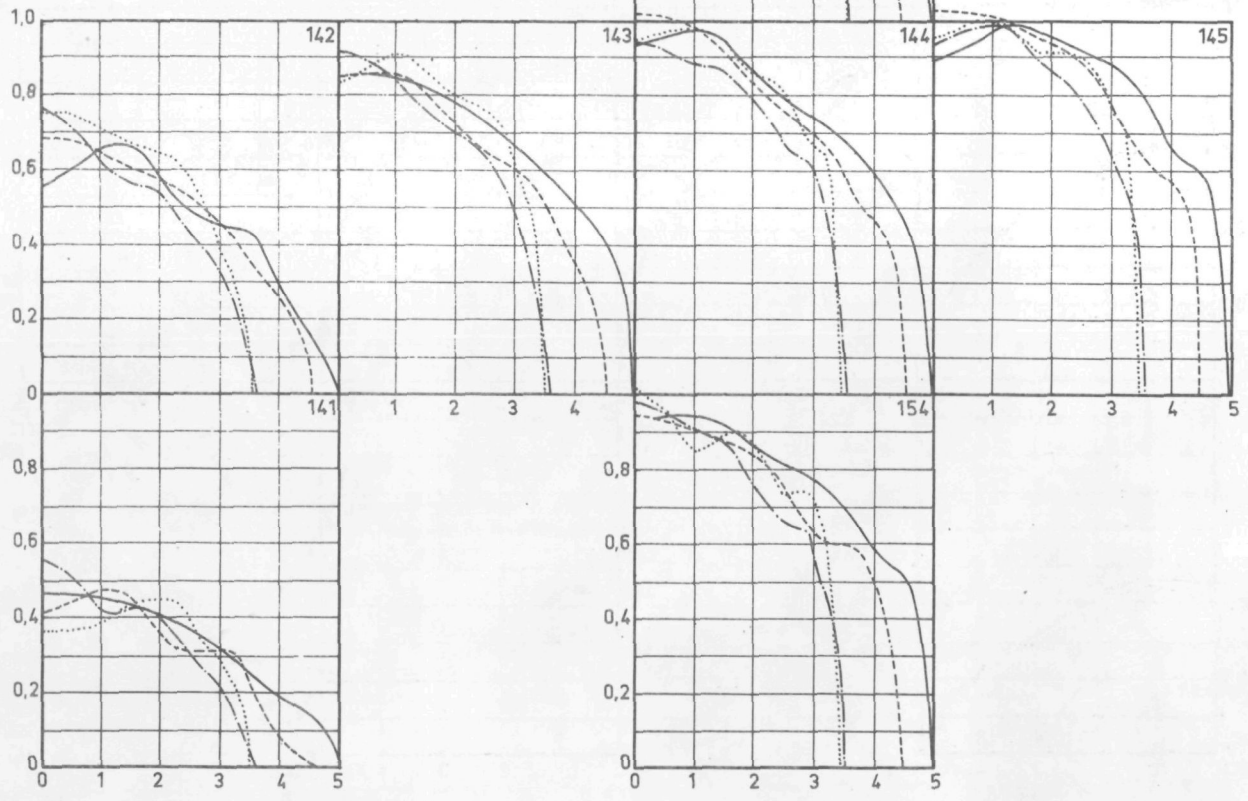


FIGURE 2-36  
*Radial distribution of the void fraction in the converging test section*



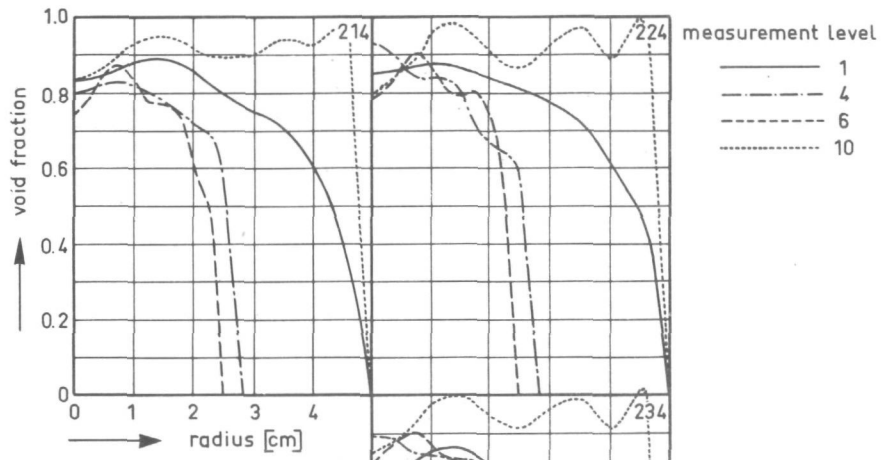
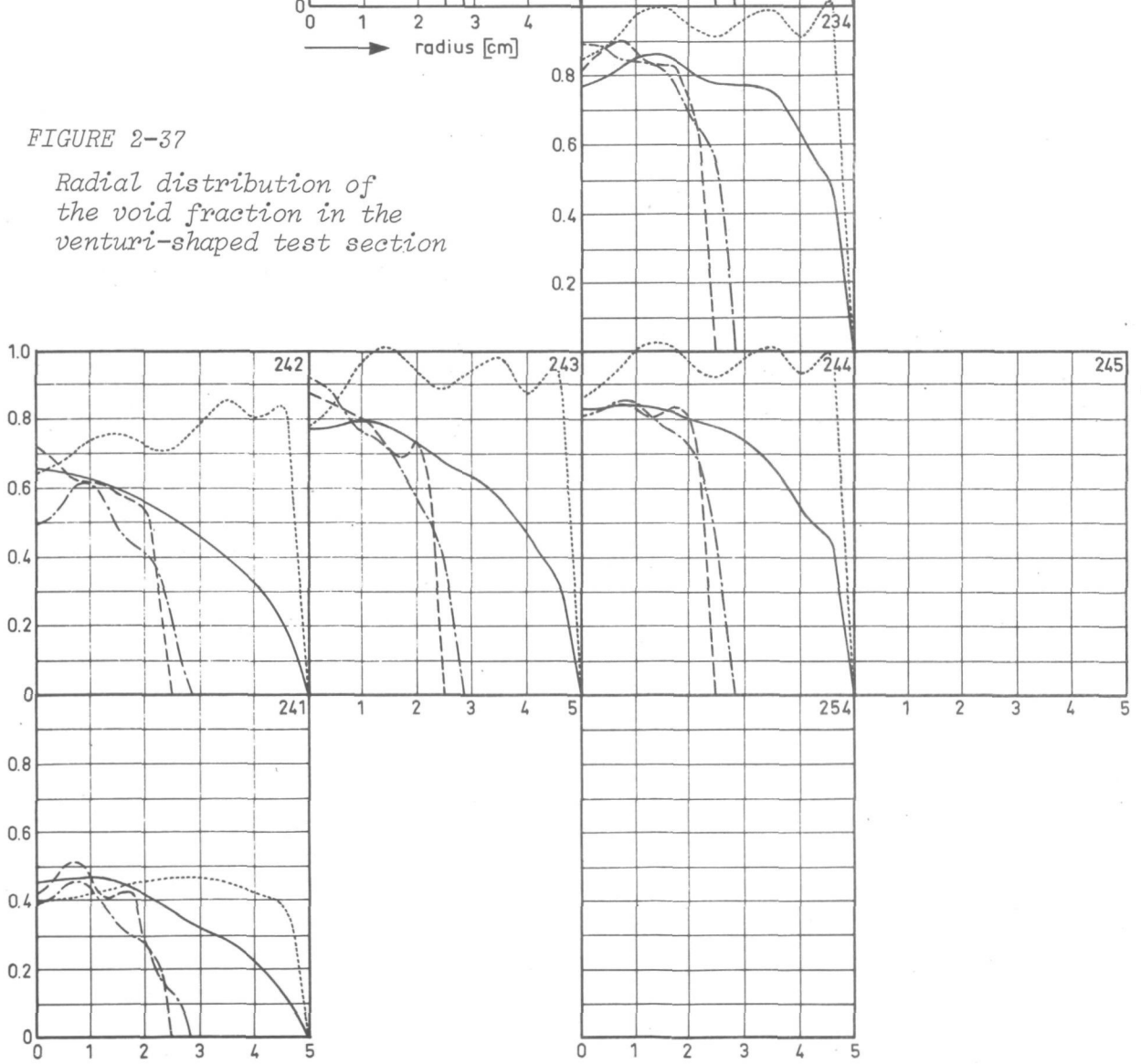


FIGURE 2-37

*Radial distribution of the void fraction in the venturi-shaped test section*



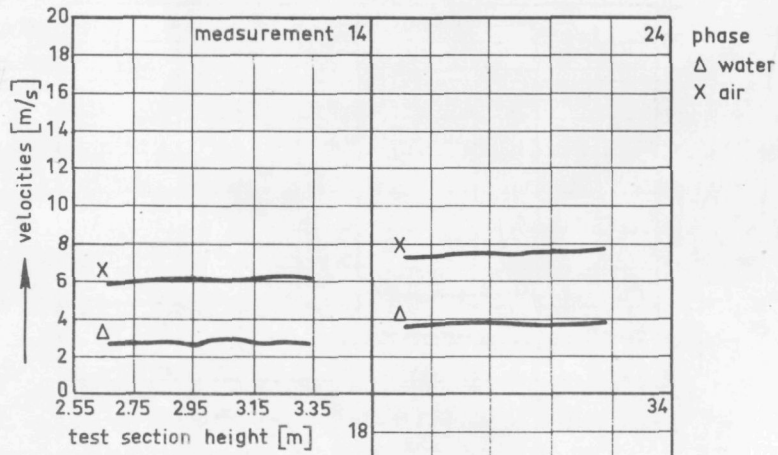
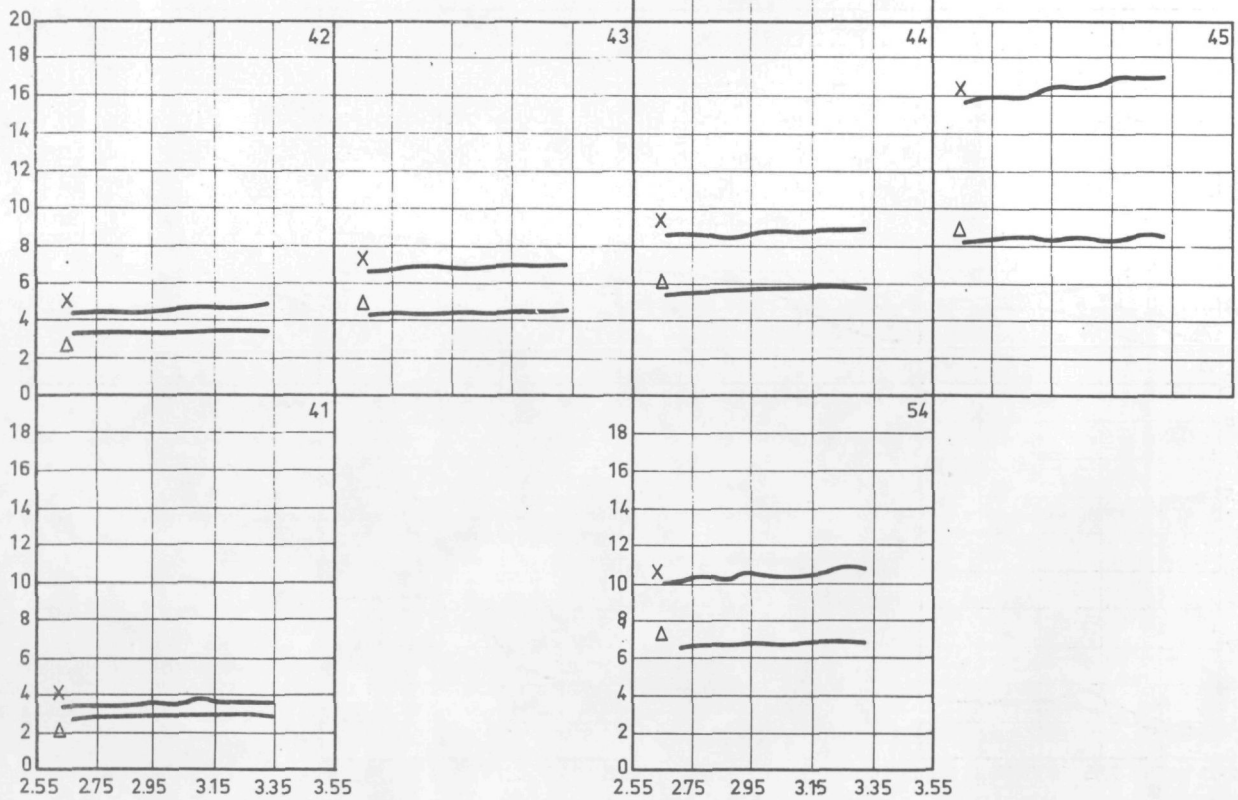


FIGURE 2-38

*Axial distribution of the phase velocities in the straight test section*



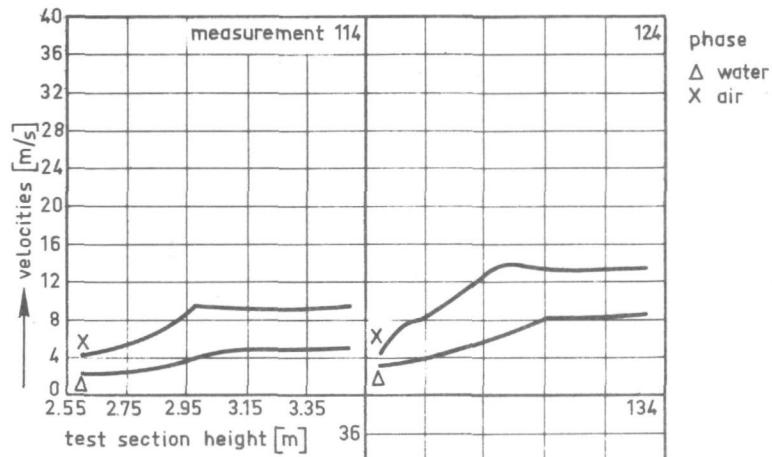
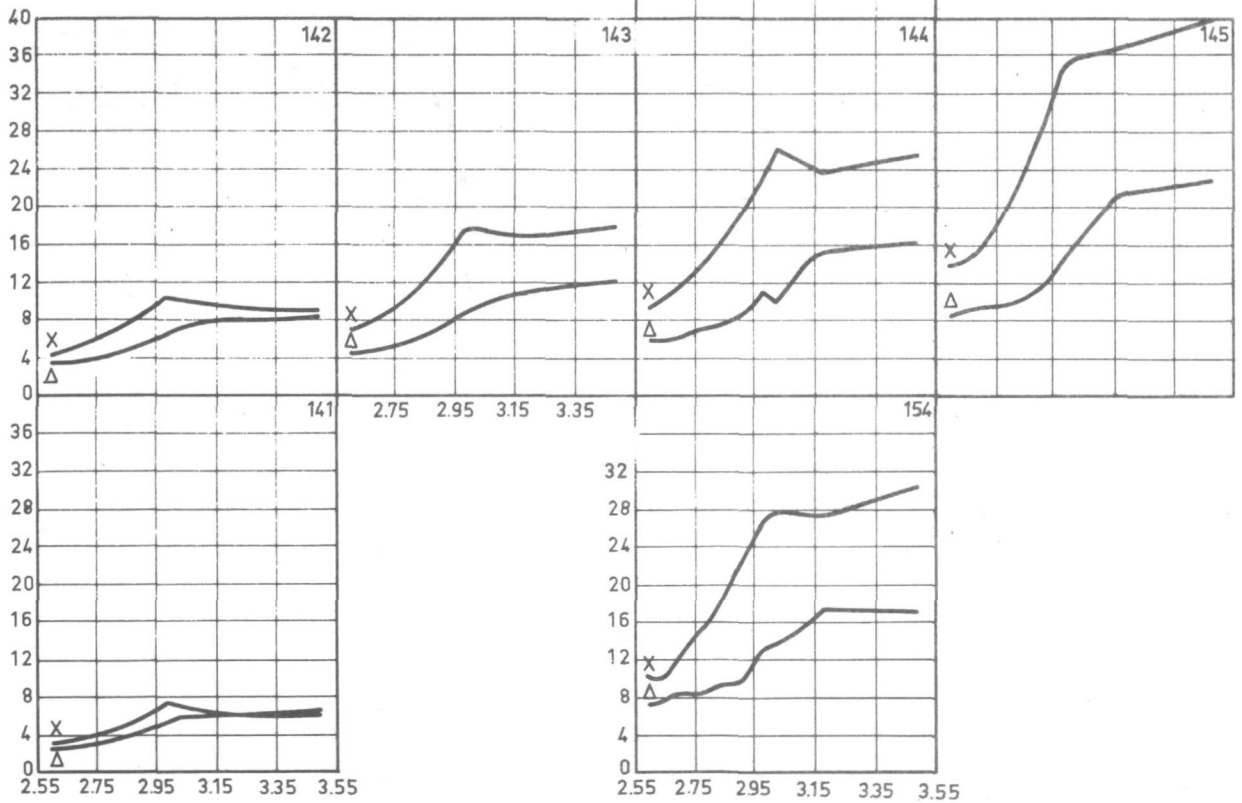


FIGURE 2-39

*Axial distribution of the phase velocities in the converging test section*



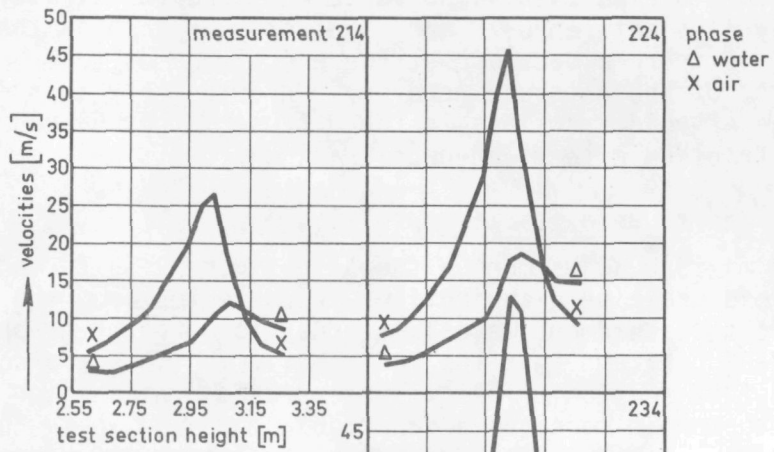
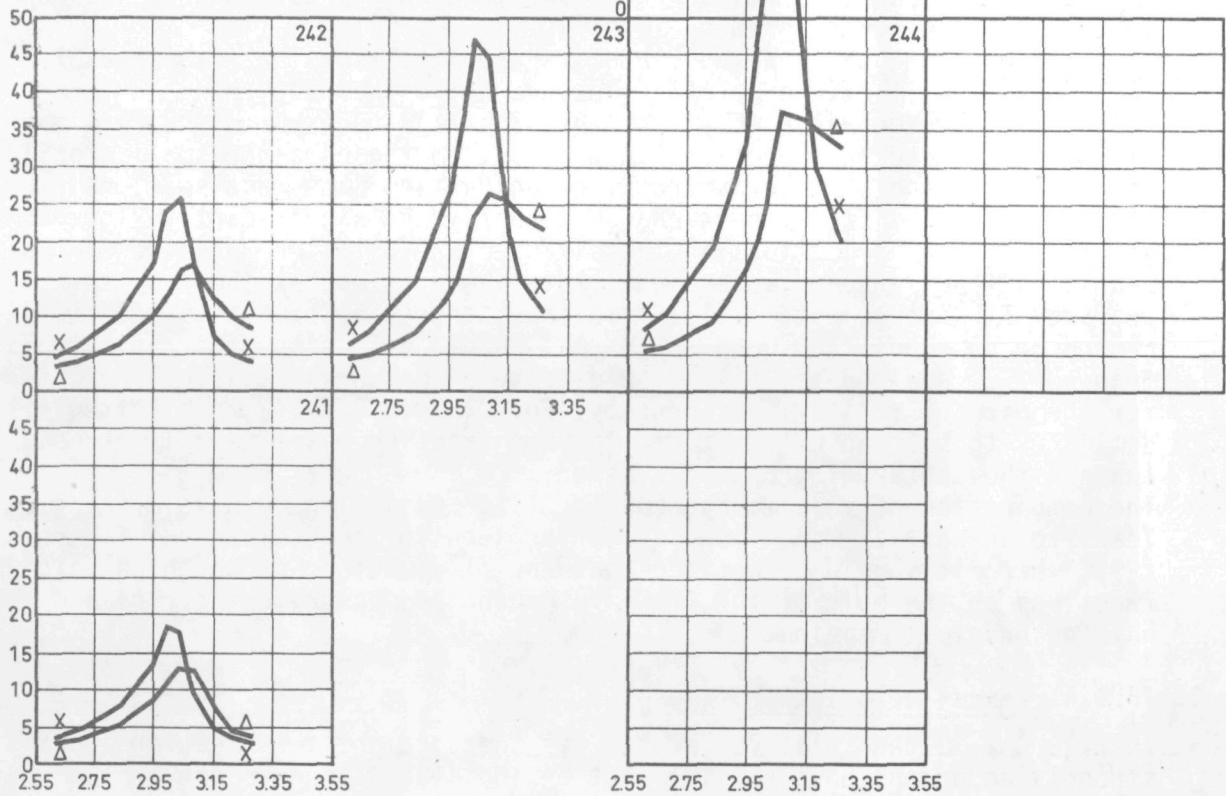


FIGURE 2-40

*Axial distribution of the phase velocities in the venturi-shaped test section*



This fact appears clearly for the experiments in the venturi-shaped test section (figure 2-34) where the void fraction increase in the throat and diffuser as well as the decrease in the lower end of the cone are more marked than in the converging test section. The increase in volumetric quality due to expansion is so large that the void fraction in the diffuser generally lies between 0.75 and 0.95: only in case of the lowest void fraction is there a decrease at the end of the diffuser due to the compression effect of the pressure recovery. Unfortunately this increase restricts the range of void fractions in the diffuser, thus hampering the investigation of void fraction effects in decelerating flows.

#### 2.3.1.6.1.3. Radial void fraction profiles

For each mixture adjustment - shown in figure 2-35 through 2-37 - four radial void fraction distributions are selected from the ten measured at the various measurement levels in order to make the graphs more transparent. Figure 2-35 confirms that the radial distributions are constant along the straight test section as was to be expected. In addition it can be concluded that the error in local void fraction  $\Delta\alpha < 0.04$ , while the maximum errors occur mostly at high local void fractions.

The profiles are in agreement with the general shape function used in subsection 2.2.4. for computing two-dimensional effects. The shape depends mostly on mean void fraction: with increasing mean void fraction the void distribution becomes more homogeneous (flatter), while there is only a slight tendency to more peaked profiles with increasing superficial water velocity.

In the converging test section (figure 2-36) the profiles become slightly more peaked in the cone, which is in agreement with the small decrease of the mean void fraction, flattening again towards the tail end as is shown by the profiles at measurement level 10.

In the converging part of the venturi-shaped test section (figure 2-37) the same somewhat steeper profiles occur, while the flattening in the throat (measurement level 6) is of the same magnitude as in the tail end of the converging test section. In contrast to these rather small profile variations in the straight and converging parts of the test sections, the profiles in the diffuser part change abruptly and significantly. The radial void fraction distributions in the diffuser are almost homogeneous for all mean void fractions and superficial water velocities, as shown by the profiles at measurement level 10. In the author's opinion this effect is caused by superposition upon the normal bubble diffusion of a radial mass transport - required to "fill" the diffuser - which is relatively greater for the air due to its lower density. For measurement 242 this latter effect dominates to such an extent that the void fraction near the wall exceeds that in the center of the test section.

The combination of this homogeneous profile and a high mean void fraction leads to an annular mist flow, as can be seen in the "column" of figure 2-37, where it should be noticed that the fluctuations of the high void fractions in the bulk of the flow are caused by measurement errors and have no physical meaning.

#### 2.3.1.6.1.4. Axial velocity profiles

In figure 2-38 the relative velocity in the straight test section appears strongly dependent on the void fraction and almost independent of the superficial water velocity. This is in agreement with the data of SMISSAERT [36] discussed in subsection 2.2.2.1.4., as borne out by figure 2-41 showing some of the present author's and Smissaert's data. The higher relative velocity found by Smissaert for the higher void fractions may be attributed to the larger frictional pressure drop caused by the smaller

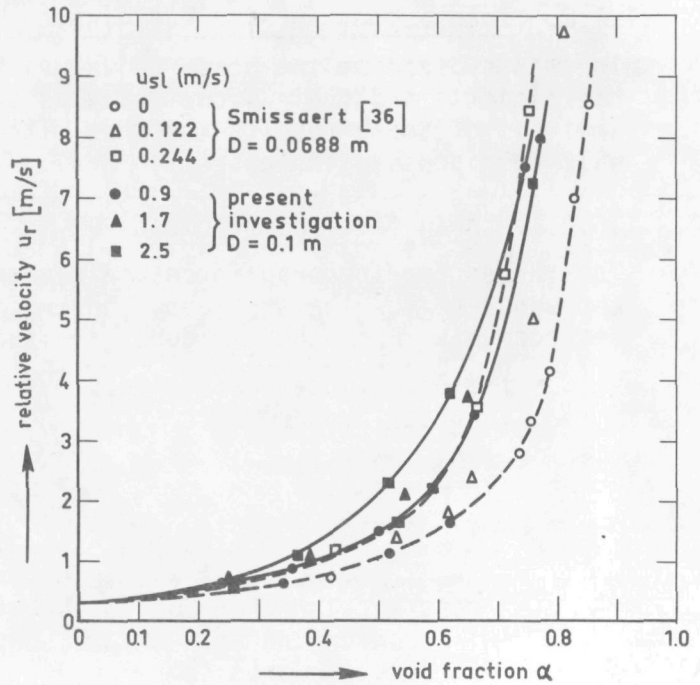


FIGURE 2-41

Comparison of Smissaert's and present data

test section diameter, an effect which becomes significant for these higher void fractions.

The acceleration in the converging test section of both water and air, the latter more marked due to the lower air density, is clearly seen in figure 2-39. There even occurs an overshoot of the air velocity at the end of the cone which, however, is eliminated in the first 0.2 m of the tail end.

The same overshoot of the air velocity occurs in the converging part of the venturi-shaped test section (figure 2-40), where in addition an "undershoot" occurs in the diffuser part. This greater deceleration of the air is even of such a magnitude that the relative velocity becomes negative in the upper part of the diffuser and the downstream tail pipe.

The magnitude of the velocities in this venturi-shaped test section - up to 74.5 m/s for the air at measurement 244 - is such as to raise the question of sonic velocity. From literature (e.g. WALLIS [7]) the velocity of sound for homogeneous flow (no slip between the phases) is known as

$$c^2 = \{(\alpha\rho_g + (1-\alpha)\rho_l)\left(\frac{\alpha}{\rho_g c_g^2} + \frac{1-\alpha}{\rho_l c_l^2}\right)\}^{-1} \quad (2-134)$$

reaching a maximum for adiabatic flow where the velocity of sound for air is determined by  $c_g^2 = \kappa_g R_g T$ . For such an adiabatic atmospheric air-water flow the velocity of sound lies between 25 and 30 m/s for void fractions between 0.2 and 0.8, values often exceeded by the air velocities in the venturi-shaped test section. However, in the present author's opinion only the continuous phase - i.e. the liquid - is relevant for the shock wave phenomena associated with the velocity of sound. Only for level 7 of measurement 244 does the water velocity exceed the velocity of sound for the actual conditions: 37.3 m/s vs. 32.1 m/s. However, even in this case no phenomena indicating supersonic flow in the diffuser occurred, confirming the present author's opinion that due to deviations from the homogeneous model underlying equation (2-134) and local variations of the void fraction and velocities in the actual cross section the water velocity did not exceed the velocity of sound.

### 2.3.1.6.2. Interaction force coefficients

In this subsection the measured values for the drag force and virtual mass coefficients and their error analyses are presented while the physical analysis of these results together with those of the steam-water experiments will be discussed in subsection 2.4..

#### 2.3.1.6.2.1. Drag force coefficient

The values for the drag force coefficient  $C_D$  are plotted in figures 2-42 through 2-44 for the straight, converging and venturi-shaped test section respectively. From these figures it is concluded that:

- ★ the drag force coefficients may be approximated with reasonable accuracy by:

$$C_D = 0.44 (1-\alpha)^6 \quad (2-135)$$

while noticing that

- the scatterband is wider for the converging and venturi-shaped test section than for the straight test section
- the converging and venturi-shaped test sections show a slight tendency towards somewhat lower coefficients
- ★ the coefficients are independent of the liquid velocity, hence the variation of the relative velocity with the liquid velocity - as measured by SMISSAERT [36] and in the present investigation (see figure 2-10 and 2-41) - must be attributed by the effects of varying frictional pressure gradient and bubble diameter
- ★ the aforementioned slight tendency to lower coefficients for accelerated flows will subsequently be found to result mainly from measurement errors and should therefore not be attributed to any significant influence of the acceleration.

Two error sources influencing the above results should be identified and corrected at this stage:

- measurement errors: in appendix 2-G it is shown that the measurement error in the liquid acceleration term - absent in case of the straight test section - results in large deviations for the measurements in the converging test section, which will further increase for the venturi-shaped test section. Appendix 2-G goes on to explain that these large deviations cause a downward shift in logarithmic graphs, which forms a plausible explanation for the differences in scatterbands visible in figures 2-42 through 2-44
- a two-dimensional effect not discussed in subsection 2.2.4., viz. the strong variation of the drag force coefficient  $C_D$  and the relative velocity  $u_r$  over a cross section due to the strong dependency of  $C_D$  on  $\alpha$ :  $C_D = 0.44 (1-\alpha)^6$  and the existence of a inhomogeneous void fraction distribution. This effect - to be further discussed and quantified in appendix 2-H - will generally cause a difference in location between the relative velocity used for computation of the coefficient  $C_D$  and the mean cross-sectional void fraction used in the proposed correlation for  $C_D$ . In appendix 2-H a numerical approximation is elaborated for the correct local void fractions: the resulting correlation for  $C_D$  based on the proper local void fractions is plotted in figure 2-45 together with some measurements from the diffuser part of the venturi-shaped test section, where this second two-dimensional effect does not exist because the void fraction distribution is almost homogeneous (cf. subsection 2.3.1.6.1.3.). Figure 2-45 shows a rather good agreement between these measurements,

FIGURE 2-42  
 Drag force coefficients in  
 the straight test section

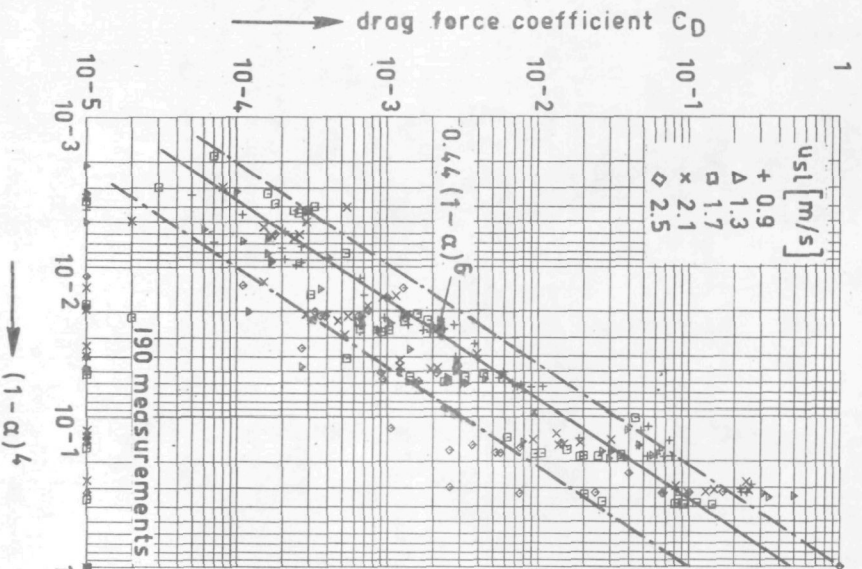
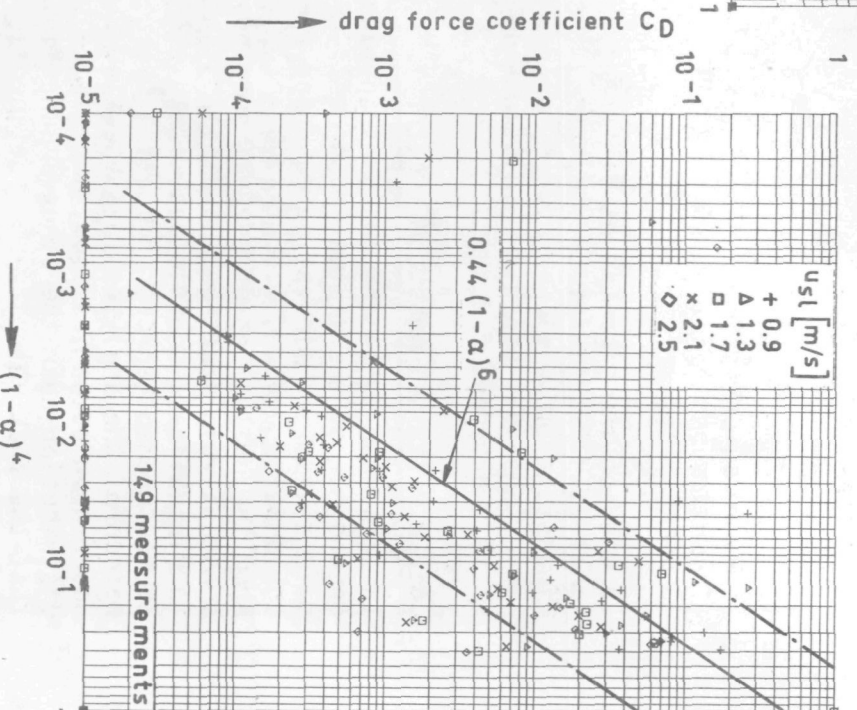
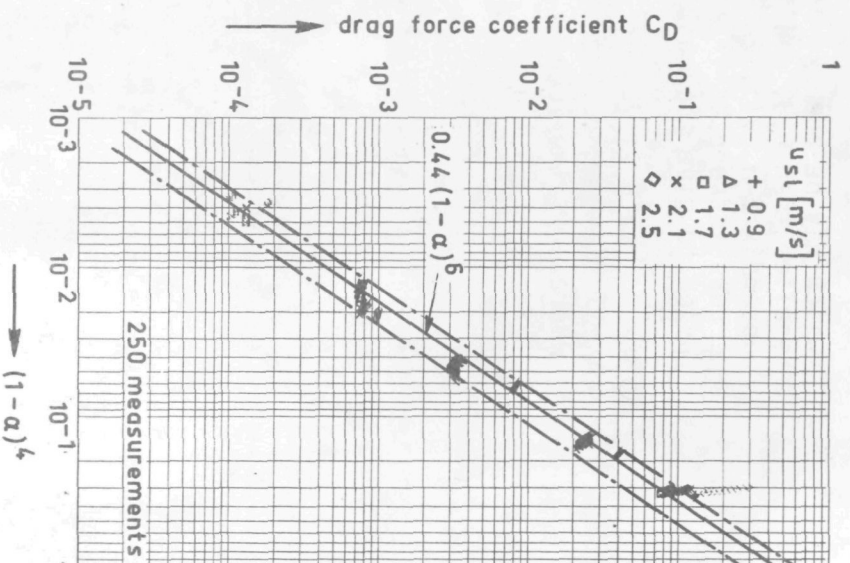


FIGURE 2-43  
 Drag force coefficients in  
 the converging test section

\* ) points at the bottomlines  
 represent negative values

FIGURE 2-44

Drag force coefficients in the venturi-shaped test section



which may be approximated by  $C_D = 0.44 (1-\alpha)^{4.25}$  for void fractions smaller than 0.8, and the numerical approximation proposed in appendix 2-H, viz.  $C_D = 0.44(1-\alpha)^{4.75}$ . In view of the possible errors introduced in appendix 2-H the actual measurements are supposed to give the most accurate correlation, yielding

$$C_D = 0.44(1-\alpha)^{4.25} \quad \text{for } \alpha < 0.8 \quad (2-136)$$

where  $\alpha$  is the local void fraction.

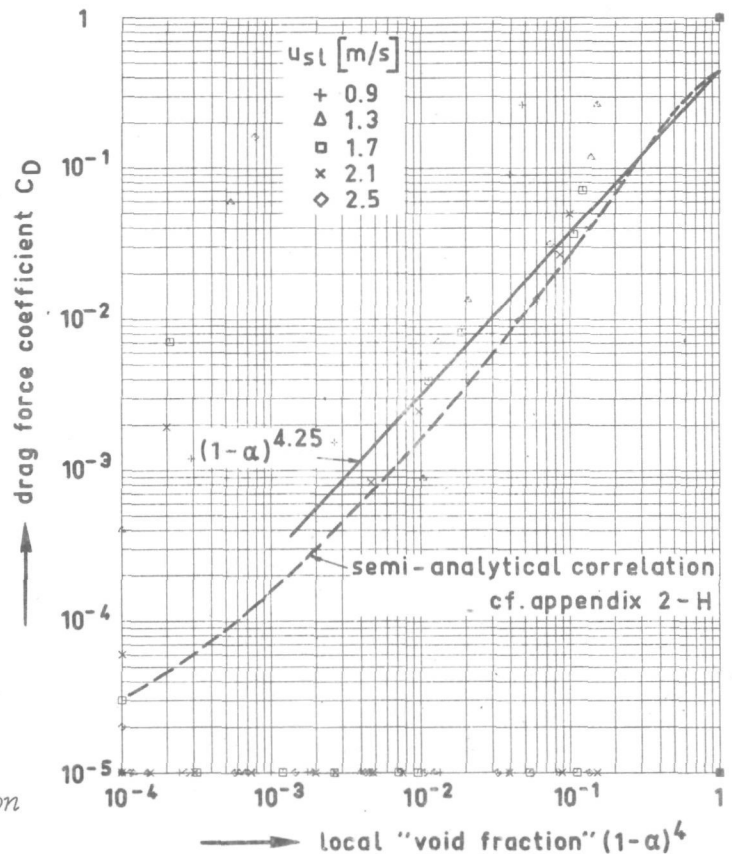


FIGURE 2-45

Measured  $C_D$ -values for homogeneous void fraction distributions

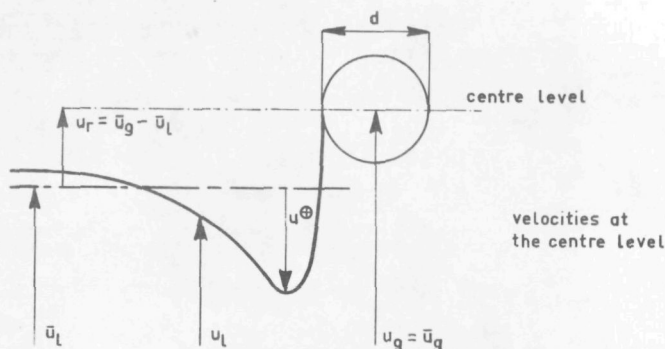
In view of the significant difference between the results on the basis of local void fractions:  $C_D = 0.44(1-\alpha)^{4.25}$  and those for the pseudo-one dimensional model:  $C_D = 0.44(1-\langle\alpha\rangle)^6$  - including the abovementioned second two-dimensional effect - a distinction will be made further on between these two types of results.

#### 2.3.1.6.2.2. Virtual mass coefficient

In accordance with the analyses in subsection 2.2.2.2. the possible dependence of the virtual mass coefficient  $B$  on void fraction  $\alpha$  and slip  $s$  was first investigated under the assumption that these dependences could be separated, i.e. that  $B = K_B \cdot g(\alpha) \cdot h(s)$ . From the evaluation of several sets of data, each having approximately constant void fraction  $\alpha$  and slip  $s$  it appears, however, that the variations in virtual mass coefficient within each group exceed the normal scatter due to measurement errors indicating the need for a third parameter. Reexamination of the analyses in subsection 2.2.2.2. shows that these are all based upon potential flow, implying a constant shape of the velocity distribution near the spheres under investigation. This in turn implies that the peak velocity  $u^{\oplus}$  - defined in figure 2-46 - for potential flow

FIGURE 2-46

Liquid velocity near a sphere



around a single sphere always equals half the relative velocity  $u_r$  (see e.g. [41]), whereas it is highly likely that the peak velocity ratio  $\frac{u^{\oplus}}{u_r}$  will in reality vary with other parameters such as the liquid viscosity. Inclusion of the peak velocity ratio  $\frac{u^{\oplus}}{u_r}$  as a relevant parameter for the virtual mass coefficients yields a general correlation:

$$B = K_B \cdot f\left(\frac{u^{\oplus}}{u_r}\right) \cdot g(\alpha) \cdot h(s) \quad (2-137)$$

The peak velocity ratio  $\frac{u^{\oplus}}{u_r}$  is analysed in appendix 2-I and it is found that:

$$\frac{u^{\oplus}}{u_r} = \frac{Re}{K_6} \left(1 - \sqrt{1 - \frac{K_7}{ReWe}}\right) \quad \text{for } ReWe \geq K_7 \quad (2-138A)$$

and

$$\frac{u^{\oplus}}{u_r} = 2 \frac{Re}{K_6} \quad \text{for } ReWe < K_7 \quad (2-138B)$$

where  $Re = \frac{(1-\alpha)\rho_l u_r d}{\eta_l}$ ,  $We = \frac{(1-\alpha)\rho_l u_r^2 d}{\sigma}$ , while the constants  $K_6$  and  $K_7$  have to be determined together with the function  $f\left(\frac{u^{\oplus}}{u_r}\right)$ .

The determination of each of the three functions  $f\left(\frac{u^{\oplus}}{u_r}\right)$ ,  $g(\alpha)$ ,  $h(s)$  and the constant  $K_B$  is discussed and described in appendix 2-J. These analyses yield as a final, slip-independent ( $h(s) = 1$ ) correlation

$$B = \frac{1}{2} \frac{2}{1+(1-\alpha)^4} \left(2 \frac{u^{\oplus}}{u_r}\right)^{0.65} = \frac{1.569}{1+(1-\alpha)^4} \cdot \left(\frac{u^{\oplus}}{u_r}\right)^{0.65} \quad (2-139)$$

in which the constants  $K_6$  and  $K_7$  - of correlation (2-138) for the peak velocity ratio  $\frac{u^{\oplus}}{u_r}$  - are determined as 10000 and 35000, respectively.

The separate dependencies on void fraction  $\alpha$  and peak velocity ratio  $\frac{u^{\oplus}}{u_r}$  are shown in figures 2-47 through 2-50. From these figures it appears that the correlation is mainly based upon the values measured in the converging test section; the scatterband found for these measurements is of the same magnitude as that for the  $C_D$  values in the converging test section (cf. figure 2-43).

The scatterband for the experiments in the venturi-shaped test section is much larger than that of the converging test section, as might be expected from the error analysis of appendix 2-G, while the shift to lower values

FIGURE 2-47

Dependence of the virtual mass coefficients on peak velocity ratio (converging test section)

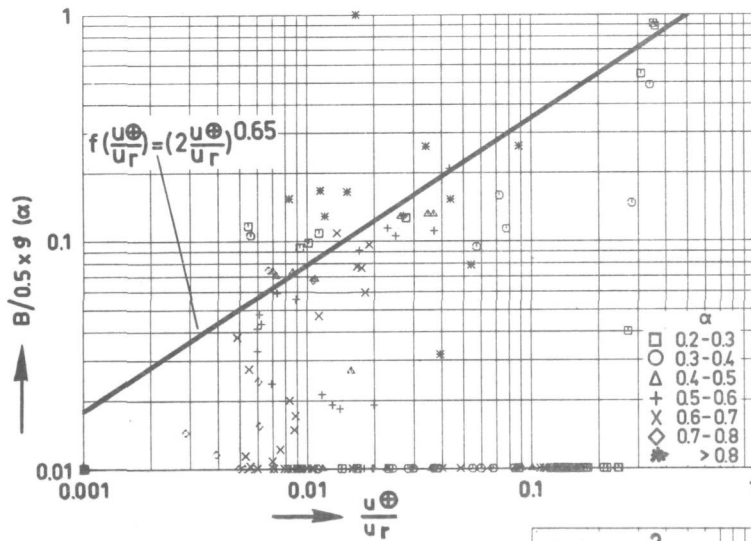
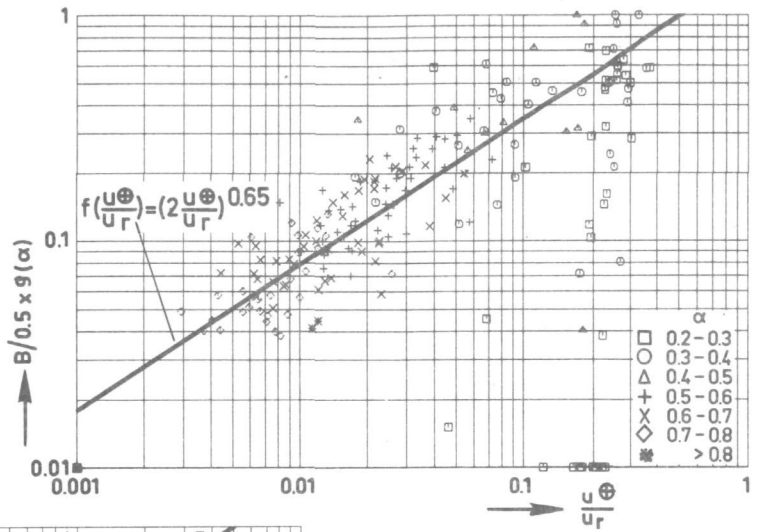


FIGURE 2-48

Dependence of the virtual mass coefficients on peak velocity ratio (venturi-shaped test section)

FIGURE 2-49

Dependence of the virtual mass coefficients on void fraction (converging test section)

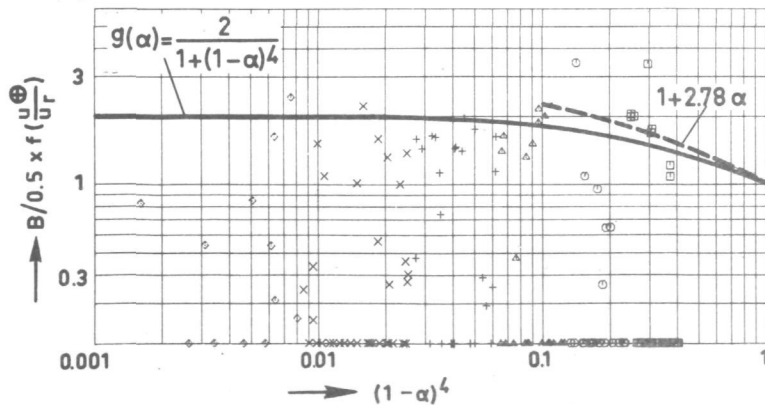
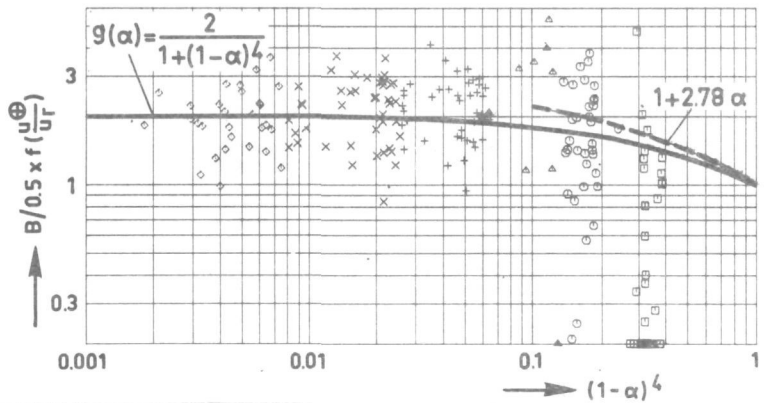


FIGURE 2-50

Dependence of the virtual mass coefficients on void fraction (venturi-shaped test section)

\* points at the bottomlines represent negative values

- also found for the drag force coefficients - should again be attributed to these large measurements errors.

The following additional remarks on correlation (2-139) appear in order:

- ★ the value  $B = 0.5$  agrees with the analysis for a single sphere in potential flow ( $\alpha \rightarrow 0$  and  $\frac{u^\oplus}{u_r} = \frac{1}{2}$ ),
- ★ in the lower range of  $\alpha$  values the dependence on the void fraction  $g(\alpha) = \frac{2}{1+(1-\alpha)^4}$  - shown in figures 2-49 and 2-50 - is in good quantitative agreement with the function  $(1+2.78\alpha)$  derived analytically by VAN WIJNGAARDEN [ 43 ].
- ★ the dependence on the void fraction is so weak that the correction from mean to local void fraction discussed in appendix 2-H and subsection 2.3.1.6.2.1. may be omitted. Hence correlation (2-139) is valid for both cross-sectional mean and local void fractions.
- ★ the independency on the slip is concluded to be very likely in appendix 2-J, but cannot be proved by large changes in accuracy of the investigated correlations with respect to the experimental results.
- ★ the virtual mass coefficients fitting this correlation exceed the values obtained from Prins' correlation (2-69):  $B = 3.155(1-\alpha)^{10.85}$  by several orders of magnitude. This significant difference is due to the fact that Prins, in obtaining his correlation from experimental results, has taken the virtual mass coefficient  $B$  constant along the test section. In this way the part  $\alpha A \rho_1 u_g u_r \frac{dB}{dz}$  of the virtual mass term  $\frac{d}{dz} \alpha A \rho_1 B u_g u_r$  is omitted from the momentum balances, whereas the present computations indicate it to be mostly large compared to the remaining part  $B \frac{d}{dz} \alpha A \rho_1 u_g u_r$  and always negative in the converging parts of the test sections due to the negative differential quotient  $\frac{dB^*}{dz}$ . Hence this omission will result in the much lower virtual mass coefficients reported in [ 1 ].

### 2.3.2. Steam-water experiments

These experiments differ significantly from the air-water experiments by the absence of the void fraction measurements. The steel pressure vessel enclosing the test sections - necessary at the process conditions ranging up to nuclear reactor operating conditions (7 MN/m<sup>2</sup> and 286°C) - makes it impossible to use the  $\gamma$ -ray technique applied for the void fraction measurement in the air-water experiments. Nor is there another void fraction measuring technique which can be readily used under these circumstances.

#### 2.3.2.1. Outline of the method

Because of the absence of measured void fractions the methods for computing the experimental values of the drag force coefficient  $C_D$  and virtual mass coefficient  $B$  will have to differ from those applied before. Mathematically spoken the lack of the void fraction measurements presents a problem with two equations: the momentum balances, and three unknowns: void fraction  $\alpha$ , drag force coefficient  $C_D$  and virtual mass coefficient  $B$ , requiring the

★) *The splitting of the virtual mass term - as announced in subsection 2.3.1.1.2. - is mostly done to evaluate the relative importance of these two parts.*

introduction of a third equation. This third equation differs for the experiments in the straight and converging\*) test sections, viz.:

- in the straight test section the acceleration due to condensation/flashing of the steam is small enough for the virtual mass term to be neglected, leaving the void fraction  $\alpha$  and drag force coefficient  $C_D$  as unknowns
- in the experiments with the converging test section a correlation for the drag force coefficient  $C_D$  is introduced, while the virtual mass coefficient  $B$  and the void fraction are computed from the two momentum balances.

This correlation for  $C_D$  will partly be based on knowledge gained from the air-water experiments and partly on the experimental data obtained from the measurements with steam-water mixtures in the straight test section. In subsection 2.3.1.6.2.1. it is concluded for the air-water mixtures that the acceleration in the converging test section does not significantly affect the values for  $C_D$ . The same is supposed to hold for the steam-water mixtures and the correlation for the drag force coefficient  $C_D$  found in the straight test section for steam-water mixtures will therefore be used in the computations for the converging test section.

Further details of these two computations will be discussed in the next two subsections.

#### 2.3.2.1.1. Drag force coefficient

As in the case of the air-water experiments the drag force coefficient  $C_D$  is computed on the basis of the liquid phase momentum balance for pseudo one-dimensional flow (2-107), yielding:

$$\frac{C_D}{d} = \frac{K_6 \rho_l \frac{d}{dz} ((1-\alpha)u_l^2) + K_7 (1-\alpha) \frac{dp}{dz} + K_8 (1-\alpha) \rho_l g + \left(\frac{dp}{dz}\right)_{fr}}{\frac{1}{4} \alpha \rho_l (K_{51} u_g^2 + K_{52} u_l^2 - K_{53} u_g u_l) \frac{|\sqrt{K_{51}} u_g - \sqrt{K_{52}} u_l|}{\sqrt{K_{51}} u_g - \sqrt{K_{52}} u_l}} \quad (2-140)$$

which differs from equation (2-113) by the elimination of the flow area  $A$  which is constant in the present computations because no drag force coefficients are computed in the converging test section.

The quotient  $\frac{C_D}{d}$  is subsequently multiplied by the bubble diameter  $d$  computed from correlation (2-98) in order to obtain the drag force coefficient  $C_D$ . The right hand side of expression (2-140) is computed from measurements of

- pressure distribution along the test section (cf. subsection 2.3.2.4.2.2.), yielding the pressure gradient  $\frac{dp}{dz}$
- the water and steam mass flows  $\phi_{ml}$  and  $\phi_{mg}$  (cf. subsection 2.3.2.4.2.1.), yielding the liquid velocity  $u_l = \frac{\phi_{ml}}{(1-\alpha)\rho_l A}$  and gas velocity  $u_g = \frac{\phi_{mg}}{\alpha \rho_g A}$ . These mass flows will be corrected for variations along the test section due to condensation/flashing, which will be expressed in term of the quality  $x = x(z)$ .

The void fraction - needed in expression (2-140) - is computed from the

\*) The experiments with the venturi-shaped test section were omitted because they yield almost no additional information, as apparent from the air-water experiments.

mixture momentum balance, which is chosen because of the absence of the drag force. This balance yields the expression

$$\alpha = \frac{K_1 \frac{d}{dz} (\alpha \rho_g u_g^2) + K_6 \rho_l \frac{d}{dz} ((1-\alpha) u_l^2) + K_3 \frac{dp}{dz} + K_8 \rho_l g + \left(\frac{dp}{dz}\right)_{fr}}{K_3 (\rho_l - \rho_g) g} \quad (2-141)$$

which is obtained by

- addition of the gas phase and liquid phase momentum balances (2-106) and (2-107) respectively
- omission of the virtual mass term (B and  $\frac{dB}{dz}$  taken equal to zero)
- substitution of  $K_7 = K_3$  and  $K_4 = K_8$  according to table 2-21
- elimination of the cross-sectional area A

The derivative  $\frac{d\alpha}{dz}$  appearing in the acceleration terms  $K_1 \frac{d}{dz} (\alpha \rho_g u_g^2)$  and  $K_6 \rho_l \frac{d}{dz} ((1-\alpha) u_l^2)$  of equations (2-140) and (2-141) should formally be obtained via an iterative computation and an additional polynomial approximation. However, these acceleration terms yield only a small correction in the momentum balances for the present steam-water flows, hence it is sufficiently accurate to obtain the derivative  $\frac{d\alpha}{dz}$  using a slip correlation and the "measured" derivative of the quality  $\frac{dx}{dz}$ . As derived in appendix 2-K this yields the expression

$$(1-\beta \frac{\partial K}{\partial \alpha}) \frac{d\alpha}{dz} = \frac{\beta^2 \rho_g}{x^2 \rho_l} \frac{dx}{dz} \quad (2-142)$$

where

- $\beta$  is the volumetric quality  $\beta = \frac{\phi_{vg}}{\phi_{vg} + \phi_{vl}}$
- the derivative  $\frac{\partial K}{\partial \alpha}$  is given by JONES and DIGHT [76] as  $\frac{\partial K}{\partial \alpha} = r(1-K_B)\alpha^{r-1}$  with  $r = 3.33 + 0.577\left(\frac{p}{p_{cr}}\right) + 4.74\left(\frac{p}{p_{cr}}\right)^2$ , while  $K_B = 0.71 + 0.29\left(\frac{p}{p_{cr}}\right)$  according to BANKOFF [4].

Because of the continuity of the polynomial approximations for the pressure and for the derivative of the void fraction, it is possible to compute the drag force coefficient and void fraction at any place along the test section. However, in order to limit the number of data and to achieve some conformity with the air-water experiments, the computations are only carried out for the locations of the pressure taps of the test section (cf. subsection 2.3.2.3.2.), resulting in ten values per mixture adjustment.

#### 2.3.2.1.2. Virtual mass coefficient

As mentioned above the virtual mass coefficient B is computed from the experiments with the conical test section, using the two available momentum balances and a correlation for the drag force coefficient  $C_D$  in order to solve for the virtual mass coefficient B and void fraction  $\alpha$ . The correlation for  $C_D$  is that obtained from the measurements in the straight test section discussed in subsection 2.3.2.6.2.1., while the virtual mass coefficient B is computed from the mixture momentum balance equation (2-114) also used for the air-water experiments. The derivative of the void fraction  $\frac{d\alpha}{dz}$  is obtained from the liquid momentum balance (2-107) yielding

$$\begin{aligned} \frac{d\alpha}{dz} = & \{-K_7(1-\alpha)A \frac{dp}{dz} - K_8(1-\alpha)A\rho_1g - (\frac{dp}{dz})_{fr}A + \\ & + \frac{3}{4}\alpha A \frac{C_D}{d} \rho_1 (K_{51}u_g^2 + K_{52}u_1^2 - K_{53}u_g u_1) \frac{|\sqrt{K_{51}u_g} - \sqrt{K_{52}u_1}|}{\sqrt{K_{51}u_g} + \sqrt{K_{52}u_1}} + \\ & + K_6\phi_{m1}(\frac{1}{A} \frac{dA}{dz} - \frac{1}{\phi_{m1}} \frac{d}{dz} \phi_{m1})\} / K_6 A u_1^2 \end{aligned} \quad (2-143)$$

The same fourth order predictor corrector method is used for the integration of  $\frac{d\alpha}{dz}$  and  $\frac{dB}{dz}$ . These two integrations of  $\frac{dB}{dz}$  and  $\frac{d\alpha}{dz}$  are carried out simultaneously because the frictional pressure drop  $(\frac{dp}{dz})_{fr}$  is affected by the acceleration terms including the virtual mass term, as mentioned at the end of subsection 2.2.3.1..

In the implementation of the abovementioned method of integration a procedure has to be found for computation of the initial values at the bottom of the test section: the absence of measured void fraction values introduces the need for an initial computation for  $\alpha$ , while application of the central difference approximation - used in the initial value computation of B for the air-water experiments - leads to wildly erratic B values in the case of steam-water experiments.

Both initial value computations are carried out for the straight part of the test section upstream of the cone and are based on:

- an iterative procedure for determining  $\frac{d\alpha}{dz}$ , in use to obtain the initial value of the void fraction
- the assumption that  $\frac{dB}{dz} = 0$  immediately ahead of the cone for obtaining the initial value of the virtual mass coefficient.

Computation of the void fraction  $\alpha$  starts with the approximation of  $\frac{d\alpha}{dz}$

- for the region from 0.17 up to 0.07 m ahead of the cone of the test section - on the basis of the derivative of the quality  $\frac{dx}{dz}$ , using equation (2-142). These derivatives  $\frac{d\alpha}{dz}$  and  $\frac{dx}{dz}$  are used in the liquid momentum balance (2-107)\* to compute the void fraction yielding

$$\alpha = \frac{K_6(\rho_1 u_1^2 \frac{d\alpha}{dz} + \frac{u_1}{A} \frac{d}{dz} \phi_{m1}) + K_7 \frac{dp}{dz} + K_8 \rho_1 g + (\frac{dp}{dz})_{fr}}{K_7 \frac{dp}{dz} + K_8 \rho_1 g + \frac{3}{4} \frac{C_D}{d} \rho_1 (K_{51}u_g^2 + K_{52}u_1^2 - K_{53}u_g u_1) \frac{|\sqrt{K_{51}u_g} - \sqrt{K_{52}u_1}|}{\sqrt{K_{51}u_g} + \sqrt{K_{52}u_1}}} \quad (2-144)$$

This equation for the void fraction  $\alpha$  is implicit because the liquid velocity  $u_1$  and the frictional pressure drop  $(\frac{dp}{dz})_{fr}$  depend on the void fraction  $\alpha$ . Hence this equation is solved using the Newton-Raphson method.

\* ) The liquid momentum balance is chosen, instead of that for the mixture used in subsection 2.3.2.1.1., because of the absence from the former of the virtual mass term which may not be omitted in the present computation.

The void fraction  $\alpha$  is thus computed at eleven equidistant points in the abovementioned region between 0.17 m and 0.07 m ahead of the cone, after which a first order polynomial approximation is computed for these void fractions. The constant first derivative  $\frac{d\alpha}{dz}$  of this polynomial is compared to the derivative used in equation (2-144) and the computation is repeated until these two derivatives differ by less than 0.0001.

The initial value computation for the virtual mass coefficient B is based on the normal forward integration of  $\frac{d\alpha}{dz}$  and  $\frac{dB}{dz}$  - as described above - starting at the end of the region considered for the void fraction computation, i.e. 0.07 m ahead of the cone. A large number of preliminary integrations using arbitrary initial values for the virtual mass coefficient B resulted - for each of the investigated mixture adjustments - in curves of the type shown in figure 2-51. The following remarks can be made pertinent to the use of these curves for the selection of appropriate initial values for the virtual mass coefficient B:

- in the conical part of the test section the curves are almost parallel, because the term  $\alpha A \rho_1 u_g u_r \frac{dB}{dz}$  is large compared to the term  $B \frac{d}{dz}(\alpha A \rho_1 u_g u_r)$ . Hence no selection criterion can be based on the values in this part of the test section.
- for each curve the derivative  $\frac{dB}{dz}$  is constant in the straight parts upstream of the cone and after about 0.2 m downstream of the cone, while the value of the derivative  $\frac{dB}{dz}$  depends strongly on the value for B because the two parts of the virtual mass term - mentioned above - are of the same magnitude.
- there exist two discontinuities in each curve, coinciding with the discontinuities in the test section. These are mathematically caused by the discontinuities of the derivative of the cross-sectional area  $\frac{dA}{dz}$  and are not realistic because the real flow contracts at these locations causing a smooth transition of the true cross-sectional area and its derivative.

The virtual mass coefficient has to be constant, i.e. its derivative must equal zero, in the straight parts of the test section. Hence the curve for which  $\frac{dB}{dz}$  equals zero both at the smoothed approximation of the transition

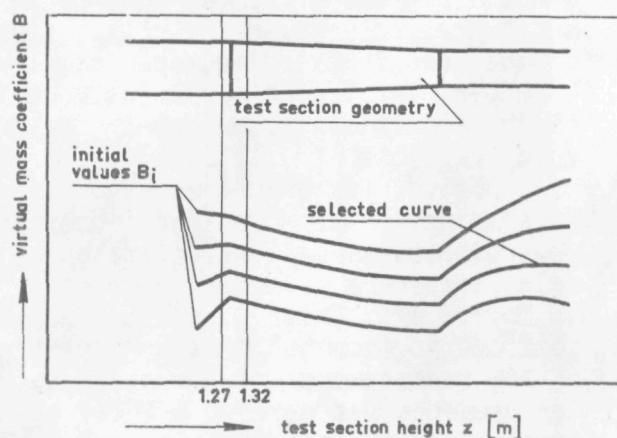


FIGURE 2-51

*Schematic curves for various initial values of the virtual mass coefficient*

from upstream cylinder to cone and at the tail end of the downstream cylinder should be selected. The former condition was mathematically reformulated to prescribe equal values for the virtual mass coefficients  $B$  some centimeters upstream and downstream of the cylinder-to-cone transition. Satisfactory results for the second condition -  $\frac{dB}{dz} \approx 0$  in the downstream part of the tail pipe - were obtained by referring this condition to the pressure taps 2 cm upstream and 3 cm downstream of that transition ( $z = 1.27$  and 1.32 m, respectively). This way of initial value computation will introduce an inaccuracy of about 35%, caused by:

- the statement  $B_{1.27} = B_{1.32}$ , whereas the decreasing curves for  $B$  in the converging part indicate that in reality the value  $B_{1.32}$  will be somewhat lower than  $B_{1.27}$ . By computing some curves for which  $B_{1.32}$  was 0.01 or 0.02 less than  $B_{1.27}$  it was found that the error introduced by the omission of this fact amounts to about 15%
- the rather arbitrary selection of  $z=1.27$  m and 1.32 m for comparison of the  $B$  values; small changes of these locations yield a variation of about 10% in the values for the virtual mass coefficient.
- the choice of 0.5 cm as a practical length of the integration step, particularly regarding the integration step straddling in the discontinuities in the test section geometry; computations with very small integration steps show a difference of about 10% in the values for  $B$  with respect to those obtained with the value of 0.5 cm actually selected to obtain a reasonable computation time.

While large by itself, this mathematically introduced inaccuracy is, however, small compared to that caused by measurements errors as apparent from the air-water experiments (cf. figures 2-47 through 2-50), and hence of minor importance.

The computation of the final curve for the coefficient  $B$  (and void fraction  $\alpha$ ) is performed for the region from 7 cm in front of the cone ( $z=1.22$  m) to 36 cm in the tail end of the test section ( $z=2.04$  m). For the reason mentioned for the drag force computations only ten values per mixture adjustment - viz. those at the pressure tap locations (cf. subsection 2.3.2.3.2.) - will be used for further evaluation of the experiments.

#### 2.3.2.2. Range of variables

The principle for establishing the mixture adjustments is the same as for the air-water experiments, viz. the combination of a number of fixed void fractions and a number of fixed superficial water velocities. For the purpose of comparison the adjustments used in the air-water experiments are included in the set of steam-water adjustments, while the omission of the void fraction measurements leads to such a reduction in the amount of experimental work per adjustment that the number of mixture adjustments can be significantly enlarged. In view of these considerations nine nominal void fractions were selected viz. from 0.1875 to 0.6875 in fixed intervals of 0.0625. Unfortunately the void fraction  $\alpha=0.75$  - as in case of the air-water experiments - could not be reached due to the large amount of carry-under steam, as will be discussed below. In addition ten superficial water velocities were selected increasing by fixed intervals of 0.2 m/s from 0.7 up to 2.5 m/s. These 90 mixture adjustments were applied in both test sections for nominal pressures of 5 and 7 MN/m<sup>2</sup>, yielding a total number of 360 measurements. Prior to these 360 measurements a full set of 90 measurements was carried out for both the straight and converging test sections - at pressures of 7 and 5 MN/m<sup>2</sup> respectively - in order to acquire experience in handling the test facility.

Because the adjustment parameters refer to the test section inlet - equal for both test sections - the adjusted flows are equal for the straight and converging test section.

The steam mass flows needed for the desired void fractions were determined from the results of the air-water experiments in the straight test section. The same void fractions are obtained for corresponding adjustments if the volumetric quality  $\beta$  is identical, as may be seen from the slip correlation of BANKOFF [ 4 ]:

$$s = \frac{1-\alpha}{K-\alpha} \quad (2-145)$$

which together with the definition of the slip

$$s = \frac{u_g}{u_l} = \frac{\phi v_g/\alpha A}{\phi v_l/(1-\alpha)A} = \frac{\beta}{1-\beta} \frac{1-\alpha}{\alpha} \quad (2-146)$$

yields

$$\alpha = K\beta \quad (2-147)$$

Because the constant K increases by about 10% by raising the pressure from atmospheric to 5 to 7 MN/m<sup>2</sup> (cf. appendix 2-K) the volumetric quality has to be reduced by 10% to obtain the same void fraction  $\alpha$ . However, this reduction of quality occurs "automatically" in the test facility, because the water - being mixed with somewhat superheated steam - is about 1 to 2°C subcooled and hence part of the steam is condensed. It appears that this condensation concerns about 10% of the steam flow, hence the initial adjustment of volumetric qualities identical to those of the air-water mixtures will result in the desired void fractions after mixing.

Table 2-52 - showing the steam flows before mixing - indicates that not all 90 adjustments have been realized. The steam flows for the lowest void fraction  $\alpha=0.1875$  are so low - less than 0.1 kg/s - as to be outside the normal range of the steam flow meters. The resulting measuring problems led to the deletion of these adjustments. For the highest void fractions carry-under flows exceed the capacity of the quench cooler (cf. subsection 2.3.2.3.1.), making it impossible to perform experiments at steam flows exceeding 1.7 kg/s. Because carry-under behaviour depends on test section geometry some of the experiments which could not be done with the straight test section succeeded with the converging test section, as apparent from table 2-52.

The final number of experiments was thus reduced to 143 for the straight test section and 136 for the converging test section, while 71 + 68 = 139 preliminary experiments were performed.

The coding system for these measurements is the same as for the air-water experiments. Each number consists of three figures. The first points to the test section geometry: 0 (which is often omitted) for the straight and 1 for the converging test section, the second figure refers to the superficial water velocity: from 1 for  $u_{s1}=0.7$  m/s up to 10 (written as 0) for  $u_{s1}=2.5$  m/s, while the third number indicates the void fraction: 1 for  $\alpha=0.1875$  up to 9 for  $\alpha=0.6875$ .

This number is followed by /5 or /7 indicating the nominal pressure of 5 or 7 MN/m<sup>2</sup> respectively, while preliminary measurements are additionally marked by a P at the end of the total code number.

It should be noticed that due to the larger number of steam-water experiments the air-water measurements bearing corresponding numbers do not have identical void fractions and superficial water velocities.

superficial water velocity m/s	water mass flow kg/s	nominal void fraction $\alpha$								
		0.1875	0.25	0.3125	0.375	0.4375	0.50	0.5625	0.625	0.6875
0.7	4.277 4.082			0.105 0.147	0.149 0.208	0.201 0.283	0.283 0.388	0.376 0.583	0.536 0.822	0.840
0.9	5.497 5.239		0.091 0.113	0.127 0.182	0.182 0.261	0.247 0.352	0.352 0.491	0.476 0.694	0.659 0.988	1.048
1.1	6.717 6.396		0.104 0.138	0.148 0.215	0.211 0.305	0.239 0.416	0.406 0.580	0.547 0.802	0.763 1.138	1.229
1.3	7.937 7.553		0.117 0.163	0.168 0.247	0.239 0.347	0.333 0.475	0.457 0.658	0.605 0.908	0.863 1.272	1.395
1.5	9.157 8.710		0.130 0.188	0.189 0.279	0.267 0.389	0.372 0.531	0.507 0.733	0.670 1.011	0.952 1.402	1.520
1.7	10.377 9.861	0.087 0.125	0.143 0.213	0.210 0.311	0.296 0.431	0.412 0.591	0.557 0.808	0.731 1.113	1.043 1.533	1.631
1.9	11.597 11.024	0.095 0.138	0.156 0.238	0.230 0.343	0.324 0.472	0.451 0.645	0.607 0.883	0.791 1.216	1.133 1.663	
2.1	12.817 12.181	0.104 0.152	0.169 0.263	0.251 0.375	0.353 0.514	0.491 0.702	0.657 0.958	0.850 1.319		
2.3	14.037 13.338	0.112 0.166	0.182 0.288	0.271 0.407	0.381 0.555	0.530 0.759	0.707 1.033	0.911 1.422		
2.5	15.257 14.495	0.120 0.180	0.195 0.313	0.291 0.439	0.409 0.597	0.570 0.816	0.757 1.108			

NOMENCLATURE

nominal pressure  $\frac{5 \text{ MN/m}^2}{7 \text{ MN/m}^2}$  test section geometry  
 ○ straight  
 △ converging

TABLE 2-52

Steam mass flows [kg/s] for the measurements at 5 and 7 MN/m<sup>2</sup>

2.3.2.3. Description of test facility

2.3.2.3.1. Steam-water loop and major components

The test facility is the same as used by PRINS [1] for his carry-under measurements, but adapted for a larger steam flow (2.2 kg/s) and equipped with a much larger number of taps for differential pressure measurements. The loop consists of five major subsystems - shown in the flow sheet figure 2-53 - viz.

- the pressure vessel - containing the test section - with its associated steam and water circulation
- the make-up water supply system for adding water during the measurements if required and to fill the pressure vessel before the first start up
- the cooling system for carry-under quenching
- the drain system for the removal of water formed by condensation of carry-under steam
- the differential pressure measuring system - not shown in figure 2-53 - consisting of 23 pressure taps, their penetrations through the vessel wall and a magnetic valve system for the same purpose as in the case of the air-water measurements: to measure a large number of pressure differences with only a few differential pressure cells (cf. figure 2-53 and subsection 2.3.1.4.3.)

The pressure vessel itself is an assembly of four interchangeable sections of 1.25 m length and 0.458 m ID and a bottom section of 0.625 m length. The sections are provided with a variety of nozzles for piping, thermocouple and electrical lead wiring penetrations, while the bottom section has in addition two water inlet nozzles and two water outlet nozzles, paired at opposite locations to enhance symmetric inlet and outlet flow. The steam entrance and exit nozzles are located in the centerline of the vessel, the former having a thermal sleeve to avoid excessive thermal stresses in the

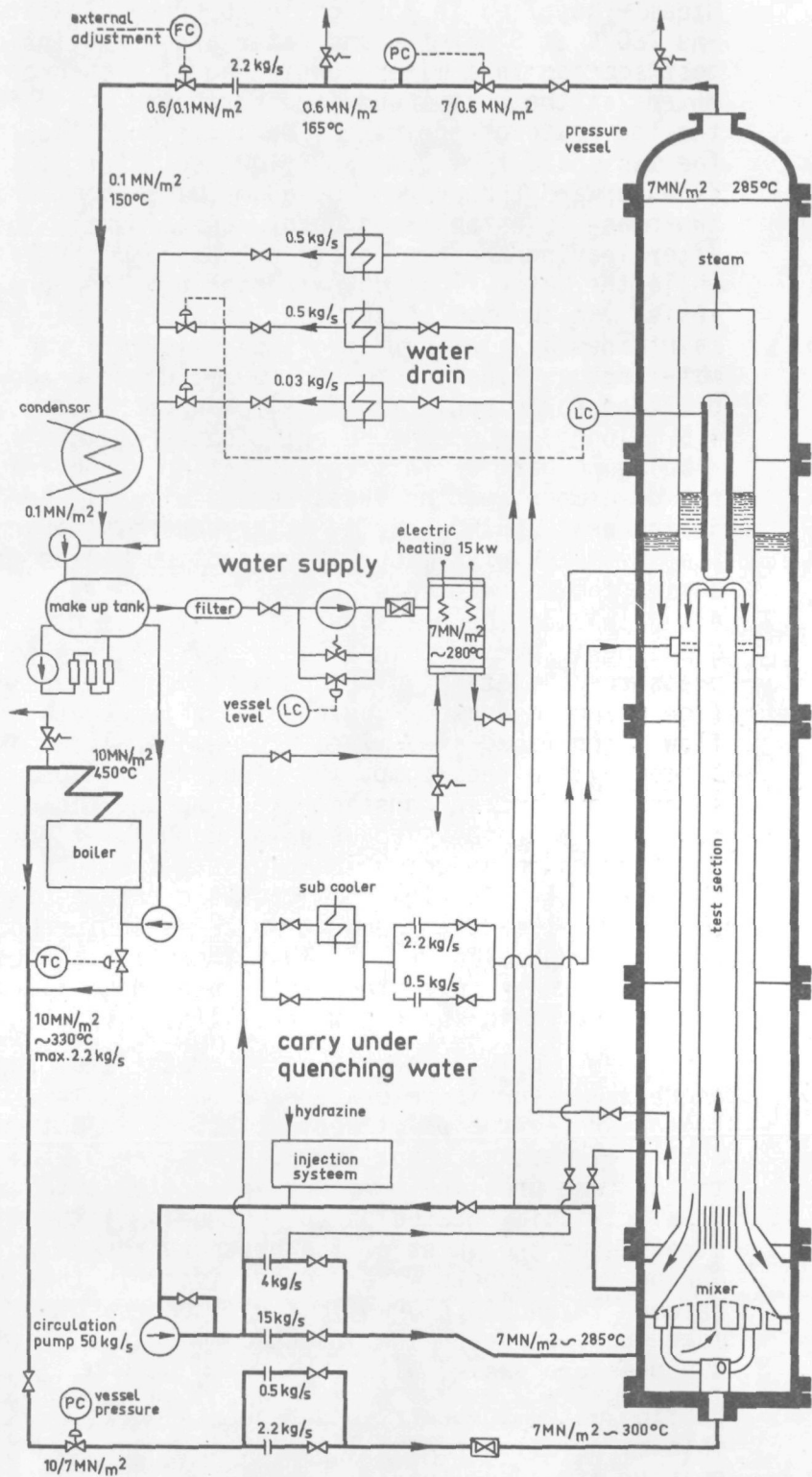


FIGURE 2-53

Flow sheet of the high pressure test facility

bottom plate.

Steam - supplied in a slightly superheated state, viz. 300°C at 7 MN/m<sup>2</sup> and 280°C at 5 MN/m<sup>2</sup> - and water are mixed inside the vessel ahead of the test section in a mixer consisting of a mushroom-shaped box where the steam enters at the bottom and is distributed over 360 holes (5 mm diameter) in the top plate of the mixer. Water is supplied through 61 pipes (16 mm ID). The two-phase flow passes a flow rectifier at the inlet of the riser and flows upward through the 0.100 m ID, 1.55 m long riser where fully developed two-phase is established before entering the test section.

After leaving the test section the steam separates at the free interface while the water flows downward through the annular downcomer, leaving the vessel via the two outlet nozzles. Forced circulation of the water is maintained by a Weise 50 kg/s circulation pump at 30 m pressure head. Two water return lines of 50 and 100 mm diameter downstream of the pump are provided for circulation flow measurements in two ranges. The 0.220 m ID, 4.5 m long downcomer tube anticipates on future separator measurements - being no part of this investigation - and leaves an annular cavity between the downcomer and the pressure vessel wall. To ensure uniform temperature during heat-up this cavity is temporarily linked with the main circulation loop by means of a manually controlled bypass flow. This flow is shut off during the measurements.

After leaving the pressure vessel via the dome the steam is reduced to atmospheric pressure in a reducing station - consisting of a pneumatic pressure-regulating valve and a hand-operated motor valve controlling the flow - and condensed. Condensate is pumped to a make-up tank, where a bypass flow is polished in a mixed bed demineralization filter and returned to the boiler by the feed pump. The reducing station in this steam outlet line serves to maintain constant pressure and flow in the test vessel. The desired flow rate is adjusted by manual set point adjustment of the motor-operated valve reducing the pressure from 0.6 down to 0.1 MN/m<sup>2</sup>. Any deviation of this flow rate causes a change of the pressure in the 0.6 MN/m<sup>2</sup> section of the steam conduit which is in turn corrected by the pneumatic pressure-regulating valve. This then affects the pressure in the test vessel which is corrected by the pneumatically operated vessel pressure control valve in the steam inlet line.

The water supply system takes its water from the atmospheric make-up tank, where the water is deaerated and purified in a mixed bed demineralization filter, while the pH is kept at 9.5 by injection of ammonia and the conductivity reaches about 10 μS. A Dosapro 0.27 kg/s pump raises the water to the test pressure. Prior to injection into the test system the water is electrically heated up to just below saturation in order to avoid thermal stresses at the inlet of the pressure vessel.

During measurements water conductivity in the pressure vessel rises to between 10 and 40 μS, while the pH decreases to about 7 because little make-up is used and the injected ammonia and hydrazine dissociate and leave the pressure vessel with the steam.

Cooling water for carry-under quenching is branched off from the 100 mm main circulation return line. It is injected into the downcomer through a sparger after cooling in a shell-and-tube subcooler. Flow and temperature of this quenching water are manually controlled - by valves at the subcooler exit and a bypass around it - in such a way that the circulation water temperature at the bottom of the downcomer is maintained at about 0.5 to 1°C below saturation to prevent cavitation in the circulating pump.

The water draining system maintains a constant level in the riser/downcomer assembly by compensating for the condensation of the steam in the mixer and downcomer. The two drain coolers - with capacities of 0.03 and 0.5 kg/s

respectively - are equipped with pneumatic valves operated by the capacitance level gage detecting the two-phase interface above the test section. A third manually controlled cooler - with a capacity of 0.5 kg/s - serves the annular cavity where overflow water from the riser/downcomer collects in the case of measurements with large mass flows.

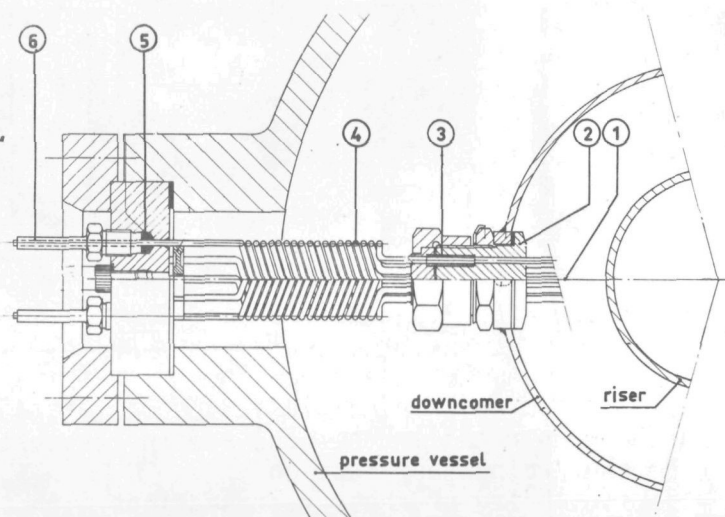
The differential pressure measuring system is essentially the same as used for the air-water experiments (cf. figure 2-25 and subsections 2.3.1.4.3.) and has the following features

- 29 pressure differences are measured with only 3 differential pressure cells, by the use of a magnetic valve system
- the central processing unit controlling the magnetic valve system provides for paired "positive" and "negative" measurements for eliminating drift, each consisting of five data recorded at intervals of 0.75 seconds to handle the stochastic character of the measured signals

The most significant difference compared to the air-water experiments is the temperature alarm causing a shutdown of all magnetic valves if any temperature in the differential pressure piping system outside the pressure vessel exceeds 40°C. This serves to prevent a meltdown of the plastic parts in the interior of the magnetic valves.

FIGURE 2-54

*Pressure tap penetration through downcomer tube and pressure vessel wall.*



1. six pressure tap connections, arising from test section and/or riser
2. conveyance through the downcomer tube
3. connection tube
4. flexible cross over
5. sealing (magnesium-silicate)
6. six outside pressure tap connections

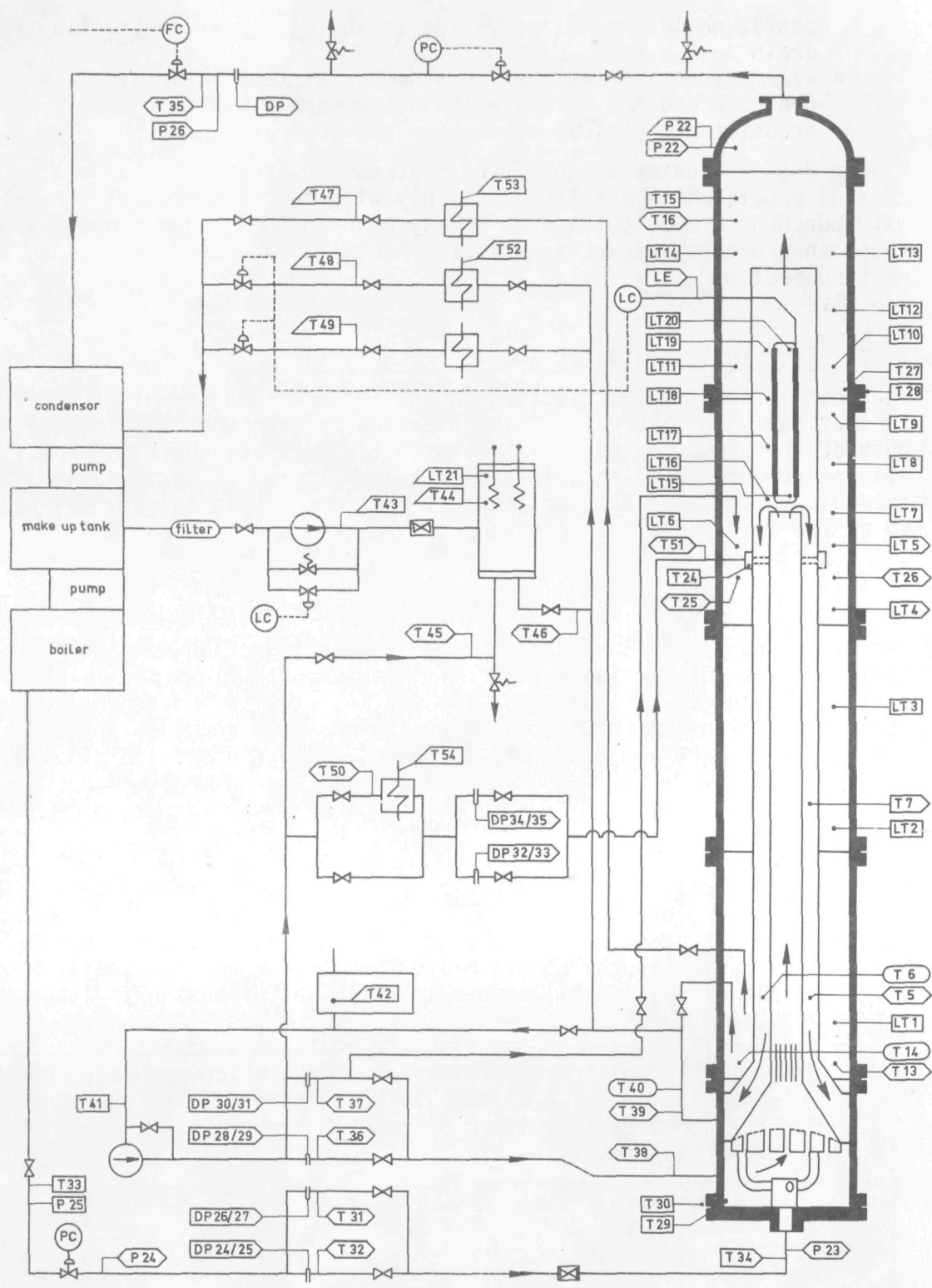
Special precautions are taken to provide for flexible connections between the pressure taps on the test section and the vessel penetrations - shown in figure 2-54 - in order to accommodate differences in thermal expansion between the carbon steel pressure vessel and the stainless steel riser/downcomer assembly.

#### 2.3.2.3.2. Test section geometries

Apart from manufacturing inaccuracies the two test sections shown in figure 2-55 are identical to the straight and converging test section of the air-water experiments.

Both test section geometries contain 18 pressure taps, the 3 lowest of which are located in the common inlet section. The remaining 15 pressure taps





- |   |  |   |                                |
|---|--|---|--------------------------------|
|  | CONTROL PANEL                              |  | DP differential pressure       |
|  | PUNCHED TAPE                               |  | P pressure                     |
|  | BOTH PANEL AND TAPE                        |  | LE level (capacitance)         |
|  | ACOUSTIC ALARM<br>(and optic at the panel) |  | LT. level test (on/off switch) |
|  | RESERVE                                    |  | T temperature                  |

FIGURE 2-56  
 Loop instrumentation diagram

panel, while the latter yields an analog signal controlling the drain

- alarm system for monitoring a number of temperatures, the vessel pressure and the level in the water supply heating vessel, with acoustic and optical signals on the control panel

Figure 2-56 indicates which of the instruments have a display at the control panel, which are linked up only with the data acquisition system with punched tape output and which may be used for both purposes. These instruments - together with the test instruments discussed in the next subsection - are listed in appendix 2-L where further particulars are given.

#### 2.3.2.4.2. Test instrumentation and data acquisition

The test instrumentation located inside the pressure vessel is shown schematically in figure 2-57; the flow and temperature instrumentation outside the pressure vessel is shown in figure 2-56, while the details of all instruments are listed in appendix 2-L. It may be worth noting that the output signal of each of the test instruments can be read out separately at the analog-digital converter of the data acquisition system.

##### 2.3.2.4.2.1. Flow measurements

This subsection describes the measuring techniques and formulae for obtaining the water and steam flow rates through the test section, needed for computation of the interaction force coefficients. Both flows are measured by venturi flowmeters according to DIN 1952 [69], with subsequent corrections for condensation/evaporation based on thermocouple readings.

The mass flows are computed from formula (2-115) (subsection 2.3.1.4.1.):

$$\phi_m = \beta A_0 \sqrt{2\rho\Delta p}$$

where

- the venturi coefficient  $\beta A_0$  is provided by the manufacturer with negligible error
- the pressure difference measurements yield a standard deviation of 2.9% caused by the normal measurement error and fluctuations on behalf of small oscillations together, as discussed in subsection 2.3.2.4.2.2.
- the density  $\rho$  is computed from the measured temperature and pressure using the subroutines of reference [77], which are based on the IFC-formulations. The errors in the temperature and pressure required for the steam density are 0.5 and 0.1% respectively, yielding a total error in the steam flow of

$$\sqrt{\frac{1}{2}2.9^2 + \frac{1}{2}(0.5^2 + 0.1^2)} = \pm 2.08\%$$

The error in the water density due to the pressure measurement is negligible, while the temperature error causes a deviation of 0.2%. The resulting error in the water-flow thus becomes

$$\sqrt{\frac{1}{2}2.9^2 + \frac{1}{2}0.2^2} = \pm 2.05\%$$

Phase change corrections are required for these mass flows because of mixing in the mixer and inlet cone and because of the effect of heat losses from riser and test section to the somewhat subcooled downcomer. The mass flow  $\phi_{1g}$  evaporating in the mixer is found from a heat and mass balance over the control volume of figure 2-58, yielding

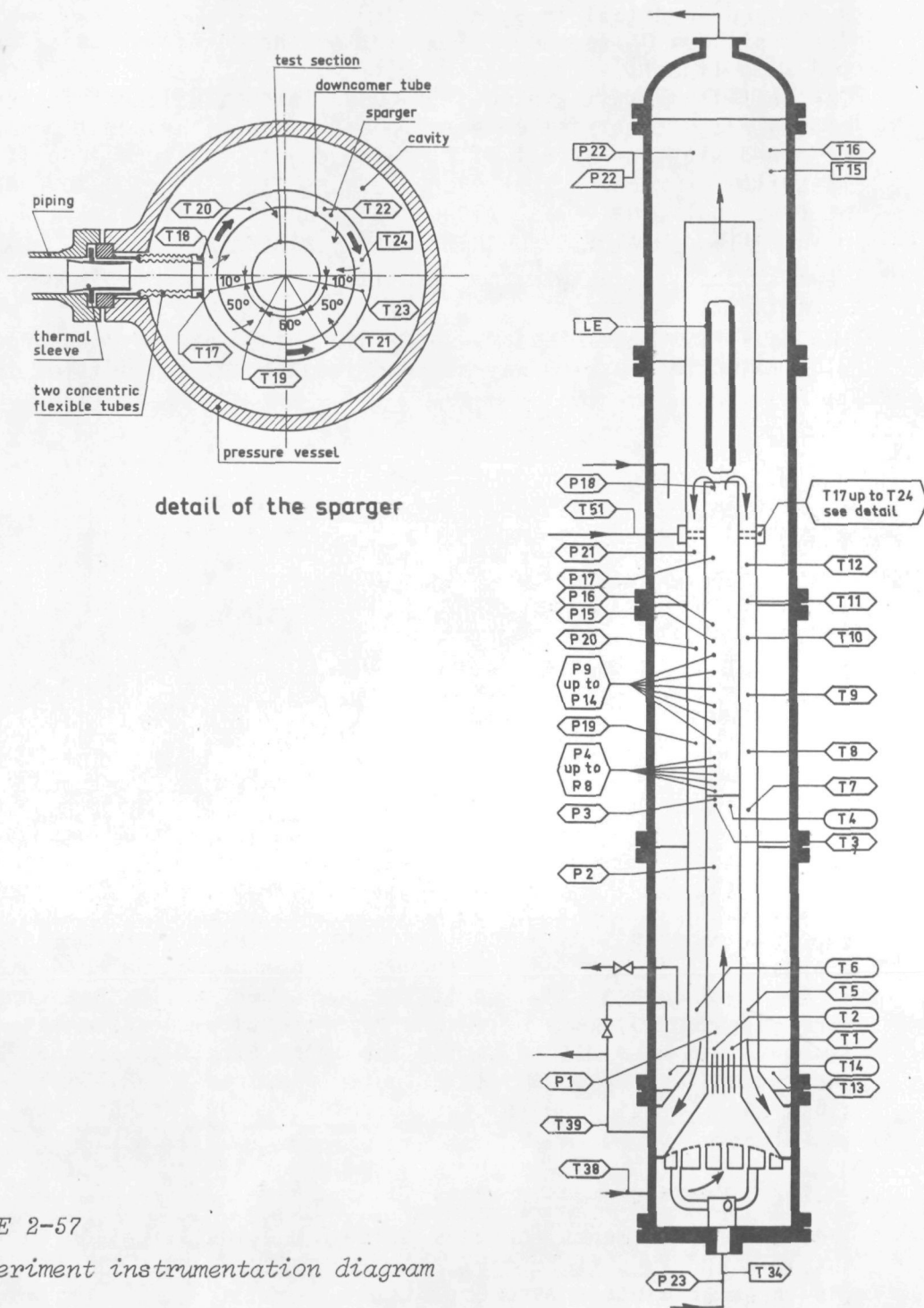


FIGURE 2-57  
 Experiment instrumentation diagram

$$\phi_{lg} = \frac{\phi_{mg}(h_g - h_{gsat}) + \phi_{ml}(h_l - h_{lsat}) - Q_M}{h_{gsat} - h_{lsat}} \quad (2-148)$$

Computation of the heat loss from riser/test section to downcomer  $Q_R$  is described in detail in appendix 2-M.

The heat loss  $Q_M$  to the bottom part of the downcomer is calculated along the same lines<sup>\*</sup>).

The heat loss  $Q_R$  is subsequently used in heat balances for successive parts of the riser/test section between each pair of adjacent pressure taps; combined with the effect of flashing due to pressure drop it yields the mass flows  $\phi_{mg}$  and  $\phi_{ml}$  at each pressure tap. In order to reduce the amount of final data these mass flows are given as total mass flow  $\phi_{mt} = \phi_{mg} + \phi_{ml}$  - which is constant through the whole riser/test section - and the quality

$$x = \frac{\phi_{mg}}{\phi_{mg} + \phi_{ml}} \text{ at each pressure tap level.}$$

The mass flow rate of carry-under quenching water is measured by a venturi flow meter in the same way as described above. In addition to cavitation

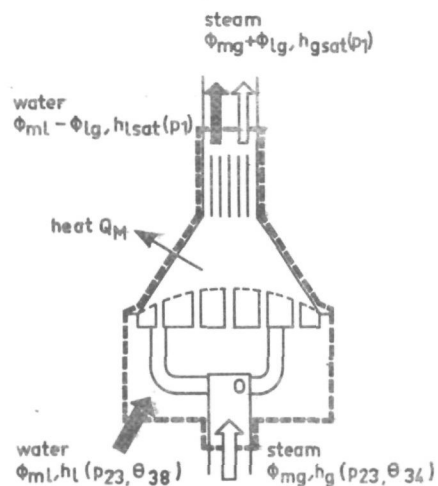


FIGURE 2-58

*Heat balance control volume over the mixer*

suppression this flow - together with the temperature measurements in the sparger (cf. figure 2-57) - serves for computing the downcomer quality from a heat balance over the top of the downcomer. While this computation will form an essential part of future experiments with steam-water separators, its only use here was to verify the improvements in sparger heat isolation and temperature measurements effected compared to PRINS [1] where heat sinks and sources gave inaccurate results. For further details the reader is referred to [78].

#### 2.3.2.4.2.2. Pressure measurements

Pressure measurements for this part of the investigation consist of 3 absolute and 29 differential pressure measurements.

The three absolute pressures, viz.

- the vessel pressure (P22)
- the boiler steam pressure (P25)
- the intermediate steam outlet pressure (P26)

<sup>\*</sup>) A detailed description of the computation of the heat flow  $Q_M$  - as well as of  $Q_R$  - is given in [78]

are measured by strain gage manometers calibrated with a dead weight tester. The formula in use for these pressures is:

$$p = K_1 + K_2 [mV] \quad (2-149)$$

where

- the calibration constant  $K_1$  including the correction for the height of the pressure tap piping system and  $K_2$  are the gauge values of the strain gage manometer
- $[mV]$  is the measured value in millivolt

The dead weight tester has an accuracy of 0.1%, while the drift of the strain gage manometers reaches 0.25%, yielding an accuracy of

$$\sqrt{0.1^2 + 0.25^2} = \pm 0.27\%$$

for the measured absolute pressures.

The 29 measured differential pressures consist of

- the seventeen differences between each two adjacent taps in the riser/test section configurations
- the two differences between the three taps in the downcomer
- three differences upstream and downstream of the riser/test section, viz. between boiler outlet and vessel inlet (dp 24-23), across the mixer in the pressure vessel (dp 23-1) and between test section outlet and vessel dome (dp 18-22)
- the total pressure difference over the mixer-riser/test section configuration (dp 23-22)
- the differences for the six venturi-tube flowmeters viz. two each (for low and high range) for steam supply, circulating water flow and carry-under quenching water flow.

These 29 differences are measured with three separate differential pressure cells actuated by the displacement of an elastic membrane. This displacement is measured by two induction coils in the cell forming a Wheatstone bridge with two resistances in the belonging carrier frequency amplifier. The stochastic character of these two-phase flow differential pressures is taken into account - in the same way as for the atmospheric air-water measurements (cf. subsection 2.3.1.4.3.) - by measuring each pressure difference 5 times at 0.75 second intervals by connecting the three amplifier outputs to 5x3 subsequent channels of the data logger. The most probable measurement value and its standard deviation are derived by the subroutine PROBMEAN previously discussed in subsection 2.3.1.5..

For these high pressure steam-water measurements the drift of the differential pressure cells is also eliminated by measuring a "positive" and "negative" pressure difference by interchanging the connections of the pressure taps to the cells and averaging the two absolute values as described for the atmospheric air-water measurements in subsection 2.3.1.4.3.. Contrary to the computation of the differential pressures for the air-water experiments (cf. equation (2-129)) the density of the water in the piping system - connecting the taps to the cells - has to be taken into account: the part of the piping system inside the pressure vessel contains water at the vessel pressure and saturation temperature  $\rho_{1sat}$ , while the piping outside the vessel contains water at the vessel pressure and 20°C:  $\rho_{1c}$ . So formula (2-129) is extended to

$$\Delta p_n = \pm K [mV]_n + \rho_{1sat} g \Delta h_n + (\rho_{1sat} - \rho_{1c}) g \Delta z_n \quad (2-150)$$

where

- $\rho_{1sat}$  and  $\rho_{1c}$  are the liquid densities at the saturation and "cold"

- temperature (of 20°C), respectively  
 -  $\Delta z_n$  is the difference in height between the piping penetration through the vessel wall for the two pressure taps under consideration

Corrected differential pressure values are obtained as described in subsection 2.3.1.4.3., using formulae (2-130) and (2-131)\*). From these corrected differential pressures the absolute pressure - subsequently used for computing the pressure gradients  $\frac{dp}{dz}$  via a polynomial approximation - are obtained by combining them with the absolute vessel pressure (P22).

The error in these pressure gradients can be estimated from the measurement error  $\varepsilon$  as defined in equation (2-130), which - in the case of the conical test section - was found to have a standard deviation of 2.9% of the overall pressure difference. Based on the reasoning given in the last alinea of subsection 2.3.1.4.3. this value will be taken as the final error in the pressure gradients  $\frac{dp}{dz}$ .

#### 2.3.2.4.2.3. Temperature measurements

All 54 temperatures are measured with chromel-alumel thermocouples. Those located in the water circulation circuit are calibrated "in situ" against pressure (cf. appendix 2-L) by comparing their measured millivolt values simultaneously with the "standard temperature" of the loop i.e. the saturation temperature in the steam dome. This is achieved by a shutdown of the quenching water cooler at a high water circulation rate thereby generating sufficient carry-under to obtain saturation temperature throughout the entire water circulation circuit. When the vessel pressure reaches its equilibrium, it is measured very accurately by use of a combination of the deadweight tester which is set to the nominal pressure and a strain gage differential pressure cell with a range of 50 kN/m<sup>2</sup> measuring the difference between the nominal pressure of the deadweight tester and the actual vessel pressure.

The maximum error of the deadweight tester is 0.1% or 7 kN/m<sup>2</sup>, whereas calibration of the cell gives an accuracy of 0.5 kN/m<sup>2</sup>. Thus the resulting error in the pressure measurement is 7.5 kN/m<sup>2</sup>, corresponding to a calibration accuracy of 0.075°C in the saturation temperature. This calibration is carried out at two pressures: 0.2 and 0.7 MN/m<sup>2</sup> below experimental pressure respectively, yielding the two gauge values  $K_1$  and  $K_2$  of the formula

$$T = K_1 + K_2 [mV_T] \quad (2-151)$$

where the constant  $K_1$  includes the calibration of the cold junction in the transostats.

For the remaining thermocouples outside the water circulation circuit the constant  $K_2$  is taken from the manufacturer's specification, while  $K_1$  equals 50°C, being the temperature of the cold junction in the Philips transostats. The accuracy of these manufacturer's specifications can be derived from the calibration of the first group of thermocouples: the standard deviation between calibrated and "manufacturer" temperatures was found to be 0.8°C, thus the uncalibrated thermocouples have a standard deviation of 0.8°C.

\* ) Due to an unsolved failure in measuring the pressure difference  $dp$  18-22, these corrections could not be elaborated in the case of the experiments with the straight test section, increasing the final error in the pressure gradients by about 0.5 to 1%.

#### 2.3.2.4.2.4. Data handling

The analog millivolt signals from the meters are converted to paper tape output by the same data logger as used for the air-water experiments (cf. subsection 2.3.1.4.5.). For these high pressure measurements 55 channels of this data logger are in use. The associated amplifiers and thermocouples are:

- channel 0: reserved for the code number of the mixture adjustment
- channel 1 through 15: consecutive connection of 5 groups of the three pressure difference cell outputs
- channel 16 and 17: strain gage meters for the absolute boiler and vessel pressure
- channel 18 and 19: steam outlet flowmeter and strain gage meter for the corresponding absolute pressure
- channel 20: capacitance level gage
- channel 21 through 52: thermocouples
- channel 53 and 54: level testers in annular cavity above sparger (LT 4 and 5)

During measurement of the pressure differences - including those of the venturi-flowmeters - only the first 16 channels are successively connected to the digital voltmeter, being repeated 27 times. This number of 27 scans stems from the number of 13 most important pressure differences in the test section (dp 3-4 up to dp 15-16), which are measured twice viz. "positive" and "negative" with a low range differential pressure cell and the control measurement of the cell's zero point.

During measurement of the absolute pressures, temperatures and levels all 55 channels are successively connected to the digital voltmeter, with the channels 1 through 15 giving only dummy values. This latter cycle is repeated manually 5 times to eliminate oscillations of the vessel pressure and corresponding temperatures.

For each channel the polarity, 5 digits and a blank are punched at a rate of 4 channels per second.

#### 2.3.2.5. Data processing

As apparent from the above all signals are measured 2 x 5 or 5 times to take account of the stochastic character of two-phase flow and of the small oscillations in steam supply and vessel pressure. The resulting paper tape consists for each mixture adjustment of:

- 27 x 16 = 432 pressure difference data, obtained by 27 scans of the first 16 channels of the data logger of which the first channel contains the code number of the adjustment and the remaining 15 channels receive the signals of the three differential pressure cells as described in subsection 2.3.2.4.2.4.
- 5 x 55 = 275 data from 5 scans of all 55 data logger connections, of which the first 16 channels give dummy values now and the last 39 channels contain data for absolute pressures, temperatures and levels.

After reordering these 707 data, the most probable measuring value and its standard deviation is computed for each set of 5 data using the subroutine PROBMEAN as discussed in subsection 2.3.1.3.4.. These most probable values and their standard deviations are combined with the gauge values of the pressure cells and thermocouples - the latter being calibrated at the beginning of each day - to form the final data set for computation of the flow parameters.

The pressure gradient  $\frac{dp}{dz}$  in the test section - required for the computations

of void fraction and interaction force coefficient as described in subsection 2.3.2.1. - is obtained from the absolute pressures at the pressure taps by polynomial approximation: a Chebyshev second degree polynomial in the case of the straight test section and a cubic spline approximation in the case of the converging test section.

The measured mass flows are corrected for condensation/flashing - as discussed in subsection 2.3.2.4.2.1. - and presented as the total mass flow  $\phi_{mt}$  and the quality  $x$  at the pressure taps, which latter data are approximated by a polynomial to obtain the derivative  $\frac{dx}{dz}$ .

### 2.3.2.6. Results

Prior to discussing the results of the interaction force coefficients and the intermediate results of the void fraction and phase velocities, it should be emphasized again that the pressure is the only parameter measured directly while all the other parameters are obtained through additional computations.

#### 2.3.2.6.1. Pressure, void fraction and velocity distributions

From the 143 and 136 measurements for the straight and converging test section respectively, the mixture adjustments having the same nominal void fraction and superficial water velocity as the air-water mixtures discussed in subsection 2.3.1.6.1., have been selected for discussion in this subsection.

It should be remarked that of these adjustments those with the highest void fraction and superficial water velocity could not be measured because of the large amount of carry-under. The adjacent mixture adjustments 88 and 188 - equivalent with the air-water tests 44 and 144 ( $\alpha = 0.625$  and  $u_{s1} = 2.1$  m/s) - have been replaced by adjustments 87 and 187 having a somewhat lower void fraction.

##### 2.3.2.6.1.1. Axial pressure profiles

These distributions are presented in the figures 2-59 through 2-62 for both test pressures and test sections.

The pressure gradients for the straight test section: figures 2-59 and 2-60 for test pressures of 5 and 7 MN/m<sup>2</sup> respectively appear to be almost constant along the test section and dominated by the hydrostatic pressure gradient  $\{(1-\alpha)\rho_l + \alpha\rho_g\}$ , i.e. constant in the "column" for constant void fraction and decreasing with increasing void fraction in the "row" for constant superficial water velocity.

A small systematic error in these pressure measurements for the straight test section was detected afterwards as a consequence of applying the polynomial approximation: it appears that the largest error in the approximation is always located at pressure tap 13, while its magnitude depends on the total pressure drop across the test section. However, this error never exceeds 1% of the total pressure drop across the test section and is thus of minor importance. In addition the Chebyshev polynomial approximation is based on weighted residuals the weighted values of which depend on the deviation itself: therefore the weighted value for this pressure is about a factor 5 lower than the other weighted values. Notwithstanding the small initial error and this suppression in the polynomial approximation, the pressure gradient  $\frac{dp}{dz}$  in the upper part of the test section will be made a little less steep by this effect.

The pressure gradients in the converging test section (cf. figures 2-61

and 2-62) are dominated by the acceleration pressure drop; the proportionality with the square of the real water velocity appears clearly from both the "row" of increasing void fraction and the "column" of increasing superficial water velocity.

The pressure gradient in the cone and tail pipe is less steep than that of the air-water mixtures (cf. figure 2-30) because of the absence of a significant gas expansion, as will be discussed in the next subsection on void fraction profiles.

#### 2.3.2.6.1.2. Void fraction profiles

In the straight test section almost all void fraction profiles increase by a few percent as apparent from figures 2-63 and 2-64 for 5 and 7 MN/m<sup>2</sup> respectively. Although the quality of the mixtures also increases - because flashing exceeds condensation due to heat leakage - the increase in void fraction is mostly caused by the error in the pressure distribution discussed in the previous subsection, as can be deduced from the contradiction between decreasing steam velocity and the increasing quality. The systematic error in the case of the straight test section resulting in a less steep pressure gradient in the upper part of the test section affects the hydrostatic pressure gradient  $\{(1-\alpha)\rho_l + \alpha\rho_g\}g$  - being the major component of the total pressure gradient - in such a way that the part  $(1-\alpha)\rho_l g$  decreases, thus causing an apparent increase in void fraction.

Because the pressure gradient is correct in the lower part of the test section and the increase in void fraction is only a few percent, it can be concluded that in general the computed void fractions will also be accurate to within a few percent, which is adequate for further computations of the drag force coefficients. However, in view of the importance of the relative velocity  $u_r$  for both the computation of the quotient  $\frac{C_D}{d}$  (cf. equation (2-140)) and the virtual mass coefficient  $B$  via the computation of the void fraction (cf. equation (2-143)) the computations are terminated if the relative error becomes large due to a small relative velocity, i.e. if the slip decreases below 1.05. For the selected measurements of the straight test section this occurs half way the test section in the case of measurement 68/7, while the same occurs with the converging test section for measurements 182/5 and 182/7.

The axial void fraction distributions for the converging test section - where no systematic error in the pressure distribution occurred - are presented in figures 2-65 and 2-66. The small decrease in the lower part of the cone - about a few percent - is identical to that of the air-water experiments (cf. figure 2-33), while the increase in the tail end of the test section by about 10 percent in the case of air-water mixtures is reduced to about 5 percent for the steam-water experiments. This latter was to be expected because the increase of the void fraction of the air-water mixtures is partly caused by the increase of the volumetric quality  $\beta$  due to the expansion of the air, whereas hardly any expansion occurs in the high pressure steam-water experiments and flashing is of minor importance. Thus it can be concluded that the void fraction computation has a good accuracy.

#### 2.3.2.6.1.3. Velocity profiles

The phase velocities for the straight test section - figures 2-67 and 2-68 for 5 and 7 MN/m<sup>2</sup> respectively - are clearly affected by the error in the computed void fraction: on the basis of increasing quality an increase of the steam velocity is to be expected instead of the rather strong decrease.

As discussed above the pressure gradient and hence the void fractions and

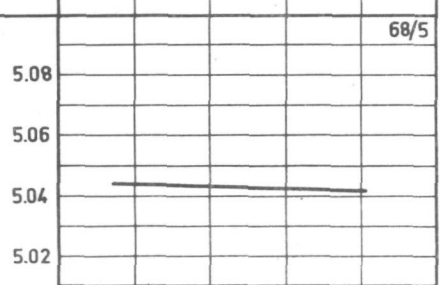
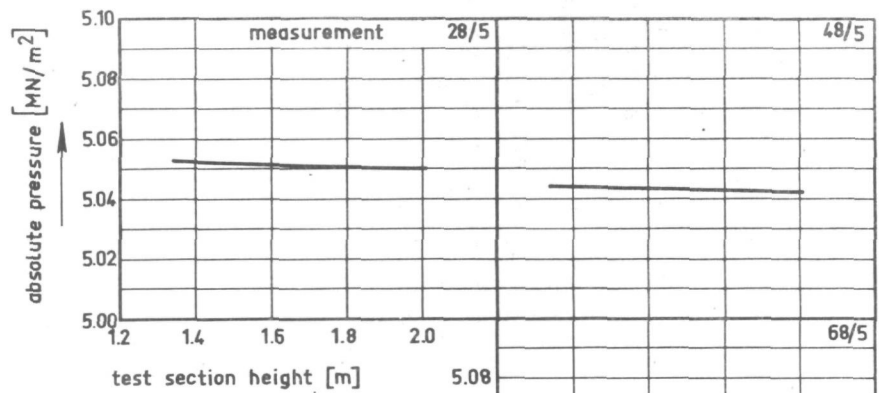
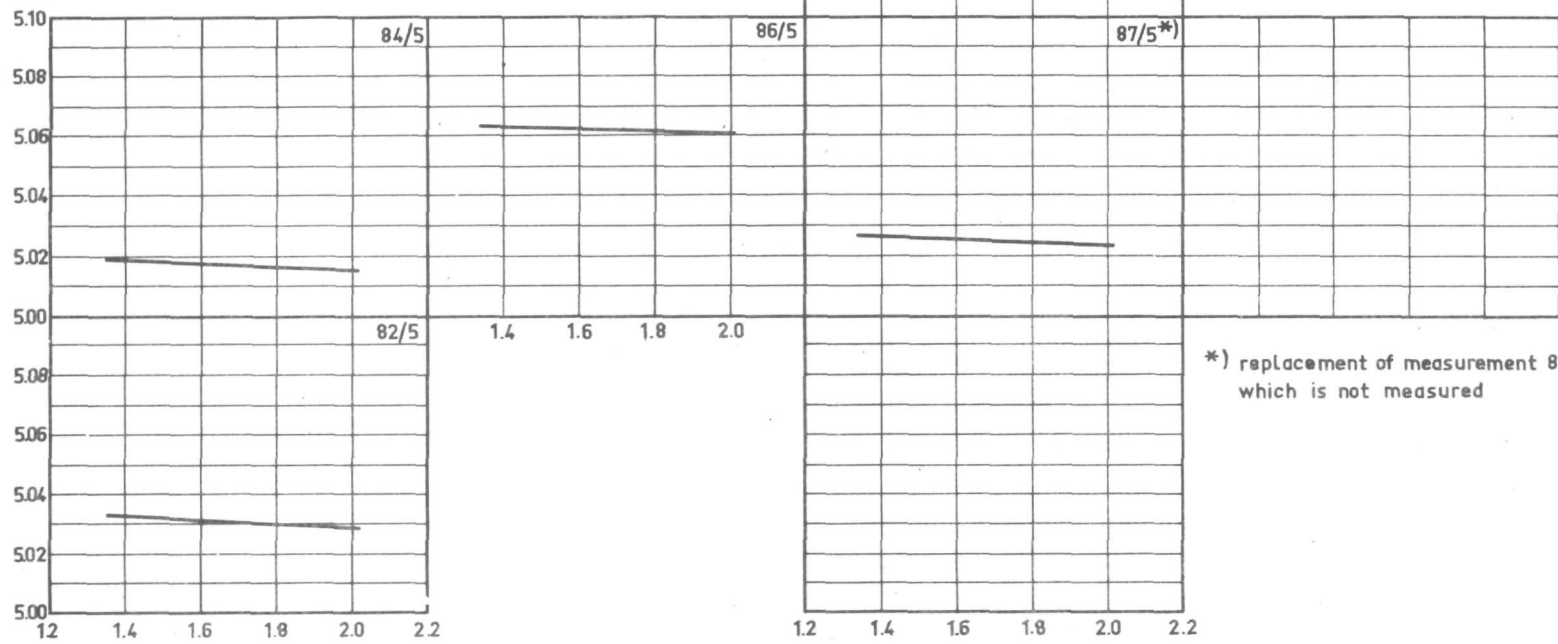


FIGURE 2-59

*Axial distribution of the pressure in the straight test section at 5 MN/m<sup>2</sup>*



\* ) replacement of measurement 88/5 which is not measured

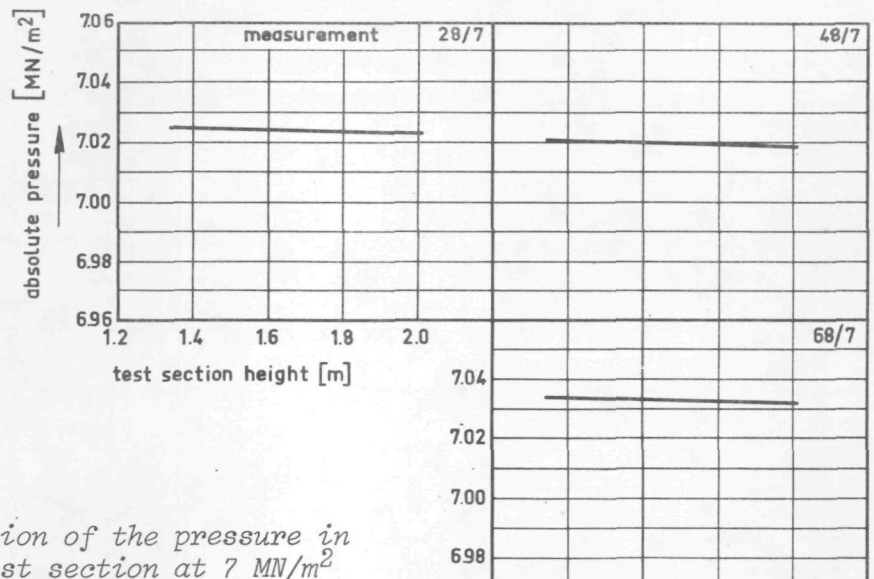
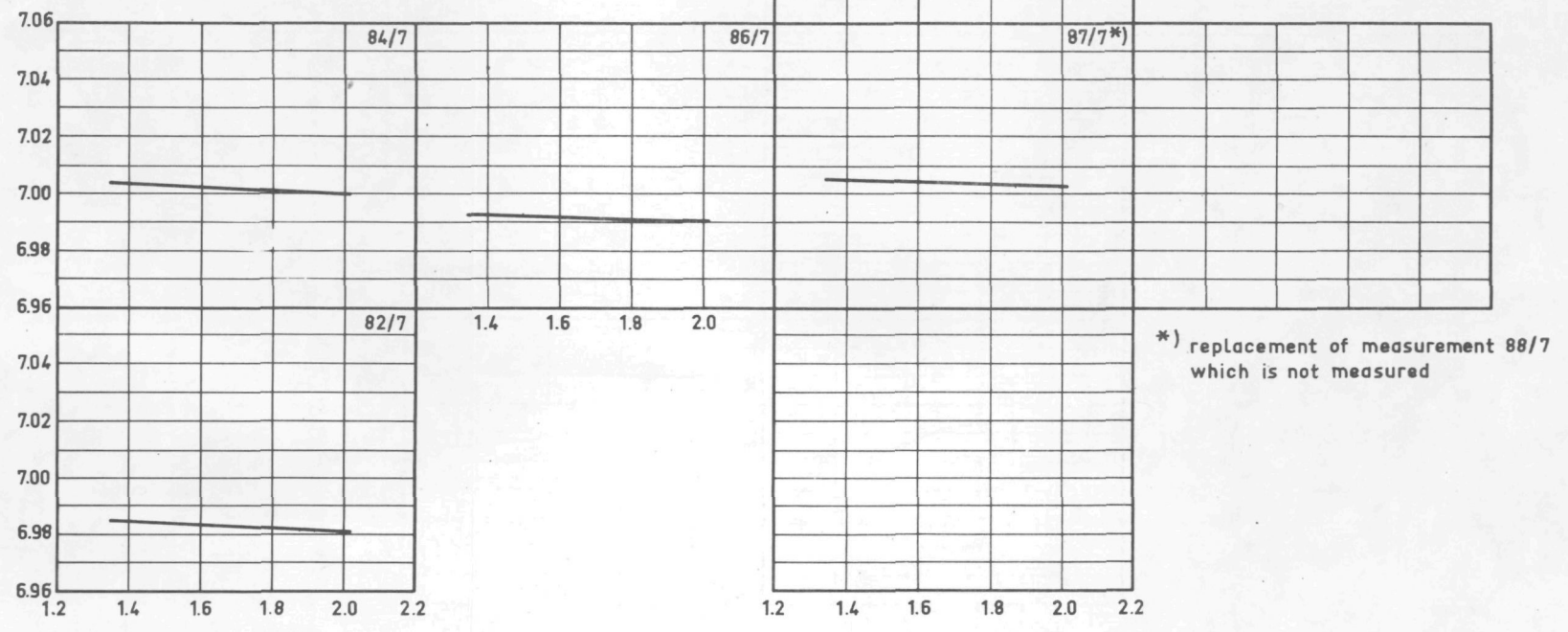


FIGURE 2-60  
 Axial distribution of the pressure in  
 the straight test section at 7 MN/m<sup>2</sup>



\*) replacement of measurement 88/7  
 which is not measured

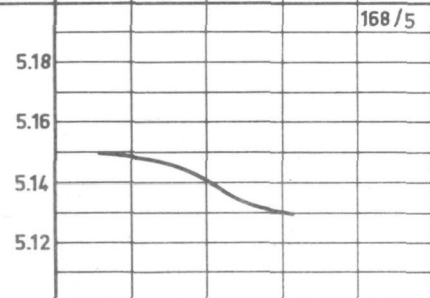
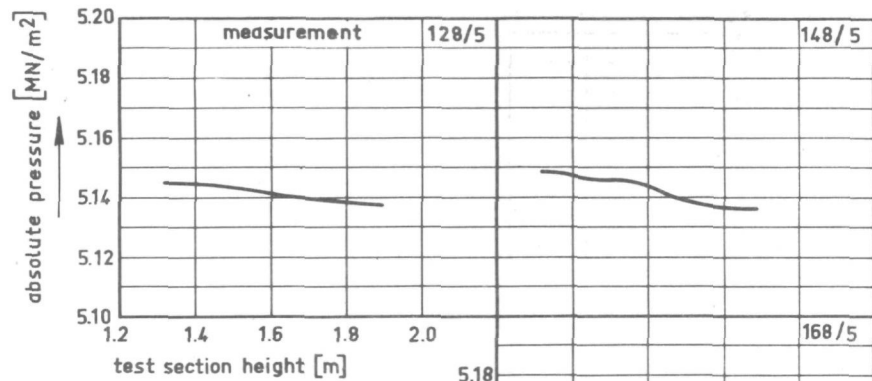
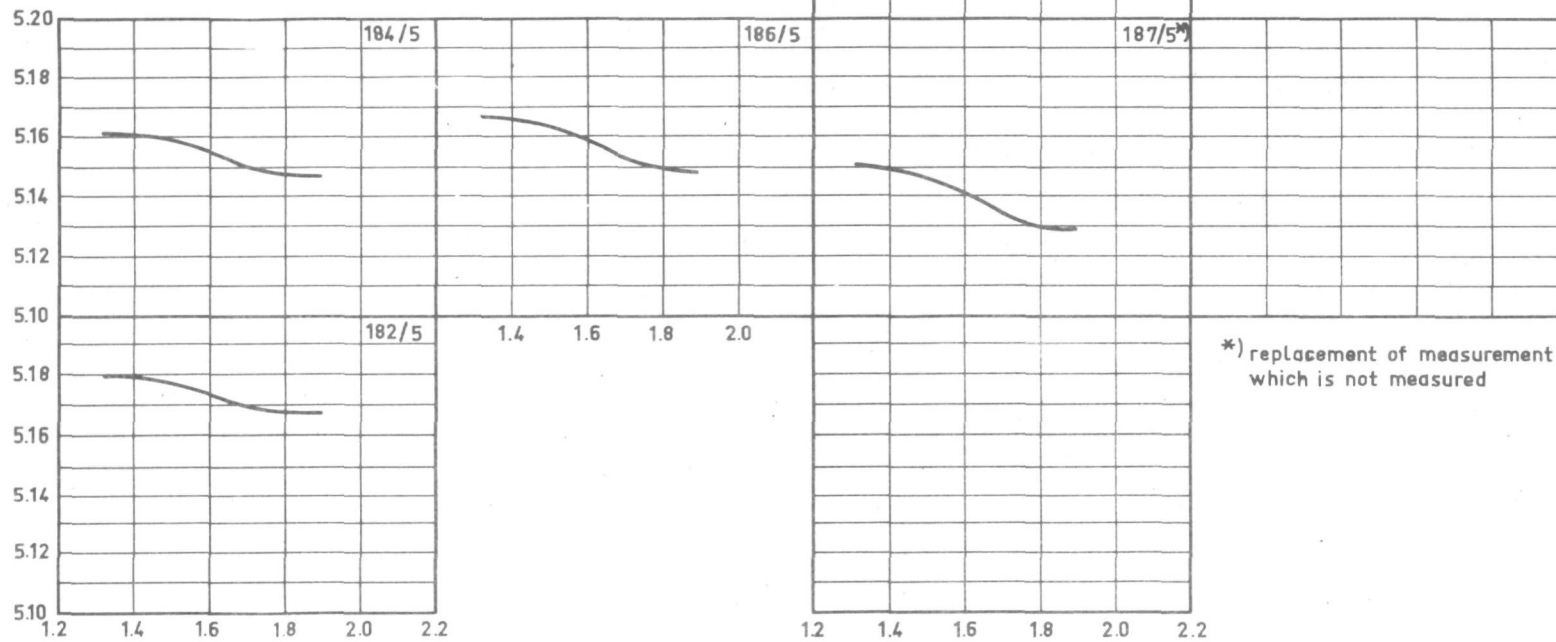


FIGURE 2-61

*Axial distribution of the pressure in the converging test section at 5 MN/m<sup>2</sup>*



\*) replacement of measurement 188/5 which is not measured

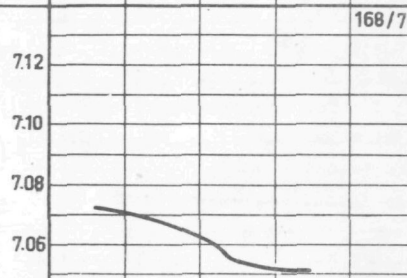
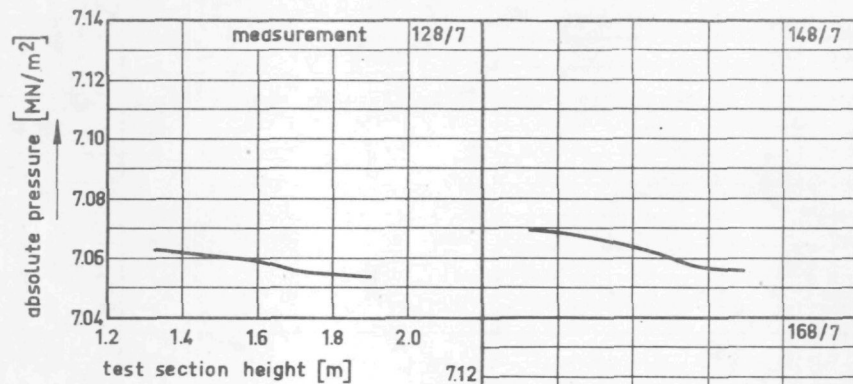
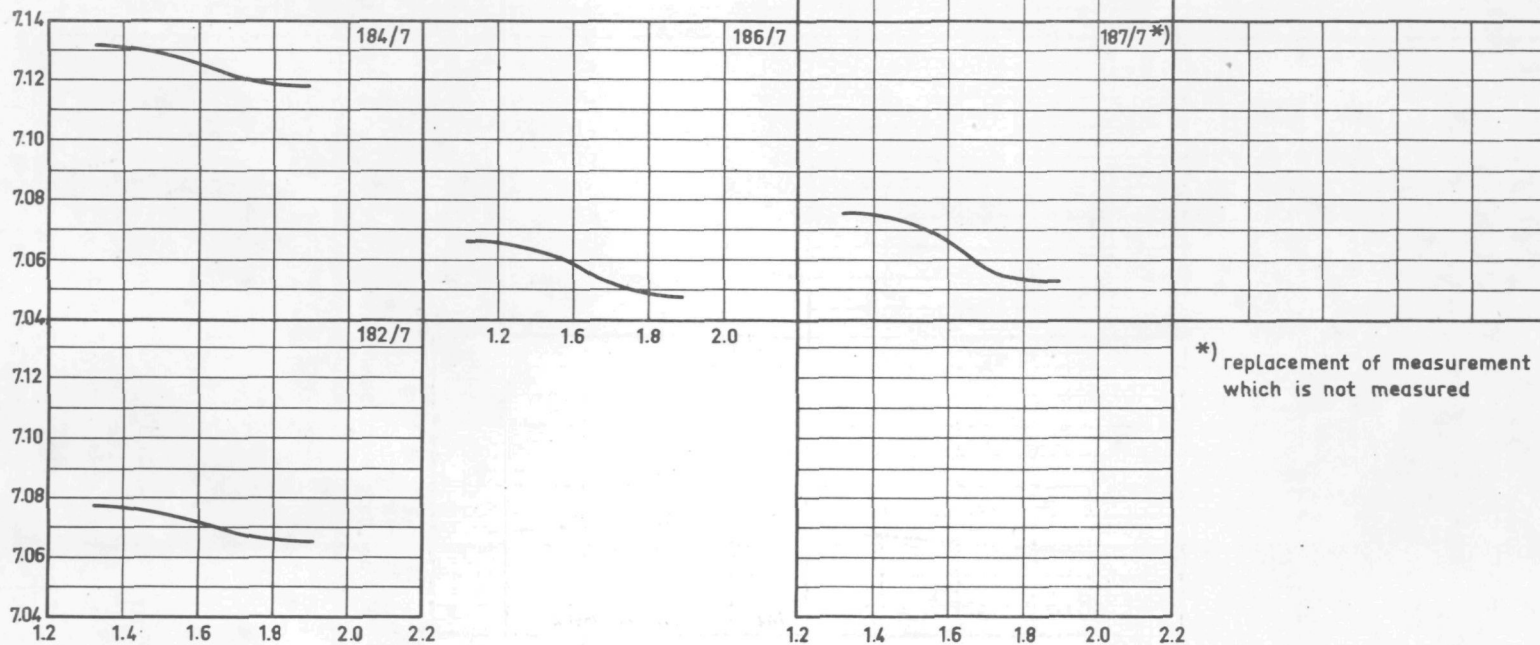


FIGURE 2-62

*Axial distribution of the pressure in the converging test section at 7 MN/m<sup>2</sup>*



\*) replacement of measurement 188/7 which is not measured

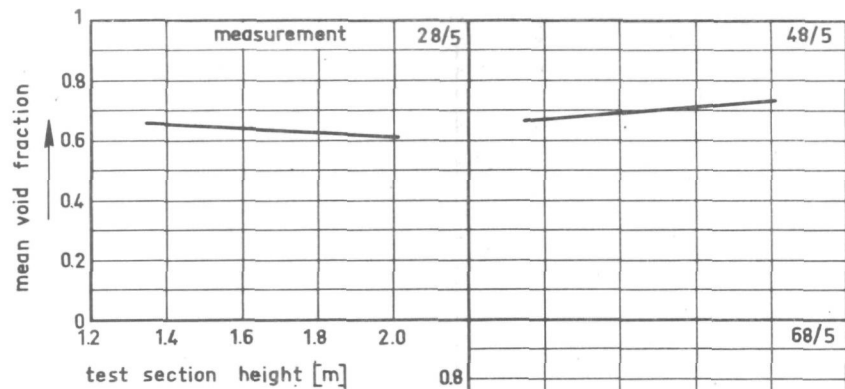
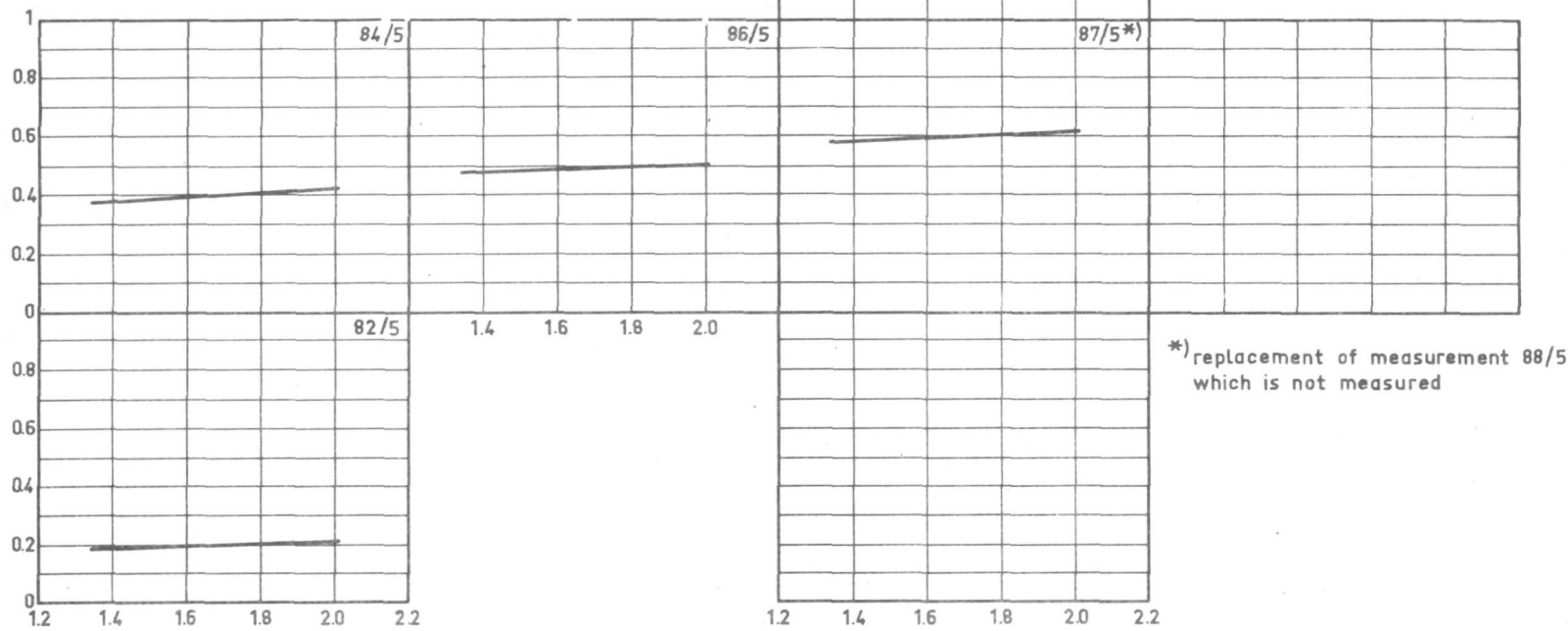


FIGURE 2-63

*Axial distribution of the void fraction in the straight test section at 5 MN/m<sup>2</sup>*



\*) replacement of measurement 88/5 which is not measured

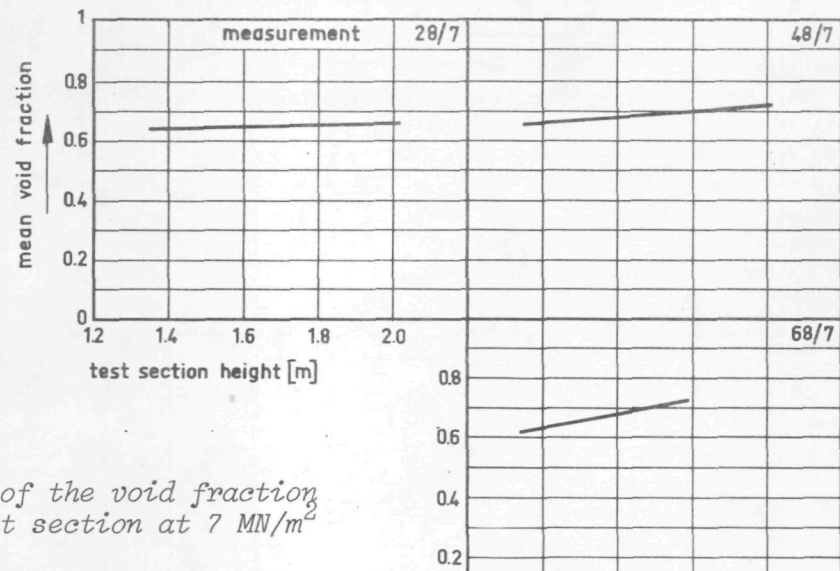
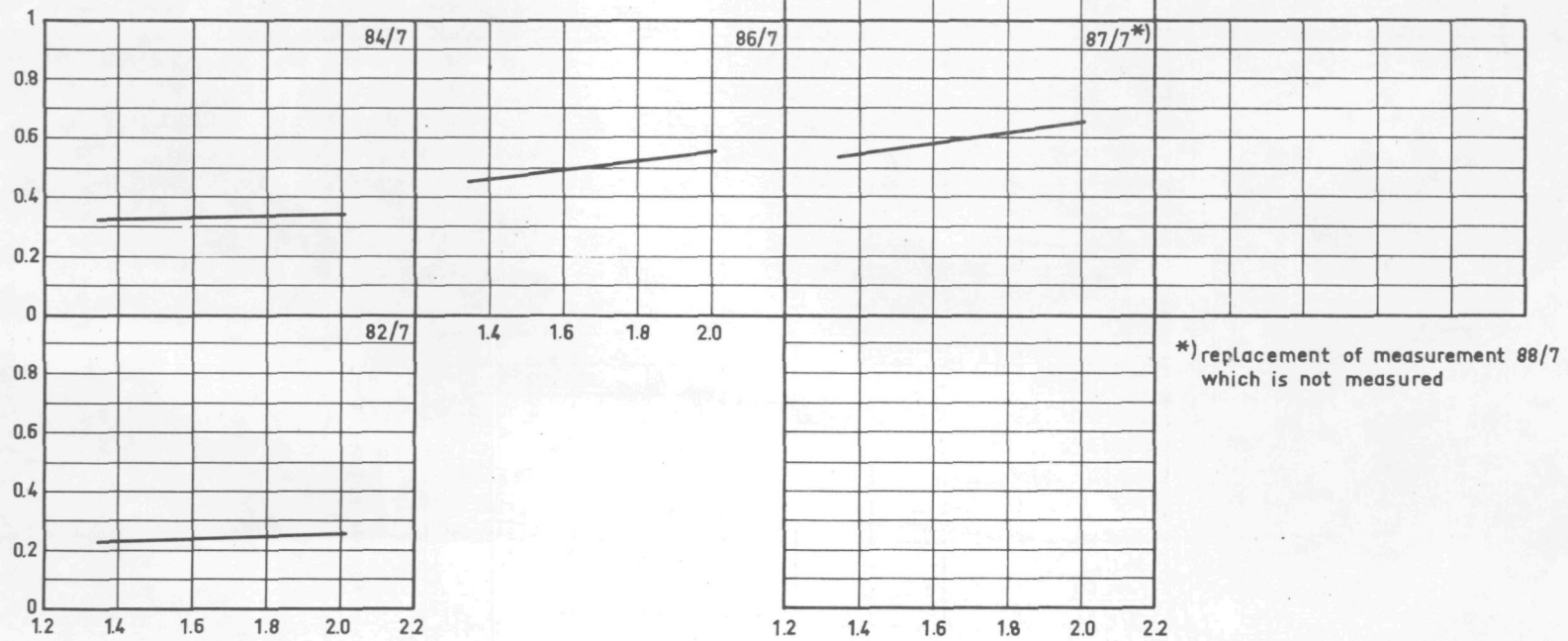


FIGURE 2-64

*Axial distribution of the void fraction  
in the straight test section at 7 MN/m<sup>2</sup>*



\*) replacement of measurement 88/7  
which is not measured

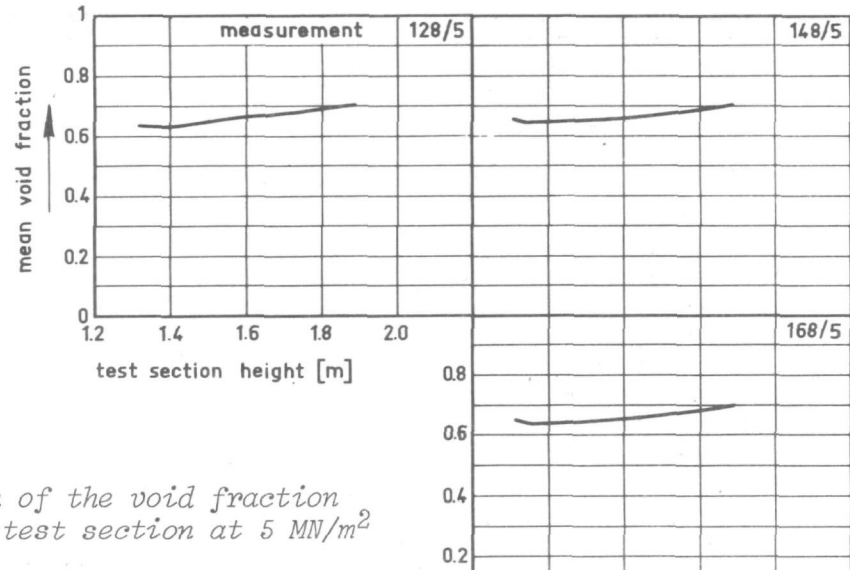
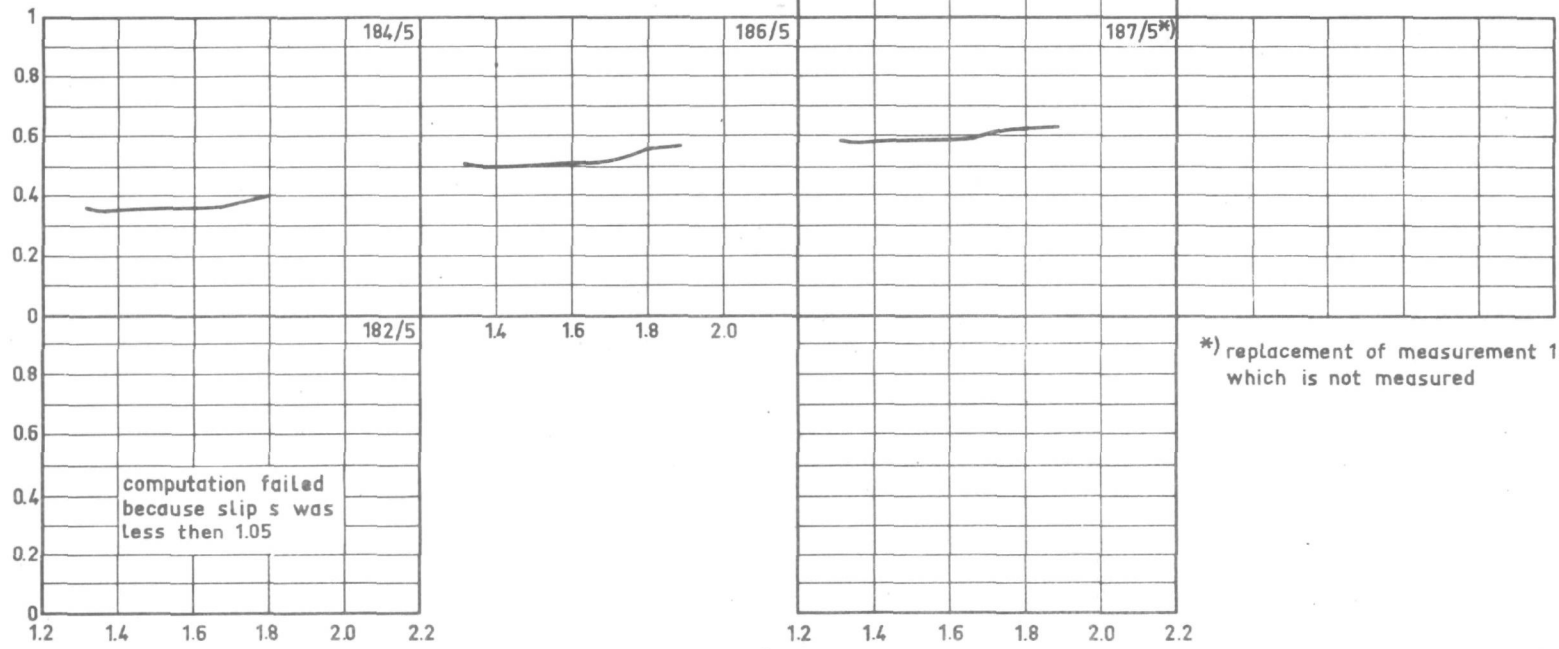


FIGURE 2-65

*Axial distribution of the void fraction in the converging test section at 5 MN/m<sup>2</sup>*



\* replacement of measurement 188/5 which is not measured

computation failed because slip s was less than 1.05

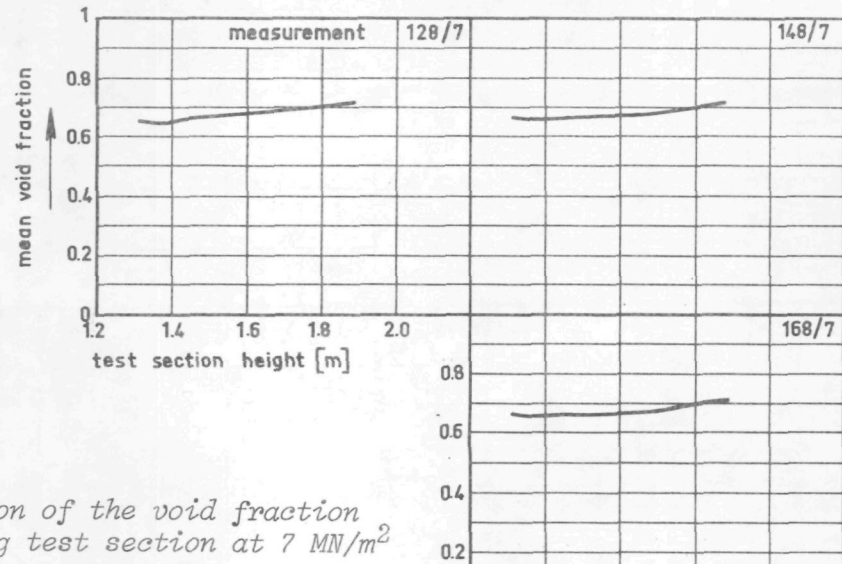
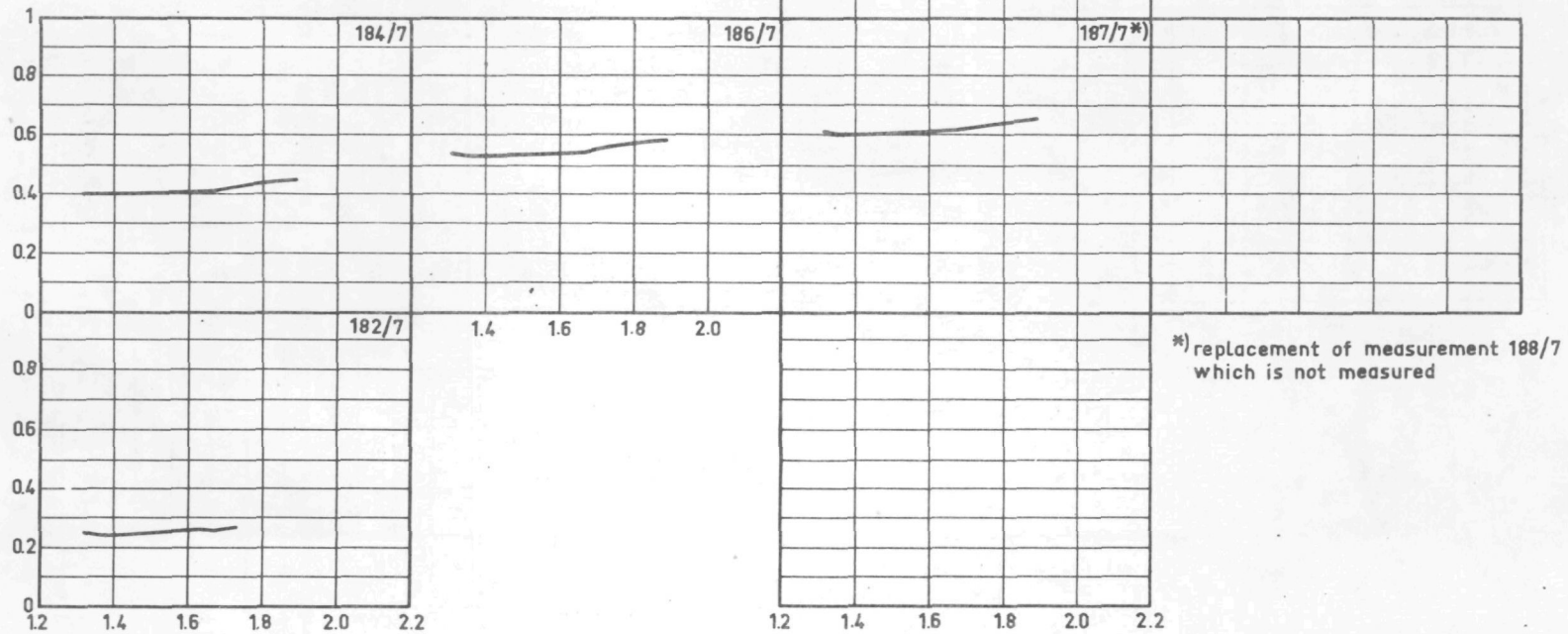


FIGURE 2-66

*Axial distribution of the void fraction  
in the converging test section at 7 MN/m<sup>2</sup>*



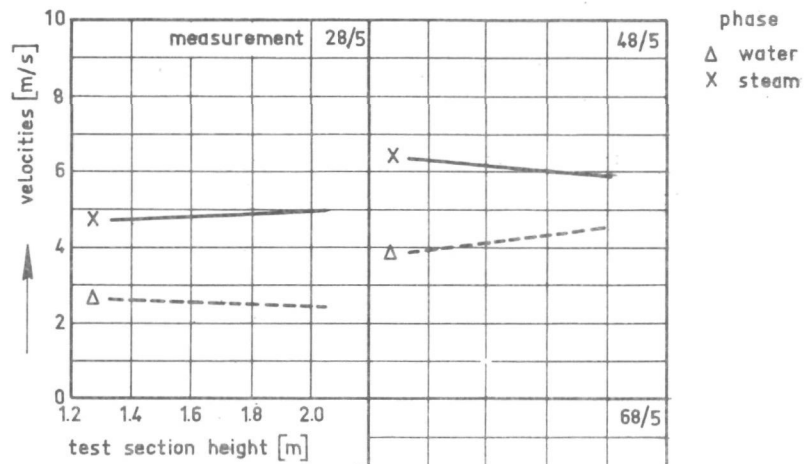
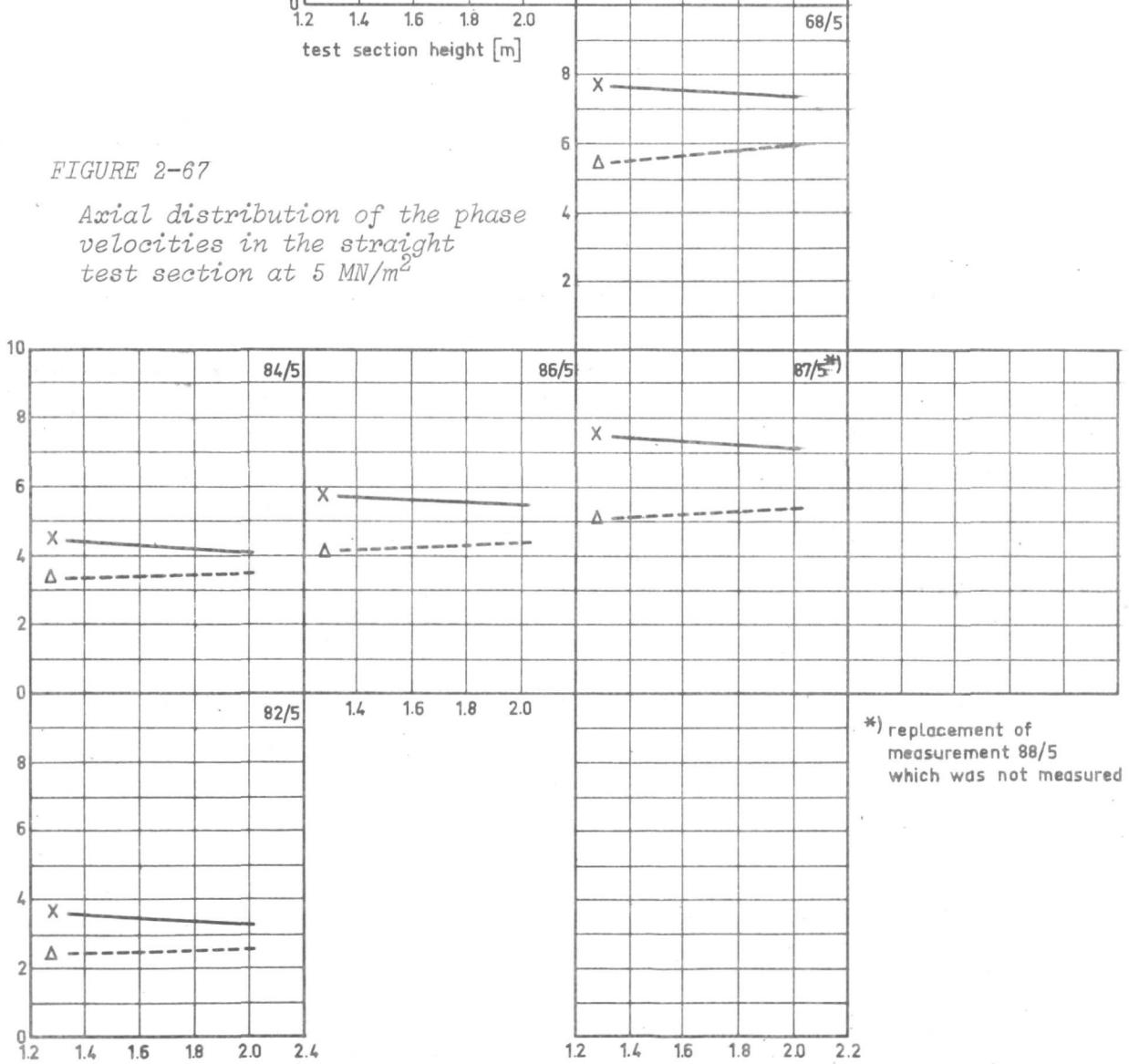


FIGURE 2-67

*Axial distribution of the phase velocities in the straight test section at 5 MN/m<sup>2</sup>*



<sup>\*)</sup> replacement of measurement 88/5 which was not measured

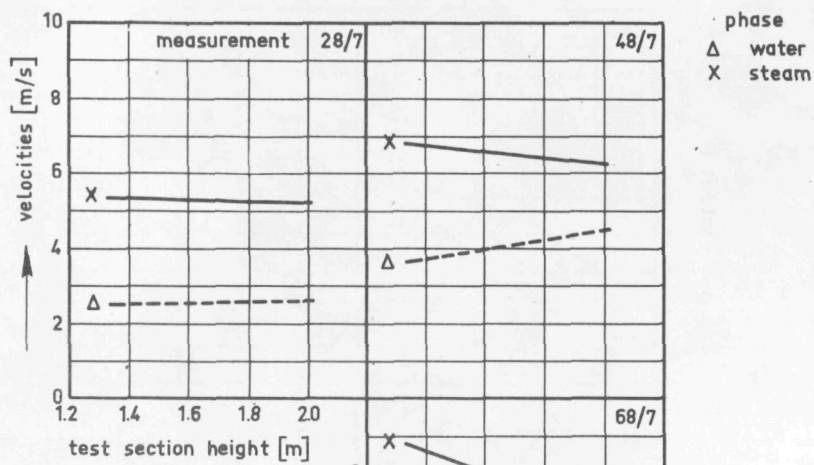
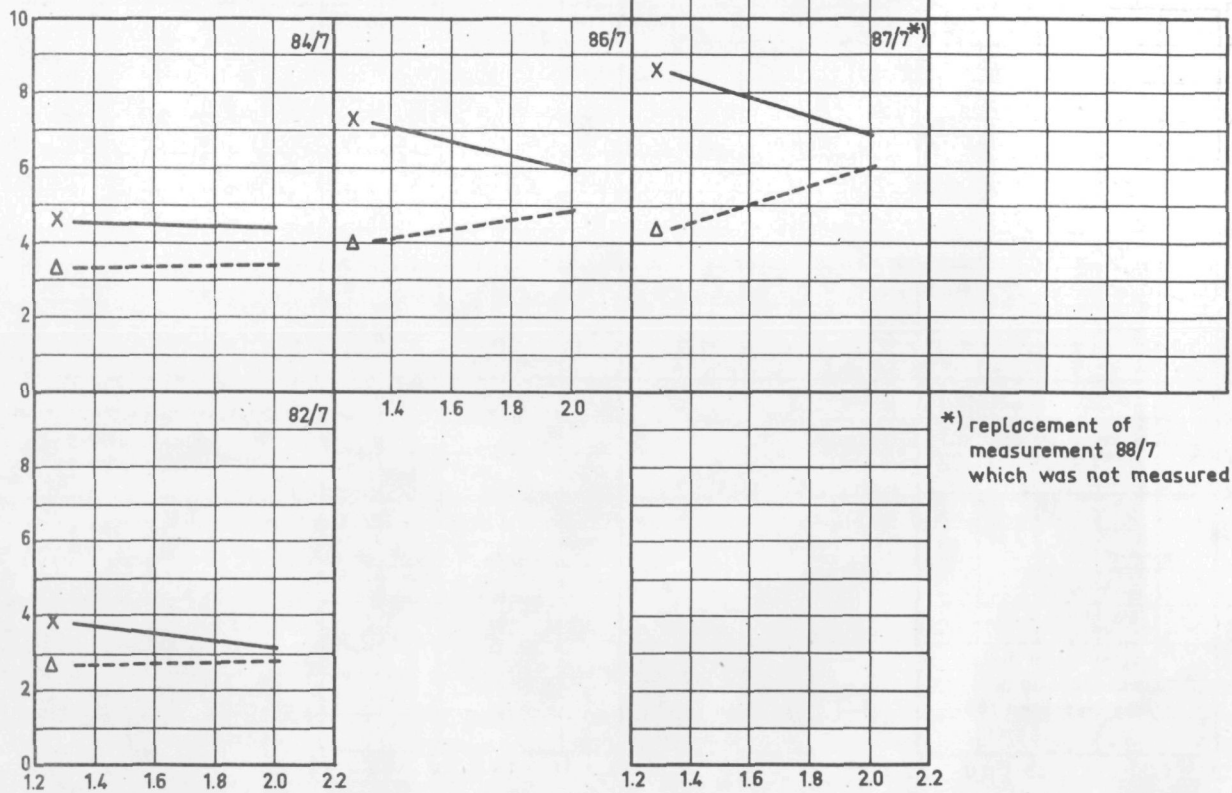
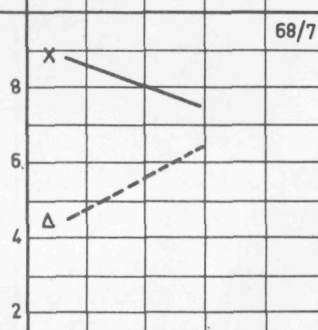


FIGURE 2-68

Axial distribution of the phase velocities in the straight test section at  $7 \text{ MN/m}^2$



\*) replacement of measurement 88/7 which was not measured

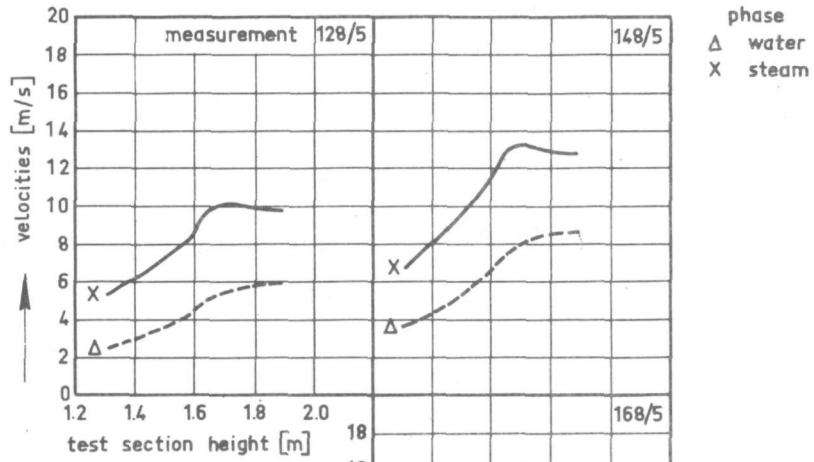
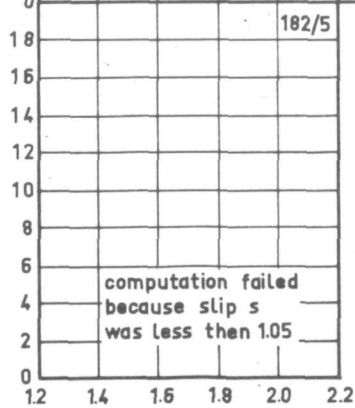
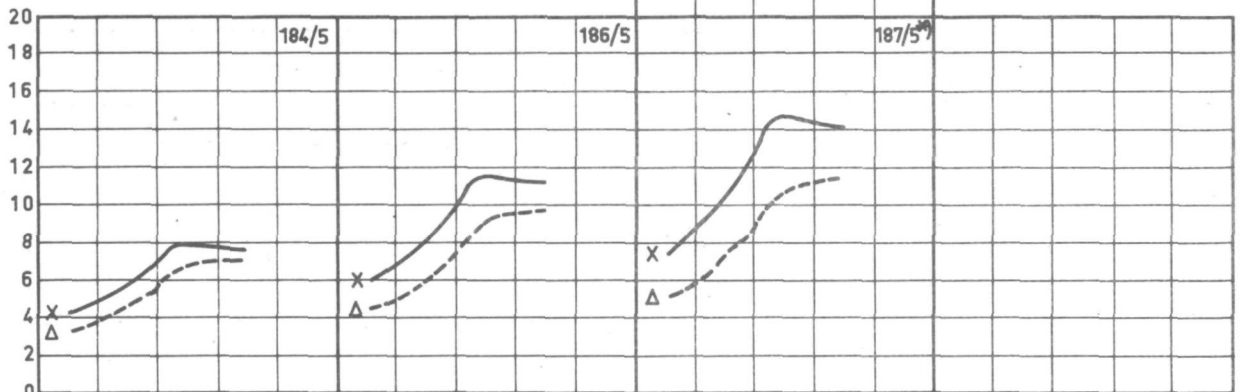
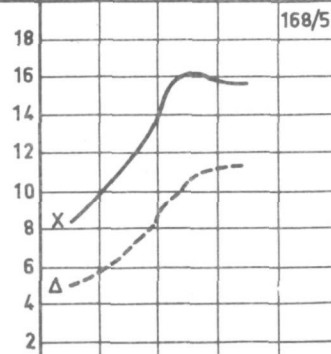


FIGURE 2-69

*Axial distribution of the phase velocities in the converging test section at 5 MN/m<sup>2</sup>*



\*) replacement of measurement 188/5 which was not measured

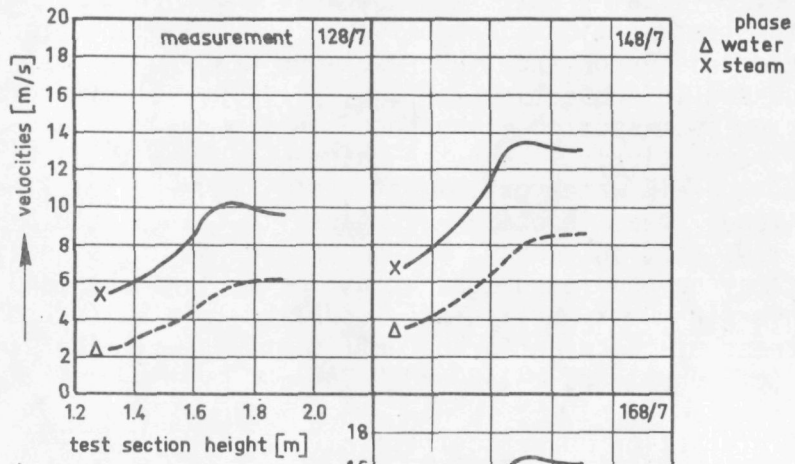
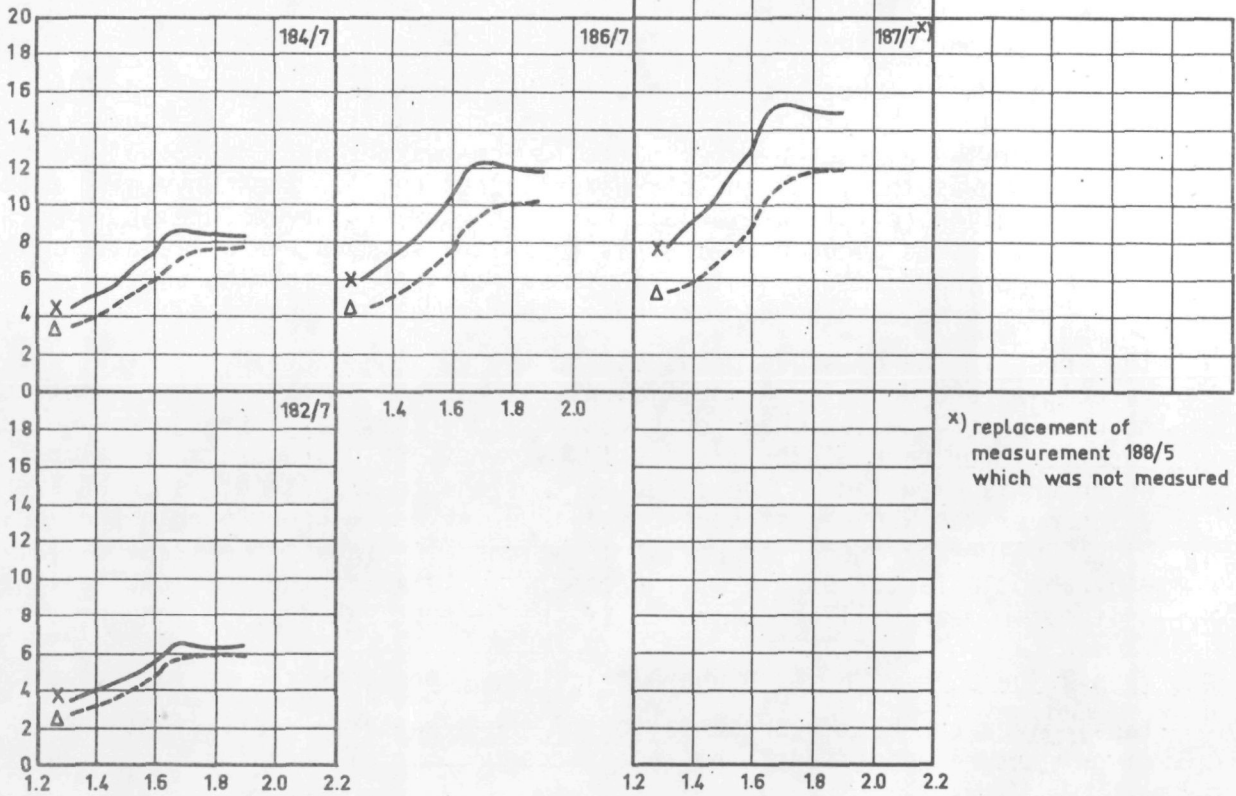
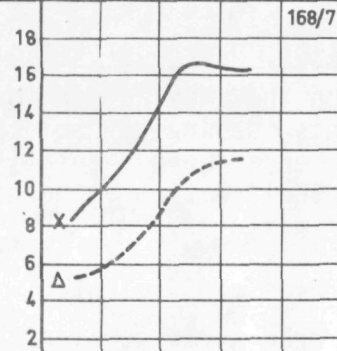


FIGURE 2-70

*Axial distribution of the phase velocities in the converging test section at 7 MN/m<sup>2</sup>*



phase velocities at the bottom of the test section are expected to be correct, which is confirmed by comparing these velocities to those of the air-water experiments (without taking into account the differences caused by the change of physical properties). Because the change in relative velocity along the test section is significant special precautions are taken to eliminate this error from the resulting drag force coefficients  $C_D$ , as will be discussed in subsection 2.3.2.6.3.1.. The velocity profiles for the converging test section - presented in figures 2-69 and 2-70 for 5 and 7 MN/m<sup>2</sup> respectively - have the shape which was to be expected on the basis of the air-water experiments (cf. figure 2-39). The only difference is the lower steam velocity - compared to that of the air - in the tail end of the test section, caused by the absence of any significant expansion. Thus it may be concluded again that the measurements and computations with the converging test section are accurate. This latter conclusion suggests correctness of the drag force coefficient correlation used in this computation (cf. equations 2-143 and 2-144).

### 2.3.2.6.2. Interaction force coefficients

The knowledge on the interaction force coefficients obtained from the air-water experiments is directly relevant for the evaluation of the steam-water results. Hence the presentation of these results will have the character of a verification rather than the development of new correlations for steam-water mixtures.

#### 2.3.2.6.2.1. Drag force coefficient

Values for the drag force coefficient  $C_D$  are plotted in figures 2-71 and 2-72A for 5 and 7 MN/m<sup>2</sup> respectively. The following conclusions can be drawn from these figures:

- the drag force coefficients may be approximated with reasonable accuracy by :  $C_D = 0.44(1-\alpha)^6$ , the correlation (2-135) found earlier for the air-water experiments<sup>\*</sup>). The scatterbands are about the same as those for the air-water experiments in the converging test section (cf. figure 2-43), hence in view of the measurement errors discussed above no reason is found to assume a new correlation.
- the independence of the liquid velocity found for the air-water mixtures also holds for these steam-water mixtures.

The error in the pressure gradient and the ensuing in void fraction, phase velocities and drag force coefficients is reduced by taking the geometric mean value of the ten drag force coefficients computed at the pressure tap locations for each of the mixture adjustments. As discussed above almost no error is expected in the lower part of the test section, hence an average value over the whole test section will be far more accurate than the individual values at the pressure tap locations. In view of the large variation - by about a factor of 5 - of the coefficients along the test section the arithmetic mean will be dominated by the largest values, thus the geometric

mean value  $\bar{C}_D = \sqrt[10]{\prod_{i=1}^{10} C_{D_i}}$  (where  $i=1\dots 10$  represents the various pressure taps) gives the best representation of the drag force coefficient for a given mixture adjustment. The same procedure is followed for the "liquid

<sup>\*</sup>) In view of the similarity of the correlation  $C_D = 0.44 (1-\alpha)^6$  for pseudo one-dimensional flow for both air-water and steam-water mixtures, there is no reason to doubt the validity of the correlation  $C_D = 0.44 (1-\alpha)^{4.25}$  derived and found for air-water mixtures (cf. subsection 2.3.1.6.2.1. and appendix 2-H) for steam-water mixtures.

FIGURE 2-71

Averaged drag force coefficients at 5 MN/m<sup>2</sup>

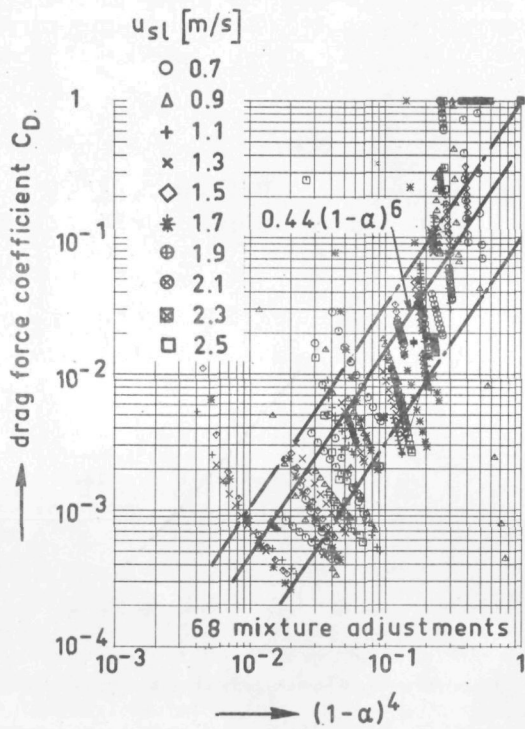
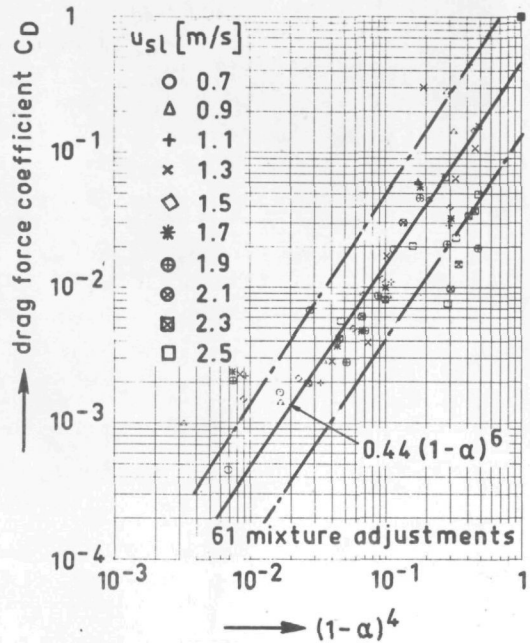


FIGURE 2-72B

All drag force coefficients at the pressure tap locations (test pressure 7 MN/m<sup>2</sup>)

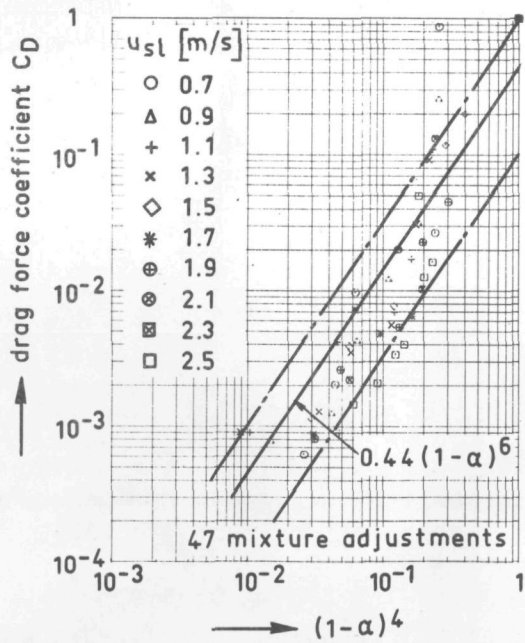


FIGURE 2-72A

Averaged drag force coefficients at 7 MN/m<sup>2</sup>

fraction"  $\overline{(1-\alpha)} = \sqrt[10]{\prod_{i=1}^{10} (1-\alpha)_i}$ . In figure 2-72B the original data are shown from which the averaged data of figure 2-72A were obtained. The mixture adjustments for which the scatterband of the original data is unduly large are omitted from figure 2-72A (the criterion being that none of the ten original data should deviate from geometric mean value by more than twice the standard deviation).

As apparent from figure 2-72B almost all original data are within the scatterband obtained from the averaged data, hence the averaging procedure only eliminates the most inaccurate measurements.

### 2.3.2.6.2.2. Virtual mass coefficient

As stated above the drag force coefficient correlation used in the simultaneously computation of void fraction (cf. equation (2-143)) and virtual mass coefficient is  $C_D = 0.44 (1-\alpha)^6$ .

In view of the results obtained from the air-water experiments no further investigation of the dependence on the slip will be undertaken. The dependence on the peak velocity ratio  $\frac{u^\oplus}{u_r}$  - defined by equation (2-138) - and void fraction  $\alpha$  is presented in figures 2-73 through 2-76 on the basis of the functions  $f(\frac{u^\oplus}{u_r}) = (2 \frac{u^\oplus}{u_r})^{0.65}$  and  $g(\alpha) = \frac{2}{1+(1-\alpha)^4}$  found for the air-water experiments.

From these figures one may conclude that:

- considering the large scatter correlation (2-139):

$B = \frac{1}{2} \frac{2}{1+(1-\alpha)^4} (2 \frac{u^\oplus}{u_r})^{0.65}$  found for the air-water experiments fits these steam-water data reasonably well. This is remarkable because the Reynolds and Weber number - on which the peak velocity ratio  $\frac{u^\oplus}{u_r}$  is based (cf. expression (2-138)) - contain physical property groups  $\frac{\rho_l}{\eta_l}$  and  $\frac{\rho_l}{\sigma}$  which differ by about a factor 7.5 and 2 respectively from those for atmospheric water.

- the largest deviations are found for data having a peak velocity ratio between 0.05 and 0.1. Rather than suggesting an increase in the power of  $f(\frac{u^\oplus}{u_r}) = (2 \frac{u^\oplus}{u_r})^{0.65}$ , this indicates in the author's opinion an error in the term  $\frac{35000}{ReWe}$  - under the square root of the peak velocity ratio (cf. expression (2-138)) - which is found to be of great importance for these data because they have a  $ReWe \approx 35000$ .

The largest deviations - mentioned above - are most probably caused by the remaining local measurement and computation errors and not by inadequacy of correlation (2-139) because:

- the region  $0.05 < \frac{u^\oplus}{u_r} < 0.1$  contains not only the largest deviations caused by overestimation of the virtual mass flow coefficients, but has in addition the highest "density" of negative coefficients - presented at the bottom line of the figures - pointing towards a large measurement and/or computation error in this region.
- the elimination of low relative velocities - by terminating the computation on the condition: slip  $s < 1.05$  (cf. subsection 2.3.2.6.1.2.) - will cause overrepresentation of too low peak velocity ratios  $\frac{u^\oplus}{u_r}$ . This effect will be significant in this region because almost all void fractions and hence the relative velocities are

FIGURE 2-73

Dependence of the virtual mass coefficients on peak velocity ratio  
(test pressure 5 MN/m<sup>2</sup>)

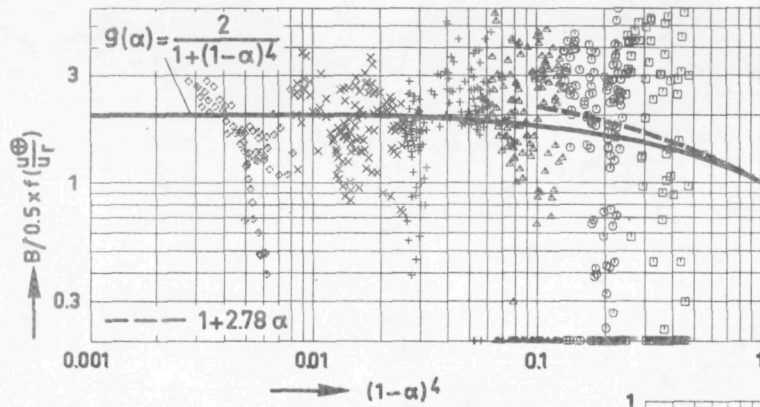
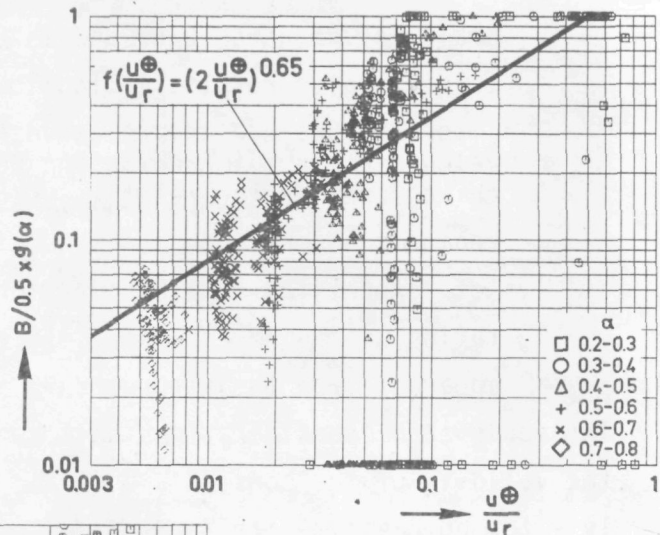


FIGURE 2-74

Dependence of the virtual mass coefficients on void fraction  
(test pressure 5 MN/m<sup>2</sup>)

FIGURE 2-75

Dependence of the virtual mass coefficient on peak velocity ratio  
(test pressure 7 MN/m<sup>2</sup>)

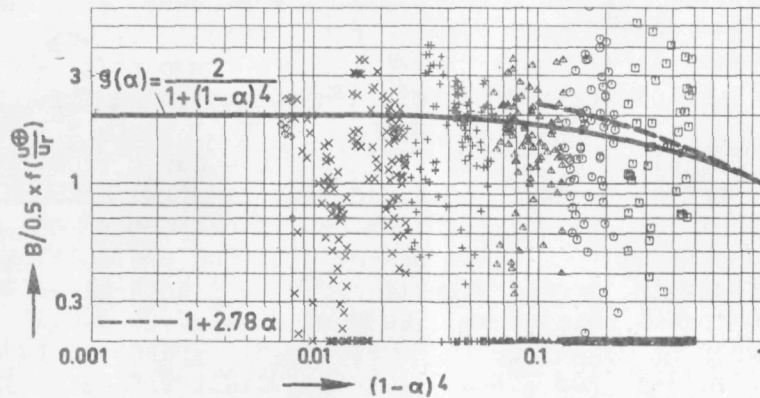
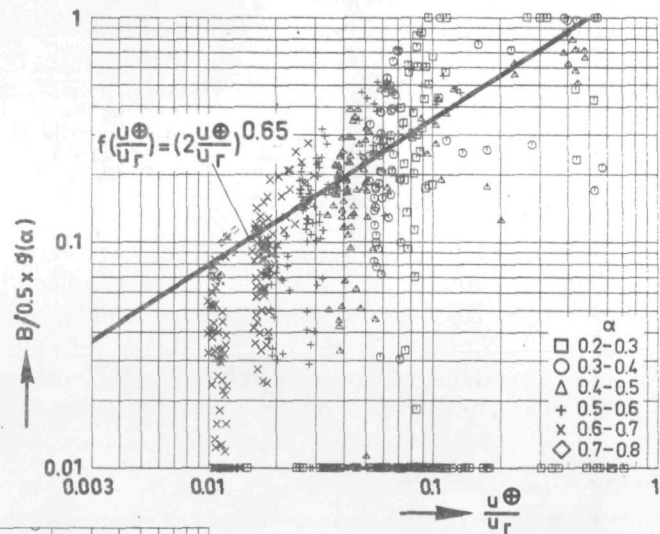


FIGURE 2-76

Dependence of the virtual mass coefficients on void fraction  
(test pressure 7 MN/m<sup>2</sup>)

\*) points at the bottomlines represent negative values

small (cf. figures 2-69 and 2-70). Overestimation of the relative velocity also results in too low values of the term  $\frac{35000}{ReWe}$ , which is important because the relative error is large for the small relative velocities in this region and because the product  $ReWe$  contains the third power of the relative velocity. Because  $ReWe \approx 35000$  in this region the corresponding reduction in the peak velocity ratio  $\frac{u^\oplus}{u_r}$  (cf. expression (2-138)) is significant and causes an overrepresentation of "measured" data left of the line  $f\left(\frac{u^\oplus}{u_r}\right) = \left(2 \frac{u^\oplus}{u_r}\right)^{0.65}$  as apparent from the figures 2-73 and 2-75.

The above error considerations have confirmed the author's confidence in the validity of the constants 0.65 and 35000 - for  $f\left(\frac{u^\oplus}{u_r}\right)$  and  $\frac{u^\oplus}{u_r}$  respectively - for both steam-water and air-water mixtures.

## 2.4. Interaction force correlations

### 2.4.1. Drag force

The final aim of this section is to derive a general correlation for the drag force coefficient, valid for both bubbly and droplet/mist flow, which is prerequisite to its use in computations for gas-liquid separators where the flow ranges from pure liquid flow at the outer wall to mist flow in the gas core. The point of departure for this purpose are the experimental results obtained on bubbly flow - void fraction  $\alpha \leq 0.75$  - described in subsections 2.3.1.6.2.1. and 2.3.2.6.2.1. for air-water and steam-water mixtures respectively. The following recommended correlations (2-135) and (2-136) - valid for the entire range from atmospheric air-water to 7 MN/m<sup>2</sup> steam-water flows - were gleaned from these subsections:

- $C_D = 0.44 (1-\langle\alpha\rangle)^6$  for pseudo one-dimensional flow
- $C_D = 0.44 (1-\alpha)^{4.25}$  for computations on the basis of local void fractions.

From these correlations it appears that for vanishing void fraction, i.e. single bubbles, the drag force coefficient equals Newton's value 0.44 which - in view of the discussion in subsection 2.2.2.1.2. on the results of BAKER and CHAO [25] - indicates that for these churn turbulent flows the turbulence is of such a magnitude that the bubbles remain grossly spherical instead of becoming mushroom-shaped.

#### 2.4.1.1. Analysis

Prior to attempting any extension of these correlations for churn turbulent bubble flow into the realm of droplet/mist flow an explanation will be given for the discrepancy with results published elsewhere for particle-liquid flow, described by:  $C_D = 0.44(1-\alpha)^{-1.7}$  for the Newton region (cf. subsection 2.2.2.1.3.).

This discrepancy cannot be explained by differences in macroscopic flow parameters and physical properties, because both the results of RICHARDSON and ZAKI [31] and the present results have - by extensive parameter variation - been proven independent from these parameters; the explanation will therefore have to be found in the microscopic aspects of both flows. The efforts on finding such an explanation will be concentrated on two effects having the right order of magnitude to cover the differences between the factors  $(1-\alpha)^{-1.7}$  and  $(1-\alpha)^{4.25}$  (or  $(1-\langle\alpha\rangle)^6$ ), viz.: cluster formation and momentum transport in the wake behind the particles/bubbles. The effects

of internal circulation, deformation, bubble diameter distribution and increased compressibility will be excluded from further consideration as being of minor importance compared to the enormous discrepancy to be explained.

#### 2.4.1.1.1. Cluster formation

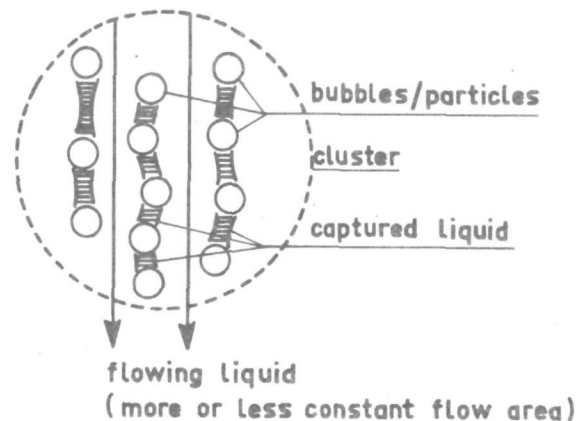
Cluster formation may be termed a variation of aggregative flow known from gas- and liquid-fluidized beds (see e.g. WALLIS [7]) where fluid "bubbles" - containing practically no solids - rise through the particle beds. In the case of gas-liquid bubble flows it is possible that - instead of "bubbles" containing only the continuous phase - clusters consisting of high concentrations of gas bubbles (the discontinuous phase) are formed. Although to date no explanation is found in literature for the formation of such fluid "bubbles", it is in the author's opinion reasonable to assume that such inhomogeneities originate from vortices from which the heavier phase is ejected by centrifugal force. This would lead to pure fluid "bubbles" in the case of particle fluidization ( $\rho_p > \rho_f$ ) and to the capture of gas bubbles in the vortices in the case of gas-liquid flow ( $\rho_g < \rho_l$ ). Some evidence for this assumption may be found in the fact that the dimension of the fluid "bubbles" strongly depends on the density ratio  $\rho_p/\rho_f$ . HARRISON et al. [80] found the ratio of fluid "bubble" and particle diameter  $D_b/d_p$  proportional to the density ratio  $(\rho_p - \rho_f)/\rho_f$ , indicating vanishing fluid "bubbles" for particle densities approaching the fluid density. This decrease of the "bubble" dimension may possibly be considered as a smooth transition from "bubbles" of the continuous phase for large  $\rho_p/\rho_f$  ratios, via no "bubbles"/clusters, to large clusters of the discontinuous gas phase in the case of gas-liquid flows with small  $\rho_g/\rho_l$  ratio. Considering the bubble clusters in the present gas-liquid flows as stable spheres moving through the remaining liquid, their effect on the values of the drag force coefficient  $C_D$  would be as follows:

- the bubble diameter  $d$  used for the computation of  $C_D$  from the intermediate result  $\frac{C_D}{d}$ :  $C_D = \frac{C_D}{d} \times d$ , has to be replaced by the much larger cluster diameter  $D_c$ , yielding much larger drag force coefficients. HARRISON et al. [80], for example, found "bubble"/particle diameter ratios up to  $10^4$  for air-fluidized beds. In the present experiments, however, the channel dimension would limit the maximum cluster diameter to about 0.07 m whereas the bubble diameter ranges from about 1 to 4 mm. The maximum cluster/bubble diameter  $D_c/d$  and hence the multiplication factor for the experimental drag force coefficient values will thus be about 70.
- the cluster is permeable for liquid, decreasing Newton's drag force coefficient below 0.44. The reduction in drag force coefficient will be especially large when assuming that part of the liquid in the cluster is captured between the bubbles, i.e. travels at the same velocity as the bubble cluster (cf. figure 2-77)): in this case the liquid passing through the cluster will flow through a more or less constant area, eliminating the velocity peaks that cause part of the drag force in flow around an individual bubble. The rate of decrease of drag force coefficient is unknown because it depends strongly on the ratio between the liquid flows through and around the cluster. In the absence of quantitative data the present author suggests a factor of magnitude 10 as a reasonable value.

Both effects together would then yield a factor  $70 \times 10 = 700$ , which is approximately equal to the discrepancy between  $(1-\alpha)^{4.25}$  and  $(1-\alpha)^{-1.7}$  for  $\alpha = 0.66$ . In view of the inaccuracies in the factor 700 it may be said

FIGURE 2-77

Constant flow area  
through a cluster



that the two effects of cluster formation, taken together, have about the right magnitude for explaining the discrepancy between solid particles and bubbles in liquid.

Two remarks are in order concerning the validity and application of the above assumption of cluster formation:

- for small values of the ratio between channel and bubble diameter  $D/d$  the cluster diameter will be affected by the channel diameter, resulting in a dependence of the drag force coefficient  $C_D$  on the channel diameter. In the present investigation the  $D/d$  ratio is considered far too large for this effect to occur, while the variation in channel diameter from 0.05 to 0.1 m is too small - with respect to the inaccuracy in the measured drag force coefficients - to even notice any such dependency should it have occurred.
- in view of the dependence of cluster formation on the density ratio  $(\rho_c - \rho_d)/\rho_c$ , the drag force coefficient  $C_D$  should also be dependent on this ratio. In all the present experiments, however, the ratio  $(\rho_l - \rho_g)/\rho_l$  has been so close to unity as to foreclose the likelihood of detecting any such dependency. For solid-liquid flows it is known from literature see e.g. [80] and [81]) that the liquid "bubbles" are small and thus of minor importance, which should explain the independency of  $(\rho_l - \rho_p)/\rho_l$  in the results from RICHARDSON and ZAKI [31] (cf. subsection 2.2.2.1.3.).

#### 2.4.1.1.2. Momentum transfer

The momentum transfer from the liquid in the wake of a bubble to a second bubble entering this wake by a stochastic lateral movement is analyzed in appendix 2-N. The model developed there is based on the assumption that a fraction  $\eta$  of the bubbles - to be discussed below - enters or has entered the wakes of preceding bubbles. This simple model correlates the "natural" drag force coefficient  $C_D$ , i.e. the coefficient acting outside the wakes, to the "measured" drag force coefficient  $C_{D_n}$  by equation (2-N-8):

$$C_{D_n} = C_D \left\{ 1 + \eta \left( \frac{\rho_l}{\rho_g + B\rho_l} - 1 \right) \frac{u_w}{u_r} \right\}^2$$

where  $\frac{u_w}{u_r}$  is the ratio between the average wake and relative velocities of preceding bubble (cf. figure 2-N-1). The "added mass" is seen to have a significant importance via the virtual mass coefficient  $B$ . For gas-liquid flows - where the virtual mass coefficient  $B < 1$  for the present experiments - the term between braces exceeds unity, i.e. the "natural" drag force coefficient  $C_D$  is larger than that "measured" in the experiments; the

magnitude of this correction term will be discussed below.

A more complex model - also derived in appendix 2-N - where infinite "chains" are formed by bubbles entering the wake of a bubble which is already in the wake of a preceding bubble itself, results in an even larger amplification

term, viz.  $C_{Dn} = C_D \left\{ 1 + \frac{\eta p}{1 - \eta p} \right\}^2$  in the case  $\eta p = \eta \left( \frac{\rho_l}{\rho_g + B\rho_l} - 1 \right) \frac{u_w}{u_r} < 1$ . As

explained in appendix N this second model is so much simplified that its only purpose here is to indicate that the real correction term will exceed the value resulting from correlation (2-N-8).

Prior to evaluating the magnitude of the correction term between braces, it should be pointed out that - as is explained in appendix 2-N - for solid-liquid flows with  $\rho_p > \rho_l$  the particles entering a wake get a velocity increase less than the wake velocity. This fact increases the relative velocity between leading and entered particle, which is expressed by the

negativity of the term  $\left( \frac{\rho_l}{\rho_p + B\rho_l} - 1 \right)$ , yielding an opposite effect of momen-

tum exchange in the wakes for solid-liquid flows compared to gas-liquid flows. Furthermore it is easy to derive that for solid-liquid flows the

absolute value of the term  $\left( \frac{\rho_l}{\rho_p + B\rho_l} - 1 \right)$  will be small compared to the corresponding term for gas-liquid flows, making the effect of momentum exchange in wakes much more important for bubble flows than for particle flows.

The magnitude of the correction term  $\left\{ 1 + \eta \frac{\rho_l}{\rho_g + B\rho_l} - 1 \right\} \frac{u_w}{u_r}$  has been

evaluated in [82] for void fractions  $\alpha < 0.7$ . The present author, however, considers it preferable to limit the consideration of this effect to void fractions not exceeding 0.4, as the occurrence of wakes may be doubtful for higher void fractions. The three distinct parts of the correction term are:

- the fraction  $\eta$  of the bubbles flowing in the wake of a preceding bubble, which is equal to the fraction of the liquid being the summation of all distinct wake volumes.

The wake volume of a single bubble can be estimated by introducing the average distance  $x$  between the centers of two bubbles and assuming the cylindrical volume between two consecutive bubbles - having the same diameter as the bubbles - to represent the wake volume of the leading bubble, yielding:

$$V_w = x \frac{\pi}{4} d^2 - 2 \cdot \frac{1}{2} \cdot \frac{\pi}{6} d^3 = 1.5 \left( \frac{x}{d} - \frac{2}{3} \right) V_b \quad (2-152)$$

- The ratio  $\frac{x}{d}$  can be related to the void fraction; taking into account void fraction  $\alpha \approx 0.7$  where the bubbles touch each other, this ratio can reasonably be approximated by:

$$\frac{x}{d} = \sqrt[3]{\frac{0.7}{\alpha}} \quad (2-153)$$

Summation over all bubbles, writing the total bubble volume as the void fraction times the total volume and dividing by the total liquid volume, yields for the wake volume fraction:

$$\eta = 1.5 \frac{\alpha}{1 - \alpha} \left[ \sqrt[3]{\frac{0.7}{\alpha}} - \frac{2}{3} \right] \quad (2-154)$$

which equals 0.54 for  $\alpha = 0.4$ .

- the quotient  $\frac{\rho_l}{\rho_g + B\rho_l}$ , which is dominated by the "added mass" for the present gas-liquid flows can therefore be approximated by the reciprocal of the virtual mass coefficient  $\frac{1}{B}$ . Although the parameters determining the virtual mass coefficient B are rather complex, it appears from figures 2-47, 2-73 and 2-75 that for a void fraction  $\alpha = 0.4$  this coefficient should not differ too much from  $B = 0.2$ , yielding  $(\frac{\rho_l}{\rho_g + B\rho_l} - 1) \approx (\frac{1}{B} - 1) = 4$
- the velocity ratio  $\frac{u_w}{u_r}$ , to be determined from experiments performed by JAYAWEERA et al. [83] on the sedimentation of two spheres of equal size falling one behind the other. For  $Re_p > 1$ , i.e. with a turbulent wake, and spacing defined by  $\frac{x}{d} < 5$  (equivalent to void fractions exceeding 0.8%), they found the trailing sphere approaching the leading one at a velocity equal to 0.35 times the relative velocity of the latter. Hence it can be concluded that the velocity ratio  $\frac{u_w}{u_r} = 0.35$ .

All together the correction term equals  $\{1 + 0.54 \times 4 \times 0.35\}^2 = 1.755^2 = 3.1$  for  $\alpha = 0.4$ , while - on behalf of the correlation  $C_D = 0.44(1-\alpha)^{4.25}$  - a factor  $\frac{1}{(1-\alpha)^{4.25}} = \frac{1}{0.6^{4.25}} = 8.75$  is needed to increase the measured drag

force coefficient  $C_D$  from 0.05 to 0.44. Hence it appears that the effect of "chain" formation has to be incorporated to obtain a correction factor of the right magnitude. The very simple model of "chain" formation yields

a correction term  $\{1 + \frac{0.755}{1-0.755}\}$ , where the second term is amplified by a factor  $\frac{1}{1-0.755} \approx 4$  compared to the model excluding "chain" formation. In

the author's opinion this amplification is excessive on behalf of the simplifications of the model and a factor of 2 seems more realistic, yielding  $C_{Dn} = \{1+1.6\}^2 C_D$ . This latter correction factor of 6.8 is of the right magnitude to explain the decrease of drag force coefficient for bubble flows.

It has to be remarked that the direct dependency - in the case of bubble flows - of the correction factor on the reciprocal virtual mass coefficient  $\frac{1}{B}$  points towards a correction factor equally complex as the correlation for the virtual mass coefficient itself, whereas the experiments yield a very simple correlation for the drag force coefficient only. This apparent contrast may be explained from graphs 2-47, 2-73 and 2-75 for the virtual mass coefficients, which indicate that the most significant parameter  $\frac{u^{\oplus}}{u_r}$  depends almost solely on the void fraction. This indicates the possibility of a rather accurate correlation for the virtual mass coefficient depending on the void fraction only and hence the existence of a correction factor for which the same would hold. In view of the simplifications in the momentum exchange model it is, however, impossible to carry this explanation beyond the stage of a plausible hypothesis.

The above evaluation of the effects of cluster formation and momentum exchange, merely confirms that they both have about the right magnitude for explaining the large discrepancy between bubble and particle flows. The actual occurrence of one of these two mechanisms cannot be proven from the available experimental data, leaving open - in addition - the possibility

of a combined occurrence. In this latter case it is even quite possible that both mechanisms cannot be separated at all: in clusters - consisting of closely spaced bubbles - it is highly likely that the momentum transfer is particularly important, while on the other hand the approach and separation of bubbles and particles respectively caused by the momentum exchange in the wake of the leading bubble/particle furthers the formation of bubble clusters and liquid "bubbles" in addition to the effect of vortices mentioned above.

#### 2.4.1.2. Extension to mist flow

So far the discussions have been limited to bubble flow. The balance equations and interaction forces for mist flow differ from those for bubble flow in three respects:

- the frictional pressure drop - forming part of the momentum balance of the continuous phase - shifts from the liquid to the gas momentum balance
- the drag force definition has to be based on droplets, i.e.

$$F_D = \frac{3}{4} (1-\alpha) \frac{C_{Dd}}{d} \rho_g u_r^2 \quad (\text{the subscript } d \text{ refers to droplets) instead}$$

$$\text{of } \frac{3}{4} \alpha \frac{C_D}{d} \rho_l u_r^2 \text{ for bubble swarms}$$

- the virtual mass term - added to the acceleration term of the discontinuous phase - shifts to the liquid momentum balance and has to be based on droplet flow.

The virtual mass term, however, is of no significance in mist flow as will be discussed in subsection 2.4.2.2. and will therefore be ignored in this analysis.

For one-dimensional pipe flow the shift of the frictional pressure drop from liquid to gas momentum balance is taken into account by the introduction of the function  $\Delta_\alpha$ , defined arbitrarily<sup>\*</sup>) by the author as

$$\begin{aligned} \Delta_\alpha &= 0 && \text{for } \alpha \leq 0.75 \\ \Delta_\alpha &= 10(\alpha - 0.75) && \text{for } 0.75 < \alpha < 0.85 \\ \Delta_\alpha &= 1 && \text{for } \alpha \geq 0.85 \end{aligned} \quad (2-155)$$

Incorporation of this delta function in the momentum balances yields

for the gas phase

$$\frac{d}{dz} (\alpha A \rho_g u_g^2) + F_A = -\alpha A \frac{dp}{dz} - \alpha A \rho_g g - F_D A - \Delta_\alpha \left(\frac{dp}{dz}\right)_{fr} \quad (2-156)$$

for the liquid phase

$$\frac{d}{dz} (1-\alpha) A \rho_l u_l^2 = -(1-\alpha) A \frac{dp}{dz} - (1-\alpha) A \rho_l g + F_D A - (1-\Delta_\alpha) \left(\frac{dp}{dz}\right)_{fr} \quad (2-157)$$

While a similar delta function approach might be followed for the drag force  $F_D$  in these balances to make the transition from bubble flow to droplet flow, a single smooth curve will be derived in order to obtain a better insight into the change in drag force caused by this transition. For this purpose the drag force definition for droplet flow has to be transformed to fit the mathematical description for bubble flow, yielding a common base

<sup>\*</sup>) Any function changing from zero to unity around a void fraction of about 0.8 can be chosen

throughout the entire range of void fractions. This implies that the drag force be defined by  $F_D = \frac{3}{4} \alpha \frac{C_D}{d^{\star}} \rho_l u_r^2$  even in the mist flow region. In this expression  $d^{\star}$  stands for the bubble diameter resulting from expression (2-97) for the actual flow conditions<sup>\*</sup>). The required transformation for droplet flow to the expression  $F_D = \frac{3}{4} (1-\alpha) \frac{C_{Dd}}{d_d} \rho_g u_r^2$  is obtained by defining the drag force coefficient  $C_D$  for this flow pattern as

$$C_D = C_{Dd} \frac{d^{\star}}{d_d} \frac{1-\alpha}{\alpha} \frac{\rho_g}{\rho_l} \quad (2-158)$$

It is reasonable to assume that the mist flow under consideration is Newtonian, yielding  $C_{Dd} = 0.44 f(\alpha)$ . The foregoing discussion on cluster formation and momentum transport in wakes indicate that the most suitable function  $f(\alpha)$  - representing the effect of neighbouring droplets - is that obtained by RICHARDSON and ZAKI [31] for particle/liquid flows. Taking into account that in the discussion of subsection 2.2.2.1.3.  $\alpha$  stands for the particle fraction the resulting expression would be  $C_{Dd} = 0.44 \alpha^{-1.7}$  (cf. correlation (2-51)). However, considering the uncertainty on the validity of this supposition and the small effect of  $f(\alpha) = \alpha^{-1.7}$  for void fractions close to unity, the simple approximation  $C_{Dd} = 0.44$  appears preferable.

The ratio between the fictitious bubble diameter  $d^{\star}$  and droplet diameter  $d_d$  is derived in appendix 2-0:

$$\frac{d^{\star}}{d_d} = \left[ \frac{(2.5-\alpha)^3}{\alpha^2(1-\alpha)} \right]^{1/5} \left[ \frac{\rho_l}{\rho_g} \right]^{2/5} \left[ \frac{1 + \frac{\alpha}{2.5-\alpha} \frac{\rho_g}{\rho_l}}{1 + \frac{1.5+\alpha}{1-\alpha} \frac{\rho_g}{\rho_l}} \right]^{3/5} \quad (2-159)$$

Substitution of the above two results in expression (2-158) yields

$$C_D = 0.44 \left[ \frac{(2.5-\alpha)^3(1-\alpha)^4}{\alpha^7} \right]^{1/5} \left[ \frac{\rho_g}{\rho_l} \right]^{3/5} (1+\xi_d)^{3/5} \quad (2-160)$$

where

$$\xi_d = 1 - \frac{1 + \frac{\alpha}{2.5-\alpha} \frac{\rho_g}{\rho_l}}{1 + \frac{1.5+\alpha}{1-\alpha} \frac{\rho_g}{\rho_l}} \quad (2-161)$$

which is small compared to unity.

The curves computed with this correlation for atmospheric air-water mixtures and steam-water mixtures at 7 MN/m<sup>2</sup> have been plotted in figure 2-78 (the values for steam-water at 5 MN/m<sup>2</sup> are about 20% below those for 7 MN/m<sup>2</sup>). The curve for atmospheric air-water blends fairly smoothly with the correlation  $C_D = 0.44(1-\alpha)^{4.25}$ <sup>\*\*</sup>), the transition occurring around  $\alpha \approx 0.57$ ,

<sup>\*</sup>) The superscript  $\star$  is used to indicate parameters based on correlations and expressions for bubble flow, while the actual flow is droplet flow. These parameters therefore have a numerical meaning only.

<sup>\*\*</sup>) The comparison is made with the correlation for local void fractions  $C_D = 0.44(1-\alpha)^{4.25}$ , because the derivation of the mist flow correlation does not allow for inhomogeneity.

which is a reasonable value for the transition from bubble to mist flow.

By contrast the curve for steam-water mixtures is seen to yield  $C_D$ -values in the intermediate void fraction range -  $0.5 < \alpha < 0.7$  - far exceeding those found with bubble flow for void fractions up to 0.65 (cf. figures 2-71 and 2-72A). The validity of this curve for mist flow therefore appears limited to void fractions  $\alpha \geq 0.9$ .

Figure 2-78 leads to the following conclusions regarding a general correlation for the drag force coefficient  $C_D$  for local void fractions:

- for high void fractions the complex void fraction dependency for mist flow found in correlation (2-160) can be approximated with reasonable accuracy by the much simpler proportionality  $C_D \sim (1-\alpha)^{0.75}$
- the above simplification of the void fraction dependency implies that the proportionality of  $C_D$  with  $(\rho_g/\rho_l)^{3/5}$  - proposed in correlation (2-160) - has to be adjusted to  $(\rho_g/\rho_l)^{0.4}$  in the high void fraction region ( $\alpha \approx 0.95$ ) in order to compensate for the elimination of the term  $(1+\xi_d)^{3/5}$  (equation (2-161)).

Implementation of these two conclusions leads to the final drag force correlation

$$C_D = 0.44(1-\alpha)^{4.25} \left( 1 + 0.25 \frac{(\rho_g/\rho_l)^{0.4}}{(1-\alpha)^{3.5}} \right) \quad (2-162)$$

for local void fractions.

Curves representing this correlation for atmospheric air-water and steam-water at  $7 \text{ MN/m}^2$  have been included in figure 2-78.

The above equation (2-162) fulfills the aim of this chapter to provide a suitable drag force correlation for use in the centrifugal flow computations of chapters 3 and 4. In addition an extension of correlation (2-135) for one-dimensional bubble flow:  $C_D = 0.44 (1-\alpha)^6$  to the mist flow region is presented in appendix 2-Q. This appendix is added in view of the dearth of formulae for one-dimensional two-phase flow and the importance of this area to engineering practice.

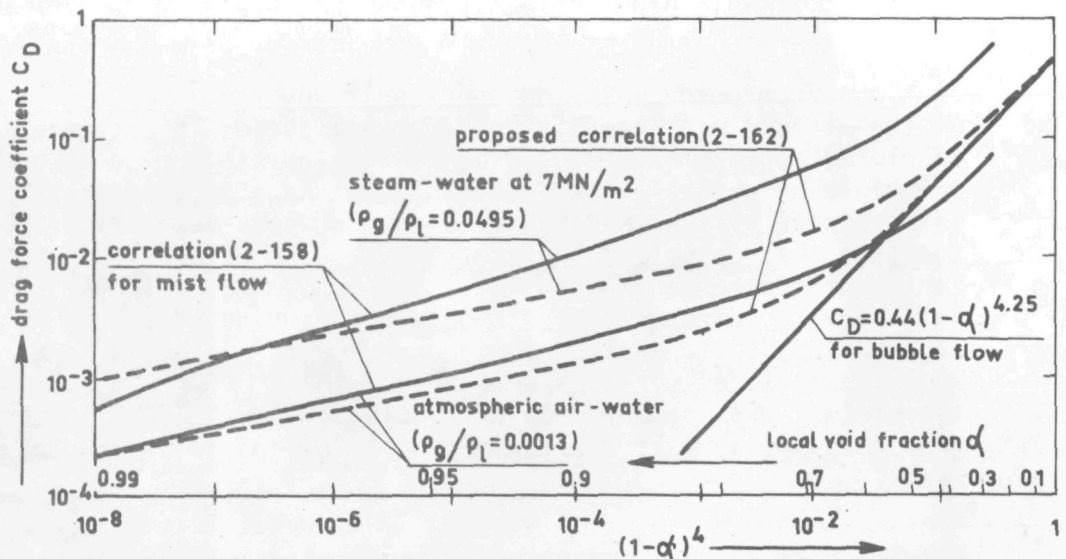


FIGURE 2-78

Correlations for the drag force coefficient over the entire range of local void fractions

## 2.4.2. Virtual mass

In conformity with its predecessor this subsection consists of two parts: an analysis of the experimental results and a discussion on the extension of the correlation into the mist flow region.

### 2.4.2.1. Analysis

The analysis is based on correlation (2-139)

$$B = \frac{1}{2} \frac{2}{1+(1-\alpha)^4} \left(2 \frac{u^\oplus}{u_r}\right)^{0.65}$$

found valid for atmospheric air-water as well as for high pressure steam-water mixtures (the peak velocity ratio  $\frac{u^\oplus}{u_r}$  is defined by correlation (2-138)).

For small void fractions the void fraction dependency  $g(\alpha) = \frac{2}{1+(1-\alpha)^4}$

has been shown to be in good agreement with the function  $(1+2.78\alpha)$  derived analytically by VAN WIJNGAARDEN [43] (cf. subsection 2.3.1.6.2.2.). For higher void fractions figures 2-49 & 50 and 2-74 & 76 indicate that the numerical value of this function asymptotically approaches 2. No further discussion on this function is required and therefore the present analysis will focus on the peak velocity ratio  $\frac{u^\oplus}{u_r}$ .

As apparent from appendix 2-I this ratio will - for the churn turbulent flows of the present investigation - mostly depend on (turbulence) liquid viscosity, an effect that cannot be evaluated by potential flow theory.

For this latter type of flow, however, the ratio  $\frac{u^\oplus}{u_r}$  is known to depend on the shape of the submerged body (see e.g. [84]). With the introduction of the generalized formula (2-137):  $B = K_B f\left(\frac{u^\oplus}{u_r}\right) g(\alpha)$  it was tacitly assumed that the effects of turbulence viscosity and shape on the virtual mass coefficient are both represented by the same function for the peak velocity ratio  $f\left(\frac{u^\oplus}{u_r}\right)$ . This hypothesis forms the rationale for comparing the experimentally obtained function  $f\left(\frac{u^\oplus}{u_r}\right) = \left(2 \frac{u^\oplus}{u_r}\right)^{0.65}$  with the theoretical predictions from potential flow considerations\*).

As the virtual mass coefficients for ellipsoids in potential flow are tabulated in many handbooks (see e.g. [84]) this type of body would in principle be suitable for investigating the effect of shape on the relationship between virtual mass coefficient and peak velocity ratio. In view of the fact that description of the flow around ellipsoids requires a large series of sources and sinks (cf. [84]), whereas a single source and sink suffice - in uniform flow - to obtain a Rankine body, the latter shape will be used instead to analyse the peak velocity ratio. This approximation appears justified since LANDWEBER and WINZER [85] empirically showed that the virtual mass of any body of revolution deviates by no more than 14% from the virtual mass coefficient of an ellipsoid having the same axis ratio.

\* ) It should be stressed that correlations (2-138) - valid for the peak velocity ratios of the flows under consideration - do not incorporate shape effects because the bubbles remain largely spherical in these churn turbulent flows as stated in subsection 2.4.1.

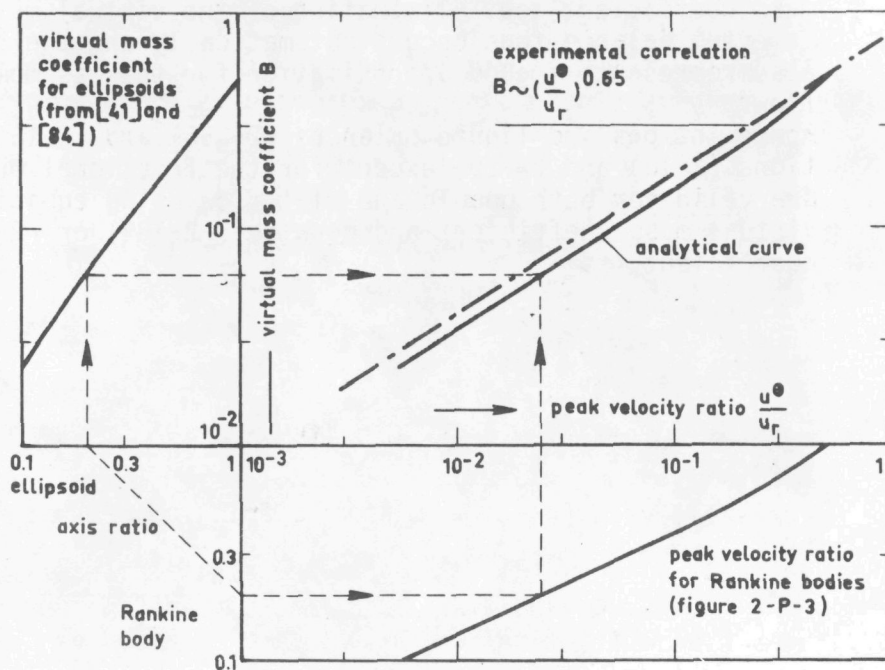


FIGURE 2-79

*Composition of the analytical curve for the dependency of the virtual mass coefficient on peak velocity ratio*

The analysis of the flow around a Rankine body given in appendix 2-P results in a numerical description of the peak velocity ratio  $\frac{u^{\oplus}}{u_r}$  as a function of the axis ratio, plotted in figure 2-P-3. Combination of this figure with the graphical presentation of the virtual mass coefficient for ellipsoids, also plotted against their axis ratio, yields a general relationship between the virtual mass coefficient and peak velocity ratio shown in figure 2-79. Excellent agreement is found between the resulting curve and the experimental correlation  $B \sim (\frac{u^{\oplus}}{u_r})^{0.65}$ , which in the author's opinion forms convincing proof of the validity of the experimental correlation (2-139).

#### 2.4.2.2. Extension to mist flow

As the virtual mass term forms part of the momentum balance of the discontinuous phase, two separate effects on this term  $F_{AA}$  can be distinguished in the momentum balances for mist flow compared to those for bubble flow ((2-16) and (2-19)), viz.:

- it shifts from the momentum balance for the gas phase (2-16) to that for the liquid phase (2-19)
- it has to be based on droplet flow.

The latter effect yields an added mass of  $BV_d\rho_g$  where  $V_d$  is the volume of the single droplet under consideration. Because of the generally small density ratio  $\rho_g/\rho_l$  this added mass may be ignored for droplet flow. Therefore the liquid momentum balance for bubble flow (2-19) is considered valid throughout the entire range of bubble and mist flow. Part of the first effect is thus fulfilled, the only remaining difference between the mist and bubble flow balances now being the elimination of this term from the gas momentum balance. However, as can be seen from figures 2-47 & 48 and 2-73 & 75, the peak velocity ratio  $\frac{u^{\oplus}}{u_r}$  in the flows under consideration vanishes for high void fractions, yielding a vanishing virtual

mass coefficient too. Elimination of the virtual mass term from the gas momentum balance thus occurs automatically and the balance equation (2-16) also represents a good approximation for the gas momentum balance for mist flow.

Hence the gas and liquid balances (2-156) and (2-157) - identical to equations (2-16) and (2-19) except for the frictional pressure drop terms - are valid for both bubble and mist flow using equation (2-139) for the virtual mass coefficient and equation (2-162) or (2-Q-1) for the drag force coefficient.

### 3. NUMERICAL PROCEDURES FOR DESCRIBING ROTATING TWO-PHASE FLOW

#### 3.1. Introduction

This chapter consists of three main parts, viz.:

- the description of the model for rotation-symmetric two-phase flow
- the description and discussion of two solution methods
- the evaluation of the application of one of the solution methods to rotating two-phase flow

As follows from chapter 2 the model is based on the two-dimensional balances for mass and momentum of both phases and completed by the introduction of an approximation for the viscosity terms and the development of special momentum equations for the flow between guide vanes.

The first solution method discussed is the so called explicit scheme, which will be shown later on to be promising for the numerical solution of (rotating) two-phase flow. This method was developed after it had become apparent that earlier developments based on the alternating direction implicit method would not result in a viable computer program. This notwithstanding the description of this latter A.D.I.-method is included because its subsequent evaluation shows clearly that the two reasons for failure lay within the structure of two-phase flow and are therefore relevant to the choice of other methods for numerical solution of two-phase flows.

The evaluation of the explicit scheme is done by comparing some of the computed data with measured data from rotating two-phase flows described and discussed in chapter 4.

#### 3.2. Model for rotation-symmetric flow

The general description of a stationary, adiabatic, three-dimensional two-phase flow yields eight unknown parameters, viz.:

- the pressure, which for the overall description of two-phase flows is always taken equal for both phases
- the void fraction, defined in equation (2-2) as the averaged time fraction during which the observed point is the gas phase
- six velocities, viz. the axial, radial and tangential velocities for both phases (these names are based on a description in cylindrical coordinates)

Application of the conservation laws in the differential form (cf. the balances presented in subsection 2.2.1. for one-dimensional flow) yields for the present case <sup>\*</sup>):

- a mass balance for each of the phases
- six momentum balances, viz. in three directions for each of the phases

stating a problem with eight unknowns and eight partial differential equations, of which the latter are completed with additional equations for physical properties and correlations for the interaction forces between the phases.

Because of the present goal, viz. the description of two-phase flow in axial up-comer separators (cf. the examples of existing separators in chapter 4) the flow is supposed to be rotation-symmetric, i.e.  $\frac{\partial}{\partial \varphi}(\dots) = 0$ , making the description of the flow two-dimensional. It should be noted that, notwithstanding the description in axial and radial coordinates,

<sup>\*</sup>) *A full description would include the energy balance, omitted for the present adiabatic flows.*

z and r respectively, the tangential velocities  $u_{g\varphi}$  and  $u_{l\varphi}$  are non-zero and of utmost significance for the present type of flows.

### 3.2.1. Conservation laws

#### 3.2.1.1. Mass balances

The mass balances are:

gas phase

$$\frac{\partial}{\partial r} (\alpha \rho_g u_{gr}) + \frac{\alpha \rho_g u_{gr}}{r} + \frac{\partial}{\partial z} (\alpha \rho_g u_{gz}) = \phi'_{lg} \quad (3-1)$$

liquid phase

$$\rho_l \frac{\partial}{\partial r} ((1-\alpha)u_{lr}) + \frac{(1-\alpha)\rho_l u_{lr}}{r} + \rho_l \frac{\partial}{\partial z} ((1-\alpha)u_{lz}) = -\phi'_{lg} \quad (3-2)$$

These mass balances are completed by some additional equations.

The first of these refers to the mass transport by evaporation  $\phi'_{lg}$  [kg/m<sup>3</sup>s]. Although in the case of gas-liquid flow some evaporation does take place even for adiabatic flow due to the decreasing pressure as the mixture passes the separator, the amount is negligible for practical purposes for both atmospheric air-water and high pressure steam-water mixtures, yielding the additional assumption

$$\phi'_{lg} = 0 \quad (3-3)$$

Furthermore the densities are supposed to be known functions of pressure and temperature, while - as apparent from equation (3-2) - the variations in the liquid density are assumed to be negligibly small, yielding:

$$\rho_g = f_1(p, \theta) \quad (3-4)$$

and

$$\rho_l = f_2(\bar{p}, \theta) = \text{constant} \quad (3-5)$$

In the case of steam-water mixtures the temperature equals the saturation temperature, while for air-water mixtures the temperature is supposed to be known.

#### 3.2.1.2. Momentum balances

For reasons discussed in subsection 3.2.1.2.2. a distinction is made between the momentum balances in the tangential direction in the free flow field above the separator guide vanes and those between the guide vanes.

##### 3.2.1.2.1. Momentum balances in a free flow field

The momentum balances for this rotation-symmetric flow contain in principle the same terms as those discussed in subsection 2.2.1.2. and 2.2.1.3. Adapting the same inaccuracy as discussed in subsection 2.2.1.2. with respect to the exchange of momentum due to change of phase, the momentum balances for the control volume  $r d\varphi dr dz$  of figure 3-1 read:

gas phase

r-direction

$$\begin{aligned} \frac{\partial}{\partial r} (\alpha \rho_g u_{gr}^2) + \frac{\alpha \rho_g u_{gr}^2}{r} + \frac{\partial}{\partial z} (\alpha \rho_g u_{gr} u_{gz}) + F_{Ar} = \\ = -\alpha \frac{\partial p}{\partial r} + \alpha \rho_g \frac{u_{g\varphi}^2}{r} - F_{Dr} \end{aligned} \quad (3-6)$$

z-direction

$$\begin{aligned} \frac{\partial}{\partial r} (\alpha \rho_g u_{gr} u_{gz}) + \frac{\alpha \rho_g u_{gr} u_{gz}}{r} + \frac{\partial}{\partial z} (\alpha \rho_g u_{gz}^2) + F_{Az} = \\ = -\alpha \frac{\partial p}{\partial z} - \alpha \rho_g g - F_{Dz} \end{aligned} \quad (3-7)$$

$\varphi$ -direction

$$\frac{\partial}{\partial r} (\alpha \rho_g u_{gr} u_{g\varphi}) + \frac{\alpha \rho_g u_{gr} u_{g\varphi}}{r} + \frac{\partial}{\partial z} (\alpha \rho_g u_{gz} u_{g\varphi}) + F_{A\varphi} = -F_{D\varphi} \quad (3-8)$$

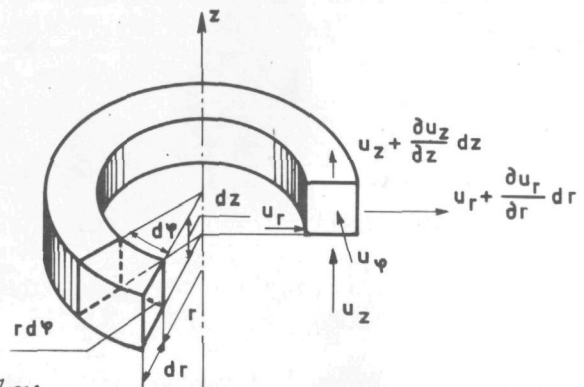


FIGURE 3-1

*Control volume for rotation-symmetric flow*

The left hand side of all three balances consists of the usual momentum transport terms and the force  $F_A$  due to the virtual mass, further discussed in subsection 3.2.2.1.

Some differences exist in the right hand sides. In the first place there are the acceleration force fields  $\frac{u_{g\varphi}^2}{r}$  and  $g$ , the negative sign of the latter being caused by taking the upward flow direction positive. No force field exists in the tangential direction and because of the rotation-symmetry there is neither a pressure gradient in this direction. The absence of viscosity terms in these balances for the gas phase is explained in subsection 2.2.1.2. for the assumption of bubble flow. As the flow in a cyclone includes the gas core formed at the centerline, the above gas phase equations have to be extended with a viscosity term in the same way as proposed for the frictional pressure drop in the case of one-dimensional mist flow (cf. subsection 2.4.1.2.). This will be discussed in subsection 3.2.2.2. where the simplification of the viscosity terms is expounded.

The momentum balances for the liquid phase include the viscosity terms, yielding:

liquid phase

r-direction

$$\begin{aligned} \rho_1 \frac{\partial}{\partial r} ((1-\alpha)u_{1r}^2) + \frac{(1-\alpha)\rho_1 u_{1r}^2}{r} + \rho_1 \frac{\partial}{\partial z} ((1-\alpha)u_{1r}u_{1z}) = \\ = - (1-\alpha) \frac{\partial p}{\partial r} + (1-\alpha)\rho_1 \frac{u_{1\varphi}^2}{r} + F_{Dr} + \\ + \frac{\partial}{\partial r} (\eta_t \frac{1}{r} \frac{\partial}{\partial r} (r(1-\alpha)u_{1r})) + \frac{\partial}{\partial z} (\eta_t \frac{\partial}{\partial z} ((1-\alpha)u_{1r})) \end{aligned} \quad (3-9)$$

z-direction

$$\begin{aligned} \rho_1 \frac{\partial}{\partial r} ((1-\alpha)u_{1z}u_{1r}) + \frac{(1-\alpha)\rho_1 u_{1r}u_{1z}}{r} + \rho_1 \frac{\partial}{\partial z} ((1-\alpha)u_{1z}^2) = \\ = - (1-\alpha) \frac{\partial p}{\partial z} - (1-\alpha)\rho_1 g + F_{Dz} + \\ + \frac{1}{r} (\eta_t r \frac{\partial}{\partial r} ((1-\alpha)u_{1z})) + \frac{\partial}{\partial z} (\eta_t \frac{\partial}{\partial z} ((1-\alpha)u_{1z})) \end{aligned} \quad (3-10)$$

$\varphi$ -direction

$$\begin{aligned} \rho_1 \frac{\partial}{\partial r} ((1-\alpha)u_{1r}u_{1\varphi}) + \frac{(1-\alpha)\rho_1 u_{1r}u_{1\varphi}}{r} + \rho_1 \frac{\partial}{\partial z} ((1-\alpha)u_{1z}u_{1\varphi}) = \\ = F_{D\varphi} + \frac{1}{r^2} \frac{\partial}{\partial r} (\eta_t r^3 \frac{\partial}{\partial r} ((1-\alpha)\frac{u_{1\varphi}}{r})) + \frac{\partial}{\partial z} (\eta_t \frac{\partial}{\partial z} ((1-\alpha)u_{1\varphi})) \end{aligned} \quad (3-11)$$

The viscosity terms in these balances are derived in appendix 3-A.

The elaboration of the drag force terms  $F_D$  using the recommended correlations of chapter 2 will be treated in subsection 3.2.2..

### 3.2.1.2.2. Tangential momentum balances between guide vanes

Between guide vanes the flow is not longer rotation-symmetric and its mathematical description becomes extremely complex due to the presence of secondary circulation. In order to achieve such a mathematical description without going to an effort far exceeding the importance of the problem, the assumption of ideal flow without secondary circulation, valid for single phase flow, has been maintained. For such a flow it is reasonable to assume that the velocities and void fraction still have an rotation-symmetric character, but the non-rotation-symmetric character of the pressure (cf. figure 3-2) is essential for the generation of the tangential velocities. Hence the momentum balances in axial and radial direction - as described above - remain valid between guide vanes, but the tangential balances should be extended with a term for the pressure gradient  $\frac{\partial p}{\partial \varphi}$ .

However, in order to keep the set of equations as simple as possible, the assumption of ideal flow between the guide vanes has been further extended in appendix 3-B to express one of the three velocities in terms of the other two velocities and the geometric parameters of the vanes. It is for vanes of constant thickness derived that:

$$u_{\varphi}(r,z) = \frac{u_z \operatorname{tg} \gamma(r,z) + u_r \sin \delta(r,z)}{\cos \delta(r,z)} \quad (3-12)$$

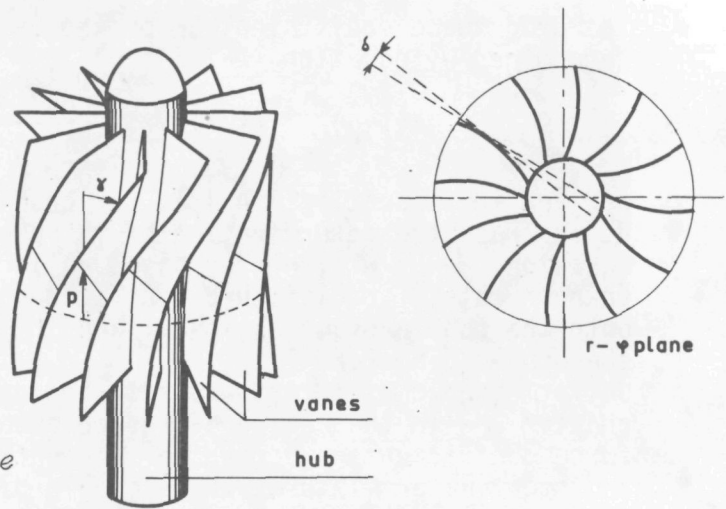


FIGURE 3-2

*Geometric parameters and pressure gradient in guide vanes*

where  $\gamma$  is the angle with the vertical in the  $z-\varphi$  plane and  $\delta$  the angle with the radius in the  $r-\varphi$  plane.

This equation is valid for both phases, yielding the two equations needed to replace the tangential momentum balances (3-8) and (3-11).

### 3.2.2. Additional equations

The momentum balances discussed in subsection 3.2.1.2.1. need to be further completed with respect to the interaction forces  $F_D$  and  $F_A$ , while the lack of a correlation for the kinematic turbulence viscosity

$\eta_t = \eta(1 + \frac{\epsilon}{\nu})$  for two-phase flow in literature results in the need for an approximation of the viscosity terms for practical applications. These two supplements and the boundary conditions for the numerical procedures will be discussed in the next three subsections.

#### 3.2.2.1. Interaction forces

This subsection deals with the determination of the  $r, z$  and  $\varphi$  components of the resultant forces.

The resultant drag force  $F_{Dt}$  has been defined in subsection 2.2.2. and its magnitude determined as  $F_{Dt} = \frac{3}{4} \alpha \frac{C_D}{d} \rho_l u_{rt}^2$ , where  $u_{rt}$  represents the resultant relative velocity.

Since the direction of the resultant drag force coincides with that of the relative velocity, the ratio between the various components and the resultant drag force is identical to that of the relative velocity, i.e.

$F_{Dr} = F_{Dt} \frac{u_{rr}}{u_{rt}}$ ,  $F_{Dz} = F_{Dt} \frac{u_{rz}}{u_{rt}}$  and  $F_{D\varphi} = F_{Dt} \frac{u_{r\varphi}}{u_{rt}}$ . Substitution of the resultant drag force yields:

$$F_{Dr} = \frac{3}{4} \alpha \frac{C_D}{d} \rho_l u_{rt} u_{rr}$$

$$F_{Dz} = \frac{3}{4} \alpha \frac{C_D}{d} \rho_l u_{rt} u_{rz}$$

and

$$F_{D\varphi} = \frac{3}{4} \alpha \frac{C_D}{d} \rho_l u_{rt} u_{r\varphi}$$

(3-13)

In these expressions the resultant relative velocity  $u_{rt} = \sqrt{u_{rr}^2 + u_{rz}^2 + u_{r\varphi}^2}$  is considered a scalar, while the various relative velocity components are vectors determining the direction as well as the magnitude of the drag force components.

The drag force coefficient  $C_D$  on the basis of local void fractions is determined by equation (2-162):

$$C_D = 0.44(1-\alpha)^{4.25} \left(1 + 0.25 \frac{(\rho_g/\rho_l)^{0.4}}{(1-\alpha)^{3.5}}\right)$$

derived in subsection 2.4.1.2. for bubble flow as well as for mist flow. By contrast the determination of the bubble diameter  $d$  according to equation (2-98) will not be based on local parameters, because of the unknown rate of radial turbulent exchange which undoubtedly occurs for both the bubble diameter itself and the energy dissipation determining the bubble diameter.

Uniform bubble diameters are selected on the basis of values found in chapter 2 - in the course of the computations leading to the interaction force coefficients - according to equation (2-98); for the air-water and steam-water mixtures these bubble diameters were around 2 and 0.5 mm, respectively.

Derivation of the components of the virtual mass force also starts from the resultant force  $F_{At}$ , having the direction of the resultant relative velocity and magnitude

$$F_{At} = \alpha \rho_l B \frac{du_{rt}}{dt_s} \quad (3-14)$$

- in Lagrangian notation - as derived before in equations (2-63) and (2-64) for one-dimensional flows.

Since the differential quotient of a vector is a vector with components equal to the differential quotients of the components of the initial vector (cf. for instance [90]), i.e.

$$\frac{du_{rt}}{dt_s} = \begin{pmatrix} \frac{du_{rr}}{dt_s} \\ \frac{du_{rz}}{dt_s} \\ \frac{du_{r\varphi}}{dt_s} \end{pmatrix} \quad (3-15)$$

the components of the resultant virtual mass force are proportional to the differential quotient of the corresponding relative velocities, viz.

$$F_{Ar} = \alpha \rho_l B \frac{du_{rr}}{dt_s}$$

$$F_{Az} = \alpha \rho_l B \frac{du_{rz}}{dt_s} \quad (3-16)$$

and

$$F_{A\varphi} = \alpha \rho_l B \frac{du_{r\varphi}}{dt_s}$$

Changing to Eulerian cylinder coordinates and taking  $F_{Ar}$  as an example yields

$$F_{Ar} = \alpha B \rho_l \frac{\partial r}{\partial t_s} \cdot \frac{1}{r} \frac{\partial}{\partial r} (r u_{rr}) + \alpha B \rho_l \frac{\partial z}{\partial t_s} \cdot \frac{\partial}{\partial z} u_{rr} + \alpha B \rho_l \frac{\partial (r\varphi)}{\partial t_s} \cdot \frac{\partial}{r \partial \varphi} u_{rr} \quad (3-17)$$

Following the same reasoning as used for equations (2-64) and (2-65), and eliminating the derivative to the  $\varphi$ -direction because of the rotation-symmetry of the present flows, the radial virtual mass force reads:

$$F_{Ar} = \frac{\partial}{\partial r} (\alpha B \rho_l u_{gr} (u_{gr} - u_{lr})) + \frac{\alpha B \rho_l u_{gr} (u_{gr} - u_{lr})}{r} + \frac{\partial}{\partial z} (\alpha B \rho_l u_{gz} (u_{gr} - u_{lr})) \quad (3-18)$$

In the same way the virtual mass forces for the z and  $\varphi$ -direction are obtained as:

$$F_{Az} = \frac{\partial}{\partial r} (\alpha B \rho_l u_{gr} (u_{gz} - u_{lz})) + \frac{\alpha B \rho_l u_{gr} (u_{gz} - u_{lz})}{r} + \frac{\partial}{\partial z} (\alpha B \rho_l u_{gz} (u_{gz} - u_{lz})) \quad (3-19)$$

and

$$F_{A\varphi} = \frac{\partial}{\partial r} (\alpha B \rho_l u_{gr} (u_{g\varphi} - u_{l\varphi})) + \frac{\alpha B \rho_l u_{gr} (u_{g\varphi} - u_{l\varphi})}{r} + \frac{\partial}{\partial r} (\alpha B \rho_l u_{gz} (u_{g\varphi} - u_{l\varphi})) \quad (3-20)$$

In the course of preliminary computations (cf. subsection 3.4.) the use of correlation (2-139) for the virtual mass coefficient B in the above equations gave rise to computational problems. These were due to the strong dependency on the relative velocities, coupled with large fluctuations in the values of these velocities due mainly to high irregular gas velocity distributions. In order to maintain computational stability in the face of these large fluctuations the author preferred to use a correlation which is independent of these unrealistic relative velocity fluctuations.

As already stated in subsection 2.4.1.1.2. the peak velocity ratio  $\frac{u^{\oplus}}{u_r}$  is - for the present type of flows - almost solely dependent on the void fraction; hence it is possible to obtain a rather accurate correlation for the virtual mass coefficient B on the basis of the void fraction only. In [82] it is found that - for the air-water mixtures of the experiments in the converging test section discussed in chapter 2 - the correlation

$$B = 0.5(1-\alpha)^{1.5} \quad (3-21)$$

represents a rather accurate relation for the experimental data, and therefore is used in the present computations of air-water flows. A similar simplified formula for B would be required for steam-water flow computations, which were not, however, carried out for the present investigation.

### 3.2.2.2. Artificial viscosity terms

The viscosity terms in the liquid momentum balances (3-9); (3-10) and (3-11) defined in appendix 3-A as the shear stress forces  $F_{\tau}$ , yield two problems, viz.:

- the kinematic turbulence viscosity  $\eta_t$  is unknown for two-phase flows
- the forces are proportional to second derivatives of the liquid velocities, requiring a very accurate computation of the liquid

velocities themselves; it is unrealistic to expect such a high accuracy for the first attempt to solve the complex problem of two-dimensional two-phase flow.

The latter problem is tackled by assuming the direction of the resultant shear stress to coincide with that of the resultant liquid velocity, yielding:

$$F_{\tau r} : F_{\tau z} : F_{\tau \varphi} = u_{1r} : u_{1z} : u_{1\varphi} \quad (3-22)$$

or equivalent

$$F_{\tau r} = Ku_{1r}, F_{\tau z} = Ku_{1z} \text{ and } F_{\tau \varphi} = Ku_{1\varphi} \quad (3-23)$$

In the author's opinion it is reasonable to expect this severe simplification to yield a more accurate estimate of the shear stress forces than a computation based on highly inaccurate second derivatives.

Through this simplifying assumptions the problem of determining a value for the turbulence viscosity is transformed to the determination of the proportionality constant K. For this purpose the axial shear stress force  $F_{\tau z}$  is integrated over a cross section, yielding:

$$\int_0^{\frac{1}{2}D} F_{\tau z} 2\pi r dr = \left(\frac{dp}{dz}\right)_{fr} A \quad (3-24)$$

or with substitution of  $F_{\tau z}$  from (3-23)

$$K = \frac{\left(\frac{dp}{dz}\right)_{fr}}{\langle u_{1z} \rangle} \quad (3-25)$$

where  $\langle u_{1z} \rangle = \frac{1}{\frac{\pi}{4} D^2} \int_0^{\frac{1}{2}D} u_{1z} 2\pi r dr$  is the mean axial liquid velocity over the actual cross section.

Thus the viscosity terms in the liquid momentum balances are replaced by the shear stress forces

$$\begin{aligned} F_{\tau r} &= \left(\frac{dp}{dz}\right)_{fr} \frac{u_{1r}}{\langle u_{1z} \rangle} \\ F_{\tau z} &= \left(\frac{dp}{dz}\right)_{fr} \frac{u_{1z}}{\langle u_{1z} \rangle} \\ F_{\tau \varphi} &= \left(\frac{dp}{dz}\right)_{fr} \frac{u_{1\varphi}}{\langle u_{1z} \rangle} \end{aligned} \quad (3-26)$$

where the axial frictional pressure drop  $\left(\frac{dp}{dz}\right)_{fr}$  is computed from correlations discussed in subsection 2.2.3.1.

It is obvious that the expressions (3-26) fail for velocities approaching zero, such as occur in boundary layers of real flows. Their use in the present context will be justified in the next subsection, where the simplifications for the boundary layers are discussed.

Since these artificial viscosity terms - just like the original terms in the liquid momentum balances (3-9), (3-10) and (3-11) - are based on bubble flow, expressions (3-26) are also inadequate for mist flow. In subsection 2.4.1.2. the shift of the frictional pressure drop from the liquid to the gas momentum balance was mathematically described for

one-dimensional flow by the introduction of the function  $\Delta_\alpha$  (equations (2-155)) as:

$$\begin{aligned} \Delta_\alpha &= 0 & \text{for } \alpha \leq 0.75 \\ \Delta_\alpha &= 10(\alpha - 0.75) & \text{for } 0.75 < \alpha < 0.85 \\ \Delta_\alpha &= 1 & \text{for } \alpha \geq 0.85 \end{aligned}$$

Although it is appreciated that the type of core-annular flow occurring in the rotating flows discussed in the chapters 3 and 4 may lead to additional errors, this same function  $\Delta_\alpha$  - now based on local instead of cross-sectional mean values of the void fractions - is used to change expression (3-26) for the artificial viscosity terms in the two-dimensional liquid momentum balances to:

$$\begin{aligned} F_{\tau 1r} &= (1 - \Delta_\alpha) \frac{u_{1r}}{\langle u_{1z} \rangle} \left( \frac{dp}{dz} \right)_{fr} \\ F_{\tau 1z} &= (1 - \Delta_\alpha) \frac{u_{1z}}{\langle u_{1z} \rangle} \left( \frac{dp}{dz} \right)_{fr} \\ F_{\tau 1\varphi} &= (1 - \Delta_\alpha) \frac{u_{1\varphi}}{\langle u_{1z} \rangle} \left( \frac{dp}{dz} \right)_{fr} \end{aligned} \quad (3-27)$$

Following the reasoning of subsection 2.4.1.2. the right hand sides of the gas momentum balances (3-6), (3-7) and (3-8) are extended with the terms:

$$\begin{aligned} F_{\tau gr} &= \Delta_\alpha \frac{u_{gr}}{\langle u_{gz} \rangle} \left( \frac{dp}{dz} \right)_{fr} \\ F_{\tau gz} &= \Delta_\alpha \frac{u_{gz}}{\langle u_{gz} \rangle} \left( \frac{dp}{dz} \right)_{fr} \\ F_{\tau g\varphi} &= \Delta_\alpha \frac{u_{g\varphi}}{\langle u_{gz} \rangle} \left( \frac{dp}{dz} \right)_{fr} \end{aligned} \quad (3-28)$$

### 3.2.2.3. Boundary conditions

The existence of boundaries affects both the physical conditions of the flow field and its mathematical description.

The former change is imposed by the centerline, inlet conditions, walls, etc. and results in turn in the degeneration of the partial differential equations describing the flow field. In addition the corresponding finite difference equations may differ; for instance, if e.g. a central difference scheme is used for the inner flow field it has to be changed in a forward or backward difference scheme at a boundary.

In this subsection only the physical conditions proper will be discussed; the effects on the numerical schemes will be discussed - where relevant - in the subsections describing these schemes. The physical conditions are prescribed at four boundaries viz. the inlet ( $z=0$ ), the outlet ( $z=z_{\max}$ ), the centerline ( $r=0$ ) and the wall ( $r=\frac{1}{2}D(z)$ ). They are:

- at the inlet ( $z=0$ )

given values for the void fraction  $\alpha$  and all velocities  $u_{gr}$ ,  $u_{gz}$ ,  $u_{g\varphi}$ ,  $u_{1r}$ ,  $u_{1z}$  and  $u_{1\varphi}$ . Because of the physical impossibility to prescribe all flow variables in one point, the pressure  $p$  at the

inlet cannot be given as a condition at this boundary for a given geometry and outlet pressure. Since the origin of the z-coordinate is taken at the inlet of the guide vanes, the tangential velocities for the actual guide vanes (cf. figure 3-2) are

$$(u_{g\varphi})_{z=0} = (u_{l\varphi})_{z=0} = 0 \quad (3-29)$$

and from the reasonable assumption that the flow is fully developed in the inlet section upstream of the guide vanes, the radial velocities

$$(u_{gr})_{z=0} = (u_{lr})_{z=0} = 0 \quad (3-30)$$

For the axial velocities a simple approximation of the 1/7 power law is chosen. For such a velocity distribution the velocity at the centerline  $u_{\zeta}$  is about 20% larger than the mean velocity, leading to the simple approximations

$$\begin{aligned} (u_{gz})_{z=0} &= u_{g\zeta} \frac{2}{7} \left(4 - \frac{2r}{D}\right) \\ (u_{lz})_{z=0} &= u_{l\zeta} \frac{2}{7} \left(4 - \frac{2r}{D}\right) \end{aligned} \quad (3-31)$$

The resulting non-zero value of the velocity at the rigid wall  $r = \frac{1}{2}D$  is discussed below.

The velocities at the centerline have to be determined via the mass flow, i.e.

$$\begin{aligned} \phi_{mg} &= u_{g\zeta} \int_{r_i}^{\frac{1}{2}D} \frac{2}{7} \left(4 - \frac{2r}{D}\right) \alpha(r)_{z=0} \rho_g(p, \theta) 2\pi r dr \\ \phi_{ml} &= u_{l\zeta} \int_{r_i}^{\frac{1}{2}D} \frac{2}{7} \left(4 - \frac{2r}{D}\right) (1 - \alpha(r))_{z=0} \rho_l 2\pi r dr \end{aligned} \quad (3-32)$$

where  $r_i$  is the radius of the hub of the guide vanes.

For reasons deriving from and therefore to be discussed in conjunction with the iterative solution scheme these mass flows - rather than the centerline velocities - are kept constant during the numerical solution.

As will be discussed in the corresponding part of this subsection the void fraction at the wall should equal zero. A 1/5 power law was selected in accordance with available information, thus

$$\alpha = \alpha_{\zeta} \left(1 - \frac{2r}{D}\right)^{1/5} \quad (3-33)$$

The void fraction at the centerline  $\alpha_{\zeta}$  should be determined through the estimated average void fraction.

- at the outlet ( $z = z_{\max}$ )

only the pressure  $p$  is given at this boundary. The flow has only to satisfy integral balances and no specific conditions in a point can be given.

For the rotational flows studied in this investigation the pressure is given only in one point of the upper boundary; in other cases, for instance, where this boundary coincides with a free surface, the pressure can be given over the whole boundary.

- at the centerline ( $r=0$ )

both the radial and tangential velocities equal zero because of the symmetry:

$$(u_{gr})_{r=0} = (u_{lr})_{r=0} = 0 \quad (3-34)$$

$$(u_{g\varphi})_{r=0} = (u_{l\varphi})_{r=0} = 0 \quad (3-35)$$

The remaining axial velocities  $u_{gz}$  and  $u_{lz}$ , the void fraction  $\alpha$  and pressure  $p$  are determined by their dependence on the in- and outlet conditions.

- at the wall ( $r=\frac{1}{2}D(z)$ )

the no-slip condition is not applied to the present flow system, because it requires a correlation for the turbulence viscosity in the wall region - which is not available for two-phase flow - and the implementation of a very fine grid in the wall region greatly increasing the computation time. Both the effort in computation time and that needed to develop a turbulence viscosity correlation far outweigh the gain for the present purpose, i.e. for computing the separation in a venturi separator, where a more accurate description of the flow in the wall region is most probably of minor importance.

The admittance of slip at the wall leaves only the condition of impermeability of the wall, i.e. the velocities perpendicular to the wall are zero, yielding the mathematical description:

$$(u_{gr})_{r=\frac{1}{2}D} = \frac{1}{2} \frac{dD}{dz} (u_{gz})_{r=\frac{1}{2}D} \quad (3-36)$$

$$(u_{lr})_{r=\frac{1}{2}D} = \frac{1}{2} \frac{dD}{dz} (u_{lz})_{r=\frac{1}{2}D}$$

The void fraction  $\alpha$  at the wall follows from a closer look at the conditions at the wall, which is taken to be cylindrical for simplicity. Since equation (3-36) - degenerated to

$(u_{gr})_{r=\frac{1}{2}D} = (u_{lr})_{r=\frac{1}{2}D} = 0$  for such a cylindrical geometry - holds along the whole wall it appears that  $(\frac{\partial}{\partial z} u_{gr})_{r=\frac{1}{2}D} = (\frac{\partial}{\partial z} u_{lr})_{r=\frac{1}{2}D} = 0$ .

Substitution of these conditions in the radial momentum balance for the gas phase (3-6), yields:

$$\alpha \frac{\partial p}{\partial r} = \alpha \rho_g \frac{u_{g\varphi}^2}{r} \quad (3-37)$$

while the radial liquid momentum balance (3-9) degenerates to

$$(1-\alpha) \frac{\partial p}{\partial r} = (1-\alpha) \rho_l \frac{u_{l\varphi}^2}{r} \quad (3-38)$$

Since it is reasonable to assume that  $u_{g\varphi} \approx u_{l\varphi}$  equations (3-37) and (3-38) can only be satisfied - for  $\rho_g \neq \rho_l$  - if either  $\alpha=0$  or  $\alpha=1$ . For the present case <sup>\*</sup>) of gas-liquid flows with  $\rho_g < \rho_l$  it is

<sup>\*</sup>) For flows without any centrifugal force field both equations (3-6) and (3-9) degenerate to  $\frac{\partial p}{\partial r} = 0$  and no condition follows for the void fraction. This failure of the set of equations is introduced by the omission of the force on the discontinuous phase caused by the wall and making  $\alpha_{r=\frac{1}{2}D} = 0$ .

obvious that  $\alpha=0$  and  $\frac{\partial p}{\partial r} = \rho_l \frac{u_{l\varphi}^2}{r}$  for  $r=\frac{1}{2}D$ , hence

$$\alpha_{r=\frac{1}{2}D} = 0 \quad (3-39)$$

For particle-liquid flow where  $\rho_g + \rho_p > \rho_l$ ,  $\alpha=1$  and  $\frac{\partial p}{\partial r} = \rho_p \frac{u_{p\varphi}^2}{r}$ .

The pressure at the wall is not prescribed, but depends on the in- and outlet conditions.

### 3.3. Solution methods

#### 3.3.1. Introduction

The first choice of the author for a method solving the above set of 8 coupled partial differential equations was the Galerkin method (cf. [91] and [92]). Being a finite element method it has the advantages of an easy fit of the element grid to the complex geometry of a separator and the general applicability to various sets of partial differential equations, while in addition extensive experience - based on finite element techniques for stress analyses - is at hand in the author's laboratory. However, the lack of experience in solving non-potential flows with finite element methods, combined with the inexperience in solving equations describing two-phase flow and last but not least the lack of a physical background (cf. the principle of minimum internal energy in the case of stress analysis) for non-potential fluid flow problems, made the author decide in favour of a finite difference method instead.

In view of the supposedly elliptical character<sup>\*)</sup> of the present set of equations the alternating direction implicit (ADI) method was then selected. This method was developed in 1955 by PEACEMAN and RACHFORD [93] and is well known. As described in the pertinent literature it has three advantages over most other finite difference schemes:

- a high degree of stability
- general applicability
- relatively short computing time

The latter advantage carries particular weight for the present large number of unknown variables; according to FRANKEL [94] the reduction in time for a set of 2400 variables (300 grid points with 8 unknowns each) is by a factor 154 compared with the next best finite difference method. Quite in contrast to this remarkable reduction, the first test runs of the completed computer program showed that despite the moderate computing time per iteration step, the large number of iteration steps required yielded an excessively large total computing time. In order to reduce the number of necessary iteration steps a rather simple computer program INIGUES was written for the purpose of providing the best possible initial guess for input to the ADI-scheme. The promising results of this INIGUES procedure, followed by the realisation that the large number of required iteration steps for the ADI-method is inherent to the combination of this method and the two-phase flow problem itself, led to the decision to abandon the ADI-method and to improve the INIGUES procedure. This improved procedure - called ANALEST (to make analytical estimations) - is based on an explicit scheme, in which each of the 8 unknown variables is

<sup>\*)</sup> *This character is hard to prove because of the relatively large number of eight equations in the system to solve and the coefficients in these equations vary strongly within the flow field.*

computed from one of the 8 available partial mass or momentum balances; hence the method will further be referred to as the explicit scheme. Because of the promising results so far obtained from the application of ANALEST to real separator flows, the main attention of this chapter will be devoted to this method. The author, however, likes to emphasize beforehand that the ANALEST procedure in its present state contains several artifices, having a practical or experimental basis rather than a mathematical background. A more exact procedure will be elaborated and published - together with extensive experimental evidence for its verification - in due course by Mr. R.v.d. Welle, who has played an essential role in its development and is presently continuing its application. Additionally a fairly complete description of the ADI-method and its evaluation are also included in order to make it clear that the reasons leading to excessive computing time are inherent to the combination of two-phase flow and the ADI-method.

### 3.3.2. Explicit scheme

It should be noted at the outset that at its present state of development ANALEST is only capable of computing 7 unknown variables out of the complete set of 8. In contrast to the ADI-scheme the void fraction  $\alpha$  is not computed in the explicit scheme; the void fraction distribution over the grid points in the flow geometry is given as input to the numerical procedure and remains unchanged during the computation of the other 7 flow parameters. This reduction of the problem still derives from the INIGUES procedure where the initial guess of the remaining 7 flow parameters was based on estimation of the void fraction distribution. Instead of immediately continuing the development towards computation of the full set of 8 unknowns the author has preferred first to improve the computational procedure for the 6 individual velocities and the pressure and to ascertain the stability of the computation as a whole. For the present version of the program the number of 8 partial differential equations is reduced to 7 by adding the radial gas and liquid momentum balance, yielding a single radial mixture momentum balance. Since computation of the full set of 8 unknowns of course remains the final aim, a scheme is presented at the end of this subsection describing the computation of the full set of unknowns. As mentioned before, the implementation of this scheme is presently underway by Van der Welle.

#### 3.3.2.1. Outline of the method

The explicit scheme is an iterative method, improving an initial guess by use of the differential mass and momentum balances. As described by VAN DER WELLE ([95], [96]) the improved values for the 6 velocities and the pressure are computed over the entire geometry for each of these flow parameters consecutively, while the cycle is repeated for all 7 parameters until the final solution is reached.

Each of the 7 unknown variables is computed using one single equation selected from the set of 7 mass and momentum balances. For the other 6 parameters present in that particular balance, values computed during the preceding step are taken (the void fractions are known a priori and kept constant during the iteration). Computation for each of the flow parameters proceeds per horizontal (radial) grid line from bottom to top of the separator. Since this procedure violates the supposedly elliptical character of the set of equations, special precautions are taken to maintain this character; these measures will be discussed in the appropriate subsection 3.3.1.4.1.

The sequence of the individual parameter computations was found to be

significant for the stability of the procedure especially during the first cycles. This aspect and the initial value computation will be discussed in subsections 3.3.1.3. and 3.3.1.2. respectively. From practical applications of the ANALEST procedure it appeared that special precautions are required to improve stability and accuracy and to ensure stable operation. These precautions will be discussed in subsection 3.3.2.4. where relevant.

### 3.3.2.2. Initial value computation

The ANALEST procedure requires only a fairly rough estimate for the initial values of the flow parameters. Therefore they are computed on the basis of rather severe simplifications.

- void fraction distribution

Up till now the ANALEST procedure has only been used for predicting the local flow parameters of the experiments discussed in chapter 4. For these flows the radial void fraction distribution is measured at 5 or 10 levels in the test section. From these measured values a Chebyshev double polynomial (in  $r$  and  $z$ ) is obtained, describing the void fraction in each grid point of the flow field for each particular operating condition. In order to avoid numerical difficulties these values are restricted between 0.02 and 0.98, except for the rigid wall where  $\alpha=0$  is prescribed (cf. subsection 3.2.2.3.). Where no void fraction distribution measurements are available a "best estimate" of this distribution should be used as fixed input until such time as ANALEST will be extended to include computation of all 8 flow parameters.

- axial velocities

Computation of the initial axial velocities is simplified by taking these velocities uniform over a cross section. Using the integral mass balance for the liquid:  $\int_0^{\frac{1}{2}D} (1-\alpha)\rho_l u_{lz} 2\pi r dr = \phi_{ml}$  the uniform velocity becomes:

$$u_{lz}(z) = \frac{\phi_{ml}}{(1-\langle\alpha\rangle)\rho_l \frac{\pi}{4} D^2(z)} \quad (3-40)$$

where a total liquid mass flow  $\phi_{ml}$  is given as a boundary condition. For the gas velocity the same procedure yields:

$$u_{gz}(z) = \frac{\phi_{mg}}{\int_0^{\frac{1}{2}D} \alpha \rho_g 2\pi r dr} \quad (3-41)$$

where the integral is computed subsequent to computation of the initial pressure distribution in order to obtain values for the gas density  $\rho_g$ .

- radial velocities

The radial velocities are supposed to be sufficiently small relatively to the axial and tangential components to permit their being taken equal to zero, thus

$$u_{lr}(z) = u_{gr}(z) = 0 \quad (3-42)$$

• tangential velocities

The tangential velocities between the guide vanes are computed in the normal way (cf. subsection 3.2.1.2.2.), i.e. based on the vane geometry and axial and radial velocities.

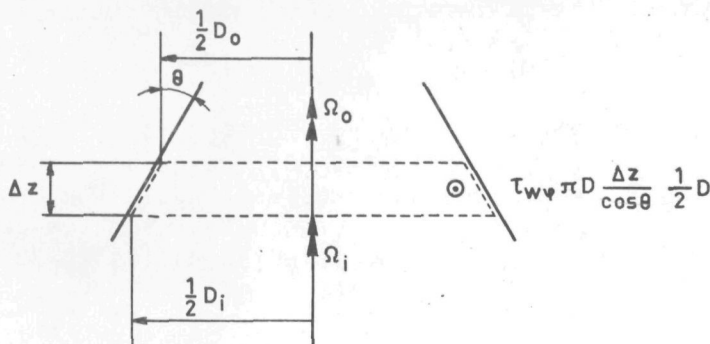
In the free flow field above the guide vanes the tangential gas and liquid velocities are assumed to be equal:  $u_{g\varphi} = u_{l\varphi} = u_{\varphi}$ , which is a reasonable assumption because of the absence of a tangential pressure gradient:  $\frac{\partial p}{\partial \varphi} = 0$ . Furthermore the distribution of this velocity  $u_{\varphi}$  is approximated by a solid body rotation, i.e.

$$u_{\varphi} = \frac{2r}{D} (u_{\varphi})_{r=\frac{1}{2}D} = \frac{2r}{D} u_{\varphi W} \quad (3-43)$$

where the tangential velocity at the wall  $u_{\varphi W}$  is obtained from the conservation law for angular momentum, as described before by PRINS [1]. Ignoring the friction forces at the upper and lower

FIGURE 3-3

*Control volume for angular momentum considerations*



boundary of the control volume shown in figure 3-3, the net angular momentum flux into the volume equals the torque exerted by the wall friction, i.e.

$$\Omega_i - \Omega_o - \tau_w \pi D \frac{\Delta z}{\cos \theta} = 0 \quad (3-44)$$

where the angular momentum flux  $\Omega$  is given by

$$\Omega = \int_0^{\frac{1}{2}D} (\alpha \rho_g u_{gz} u_{g\varphi} + (1-\alpha) \rho_l u_{lz} u_{l\varphi}) r^2 \pi r dr \quad (3-45)$$

Following the reasoning of subsection 3.2.2.2. the shear stress at the wall  $\tau_w$  can be derived by

$$\tau_w = \frac{D}{4} \left( \frac{dp}{dz} \right)_{fr} \frac{u_{\varphi W}}{\langle u_{lz} \rangle} \quad (3-46)$$

Combining equations (3-44) and (3-45) yields for the tangential wall velocity at the upper boundary

$$u_{\varphi W} = \frac{D_o}{2} \frac{\int_0^{\frac{1}{2}D_i} \{ \alpha \rho_g u_{gz} u_{g\varphi} + (1-\alpha) \rho_l u_{lz} u_{l\varphi} \} r^2 dr}{\int_0^{\frac{1}{2}D_o} \{ \alpha \rho_g u_{gz} + (1-\alpha) \rho_l u_{lz} \} r^3 dr + \frac{D^4}{32} \left( \frac{dp}{dz} \right)_{fr} \frac{\Delta z}{\cos \theta}} \quad (3-47)$$

The wall velocities  $u_{\phi W}$  and subsequently the tangential velocities at the inner grid points are computed from bottom to top of the separator.

• pressure distribution

A first approximation of the axial pressure distribution is obtained by the integral axial momentum balance of the mixture. Since the pressures have to be computed before the axial gas velocities, because of the unknown gas density required for the latter, the gas terms in this mixture balance are ignored, including the virtual mass terms. For the sake of simplicity the friction term is also ignored. The integral axial momentum balance thus reads:

$$\int_0^z \left\{ \frac{d}{dz} ((1-\langle\alpha\rangle)\rho_1 u_{1z}^2) \right\} dz = - \int_0^z \left\{ \frac{dp}{dz} - (1-\langle\alpha\rangle)\rho_1 g \right\} dz \quad (3-48)$$

Since the pressure level cannot be obtained from the momentum balances, this equation is only used to compute the reduced pressure  $p^*$ , starting at the lower boundary  $z=0$  with  $p_{z=0}^* = 0$ , i.e.

$$p^* = - \phi_{m1} \{ (u_{1z})_z^2 - (u_{1z})_0^2 \} - \int_0^z (1-\langle\alpha\rangle)\rho_1 g dz \quad (3-49)$$

This reduced pressure is assumed to represent a reasonable approximation of the axial pressure distribution at the radius where the pressure equals the cross sectional mean value of the pressure. For the test section geometries of the present investigation the selected radius is 30% of the 5 cm inlet radius of the test sections, i.e.  $p_{0.15,z}^* = p_z^*$ .

From these reduced pressures  $p_{0.15,z}^*$  the radial pressure distribution at each horizontal grid line is computed using the radial mixture momentum balance (addition of the individual balances (3-6) and (3-9)) with zero interaction forces  $F_{Dr}$  and  $F_{Ar}$  due to the zero radial velocities. Again ignoring the gas terms and the friction term this mixture balance degenerates to:

$$0 = - \frac{\partial p}{\partial r} + (1-\alpha)\rho_1 \frac{u_{1\phi}^2}{r} \quad (3-50)$$

Integration of this balance yields the complete reduced pressure field:

$$p_{r,z}^* = p_{0.15,z}^* + \int_{0.15}^r (1-\alpha)\rho_1 \frac{u_{1\phi}^2}{r} dr \quad (3-51)$$

Finally these reduced pressures are converted to real pressures by fulfilling the pressure boundary condition at the outlet  $z=z_H$ , where the pressure at the wall  $r=r_w = \frac{1}{2}D(z_H)$  is prescribed as  $p_{r_w,z_H}$ , yielding:

$$p_{r,z} = p_{r,z}^* + (p_{r_w,z_H} - p_{r_w,z_H}^*) \quad (3-52)$$

3.3.2.3. Program sequence

The simplified flow diagram in figure 3-4 shows the sequence of the iteration loop in ANALEST. This sequence was selected rather arbitrarily. Since the iteration is a continuous cycle along the individual subroutines, the sequence of the iteration loop can only be significant at the start

and at the end of this cycle. At the end, however, convergence is reached and thus the invariance of the flow parameters makes it indifferent at which stage the cycle is ended; hence potential significance of the sequence is limited to the start of the iteration cycle. Evidence obtained to date indicates this influence to be weak, except that computation of the liquid velocity components should precede that of the corresponding gas velocities for reasons of numerical stability. This is due to the lower density of the gas resulting in greater sensitivity of the gas velocity to numerical disturbances of the pressure gradient. If the gas velocity is

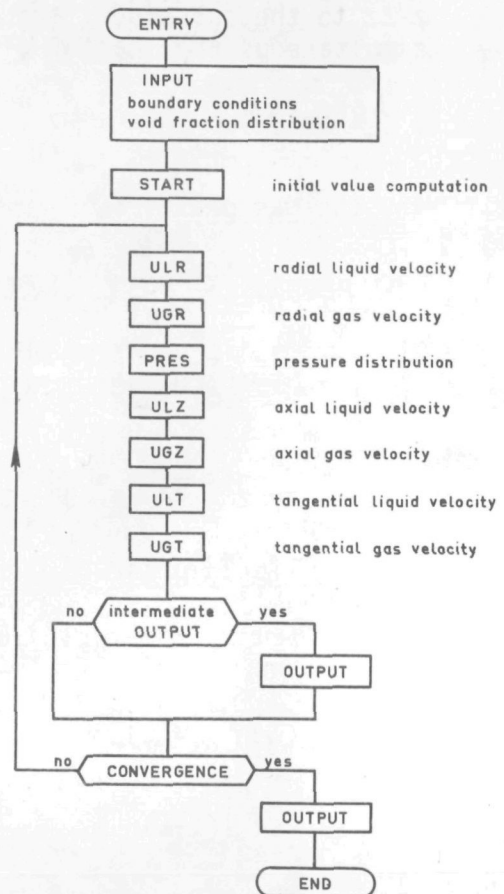


FIGURE 3-4

*Flow diagram of the ANALEST procedure*

computed first the large deviation of this velocity in case of a numerical disturbance of the pressure gradient yields in turn a successive large deviation of the interaction forces via the deviated relative velocity (cf. expressions (3-13) and (3-18)/(3-20)) during the subsequent computation of the liquid velocity and thus an excessive deviation of the latter. This amplifying effect is eliminated by computing the liquid velocities prior to those of the gas phase.

As soon as the convergence criterion, to be discussed in the next subsection, has been satisfied the iteration is stopped upon completion of the current cycle, i.e. after computation of the tangential velocities.

### 3.3.2.4. Computation of velocity and pressure fields

#### 3.3.2.4.1. Axial velocities

As described in [95] the axial velocities of the two phases are computed from their respective axial momentum balances. These gas and liquid balances, (3-7) and (3-10) respectively, in combination with the appropriate additional expressions for the interaction forces and artificial viscosity terms (cf. subsection 3.2.2.) are integrated gridline by gridline from bottom to top. For a given integration, at a specific radius  $r$ , from the gridline at  $z-\Delta z$  to the subsequent gridline at level  $z$  these equations become, with simultaneous application of the trapezium rule for the drag force:

$$\int_{z-\Delta z}^z F_{Dz} dz = \frac{1}{2} \{ [F_{Dz}]_{z-\Delta z} + [F_{Dz}]_z \} \Delta z :$$

for the gas phase

$$\begin{aligned} & [ \alpha \rho_g \pm \frac{\Delta z}{2} F_{Dz}^* ]_{r,z}^{n-1} [u_{gz}^2]_{r,z}^n \mp [ \Delta z F_{Dz}^* u_{gz} ]_{r,z}^{n-1} [u_{gz}]_{r,z}^n \pm \\ & \pm [ \frac{\Delta z}{2} F_{Dz}^* u_{gz}^2 ]_{r,z}^{n-1} - [ \alpha \rho_g u_{gz}^2 ]_{r,z-\Delta z}^{n-1} + [ \frac{\Delta z}{2} F_{Dz}^* (u_{gz} - u_{lz}) |u_{gz} - u_{lz}| ]_{r,z-\Delta z}^{n-1} + \\ & + \int_{z-\Delta z}^z [ \alpha \frac{\partial p}{\partial z} + \alpha \rho_g g + F_{\tau gz} + F_{Az} - \frac{1}{r} \frac{\partial}{\partial r} (r \alpha \rho_g u_{gr} u_{gz}) ]_r^{n-1} dz = 0 \end{aligned} \quad (3-53)$$

for the liquid phase

$$\begin{aligned} & [ (1-\alpha) \rho_l \mp \frac{\Delta z}{2} F_{Dz}^* ]_{r,z}^{n-1} [u_{lz}^2]_{r,z}^n \pm [ \Delta z F_{Dz}^* u_{gz} ]_{r,z}^{n-1} [u_{lz}]_{r,z}^n \mp \\ & \mp [ \frac{\Delta z}{2} F_{Dz}^* u_{gz}^2 ]_{r,z}^{n-1} - [ (1-\alpha) \rho_l u_{lz}^2 ]_{r,z-\Delta z}^{n-1} - [ \frac{\Delta z}{2} F_{Dz}^* (u_{gz} - u_{lz}) |u_{gz} - u_{lz}| ]_{r,z-\Delta z}^{n-1} + \\ & + \int_{z-\Delta z}^z [ (1-\alpha) \frac{\partial p}{\partial z} + (1-\alpha) \rho_l g + F_{\tau lz} + \frac{1}{r} \frac{\partial}{\partial r} (r(1-\alpha) \rho_l u_{lr} u_{lz}) ]_r^{n-1} dz = 0 \end{aligned} \quad (3-54)$$

In these equations the superscript  $n$  or  $n-1$  indicates the number of the iteration step in which the value of the actual element is computed and is the specific drag force  $F_{Dz}^*$  the product of the velocity independent factor of the drag force  $\frac{3}{4} \alpha \frac{C_D}{d} \rho_l$  and the correction factor for the direction of the drag force  $\left| \frac{u_{rt}}{u_{rz}} \right| = \sqrt{1 + \left( \frac{u_{rr}}{u_{rz}} \right)^2 + \left( \frac{u_{r\theta}}{u_{rz}} \right)^2}$ , which for the present type of flows is close to unity. This latter rectification is introduced by expressing the drag force in terms of the axial relative velocity  $F_{Dz} = F_{Dz}^* (u_{gz} - u_{lz})^2$  rather than  $F_{Dz} = \frac{3}{4} \alpha \frac{C_D}{d} \rho_l u_{rt} u_{rz}$  as derived in subsection 3.2.2.1. The absolute value

\*) In spite of the use of the symbol  $F$  this axial parameter should not be mistaken for a force.

$\left| \frac{u_{rt}}{u_{rz}} \right|$  is introduced instead of the correct factor  $\frac{u_{rt}}{u_{rz}}$  because this correction factor is determined from values obtained from the preceding step in the computation, while it is preferable to determine the sign of the drag force from the actual computation of the phase velocities. Application of this absolute value eliminates the sign of the drag force with respect to a positive or negative value for the axial relative velocity  $u_{rz}$ ; therefore a double sign is introduced in the equations (3-53) and (3-54) for the factor  $F_{Dz}^*$ . The axial phase velocities are computed for both cases and the irrelevant value - violating the initial assumption for the sign of the relative velocity - is rejected. Incorporation of this selection of the correct sign into the appropriate subroutine posed no problem, as discussed in detail in [95]. The terms with superscript  $n-1$  in equations (3-53) and (3-54) are computed from flow parameter values known from the preceding computation step, yielding quadratic equations of the type:

$$a_{r,z}^{n-1} [u_z^2]_{r,z}^n + b_{r,z}^{n-1} [u_z]_{r,z}^n + c_{r,z}^{n-1} = 0 \quad (3-55)$$

This solution method with quadratic equations for  $[u]^n$  was developed after it was found that linearized equations yield unsatisfactory results with respect to the stability of the procedure. Of the two roots of equation (3-55) only the one with the positive sign for the determinant has a physical meaning (cf. appendix 3-C), hence:

$$[u_z]_{r,z}^n = \frac{-b + \sqrt{b^2 - 4ac}}{2a} \quad (3-56)$$

In some grid points neither of the two solutions for positive and negative relative velocity fulfill the appropriate initial assumption. For these grid points the value of the preceding step is taken as a temporarily solution during the actual iteration cycle. These cases are caused by the violation of the additional condition for the determinants derived in appendix 3-C, viz.  $\sqrt{D_1}, \sqrt{D_2} > 2\alpha\rho g|z$  for the gas velocity computations and  $\sqrt{D_1}, \sqrt{D_2} > 2(1-\alpha)\rho_l u_{gz}$  for the liquid velocity computations. Because it is reasonable to attribute such violations to relatively large temporary deviations of the flow parameters from the exact solution, they may be considered a measure for the accuracy of the actual flow parameter values compared to the exact solution. This is confirmed by the experience that whereas this "both determinants too small" case occurs in about 10% of the grid points for both the gas and liquid velocity computation during the first iteration cycle, the frequency of its occurrence gradually decreases during successive iteration to less than 0.5% for the gas velocity computation and a persistent percentage of about 2 for the liquid velocity computation. Once these rest percentages are reached, further iteration steps do not affect the flow parameters apart from small variations around the final solution.

Based on this experience the final solution is considered to be reached when the number of grid points where "both determinants are too small" show no further decrease, which is an easy detectable criterion for convergence.

The axial gas and liquid velocities thus computed are subsequently corrected for the violation of the supposedly elliptical character of the initial set of balances inflicted by computing the velocities grid line by grid line from bottom to top through the flow geometry yielding instabilities in the numerical procedure. The elliptical character is

enforced upon the solution method by imposing the requirement that the integral mass balances of the individual phases must be met. Immediately after completion of the computation of a phase velocity distribution along a grid line this distribution is integrated over the cross section, i.e.

$$[\phi_{mg}]_z^n = \int_0^{D/2} [\alpha \rho_g u_{gz}]_{r,z}^n 2\pi r dr \quad \text{and} \quad [\phi_m]_z^n = \int_0^{D/2} [(1-\alpha)\rho_l u_{lz}]_{r,z}^n 2\pi r dr$$

and these mass flows are equalized to the inlet mass flows  $[\phi_{mg}]_0$  and  $[\phi_m]_0$  (boundary conditions) by adjusting the velocities as:

$$\begin{aligned} [u_{gz}]_{r,z}^n &\rightarrow [u_{gz}]_{r,z}^n \frac{[\phi_{mg}]_0}{[\phi_{mg}]_z} \\ [u_{lz}]_{r,z}^n &\rightarrow [u_{lz}]_{r,z}^n \frac{[\phi_m]_0}{[\phi_m]_z} \end{aligned} \quad (3-57)$$

It is obvious that these correction factors  $[C_g]_z = \frac{[\phi_{mg}]_0}{[\phi_{mg}]_z}$  and  $[C_l]_z = \frac{[\phi_m]_0}{[\phi_m]_z}$  should approach unity when the final solution is reached. Hence the introduction of these correction factors does not affect the above mentioned criterion for convergence.

#### 3.3.2.4.2. Radial velocities

Contrary to what might be expected from the above the radial velocities will be computed from the mass rather than from the momentum balances, the latter being combined into a single mixture balance, in order to obtain the required reduction to 7 equation (cf. subsection 3.3.2.). As will be discussed in subsection 3.3.2.4.4. this radial mixture balance is used to compute the pressure distribution.

Excluding change of phase ( $\phi'_g = 0$  in equation (3-3)) radial integration of the mass balances (3-1) and (3-2) yields

for the gas phase:

$$[r\alpha\rho_g u_{gr}]_{0,z}^{r,z} = - \int_0^r r \frac{\partial}{\partial z} [\alpha\rho_g u_{gz}]_z dr \quad (3-59)$$

for the liquid phase:

$$[r(1-\alpha)\rho_l u_{lr}]_{0,z}^{r,z} = - \int_0^r r \frac{\partial}{\partial z} [(1-\alpha)\rho_l u_{lz}]_z dr \quad (3-60)$$

Since at the lower boundary  $r = 0$  as well as  $u_r = 0$  the radial velocities for  $r \neq 0$  are found as:

$$[u_{gr}]_{r,z}^n = \frac{- \int_0^r r \frac{\partial}{\partial z} [\alpha\rho_g u_{gz}]_{r,z}^{n-1} dr}{[r\alpha\rho_g]_{r,z}^{n-1}} \quad (3-61)$$

$$[u_{lr}]_{r,z}^n = \frac{- \int_0^r r \frac{\partial}{\partial z} [(1-\alpha)\rho_l u_{lz}]_{r,z}^{n-1} dr}{[r(1-\alpha)\rho_l]_{r,z}^{n-1}} \quad (3-62)$$

where the numerators are integrated numerically over the grid points of the appropriate level  $z$ .

### 3.3.2.4.3. Tangential velocities

Apart from the distinction between the flow in the guide vane area and in the free channel flow field, additional accommodations are made for both flow fields in order to obtain a proper computation of the tangential velocity component.

In the former case the actual flow deviates from the ideal flow described in subsection 3.2.1.2. and appendix 3-B, to the extent - confirmed by visual observations during the experiments reported in chapter 4 - that flow separation occurs at the convex side of the guide vanes, lowering the tangential velocity as compared to ideal flow (cf. figure 3-5).

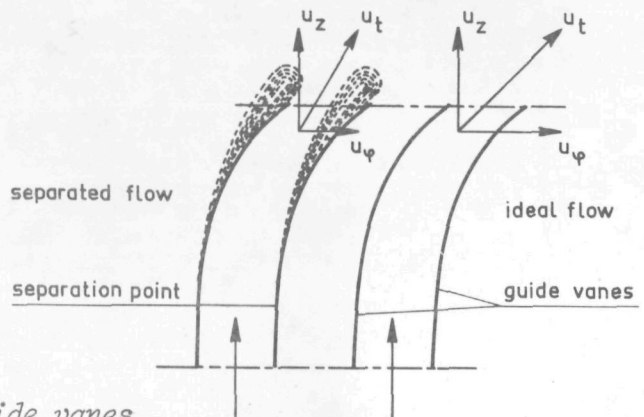


FIGURE 3-5

*Ideal and separated flow between guide vanes*

The resulting difference may be expressed in terms of a correction factor  $\zeta_b$ , extending the validity of equation (3-12) to real flows:

$$u_{\varphi}(r,z) = \zeta_b \frac{u_z \operatorname{tg} \gamma(r,z) + u_r \sin \delta(r,z)}{\cos \delta(r,z)} \quad (3-63)$$

For single phase flows this correction factor, which determines to a large extent the value of the blade efficiency, so important to turbomachinery designers and users, may be gleaned with sufficient accuracy from the extensive literature on the subject. This is not the case for two-phase flow, where the mixture quality and slip may be expected to influence its magnitude. For the experiments discussed in section 4.4. the value  $\zeta_b = 0.65$  was found to yield satisfactory results for all mixtures and all four different guide vane geometries.

In contrast to the above adaption to reality for the computation between the guide vanes, the tangential velocity computation in the free flow field requires further simplification because of the failure of the existing model based on the tangential momentum balances (3-8) and (3-11) together with the appropriate additional equations. Evaluation of tangential velocities computed by a subroutine, in which the tangential velocities were obtained via the same type of quadratic equations as used for the axial velocity computation (cf. subsection 3.3.2.4.1.), clearly indicates that - for the flows discussed in chapter 4 - the lack of viscous radial interaction in the model leads to erroneous velocity peaks, as for example presented in figure 3-6.

Since these erroneous peaks in the tangential velocities strongly affect the pressure distribution via the centrifugal term  $\rho \frac{u_{\varphi}^2}{r}$ , and hence indirectly affects the other velocities, these peaks had to be eliminated.



This was achieved imposing a radial distribution function for the tangential velocities. As can be seen from figure 3-6 the radial distribution function can be approximated with reasonable accuracy by a solid body distribution which flattens in the wall region. Additionally it appears that the approximations for gas and liquid velocity may be taken equal, as could be expected because of the absence of a tangential pressure gradient:  $\frac{\partial p}{\partial \varphi} = 0$ . Therefore the tangential velocities are prescribed as:

$$\begin{aligned}
 [u_{g\varphi}]_{r,z} &= [u_{l\varphi}]_{r,z} = C(z) \frac{2r}{D} & \text{for } r < 0.8 \frac{D}{2} \\
 [u_{g\varphi}]_{r,z} &= [u_{l\varphi}]_{r,z} = 0.8 C(z) & \text{for } r \geq 0.8 \frac{D}{2}
 \end{aligned}
 \tag{3-64}$$

The computations of the tangential velocities thus reduces to that of the constants  $C(z)$  at each grid line.

#### 3.3.2.4.4. Pressure distribution

While axial and radial pressure distributions can be computed by integrating the pressure gradients  $\frac{\partial p}{\partial z}$  and  $\frac{\partial p}{\partial r}$  obtained from the axial and radial momentum balances respectively, no equation is available for coupling these axial and radial distributions to a single pressure distribution. This problem is illustrated for the grid of figure (3-7): starting from known pressures at the level of grid line  $k-1$ , the pressure at the grid point  $h,k$  can be computed via many integration routes. Two examples of these routes - both starting at the grid point  $h,k-1$  - are:

$$p_{h,k}\{(h,k-1),(h,k)\} = p_{h,k-1} + \int_{z_{k-1}}^{z_k} \left[\frac{\partial p}{\partial z}\right]_h dz$$

and

$$\begin{aligned}
 p_{h,k}\{(h,k-1),(h+1,k-1),(h+1,k),(h,k)\} &= \\
 &= p_{h,k-1} + \int_{r_h}^{r_{h+1}} \left[\frac{\partial p}{\partial z}\right]_{h+1} dz + \int_{r_{h+1}}^{r_h} \left[\frac{\partial p}{\partial r}\right]_k dr
 \end{aligned}$$

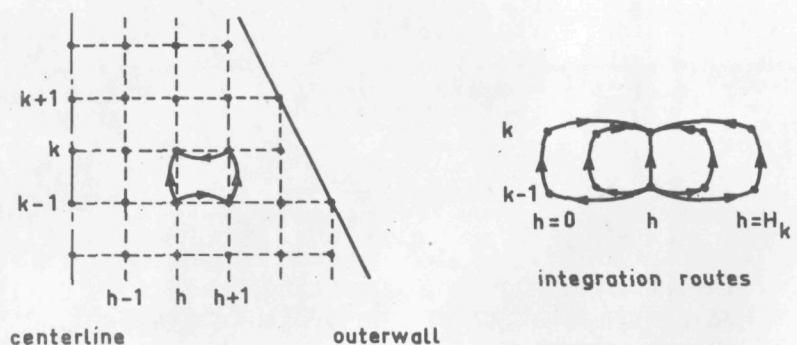


FIGURE 3-7

*Gridlines and integration routes*

During the iteration - while the velocity and pressure distributions are not yet established - these two pressures will deviate from each other and a choice must be made as to how the pressure  $p_{h,k}$  is coupled to the pressure  $p_{h,k-1}$ , i.e. the coupling equation has to be defined. Since no preference exists for the selection of a particular route, the most probable value is assumed to be the mean value for all possible routes. In view of the serial computation from bottom to top of the separator the author restricted the routes considered to those passing via two adjacent horizontal grid lines  $k-1$  and  $k$ . The mathematical description of this approach becomes:

$$p_{h,k} = p_{h,k-1} + \frac{1}{H_k+1} \sum_{m=0}^{H_k} \left\{ \int_{r_h}^{r_m} \left[ \frac{\partial p}{\partial r} \right]_{k-1} dr + \int_{z_{k-1}}^{z_k} \left[ \frac{\partial p}{\partial z} \right]_m dz + \int_{r_m}^{r_h} \left[ \frac{\partial p}{\partial r} \right]_k dr \right\} \quad (3-65)$$

where  $H_k$  is the maximum value for  $h$  at the  $k^{\text{th}}$  horizontal grid line, as indicated in figure 3-7 where all the integration routes in use are shown.

In addition this averaging along various integration routes serves to solve a second problem introduced by the repeated use of the axial momentum balances previously applied to compute the axial velocities (cf. subsection 3.3.2.4.1.). Integrating these balances along the same integration route, to obtain the pressure difference  $p_{h,k} - p_{h,k-1}$ , will yield the existing pressure difference. Thus no improvement of the initial pressure field will occur during the iteration, obstructing the aim and limiting the usefulness of the iteration procedure.

By contrast use of the average equation (3-65) leads to adaptation of the existing pressure difference  $p_{h,k} - p_{h,k-1}$  to the surrounding flow field through the corrections in the right hand side of this equation. Thus the use of the average equation (3-65) justifies the repeated use of the axial mixture balance to substitute an expression for the pressure gradient

$\frac{\partial p}{\partial z}$ . This mixture balance yields:

$$\begin{aligned} \frac{\partial p}{\partial z} = & -\frac{1}{r} \frac{\partial}{\partial r} (r((1-\alpha)\rho_l u_{lz} u_{lr} + \alpha\rho_g u_{gz} u_{gr})) - \frac{\partial}{\partial z} ((1-\alpha)\rho_l u_{lz}^2 + \alpha\rho_g u_{gz}^2) + \\ & - F_{Az} - ((1-\alpha)\rho_l + \alpha\rho_g)g - F_{\tau z} \end{aligned} \quad (3-66)$$

The expression for the radial pressure gradient  $\frac{\partial p}{\partial r}$  is based on the radial mixture balance, yielding:

$$\begin{aligned} \frac{\partial p}{\partial r} = & \frac{1}{r} \frac{\partial}{\partial r} (r((1-\alpha)\rho_l u_{lr}^2 + \alpha\rho_g u_{gr})) - \frac{\partial}{\partial z} ((1-\alpha)\rho_l u_{lr} u_{lz} + \alpha\rho_g u_{gr} u_{gz}) + \\ & - F_{Az} + (1-\alpha)\rho_l \frac{u_{l\varphi}^2}{r} + \alpha\rho_g \frac{u_{g\varphi}^2}{r} - F_{\tau r} \end{aligned} \quad (3-67)$$

The remainder of the computing process is similar to that of the initial value computation of the pressure field  $\star$ ).

$\star$ ) The described procedure based on the mixture balances (3-66) and (3-67) is proceeded in the region between the guide vanes. In view of the existing pressure gradient  $\frac{\partial p}{\partial \varphi}$  the resulting pressures in this region are considered to represent the average pressure  $p(r,z) = \frac{1}{2\pi} \int_0^{2\pi} p(r,z,\varphi) d\varphi$ .

During the first trial runs with ANALEST the flow field computation was found to be very sensitive to the pressure distribution, leading to excessive velocity changes where the changes in pressure gradient from one iteration step to another become relatively large. Therefore an underrelaxation was introduced for the pressure computation, i.e. the pressures of the  $n^{\text{th}}$  iteration step are partly based on the values  $p_{r,z}^{n-1}$  obtained in the preceding iteration step, via:

$$p_{r,z}^{n+} = (1-R) p_{r,z}^{n-1} + R p_{r,z}^n \quad (3-68)$$

where  $p_{r,z}^n$  are the values for the pressure obtained by the above computation method, and  $p_{r,z}^{n+}$  the corrected final values for the  $n^{\text{th}}$  iteration step.

A value of 0.2 for the underrelaxation factor R was found to yield reasonably stable computations and hence retained for the time being, though this should certainly not be considered an optimized value.

### 3.3.2.5. Extension to computed void fraction distribution

While at the present stage the explicit scheme is restricted to the computation of only 7 flow parameters out of the total set of 8, the final aim is to develop a procedure computing the full set of unknowns. Although this further development is being undertaken by the author's successor, as stated before the proposed scheme for the full computation will be outlined here in order to provide an impression of the capabilities of the explicit scheme.

The most significant extension of the present ANALEST procedure for the purpose of computing the full set of unknowns is the computation of the void fraction distribution. As already described by VAN DER WELLE [96] it seems logical to base this computation on a mass balance. Since no preference exists for either the gas or liquid balance, the mixture balance is selected to compute the void fractions.

Because of this use of the mixture mass balance, one of the radial velocities - previously computed from the phase mass balances - will have to be computed via one of the radial momentum balances not previously used. For reasons of computational stability the liquid velocity is selected to be computed from the radial liquid momentum balance. Hence the proposed sequence for the iteration loop for the full computation becomes:

- radial liquid velocity via radial momentum balance
- radial gas velocity via gas mass balance
- pressure via axial and radial mixture momentum balances
- axial liquid velocity via axial liquid momentum balance
- axial gas velocity via axial gas momentum balance
- tangential liquid velocity } either via the appropriate balance or
- tangential gas velocity } as single tangential velocity via conservation of angular momentum
- void fraction via mixture mass balance

The void fraction is proposed to be computed last because the computations are expected to be very sensitive for errors in the void fraction distribution, hence the best approximations of the velocities should be known prior to the void fraction computation. This consideration may even lead to the introduction of an underrelaxation for the void fraction.

While it is proposed to base the computation of the radial liquid velocity on the radial liquid momentum balance (3-10) <sup>\*</sup>) via the type of quadratic equation derived earlier for the axial velocity computation (cf. sub-section 3.3.2.4.1.), this quadratic equation cannot, however, be obtained by radial integration of the radial momentum balance, because the

acceleration term  $\frac{1}{r} \frac{\partial}{\partial r} (r(1-\alpha)\rho_1 u_{1r}^2)$  cannot be integrated analytically.

Therefore the momentum balance will be used in its differential form, in which the acceleration term is approximated numerically.

Rewritten in a quadratic form such an equation can be solved - starting at the centerline where  $u_{1r} = 0$  - by same type of procedure as used for the axial velocity computations.

### 3.3.3. Alternating direction implicit method

As stated earlier, the discussion of this method is mainly intended to point out the causes for the excessively large computing times having led to its rejection. The present subscription is therefore limited to a brief description of the mathematical background of the computer program developed, while the discussion of its practical application is restricted to these causes for failure. For an extensive description of the method and of the program structure the reader is referred to [99] and [100], while a complete listing of the program is presented in [89].

#### 3.3.3.1. Outline of the method

For convenience the set of 8 partial differential equations available for the solution of the 8 unknowns, is written in matrix notation as:

$$A \frac{\partial}{\partial r} \underline{u} + C \frac{\partial}{\partial z} \underline{u} + \underline{w} = 0 \quad (3-69)$$

where  $\underline{u}$  is the vector of 8 variables, A and C stand for 8 x 8 matrices easy to derive from the differential equations, and  $\underline{w}$  is the vector of non-differential terms.

In order to save computing time this set of 8 coupled equations is split into two sets of equations which are separately solved: a leading set of 6 equations for which the vector of variables is defined by:

---

<sup>\*</sup>) *In a late stage during the writing of this chapter the author became aware of STUHMILLER's [97] recently developed two-phase momentum balances in which an extra term - the so called dynamic pressure term - occurs, not present in the momentum balances used in the present investigation. This dynamic pressure term is briefly discussed and analyzed in appendix 3-D. The analysis indicate that for the present flows this term is unimportant in the axial and tangential momentum balances, but by contrast may - if the suppositions are correct - be rather significant for computations of radial velocities from the radial liquid momentum balance. Prior to future applications of the proposed complete explicit scheme further investigation of the provisional analyses of appendix 3-D is therefore required.*

*The maximum possible inaccuracy in the ANALEST procedure due to omission of the dynamic pressure term, is estimated in appendix 3-D to be in the order of the inaccuracy of the procedure itself and therefore accepted by the present author.*

$$\underline{u} = \begin{pmatrix} \alpha \\ p \\ u_{gr} \\ u_{gz} \\ u_{\varphi r} \\ u_{\varphi z} \end{pmatrix} \quad (3-70)$$

and the 6 x 6 matrices A and C are derived from the two mass balances, two radial and two axial momentum balances, and an additional set based on the two tangential momentum balances for which

$$\underline{u} = \begin{pmatrix} u_{g\varphi} \\ u_{\varphi} \end{pmatrix} \quad (3-71)$$

The saving in computing time stems from the fact that solution of a set of matrices requires a number of computational operations proportional to the order of the matrix cubed, i.e. 512 for a 8 x 8 matrix and 216 + 8 = 224 for successive solution of the 6 x 6 and 2 x 2 matrices. The separate solution procedure appears justified because the leading six equations indeed do not contain differential quotients of the tangential velocities, while the dependence of the two additional equations from the leading six parameters is weak. In the additional system the differential quotients for the two radial and axial velocities are computed from the values obtained from the foregoing solution of the leading system. Since the ADI method treats the problem as an initial value problem where the initial guess is improved during the successive iteration steps until the steady state solution is reached, ignoring of the coupling will at worst cause some increase in the number of iteration steps and will not affect the essence of the solution method.

Although a complete single iteration step consists of the successive solution of the leading and additional system, only the leading system will be discussed here because of the great similarity in the mathematical description of both systems.

For the present purpose the vector  $\underline{w}$  will be expressed as:

$$\underline{w} = D \underline{u} \quad (3-72)$$

which is possible because  $\underline{w}$  is dependent on  $\underline{u}$ , but nevertheless leaves 30 degrees of freedom for the 36 terms of the 6 x 6 D matrix. These 30 degrees of freedom will be prescribed by stability considerations, as discussed in the next subsection.

Substitution of equation (3-72) in (3-69) yields:

$$(A \frac{\partial}{\partial r} + C \frac{\partial}{\partial z} + D) \underline{u} = \underline{0} \quad (3-73)$$

Because the left hand side is based on an initial guess it will not equal zero. The ADI method uses these deviations to improve the initial guess by stating \*):

\* ) In literature these deviations are generally referred to as pseudo time dependencies, denoted by  $\frac{\partial}{\partial t} \underline{u}$  instead of  $\frac{\partial}{\partial s} \underline{u}$ . In order to avoid confusion the author prefers to describe them on the basis of an integration route s.

$$\frac{\partial}{\partial s} \underline{u} = (A \frac{\partial}{\partial r} + C \frac{\partial}{\partial r} + D) \underline{u} \quad (3-74)$$

The original system (3-69) is solved if the integration along the route  $s$  arrives at  $\frac{\partial}{\partial s} \underline{u} = \underline{0}$ . As extensively described in [99], [100] the ADI method was extended for the present investigation by the introduction of a so called stability matrix  $M^{-1}$ , equaling the deviations to  $M^{-1} \frac{\partial}{\partial s} \underline{u}$ :

$$M^{-1} \frac{\partial}{\partial s} \underline{u} = (A \frac{\partial}{\partial r} + C \frac{\partial}{\partial z} + D) \underline{u} \quad (3-75)$$

which is transformed to:

$$\frac{\partial}{\partial s} \underline{u} = (MA \frac{\partial}{\partial r} + MC \frac{\partial}{\partial z} + MD) \underline{u} \quad (3-76)$$

being the system to be iterated until  $\frac{\partial}{\partial s} \underline{u} = \underline{0}$ .

The effect on the computational stability of introducing  $M^{-1}$  will be discussed in the following subsection.

The solution  $\underline{u}(s + \Delta s)$  for the system (3-76) in a point  $r, z$  can be obtained by integration along the route  $s$ , yielding:

$$[\underline{u}]_{r,z}^{s+\Delta s} = \exp\{([MA]_{r,z}^s \frac{\partial}{\partial r} + [MC]_{r,z}^s \frac{\partial}{\partial z} + [MD]_{r,z}^s) \Delta s\} [\underline{u}]_{r,z}^s \quad (3-77)$$

where the matrices  $[MA]_{r,z}^s$ ,  $[MC]_{r,z}^s$  and  $[MD]_{r,z}^s$  vary along the integration route (dependent on  $s$ ).

Discretization of this solution for the integration route  $s$  after  $n$  and  $n+1$  iteration steps, as well as for the flow field to nodal points of a grid, yields for the grid point  $r = r_h = h\Delta r$  and  $z = z_k = k\Delta z$ :

$$[\underline{u}]_{h,k}^{n+1} = \exp\{\Delta s ([MA]_{h,k}^n \frac{\partial}{\partial r} + [MC]_{h,k}^n \frac{\partial}{\partial z} + [MD]_{h,k}^n)\} [\underline{u}]_{h,k}^n \quad (3-78)$$

In the ADI method this equation is rewritten as:

$$\begin{aligned} & \exp\{-\frac{\Delta s}{2} [MA]_{h,k}^n \frac{\partial}{\partial r}\} \cdot \exp\{-\frac{\Delta s}{2} [MC]_{h,k}^n \frac{\partial}{\partial z}\} \cdot \exp\{-\frac{\Delta s}{2} [MD]_{h,k}^n\} [\underline{u}]_{h,k}^{n+1} = \\ & = \exp\{\frac{\Delta s}{2} [MA]_{h,k}^n \frac{\partial}{\partial r}\} \cdot \exp\{\frac{\Delta s}{2} [MC]_{h,k}^n \frac{\partial}{\partial z}\} \cdot \exp\{\frac{\Delta s}{2} [MD]_{h,k}^n\} [\underline{u}]_{h,k}^n \end{aligned} \quad (3-79)$$

The exponential functions are subsequently expanded in Taylor series, i.e. for example:

$$\begin{aligned} \exp\{\frac{\Delta s}{2} [MA]_{h,k}^n \frac{\partial}{\partial r}\} &= I + \frac{\Delta s}{2} [MA]_{h,k}^n \frac{\partial}{\partial r} + \frac{1}{2!} \{\frac{\Delta s}{2} [MA]_{h,k}^n \frac{\partial}{\partial r}\}^2 + \\ &+ \frac{1}{3!} \{\frac{\Delta s}{2} [MA]_{h,k}^n \frac{\partial}{\partial r}\}^3 + \dots \end{aligned}$$

and it is assumed that the integration interval  $\Delta s$  is sufficiently small to satisfy the conditions:

$$\frac{\Delta S}{2} [MA]_{h,k}^n \frac{\partial}{\partial r} \ll I$$

$$\frac{\Delta S}{2} [MC]_{h,k}^n \frac{\partial}{\partial z} \ll I \quad (3-80)$$

$$\frac{\Delta S}{2} [MD]_{h,k}^n \ll I$$

Thus the Taylor expansions can be approximated by the first two terms only, and substitution of these terms in (3-79) yields:

$$\begin{aligned} \{I - \frac{\Delta S}{2} [MA]_{h,k}^n \frac{\partial}{\partial r}\} \{I - \frac{\Delta S}{2} [MC]_{h,k}^n \frac{\partial}{\partial z}\} \{I - \frac{\Delta S}{2} [MD]_{h,k}^n\} [\underline{u}]_{h,k}^{n+1} &= \\ &= \{I + \frac{\Delta S}{2} [MA]_{h,k}^n \frac{\partial}{\partial r}\} \{I + \frac{\Delta S}{2} [MC]_{h,k}^n \frac{\partial}{\partial z}\} \{I + \frac{\Delta S}{2} [MD]_{h,k}^n\} [\underline{u}]_{h,k}^n \end{aligned} \quad (3-81)$$

An intermediate solution  $[\underline{u}]_{h,k}^{n*}$  is then introduced, which splits the system (3-81) into two systems according to:

$$\{I - \frac{\Delta S}{2} [MA]_{h,k}^n \frac{\partial}{\partial r}\} [\underline{u}]_{h,k}^{n*} = \{I + \frac{\Delta S}{2} [MC]_{h,k}^n \frac{\partial}{\partial z}\} \{I + \frac{\Delta S}{2} [MD]_{h,k}^n\} [\underline{u}]_{h,k}^n \quad (3-82A)$$

$$\{I - \frac{\Delta S}{2} [MC]_{h,k}^n \frac{\partial}{\partial z}\} \{I - \frac{\Delta S}{2} [MD]_{h,k}^n\} [\underline{u}]_{h,k}^{n+1} = \{I + \frac{\Delta S}{2} [MA]_{h,k}^n \frac{\partial}{\partial r}\} [\underline{u}]_{h,k}^{n*} \quad (3-82B)$$

For successive solution of the systems (3-82A) and (3-82B) the right hand sides are known and the left hand sides each contain only one operator in one direction. This alternating integration in one direction only yields a much simpler set of equations to solve, causing the reduction in computing time mentioned in subsection 3.3.1.

The remaining final step in the numerical solution procedure is discretization in space, i.e. replacement of the differential operators  $\frac{\partial}{\partial r}$  and  $\frac{\partial}{\partial z}$  by finite differences. In the present case the central difference scheme was chosen. The differential operators  $\frac{\partial}{\partial r}$  and  $\frac{\partial}{\partial z}$  are replaced by the finite difference operators  $\frac{\delta r}{\Delta r}$  and  $\frac{\delta z}{\Delta z}$ , respectively, where

$$\begin{aligned} \delta_r [\underline{u}]_{h,k}^n &= \frac{1}{2} ([\underline{u}]_{h+1,k}^n - [\underline{u}]_{h-1,k}^n) \\ \delta_z [\underline{u}]_{h,k}^n &= \frac{1}{2} ([\underline{u}]_{h,k+1}^n - [\underline{u}]_{h,k-1}^n) \end{aligned} \quad (3-83)$$

Substitution of these operators in the system (3-82), yields:

$$\{I - \frac{\Delta S}{2} [MA]_{h,k}^n \frac{\delta r}{\Delta r}\} [\underline{u}]_{h,k}^{n*} = \{I + \frac{\Delta S}{2} [MC]_{h,k}^n \frac{\delta z}{\Delta z}\} \{I + \frac{\Delta S}{2} [MD]_{h,k}^n\} [\underline{u}]_{h,k}^n \quad (3-84A)$$

$$\{I - \frac{\Delta S}{2} [MC]_{h,k}^n \frac{\delta z}{\Delta z}\} \{I - \frac{\Delta S}{2} [MD]_{h,k}^n\} [\underline{u}]_{h,k}^{n+1} = \{I + \frac{\Delta S}{2} [MA]_{h,k}^n \frac{\delta r}{\Delta r}\} [\underline{u}]_{h,k}^{n*} \quad (3-84B)$$

In general each of these systems results in a set of equations shaped as a band matrix each containing three diagonals of which the elements are 6 x 6 matrices in the case of the leading system of 6 unknowns.

Some irregularities in these diagonals occur for the grid points at the boundaries where the central difference scheme has to be replaced by either a forward or a backward finite difference operator. These effects are extensively discussed by DE RUITER [100] as is the incorporation of the boundary conditions mentioned in subsection 3.2.2.3.

### 3.3.3.2. Criteria for stability

Stability will be discussed here rather than referring to [99], [100] because it will be shown to require an extremely small iteration step, thereby rendering the ADI method unsuitable for application to two-phase flow.

In view of this reason only the major aspects are discussed in this subsection; for the details the reader is referred to [100], where convergence, consistency and the effects of linearization and iteration are also discussed.

The Von Neumann criterion (see e.g. [101]) was selected for stability assessment in spite of some doubts voiced by mathematicians concerning its applicability to the present problem.

The Von Neumann method is based on a Fourier series expansion of the unknown function. For the present flow field,  $0 \leq r \leq \frac{1}{2}D$  and  $0 \leq z \leq z_H$ , this yields:

$$\underline{u}(r,z,s) = \sum_{\beta=-\infty}^{\infty} \sum_{\gamma=-\infty}^{\infty} v_{\beta\gamma}(s) e^{i2\pi\beta \frac{2r}{D}} e^{i2\pi\gamma \frac{z}{z_H}} \quad (3-85)$$

For the system of interest, i.e. (3-81), the criterion is applied to each of the grid points. Substitution of  $[\underline{u}]_{h,k}^n$  on the basis of (3-85) into (3-81) yields:

$$[v_{\beta\gamma}]_{h,k}^{n+1} = [G_{\beta\gamma}]_{h,k}^n [v_{\beta\gamma}]_{h,k}^n \quad (3-86)$$

where  $[G_{\beta\gamma}]_{h,k}^n$  is the so called amplification matrix for each grid point. The Von Neumann criterion requires that the spectral radius  $\rho$  of each amplification matrix satisfies the inequality:

$$\rho([G_{\beta\gamma}]_{h,k}^n) \leq 1 + K\Delta s \quad (\text{for all integer } \beta \text{ and } \gamma) \quad (3-87)$$

for any existing constant K.

This criterion is necessary for stability. It is sufficient if the amplification matrix is a Hermitian matrix.

#### 3.3.3.2.1. Necessary condition

The amplification matrix  $[G_{\beta\gamma}]_{h,k}^n$  is obtained by substitution of  $[\underline{u}]_{h,k}^n$  in terms of a Fourier expansion like (3-85) in the system (3-81).

In this latter equation - being the representation of the complete iteration step - the differential operators  $\frac{\partial}{\partial r}$  and  $\frac{\partial}{\partial z}$  are replaced by the finite difference operators as defined in (3-83), yielding:

$$\delta_r [\underline{u}]_{h,k}^n = \sum_{\beta=-\infty}^{\infty} \sum_{\gamma=-\infty}^{\infty} \frac{1}{2} (e^{i2\pi\beta \frac{\Delta r}{\frac{1}{2}D}} - e^{-i2\pi\beta \frac{\Delta r}{\frac{1}{2}D}}) [v_{\beta\gamma}]_{h,k}^n e^{i2\pi\beta \frac{r}{\frac{1}{2}D}} e^{i2\pi\gamma \frac{z}{z_H}} \quad (3-88)$$

$$\delta_z [\underline{u}]_{h,k}^n = \sum_{\beta=-\infty}^{\infty} \sum_{\gamma=-\infty}^{\infty} \frac{1}{2} (e^{i2\pi\gamma \frac{\Delta z}{z_H}} - e^{-i2\pi\gamma \frac{\Delta z}{z_H}}) [v_{\beta\gamma}]_{h,k}^n e^{i2\pi\beta \frac{r}{\frac{1}{2}D}} e^{i2\pi\gamma \frac{z}{z_H}}$$

Substitution of these expressions with application of the equality  $i \sin x = \frac{1}{2}(e^{ix} - e^{-ix})$  and defining, for brevity's sake:

$$\begin{aligned}\mu &= \frac{\Delta S}{2\Delta r} \sin \left( 2\pi\beta \frac{\Delta r}{\frac{1}{2}D} \right) \\ \zeta &= \frac{\Delta S}{2\Delta Z} \sin \left( 2\pi\gamma \frac{\Delta Z}{Z_H} \right) \\ \kappa &= \frac{\Delta S}{2}\end{aligned}\tag{3-89}$$

transforms system (3-81) into:

$$\begin{aligned}\sum_{\beta=-\infty}^{\infty} \sum_{\gamma=-\infty}^{\infty} (I - i\mu [MA]_{h,k}^n) (I - i\zeta [MC]_{h,k}^n) (I - \kappa [MD]_{h,k}^n) [\underline{v}]_{h,k}^{n+1} e^{i2\pi\beta \frac{r}{\frac{1}{2}D}} e^{i2\pi\gamma \frac{Z}{Z_H}} = \\ = \sum_{\beta=-\infty}^{\infty} \sum_{\gamma=-\infty}^{\infty} (I + i\mu [MA]_{h,k}^n) (I + i\zeta [MC]_{h,k}^n) (I + \kappa [MD]_{h,k}^n) [\underline{v}]_{h,k}^n e^{i2\pi\beta \frac{r}{\frac{1}{2}D}} e^{i2\pi\gamma \frac{Z}{Z_H}}\end{aligned}\tag{3-90}$$

From this equation and (3-86) the amplification matrix becomes:

$$\begin{aligned}[G_{\beta\gamma}]_{h,k}^n = \{ (I - i\mu [MA]_{h,k}^n) (I - i\zeta [MC]_{h,k}^n) (I - \kappa [MD]_{h,k}^n) \}^{-1} \\ (I + i\mu [MA]_{h,k}^n) (I + i\zeta [MC]_{h,k}^n) (I + \kappa [MD]_{h,k}^n)\end{aligned}\tag{3-91}$$

where the matrices  $[A]_{h,k}^n$  and  $[C]_{h,k}^n$  are known from the set of governing balances, while matrix  $[D]_{h,k}^n$  still has 30 degrees of freedom because it has only to satisfy the six equation (3-72) and the matrix  $[M]_{h,k}^n$  has to satisfy the stability criterion (3-87).

In order to simplify the analyses on this amplification matrix  $[G_{\beta\gamma}]_{h,k}^n$  as much as possible, the conditions for the stability matrix  $[M]_{h,k}^n$  are stated in advance and subsequently elaborated to demonstrate the fulfilling of condition (3-87). The requirements for  $[M]_{h,k}^n$  are:

- the matrices  $[MA]_{h,k}^n$  and  $[MC]_{h,k}^n$  are symmetric, i.e.

$$\begin{aligned}[MA]_{h,k}^n &= ([MA]_{h,k}^n)^T \\ [MC]_{h,k}^n &= ([MC]_{h,k}^n)^T\end{aligned}\tag{3-92}$$

- the matrix  $[MD]_{h,k}^n$  equals the negative unity matrix, i.e.

$$[MD]_{h,k}^n = -I\tag{3-93}$$

To avoid the computation of  $[D]_{h,k}^n$  equation (3-72) is substituted in (3-93), transferring this latter condition into:

$$[\underline{Mw}]_{h,k}^n = -[\underline{u}]_{h,k}^n\tag{3-94}$$

This system consists of 6 equations, while each of the conditions (3-92) represents 15 equations, i.e. a total of 36 equations permitting the determination of the 36 elements of  $[M]_{h,k}^n$ .

For the analyses of the stability condition (3-87), the spectral radius  $\rho([G_{\beta\gamma}]_{h,k}^n)$  is replaced by the eigenvalues  $\lambda_G$  of the amplification matrix. Application of the inequality

$$\rho([G_{\beta\gamma}]_{h,k}^n) \leq \max |\lambda_G| \quad (3-95)$$

shows that the condition (3-87) is satisfied if

$$|\lambda_G| \leq 1 + K\Delta s \quad (3-96)$$

focussing the further discussion on the eigenvalues  $\lambda_G$ .

Substitution of (3-93) yielding  $(1-\kappa[MD]_{h,k}^n) = (1+\kappa)I$  and  $(1+\kappa[MD]_{h,k}^n) = (1-\kappa)I$ , and introduction for brevity's sake of the matrix:

$$[N_{\beta\gamma}]_{h,k}^n = (I - \mu\zeta[MA]_{h,k}^n [MC]_{h,k}^n) (\mu[MA]_{h,k}^n + \zeta[MC]_{h,k}^n) \quad (3-97)$$

transforms the amplification matrix (3-91) into:

$$[G_{\beta\gamma}]_{h,k}^n = \frac{1-\kappa}{1+\kappa} (I - i[N_{\beta\gamma}]_{h,k}^n)^{-1} (I + i[N_{\beta\gamma}]_{h,k}^n) \quad (3-98)$$

which implies a dependency of  $\lambda_G$  on the eigenvalues  $\lambda_N$  of  $[N_{\beta\gamma}]_{h,k}^n$ . Calculation of  $\lambda_G$  via

$$|\lambda_G I - \frac{1-\kappa}{1+\kappa} (I - i[N_{\beta\gamma}]_{h,k}^n)^{-1} (I + i[N_{\beta\gamma}]_{h,k}^n)| = 0$$

yields

$$|\lambda_G I (I - i[N_{\beta\gamma}]_{h,k}^n) - \frac{1-\kappa}{1+\kappa} (I + i[N_{\beta\gamma}]_{h,k}^n)| = 0$$

and

$$|(\lambda_G - \frac{1-\kappa}{1+\kappa}) I - i(\lambda_G + \frac{1-\kappa}{1+\kappa}) [N_{\beta\gamma}]_{h,k}^n| = 0$$

which, according to the definition of the eigenvalues, leads to:

$$i\lambda_N = \frac{\lambda_G - \frac{1-\kappa}{1+\kappa}}{\lambda_G + \frac{1-\kappa}{1+\kappa}}$$

and thus

$$\lambda_G = \frac{1-\kappa}{1+\kappa} \cdot \frac{1+i\lambda_N}{1-i\lambda_N} \quad (3-99)$$

Application of the generalized expression  $\lambda_N = \text{Re}\lambda_N + i\text{Im}\lambda_N$  yields:

$$|\lambda_G| = \frac{1-\kappa}{1+\kappa} \left| \frac{1 - \text{Im}\lambda_N + i\text{Re}\lambda_N}{1 + \text{Im}\lambda_N - i\text{Re}\lambda_N} \right| = \frac{1-\kappa}{1+\kappa} \left\{ \frac{(1 - \text{Im}\lambda_N)^2 + (\text{Re}\lambda_N)^2}{(1 + \text{Im}\lambda_N)^2 + (\text{Re}\lambda_N)^2} \right\}^{\frac{1}{2}}$$

$$|\lambda_G| = \frac{1-\kappa}{1+\kappa} \left\{ 1 - \frac{4\text{Im}\lambda_N}{(1 + \text{Im}\lambda_N)^2 + (\text{Re}\lambda_N)^2} \right\}^{\frac{1}{2}} \quad (3-100)$$

Substitution of this expression in condition (3-96), shows that

- ★ the criterion is satisfied whenever  $\text{Im}\lambda_N \geq 0$
- ★ if  $\text{Im}\lambda_N < 0$ , then  $\text{Im}\lambda_N$  must be of the same magnitude as  $\Delta s$

This latter requirement will be derived by the development of an expression for  $\text{Im}\lambda_N$ . On the basis of the definition for the eigenvectors  $\underline{x}_N$  of the matrix  $[N_{\beta\gamma}]_{h,k}^n : [N_{\beta\gamma}]_{h,k}^n \underline{x}_N = \lambda_N \underline{x}_N$ , it follows (omitting the subscripts  $h, k, n, \beta$  and  $\gamma$ ) that:

$$\underline{x}_N^T N \underline{x}_N = \lambda_N \underline{x}_N^T \underline{x}_N \quad (3-101A)$$

And via  $N\underline{x}_N = \lambda_N \underline{x}_N \rightarrow \underline{x}_N^T N\underline{x}_N = \bar{\lambda}_N \underline{x}_N^T \underline{x}_N$  and subsequent transformation  $(\underline{x}_N^T N\underline{x}_N)^T = (\bar{\lambda}_N \underline{x}_N^T \underline{x}_N)^T$ , it yields:

$$\underline{x}_N^T N^T \underline{x}_N = \bar{\lambda}_N \underline{x}_N^T \underline{x}_N \quad (3-101B)$$

Subtraction of these two expressions gives:

$$\begin{aligned} \underline{x}_N^T (N - N^T) \underline{x}_N &= (\lambda_N - \bar{\lambda}_N) \underline{x}_N^T \underline{x}_N \quad \text{and thus} \\ (\lambda_N - \bar{\lambda}_N) &= 2i\text{Im}\lambda_N = \frac{\underline{x}_N^T (N - N^T) \underline{x}_N}{\underline{x}_N^T \underline{x}_N} \end{aligned} \quad (3-102)$$

For further elaboration of  $\text{Im}\lambda_N$  the matrix  $(N - N^T)$  is obtained by substitution of definition (3-97) for  $N$ , yielding:

$$\begin{aligned} (N - N^T) &= (I - \mu\zeta MAMC)^{-1} [\mu(MA - (MA)^T) + \zeta(MC - (MC)^T) + \mu\zeta^2(MAMC(MC)^T + \\ &\quad - MC(MC)^T(MA)^T) + \mu^2\zeta MA(MC - (MC)^T)] (I - \mu\zeta(MC)^T(MA)^T)^{-1} \end{aligned} \quad (3-103)$$

Since  $\mu MA \ll I$  and  $\zeta MC \ll I$  - being the discretized version of condition (3-80) which was introduced for the approximation of the Taylor series - the cubic terms in expression (3-103) are much smaller than the linear components  $\mu MA$  and  $\zeta MC$ . Thus the symmetry conditions (3-92):  $MA = (MA)^T$  and  $MC = (MC)^T$ , yield the smallest possible value for  $(N - N^T)$  and thus for  $\text{Im}\lambda_N$ .

Further approximation of  $(N - N^T)$  by taking the sine functions in  $\mu$  and  $\zeta$  (cf. definitions (3-89)) equal to unity for this minimum value of  $(N - N^T)$ , results in

$$(N - N^T) \leq \frac{\Delta s^3}{8\Delta r\Delta z^2} (I - \frac{\Delta s^2}{4\Delta r\Delta z} MAMC)^{-1} (MAMCMC - MCMCMA) (I - \frac{\Delta s^2}{4\Delta r\Delta z} MCMA)^{-1} \quad (3-104)$$

Because of this proportionality with the iteration step  $\Delta s$  cubed, it is possible by an adequate selection of this iteration step to satisfy the condition:

$$\text{Im}\lambda_N = \frac{\overline{x}_N^T (N - N^T) x_N}{\overline{x}_N^T x_N} = 0(\Delta s) \quad (3-105)$$

fulfilling the necessary condition of the Von Neumann criterion.

### 3.3.3.2.2. Sufficient condition

As stated above condition (3-87) is sufficient for stability if the amplification matrix  $[G_{\beta\gamma}]_{h,k}^n$  is Hermitian, i.e.

$$[G_{\beta\gamma}]_{h,k}^n = \overline{([G_{\beta\gamma}]_{h,k}^n)^T} \quad (3-106)$$

In this subsection the effects of this Hermitian condition on the stability condition  $\rho([G_{\beta\gamma}]_{h,k}^n) < 1 + K\Delta s$  will be analyzed. Hereto expression (3-98) is substituted in condition (3-106), yielding:

$$\begin{aligned} \frac{1-\kappa}{1+\kappa} (I - i[N_{\beta\gamma}]_{h,k}^n)^{-1} (I + i[N_{\beta\gamma}]_{h,k}^n) &= \\ &= \frac{1-\kappa}{1+\kappa} (I - i[N_{\beta\gamma}]_{h,k}^n)^T (I + i([N_{\beta\gamma}]_{h,k}^n)^T)^{-1} \end{aligned} \quad (3-107)$$

showing that this condition is satisfied if  $[N_{\beta\gamma}]_{h,k}^n$  is anti-symmetric, i.e.

$$[N_{\beta\gamma}]_{h,k}^n = -([N_{\beta\gamma}]_{h,k}^n)^T \quad (3-108)$$

This latter condition affects the eigenvalues  $\lambda_N$ ; considering expression (3-102) for  $\text{Im}\lambda_N$  it appears that condition (3-108) leads to:

$$\text{Im}\lambda_N = \frac{\overline{x}_N^T N x_N}{\overline{x}_N^T x_N} \quad (3-109)$$

The real part of  $\lambda_N$  is obtained by adding the expression (3-101A) and (3-101B), yielding:

$$(\lambda_N + \overline{\lambda}_N) = 2\text{Re}\lambda_N = \frac{\overline{x}_N^T (N + N^T) x_N}{\overline{x}_N^T x_N} \quad (3-110)$$

which for condition (3-108) transforms into:

$$\text{Re}\lambda_N = 0 \quad (3-111)$$

Thus in the case of a Hermitian matrix  $[G_{\beta\gamma}]_{h,k}^n$  expression (3-100) for the eigenvalues reduces to:

$$|\lambda_G| = \frac{1-\kappa}{1+\kappa} \left| \frac{1 - \text{Im}\lambda_N}{1 + \text{Im}\lambda_N} \right| \quad (3-112)$$

Evaluation of these eigenvalues on the basis of expression (3-109) and definition (3-97) for  $N$ , shows that  $\text{Im}\lambda_N$  is proportional with either

$\mu = \frac{\Delta S}{2\Delta r} \sin(2\pi\beta \frac{\Delta r}{\frac{1}{2}D})$  or  $\zeta = \frac{\Delta S}{2\Delta z} \sin(2\pi\gamma \frac{\Delta z}{z_H})$ , dependent on the ratio of  $\mu[MA]_{h,k}^n$  and  $\zeta[MC]_{h,k}^n$ . Generalizing this proportionality as:

$$\text{Im}\lambda_N = \frac{\Delta S}{2\Delta r} C_N \quad (3-113)$$

where the proportionality constant  $C_N$  depends on the above mentioned ratio as well as on  $N$ ,  $\beta$ ,  $\gamma$  and the ratio between  $\Delta s$  and  $\Delta z$ . Substitution of (3-112) and (3-113) transforms stability condition (3-96) into:

$$\frac{1 - \frac{\Delta S}{2}}{1 + \frac{\Delta S}{2}} \left| \frac{1 - \frac{\Delta S}{2\Delta r} C_N}{1 + \frac{\Delta S}{2\Delta r} C_N} \right| \leq 1 + K\Delta s \quad (3-114)$$

Further elaboration of this condition, yields:

$$-(1 + K\Delta s) \leq \frac{1 - (\frac{1}{2} + \frac{C_N}{4\Delta r})\Delta s + \frac{C_N}{4\Delta r}\Delta s^2}{1 + (\frac{1}{2} + \frac{C_N}{4\Delta r})\Delta s + \frac{C_N}{4\Delta r}\Delta s^2} \leq 1 + K\Delta s$$

Subtracting 1 from each of the three expressions and subsequent multiplication with the denominator of the middle expression, yield the two inequalities:

$$2(\frac{1}{2} + \frac{C_N}{4\Delta r}) \geq K [1 + \{\frac{1}{2} + \frac{C_N}{4\Delta r}\} \Delta s + \frac{C_N}{4\Delta r} \Delta s^2] \quad (3-115A)$$

and

$$2 + \{2(\frac{1}{2} + \frac{C_N}{4\Delta r}) + K\} \Delta s + \{2 \frac{C_N}{4\Delta r} + K(\frac{1}{2} + \frac{C_N}{4\Delta r})\} \Delta s^2 + K \frac{C_N}{4\Delta r} \Delta s^3 \geq 2(\frac{1}{2} + \frac{C_N}{4\Delta r}) \Delta s$$

which latter is rewritten as:

$$2 + K\Delta s + \{2 \frac{C_N}{4\Delta r} + K(\frac{1}{2} + \frac{C_N}{4\Delta r})\} \Delta s^2 + K \frac{C_N}{4\Delta r} \Delta s^3 \geq 0 \quad (3-115B)$$

These two conditions - obtained for a Hermitian amplification matrix  $[G_{\beta\gamma}]_{h,k}^n$  - can both be satisfied if  $C_N \geq 0$ , i.e.  $\text{Im}\lambda_N \geq 0$ .

If  $C_N < 0$  no  $K$  exists to satisfy condition (3-115A) for  $\Delta r$  and  $\Delta s$  approaching zero, i.e. the specific stability condition (3-114) for a Hermitian amplification matrix cannot be satisfied.

Thus the Von Neumann criterion (3-87) cannot be satisfied for a Hermitian amplification matrix, which implies that the sufficient condition for stability cannot be satisfied, leaving an uncertainty about the stability. It should, however, be noticed that this conclusion is reached using expression (3-93), leaving the possibility that the sufficient condition might be satisfied if using an alternative formulation of the matrix  $[D]_{h,k}^n$ . The complexity of such analyses, however, has prevented the search for such an alternative.

### 3.3.3.3. Evaluation of the ADI procedure

The major points of interest, as in any other computer code, are the proof of stability and the required computation time.

The determination of the maximum stable integration interval is discussed in subsection 3.3.3.3.1., together with the proof of stability. Subsection 3.3.3.3.2. deals with the required computation time and methods to reduce this time as much as possible.

### 3.3.3.3.1. Determination of the integration interval

The maximum integration step  $\Delta s$  satisfying the necessary stability condition (3-96) can be obtained by computing the eigenvalues  $\lambda_G$  from expression (3-100). But since such computations must be made for each of the grid points and for a large number of values for  $\beta$  and  $\gamma$  and has to be repeated for each iteration, this integration interval will be determined in a more generalized way.

From expression (3-105) it appears that  $\text{Im}\lambda_N$  has to be determined to fulfill the necessary condition for stability. In order to estimate the magnitude of this part of  $\lambda_N$ , a number  $m$  is introduced, which is - considering expressions (3-102) and (3-104) - defined by:

$$\text{Im}\lambda_N = \frac{\Delta s^3}{16\Delta r\Delta z^2} m^3 \quad (3-116)$$

The factors  $(I - \frac{\Delta s^2}{4\Delta r\Delta z} \text{MAMC})^{-1}$  and  $(I - \frac{\Delta s^2}{4\Delta r\Delta z} \text{MCMA})^{-1}$  - occurring in expression (3-104) - can both be approximated by the unity matrix  $I$  because  $\frac{\Delta s}{\Delta r} \text{MA} \ll I$  and  $\frac{\Delta s}{\Delta z} \text{MC} \ll I$  as a consequence of the conditions (3-80) introduced to approximate the Taylor series.

In combination with expression (3-102) it follows that  $m^3$  represents the term  $(\text{MAMCMC} - \text{MCMCMA})$  occurring in expression (3-104).

With respect to this term it is reasonable to assume that the magnitude of the elements of this matrix  $(\text{MAMCMC} - \text{MCMCMA})$  is the same as the magnitude of the elements of the separate matrices  $\text{MAMCMC}$  and  $\text{MCMCMA}$ . Furthermore the character of the governing mass and momentum balances leads to the expectation that the magnitude of the elements of the matrices  $A$  and  $C$  are identical, hence the foregoing will also be valid for the matrices  $\text{MA}$  and  $\text{MC}$ . Since  $\text{Im}\lambda_N$  is expected to be mostly determined by the largest terms of the constituent matrices, it is finally concluded that  $m$  represents the largest elements of the matrices  $\text{MA}$  and  $\text{MC}$ , i.e.:

$$m \approx \max |(ma)_{ij}| \approx \max |(mc)_{ij}| \quad (3-117)$$

The number  $m$  is determined applying the computer code - including the computation of the stability matrix  $M$  via the requirements (3-93) and (3-94) - to one of the flows measured in chapter 4\*), viz. measurement 3043 for a rotating mixture in a cylindrical geometry. It was found that

$$\max |(ma)_{ij}| \approx \max |(mc)_{ij}| \approx 10^6 \text{ \AA } 10^7 = 5 \cdot 10^6 \quad (3-118)$$

Substitution of this result in (3-116) via (3-117) yields:

$$\text{Im}\lambda_N \approx \frac{\Delta s^3}{\Delta r\Delta z^2} 8 \cdot 10^{18}$$

For the flow geometries described in chapter 4 the grid sizes were defined by  $\Delta r = 5 \cdot 10^{-3}$  and  $\Delta z = 5 \cdot 10^{-2}$  meter. Application of these grid sizes and

\*) *Similar results were found on the basis of computations for more arbitrary flows.*

the above result to condition (3-105), stating that  $\text{Im}\lambda_N$  has to be of the magnitude  $\Delta s$ , yields  $\frac{\Delta s^3}{125 \cdot 10^{-7}} 8 \cdot 10^{18} = \Delta s$  resulting in:

$$\Delta s = 1.3 \times 10^{-12} \quad (3-119)$$

Since the above derivation is based on a number of assumptions and approximations, it is worthwhile to verify this result by comparison to the complete computations of an iteration step. In addition such an approach may serve to remove the doubt concerning stability caused by not having satisfied the sufficient condition for stability.

The verification presented here is based on an expression known from analyses on the rate of convergence (see e.g. [102], [103]) correlating the deviations from the exact solution  $[\underline{u}]_{h,k}^\infty$  for subsequent iteration steps, i.e.

$$[\underline{u}]_{h,k}^{n+1} - [\underline{u}]_{h,k}^\infty = \rho([G_{\beta\gamma}]_{h,k}^n) ([\underline{u}]_{h,k}^n - [\underline{u}]_{h,k}^\infty) \quad (3-120)$$

As before the spectral radius  $\rho([G_{\beta\gamma}]_{h,k}^n)$  is replaced by the maximum eigenvalue  $\max |\lambda_G|$ , resulting in:

$$[\underline{u}]_{h,k}^{n+1} - [\underline{u}]_{h,k}^\infty = (\max |\lambda_G| - 1) ([\underline{u}]_{h,k}^n - [\underline{u}]_{h,k}^\infty) \quad (3-121)$$

For the above small value of  $\Delta s$  - and thus of  $\text{Im}\lambda_N$  - condition (3-96) and expression (3-100) imply that for a stable computation

$$(\max |\lambda_G| - 1) \sim \Delta s \quad (3-122)$$

resulting in:

$$[\Delta \underline{u}]_{h,k}^{n+1} = ([\underline{u}]_{h,k}^{n+1} - [\underline{u}]_{h,k}^n) \sim \Delta s ([\underline{u}]_{h,k}^n - [\underline{u}]_{h,k}^\infty) \quad (3-123)$$

Thus it is concluded that for a computation satisfying the necessary condition for stability the variation of the unknowns  $[\Delta \underline{u}]_{h,k}^{n+1}$  is proportional

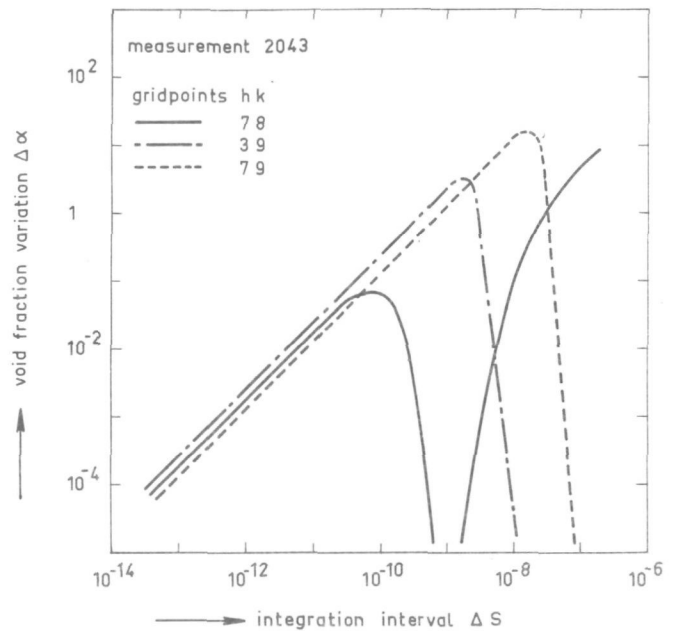
to the integration interval  $\Delta s$ , as long as the deviation from the exact solution in the previous iteration step is kept constant. In order to verify this conclusion the first iteration step for the computations of measurement 3043 was repeated several times with intergration intervals ranging from  $\Delta s = 10^{-13}$  upto  $10^{-7}$ . A typical example of the results is presented in figure 3-8; the above proportionality with  $\Delta s$  is found to occur only for  $\Delta s < 10^{-11}$ . Above this value the variations become wildly erratic; for this specific case of  $\Delta \alpha$  the variation sometimes even exceeds unity, causing a void fraction beyond the physical range  $0 \leq \alpha \leq 1$ .

The wild character for  $\Delta s > 10^{-11}$  points to an unstable iteration procedure, while the smooth behaviour for  $\Delta s < 10^{-11}$  suggests a stable computation, notwithstanding absence of proof of the sufficient conditions for stability. The rather good agreement between the value of  $\Delta s = 10^{-11}$  thus obtained and the integration interval  $\Delta s = 10^{-12}$  derived on the basis of the Von Neumann criterion points to the validity of this criterion for the present set of equations, notwithstanding the doubt on its applicability expressed in the introduction of subsection 3.3.3.2.

Although stable computation thus appears possible with  $\Delta s = 10^{-11}$ , it is suggested to maintain an upper limit of  $\Delta s = 10^{-12}$  integration interval for safety reasons.

FIGURE 3-8

*Typical example of dependency of parameter variation on integration interval*



### 3.3.3.3.2. Computation time

In order to evaluate the computation time and possible ways for its reduction, some characteristics of the procedure will first be presented. The ADI procedure - written in PL1 - is implemented on an IBM 370/65 computer, requiring:

- a memory of about 500 kbytes
- a computation time of 0.4 second per grid point per iteration step

For application to the flows of the present investigation the grid consists of 10 radial and 20 axial grid points, yielding 80 seconds computing time per iteration step. Here it should be remarked that:

- about half the computing time is required for computation of the stability matrix  $M$  (obtained by solving 36 equations for the 36 elements). After establishing the procedure this half might possibly be reduced either by computing the matrix  $M$  only once per 3 to 5 iteration steps or by application of one single matrix  $M$  for a group of neighbouring nodal points. Application of such techniques may reduce the computation time to about 50 seconds per iteration step.
- the procedure is not yet completely optimized with respect to computation time
- a further reduction can be achieved by writing the essential subroutines in ASSEMBLER rather than in a higher computer language and by using FORTRAN instead of PL1, the latter having been selected for convenience during the development of the procedure.

Such improvements will further reduce the computing time from 50 to about 20 seconds, which is taken as the representative computing time in the further discussion.

A value for the required number of iteration steps can be obtained analytically by application of equation (3-120); replacing the spectral radius by  $\max |\lambda_G|$  and subsequent series expansion, yields:

$$[\underline{u}]_{h,k}^{n+1} - [\underline{u}]_{h,k}^{\infty} = (\max |\lambda_G|)^{n+1} ([\underline{u}]_{h,k}^0 - [\underline{u}]_{h,k}^{\infty}) \quad (3-124)$$

where  $[\underline{u}]_{h,k}^0$  stands for the values of the initial guess.

Assuming the initial deviation  $[\underline{u}]_{h,k}^0 - [\underline{u}]_{h,k}^\infty$  to be about 25% of the exact solution and terminating the computation if the deviation equals 1%, it follows that:

$$(n + 1) = \frac{\ln 1/25}{\ln(\max |\lambda_G|)} \quad (3-125)$$

Taking the most optimistic value of  $\max |\lambda_G|$ , i.e.  $\text{Im}\lambda_N = 0$ , expression (3-100) reduces to  $|\lambda_G| = \frac{1-\kappa}{1+\kappa}$ , and it follows via definition (3-89) that for the small value of  $\Delta s$  the eigenvalue can be approximated as  $|\lambda_G| \approx 1 - \Delta s$ . Thus  $\ln(\max |\lambda_G|)$  can be approximated as  $-\Delta s$ , yielding for the total number of iteration steps:

$$n + 1 = \frac{3.2}{\Delta s} \approx 3.10^{12} \quad (3-126)$$

Again this analytical result is verified by computing a complete iteration step. The relative variations of the flow parameters for a single iteration step are presented for measurement 3043 in the first column of table 3-9, showing that the smallest relative variation occurs for the pressure, i.e.  $\frac{\Delta p}{p} \approx 10^{-13}$ . In order to obtain a relative variation of 25%, at least  $2.5 \times 10^{12}$  iteration steps are thus required, confirming the analytical result (3-126).

TABLE 3-9

Relative parameter variation  
for various conditions

parameter	relative parameter variation for $\Delta s = 10^{-12}$	
	straight forward	scaling to $\underline{u}^* \approx 1$
$\alpha$	$10^{-3}$	$10^{-12}$
$p$	$10^{-13}$	$10^{-9}$
$u_{gr}$	$10^{-4}$	$10^{-12}$
$u_{gz}$	$10^{-4}$	$10^{-9}$
$u_{1r}$	$10^{-3}$	$10^{-12}$
$u_{1z}$	$10^{-4}$	$10^{-9}$

Since this number of iteration steps requires  $20 \times 3.10^{12} = 6.10^{13}$  seconds  $\approx 2.10^6$  year, it is evident that without drastic reduction of this time the procedure will not be applicable.

For this purpose the effect of scaling was investigated. It was found that scaling of the separate equations in order to alter  $\frac{\partial}{\partial s} \underline{u}$  is of no avail because the values of the matrices MA, MC and MD remain unaffected by the scaling operation as M offsets the effect on A, C and D. The scaling of the flow parameters, however, does affect the overall characteristics. By trial and error it was found that scaling such that the scaled parameters  $\underline{u}^* \approx 1$ , yield the best results. From the second column of table 3-9 it appears that the minimum relative variation is increased to  $10^{-12}$  for  $\Delta s = 10^{-12}$ , reducing the number of iteration steps by a factor 10. Furthermore it was found that the elements of the matrices MA and MC - and thus

$m \approx \max |(ma)_{ij}| \approx \max |(mc)_{ij}|$  - reduce by about a factor 10, increasing in turn the maximum possible time step by a factor 30. Thus the total effect of parameter scaling is to reduce the required computation time by a factor 300 to 6000 year.

In view of this result no effort was made to investigate the potential of the various methods for convergence acceleration (see e.g. [102], [103]) and it was concluded that computation by the ADI procedure on the basis of a stable iteration scheme is not a viable proposition applicable for the present class of flow problems.

In view of the above conclusion the only possibility for application of the ADI method is to ignore all the conditions originating from the stability requirements. Such a computation is carried out by prescribing the stability matrix  $M$  as the unity matrix, i.e. multiply the original matrices  $MA$ ,  $MC$  and  $MD$  with  $M^{-1}$ . Fulfilling the only remaining conditions, viz. (3-80) for the approximation of the Taylor series, which are now transformed into

$\frac{\Delta S}{\Delta r} A \ll I$  and  $\frac{\Delta S}{\Delta z} C \ll I$ , it was found that the minimum relative variation

$\frac{\Delta p}{p} \approx 10^{-7}$ . Even this relative variation causes an excessive computation time, viz.  $20 \times 2.5 \times 10^6 = 5 \cdot 10^7$  seconds  $\approx 1.5$  year, while some of the results suggest instable behaviour.

#### 3.3.3.4. Conclusion

Introduction of a stability matrix results in an ADI procedure satisfying the necessary condition for stability. Compared to a straight forward computation ignoring the stability conditions - resulting in all probability in instability - the stable computation increases the number of iteration steps and thus the computation time by a factor  $10^6$ . Even after the introduction of parameter scaling - which reduces the computing time by about a factor 300 - and convergence acceleration methods (not investigated here) stable computation would require at least several centuries. Therefore the present ADI procedure is concluded to be inapplicable for the flows under consideration.

The most pronounced characteristic of the stable computation is its suppression of the variation in pressure (cf. table 3-9). In the author's opinion this is due to the combined characteristics of gas-liquid flow and of the present ADI procedure. The stability conditions of the present scheme are mainly determined by the characteristics of the matrices  $MA$  and  $MC$ , as apparent from equations (3-116) through (3-119), where the maximum stable iteration interval is determined on the basis of the matrices  $MA$  and  $MC$ . These matrices form part of the terms defining the pressure gradients and acceleration forces in the momentum balances (3-76). In the momentum balances for the relatively heavy liquid phase the pressure gradients are more or less balanced by the acceleration forces, hence the major terms of these liquid balances are involved in the stability conditions. In the gas momentum balances, however, the pressure gradients are balanced by the interaction forces, especially the drag forces  $F_{Dj}$ . These drag forces are part of the vector  $w$ , which is transformed into  $Mw = MDu = -u$  and is of minor importance with respect to the stability conditions. Thus it is reasonable to assume that the stability conditions - defined by  $MA$  and  $MC$  - suppress the variation of the pressure to the extent that the variation of the relatively small acceleration terms is maintained at an acceptable magnitude rather than relating the pressure variation to the major drag force term. These considerations yield the following theoretical possibilities to improve the

present ADI scheme:

- changing conditions (3-93) and (3-94) for the stability matrix  $M$  in such a way that the resulting change in  $Mw = MDu = -u$  causes the drag forces to have a significant effect on the stability conditions. As evident from relation (3-93) this approach would necessitate reformulation of the  $D$  matrix. As stated at the end of subsection 3.3.3.2.2. this would lead to complex analyses, preventing the implementation of this approach.
- replacing the gas momentum balances by 'interaction force expressions' i.e. eliminating the pressure gradients in the gas momentum balances by substitution of the pressure gradients from the liquid momentum balances, yielding expressions for the interaction forces. Possibly this will reduce or perhaps even eliminate the effect of the pressure gradients on the gas acceleration terms, considered to be at the root of the present problem. However, for this approach to be fully effective the drag force should be properly represented by quadratic velocity terms, which is basically impossible in the ADI method because the vector  $w$  has to be linearized as  $w = Du$ . This imperfect representation of the drag force makes it doubtful whether the effort should be undertaken.

As a matter of fact the present author became only aware of this significant role of the drag force in the course of the development of the explicit scheme, which at that time had reached the stage where its continued development appeared preferable to further efforts on improving the ADI procedure.

Apart from the time consuming stability requirements the implicit approach has an inherent disadvantage in computing time due to the fact, stated in subsection 3.3.3.1., that the number of computational operations required for solving a given set of matrix equations is proportional to the order of the matrix cubed. The present ADI procedure, despite the splitting in two sets of 6 and 2 equations respectively, thus compares poorly with an explicit scheme, i.e. by a ratio of 224 ( $= 6^3 + 2^3$ ) to 8 ( $= 8 \times 1^3$ ). This effect is particularly significant for two-phase flow, where the number of flow parameters is doubled compared to single-phase flow.

In view of the above considerations it is concluded that the excessive computation time required for the present ADI procedure is inherent to the combined characteristics of both the gas-liquid flows and the ADI method, and adequate reduction cannot be expected.

#### 3.4. Application of the explicit scheme to separator analysis

The ANALEST procedure as described above was applied to the experimental data on rotating flows given in chapter 4, viz.:

- 24 preliminary experiments with rotating flow in each of the three test sections shown in figure 2-24. These test sections were equipped with entrance vanes to obtain rotation but had no vortex finder for separation.
- separator experiments with a venturi separator, i.e. 7 introductory experiments and 9 measurements under simulated full and part load BWR conditions.

For the present evaluation of the explicit scheme only the computations for the 72 preliminary atmospheric air-water experiments will be discussed. In each set of 24 measurements 4 blade shapes were tested - coded as 1\*\*\*, 2\*\*\*, 3\*\*\* and 4\*\*\* in addition to the three number code defined in chapter 2 -

having an outlet angle of deflection at the wall of 30, 40, 50 and 60° respectively, i.e. increasing rotation with increasing code number. The 6 measurements per test section per blade geometry consist of 5 flows - coded as \*\*41 up to \*\*45 - having an axial superficial water velocity of 2.1 m/s and a void fraction at the inlet increasing from 0.25 to 0.75, the 6th measurement \*\*24 has a superficial water velocity of 1.3 m/s and a void fraction of about 0.62.

Only 36 measurements out of the above 72 were analyzed with the ANALEST procedure, viz. 18 experiments each for the straight and converging test section - coded as \*0\*\* and \*1\*\* respectively - consisting of the 6 measurements for 40, 50 and 60° blade angles. The experiments with the venturi shaped test section and with the 30° blades were not computer analyzed, as it was found from preliminary hand calculations that these flows are not significant for the further development of a venturi separator (cf. chapter 4).

The computer listings for these computations are presented in [104] and [95]. For all 36 cases the grid sizes were 50 and 5 mm for the axial and radial directions, respectively. The bottom grid line coincided with the bottom of the blade package (cf. figure 3-10 for the converging test section).

Some characteristics of these computations - performed on an IBM 370/65 computer - are:

- a computation time of 0.01 second per grid point per iteration step. Considering this type of computation as the solution of five  $1 \times 1$  matrices (pressure, two axial and radial and one tangential velocity), the proportionality constant for the number of computational operations (cf. subsection 3.3.3.1.) is  $5 \times 1^3 = 5$ , while the same constant for the ADI procedure equals  $6^3 + 2^3 = 224$ . This ratio of 45 corresponds to that of the computation time of 0.4 second for the ADI procedure (cf. subsection 3.3.3.2.) to the present 0.01 second,
- a required memory of 320 kbytes, in the case of the present 244 grid points
- the required number of iteration steps is found to be 15, both from considering the limit of "both determinants too small" discussed in subsection 3.3.2.4.1. and from the requirement that the values for all flow parameters remain constant during additional iteration steps.

The resulting total computation time for each of the 36 computations is around 35 seconds.

#### 3.4.1. Comparison with experimental results

In the analyses of the rotating flow experiments - extensively discussed in chapter 4 - all the flow parameters are taken into account, but for the present purpose, evaluation of the ANALEST procedure, only the computed pressure at the wall can be compared to measured data. This is because the second measured parameter, the radial void fraction distribution, is used as input at the actual stage of development of the ANALEST procedure. None of the remaining 6 parameters is measured locally, only the average axial velocities are calculated via the volumetric flow rates and the average cross sectional void fractions.

Prior to the comparison of computed and measured wall pressures presented in subsection 3.4.1.2., an impression of all the individual flow parameters will be given in subsection 3.4.1.1. using the computed data of measurement 3144.

### 3.4.1.1. Impression of local values for all flow parameters

Measurement 3144 was selected for the present purpose, because geometry and flow rates are fairly similar to the design conditions of the venturi separator to be developed.

The grid for the computations in the conical test section is presented in figure 3-10. For the present impression the radial distribution of all parameters is presented for 5 equidistant grid lines at a mutual distance of 200 mm, starting at the blade outlet, as indicated in figure 3-10. These radial distributions, presented in figure 3-11, give rise to the following comments:

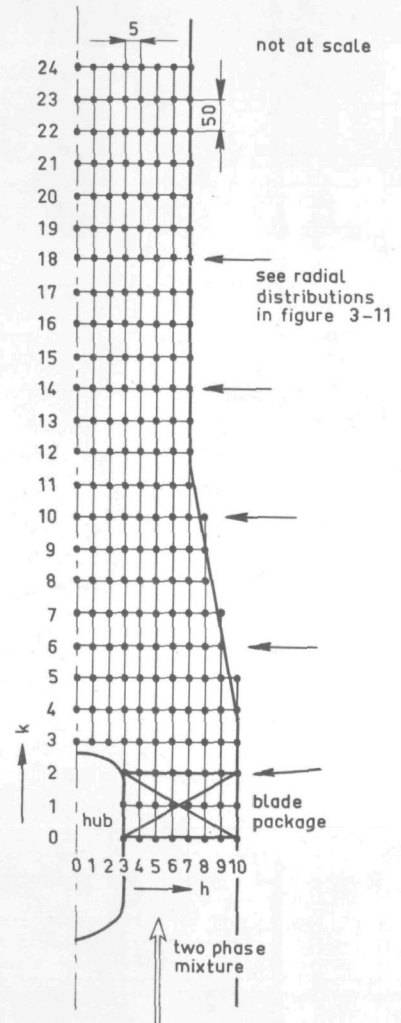


FIGURE 3-10

*Gridlines in the converging test section*

- void fraction

the radial distributions obtained by manual smoothing<sup>\*)</sup> of the data, show a dip at the centerline for the grid lines 6 and 10. This decrease of void fraction at the centerline was consistently measured for all flows. No indication could be found as to whether this was due to a measurement error or to an unexplained physical effect.

<sup>\*)</sup> To avoid irregularities caused by the Chebyshev double polynomial approximation, which otherwise might obscure a proper insight in the working of the ANALEST procedure.

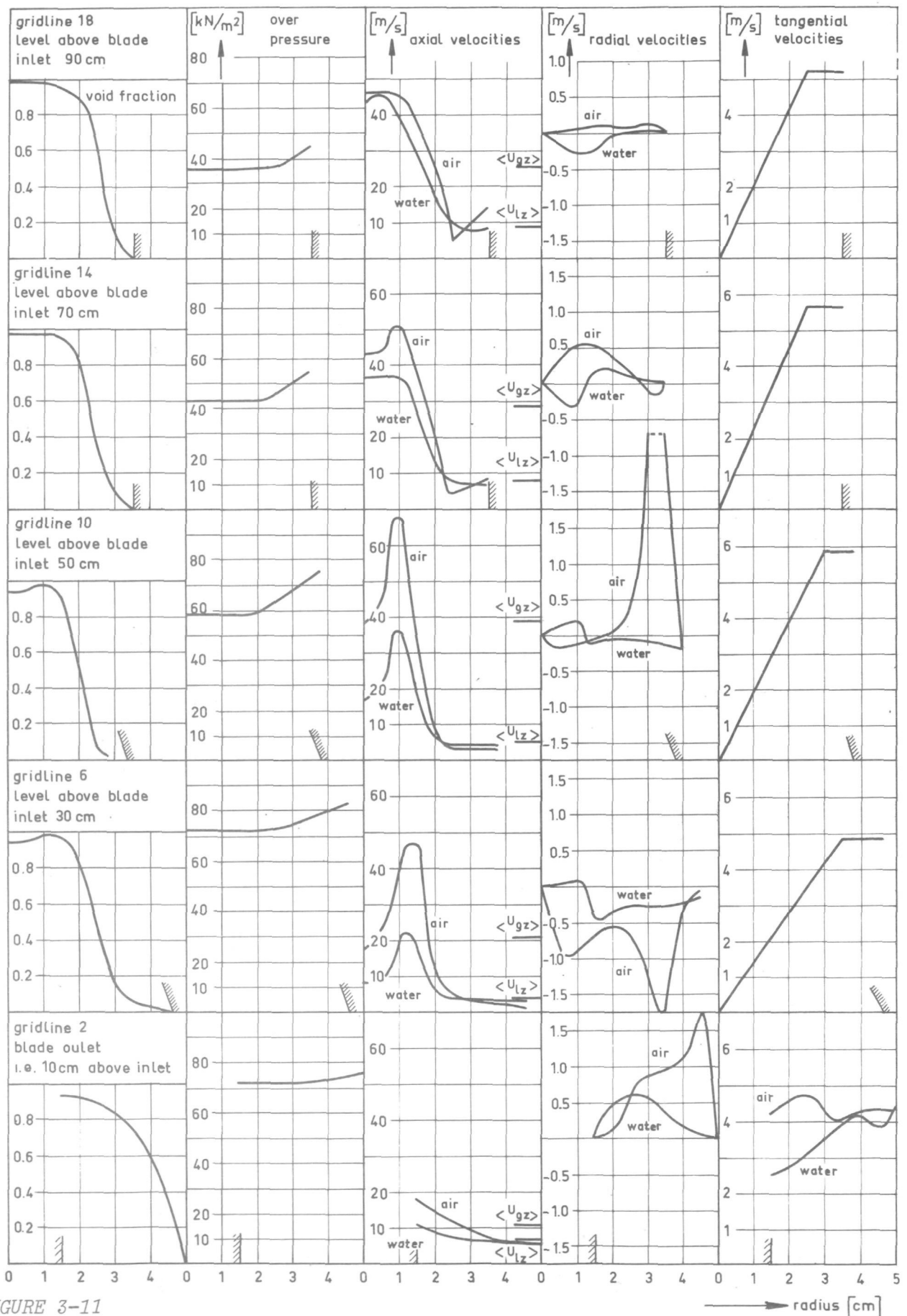


FIGURE 3-11

Radial distribution at various levels of all flow parameters for measurement 3144

- pressure

the increase in pressure from centerline to the wall is to be expected on the basis of the centrifugal force field  $\{(1-\alpha)\rho_l + \alpha\rho_g\} \frac{u^2}{r}$ . For  $\alpha > 0.5$ , i.e. in the gas core, the mixture density and tangential velocity are so small that the pressure is almost constant, while in the water layer  $\frac{\partial p}{\partial r}$  is nearly constant. The axial pressure profile shows a continuous decrease from bottom to top at the centerline; at the wall, however, a maximum exists around grid line 6 caused by the variation in the radial gradient  $\frac{\partial p}{\partial r}$  along the test section.

For the present measurement 3144 the radial pressure gradient in the water layer at the end of the cone, i.e. grid line 10,  $\frac{\partial p}{\partial r} \approx 10^6 \text{ N/m}^3$ , is high compared to the axial pressure gradient  $\frac{\partial p}{\partial z} \approx 0.8 \times 10^5 \text{ N/m}^3$ .

The ratio of radial to axial pressure gradients depends on that of the tangential and axial liquid velocities, i.e. on the blade geometry reaching the order  $10^2$  for a blade angle of  $60^\circ$  (measurement 4145).

- axial velocities

most conspicuous in the radial distributions of the axial velocities are the peaks at a radius of about 10 mm. The unrealistic magnitude of these peaks is due to the approximation of the second order viscosity terms for the gas phase by the artificial terms of expression (3-28). Correct viscosity forces will lower the gas peaks and subsequently the water velocity peaks via the interaction forces. What will then remain is a small peak, due to the maximum of the void fraction at this radius, causing a minimum in the drag force coefficient  $C_D$ . Comparison of grid line 14 to grid lines 6 and 10 confirms that a certain minimum peak height is required for the gas velocity to cause a noticeable peak in the liquid velocity.

A second point of interest in figure 3-11 is the negative relative velocity in the wall regions. This error in the gas velocities is caused by the computational velocity adjustments (3-57). The gas correction factor  $[C_g]_z$  gradually decreases from around 1 at the bottom of the grid to 0.85 at the top, yielding gas velocities in this latter region which are 15% below the values obtained from the gas momentum balance. For an explanation of this difference the reader is referred to subsection 3.4.2.

By contrast the correction factors for the liquid phase  $[C_l]_z$  are all between 0.94 and 1.03.

After averaging of the irrelevant peak, the gas velocity in the gas cone exceeds the average gas velocity  $\langle u_{gz} \rangle$  based on the volumetric flow rate and the average void fraction by a factor of about 1.5. The liquid velocity in the gas core exceeds the average velocity  $\langle u_{lz} \rangle$  by a factor of about 4 at the test section exit.

- radial velocities

the radial velocities are much too peaky to represent accurate values. Nevertheless it can be concluded that the magnitude of these velocities during separation, i.e. between grid lines 2 and 6, is about 0.5 and 1 m/s for the water and air respectively.

Figure 3-12 shows the sign of the radial velocities of both phases. A negative gas velocity and a positive liquid velocity causes the desired separation effect. Analyzing the flow from bottom to top it

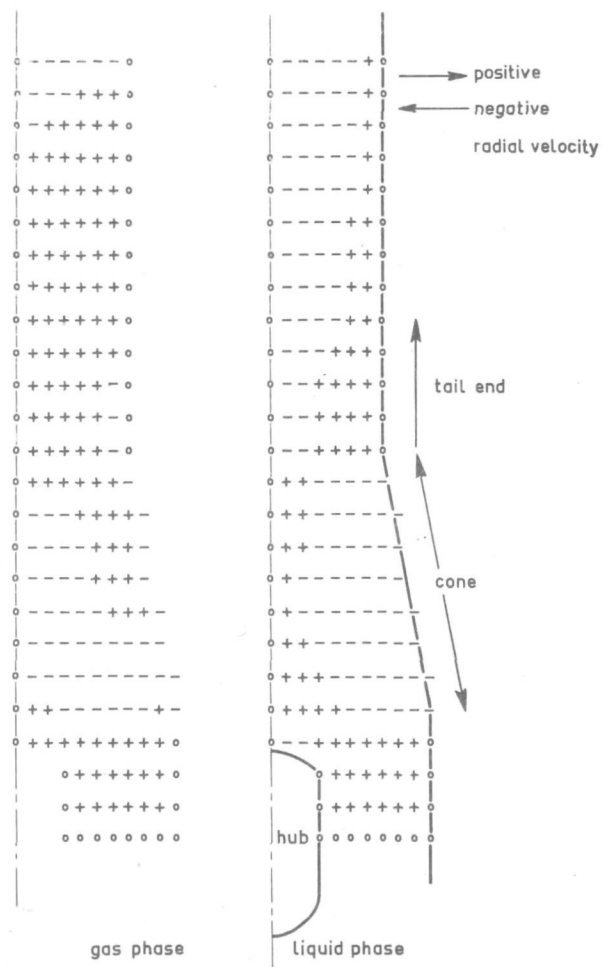


FIGURE 3-12

*Direction of radial velocities  
(measurement 3144)*

appears that:

- in the blade package both phases have a positive direction, which is undesirable for the gas phase but depends strongly on the blade geometry (cf. chapter 4).
- immediately above the hub some water is sucked towards the centerline, but subsequently removed from the center further downstream of the hub. The negative water velocity in the remainder of the cone is caused by the contraction effect.
- at the end of the cone air penetrates in the water layer, notwithstanding the high pressure gradient  $\frac{\partial p}{\partial r}$ . Most probably there is an exchange of air and water in the transition zone between the gas core and the water layer, due to the high relative axial velocity between these two flow regions.
- upon entering the straight tail end of the test section the air immediately remixes with the water while the penetration of the water in the gas core occurs only gradually.

• tangential velocity

since the radial distribution of the tangential velocities in the free flow field above the blades is obtained by imposing a radial distribution function (cf. subsection 3.3.2.4.3.), only the magnitude of the maximum velocity in the water layer can be analyzed. This maximum at the wall increases from 4 m/s at the blade outlet to 6 m/s at the end of the cone. This fulfills the aim of increasing the tangential velocity for separation reasons by decreasing the diameter of the test section, notwithstanding the tendency towards decreasing

tangential velocity due to concentration of the heavy phase at the wall of the test section at a constant angular momentum. In the straight part of the test section the decrease of the angular momentum and hence the tangential velocity due to wall friction becomes predominant.

#### 3.4.1.2. Wall pressures

The measured and computed pressures at the wall are presented in figures 3-13 and 3-14 for the straight and converging test section, respectively. Although the axial distribution of wall pressures will be discussed in chapter 4, the various causes affecting the measured and computed pressure gradients will be listed below in order to provide a better insight for their subsequent comparison.

The first measuring point (at  $z = 2.25$  m) is upstream of the hub of the blade package, upon passing the hub the mixture is accelerated - because of the 9% reduction in cross section area - causing a pressure decrease. Since the grid of the computation starts at the blade inlet ( $z = 2.418$  m) this acceleration pressure difference is not computed. Upon entering the guide vanes the pressure near the hub decreases due to the hydrostatic and frictional pressure gradients, but the gradual creation of a radial pressure gradient causes an increase of the wall pressure.

In the straight test section two effects are added - downstream of the guide vanes - to the hydrostatic and frictional pressure gradient, viz.:

- a deceleration of the mixture as a whole, because of the cross section enlargement at the end of the hub
- an acceleration of the gas, as a consequence of the separation: the interaction force of the gas in the core is lower than in a bubble swarm. This gas acceleration causes a deceleration of the liquid, the latter being dominant for the pressure gradient.

Both deceleration effects on the liquid will cause an increase of the pressure; the former at the end of the hub and that due to separation stretched over the separation region of which the length and the location depends on the axial and tangential velocity.

Two additional effects occur in the converging test section, due to the reduction in test section diameter, viz.:

- increasing rotation, which causes an increase in wall pressure via the radial pressure gradient
- acceleration of the mixture, yielding a pressure decrease

Finally two other effects occur in the straight tail end, viz.:

- some remixing takes place upon entering the straight part, yielding an extra pressure decrease opposite to the above separation effect
- a rather high frictional pressure gradient exists because the velocity is doubled by the diameter reduction from 0.1 to 0.07 m.

Considering figure 3-13A for the straight test section and the lowest tangential velocities (blade deflection  $40^\circ$ ), it is seen that the computations yield an almost exact prediction of the measured wall pressures. For the smallest void fraction (measurement 2041) separation is completed within the guide vanes and the pressure gradient is fully dominated by the hydrostatic pressure gradient of a thick film annular flow. With increasing void fraction this pressure gradient decreases, while due to the increased real velocities separation occurs downstream of the guide vanes. In the case of measurement 2045 the increase in pressure due to the separation continues up to the coordinate 3.2 m, followed by a decrease caused by the hydrostatic gradient of the annular flow regime.

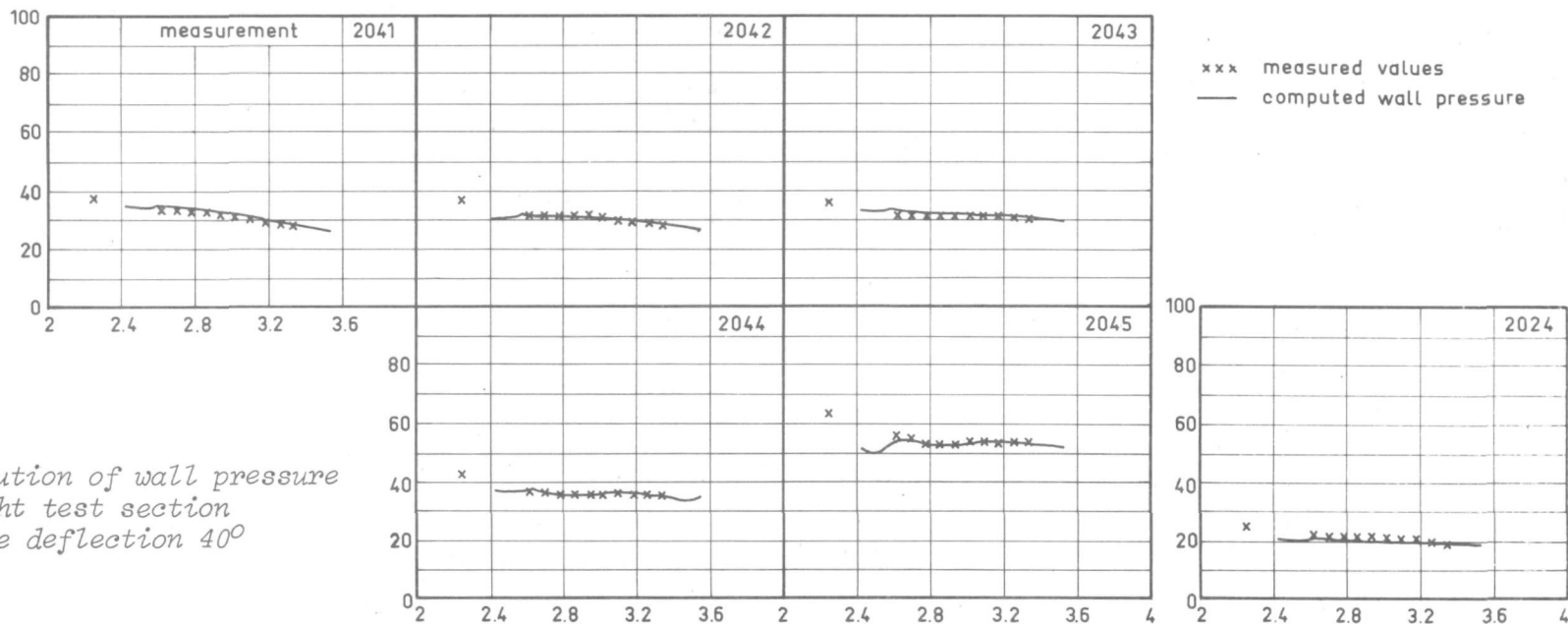


FIGURE 3-13A

*Axial distribution of wall pressure  
in the straight test section  
Angle of blade deflection 40°*

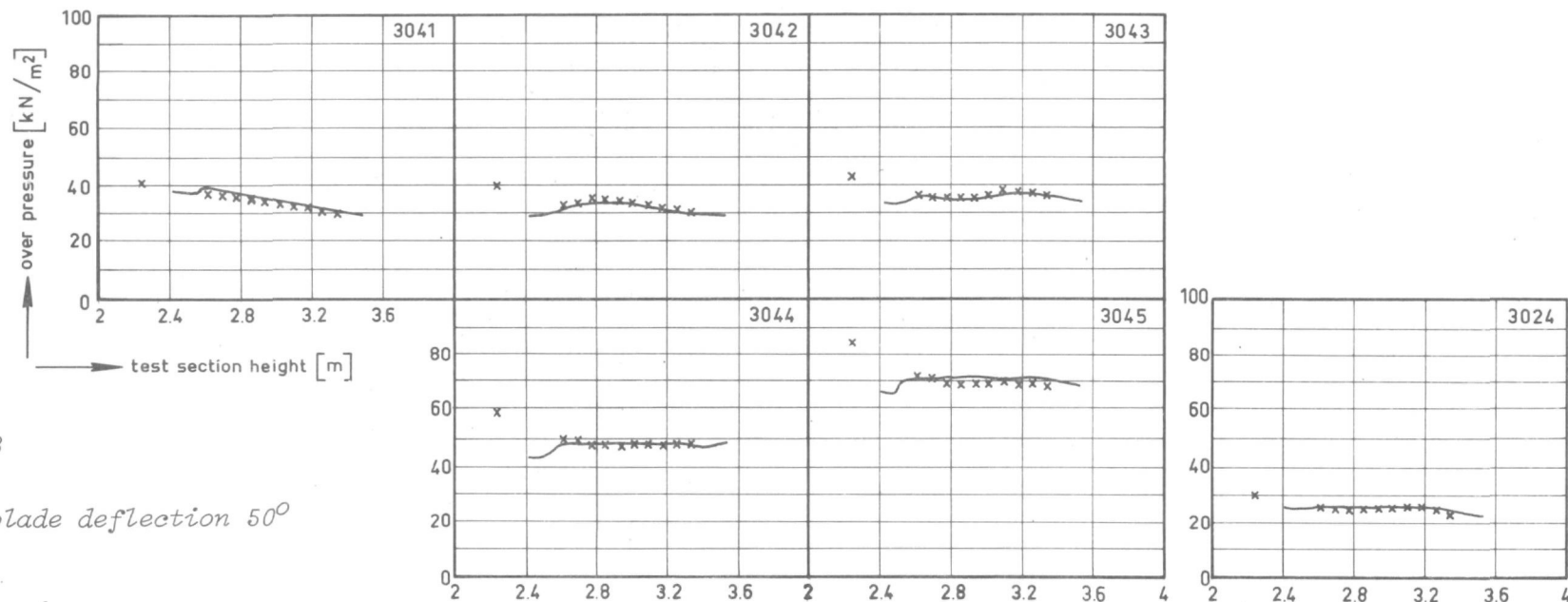


FIGURE 3-13B

*Idem  
Angle of blade deflection 50°*

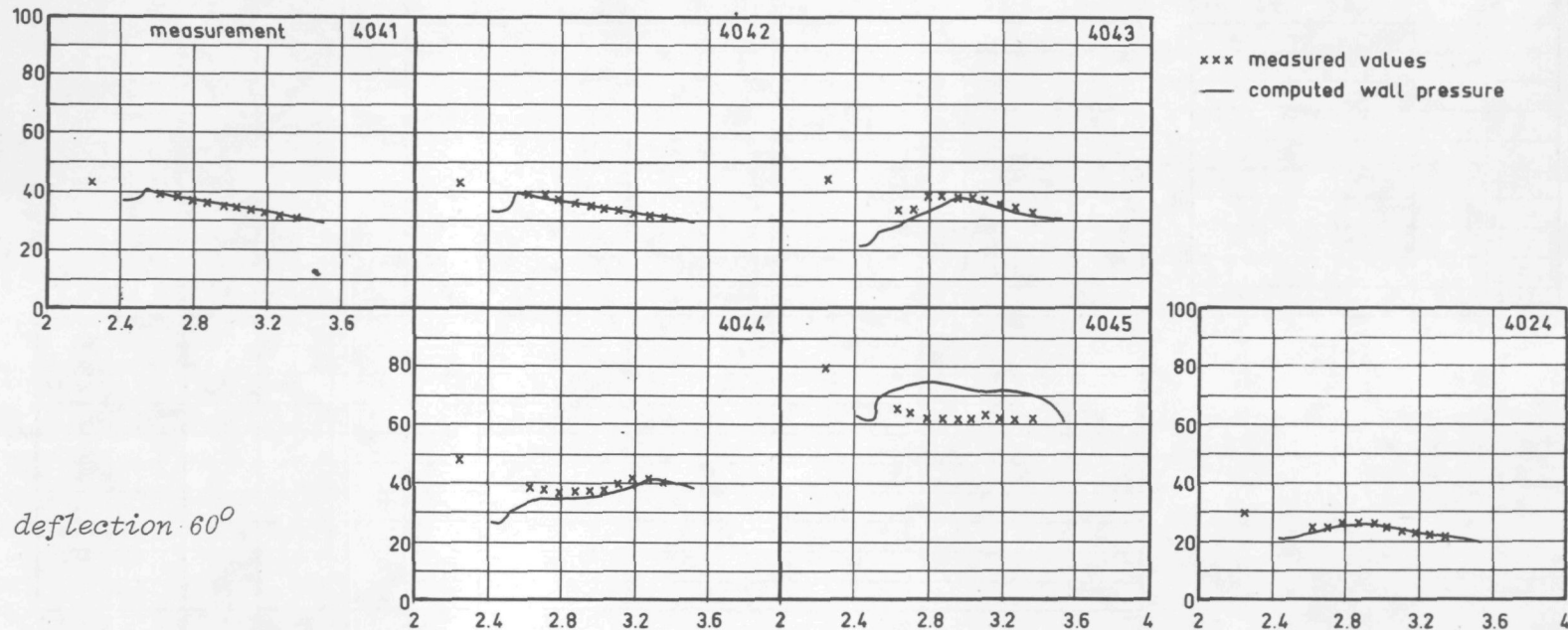


FIGURE 3-13C

Idem  
Angle of blade deflection  $60^\circ$

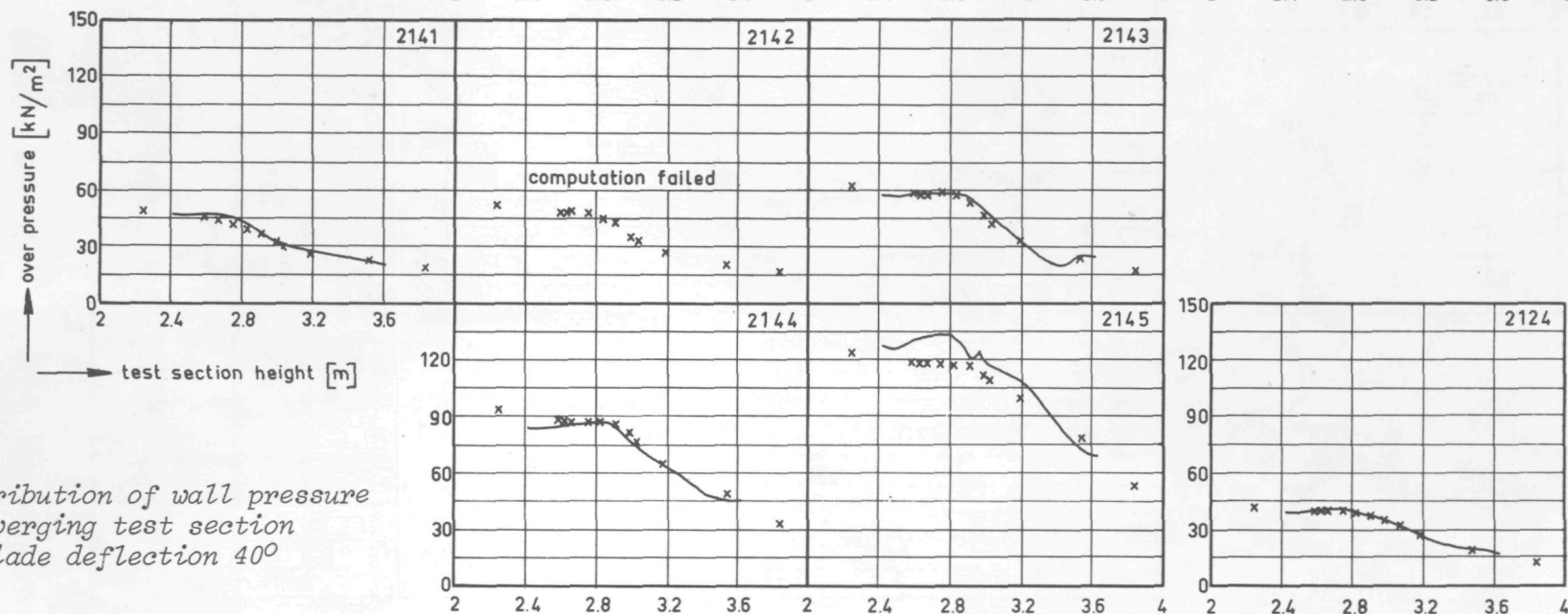


FIGURE 3-14A

Axial distribution of wall pressure  
in the converging test section  
Angle of blade deflection  $40^\circ$

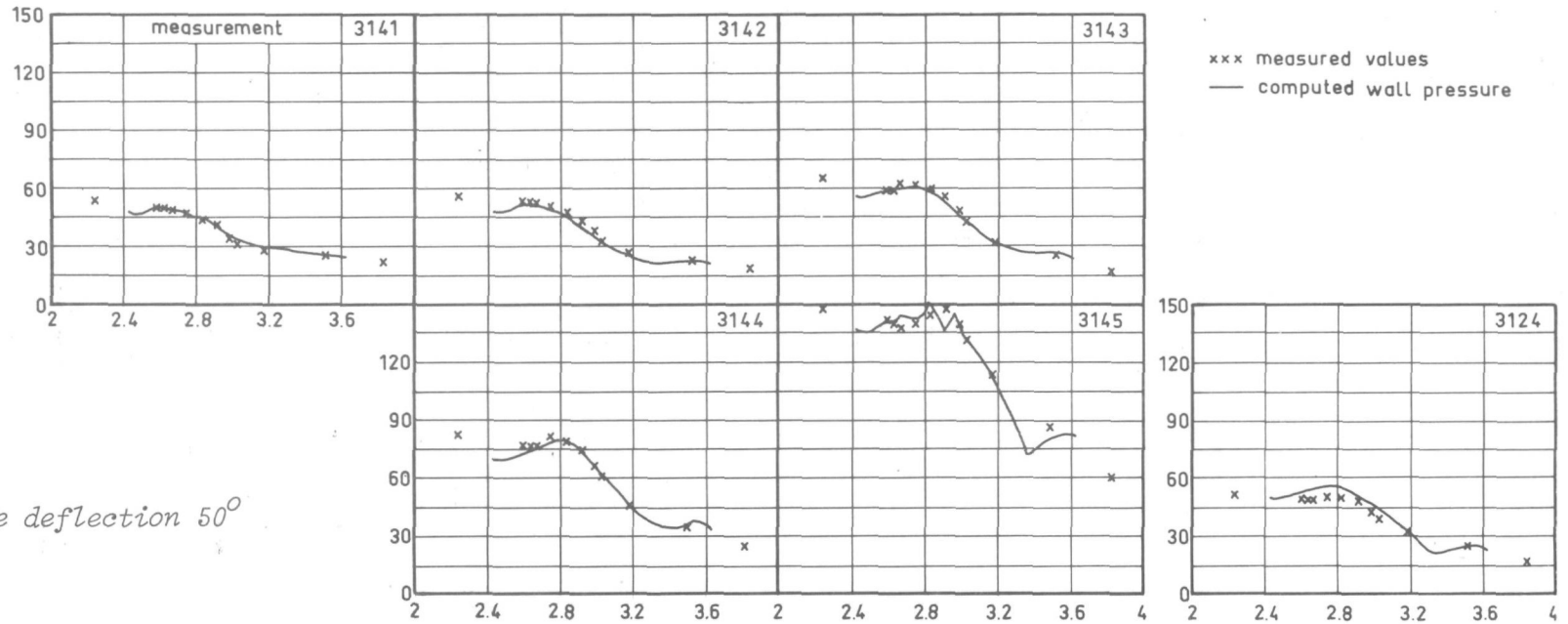


FIGURE 3-14B

Idem  
Angle of blade deflection 50°

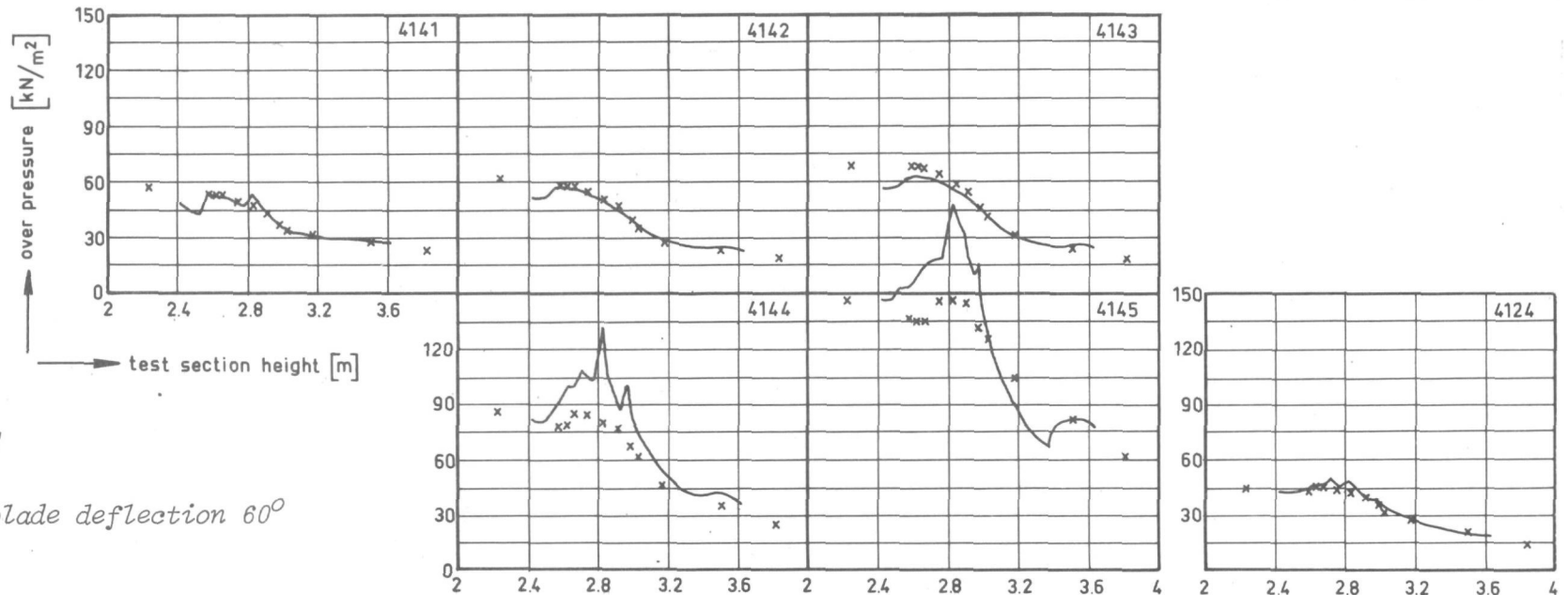


FIGURE 3-14C

Idem  
Angle of blade deflection 60°

Although for the small rotation of these  $40^\circ$  blades the prediction of the pressure gradient is rather simple because of the dominance of the hydrostatic pressure gradient, these results prove that the ANALEST procedure is able to handle a pressure gradient which is almost uniform over the cross section in combination with a strong variation in local void fraction from almost unity at the centerline to almost zero in the wall region. For the blade geometry with  $50^\circ$  deflection the computed values agree slightly less with the measured pressures. The increased rotation extends the distance over which separation takes place: for example up to 2.85 m for measurement 3042, while in the case of measurement 2042 separation is completed in the blade region.

For flows with  $60^\circ$  blade deflection the computed pressures at the inlet of the test section show some deviation for measurements 4043 and 4044. This is probably caused by the inaccuracy of the single value of 0.65 for the blade correction factor  $\zeta_b$  used for all flows and guide vane geometries (cf. subsection 3.3.2.4.3.). The deviation vanishes towards the end of the test section because the outlet pressure is fixed as a boundary condition. The extreme deviation for measurement 4045 is probably caused by inaccuracy of the Chebyshev double polynomial approximation of the local void fraction: an erroneous remixing at the end of the test section causes a steep pressure gradient towards the fixed outlet pressure. Because of the fixed void fraction distribution and mass flows, this error cannot be corrected by the procedure itself.

Out of the 18 computations for the converging test section - presented in figure 3-14 - only the measurement 2142 yielded no meaningful results. No specific reason could be found for this failure; the search for this reason is impeded by the rather erratic behaviour of the parameter values obtained in the first iteration step. This holds for all the computations but whereas general these erratic values gradually approach the final solution during subsequent iterations, the values become more erratic in the case of measurement 2142.

Large errors occur in the computation for measurements 4144 and 4145 and to a lesser extent in those for measurements 2145 and 3145. These are the flows with the largest tangential velocities, which enhances the effect of the inaccuracies, present in the computation of this parameter, i.e. fixed radial profile, single blade correction factor  $\zeta_b = 0.65$  and approximation of tangential viscous forces, on the resultant wall pressures. Concerning only the level of the pressure for the moment, and remembering the fixed pressure at the outlet; it appears that the too high level around the coordinate  $z = 2.8$  m is caused by a too steep pressure drop between 2.8 and 3.6 m, i.e. in the tail end of the test section. Since the pressure gradient in the tail end is dominated by the decrease of tangential velocity it is concluded that the too high pressure level for measurements 4144 and 4145 is caused by a too strong decrease of angular momentum on behalf of the imperfect representation of the viscous forces in tangential direction (cf. equations (3-27), (3-28) and (3-46)).

The peaks in the pressure distribution are caused by discontinuities: the stepwise reduction of radial grid points in the cone causes a stepwise change of the region where the prescribed radial distribution of the tangential velocity flattens (cf. expression 3-64). These two spatial discontinuities cause discontinuities in the tangential velocity and thus in the radial pressure gradient and axial wall pressure distribution: the axial location of the three peaks (most pronounced in measurement 2144) coincides with the grid lines where the number of grid points is reduced stepwise with respect to the preceding grid line. In view of the large

radial pressure gradient -  $\frac{\partial p}{\partial r} = 12 \text{ MN/m}^3$  for measurement 4145, i.e.  $12 \text{ kN/m}^2$

per millimeter of radial distance - the magnitude of the peak values is quite understandable. The possibilities for eliminating this error are discussed in subsection 3.4.2.

Apart from measurements 2145, 4144 and 4145 where the pressure level is too high and the failure for measurement 2142, the computations are in good agreement with the measured data. For low rates of rotation it is seen that in the cone ( $z = 2.518$  up to  $2.908$  m) the increase in wall pressure due to increasing rotation and the separation effect is more or less balanced by the acceleration pressure drop, causing a rather flat axial wall pressure profile. For larger rotations the wall pressure increases in the cone. In the tail end ( $z > 2.908$  m) the steep decrease at the wall (not at the centerline) is caused by the decreasing radial pressure gradient (friction losses for the angular momentum) and the rather high frictional pressure drop.

### 3.4.2. Evaluation and further development

From the above discussion in subsection 3.4.1.1. on the individual flow parameters and the general good agreement of the wall pressures compared with measured data (cf. subsection 3.4.1.2.) it is concluded that the ANALEST procedure is true to its name, i.e. is able to produce an analytical estimation of the various flow parameters. In its present stage it is therefore helpful to improving the insight in local flow parameter values and in detecting trends dependent on geometry, mass flows, etc. The accuracy of the computed values is found to vary for the different parameters, viz.

- the radial gas and liquid velocities are the most inaccurate parameters: only their magnitude and direction can be predicted
- the accuracy of the tangential velocity is mainly determined by the validity of the prescribed radial profile and the value of the blade correction factor  $\zeta_b = 0.65$  (cf. subsection 3.3.2.4.3.). No knowledge exists on the accuracy of these two constraints
- the maximum deviations of the axial velocities - estimated on the basis of the correction factors  $[C_g]_z$  and  $[C_l]_z$  (cf. subsection 3.4.1.1.) - are 15 to 20% for the gas and around 10% for the liquid
- the accuracy of the local pressures is generally within 5% of the total axial pressure difference over the test section

Most of the possibilities to improve the above inaccuracies lie within the mathematical model of the two-phase flow.

Here the greatest improvement of the results is expected from a better representation of the viscosity forces, up till now represented by the artificial viscosity forces (3-27) and (3-28). A correct description of these forces will:

- allow the computation of the tangential velocities without prescribing the radial distribution, because the unrealistic peaks (cf. subsection 3.3.2.4.3.) will be eliminated by the application of second order velocity derivatives
- eliminate peaks in the computed wall pressures, caused by overestimation of the frictional loss of angular momentum as discussed in subsection 3.4.1.2.
- reduce the erroneous peaks in the gas and liquid velocities at a radius around 10 mm (cf. figure 3-11 and subsection 3.4.1.1.)

The best result will undoubtedly be obtained if the viscosity forces are represented by the original second order terms as given in equations (3-9) up to (3-11), requiring a correlation for the turbulence viscosity of two-phase flow and a numerical procedure to obtain accurate values for the

second order velocity derivatives even when the velocity distributions are somewhat peaky. On the other hand the oversimplification introduced by the present expressions for the artificial viscosity terms is such that a reasonable improvement can already be expected from an improved model for these terms in which the effect of neighbouring velocities is somehow taken into account.

A second source of improvement of the mathematical model is presented by the approximations for the mist flow region contained in correlation (2-162) for the drag force coefficient. The 15% deviation of the axial gas velocities at the exit of the converging test section pointed out in subsection 3.4.1.1. is most probably due to underestimation of the drag force coefficient for the annular flow regime existing in that part of the test section. Such an improvement of correlation (2-162) requires experimental data on mist flows.

The third possibility for improvement is to differentiate values for the blade correction factor  $\zeta_b$  according to blade geometry and mixture composition.

The only improvement to be obtained via a change in the solution procedure is by application of variable grid sizes, i.e. by adapting the grid to the real geometry and thus avoiding discontinuities and peaks in the wall pressure as discussed in subsection 3.4.1.2. A partial solution for this problem - only reducing the effect of grid discontinuities - is applied in the computations for the venturi separator (cf. chapter 4), where a more continuous radial distribution of the tangential velocities is used:

$$[u_{g\varphi}]_{r,z} = [u_{l\varphi}]_{r,z} = C(z) \sin\left(\frac{\pi}{2} \frac{2r}{D}\right) \quad (3-127)$$

instead of the former expression (3-64).

The author expects the implementation of the above possible improvements to yield an increase in accuracy for the axial and tangential velocities and the pressure of up to 5 to 10%. Although the accuracy of the radial velocities will also slightly increase, these velocities are so dependent on the void fraction that accurate values can only be achieved if the void fraction itself is computed, rather than imposed. For this computation a further analysis of the radial momentum balances is required with respect to the dynamic pressure term as discussed in appendix 3-D.

In summary it is concluded that with a reasonable effort the present ANALEST procedure can be developed into a computer program capable of predicting fairly accurate values for the flow parameters of rotating two-phase flow.

## 4. GAS-LIQUID SEPARATION

### 4.1. Introduction

Equipment for the mechanical separation of gas and liquid in steady two-phase flow consists of two categories: separators for low quality inlet flows (typically: up to  $x = 0.25^*$ ) and driers/demisters for high quality inlet flows (typically:  $x > 0.8^{**}$ ). As evidenced by chapter 1 the present investigation deals exclusively with the former category and more specifically with centrifugal separators.

This latter type of separators is widely applied in (petro)chemical and power engineering. In the first case the aim is mostly to remove entrained non-condensable gases, while in the latter case the aim is to obtain dry steam from circulation boilers producing steam-water mixtures with steam contents not exceeding about 25% by weight in view of the requirements for the circulation in the boiler circuit.

The most sophisticated applications in steam supply systems are the centrifugal separators of a nuclear boiling water reactor (BWR), because of the size limitations imposed by the space available above the nuclear core and the high separating efficiency required to minimize carry-under; both of these items are prerequisite for the economic and technical feasibility of such a reactor. In U-tube steam generators for pressurized water reactors (PWR's) and in fossil-fueled boilers the available space is larger, while in the latter case the steam is subsequently superheated and therefore the main purpose of steam drying is to protect the superheater against corrosion and solids deposition. At the time of initiation of the work reported here there appeared to be a continuing need in BWR energy systems for separators of higher specific loading (capacity per built-in area) concomitant with the trend towards increased unit rating, i.e. a relatively decrease in available space [1]. An indication of this need was given by the successive development by General Electric [105] of first, second and third generation separators for its BWR steam supply systems, with specific steam loading increasing from 0.385 up to 0.82 kg/sm<sup>2</sup>. As noticed in chapter 1 this apparent need for further development was one of the reasons that caused the Laboratory of Thermal Power Engineering of Delft University of Technology to embark in the mid sixties upon the development of a steam-water separator based on the specifications of a BWR. This chapter deals with the implications of the present investigation for this development initiated by PRINS [1]. Before going into the results of the present investigation a short introduction is given on the BWR system, various types of centrifugal separators and the separating requirements.

### 4.2. Steam-water separation in boiling water nuclear reactors

#### 4.2.1. BWR steam supply system

A simplified flow diagram of the steam and water circulation loops in a BWR power plant is given in figure 4-1. It is usually a single cycle system

---

\**) The distinction between both categories of separators is essentially determined by the void fraction ( $\alpha \approx 0.8$ ), but for the readers interested in nuclear power systems this value is transformed to weight quality based on steam-water properties at 7 MN/m<sup>2</sup>.*

\*\**) The droplets in mist flow may also be removed in cyclones, and there exists special equipment for non-steady flow: knock-out drums and slug catchers.*

with forced circulation through the nuclear core where - in modern plants - 15% by weight of the water is evaporated. The mixture released from the core passes the primary separators - forming the subject of this investigation - whence the water is returned to the downcomer for recirculation, whilst the wet steam is led to the driers. This secondary separation removes the last water from the steam: a few percent during steady operation at rated load but possibly up to 15% during start up and part load conditions. The dry steam passes to and through the turbine, is condensed and returned to the reactor as feedwater.

The two step steam-water separation serves various goals. The 'carry-over' of droplets in the steam must be minimized to protect the turbine buckets against erosion and solids deposition and to avoid high radiation levels

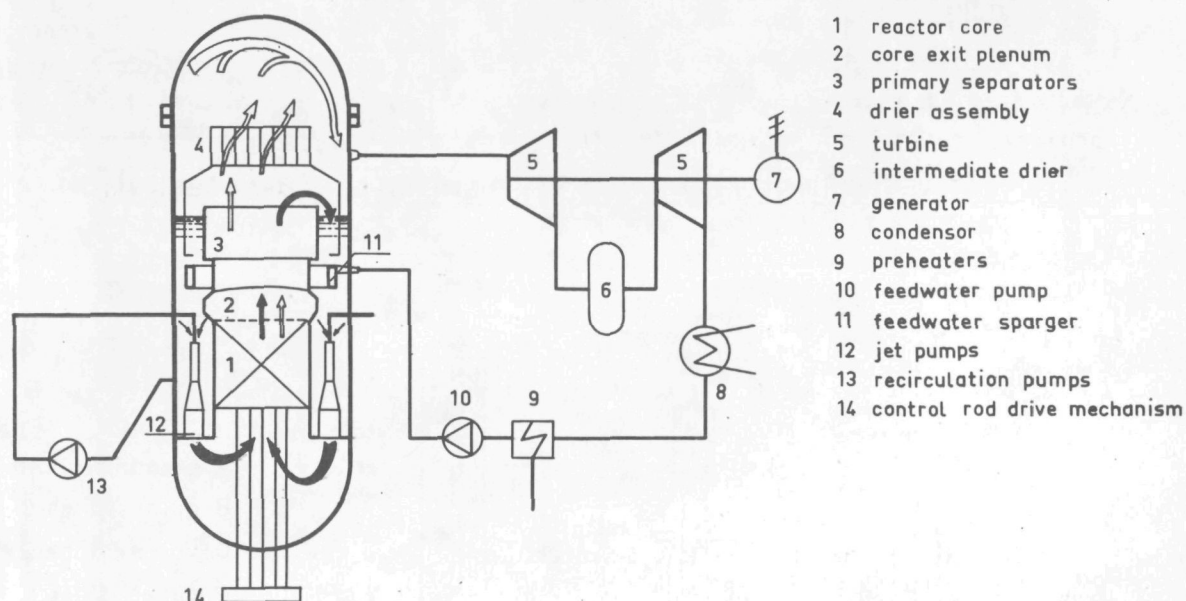


FIGURE 4-1

*Schematic flow diagram of a BWR power plant*

in the vicinity of the turbine. At the other side of the separation the entrainment of bubbles in the downcomer, termed 'carry-under', must be prevented because of the resulting cavitation risk for the recirculation pumps, reduced shielding effect of the downcomer water and decreased subcooling at the core inlet. The latter would reduce power output, due to the lower moderator-to-fuel ratio, stability margin and critical heat flux ratio. Furthermore both carry-over and carry-under reduce the efficiency of the power plant, as set forth in subsection 4.2.3.

#### 4.2.2. Types of mechanical separator

At present all primary separators are of the centrifugal type: the evolution from gravity separation in the first small size BWR's to these mechanical separators has been described by Prins [1]. Several types of centrifugal separator have been installed so far by the various BWR suppliers. Those known from the open literature are shown in figure 4-2 \*).

\* ) The radial vane separator [28] is not included in this summary because it was never been applied for commercial size plants.

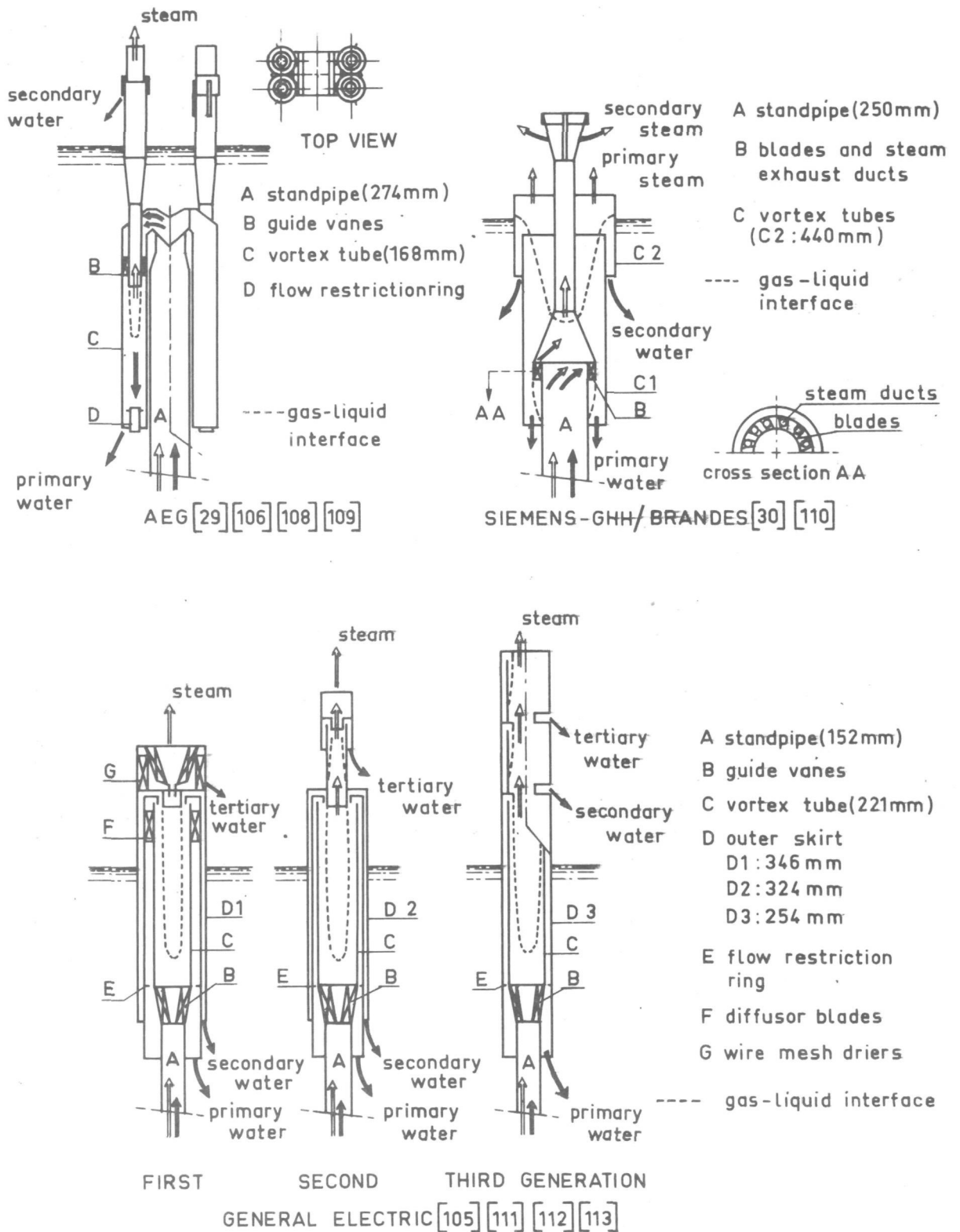


FIGURE 4-2  
Industrial separators

AEG developed a down-flow cyclone [29] for installation in the down comer adjacent to the reactor core. This location, applied in the Lingen and Würgassen BWR's [106], has the advantage of direct access to the core during refueling, but the associated increase in pressure vessel diameter makes it less attractive for increasing plant size. In addition, its separation effect in the Würgassen plant was found inadequate [107] <sup>\*</sup>). For both reasons the configuration shown in figure 4-2 was subsequently developed by AEG ([108] and [109]). The separator itself is essentially unchanged but the total configuration is adapted by the introduction of a standpipe - mounted on the plenum on top of the core - feeding four down-flow separators, while in addition a centrifugal predryer is installed near the top of the steam discharge pipe in order to increase the separation efficiency. Notwithstanding the gain in radial space - obtained at the expense of core accessibility - this configuration still requires a rather large built-in area mainly due to the complicated flow pattern: upward flow of the mixture through the standpipe, downward flow of the mixture in the vortex tube and finally upward flow of the steam the discharge tube passing through the vortex tube. The capacity of such a quadruple assembly is 131 kg/s for a steam-water mixture at 7 MN/m<sup>2</sup> and a quality of 14%; under these conditions the pressure difference between just in front of the guide vanes and the waterlevel in the pressure vessel equals 45 kN/m<sup>2</sup>[108].

The separator development described by BRANDES ([30] and [110]) in co-operation with Siemens/GHH (cf. figure 4-2) is somewhat beyond the scope of the present review, being primarily intended for application in PWR steam generators. This follows from the co-operation with Siemens and GHH, at that time exclusively interested in PWR's and steam generators respectively, and from the separators' capacity: 70 kg/s water at about atmospheric pressure with a volumetric quality  $\beta = 0.774$  <sup>\*\*</sup>) (corresponding to a quality by weight of  $x = 0.146$  for steam-water mixtures at 7 MN/m<sup>2</sup>), which is rather low for its outer diameter of 440 mm. Comparing the resulting loading of 323 kg/sm<sup>2</sup> (based on a triangular pitch of 500 mm and atmospheric air-water mixtures) with that of 555 kg/sm<sup>2</sup> for the above AEG quadruple assembly, it becomes apparent that a further increase in capacity would be required before this separator could be used in a BWR. In the author's opinion such a development would be difficult to achieve because the complex flow geometry practically precludes a systematic evolution to the optimal geometry, leaving only the expensive path of trial and error.

ASEA is known to possession a test facility for separator development, but no data on the design and performance of its separators were found in the open literature.

By contrast the General Electric separators shown in figure 4-2 are well known from literature and will therefore be used as a yardstick for the characteristics and performance of the venturi-separator forming the subjects of the present investigation.

Up till 1972 the General Electric development program for mechanical steam-water separation, started in 1958, had resulted in four successive separator designs: the first, modified first, second and third generation,

<sup>\*</sup>) *This plant had to be derated to 80% of its design value for about a year until new separators were installed, indicating the importance of good separator performance.*

<sup>\*\*</sup>) *Only atmospheric air-water tests have been published.*

the first and the latter two of which are shown in figure 4-2 [105],[111], [112], [113].

As apparent from this figure the vortex tube and thus the first separation stage is the same for all separators (length 950 mm, diameter 216 mm). The differences occur in the secondary and tertiary separation, the latter being a wire-mesh dryer in the first generation and a centrifugal separator for the modified first and subsequent generations. The most significant aspect of the third generation is the changed flow path of the second separation stage, which no longer extends along the full length of the separator but leaves the separator at the top of the vortex tube. This allows a reduction of the outer diameter from 324 mm to 254 mm, yielding a smaller built-in area and thus higher specific separator loading.

generation	outer diameter [ mm ]	triangular pitch [ mm ]	total mass flow $\phi_{mt}$ [ kg/s ]	quality [ % ]	steamflux [ kg/s.m <sup>2</sup> ] *)	waterflux [ kg/s.m <sup>2</sup> ] *)	mixture velocity $u_m = u_{sl} + u_{sg}$ [ m/s]**)	total pressure drop [ kN/m <sup>2</sup> ]
first	336	343	56.6	8	44.6	512	5.35	48
modified first	336	343	56.6	10	55.5	500	6.14	56.2
second	324	343	61.7	13	78.4	524	8.02	75.7
third	254	305	51.0	15	94.6	536	7.32	52.6

\*) based on built-in area (triangular pitch)  
\*\*) based on the cross section of the vortex tube (  $\phi$  216 mm for all separators)

TABLE 4-3

*Characteristics of GENERAL ELECTRIC separators*

Table 4-3, summarizing the characteristics of the four separators, shows a decrease in total mass flow per separator (by increasing the number of separators) and a corresponding decrease of total pressure drop for the third generation. The liquid mass flux (with reference to the built-in area) has remained almost constant for all four designs, while the steam flux has more than doubled through the increased entrance quality. The mass fluxes and qualities mentioned in table 4-3 will serve as a guide-line for the development tests of the venturi separator in the present investigation.

4.2.3. Separator performance evaluation

Figure 4-4 shows typical design point carry-under and carry-over values for each of the three General Electric separator generations. With respect to carry-under General Electric specifies a maximum downcomer quality of 0.25%, which requirement is satisfied in the third generation separator for inlet qualities ranging from 7.5 up to 17% at the rated mass flow of 51.0 kg/s (cf. figure 4-4).

As discussed in [105] and [111] the amount of carry-under depends on the water level surrounding the separator as well as on the entrance quality and mass flow. In BWR's the latter two values change with radial position of the separator due to the inhomogeneous power distribution in the core and imperfect mixing in the upper plenum. Therefore the maximum separating

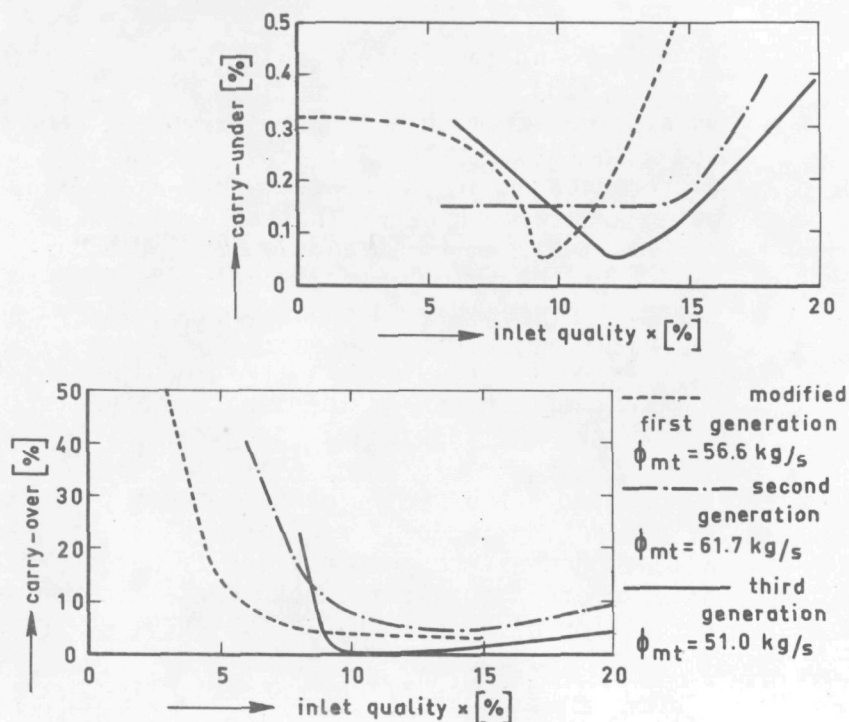


FIGURE 4-4

*Performance of GENERAL ELECTRIC separators*

efficiency corresponding to rated conditions is only achieved in a few separators, which increases the average carry-under and carry-over values. For the first generation of General Electric separators this effect is discussed in [114] and [115] on the basis of measurements from operating BWR's: for all plants discussed except one the carry-under reached about 0.13% at rated conditions, whereas the minimum value during the separator development tests was about 0.05%. The only exception is Kernkraftwerk RWE/Bayernwerk (KRB) at Gundremmingen where the carry-under reached 0.6%, as against the design value of 0.17%

The requirement for a minimum carry-over quality  $x_{CO} = 0.99$  - for GE-designed BWR's - refers to the steam exiting from the reactor pressure vessel; the moisture carry-over from the primary separators is allowed to go up to 15%, further water removal taking place in the impingement dryers near the top of the pressure vessel.

Separator performance, with respect to the above requirements, may be assessed in at least three ways:

- by the purity of the phases (or components) exiting from the separator, i.e. by carry-over and carry-under; the characteristic quantitative value might be termed "separating effect"
- by the loss in available energy (or exergy) required to achieve the above mentioned purities of both separator exits. The expression quantifying this loss caused by the irreversibility of the separating process, which might be termed "separator efficiency", is derived in [116]
- by evaluating both effects of purity and pressure loss on the performance of the entire process of which the separator forms part.

In order to evaluate the separating effect various definitions can be used. For example Prins [1] used a carry-under effect:

$$\eta_D = 1 - \frac{\beta_D}{\beta_R} \quad (4-1)$$

and a carry-over effect:

$$\eta_E = 1 - \frac{1 - \beta_E}{1 - \beta_R} \quad (4-2)$$

where the volumetric qualities refer to:

- the inlet in the riser/standpipe of the separator:  $\beta_R$
- the downflow of the separated water:  $\beta_D$
- the exiting steam:  $\beta_E$

As pointed out by Prins himself these definitions have the disadvantage of presenting two criteria for evaluating a single separator, each of which moreover changes in value if defined on the basis of weight instead of volumetric qualities. Both these disadvantages are overcome by the definition of a compound efficiency:

$$\eta_C = \left| \frac{\phi_g - \phi_{cu}}{\phi_g} - \frac{\phi_{co}}{\phi_l} \right| = \left| \frac{\phi_{cu}}{\phi_g} - \frac{\phi_l - \phi_{cu}}{\phi_l} \right| \quad (4-3)$$

This compound efficiency - previously used by VAN ROSSUM [117] and VAN EBBENHORST TENGBERGEN [118] for hydrocyclones - yields the same value for both volumetric and mass flows. For small values of  $(1 - \beta_E)$  and  $\beta_D$  Prins had transformed this definition to:

$$\eta_C = 1 - \frac{\beta_R(1 - \beta_E)}{\beta_E(1 - \beta_R)} - \frac{\beta_D(1 - \beta_R)}{\beta_R(1 - \beta_D)} \quad (4-4)$$

where  $x$  may be substituted for  $\beta$  without changing the value of  $\eta_C$ .

This compound efficiency has the disadvantage of attributing equal weight to both carry-under and carry-over, whereas the above discussion on secondary separation in the dryers indicates that the limit for carry-under is likely to be more restrictive than that for carry-over. Thus it is concluded that none of the above definitions for the efficiency of the separating effect yields an appropriate basis for evaluation of the dual purpose BWR separators.

For the "separator efficiency" - on the basis of exergy - numerical analyses are elaborated [116] for the present application to BWR conditions. It appears that in general this efficiency is close to unity, e.g. about 0.997 for the above conditions of the General Electric separator: irrespective of pressure drop and purities. Therefore this separator efficiency is rejected for the present comparison of separators, and evaluation of the pressure drop - characterizing the irreversibility - will be made on the basis of a specific pressure drop coefficient discussed in subsection 4.2.3.2.

An evaluation of separator performance on the basis of the entire process of which the separator forms part is particularly appropriate for thermal power cycles such as the BWR steam cycle, because all possible consequences of exceeding the carry-under and carry-over limits can be expressed in terms of capital cost and power output variations. Since a BWR power plant is the intended application for the separators of the present investigation,

a study on the economic consequences is carried out on a standard General Electric BWR-6-219/592 power plant - for which the main characteristics are given in table 4-5 - and reported in [120]; its results will be summarized briefly in subsections 4.2.3.1. and 4.2.3.2 and more extensively in appendix 4-A. The separators used in this BWR design are third generation separators.

In this study the original plant components and/or performance are adapted to assumed variations in separator performance and the - estimated - results compared in terms of capital cost and power output variations.

pressure vessel diameter	[ m ]	5.54 (218")
number of fuel bundles		592
core power	[ MW <sub>t</sub> ]	2894
generator power	[ MW <sub>e</sub> ]	980
core flow	[ kg/s]	10633
number of separators		209
power per circulation pump (two pumps installed)	[ MW]	4.4

TABLE 4-5

*Characteristics of a GENERAL ELECTRIC BWR-6-218/592 plant*

#### 4.2.3.1. Economics of the separating effect

An increase in carry-over from the primary separators is assumed to be cancelled by enlargement of the dryers so as to maintain the final exhaust quality at 99.90% as reached in this General Electric design for the BWR-6-218/592. The resulting increase in capital cost<sup>\*)</sup> consists of three components:

- increased dryer size
- increased height of the pressure vessel needed to accommodate the enlarged dryer
- increased height of the containment needed to accommodate the enlarged pressure vessel

Assuming 10% initial (= design point) carry-over from the primary separators (a figure unsupported by test data for operating conditions) a doubling of this figure to 20% due to less efficient primary separators, causes additional capital costs of Dfl.  $0.52 \times 10^6$  (1976 value).

An increase in carry-under - over the design value at rated load of 0.17% - causes several interacting changes in the thermal performance and design of the power plant, viz.:

- decreased turbine-generator output due to the decreased supply of live steam
- reduction of the amount of bled steam supplied to the high pressure feedwater heater. This is needed for lowering the final feedwater temperature to the extent required for quenching the excess carry-under steam

<sup>\*)</sup> Prices and costs mentioned in this and the next subsection are substantiated in appendix 4-A.

- the latter change increases the steam flow through the low pressure turbine, causing an increase of power output to the generator
- the foregoing changes will necessitate partial redesign of the turbine and condenser

A first estimate of the costs of these effects indicated the latter effect to be of minor importance, hence the costs of carry-under increase are based on the first three effects only.

An assumed doubling of carry-under quality from 0.17% to 0.34% yields a decrease in income of Dfl.  $9.82 \times 10^6$  during a reactor life time of 35 years (based on a price of Dfl. 0.045 per kWh).

While the above costs are in the range of promilles only of the total costs over 35 year, viz. about Dfl.  $8.8 \times 10^9$ , it is obvious that most attention should be paid to the carry-under, which must not in any case increase to the range of percents.

#### 4.2.3.2. Pressure loss evaluation

The same approach as used above with respect to the separating effect, has been used in appendix 4-A to evaluate the savings resulting from a decrease in separator pressure loss.

In this evaluation no account was taken of the possible need for redesign of the circulation pumps due to the change in pressure head, because it was considered quite possible and even likely that - within certain limits - such adjustments would be simple to effect. Therefore only the saving due to the reduction in motor power for the two pumps is taken into account. A decrease in separator pressure loss from the value of  $52.6 \text{ kN/m}^2$  - given in table 4-3 - to  $40 \text{ kN/m}^2$ , results in present worth savings of Dfl.  $3.9 \times 10^6$ .

Although this figure gives a fair impression of the relative importance of the effort put into a pressure loss reduction, it cannot be used to compare various types of separators under various conditions. Such a comparison requires the inclusion of capacity and mixture composition. Therefore the pressure loss coefficient  $\zeta$ , defined by the expression:

$$\Delta p = \zeta M_{tp} \quad (4-5)$$

seems to be a better yardstick for the comparison of various separators. However, for the two-phase momentum  $M_{tp}$  - as defined in expression (2-74) - the void fraction  $\alpha$  has to be known, which is mostly unknown in engineering practice and in addition is not constant in the separator. A definition based on

$$M_{tp}^* = (1 - \beta) \rho_l u_m^2 + \beta \rho_g u_m^2 \quad (4-6)$$

appears more practical <sup>\*)</sup>. Compared to expression (2-74) this definition of  $M_{tp}$  in fact assumes homogeneous flow, yielding  $\alpha = \beta$  and  $u_g = u_l = u_m = u_{sl} + u_{sg}$ , which seems to be a reasonable approximation for engineering purposes. Further pressure drop comparisons between separators of various types and conditions will hence be based on the pressure loss coefficient

$$\zeta^* = \Delta p / M_{tp}^* \quad (4-7)$$

\*) Or:  $M_{tp}^* = \frac{\phi_{mt}^2}{\rho_l A^2} \left\{ (1-x) + x \frac{\rho_l}{\rho_g} \right\}$ , expressed in weight quality.

#### 4.3. Selection of separator type

A venturi type separator - previously introduced in figure 1-1 - was selected by PRINS [1] for further study. Although the results obtained on the first two prototypes, as reported by Prins, indicated lower separating efficiencies and higher pressure loss than those reported for the GE upcomer type, investigation of the former type was continued, mainly because its simpler flow path renders it more suitable for the primary aim of the present investigation, viz. experimental verification of the proposed computational model for rotating two-phase flow. A second, more practical advantage of the venturi separator is the absence of a passage for the downflow of separated water. As can be seen from the successive GE separator designs (cf. figure 4-2 and table 4-3) part of the effort of this continuing development was spent on reducing the outer diameter of the separators by decreasing the size and number of the downflow passages. The advantage of the significant decrease in outer diameter achieved for the third generation separator stands out clearly from table 4-3 in the combination of decreased pressure drop - due to lower mass flow in the vortex tube - and decreased specific built-in area. The absence of a downflow passage in the case of a venturi separator enhances the latter advantage, which is particularly relevant for separator assemblies mounted on top of the nuclear core of a BWR. Figure 4-6 shows the effect of this advantage for this latter application by direct comparison of the two separator designs, indicating that the GE-separators require a larger spacing as a consequence of the downflow passage.

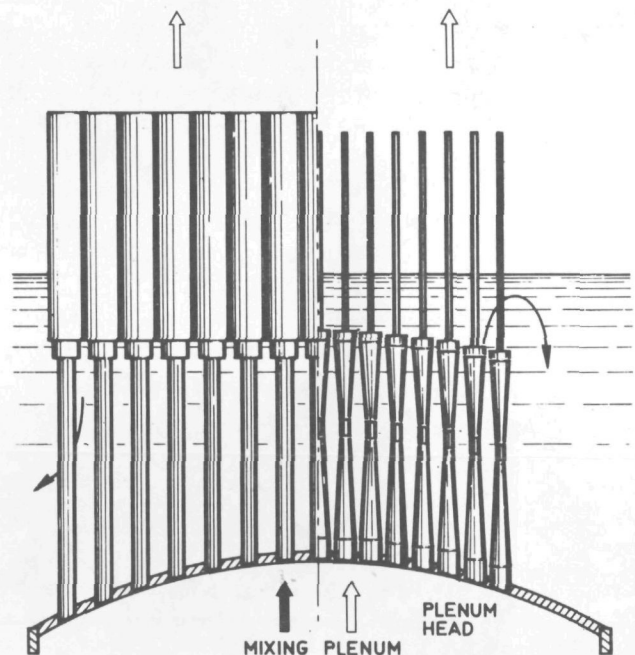


FIGURE 4-6

*Comparison of separator assembly diameter for venturi separators and GENERAL ELECTRIC separators*

For the third generation G.E. separator the down flow accounts for 24% of the maximum separator cross-section. Hence the elimination of the down flow would permit installation of 24% more separators in the same area assuming the separating efficiency to remain unchanged. This either permits a 24% decrease in specific vortex tube loading, causing a decrease of separator pressure loss, or a 24% core flow and thus power increase at the initial specific vortex tube loading.

The converging/diverging shape of the venturi separator yields the third advantage of this separator type, viz. through the corresponding increase of rotation in the converging part and the decrease of water velocity after separation. The former implies that only part of the rotation required for effective separation has to be generated by the guide vanes, which should reduce the pressure losses due to flow separation from and friction on the vanes. In addition the total pressure drop over the separator is decreased by the diffuser where part of the kinetic energy is converted to pressure head.

#### 4.4. Introductory air-water experiments

##### 4.4.1. Objectives

The purpose of these introductory experiments is to provide insight into and characteristic data of rotating gas-liquid flow in straight and converging channels, the latter representing the vortex tube of a venturi separator. In order to avoid secondary effects the test section geometries (cf. subsection 4.4.2.2.) are chosen as simple as possible, i.e. no vortex finder is mounted to remove the gas core; the air leaves the test section together with the water.

The specific aspects investigated in these experiments are:

- the effect of rotation intensity: four blade geometries with various angles of deflection are applied in these experiments (cf. subsection 4.4.2.2.)
- the stability of the gas core. PRINS [1] has reported a remixing of the separated air and water just ahead of the vortex finder, but was unable to determine whether this was caused by an 'hydraulic jump' of the water layer or the unbalance of the pressure drop along the gas and water outlet paths. The present experiments yield the possibility to investigate the stability of a supercritical ( $Fr > 1$ ) water layer in the absence of a vortex finder
- the gas core diameter, required for sizing the inlet diameter of the vortex finder
- the length, required to obtain the best possible separation
- an estimation of the obtainable separation effect, i.e. the purity of the phases

Furthermore the experiments itself yield an insight into blade performance, pressure difference over the converging part of a venturi separator and average axial velocities of both phases, while additional computations with the ANALEST procedure (cf. subsection 3.3.2.) will provide an estimation of tangential and radial velocities and a more precise description of the radial distributions of the axial velocities.

##### 4.4.2. Test facility

###### 4.4.2.1. Test loop

The test loop is the same as that described in subsection 2.3.1.3.1. (cf. figure 2-22), while the instrumentation and data acquisition are also identical to the descriptions in appendix 2-E and subsection 2.3.1.4.

#### 4.4.2.2. Test section geometries

The three test sections used for these introductory experiments are the same as those used for the air-water interaction force experiments described in chapter 2 (cf. subsection 2.3.1. and figure 2-24). The resultant downscaling of the inlet diameter of the vortex tube - which is around 220 mm in actual BWR practice (cf. figure 4-2) - to 100 mm is necessitated by the capacity<sup>\*</sup>) of the steam supply for subsequent high pressure steam-water tests not described here. The rules for upscaling to industrial sizes are discussed in subsection 4.5.7.3.

In the present air-water tests four blade shapes are tested, with outlet angles of deflection - measured at the test section wall - of 30, 40, 50 and 60°, respectively (cf. figure 4-7 for the definition of this nominal value).

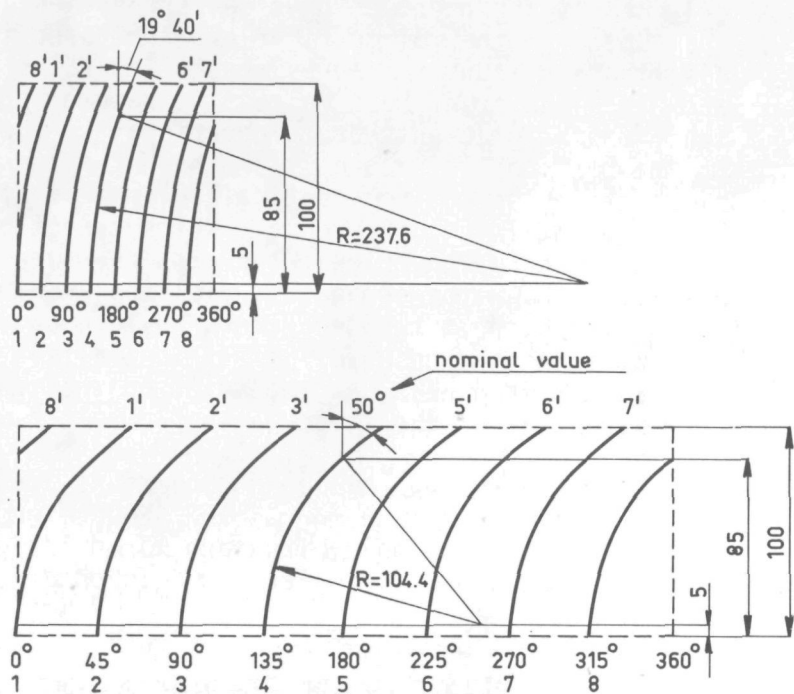


FIGURE 4-7

*Guide vane development at the wall and the central hub for a 50° angle of deflection nominal value*

Since the interest in this variation in swirl generation is focussed on the effect of rotation intensity, the main consideration in selecting the shape of the blades shown in figure 4-7 was ease of manufacturing.

The 8 brass blades are formed from flat plate, i.e. without curvature in the  $r-\varphi$  plane and soldered to the central tube. A discussion on optimal blade profiles is presented in subsection 4.5.3.3. with respect to the blades applied in the air-water separator.

<sup>\*</sup>) *The maximum capacity of 2.2 kg/s high pressure steam in the Laboratory for Thermal Power Engineering is well below that delivered to the second and third generation of G.E. separators, viz. around 8 kg/s.*

### 4.4.3. Scope of experiments

#### 4.4.3.1. Range of flow parameters

In view of the purpose of these introductory experiments to provide information relevant to steam-water venturi separators, it is essential to define the scaling rules pertinent to these two types of gas-liquid flows with different physical properties.

For equal volume flows in the low quality range of the bubble flow region it is reasonable to expect the pressure gradients to be nearly proportional to the liquid density. Because the drag and virtual mass forces  $F_D$  and  $F_A$  are proportional to the liquid density, and the physical properties have only a minor indirect effect via the bubble diameter and peak velocity ratio (cf. correlations (2-162) and (2-129)), the relative velocity is only weakly dependent on physical properties. Hence it can be concluded that whenever the volumetric flows are taken identical, the void fraction distribution - determined by these flow rates and the relative velocities - and hence the true phase velocities become approximately identical, while the pressure gradients are proportional to the liquid density.

On the basis of this conclusion the high pressure steam-water flows are simulated by selecting identical volumetric atmospheric air and water flows. The only remaining difference - which cannot be eliminated - is in the expansion of the gas flows: the high pressure steam hardly expands while passing through the separator, yielding an almost constant volumetric quality throughout the separator, while expansion of the nearly atmospheric air causes an increase in volumetric quality. In the present experiments the volumetric quality at the inlet of the test section is made to correspond with that of the steam-water flow.

Data on BWR part and full load conditions are given in [123] and found to be essentially the same for GE and AEG designs. For the present investigation the GE data [124] are taken for guideline. In figure 4-8 it is shown that load control of a BWR is obtained by varying both control

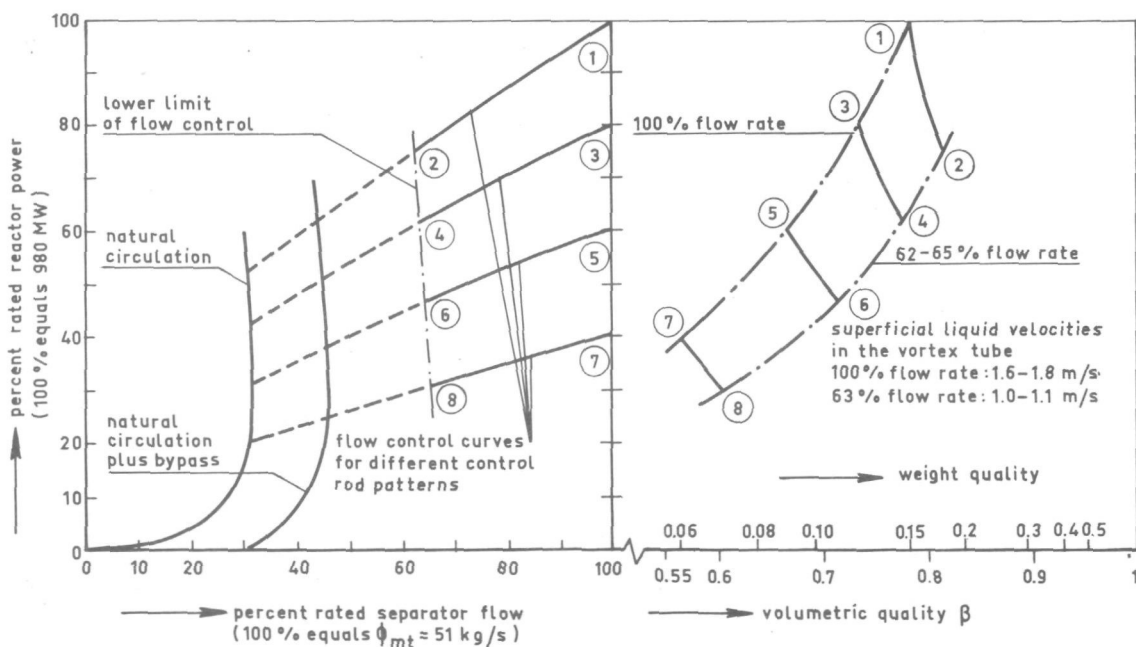


FIGURE 4-8  
Separator flow conditions in a BWR-6-218/592

rod pattern and total mass flow through the core. The latter control parameter - which is of interest for the separator load - varies between 63 and 100% of rated flow.

Because of the relatively small weight fraction of the steam in these mixtures the water flow rate - and thus superficial water velocity in the separator - may also be assumed to vary approximately between 63 and 100% of its rated value. Figure 4-8 shows that combination of both parameter variations cause the volumetric quality  $\beta$  to vary from 0.57 up to 0.82 (corresponding to a quality range by weight  $x = 0.06 - 0.18$ ).

In accordance with these power plant data the introductory air-water experiments were carried out at two superficial water velocities applied earlier in the air-water experiments of chapter 2, viz 1.3 and 2.1 m/s, corresponding to the range of the second generation GE separator and exceeding that of the third generation by about 20%. The variation in volumetric quality is simulated by the same series of nominal inlet void fractions as applied in the air-water experiments discussed in chapter 2, viz. 0.25, 0.38, 0.50, 0.63 and 0.75. In order to restrict the total amount of experimental work this full range of 5 void fractions was only investigated for the superficial water velocity of 2.1 m/s; tests at 1.3 m/s velocity were restricted to a void fraction of 0.63.

These 6 different flows, in combination with 3 test sections and 4 blade geometries, result in a total of 72 measurements which are coded by a number consisting of four figures:

- the first figure refers to the angle of blade deflection: 1 stands for the smallest deflection ( $30^\circ$ ) and 4 for the largest deflection ( $60^\circ$ )

The last three figures contain the same code as previously described in subsection 2.3.2.1.2., i.e.:

- the second figure refers to the test section, viz. 0,1 or 2 for the straight, converging or venturi-shaped test section respectively.
- the third figure refers to the superficial water velocity: 2 stands for 1.3 m/s and 5 for  $u_{s1} = 2.1$  m/s
- the fourth number refers to the nominal void fraction: 1 stands for the lowest (0.25) and 5 for the highest nominal void fraction (0.75).

#### 4.4.3.2. Measured data

As stated before data acquisition and data processing for these 72 rotating flow measurements - extensively discussed in [125] - are identical to those previously described in subsections 2.3.1.4. and 2.3.1.5., i.e.

- water and air flow rates are measured
- wall pressures are measured at 13 pressure taps along the test sections (cf. figure 2-24)
- void fraction distributions are measured in ten cross sections along the test sections (cf. figure 2-24)

For discussion of the measurement techniques and error analyses the reader is referred to the above-mentioned subsections of chapter 2.

Apart from the axial distribution of wall pressure, velocities and cross-sectional mean void fraction, special attention is paid to the radial void fraction distributions in each of the ten cross sections, because of their importance to separator performance.

As described in appendix 2-F the radial void fraction distribution is obtained from the set of 41 mean void fractions (cf. subsection 2.3.1.4.2.)

by a least square approximation based on the seven terms general polynomial

$$\alpha(r) = C_0 + C_2 r^2 + \dots + C_{2n} r^{2n} + \dots + C_{12} r^{12} \quad (4-8)$$

where  $r$  is the relative radius.

No exact error analysis can be applied to this local void fraction  $\alpha(r)$ , because only measured mean chordal void fractions are available for comparison and local errors will be more or less cancelled out in the integration of polynomial (4-8) over a chord. However, in [72] it is argued that this canceling effect may be minor or negligible for chords having a large measurement error with respect to the integration value from expression (4-8), thus providing an indication of the mean local error for such chords. It was found that 80% of all measured mean chordal void fractions have a smaller measurement error than 0.06; in the strength of the above reasoning the standard deviation for the local void fraction is estimated as 0.06.

#### 4.4.3.3. Application of the ANALEST procedure

The parameters characterizing separating performance, such as separating effect, separator pressure loss and gas core stability were evaluated in [125] for all the 72 introductory experiments on the basis of severe simplifications with respect to local phase velocities and simplified radial void fraction distributions. Because of these simplifications these analyses only indicate general trends. In order to obtain more accurate results computations with the ANALEST procedure were subsequently carried out [104], though only for the guide vanes with 40, 50 and 60° angles of deflection and for the straight and converging test sections. This restriction appeared justified because the approximate analyses had already made it clear that a 30° deflection and the strong convergence of the inlet cone of the venturi-shaped test section were both unsuited for further separator development.

Thus 36 flows - coded 20\*\*, 30\*\*, 40\*\*, 21\*\*, 31\*\* and 41\*\* - were evaluated using the ANALEST procedure. With respect to the results of these computations - to discuss in the next two subsections - it should be stressed again that the ANALEST procedure provides only estimations of the local flow conditions, having a relatively large standard deviation as explained in subsection 3.4.2.

#### 4.4.4. Results

The direct results, viz. axial wall pressure distribution and axial and radial void fraction distributions, of 12 out of the total set of 72 measurements have been selected for each of the three test sections to show the influences of rotation intensity and void fraction.

These measurements were selected to correspond with GE separator conditions, i.e. void fractions of 0.63 and 0.75 and a superficial water velocity of 2.1 m/s (measurements \*\*44 and \*\*45) to show the effect of rotation intensity, while the influence of void fraction is demonstrated by selecting 5 measurements containing the complete series of void fractions and a fixed blade geometry with 50° angle of deflection (coded as 3\*4\*). For the flows with 63% water flow rate, i.e. 1.3 m/s superficial water velocity and the corresponding inlet void fraction of 0.63, only one measurement with 50° blades (coded 3\*24) is presented for each test section.

#### 4.4.4.1. Axial and radial pressure profiles

The axial pressure distributions for each of the three test sections are presented in figures 4-10 through 4-12.

The wall pressure profiles in the straight test section (figure 4-10) can be characterized, in general, by a pressure drop between the test section levels  $z=2.250$  and  $2.618$  m - i.e. the first and second pressure tap - and a more or less constant pressure downstream  $2.618$  m. The pressure drop between the first two pressure taps is mainly caused by the mixture acceleration due to the flow area reduction by the hub of the guide vanes. The constant pressure is the result of a balance between the negative hydrostatic pressure gradient and a positive gradient due to deceleration of the liquid, caused by the axial decrease in void fraction as a consequence of slowly proceeding separation. As will be discussed in subsection 4.4.4.2. a fast separation occurs in the test section for measurements 3042, 3043 and 4044, causing a sharp decrease of the mean void fraction and consequently an increase in pressure due to deceleration of the liquid. Downstream of such a fast separation the void fraction remains constant and the pressure gradient equals the hydrostatic pressure gradient. For measurement 3041 - with a low inlet void fraction  $\alpha_{in} \approx 0.25$  - separation is completed between the guide vanes and can therefore not be detected via the wall pressures.

The pressures at the centerline - computed with the ANALEST procedure - are seen to follow smoothly the overall pressure gradient at the wall. With increasing void fraction (measurements 304\*) the radial pressure difference remains more or less constant, due to two counteracting effects. In the first place the true liquid velocities - and thus the tangential velocity - increase with increasing void fraction at constant superficial water velocity, yielding a larger radial pressure gradient  $\frac{\partial p}{\partial r}$  in the water layer. On the other hand, however, the water layer thickness  $\delta$  decreases, leading to the more or less constant total radial pressure difference. For increasing angle of blade deflection, i.e. increasing tangential velocity - with constant inlet void fraction -, the radial pressure gradient in the liquid layer increases yielding an increasing radial pressure difference across the water layers with equal thickness \*).

The pressure distributions for the converging test section are presented in figure 4-11. For measurements 1144 and 1145, i.e. for the lowest rotation intensity, the axial wall pressure distributions are almost the same as those of the non-rotating measurements 144 and 145 (cf. figure 2-30) discussed in chapter 2. In the upper range of blade angles and water velocities a peak occurs in the wall pressure around level  $z=2.7$  m, i.e. in the lower part of the cone of this test section. This wall pressure peak is caused by the increase in rotation intensity due to the diameter reduction, being dominated by the acceleration pressure drop in the upper part of the cone. The result of this effect is a smaller pressure difference at the wall between the test section inlet  $z=2.225$  m and the end of the cone  $z=2.998$  m compared to non-rotating flows.

The centerline pressure - computed with the ANALEST procedure - smoothly follows the axial profile of the wall pressure as long as the rotation \*\*)

\* ) The apparently small radial pressure difference for measurement 4045 is caused by erroneous computation of the pressure; in figure 3-13C the computed wall pressure - and thus the centerline pressure - is seen to be too high.

\*\* ) The excess of centerline pressure above wall pressure at the inlet of measurements 2145, 4144 and 4145 is not realistic, being caused by computational inaccuracies.

intensity is not excessively high. For the measurements with the highest rotation intensity (3145, 4144 and 4145) the centerline pressure drops sharply in the cone ( $z=2.608$  to  $2.998$  m), indicating that the axial pressure gradient in the water layer at the wall is dominant compared to that of the gas core and thus the axial pressure gradient of the latter is determined by the former and the large radial pressure difference due to high rotation intensity. The resultant steep pressure gradient at the centerline causes a strong acceleration of the gas core (cf. subsection 4.4.4.3.).

The recovery of centerline pressure at the inlet of the tail end is caused by the dispersion (cf. subsection 4.4.4.2.) and resulting strong deceleration of the gas core.

For the venturi-shaped test section (figure 4-12) the pressure peak around  $z=2.7$  m is less than for the converging test section, indicating that the pressure increase due to rotation and liquid deceleration by separation is surpassed by the liquid acceleration caused by the stronger convergence of

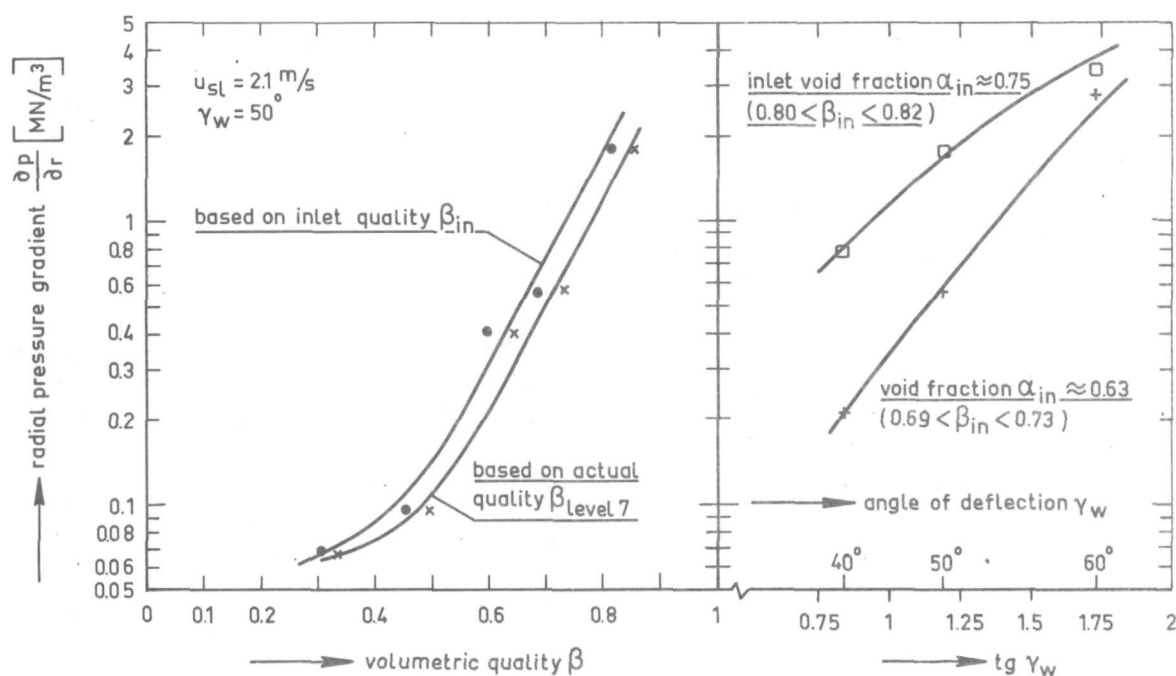


FIGURE 4-9

Radial pressure gradient  $\frac{\partial p}{\partial r}$  for the converging test section (level 7) as a function of volumetric quality and blade deflection

the cone. The decrease in wall pressure difference over the cone for rotating flow is more pronounced compared to the flows in the converging test section; for example the pressure drop between  $z=2.250$  and  $2.988$  m is only  $145 \text{ kN/m}^2$  for measurement 3244 while it reaches  $260 \text{ kN/m}^2$  for the non-rotating flow 244 (cf. figure 2-31).

Pressure recovery in the diffuser hardly exists at the wall, but is likely to occur at the centerline in view of the computed pressure values found at this location for the converging test section.

The radial pressure gradient  $\frac{\partial p}{\partial r}$ , in addition to providing the driving force for separation, is also responsible for keeping the gas core and water layer apart once separation has taken place. To analyse this latter effect

the gradient  $\frac{\partial p}{\partial r}$  in the transition zone between gas core and water layer was derived from the ANALEST computations for measurement level 7 of the converging test section <sup>\*</sup>), i.e. 1 cm upstream of the end of the cone. The changes in pressure and radius figuring in the quotients  $\frac{\Delta p}{\Delta r}$  presented in figure 4-9 refer to the radial locations where the void fraction equals 0.7 and 0.3, i.e. in the middle of the transition zone. The gradient is seen to grow exponentially with increasing volumetric quality (void fraction). The increase with angle of blade deflection, however, appears to reach a maximum for angles above 70°.

#### 4.4.4.2. Axial and radial void fraction profiles

The axial profiles for the mean cross-sectional void fractions are presented in figures 4-13 through 4-15, and the radial profiles of the local void fractions in figure 4-16 through 4-18 <sup>\*\*</sup>). For each measurement the radial profiles are given at four of the ten measurement levels (cf. figure 2-24), viz.:

- for the straight test section at levels 1, 4, 7 and 10, i.e. spread equidistant over the length of the test section
- in the converging test section attention is focussed on the end of the cone, i.e. levels 6 and 7, with levels 1 and 4 at the inlet and halfway the cone added for completeness
- for the venturi-shaped test section level 8 - halfway the diffuser - is combined with levels 1, 3 and 5, i.e. at the inlet, halfway and the end of the confuser.

For the straight test section the 'row' for varying void fraction (measurements 304<sup>\*</sup>) in figure 4-13 shows a great variety in axial profile of the mean void fraction: the profile is almost uniform for measurement 3041, shows a large dip for 3042 and 3043 and a slow decrease for measurements 3044 and 3045. The reason for this variety becomes clear from the radial profiles of the local void fraction shown in figure 4-16. The four radial profiles of measurement 3041 do not change along the test section, meaning that separation of the low void fraction is obviously completed between the guide vanes of the swirl generator. For the somewhat higher void fraction of measurement 3042 separation takes a little more time, shifting the point of completion downstream in the test section, while the increased mixture velocity compared to 3041 causes an additional shift in this direction. The uniform radial void fraction profiles downstream of level 4 indicate completion of separation before level 4. The dip in the mean void fraction profile (figure 4-13) occurs upon completion of the separation, because the drag force of the gas core is much lower than the drag force of the bubble swarm, resulting in a much higher relative velocity and consequently a lower mean void fraction.

The increase in separation length continues for measurements 3043 through 3045. For measurements 3044 and 3045 the separation length even exceeds the test section length; slowly decreasing mean void fraction and slowly changing radial profile indicate only the onset of separation. Comparing measurement 4044 with 3044 (60 and 50° angle of deflection respectively) confirms that the increased rotation causes a shorter separation length. For the low rotation intensities of measurements 1044 and 2044 the separation length exceeds the test section length, as it does

<sup>\*</sup>) For the straight test section no uniform separation length exists; in most cases separation is not completed in the test section.

<sup>\*\*</sup>) The local void fractions above 1 and below 0, are only inaccuracies of the polynomial approximation and have obviously no physical meaning.

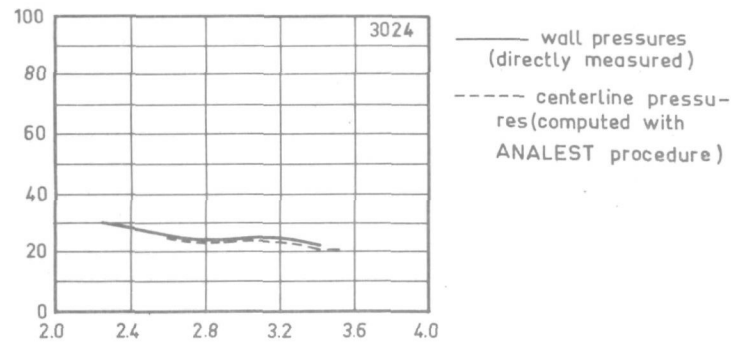
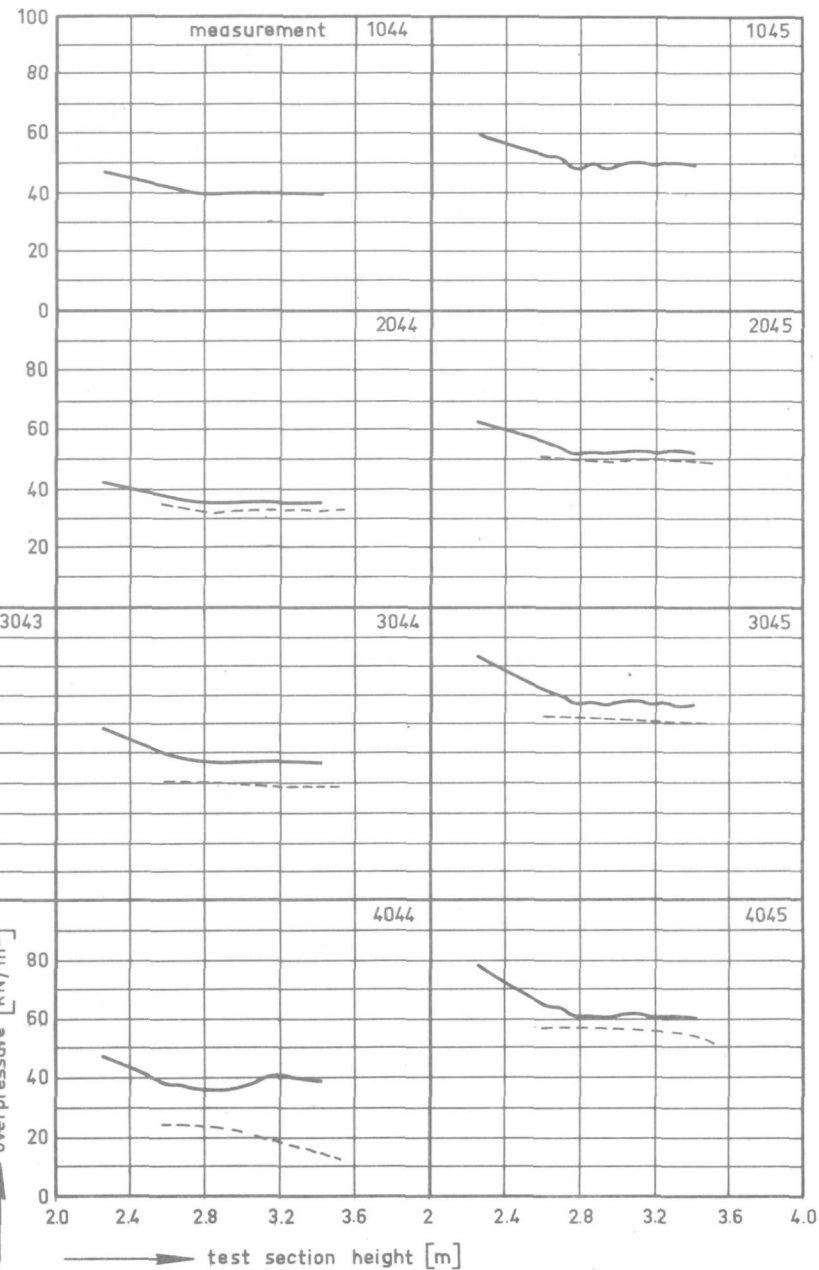


FIGURE 4-10  
Axial distributions of the overpressure at the wall and the centerline of the straight test section



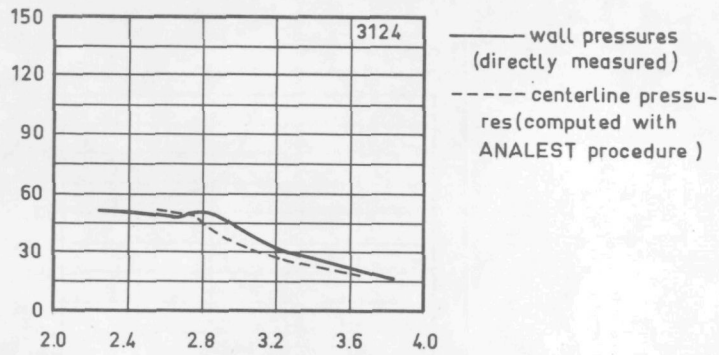
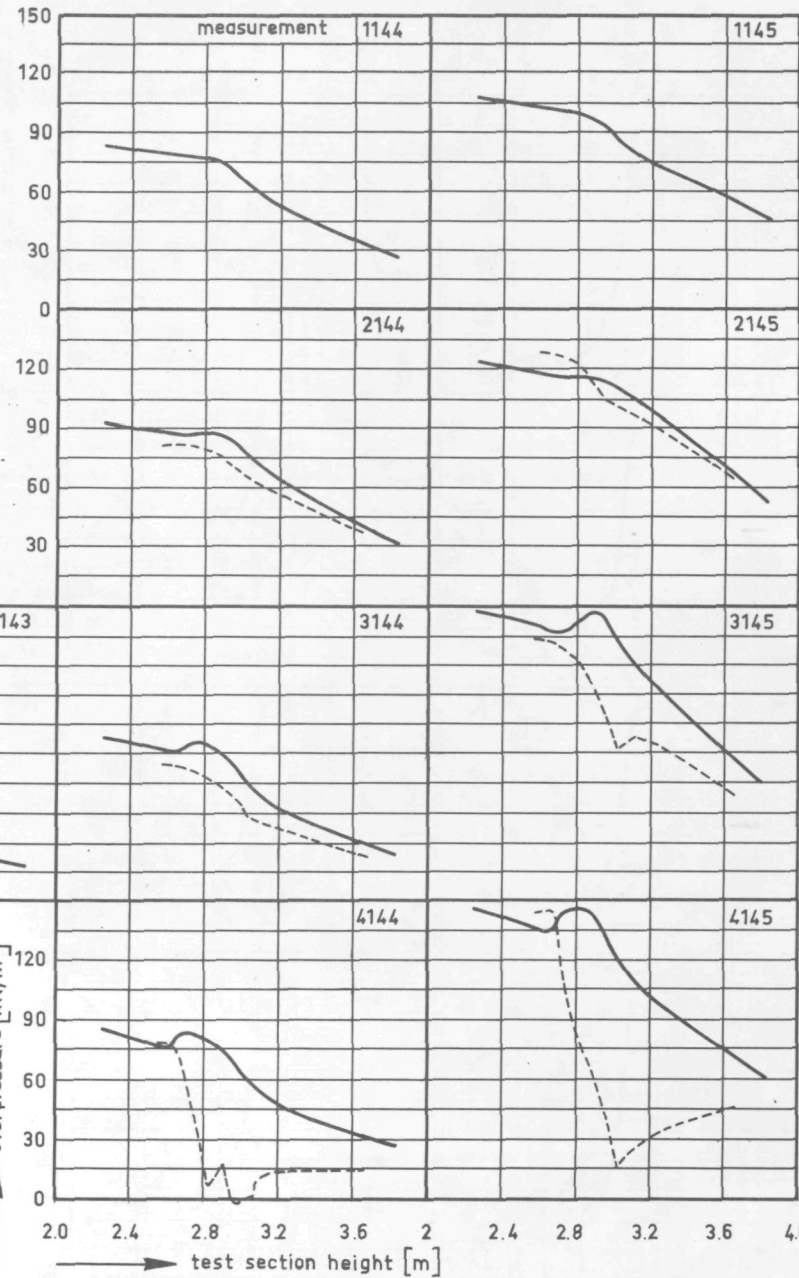


FIGURE 4-11

*Axial distributions of the overpressure at the wall and the centerline of the converging test section*



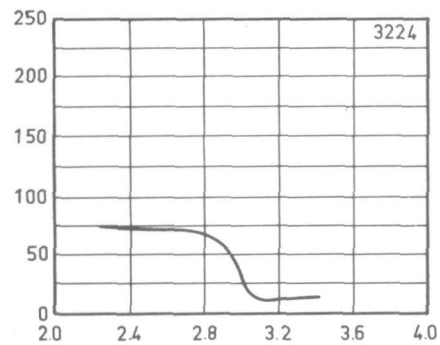
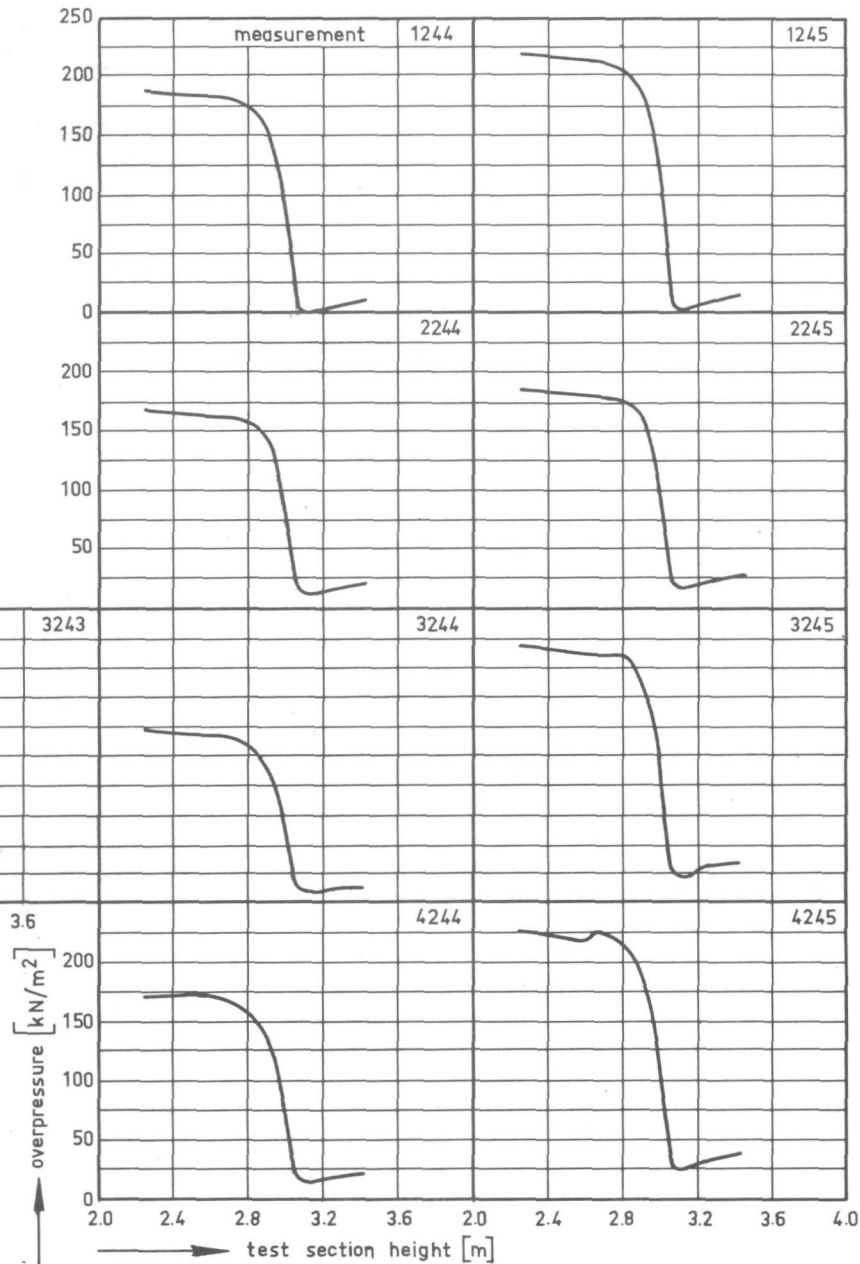
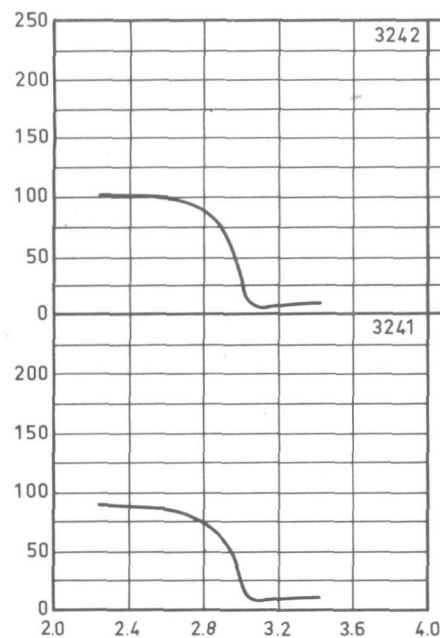


FIGURE 4-12

*Axial distribution of the overpressure at the wall of the venturi-shaped test section*



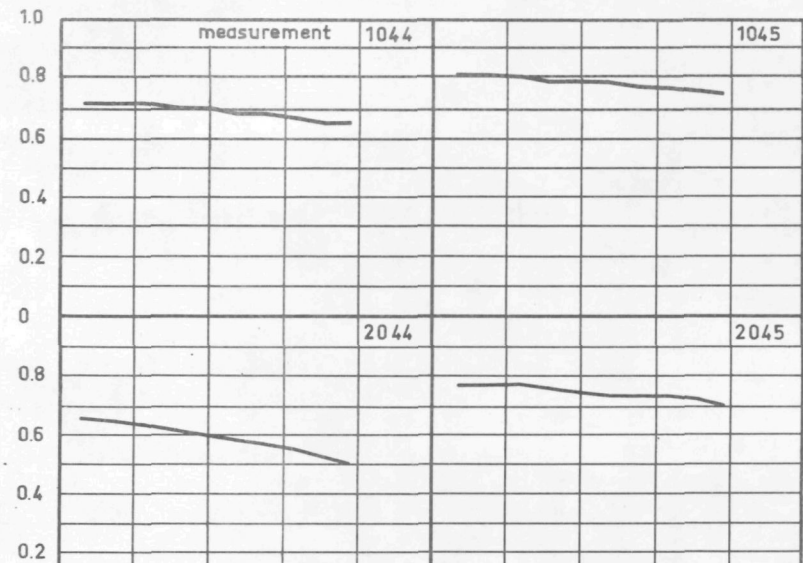
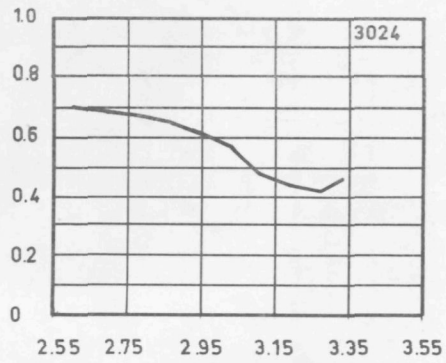
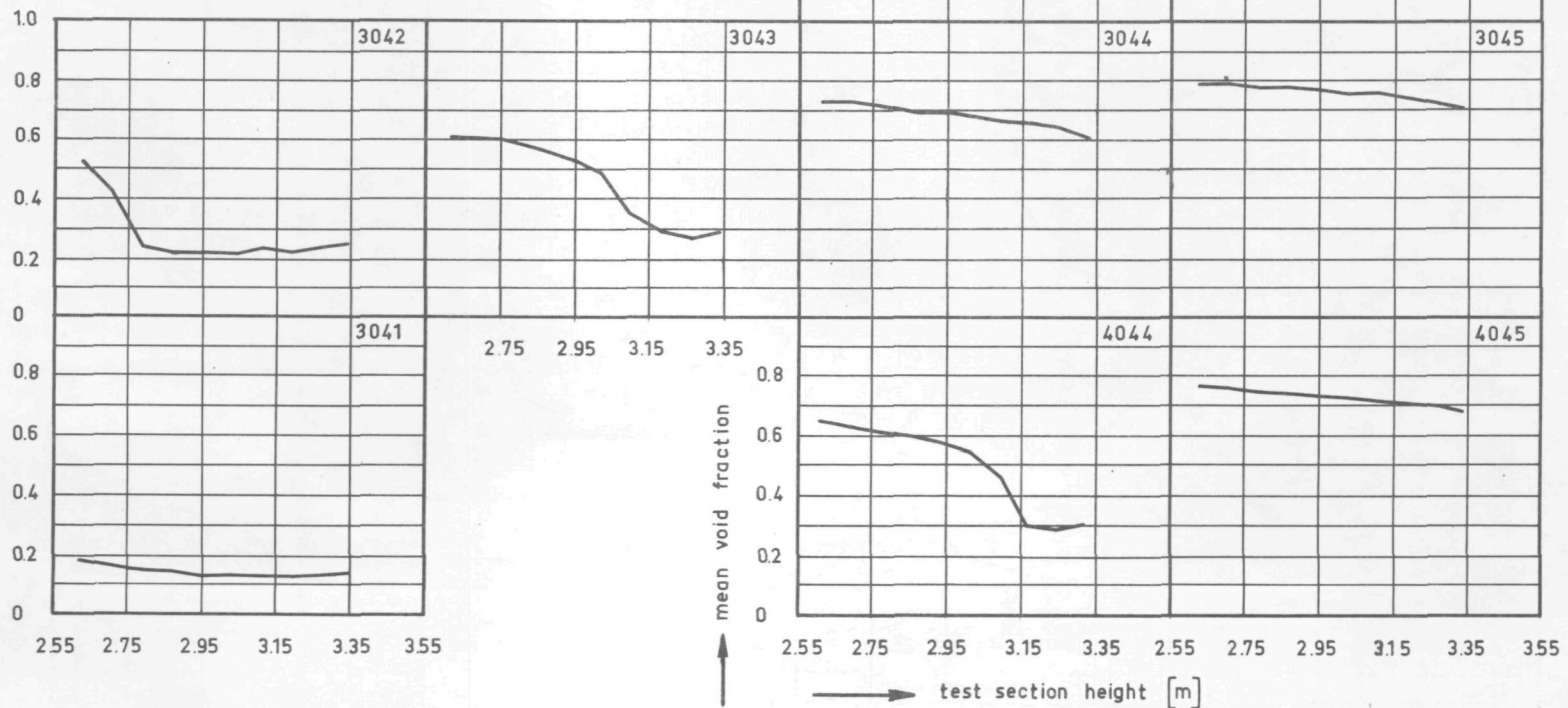


FIGURE 4-13

*Axial distribution of the mean void fraction in the straight test section*



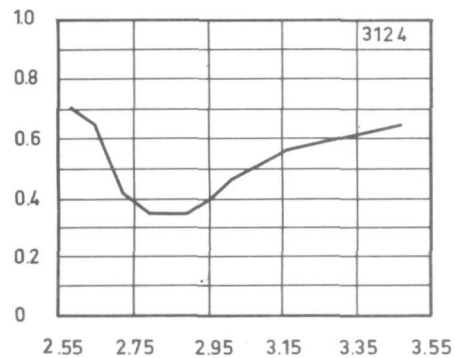
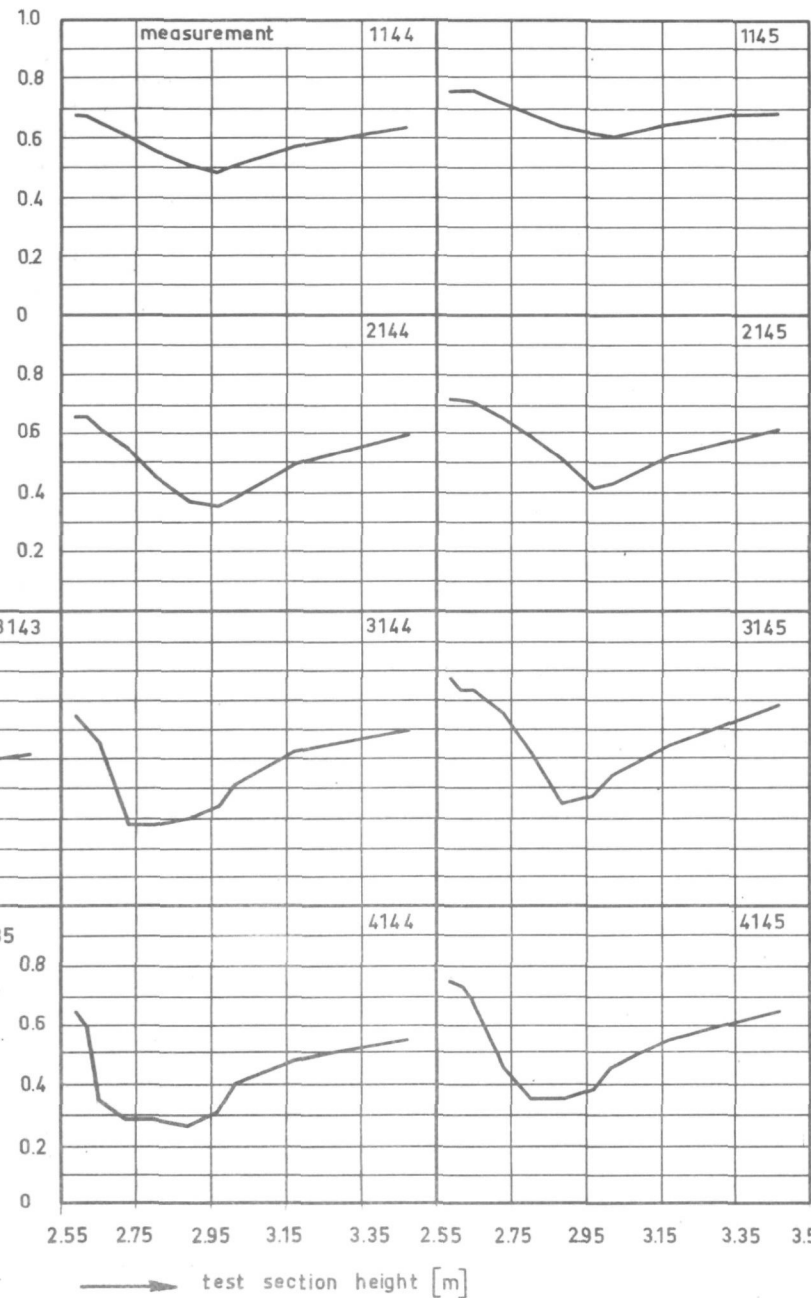


FIGURE 4-14

*Axial distribution of the mean void fraction in the converging test section*



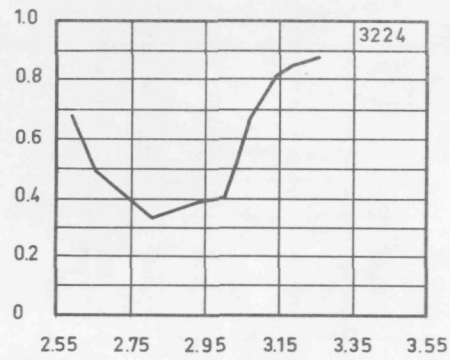
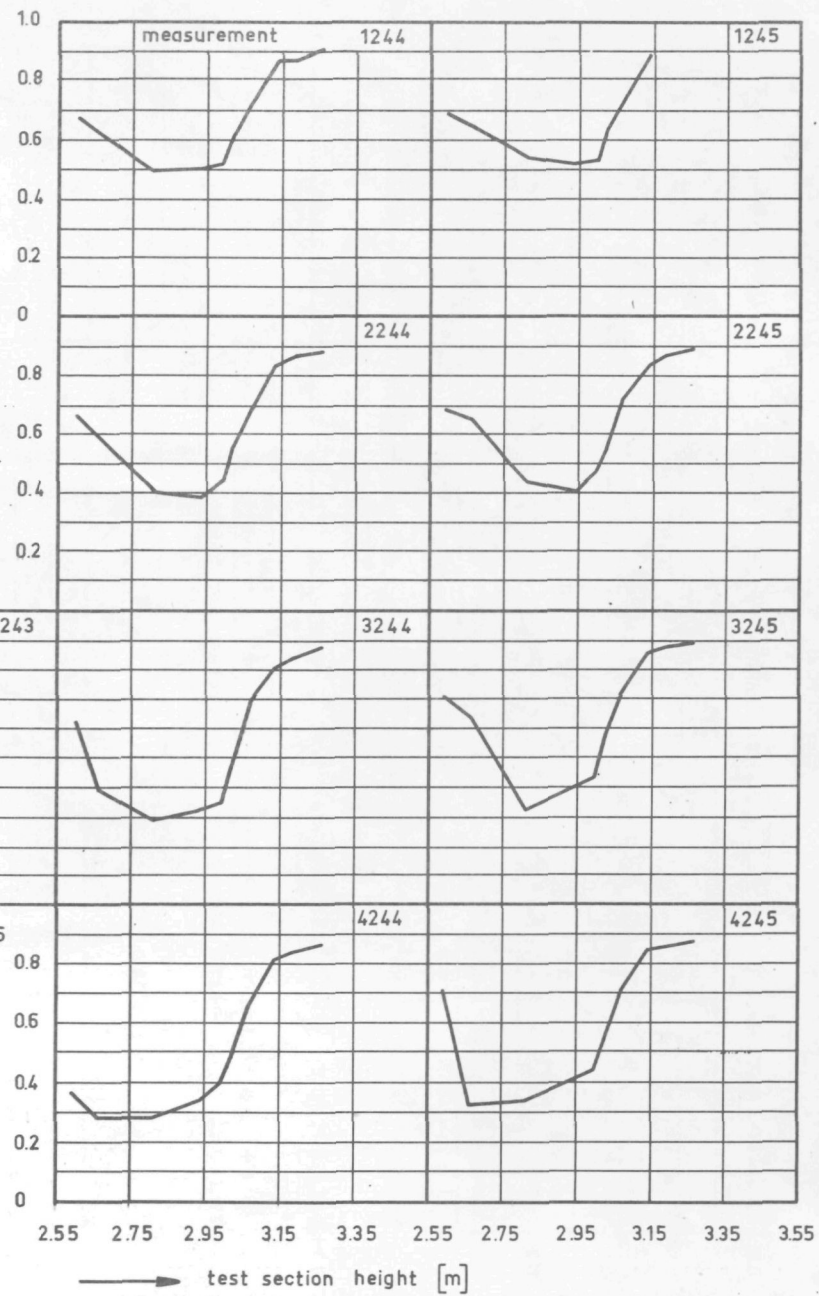


FIGURE 4-15

*Axial distribution of the mean void fraction in the venturi-shaped test section*



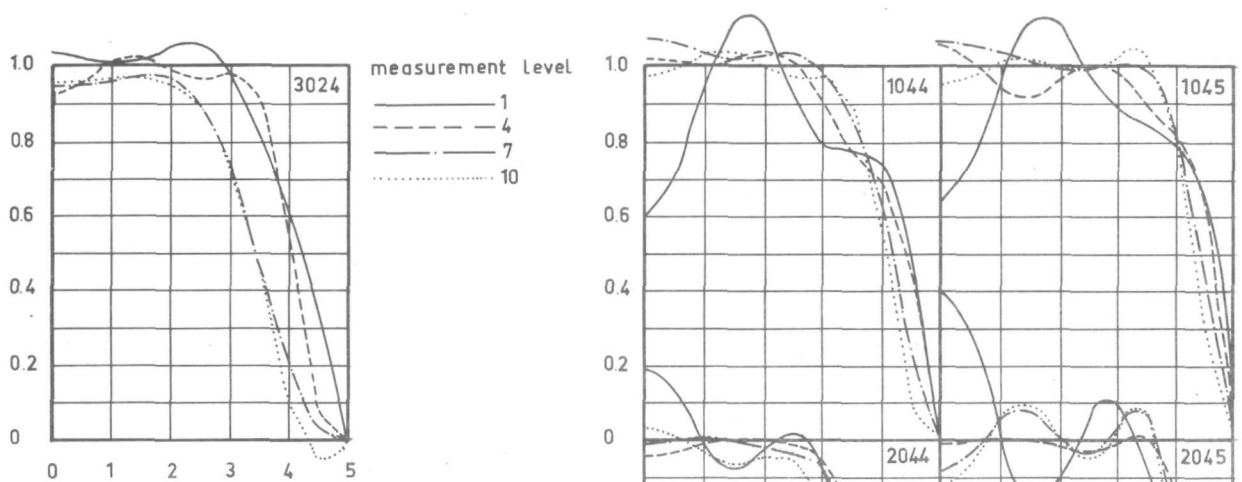
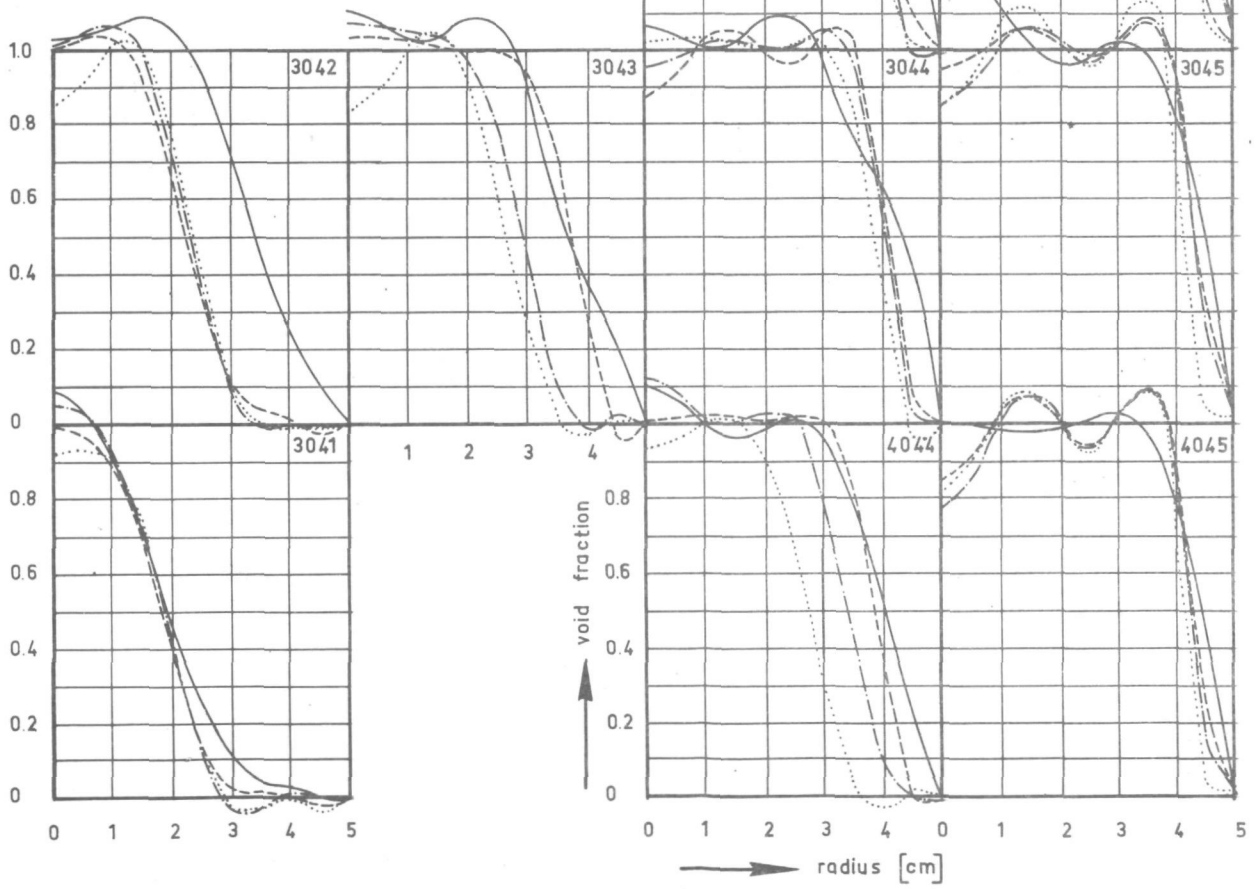


FIGURE 4-16  
*Radial distribution of  
 the void fraction in the  
 straight test section*



\*) void fractions above 1 and below 0, being caused by inaccuracies of the polynomial approximation, have no physical meaning

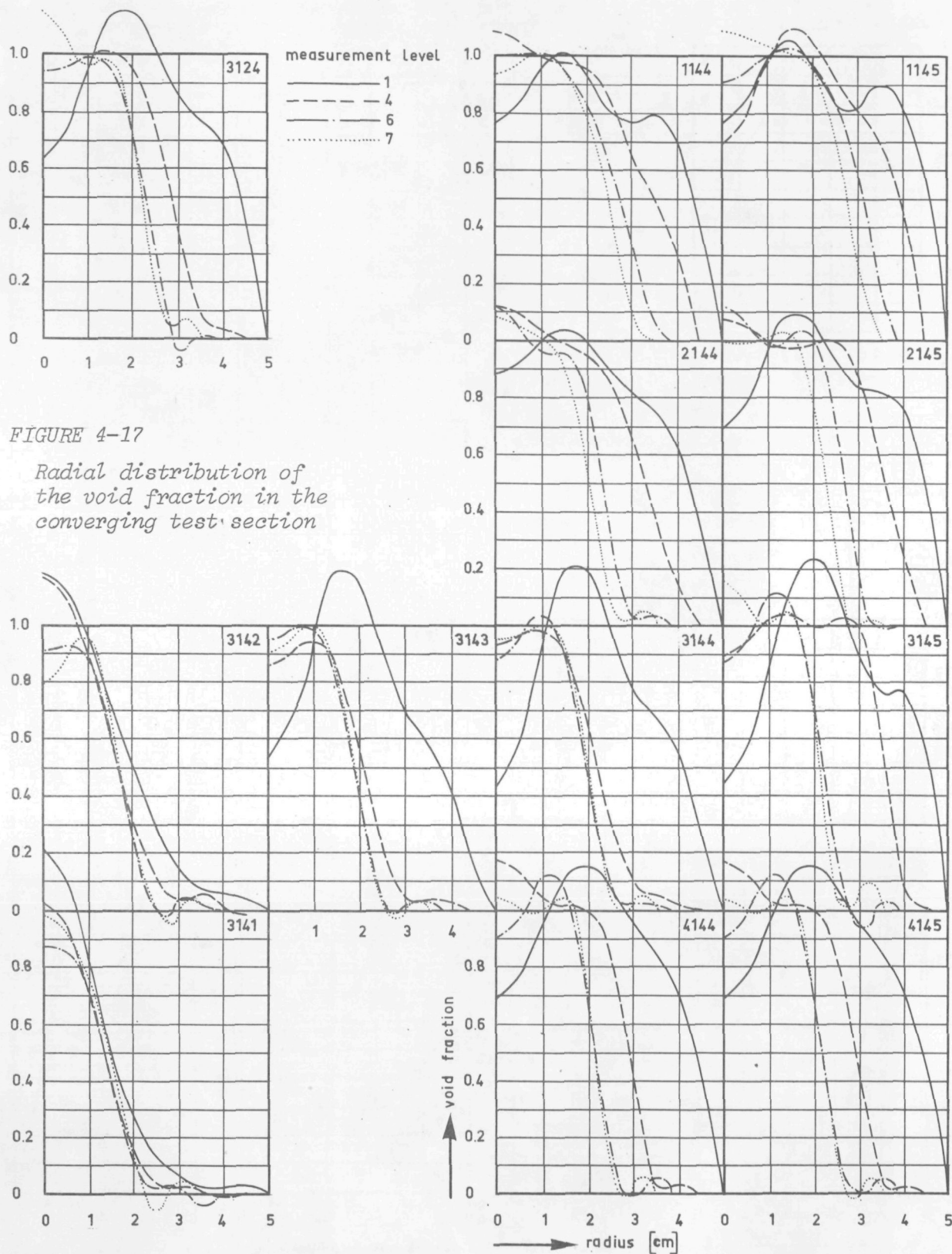


FIGURE 4-17

*Radial distribution of the void fraction in the converging test section*

\* ) void fractions above 1 and below 0, being caused by inaccuracies of the polynomial approximation, have no physical meaning

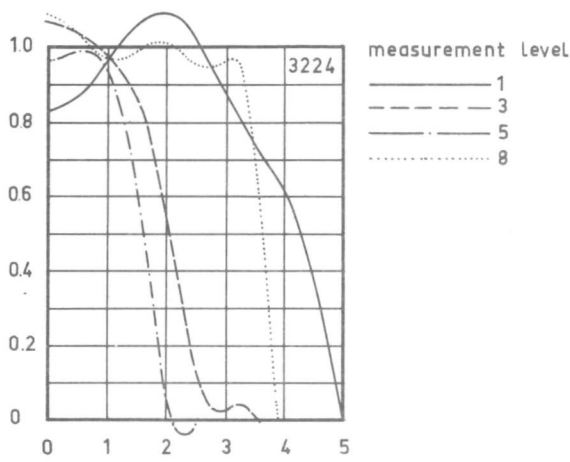
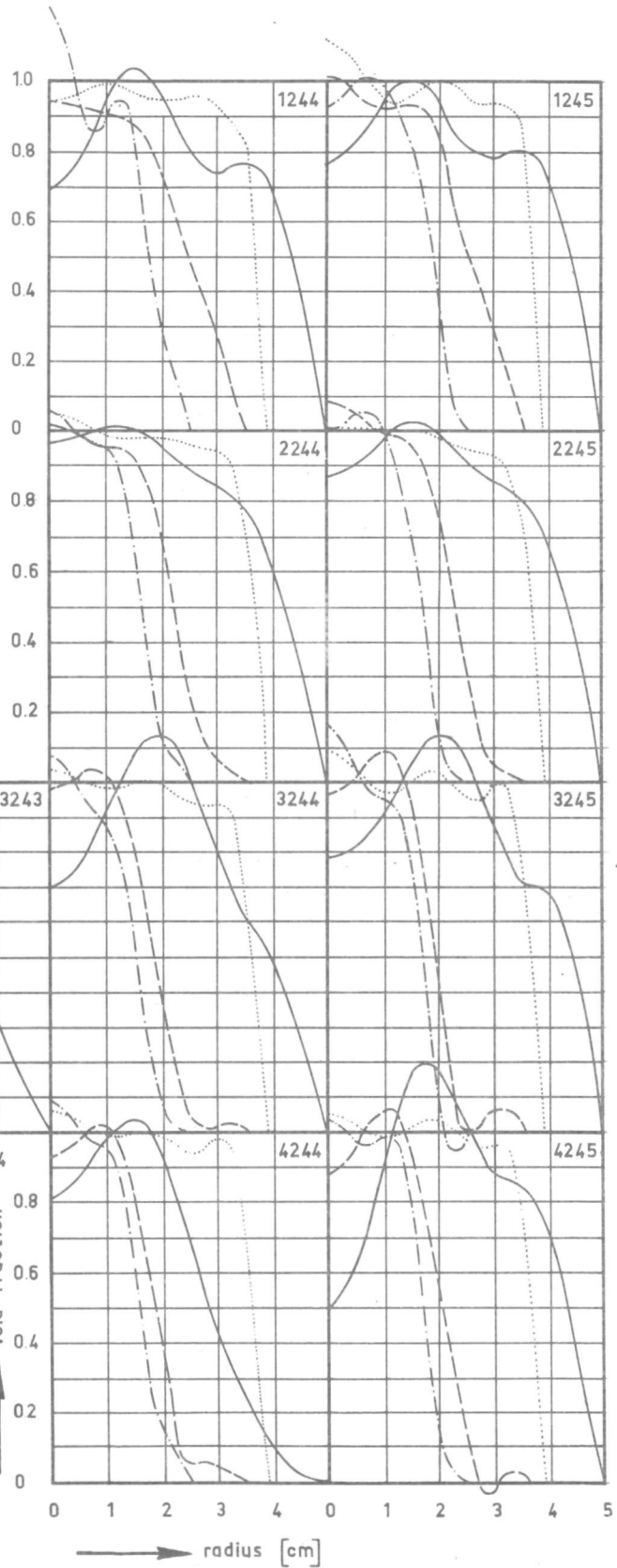


FIGURE 4-18

*Radial distribution of the void fraction in the venturi-shaped test section*



\*) void fractions above 1 and below 0, being caused by inaccuracies of the polynomial approximation, have no physical meaning

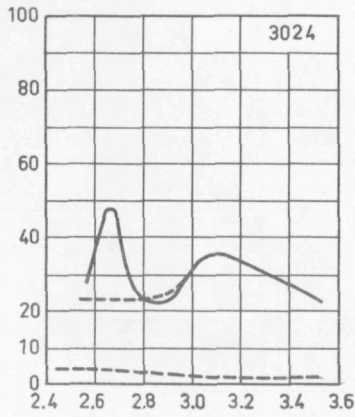


FIGURE 4-19

Axial distribution of the gas core and liquid wall layer velocities in the straight test section

gas core velocity  
 ——— computed with ANALEST procedure  
 - - - likely gas core velocity  
 liquid wall layer velocity ———

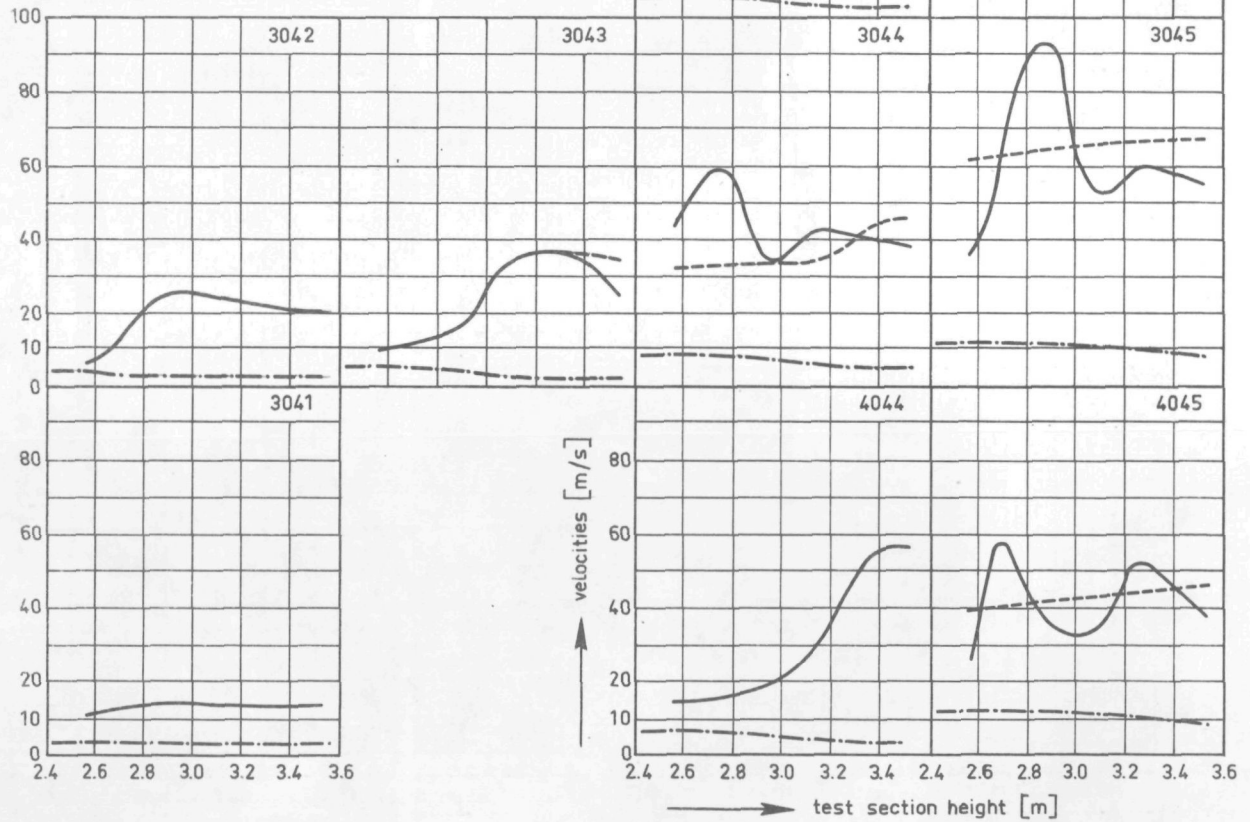
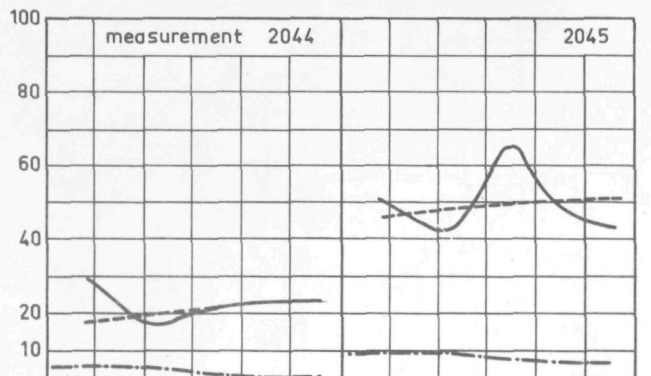
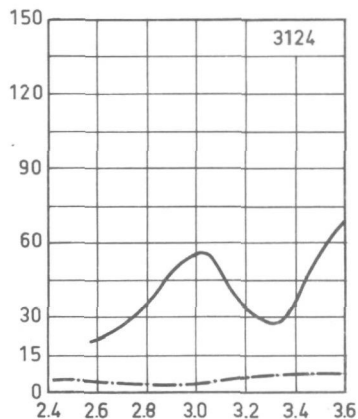


FIGURE 4-20

*Axial distribution of the gas core and liquid wall layer velocities in the converging test section*



gas core velocity  
 ——— computed with ANALEST procedure  
 - - - - - likely gas core velocity  
 liquid wall velocity - - - - -

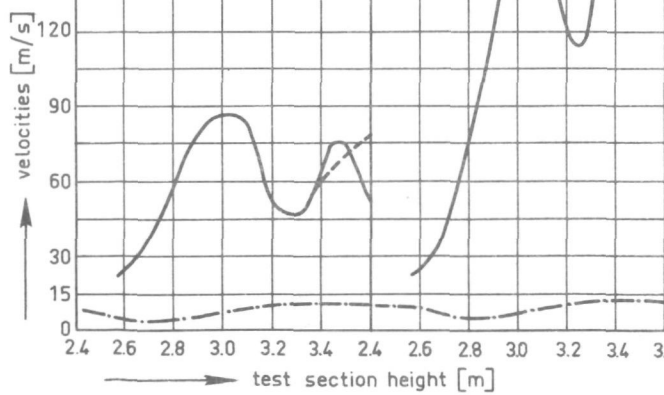
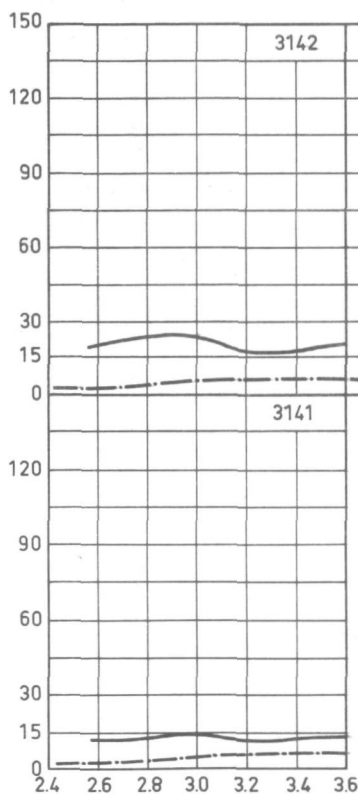
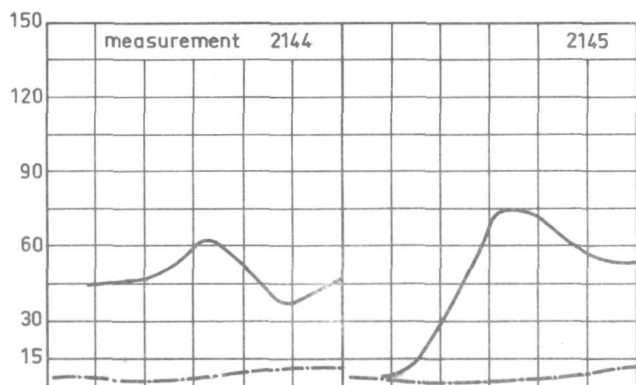


FIGURE 4-21

*Axial distribution of the tangential wall velocities in the straight test section*

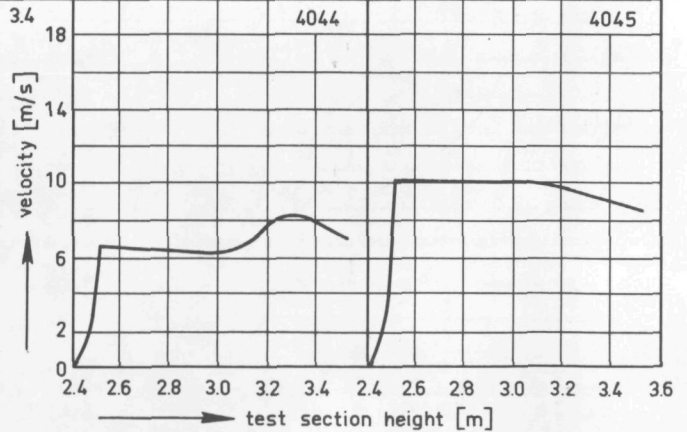
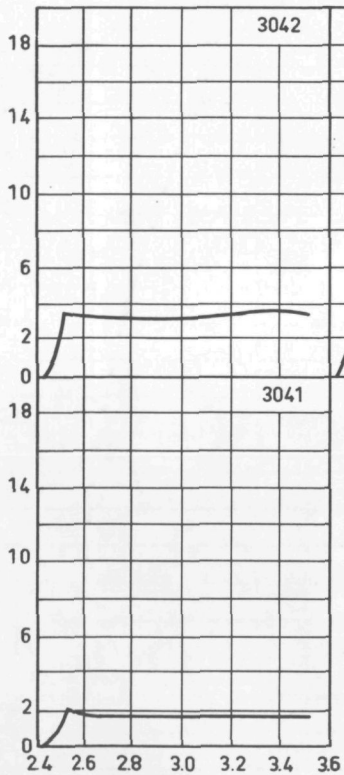
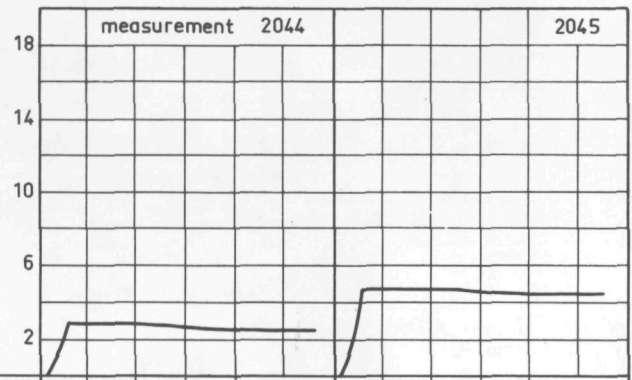
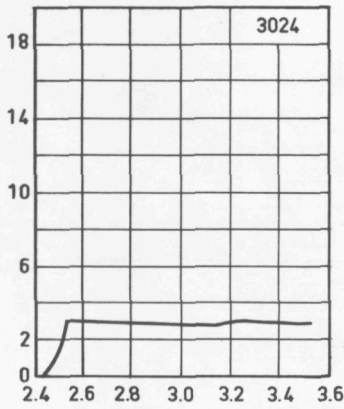
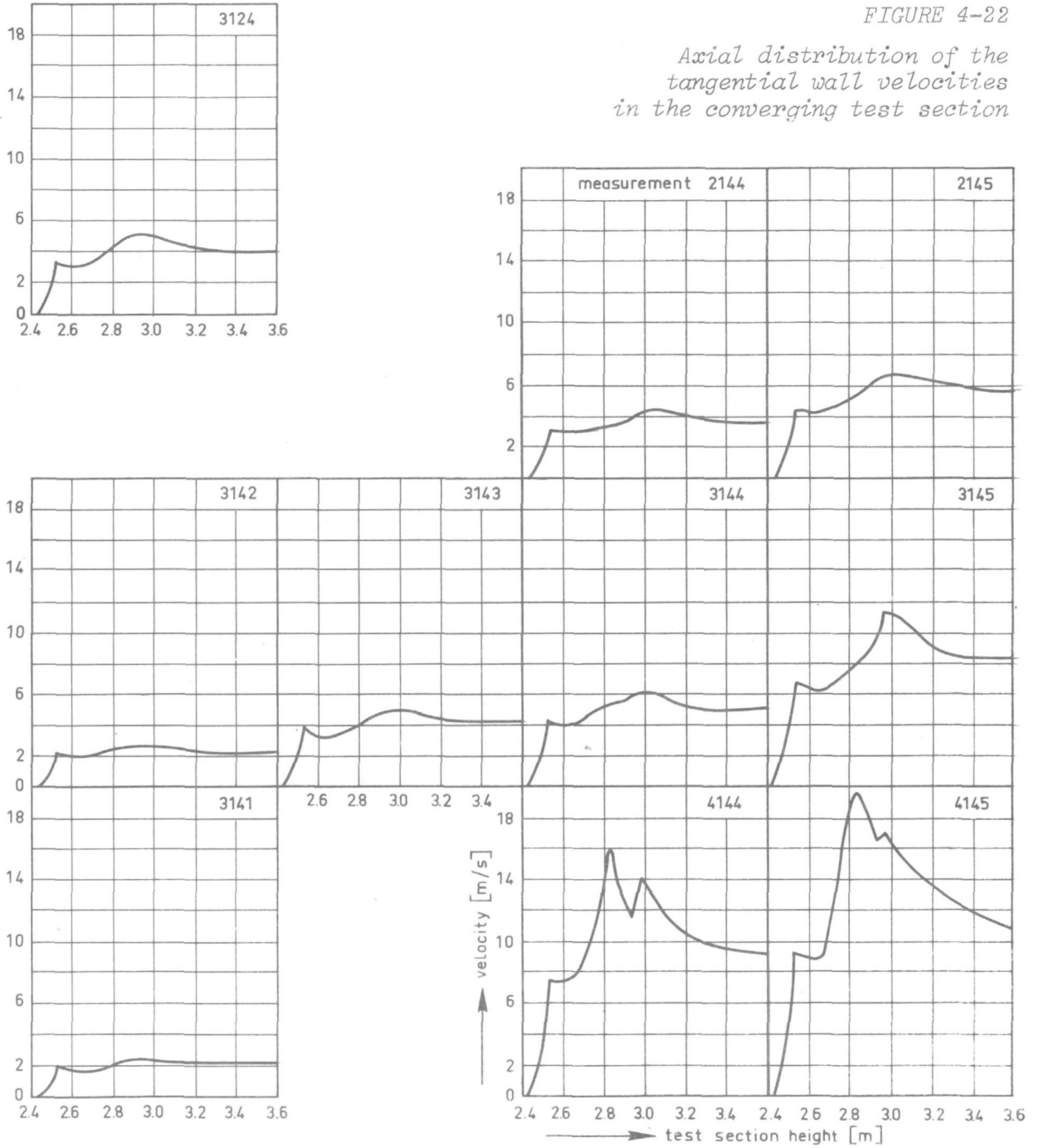


FIGURE 4-22

*Axial distribution of the tangential wall velocities in the converging test section*



for the entire 'column' of highest void fractions \*045 due to the higher mixture velocities.

In the converging test section (figures 4-14 and 4-17) separation length is restricted to the length of the cone, because the gas core disperses upon entering the tail end. For the details of the radial profiles after this breaking up the reader is referred to [125]. In figure 4-14, this dispersion is sharply marked by the increase in mean void fraction downstream of the end of the cone ( $z=2.998$  m), which for the largest angles of deflection (measurements 314\* and 414\*) is preceded by a sharp decrease and a subsequent more or less constant void fraction: the latter region indicating completed separation. The separation length is decreased compared to the measurements in the straight test section, which is undoubtedly a consequence of the increase of rotation intensity due to convergence of the test section. Although the same sort of separation length decrease occurs for the measurements with the smaller angles of blade deflection (measurements 114\* and 214\*) the continuing decrease of mean void fraction until the end of the confusor indicates incomplete separation.

For the venturi-shaped test section (figures 4-15 and 4-18) the separation length is further decreased compared to the converging test section, yielding complete separation for the blades with 40, 50 and 60° angle of deflection and almost complete separation for the 30° blades. A new aspect is the increase of the mean void fraction in the last part of the confusor (up to level  $z=2.998$  m), which is caused by the fact that the gas core reaches its minimum diameter halfway the confusor and remains unchanged in the last part.

The radial void fraction profiles in the diffuser (level 8) show, in general the same mist flow characteristics as found in chapter 2 (cf. figure 2-37) for non-rotating flows, thus it is concluded that separation does not exist any more at this level.

The steepness of the void fraction gradient  $\frac{\partial \alpha}{\partial r}$  after completion of the separation is one of the determining parameters for the separating effect.

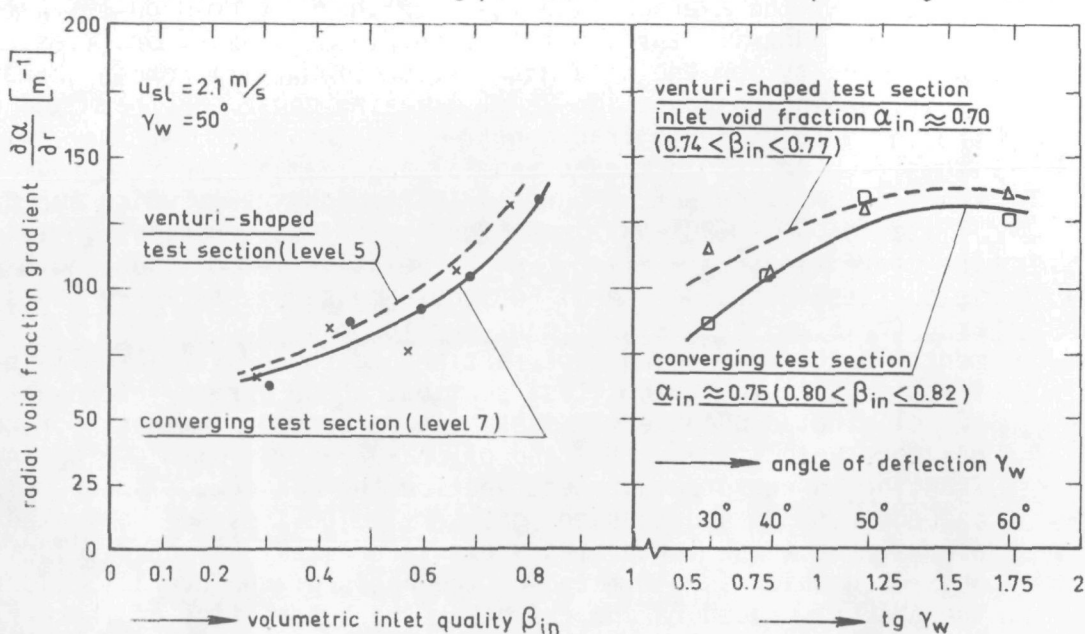


FIGURE 4-23

Dependency of the radial void fraction gradient in the transition zone on the volumetric quality and the angle of deflection

A selection of values of the quotient  $\frac{\Delta\alpha}{\Delta r}$  - referring to the radii where the local void fraction equals 0.7 and 0.3 - is presented in figure 4-23 for the converging and venturi-shaped test sections. The end of the confusors is considered to define the separation length, and thus measurement levels 7 and 5, respectively are selected, both located 1 cm upstream of the end of the cone.

In the left part of figure 4-23 the void fraction gradient  $\frac{\partial\alpha}{\partial r}$  is seen to increase with increasing volumetric quality (mean void fraction). This is caused by the increase in tangential velocity. The increase in turbulence in the transition zone between gas core and water layer due to larger velocities - which is expected to lower the gradient - is apparently dominated by the increase of rotation intensity. The higher values for the venturi-shaped test section are caused by the stronger increase of rotation due to the stronger diameter decrease of the confusor. In the right hand side of figure 4-23, it is seen that the effect of increasing blade deflection vanishes for large angles: the void fraction gradient  $\frac{\partial\alpha}{\partial r}$  becomes constant. This is caused by the balance of two counteracting effects: the increase in rotation intensity raising the gradient and the increase in axial gas velocity raising the turbulence in the transition zone, i.e. lowering the radial gradient (both effects will be discussed in subsections 4.4.4.4. and 4.4.4.3., respectively, for the straight and converging test sections).

#### 4.4.4.3. Axial velocity profiles

From the view point of separation the main interest lies in the gas velocity in the gas core and the liquid velocity in the water layer. These velocities - obtained with the ANALEST procedure - are presented in figures 4-19 and 4-20 for the straight and converging test section, respectively.

The peaks in the radial distribution of the axial gas velocity discussed in subsection 3.4.1.1. are taken into account by computing the gas core velocity as the average velocity over the four grid points with  $r=0, 5, 10$  and  $15$  mm. Notwithstanding this smoothing the axial profiles of the gas core velocity for the straight test section still retain the erroneous peaks, shown in subsection 3.4.1.1. being caused by the strong variation of the volumetric liquid fraction  $(1-\alpha)$  in the gas core. The variation in  $(1-\alpha)$  stems from errors in the polynomial approximation of the radial void fraction profiles (cf. figures 4-16 through 4-18), which are used - with a limitation  $\alpha \leq 0.98$  - as input for the ANALEST procedure, yielding - via the coefficient  $C_D$  - errors in the relative velocity and both phase velocities in the gas core. For those measurements where the smoothing area ( $r=15$  mm) is a significant portion of the gas core, i.e. all measurements in the converging test section and those with a small inlet void fraction in the straight test section, these errors in the gas velocity are eliminated because the mass balance becomes dominant for the resulting gas core velocity. In the case of measurements with a high inlet void fraction in the straight test section the gas core diameter significantly exceeds  $r=15$  mm and thus the gas core velocities are dominated by local errors. For these latter measurements a likely gas core velocity is presented which is estimated on the basis of the overall velocity from the ANALEST procedure and the other characteristics of these flows such as radial and axial void fraction profiles and axial pressure profiles.

In the straight test section the gas core velocities (cf. figure 4-19) are characterized by a slow increase before separation, a strong increase over the separation stretch and a decrease after separation (for those cases

where separation is completed in the test section). The actual profile for each of the measurements thus depends on the location of the separation. The increase during separation is caused by the decrease in total drag force for the core flow compared to bubble flow before separation, while the decrease after separation (cf. measurements 3024 and 3042) is caused by the dispersion of the gas core; increasing the drag force and thus decelerating the gas.

The water layer velocities are constant before separation, decrease in the separation stretch and remain constant afterwards. The decrease is caused by the decrease in cross-sectional mean void fraction as a consequence of the gas velocity increase.

In the converging test section the gas core velocity shows the same behaviour as in the straight test section before, during and immediately after separation, followed by a second increase towards the end of the tail. This increase in gas velocity is caused by a second separation in the tail end after the dispersion, due to the still existing tangential velocity.

The water layer velocity decreases again over the separation stretch, but increases afterwards in the last part of the confusor and the first part of the tail end. In the confusor convergence of the test section is one of the causes, a second cause - also acting in the first part of the tail end - being the very high relative velocity (up to 200 m/s for measurement 4145) yielding - notwithstanding the low overall drag force coefficient - a rather high drag force accelerating the liquid.

#### 4.4.4.4. Tangential velocity

Because of the prescribed radial distribution of both phase velocities in the ANALEST procedure (cf. subsection 3.3.2.4.3.) the tangential velocities at the test section wall contain all the information required on the tangential velocities.

In the straight test section (cf. figure 4-21) the velocity at the wall remains almost constant after leaving the guide vanes, except for measurements 3024, 3043 and 4044, where separation takes place within the test section and the tangential velocity is seen to increase in the separation stretch. This increase is caused by the decrease in axial liquid velocity; the most important term for determination of the tangential velocity being  $(1-\alpha)\rho_l u_{1z} u_{1\phi}$  (cf. equations 3-11 and 3-47).

In the converging test section (cf. figure 4-22) the tangential velocity is seen to increase in the confusor, in keeping with the purpose of this component. The ratio between the tangential wall velocities at the end of the confusor and those at the guide vane outlet increases both with increasing void fraction (measurements 314\*) and increasing angle of deflection ("columns" \*144 and \*145). This deviation from the expected constant ratio is again caused by the deceleration of the axial liquid layer velocity which is more pronounced with increasing void fraction and angle of deflection.

The peakiness of measurements 4144 and 4145 is caused by the spatial discontinuities in the ANALEST grid, as discussed in subsection 3.4.1.2.

#### 4.4.5. Analyses of separating performance

The results of the present introductory air-water measurements are used to design the air-water separator discussed in subsection 4.5. To this end the measured results as well as the values obtained with the ANALEST procedure are used to predict the separating performance should there be a vortex finder.

#### 4.4.5.1. Separation length

The axial profiles of the mean cross-sectional void fraction are best suited to define the separation length. From figure 4-13 through 4-15 it appears that separation length increases with increasing volumetric quality and superficial water velocity and decreases with increasing blade angle and increasing convergence of the confusor. This latter effect of convergence shows the advantage of a venturi separator compared to separators with a cylindrical vortex tube: for the flows under investigation the maximum separation length is reduced from over 1 meter for the straight test section to around 50 cm for a confusor with half a top angle of  $20^{\circ}12'$  (converging test section) and to only 30 cm for a confusor with half a top angle of  $30^{\circ}40'$  (venturi-shaped test section).

Considering the effect of the angle of deflection for a fixed separation length of 48 cm, i.e. the end of both confusors, and for the highest volumetric quality, which is close to the rated flow condition in a BWR, it appears from figures 4-14 and 4-15 that this separation length suffices for complete separation in combination with an angle of  $45^{\circ}$  for the converging test section and an angle of  $30^{\circ}$  for the venturi-shaped test section. Increase of these angles of deflection - for unchanged throat diameter - allows a decrease in confusor length.

#### 4.4.5.2. Gas core diameter

The gas core diameter can be defined in several ways, e.g. the diameter for which a fixed exit or downcomer quality is obtained, the radius at which the radial void fraction gradient  $\frac{\partial \alpha}{\partial r}$  is steepest, the radius where the local void fraction reaches a fixed value, etc. Although the diameters will differ slightly for each of these definitions, the trends with respect to the dependencies on volumetric quality, angle of blade deflection and vortex tube geometry will remain unchanged. It is therefore logical to use the most simple definition, viz. the radius at which the local void fraction equals 0.5. These radii are derived from the radial void fraction distributions at the end of the straight test section, i.e. level 10, and the top of both confusors, i.e. levels 7 and 5 for the converging and venturi-shaped test sections, respectively.

The left hand side of figure 4-24 shows a rather strong dependency on the volumetric quality, roughly characterized by  $r_c = K\sqrt{\beta_{in}}$ , with different constants for the various vortex tubes. The discontinuity for the straight test section is caused by the difference between complete separation for the lower volumetric qualities and the absence of separation within the test section for the higher qualities.

The characteristic  $r_c = K\sqrt{\beta_{in}}$  stems from the fact that for core flow with a "top hat" void fraction distribution the core diameter  $d_c = \sqrt{\langle \alpha \rangle} D$ , and the mean void fraction is, in general, proportional to the volumetric quality. From comparison of the two correlations it can be concluded that the mean void fraction after separation remains more or less proportional to the inlet void fraction. Since the vortex finder of a separator has a fixed diameter a strong effect on the separating effect is to be expected from variations of the volumetric inlet quality.

For a given volumetric inlet quality the gas core radius is seen in the right hand part of figure 4-24 to be independent of the angle of deflection (except for the smallest angle), and solely dependent on the vortex tube geometry. The high volumetric qualities in this right hand part of the figure are not separated in the straight test section, but analysing the gas core radii after complete separation in the left part of figure 4-24

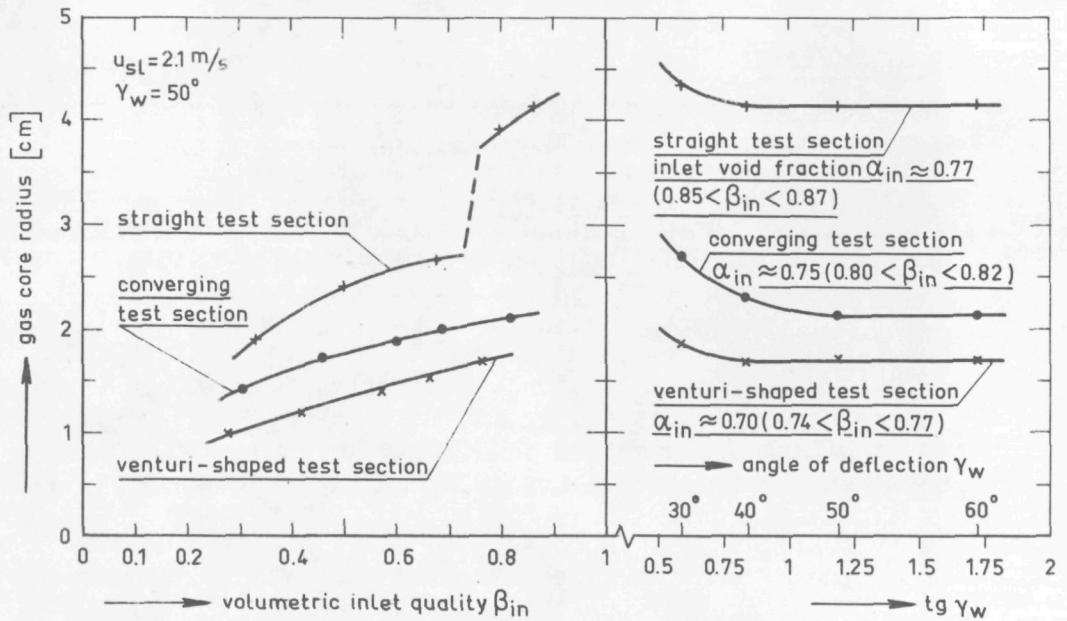


FIGURE 4-24

Dependency of the gas core radius ( $\alpha = 0.5$ ) on the volumetric quality and the angle of deflection

the radii for a fixed volumetric inlet quality  $\beta_{in} = 0.75$  are 2.75, 2.08 and 1.67 cm for the straight, converging and venturi-shaped test sections respectively.

The ratios between these values and the test section radii at the levels of interest, i.e. the relative gas core radii, are 0.55, 0.59 and 0.67, respectively. This relatively small variation confirms that the gas core radius is dominated by the volumetric inlet quality and yields a rather simple design rule for the diameter of the vortex finder.

#### 4.4.5.3. Gas core stability

In contrast with the experiments with a vortex finder described by PRINS [1], the gas core does not disintegrate in the present introductory experiments without vortex finder, as evidenced by the radial void fraction profiles (cf. figures 4-16 through 4-18) which remain unchanged after completion of the separation until the end of the confusor.

The dispersion of the gas core entering the tail end of the converging test section or the throat of the venturi is most probably caused by the contraction of the flow at these locations and the subsequent diffusion. As mentioned in subsection 2.3.1.6.1.3. the required radial transport in a diffusing two-phase flow is dominated by the gas phase because this light phase is much easier to accelerate, while the heavy liquid phase tends to maintain its original axial flow direction.

PRINS [1] describes two possible causes for the disintegration of the gas core in his experiments, viz. the occurrence of a hydraulic jump and the so called pressure drop unbalance for the gas and liquid outlet paths separated by the vortex finder. In view of the absence of a vortex finder the present introductory experiments have been used to investigate whether a hydraulic jump exists and whether the condition for a hydraulic jump is fulfilled.

The hydraulic jump is well known in open channel flow (see e.g. STREETER [84]) and is characterized by a sudden change in flow depth (jump). This phenomenon exists thanks to the possibility for the liquid to flow at two different depths at a given throughput possessing equal energy: deep flow with a low

kinetic energy and high potential energy and shallow flow where these energies are reversed in magnitude. The condition at which both depths are equal, is defined by a Froude number equal to unity:  $Fr = \frac{u^2}{gh} = 1$ . For supercritical flow, i.e.  $Fr > 1$ , a jump can occur, changing the flow to subcritical flow  $Fr < 1$ , while dissipating some energy in the turbulent mixing zone at the location of the jump. For rotating annular flow the same conditions apply as for open channel flow: a layer of flowing liquid with a free surface and a force field perpendicular to the direction of motion. The existence of hydraulic jump in rotating flows was proved by BINNIE [126] for a rotating annular liquid layer in vertical downflow, where he observed a sudden increase in thickness of the liquid layer with a simultaneous reduction in diameter of the gas core. Further proof was obtained by KEDL [127] with an axial flow separator with cylindrical vortex tube, having found that the gas core disintegrated into very small diameter bubbles before reaching the vortex finder, followed by remixing of the separated air with the water. Subsequent analysis of the rotating annular flow showed [128], [129] that a reasonable similitude with open channel flow is obtained if the Froude number definition suggested by BINNIE and SHAW [128] is used. This definition may be written as:

$$Fr = \frac{u_{1z}^2}{\frac{u_{\phi c}^2}{r_c} \frac{R^2 - r_c^2}{2r_c}} \quad (4-9)$$

where  $u_{1z}$  is the axial liquid velocity,  $u_{\phi c}$  the tangential velocity at the interface,  $R$  the test section radius and  $r_c$  the radius of the interface. The difficulty in applying this definition to the flows under consideration consists of determining the interface radius  $r_c$  and the corresponding tangential velocity  $u_{\phi c}$ , because a transition zone rather than a sharp interface exists between liquid layer and gas core. Since, however, such a sharp interface is described by a "top hat" void fraction distribution for which  $\left(\frac{r_c}{R}\right)^2 = \langle \alpha \rangle$ , it seems logical to rewrite definition (4-9) as:

$$Fr = \frac{2\langle \alpha \rangle}{(1-\langle \alpha \rangle)} \frac{u_{1z}^2}{u_{\phi c}^2} \quad (4-10)$$

Consequently the tangential velocity  $u_{\phi c}$  has to be determined at  $r_c = \sqrt{\langle \alpha \rangle} R$ . For the tangential velocities obtained with the ANALEST procedure, in which the radial distribution of this velocity is prescribed by equation (3-64):  $u_{\phi} = 1.25 \frac{r}{R} u_{\phi W}$  for  $\frac{r}{R} < 0.8$ , one obtains:

$$u_{\phi c}^2 = 1.56 \langle \alpha \rangle u_{\phi W}^2 \quad \text{for } \langle \alpha \rangle < 0.64 \quad (4-11)$$

Because the mean void fractions  $\langle \alpha \rangle < 0.64$  after separation for all flows under consideration, it follows that:

$$Fr = \frac{1.28}{(1-\langle \alpha \rangle)} \frac{u_{1z}^2}{u_{\phi W}^2} \quad (4-12)$$

In figure 4-25 the values for this Froude number are presented for the outlet of the confusor (level 7) of the converging test section and for the exit of the straight test section (level 10). For the former test section the data cover all test results (measurements 314\* and \*145), but for the straight test section the results are restricted to the measurements with complete separation at the exit. On the left hand side of this figure the Froude numbers are seen to depend very strongly on the volumetric inlet quality, while on the right hand side the effect of blade deflection is as expected, i.e. decreasing Froude number with increasing blade deflection.

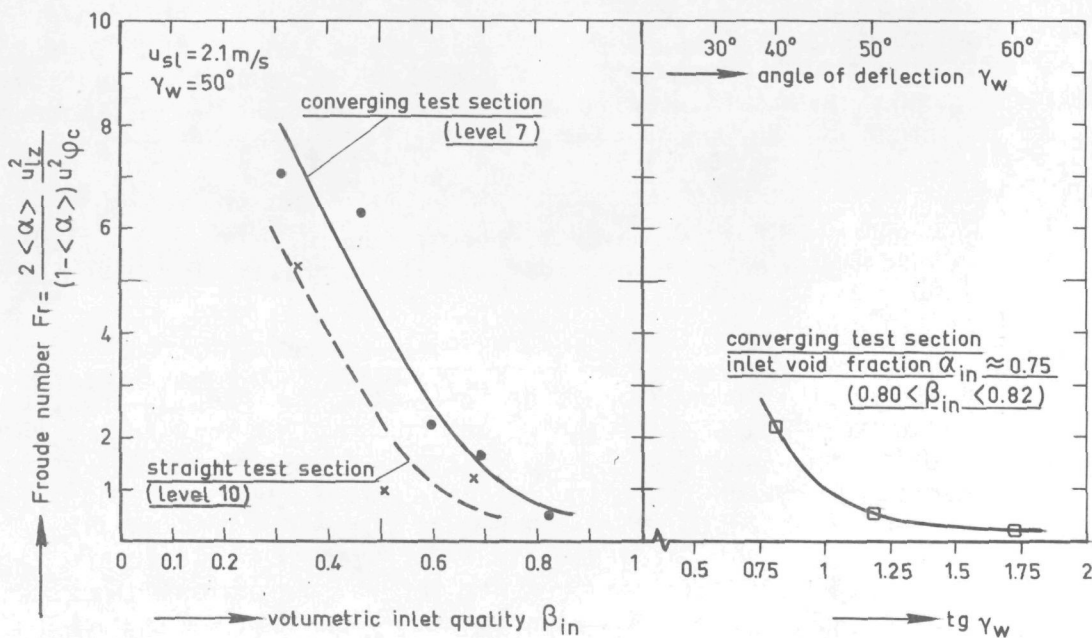


FIGURE 4-25

*Dependency of the Froude number for rotating liquid layers on the volumetric quality and the angle of deflection*

For open channel flow STREETER [84] presents the following classification of the hydraulic jump phenomenon:

- $Fr < 1$ , subcritical flow; no jump
- $1 < Fr < 3$ , undular jump; i.e. small undulations appear on the surface vanishing over a short distance
- $3 < Fr < 6.3$ , weak jump; small rollers develop on the surface, but the downstream surface still remains smooth
- $6.3 < Fr < 20$ , oscillating jump; a jet oscillates at the front of the jump, producing large waves which remain existent far downstream of the jump
- $20 < Fr < 80$ , steady jump; a well balanced and stable jump is formed
- $Fr > 80$ , strong jump; a strong energy dissipation occurs by intermittent slugs and a rough surface.

Considering the Froude numbers presented in figure 4-25 the numbers for low volumetric quality and low rotation intensity are seen to exceed unity up to a maximum around 7. Hence only small waves and rollers are to be expected in view of the above classification. These disturbances are likely to contribute to the existence of the transition zone between water layer and gas core, but it was found that the width of this zone does not correlate to the Froude number as is the case for the height of the jump

in open channel flow. This inadequacy of the liquid Froude number to yield an accurate correlation for the wave height is quite understandable, because the present separator flow - bounded by the centerline and the wall - is in fact a cocurrent gas-liquid closed channel flow. The determination of wave heights for cocurrent closed channel flow, however, is a problem too complex for theoretical analysis at the present state of knowledge, notably for complex channel geometries and significant wave heights. This complexity is illustrated by analyses of LONG [130], which yield highly complex correlations based on the Froude numbers of both phases even for inviscous flow, a simple rectangular channel geometry and restricted relative wave heights.

From the above qualitative considerations it is concluded - in the absence of a theoretical description - that while the present flows are expected to be supercritical both for low volumetric qualities and low rotation intensities the resulting waves or rollers will be small and no strong steady jump will occur. Stretching this conclusion to the experiments of PRINS [1] it is subsequently concluded that the disintegration of the gas core in those flows is caused by an unbalance of pressure drop for the gas and liquid path, which therefore should be given special attention in the design of the vortex finder and diffuser of the venturi separator.

#### 4.4.5.4. Liquid carry-over and gas carry-under

Although it is common practice in reactor engineering to assess separator performance in terms of the weight qualities  $x_E$  and  $x_D$  the volumetric qualities  $\beta_E$  and  $\beta_D$  will be utilized for the present air-water measurements. The reason for this choice is given by the argument presented in subsection 4.4.3.1., viz. the use of the volumetric quality as a suitable parameter for obtaining similitude between steam-water and air-water flows. The General Electric requirements for BWR separators discussed in subsection 4.2.3. are hence transformed\*) into conditions for the volumetric qualities: the maximum of 15% moisture carry-over in the separated steam, i.e.  $x_E > 0.85$ , corresponds with  $\beta_E > 0.991$  and the maximum carry-under of 0.25% steam is represented by  $\beta_D < 0.048$ .

The volumetric flow rates required to derive the values of  $\beta_E$  and  $\beta_D$  for the present experiments at the actual test section levels are obtained [104] by using the measured void fractions in combination with the axial phase velocities computed with the ANALEST procedure. For any discrete radius considered as the inlet radius of a fictitious vortex finder the exit quality  $\beta_E$  may be computed as the volumetric quality of the flow inside this radius, while the flow between this specific radius and the wall of the test section yields the downcomer quality  $\beta_D$ . By repeating these computations for a number of radii the dependency of the qualities on the radius of the vortex finder is obtained. The results of such computations are given in figures 4-26 and 4-27, be it that the exit quality is shown in terms of  $(1-\beta_E)$  for the sake of convenient representation.

The accuracies for  $(1-\beta_E)$  and  $\beta_D$  are poor in the gas core and near the wall respectively, due to the void fraction limitations of 0.98 and 0.02 for the input of the ANALEST procedure (cf. subsection 3.3.2.2.). Because this input for the present ANALEST procedure is based on the measured void fractions which have a standard deviation of 0.06 (cf. subsection 4.4.3.2.) more accurate estimations can only be achieved when the ANALEST

\*) The weight and volumetric qualities are related to each other via the

$$\text{definition } \frac{x}{1-x} \frac{\rho_l}{\rho_g} = \frac{\beta}{1-\beta} .$$

FIGURE 4-26

Dependency of the volumetric separation "qualities" on the radius of a fictitious vortex finder in the straight test section at level 10

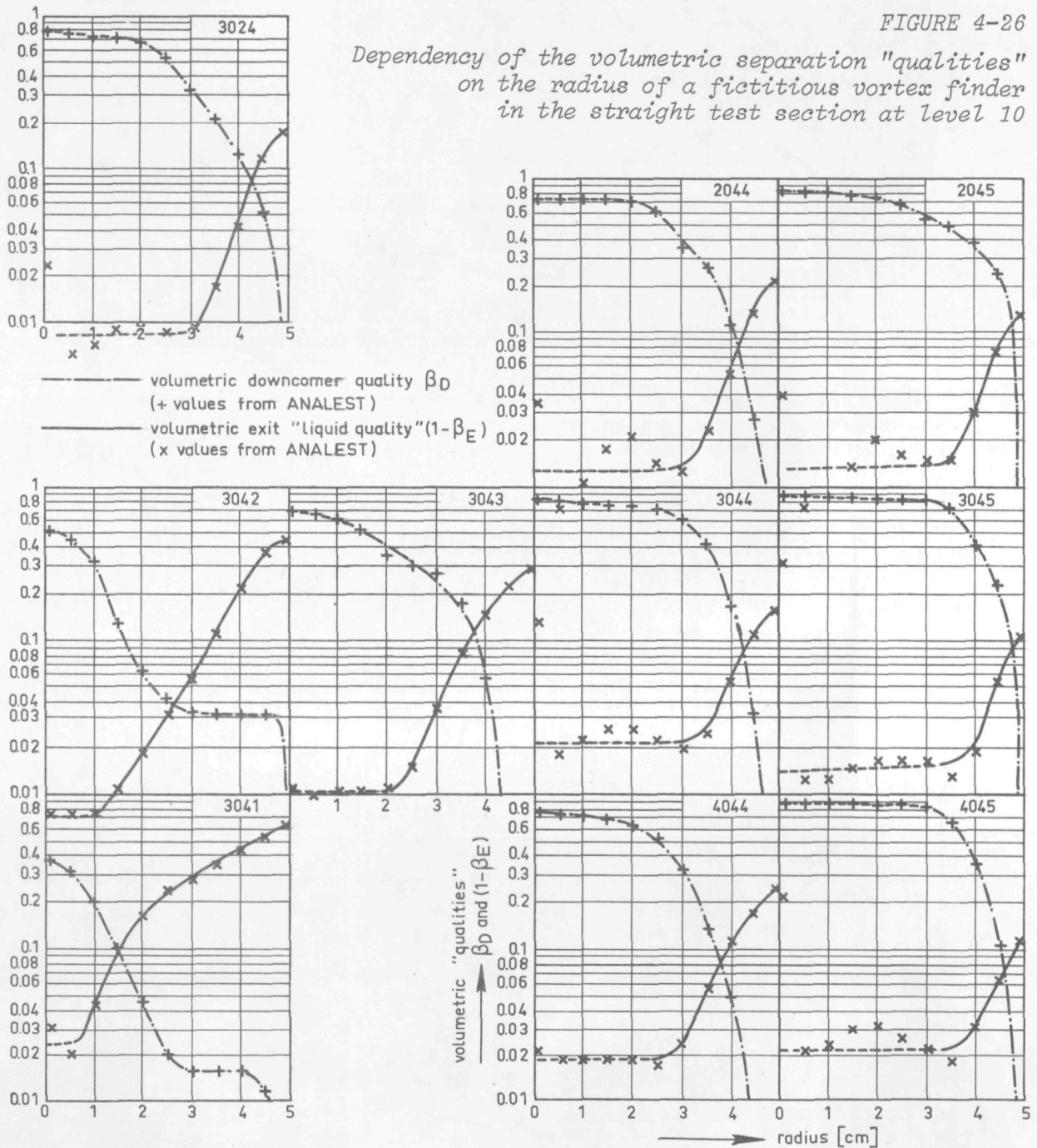
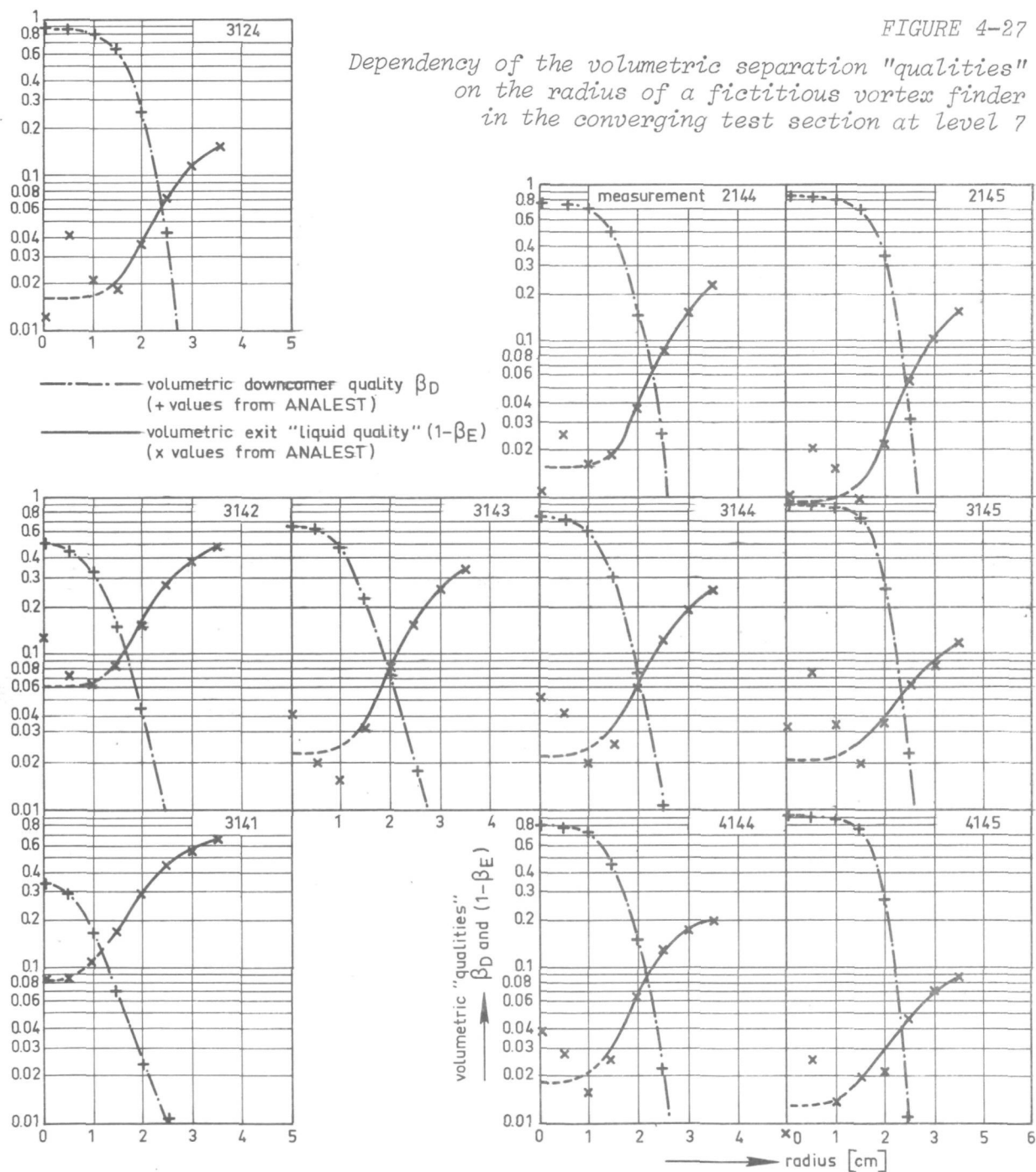


FIGURE 4-27

Dependency of the volumetric separation "qualities" on the radius of a fictitious vortex finder in the converging test section at level 7



procedure is extended to include computation of the void fraction distribution. Based on the definition  $s = \frac{\beta}{1-\beta} \frac{1-\alpha}{\alpha}$  the present limitations for the void fraction result in limitations for  $(1-\beta_E)$  and  $\beta_D$ :  $(1-\beta) \approx \frac{1-\alpha}{s}$  for  $\alpha \approx 1$  and  $\beta = \alpha s$  for  $\alpha \approx 0$ , hence  $(1-\beta_E)$  is restricted to  $\frac{0.02}{s}$  in the gas core and  $\beta_D$  to  $0.02s$  in the liquid layer.

The former limitation is evident throughout figures 4-26 and 4-27 where  $(1-\beta_E)$  reaches a minimum level in the gas core. The limitation for  $\beta_D$  is only significant for measurements with a relatively thick water layer, i.e. 3041 and 3042.

Despite these limitations it is evident that for none of the experiments both requirements -  $(1-\beta_E) < 0.009$  and  $\beta_D < 0.048$  - are fulfilled at the same radius, i.e. that secondary separation is required to reach the General Electric specifications.

Because separation is not complete for all the measurements in the straight test section, subsequent analyses will be based on the results for the converging test section presented in figure 4-27. The curves for  $(1-\beta_E)$  are seen to rise with decreasing inlet quality, indicating that the requirement for limited liquid carry-over  $(1-\beta_E) < 0.009$  becomes more difficult or even impossible to meet for low inlet qualities.

The curves for  $\beta_D$  rise at the centerline with increasing inlet quality and show a significant steepening, i.e. an increase of the radius for which  $\beta = 0.048$  (from  $r=17$  mm for measurement 3141 up to  $r=23$  mm for measurement 3145). In view of the actual test section radius  $R=35$  mm it is concluded that the GE specification  $\beta_D < 0.048$  is satisfied for a relatively large region.

Variation of the angle of blade deflection ("columns" \*144 and \*145) is seen hardly to affect the exit and downcomer qualities, as was to be expected on the basis of the void fraction characteristics presented in figures 4-23 and 4-24.

#### 4.4.5.5. Compound efficiency of the separating effect

Despite the disadvantage of attributing equal weight to both carry-under and carry-over - as discussed in subsection 4.2.3. - the compound efficiencies (cf. definition (4-3)) will be shown to provide a better insight for the selection of a vortex finder inlet radius.

The compound efficiencies are computed on the basis of the volumetric qualities  $\beta_E$  and  $\beta_D$  presented in the previous subsection, while the riser (inlet) quality  $\beta_R$  is represented by the volumetric quality at the actual level in order to take into account the expansion of the gas in the course of its rise through the test section.

The results are shown in figure 4-28 for the straight and converging test sections; for the straight test section only those measurements are included for which separation is completed at level 10.

In the upper part of figure 4-28 the radial distribution of the compound efficiency for the straight test section is seen to vary strongly with the inlet void fraction (inlet volumetric quality), obviously causing a strong variation in separator performance for a fixed vortex finder inlet radius. By contrast the curves for the converging test section show for each of the angles of blade deflection a fixed location for the maximum efficiency. The radii of these maxima decrease slightly with increasing rotation intensity (blade deflection), but are practically independent of the volumetric inlet quality, notwithstanding the variation of the individual

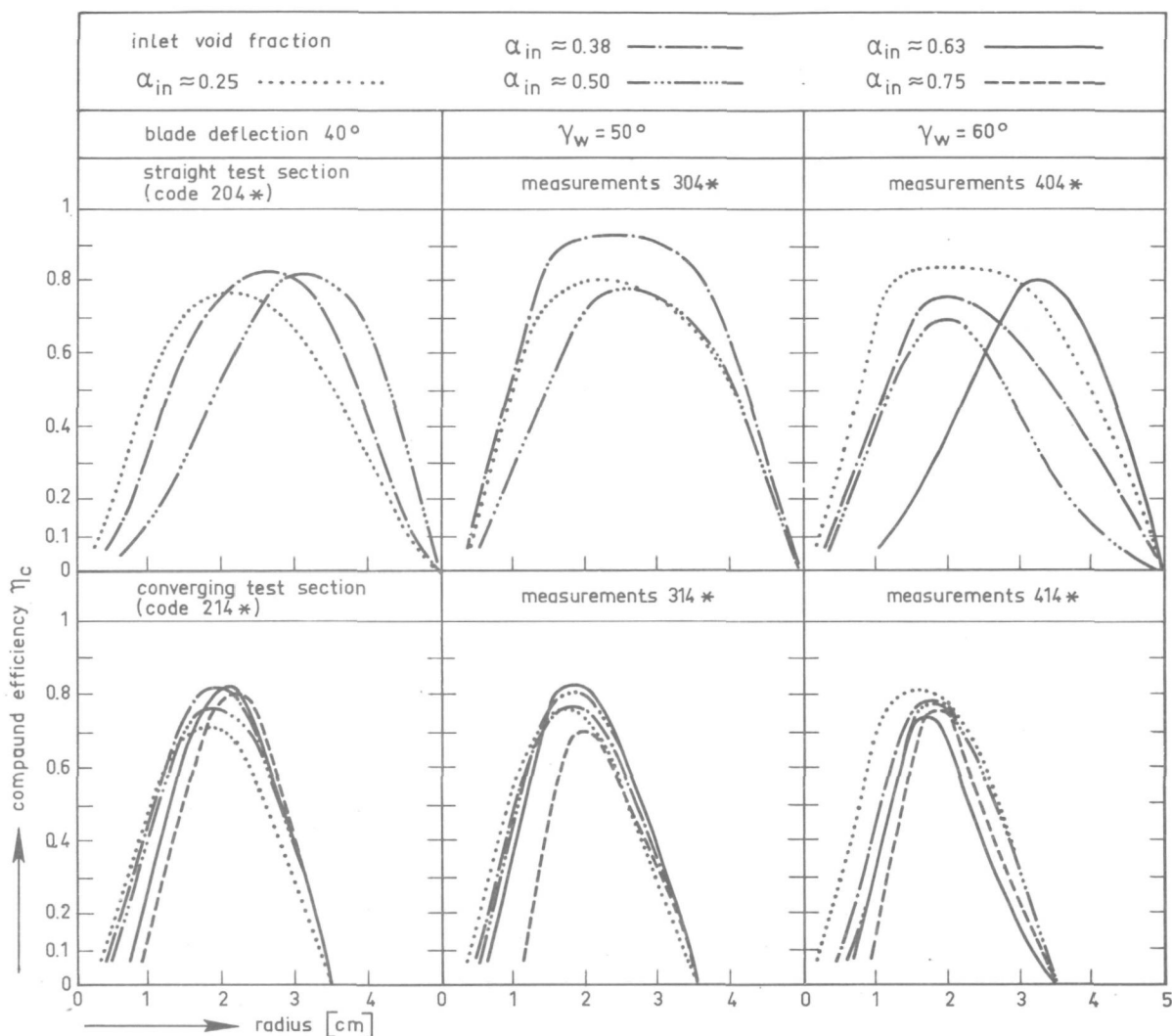


FIGURE 4-28

*Compound efficiency of the separating effect as a function of the inlet radius of a fictitious vortex finder*

outlet qualities  $\beta_E$  and  $\beta_D$  discussed in the previous subsection<sup>\*)</sup>).

#### 4.4.5.6. Pressure loss

For the present introductory measurements without vortex finder the separator pressure loss is defined as the pressure difference between the cross sections immediately upstream of the guide vanes and at the inlet of the fictitious vortex finder, i.e. at the end of the confusor (level 7) for the converging test section or level 10 of the straight test section. At these latter locations two pressures can be distinguished, viz. the measured pressure at the wall and the centerline pressure computed with the ANALEST procedure. The pressure difference on the basis of the latter is the largest of the two and considered representative for the separator pressure loss, as explained in the next subsection. For the straight test section both pressure differences are always small (less than  $10 \text{ kN/m}^2$ ), and will be omitted from further discussion because

<sup>\*)</sup> *The optimum vortex finder inlet radius, however, will have to be selected on considerations of outlet qualities rather than on the maximum compound efficiency (cf. subsection 4.2.3.1.).*

of the irrelevance of this geometry for further separator development. For the converging test section both pressure differences are presented in figure 4-29; the wall pressure differences are obtained from the direct measurements for pressure taps 2 and 9 (cf. figure 2-24) and the centerline difference is composed from this former measured difference and the computed radial pressure difference.

In the left part of figure 4-29 the centerline pressure difference is seen to increase rather steeply with increasing quality, while the wall pressure difference remains small and even decreases for large inlet qualities. This low wall pressure difference is caused by the absence of acceleration, or sometimes even deceleration, of the liquid layer at the wall (cf. figure 4-20). The centerline pressure difference for large rotation intensities

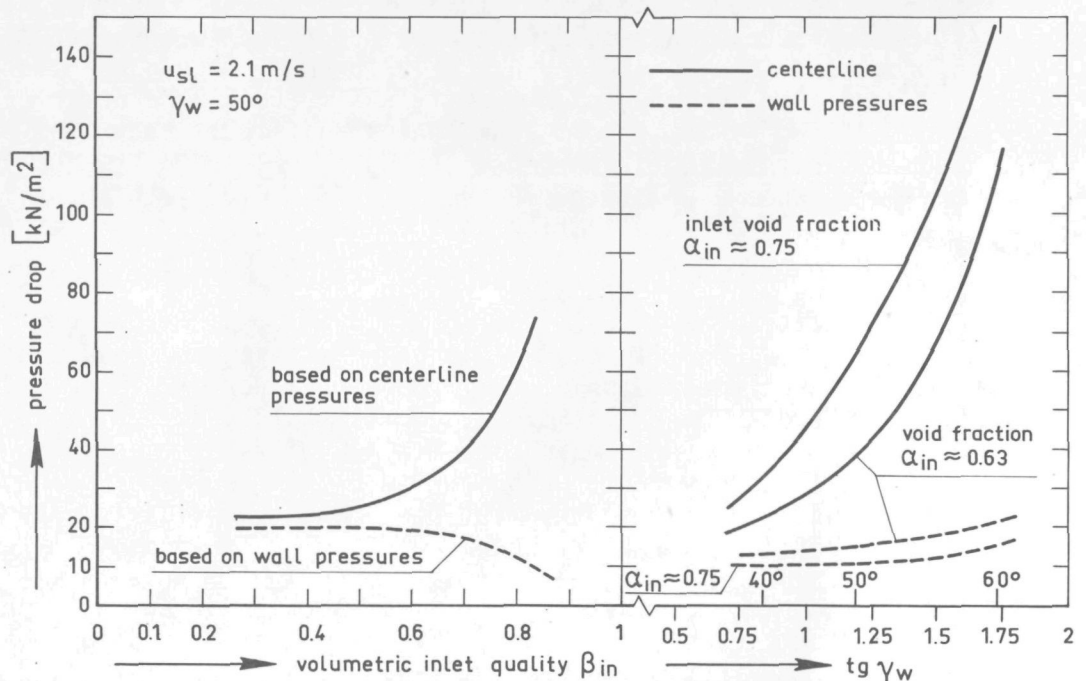


FIGURE 4-29

*Pressure drop over the separation section (guide vanes and confusor) of the converging test section*

(cf. the right hand part of figure 4-29) is almost completely determined by the radial pressure difference, corresponding to the very large radial pressure gradient  $\frac{\partial p}{\partial r}$  presented in figure 4-9. Since this latter difference causes separation of the phases, it is concluded that even for a converging vortex tube a significant part of the separator pressure loss - i.e. the centerline pressure difference - is utilized for separation rather than for acceleration of the mixture.

#### 4.4.6. Discussion

The above results lead to three main conclusions concerning separating performance:

- ★ a converging vortex tube is preferable over a cylindrical vortex tube because of the corresponding increase of tangential velocity. The resulting increase in radial pressure gradient leads to a reduction in separator length, while furthermore the radial distribution of separating performance - expressed in terms of compound efficiency -

becomes independent of the inlet quality. The only disadvantage is the concurrent increase in separator pressure loss, which, however, is not unduly large for moderate rotation intensities.

- \* single stage separation cannot satisfy both BWR requirements:  
 $\beta_E > 0.991$  and  $\beta_D < 0.048$
- \* a stable gas core is obtained after completion of the separation, hence the dispersion of the gas core observed by PRINS [1] must be attributed to different pressure drops of the two phases along the outlet paths. The solution of this problem should be given special attention in further venturi separator development.

While the first conclusion should make it worthwhile to develop a venturi separator as an improvement of existing separators with cylindrical vortex tubes, the second conclusion makes it clear that such a separator will have to be followed by a secondary stage. According to the economics of separator performance (cf. subsection 4.2.3.1.) priority should be given to satisfying the condition for downcomer quality ( $\beta_D < 0.048$ ). Moreover elimination of droplets from a gas stream appears less difficult than that of isolated bubbles from a liquid. It hence stands to reason to try and achieve the maximum downcomer quality requirement ( $\beta_D < 0.048$ ) in the first stage and to apply secondary separation to the mist flow leaving from the vortex finder. The consequences of this recommendation can be envisaged by considering measurements 3142 through 3145, covering the range of volumetric inlet qualities  $\beta_{in} = 0.50 - 0.88$  typical for BWR flow conditions (cf. figure 4-8). From figure 4-27 it appears that for measurement 3145  $\beta_D = 0.048$  at the radius  $r = 23.6$  mm; for a vortex finder with this inlet radius the downcomer quality  $\beta_D$  decreases with decreasing inlet quality down to  $\beta_D = 0.015$  for measurement 3142, whilst the corresponding exit quality  $\beta_E$  reduces from 0.945 down to 0.74. The latter value, however, is still expected to be in the mist flow range, considering also the gas core velocity of 25 m/s (cf. figure 4-20).

Notwithstanding the multitude of parameters involved it is possible to derive from the above data a set of design rules leading towards an optimal design for a first stage venturi separator.

The design starts by considering the radial void fraction gradient and separator pressure loss. In figure 4-23 the void fraction gradient  $\frac{\partial \alpha}{\partial r}$  for converging vortex tubes is seen to reach a limit for angles of blade deflection exceeding  $50^\circ$ , hence the maximum separating effect will be reached for  $50^\circ$ . In figure 4-29 the separator pressure loss appears to increase sharply with increasing blade deflection, requiring the lowest possible blade deflection. Selecting  $50^\circ$  blade deflection the maximum separating effect is obtained without undue pressure loss, i.e.  $50^\circ$  is the optimal angle of blade deflection.

The next step is to select a combination of throat diameter and separation length on the basis of measurements 314\*, referring to a blade deflection of  $50^\circ$ . From figure 4-14 it appears that for a throat diameter of 70 mm separation for the highest inlet quality (3145) is completed a few centimeters upstream of the end of the confusor, i.e. a separation length of about 35 cm. In view of the separator pressure loss, it is desirable to apply the largest possible throat diameter without, however, affecting the convergence of the vortex tube. A throat diameter of 80 mm is expected to serve both purposes well and will hence be marked as the optimal throat diameter. Compared to the measurements in the converging test section this enlarged throat diameter will cause an increase in separation length, estimated at around 45 cm.

The inlet radius of the vortex finder depends on the required separating effect for the application in question, and can be derived by comparison

with the separating characteristics for measurements 314\* (cf. figure 4-27). Using the definition of gas core radius given in subsection 4.4.5.2. i.e. the radius for which  $\alpha = 0.5$ , these measurements indicate relative radii of 0.55, 0.59 and 0.67 for a volumetric inlet quality  $\beta_{in} = 0.75$  for the straight, converging and venturi-shaped test section, respectively. By interpolation on the basis of throat diameter it is found that for a throat diameter of 80 mm the condition  $\alpha = 0.5$  occurs at the relative radius 0.574, and consequently corresponding separating characteristics in the transition zone are expected to occur at a relative radius  $\frac{0.574}{0.59} = 0.973$  times the relative radius of the converging test section, i.e. the actual radius has to be multiplied by  $0.973 \times \frac{80}{70} = 1.112$  to obtain qualities  $\beta_E$  and  $\beta_D$  equal to those appearing in figure 4-27.

For the remaining parts of the venturi separator, viz. the diffuser for the liquid outlet and the gas exhaust pipe, the third conclusion is in order, i.e. that equal pressure drops have to be achieved for both phases. The analysis of this requirement starts with the downcomer side: it is assumed - in accordance with BWR requirements - that the downcomer quality is low enough to approximate the flow as a single phase liquid. For the BWR conditions with equal liquid flow rate, i.e. conditions 1, 3, 5 and 7 as presented in figure 4-8, the downcomer flow is thus found to be independent of the inlet mixture, yielding a constant pressure drop along the water outlet path. In order to fulfill the requirement for equal pressure drop, the pressure drop along the gas exit path must also be constant for these flow conditions irrespective of the abovementioned variation in gas exit quality  $\beta_E$  and the associated variation of momentum flux. The only way to achieve this is by keeping the gas pressure drops zero under all conditions. For this purpose part of the gas exhaust pipe is designed as a diffuser whose pressure recovery - being proportional with the momentum flux - balances the frictional and exhaust pressure losses.

The water outlet path has to be designed accordingly: a slightly diffusing cross-section to overcome frictional, hydrostatic and exhaust pressure losses, yielding zero pressure drop. This design method annihilates one of the intended advantages of the venturi separator, viz. the pressure recovery in the diffuser part, but since the liquid layer is not accelerated in the confuser (cf. subsection 4.4.4.3.) this will not cause a major increase in total separator pressure loss.

Application of the above considerations to the optimal design for a first stage venturi separator with a 100 mm downscaled inlet diameter (cf. subsection 4.4.2.2.) and for a liquid mass flow rate equivalent with a superficial inlet velocity of 2.1 m/s - as derived in subsection 4.4.3.1. -, results in:

- a 50° angle of blade deflection
- a throat diameter of 80 mm
- a confuser length of 45 cm
- a vortex finder inlet radius depending on the actual separating requirements (for example  $1.112 \times 23.6 = 26.3$  mm to obtain  $\beta_D < 0.048$  for all mixture qualities)
- a slightly diverging gas exhaust pipe and water outlet path, both designed for zero pressure loss for all mixture qualities

The separating effect and pressure loss measured for such a venturi separator design\*) are discussed in the next section.

\*) The air-water separator discussed in section 4.5. deviates somewhat from the optimal geometry derived in this subsection for reasons explained in section 4.5.

## 4.5. Air-water separator test

### 4.5.1. Introduction

Prior to describing the air-water separator test two remarks appear in order for this separator:

- the separator tested is only a first stage device as described in section 4.4., i.e. no secondary separation was carried out to satisfy both BWR conditions: the development of a droplet separator for the gas exit is part of the continuing investigation not reported here
- the separator deviates from the optimal design described in subsection 4.4.6. in two respects:
  - the geometry of the converging vortex tube is intermediar between the optimal geometry and the converging test section of the introductory experiments (cf. subsection 4.5.3.1.), in order to obtain a better basis for comparison with the latter experiments.
  - the guide vane angle of deflection is  $45^{\circ}$  rather than  $50^{\circ}$ , for reasons discussed in subsection 4.5.3.3.

Within the continuing series of experiments for the development of a venturi separator for BWR conditions the test described hereafter should primarily be considered as an investigation on the performance and side effects of a vortex finder, not included in the introductory experiments. Therefore the design of the vortex finder inlet radius is not only meant to achieve an as good as possible separating effect, but is selected too to obtain a better insight in the vortex finder performance as a whole; the specific aspects for the vortex finder with respect to this goal are discussed in subsection 4.5.3.2.

### 4.5.2. Test facility

The same test facility was used as for the measurements described in subsections 2.3.1. and 4.4., except for the added possibility to measure the separated exit flows. Figure 4-30 shows how each of the two exiting gas flows, viz. the mist exhausted from the vortex finder and the carry-under air released from the free surface in the liquid collecting vessel, is passed through a mist separator. The air and water flows separated from the vortex finder exhaust are used to compute the gas exit quality, while the droplet removal from the carry-under air serves to dry the air before measurement; the water flow is only measured to yield an impression of the amount of liquid entrained from the free surface. For computation of the downcomer quality this air flow is combined with the entrained air released from the settling tank<sup>\*)</sup>.

The air and water flow measurements are discussed in some detail in subsection 4.5.4.

In order to simulate real separator conditions, where pressures at the vortex finder exhaust and liquid downcomer exit are identical, precautions were taken to equalize the test exhaust pressure  $p_{15}$  and  $p_{16}$  (cf. figure 4-30). This was done indirectly by equalizing the final pressures  $p_{17}$  and  $p_{18}$  and selecting large diameter piping for the blowdown lines connecting the pressure locations  $p_{15}$  and  $p_{16}$  to the exhaust manifolds A and B. Notwithstanding this precaution the pressure  $p_{16}$  was always found to be  $0.7 - 0.9 \text{ kN/m}^2$  in excess of pressure  $p_{15}$ ; this situation, however,

<sup>\*)</sup> *No water was ever collected in the mist separator installed in the air removal line from the settling tank.*

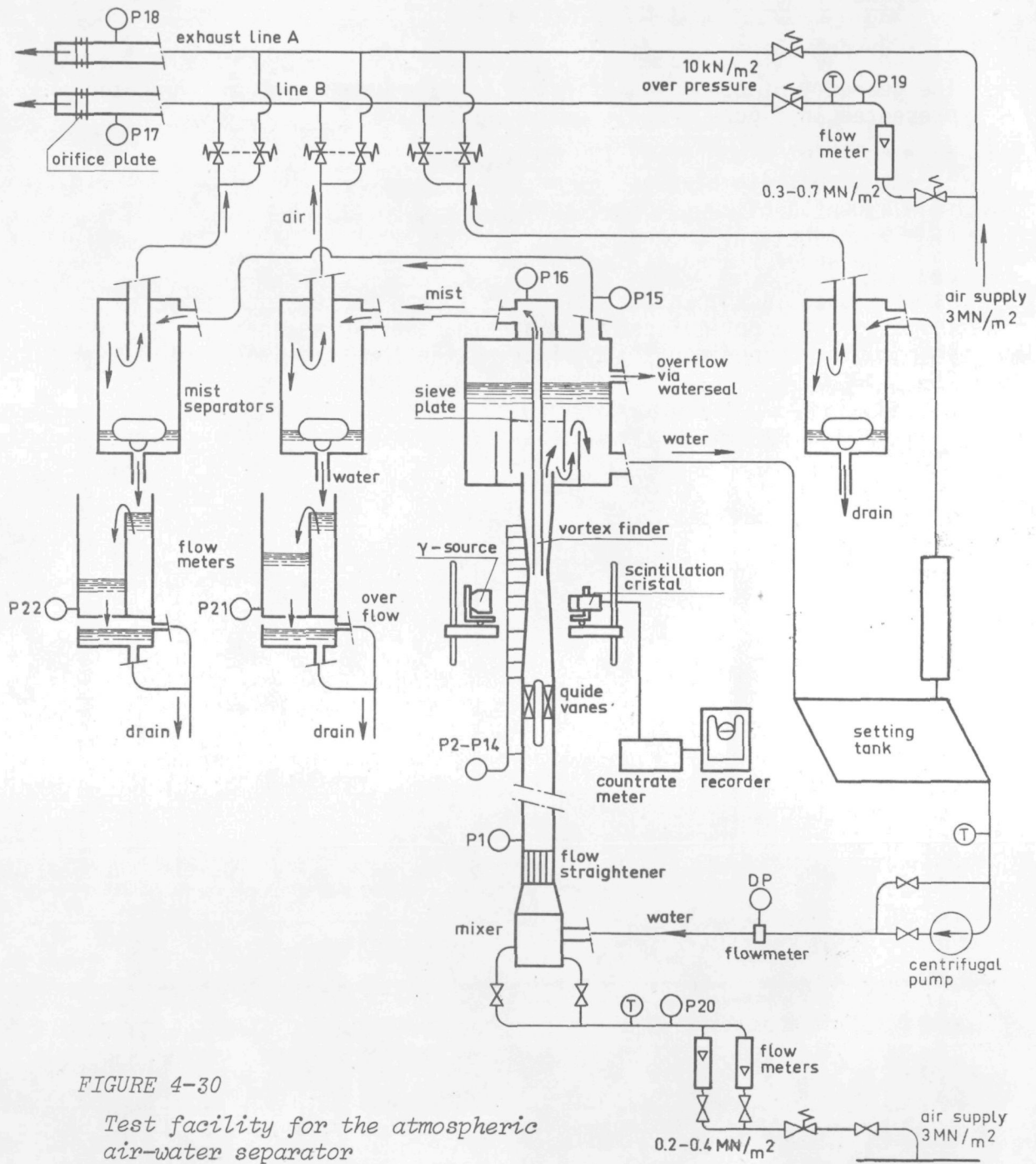


FIGURE 4-30  
 Test facility for the atmospheric  
 air-water separator

corresponds to a fictitious liquid level - at equal exhaust pressures - in the liquid collecting vessel 7 to 9 cm higher than the actual one, which represents a variation in level well within actual practice for BWR conditions.

#### 4.5.3. Separator geometry

##### 4.5.3.1. Channel shape

The geometry of the actual first stage air-water venturi separator as presented in figure 4-31 is characterized by:

- an inlet diameter of 100 mm
- a throat diameter of 75 mm
- a confusor length of 40 cm
- a slightly diffusing liquid channel, with an exit area exceeding the annulus area at the throat by 14.5%.

As mentioned in the introduction 4.5.1. the vortex tube geometry is chosen in between the optimal geometry and the converging test section of the introductory experiments. Considering the throat diameter of 80 and 70 mm

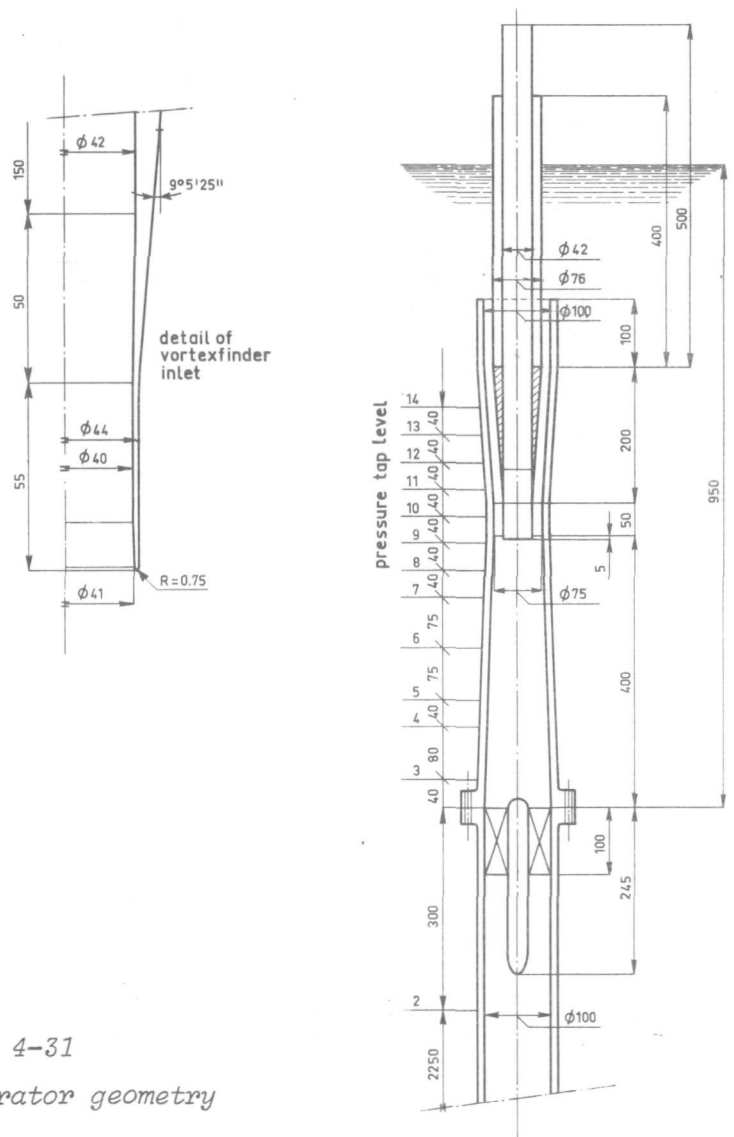


FIGURE 4-31  
Separator geometry

respectively, the actual throat diameter was taken 75 mm. In view of the dependence of the separation length on the throat diameter, viz. 35 cm for  $D = 70$  mm and 45 cm for  $D = 80$  mm (cf. subsection 4.4.6.), the length of the present vortex tube was taken 40 cm.

The slightly diffusing liquid channel is meant to overcome the pressure loss incurred by friction in the narrow gap between the wall and vortex finder and the hydrostatic pressure drop caused by 55.5 cm of water column above the level of the vortex finder inlet, as well as to compensate the effect of carry-under gas. The kinetic energy at the outlet is supposed to be completely dissipated in the water of the collecting vessel, and thus not taken into account for the diffuser design.

Because an outlet diameter of 100 mm is imposed by the design of the liquid collecting vessel a blank space is introduced between the gas exit pipe and the downcomer exit (cf. figure 4-31) in order to obtain the desired outlet area for the latter. For real separators no such blank space will of course be required.

#### 4.5.3.2. Vortex finder

The equivalent vortex finder inlet radius for the actual 75 mm throat is derived in the same way as discussed in subsection 4.4.6. for a 80 mm throat. Interpolation indicates that for the 75 mm throat the condition  $\alpha = 0.5$  should be reached for a relative radius 0.582, i.e.

$\frac{0.582}{0.59} \times \frac{75}{70} = 1.057$  times the absolute radius of the converging test section.

In order to fulfill the BWR carry-under condition  $\beta_D < 0.048$  the vortex finder inlet radius for the 70 mm throat of the converging test section has to be 23.6 mm as explained in subsection 4.4.6. Such an inlet radius - or its equivalent of  $1.057 \times 23.6 = 24.9$  mm for a 75 mm throat - yields, however, a rather low exit quality  $\beta_E$  for all flow conditions, preventing a conclusive answer with respect to the maximum obtainable gas core quality. In order to improve this situation a smaller inlet radius was selected, viz. 20.875 mm (cf. figure 4-31), corresponding to 20 mm in the converging test section.

To satisfy the design condition of zero pressure drop the gas exit pipe flares to 42 mm - over a length of 50 mm - to compensate the friction loss; the kinetic energy at the pipe outlet is - as for the liquid channel - supposed to be completely dissipated in the receiving vessel.

The vortex finder is designed to withdraw the gas core 5 mm upstream of the throat entrance. Some short tests were carried out - by vertical adjustment of the entire vortex finder - to verify by visual observation of the gas core entrance into the vortex finder and of the downcomer void fraction that this was indeed the optimum level for gas core removal.

#### 4.5.3.3. Blade profile

The required rotation intensity is obtained by guide vanes with an improved blade profile having an angle of deflection of  $45^\circ$  (cf. figure 4-32) instead of  $50^\circ$  selected for the optimal separator (cf. subsection 4.4.6.) with the blade design applied in the introductory experiments.

The improvement consists of a constant rate of deflection increase  $\frac{\partial \gamma}{\partial z}$

along the height of the blades, eliminating the high rate of deflection in the upper part of the original blade profile, and thus the obstruction to axial flow near the wall. In [131] it was found that the radial velocity

for single phase flow decreases by about 20% compared to the original design. The improvement over the original design was confirmed by two-phase computations with the ANALEST procedure for the separator tests [132], where a correction factor  $\zeta_b = 0.75$  was found to yield the best fit for the wall pressure; this value should be compared to  $\zeta_b = 0.65$  for the original design. Considering equation (3-63) for the tangential velocities - which for the straight blades (angle  $\delta = 0$ ) for both designs reduces to  $u_\phi(r,z) = \zeta_b u_z \text{tg}\gamma(r,z)$  - the present  $45^\circ$  angle of deflection yields  $u_\phi = 0.75 \times 1 \times u_z$  at the wall of the blade exit, while the original design with  $50^\circ$  angle results in  $u_\phi = 0.65 \times 1.19 \times u_z = 0.77 u_z$ . Thus the rotation intensity with the improved  $45^\circ$  blade profile is almost the same as for the  $50^\circ$  blades of the introductory experiments, as required for optimal separation.

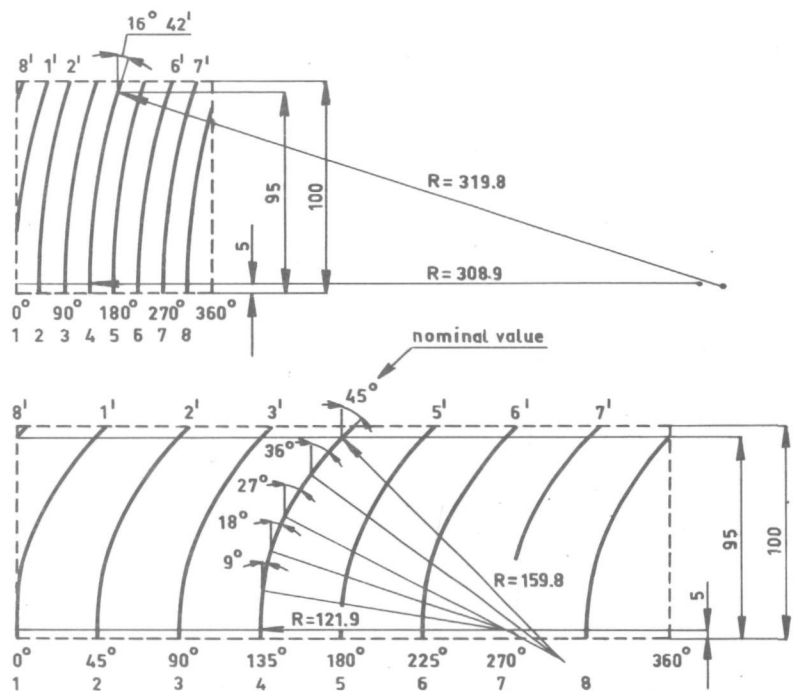


FIGURE 4-32

*Development at the wall and central hub of the separator guide vanes with a constant blade deflection rate*

#### 4.5.4. Data acquisition

Apart from the separated flow measurements the only difference with respect to the description in subsection 2.3.1.4. is in the number of cross-sections for which the void fraction distribution is measured. Because separating performance rather than detailed flow distribution form the main goal of the present tests, this number was reduced from ten to five cross-sections, viz. the levels 3, 5, 6, 7 and 9 (cf. figure 4-31).

The extension for the flow measurements of the separated air and water flows is essentially based on the same sorts of equipment. The drain flows are measured by an orifice plate in the bottom of each collecting vessel. The liquid height  $h$  is measured via the pressure ( $p_{21}$  and  $p_{22}$ , respectively) at the bottom of each vessel. The constant  $K$  in the formula

$$\phi_{ml} = K\sqrt{\Delta p} \quad (4-13)$$

is obtained by calibration for each of the measurement vessels. The downcomer water flow rate - exiting via the liquid collecting vessel - is derived by subtracting the sum of the separator mist water flows from the measured inlet water flow rate.

The measurement of the air flows - exiting from the mist separators - is much more complicated because the measurement itself may not affect the pressure distribution in the test facility and the separator outlets. The measurement procedure developed to achieve this requirement is described in appendix 4-B. In this appendix the relative measurement error is discussed to be rather high; especially for the downcomer gas flow. Therefore the standard deviation for each of the separating measurements is incorporated in the presentation of the resulting data in the next subsections.

#### 4.5.5. Scope of the separating tests

The main goal is to test the air-water separator under simulated BWR conditions. As apparent from figure 4-8 these flow conditions are related to the maximum flow capacity of the separator, i.e. the water flow ranges from 62 to 100% of the maximum, while the volumetric inlet quality  $\beta$  ranges from 0.55 up to 0.80. Therefore a first series of tests was carried out to determine the capacity corresponding to the optimal separating effect. This capacity will subsequently be considered the separator's rated condition, i.e. equivalent to condition 1 from figure 4-8. Nine of such preliminary tests were carried out, all having a volumetric inlet quality  $\beta = 0.78$  equivalent to  $x_{in} = 0.15$  for steam-water at  $7 \text{ MN/m}^2$ , i.e. the full power conditions for a General Electric BWR-6. The inlet superficial water velocity ranged from 1.3 to 2.9 m/s with intervals of 0.2 m/s.

The resulting volumetric exit and downcomer qualities are presented in figure 4-33. The exit quality  $\beta_E$  is seen to remain fairly constant between 0.981 and 0.987, equivalent to  $\bar{x} = 0.718$  to 0.789 for BWR conditions, but the volumetric downcomer quality  $\beta_D$  decreases significantly from 0.49 down to a minimum of 0.37 for  $u_{sl} = 2.5 \text{ m/s}$  (equivalent to  $x = 0.0452$  and 0.0281, respectively for BWR conditions).

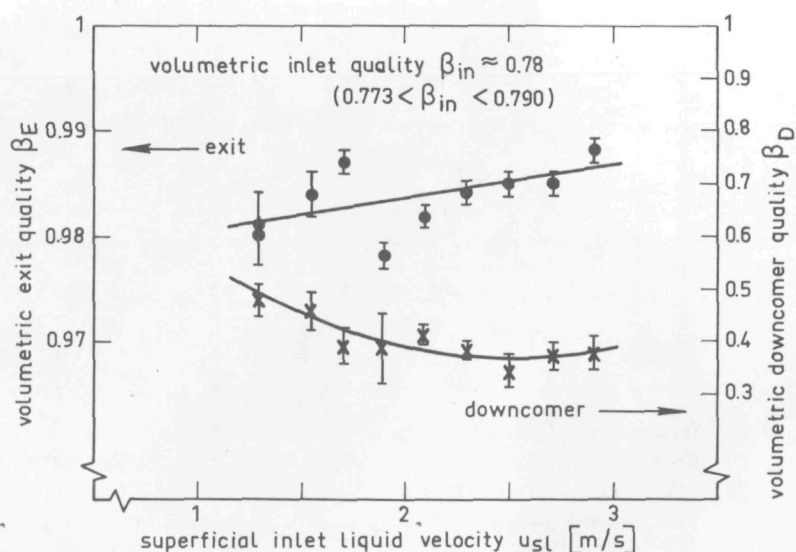


FIGURE 4-33

*Volumetric exit qualities for the primary separator tests*

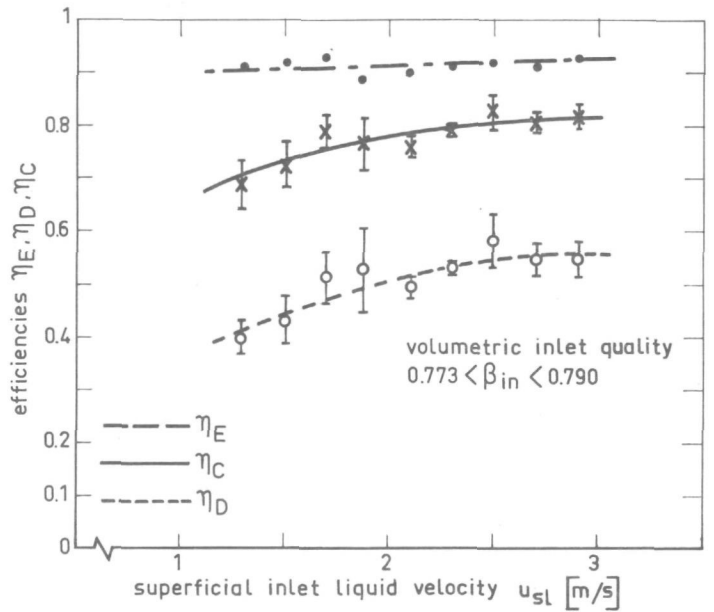


FIGURE 4-34

*Exit, downcomer and compound efficiency for the primary separator tests*

Because the minimum in the downcomer quality is not very pronounced the three efficiencies for the separating effect  $\eta_E$ ,  $\eta_D$  and  $\eta_C$  - defined in subsection 4.2.3. on a volumetric basis - were computed and are presented in figure 4-34. None of the three exhibits a pronounced maximum either, but the downcomer and compound efficiencies make it clear that the optimum separator capacity will be attained around a superficial inlet water velocity of 2.5 m/s.

Hence the rated separator capacity is taken around 2.5 m/s, viz. at  $\phi_{m1} = 20$  kg/s, corresponding to 2.55 m/s superficial inlet water velocity.

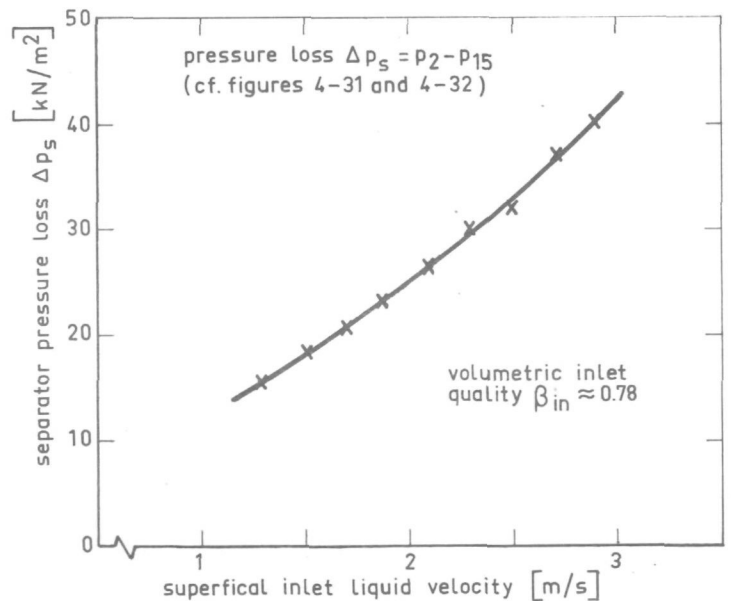


FIGURE 4-35

*Separator pressure loss for the primary separator tests*

water loading 20 kg/s ( $u_{s1} = 2.55$ m/s)			water loading 12.5 kg/s ( $u_{s1} = 1.59$ m/s)		
test number	qualities		test number	qualities	
	volumetric	equivalent BWR weight quality		volumetric	equivalent BWR weight quality
1	0.778	0.148	2	0.801	0.166
3	0.739	0.123	4	0.775	0.145
5	0.656	0.086	6	0.706	0.106
7	0.545	0.056	8	0.590	0.066

TABLE 4-36

*Separator test conditions*

For this capacity the separator pressure loss is about  $33 \text{ kN/m}^2$  according to figure 4-35, which appears a reasonable value.

The separator test proper consists of the simulation of the eight BWR conditions presented in figure 4-8 as 1 through 8. Of these conditions 1, 3, 5 and 7 are measured at the rated water capacity of 20 kg/s, and conditions 2, 4, 6 and 8 at the reduced capacity of 12.5 kg/s (62.5%). The corresponding volumetric inlet qualities - presented in table 4-36 - cover the full range of BWR volumetric qualities from 0.55 up to 0.80.

#### 4.5.6. Results

The results presented in this subsection focus exclusively on the separating performance. The results of the detailed flow computations in the confuser, using the ANALEST procedure ([132]) are only used to compare the measured outlet qualities with the computed ones; the local flow data were found to have the same characteristics as discussed in subsection 4.4.4. for the introductory measurements.

##### 4.5.6.1. Radial void fraction profiles

The radial void fraction profiles are presented in figure 4-37. They demonstrate the stability of the gas core in the presence of a vortex finder and confirm the completion of separation for the new venturi design and guide vane geometry.

Four out of the five measured distributions were selected for presentation. With respect to the core stability and completion of the separation especially levels 7 and 9 - 8.5 and 0.5 cm upstream the vortex finder inlet, respectively - are particularly relevant. For the lowest inlet qualities - measurements 7 and 8 - these two distributions are seen to be identical as far as the transition zone is concerned, indicating completion of the separation already at level 7 and stability of the core at least up to 0.5 cm ahead of the vortex finder inlet. For the somewhat larger inlet qualities of measurements 5 and 6 complete separation is achieved somewhat downstream of level 7. However, even for measurements 1 and 2, i.e. the highest inlet qualities, the rather small differences between the void fraction distributions at levels 7 and 9 indicate that complete separation is achieved at level 9.

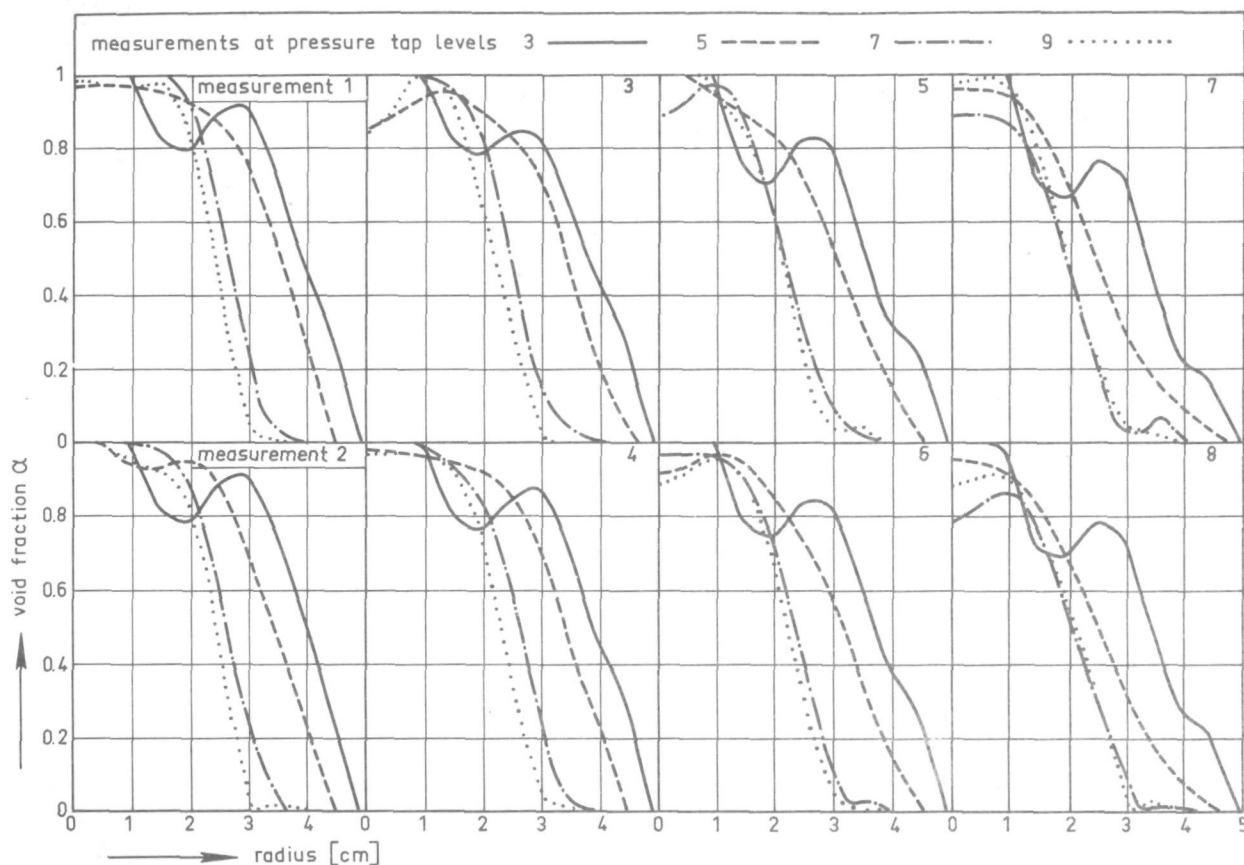


FIGURE 4-37

*Radial void fraction profiles in the confusor of the separator*

The steepness of the radial void fraction gradient  $\frac{\partial \alpha}{\partial r}$  and the void fraction value in the core at levels 7 and 9 indicate no dispersion on the gas core, in contrast to the remixing cores, reported by PRINS [1], of which the centerline void fraction decreases - sometimes down to 0.55 - preceded by gas core diameter increase immediately ahead of the vortex finder inlet. It is therefore concluded that the present design, by ensuring equal pressure drops for both outlet paths, prevents remixing and provides a stable gas core.

Comparison of the upper ( $\phi_{m1} = 20$  kg/s) and lower ( $\phi_{m1} = 12.5$  kg/s) rows of figure 4-37 shows that the void fraction distribution at the vortex finder inlet (level 9) is not affected by the water flow rate but only depends on the inlet quality. This fact is further discussed in subsection 4.5.6.3. on the separating performance.

#### 4.5.6.2. Axial pressure profile

In the present design the axial pressure drop at the wall between the vortex finder inlet ( $z = 2.945$  m) and the free surface in the liquid collecting vessel ( $z = 3.50$  m) must equal the radial pressure difference over the water layer at the vortex finder inlet level, because the gas core pressure is equal at these two levels. Thus the sharp pressure drop at the wall, evident in the profiles presented in figure 4-38, marks the vanishing radial pressure difference in the water exit path, i.e. the rapid dissipation of the tangential velocity in the narrow gap between outer wall and vortex finder. After this dissipation in the throat and the first part of the diffuser the axial pressure decreases only gradually.

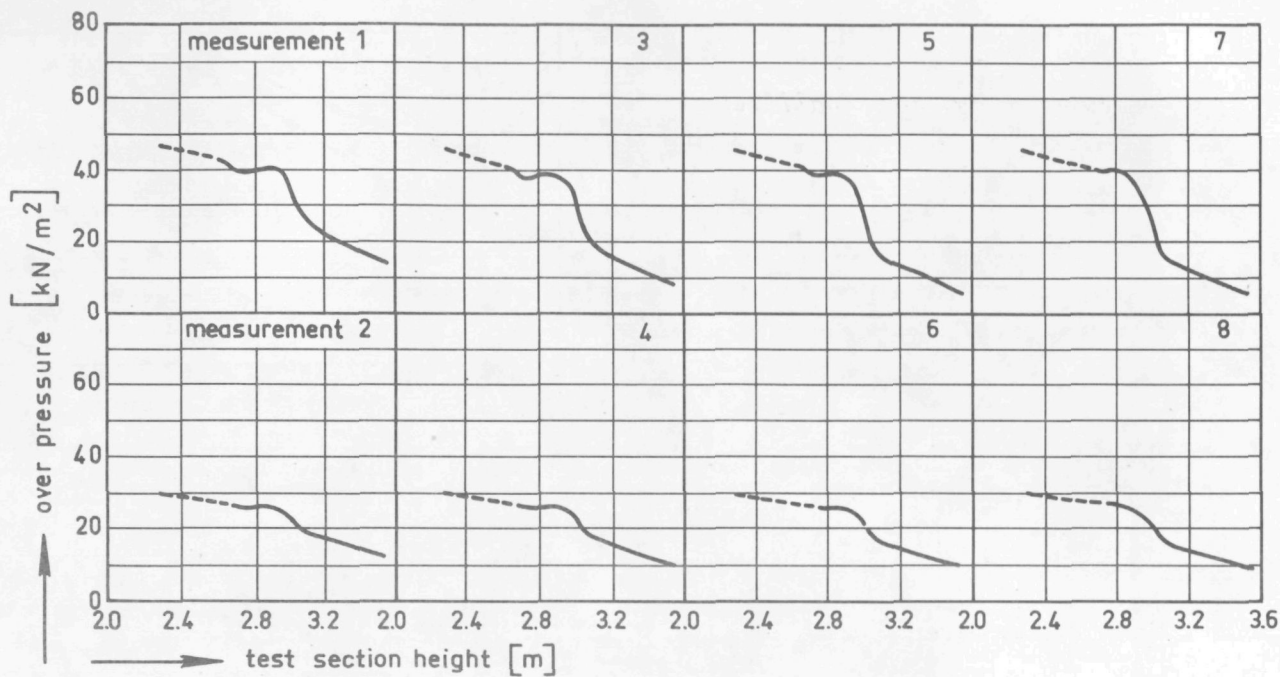


FIGURE 4-38

*Axial pressure profile at the wall of the separator*

It will be clear that this effect will be more marked at higher water flow rates, i.e. higher tangential velocities at the end of the confusor, a fact well borne out by the differences in pressure profile evident between the upper and lower rows of figure 4-38. Because the major part of separator pressure loss is seen to be caused by the radial pressure difference - being in turn the cause of phase separation - it is concluded that almost the full pressure loss is employed to obtain separation.

#### 4.5.6.3. Separator performance

The separator exit qualities are presented in figures 4-39 and 4-40 for gas and downcomer liquid, respectively. In addition to the measured volumetric qualities, figures are added for the equivalent weight qualities for steam-water mixtures at 7 MN/m<sup>2</sup> for the benefit of readers accustomed to BWR engineering practice.

The most striking fact to be gleaned from these figures is the significant worsening of the separating effect with decreasing liquid flow rate, evidenced by both lower gas exit qualities and higher downcomer qualities. While this fact is consistent with the lower rotation intensity corresponding to the lower flow rate, it is not predicted by the radial void fraction distributions of figure 4-37 seen to be quite similar for the two flow rates. No physical explanation - except dispersion of the gas core between measurement level 9 and the vortex finder inlet - was found for this discrepancy between exit qualities and void fraction distributions.

The maximum gas exit quality value  $\beta_E = 0.982$  measured for the rated BWR condition falls short of the BWR requirement  $\beta_E > 0.991$  in spite of the actual undersized vortex finder inlet (cf. subsection 4.5.3.2.). The computed exit qualities from ANALEST were found ([132]) to be in good

FIGURE 4-39A

Measured volumetric qualities

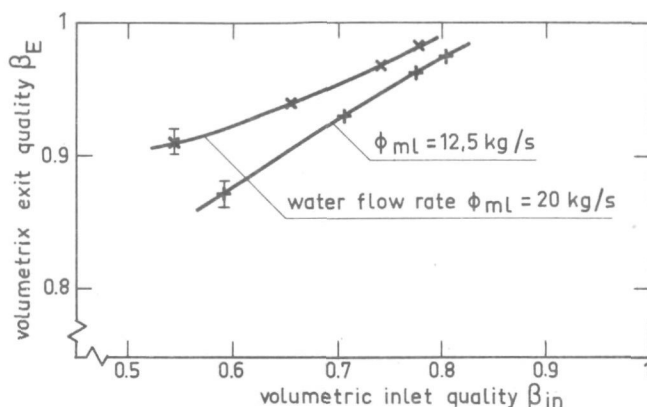


FIGURE 4-39B

Equivalent steam-water weight qualities at  $7 \text{ MN/m}^2$

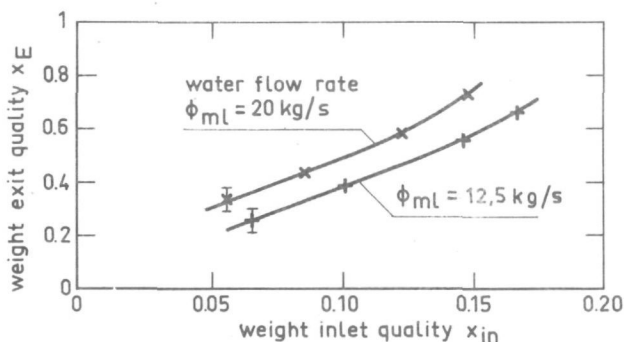


FIGURE 4-39

Gas exit qualities for the separator tests

agreement with the measurements; the relative error for  $(1-\beta_E)^*$  having a standard deviation of 19.2%, for  $(1-\beta_E)$  ranging from 0.018 up to 0.133. Apart from offering the conclusion that the void fraction limitation  $\alpha \leq 0.98$  for the ANALEST input does not impair the validity of the computations, this agreement confirms the finding of the introductory experiments that a single stage separator cannot satisfy the requirement  $\beta_E > 0.991$ .

The exit quality decreases for lower inlet qualities, as was to be expected from the decreasing gascore diameter observed in the introductory measurements (cf. subsection 4.4.5.2.); the lowest measured volumetric exit quality is 0.867.

The same decreasing trend with lower inlet qualities is found for the downcomer quality  $\beta_D$ , again in keeping with the introductory experiments (cf. subsection 4.4.5.4.). In figure 4-41 the measured values for  $\phi_{mL} = 20 \text{ kg/s}^{**}$  are presented together with the computed values obtained from the ANALEST procedure. The good agreement for the highest inlet quality (measurement 1) makes it likely that the ANALEST procedure yields reliable values for  $\beta_D$  and that the discrepancies at the lower inlet qualities may be due to a physical reason not covered by ANALEST.

\* ) The value  $(1-\beta_E)$  is a better measure for the error than  $\beta_E$  itself, because - for these high  $\beta_E$  values -  $(1-\beta_E)$  is almost equal to the ratio of the volumetric flows  $\frac{1-\beta_E}{\beta_E}$ .

\*\* ) A similar trend is found [132] for  $\phi_{mL} = 12.5 \text{ kg/s}$ .

FIGURE 4-40A

Measured volumetric qualities

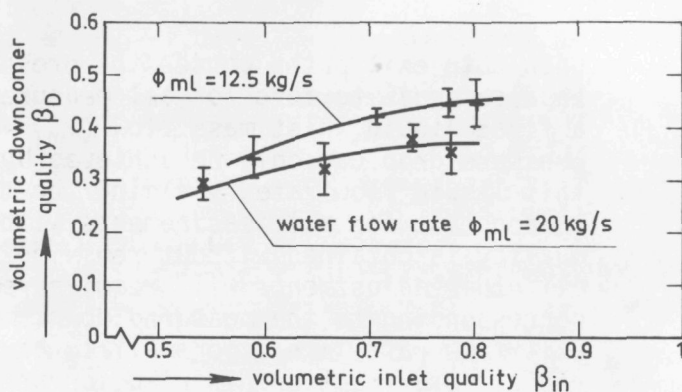


FIGURE 4-40B

Equivalent steam-water weight qualities at  $7 \text{ MN/m}^2$

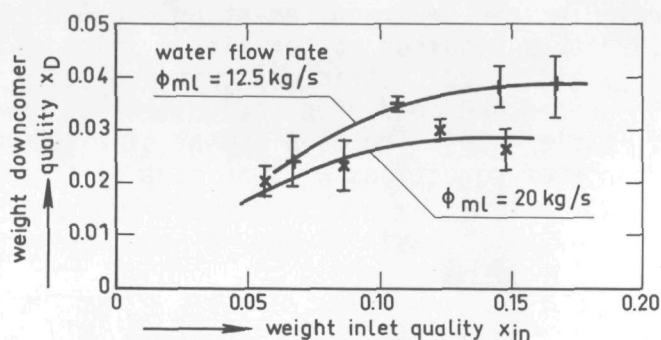


FIGURE 4-40

Downcomer qualities for the separator tests

Such a reason may be found in the fact that the ANALEST computations, being restricted to the confusor of the test separator, cannot take account of any subsequent unbalance between the gas and liquid pressure drop along the exit paths. Thus the ANALEST results represent the exit qualities should there be no remixing due to pressure drop unbalance. In view of the agreement between measured and computed quality for measurement 1 ( $\beta_{in} = 0.778$  and  $\phi_{ml} = 20 \text{ kg/s}$ ) it appears reasonable to attribute the discrepancies for the lower inlet qualities to small scale remixing of gas with the water layer. This tentative conclusion is lent credibility by the following reasoning: because the zero pressure drop over the gas exhaust pipe holds for all measurements due to its special design, the pressure balance forced

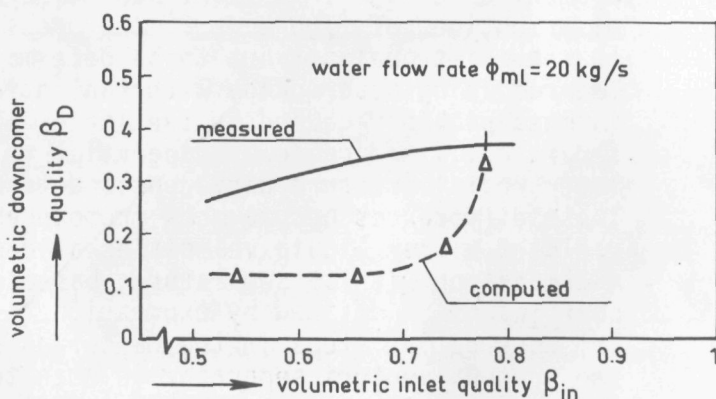


FIGURE 4-41

Comparison of measured and computed volumetric downcomer qualities

upon both exit paths causes the pressure drop along the downcomer gap to be also equal to zero for all measurements. For varying inlet qualities at a fixed liquid inlet mass flow ( $\phi_{ml} = 20 \text{ kg/s}$ ) this uniform downcomer pressure drop can only be achieved by adding a constant gas flow rate to this liquid flow rate, yielding the tendency to keep the downcomer quality  $\beta_D$  constant for all measurements with equal liquid flow rate. This downcomer quality is obtained without remixing for only one inlet mixture adjustment, all other adjustments will require remixing. The amount of remixed gas corresponding to the measured downcomer qualities is at most 13% of the gas exit flow rate, i.e. too small to cause a detectable change in the measured radial void fraction distribution at level 9 (5 mm upstream of the vortex finder inlet).

Because the downcomer qualities are highest for the low liquid flow rate  $\phi_{ml} = 12.5 \text{ kg/s}$ , these flow conditions will determine the vortex finder inlet radius for the final separator development required to satisfy the General Electric BWR requirement  $\beta_D \leq 0.048$ . On the basis of the computations in [132] this required vortex finder inlet radius is estimated between 29 and 30 mm, yielding volumetric gas exit qualities ranging from about  $\beta_E = 0.913$  for the rated BWR condition (adjustment 1) down to  $\beta_E = 0.735$  for adjustment 8 (cf. table 4-36). The development of a second stage droplet separator for this range of conditions will be part of future investigations not reported here.

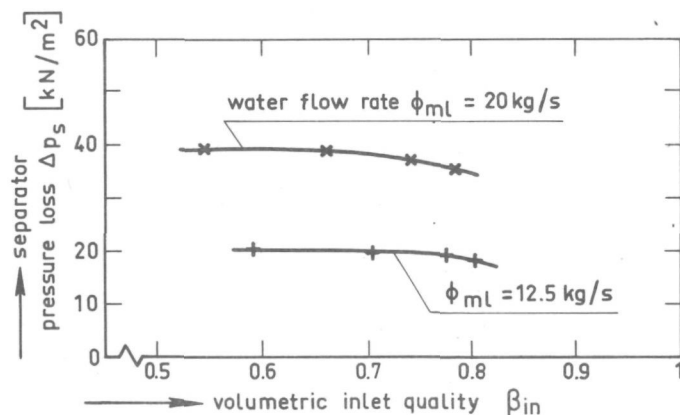


FIGURE 4-42

Separator pressure loss

The separator pressure losses, i.e. the pressure difference between tap 2 upstream of the guide vane hub and tap 15 above the free surface, are presented in figure 4-42. As was to be expected from the axial pressure distributions of figure 4-38 the pressure loss is seen hardly to depend on the inlet quality, but to be determined by the liquid flow rate alone. The resulting discrepancy with the introductory experiments (cf. figure 4-29) is most probably caused by the larger throat diameter of the actual separator, yielding lower tangential velocities at the throat and subsequently lower radial pressure differences determining the separator pressure losses. These differences become more pronounced for high volumetric qualities, yielding higher liquid velocities at constant superficial inlet velocity. A comparison with GE separators, based upon the specific pressure loss coefficient  $\zeta^*$  defined by expression (4-7), is presented in figure 4-43. The consecutive steps in the GE series show a continuous improvement, but the present venturi separator is seen to yield coefficients about half those of the GE separators. For the flow conditions of a third generation GE separator the present 100 mm venturi separator is expected to have a pressure loss of  $26.9 \text{ kN/m}^2$  as compared to  $52.6 \text{ kN/m}^2$  for the GE separator (cf. table 4-3).

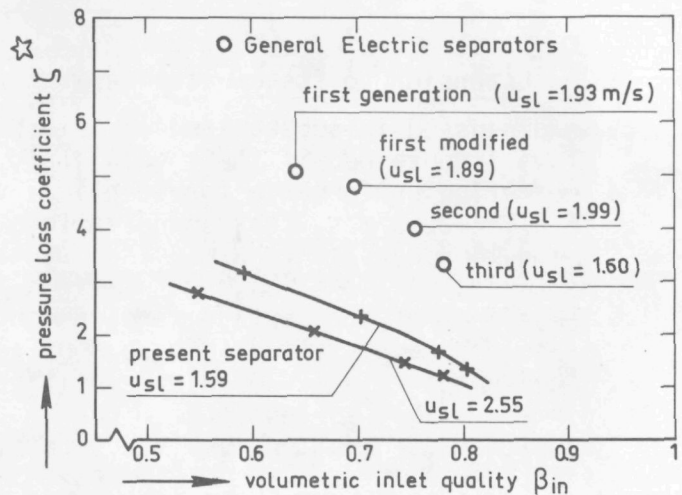


FIGURE 4-43

Comparison of specific separator pressure loss coefficients

Although the implementation of a second stage droplet separator in the venturi separator gas exit will undoubtedly affect the total separator loss, the present difference with the GE third generation separator appears sufficiently large to expect a lower pressure loss for the complete venturi separator.

#### 4.5.7. Discussion

##### 4.5.7.1. Air-water separator

For the tested separator (cf. figure 4-31) the BWR requirement for downcomer quality  $\beta_D \leq 0.048$  is satisfied for all BWR conditions by taking a vortex finder inlet with a radius between 29 and 30 mm.

The resulting gas exit qualities will range from  $\beta_E = 0.913$  down to 0.735, requiring a second stage droplet separator to satisfy the requirement  $\beta_E > 0.991$ , thus confirming the main conclusion of the introductory air-water measurements. In [133] several possible designs are proposed for such a droplet separator, which are not discussed here because their evaluation requires further experimental investigation. In order to maintain zero pressure drop along the gas exhaust path as a design property, the first part of the gas exhaust pipe should have sufficient flare for building up pressure increase capable of overcoming the pressure loss of the droplet separator.

The advantages of such a venturi separator are:

- almost constant downcomer quality  $\beta_D$  for all flow conditions, due to variable remixing for constant water flow rates. This is in contrast with the GE separators which are seen - in figure 4-4 - to have a relatively strong variation in carry-under
- total separator pressure loss is expected to be lower than in known GE separators for equal separating performance
- the specific volumetric liquid flow rate - based on the vortex tube area - of the tested separator is 59% in excess of the third generation GE separator ( $u_{sl} = 2.55$  versus 1.60 m/s). The absence of a downflow area, accounting for a 24% increase in cross-sectional area in the third generation separator, increases the specific loading - based on the built-in-area - to a factor of 1.98 compared to said GE separator.

In view of the above advantages it appears worthwhile to the author to proceed with the development of the venturi separator.

#### 4.5.7.2. Extension to steam-water separators

As discussed in subsection 4.4.3.1. similarity for air-water and steam-water flows is obtained if their volumetric flow rates are equal. Thus similar separating performance for identical volumetric inlet qualities is expected if  $u_{s1} = 2.55$  m/s, corresponding to a rated liquid flow rate of  $\phi_{m1} = 14.8$  kg/s at  $7$  MN/m<sup>2</sup>, is also taken for the high pressure steam-water mixtures.

The effect of the surface tension mentioned in subsection 4.4.3.1. will cause a somewhat slower progress of separation in steam-water mixtures, because the relative bubble velocities are smaller for the smaller bubble diameters, but is deemed of minor importance since for most of the flow conditions separation is already completed upstream of the vortex finder inlet.

A more significant difference is the absence of any significant gas expansion in the case of high pressure steam-water flows, causing a lower gas exit velocity and a somewhat smaller gas core diameter. Taking the volumetric quality as a measure for the void fraction, i.e. for the gas core diameter, the effect is seen to be rather small because the increase in volumetric quality for the air-water mixtures passing through the separator is only around 5%, yielding an estimated initial decrease of 2.5% in gas core diameter. This decrease, which will be enhanced by some secondary effects discussed in [134] yields in turn a larger liquid area, decreasing the liquid velocity and thus causing a lower axial pressure gradient due to the lower liquid layer acceleration (or perhaps larger liquid deceleration). Because this pressure gradient is the driving force for the relative axial velocity, the steam core velocity will be lowered with respect to the above initial increase, causing a countervailing effect to the decrease in steam core diameter. In view of these considerations the decrease in core diameter is estimated to be limited to 3 to 4%.

Apart from the steam core diameter the somewhat smaller volumetric quality at the venturi throat will also affect the width of the transition zone between gas core and water layer, directly affecting the separation effect. In order to determine the trend of this effect it is for comparison related to the trends for a smaller volumetric quality observed for the introductory air-water experiments. In figure 4-23 the radial void fraction gradient  $\frac{\partial \alpha}{\partial r}$  - reciprocal to the width of the transition zone - is seen to decrease with decreasing volumetric quality. The increase in transition zone width to be expected from this comparison also follows from the trend in Froude number (cf. figure 4-25) discussed in subsection 4.4.5.3. There the increase in Froude number for lower volumetric qualities was found to be related to an increase in transition zone width.

Although the increase in transition zone width is expected to be only small it will lower the separating effect for steam-water mixtures. In view of the proposition to satisfy the BWR requirement  $\beta_D < 0.048$  under all conditions, this effect will probably result in a further reduction in gas exit quality  $\beta_E$  and thus increase the performance requirements of the second stage droplet separator to be developed.

With respect to the separator pressure loss there is no reason to expect significant deviations from the values for  $\zeta^*$  presented in figure 4-43. Because the two-phase momentum  $M_{tp}^*$  - defined by expression (4-6) - is hardly affected by the gas density, it is - for equal volumetric qualities - proportional to the liquid density and hence the separator pressure loss too. On this basis the maximum steam-water separator pressure loss will be  $29.0$  kN/m<sup>2</sup> rather than  $39.2$  kN/m<sup>2</sup> as apparent from figure 4-42 for the air-water separator.

In view of the above discussion it is concluded that application of the venturi separator to steam-water mixtures will - apart from a significantly lower pressure loss - cause only minor changes with respect to the tested separator as long as the volumetric water and steam flows are taken equal to the corresponding water and air values. Hence the characteristics and advantages described in subsection 4.5.7.1. remain valid for steam-water separators.

#### 4.5.7.3. Size extrapolation

In order to lower manufacturing costs the number of separators should be kept to a minimum, which can be obtained by increasing the dimensions of the separator. As an example the consequences are investigated of size extrapolation of the venturi separator from the present inlet diameter of 100 mm to 216 mm; the vortex tube diameter of the GE separators. For this purpose all other dimensions are assumed to be upscaled by the same factor of 2.16. The blade deflection shall be maintained at its nominal value of  $45^\circ$ , while similarity for the mixture adjustments is obtained by taking the same superficial gas and liquid velocities as for the tested 100 mm venturi separator.

Because the radial pressure difference is the determining factor for both separating effect and separator pressure loss the discussion is concentrated on the effect of the above scaling for this flow parameter. The radial pressure gradient is evaluated on the basis of the radial mixture momentum balance: summation of the phase balances (3-6) and (3-9), with the acceleration and viscosity terms omitted for simplicity, yields:

$$\frac{\partial p}{\partial r} = (1-\alpha)\rho_l \frac{u_{l\varphi}^2}{r} + \alpha\rho_g \frac{u_{g\varphi}^2}{r} \quad (4-14)$$

Considering that the tangential velocities initially remain unchanged due to the unchanged axial velocities and equal blade deflection, and that the void fraction will also remain unchanged due to the equality of the volumetric quality, it appears that the radial pressure gradient is inversely proportional to the radius, i.e. reduced by a factor 2.16. Because the liquid layer thickness is increased with the same factor the radial pressure difference remains unchanged, yielding a separator pressure loss initially independent of the upscaling.

On the basis of the equal radial pressure difference at the throat and the experimental result of almost constant wall pressure in the confusor, it is concluded that the axial pressure difference at the centerline will also remain unchanged. In combination with the increase in confusor length it follows that the axial pressure gradient  $\frac{\partial p}{\partial z}$  decreases by a factor 2.16 at the centerline. Through the axial momentum balances (3-7) and (3-10) this is expected to reduce the drag force (and other terms), yielding lower relative and gas velocities and thus an increase in mean void fraction, i.e. increased gas core diameter. Furthermore the radial void fraction gradient  $\frac{\partial \alpha}{\partial r}$  in the transition zone between gas core and liquid layer will be lowered due to the reduced pressure gradient  $\frac{\partial p}{\partial r}$ , but as long as the transition zone width is also enlarged by a factor 2.16 the separating effect is expected to remain unchanged.

A second aspect of separation is the radial gas velocity through the liquid layer, determining the required separation length. Substitution of the pressure gradient expressed by equation (4-14) in the radial gas momentum balance (3-6), and neglection of the acceleration terms yields:

$$F_{Dr} = -\alpha(1-\alpha)\left\{\rho_l \frac{u_{1\varphi}^2}{r} - \rho_g \frac{u_{g\varphi}^2}{r}\right\} \quad (4-15)$$

Substitution of expression (3-13) for  $F_{Dr}$  gives:

$$\frac{C_D}{4} \frac{d}{d} \rho_l u_{rt} u_{rr} = - (1-\alpha)\left\{\rho_l \frac{u_{1\varphi}^2}{r} - \rho_g \frac{u_{g\varphi}^2}{r}\right\} \quad (4-16)$$

Because the resultant relative velocity  $u_{rt}$  is strongly dominated by the axial relative velocity  $u_{rz}$ , i.e. almost independent of the radial relative velocity  $u_{rr}$ , this latter radial velocity appears - for initially unchanged void fraction and tangential velocities - to be inversely proportional to the actual radius, i.e. decreases with the upscaling factor 2.16. By contrast completion of the separation in the scaled length requires an unchanged relative radial bubble velocity, because both the distance through the liquid layer and the residence time in the confusor increase by a factor 2.16. Thus it is concluded that the separation length becomes significantly larger than the scaled confusor length.

This latter effect is considered to be unacceptable, and therefore the blade deflection will have to be redesigned to yield a higher rotation intensity and thus decreases the separating length. The tangential velocity is increased by a factor equal to the square root of the scaling factor  $\sqrt{2.16} = 1.47$ . For this purpose the tangent of the angle of deflection is increased by a factor 1.47, i.e. the angle of deflection becomes  $55^{\circ}46'$  rather than  $45^{\circ}$ . This increase in tangential velocity by a factor  $\sqrt{2.16}$ , yields with respect to the unscaled 100 mm venturi separator:

- a proportionally upscaled separation length, due to the fact that the radial bubble velocity through the liquid layer remains unchanged
- an improved separating effect due to the unchanged radial pressure gradient, which latter is expected to yield an unchanged transition zone width, i.e. a width decreased relatively to the scaled liquid layer and gas core dimension. Some uncertainty exists on this separating improvement because in the introductory measurements increasing blade deflection above  $50^{\circ}$  was found to have a limited effect on the radial void fraction gradient in the transition zone (cf. figure 4-23)
- an unchanged axial pressure gradient  $\frac{\partial p}{\partial z}$  at the centerline, keeping the mean void fraction equal and scaling the gas core diameter proportionally
- a separator pressure loss increased by a factor 2.16. The corresponding increase - by a factor 2.16 - of the specific pressure loss coefficient  $\zeta^*$  yields coefficients almost exactly equal to the values for GE separators (cf. figure 4-43) eliminating the pressure loss advantage of the venturi separator.

In summary it is concluded that multiplying the tangent of the angle of deflection by the square root of the dimensional scaling factor, results in a slightly improved - or at least unchanged - separating performance, but increases the separator pressure loss proportional with the dimensional scaling factor.

## 5. CONCLUSIONS

Two of the three objectives of this study formulated in the introduction were only partly attained.

The investigation on the interaction forces in bubble swarms did result in correlations for the drag force and virtual mass coefficients applicable to the numerical solution of the momentum balances. The validity of these correlations for bubble swarms was experimentally verified on both atmospheric air-water mixtures and high pressure steam-water mixtures (up to  $7 \text{ MN/m}^2$ ). Thanks to the development of a correlation for bubble diameters it was possible to identify the effect of void fraction on the drag force coefficient, which could be defined by a single simple expression valid for the entire range of experiments. Despite this experimentally proven validity of the drag force correlation the significant difference with an expression of the same kind developed for swarms of solid particles, occurring e.g. in fluidization and sedimentation, remains an open question.

The virtual mass coefficient for bubble swarms was found to depend on both the void fraction and a second parameter, the peak velocity ratio. The dependence on this latter, newly introduced parameter and hence implicitly on fluid properties covers the full range of the present experiments. In addition it was also proven valid for potential flow around submerged Rankine bodies. The experimentally found dependence of the virtual mass coefficient on the void fraction is in agreement with analytically derived expressions.

The development of the so called ANALEST procedure for computation of rotating gas-liquid flows on the basis of differential mass and momentum balances was not completed. Only seven out of the eight flow variables can at present be computed; the void fraction distribution has to be provided as input to the computer program. However, even in its present state, the procedure proved a powerful tool for obtaining detailed information on separator flows. Comparison with measured pressure distributions of separator flows and exit qualities after separation show general agreement. Further development of this procedure aimed at computation of all eight flow variables is worthwhile and is under way.

By contrast a computer program based on the alternating direction implicit (ADI) method failed because it requires at least several centuries of computation time. The cause of this excessive computation time was found to be inherent to the combined characteristics of gas-liquid flows and the ADI method.

The venturi separator design tested in the present investigation can only serve as a first stage because it cannot satisfy both BWR separation requirements, viz. maximum downcomer and minimum gas exit quality. It is recommended to fulfill the downcomer requirement with this first stage separation and to develop a droplet separator for the gas exit. Such a first stage venturi separator has the advantage of almost constant downcomer quality over the entire range of BWR conditions. The separating effect is discussed to remain unchanged for application to steam-water mixtures compared to the actual atmospheric air-water tests. Design rules are provided to translate the separating effect obtained on reduced scale separators to full-scale separators.

The separator pressure loss of the actual 100 mm inlet diameter venturi separator is found to be far lower than that of existing General Electric separators, but - because of the proportionality of the separator pressure

loss with the vortex tube radius - this advantage is eliminated for venturi separators with an inlet diameter upscaled to 216 mm, i.e. equal to the vortex tube diameter of GE separators.

## ACKNOWLEDGEMENTS

The author wishes to express his thanks to all those who took an active part in the work, which was carried out in the Laboratory for Thermal Power Engineering of Delft University of Technology.

The many hours invested by Messrs. C.A.C.M. van den Bergh, L.C. Boogaars, C.M. van Dissel, A.C. Groot, G.J. Jonk, J. Kerkhof, F.C.J. Kroos, W. Landlust, C. Pronk, M.A. Terveer, A.J.J. Vincenten and C.J. Vis in construction, maintenance and operation of the test loops are gratefully acknowledged, as is the participation of Messrs. A.T.G. Maissan and W.A.J. Middelkoop in the design of these facilities.

Thanks also goes to the students Len Leyten, Nol Herfkens, Henk Hagreis, Jan van Bekkum, Henk Siteur, Hans Hogenes, Peter Stoop, Peter van Bruggen, André Christiaan, Jos Jehee, Jan Janssen and Peter Koelemij, who in the course of their studies built a 60 cm pile of reports in gathering experimental data and all sorts of information as a firm base mainly for the chapters 3 and 4.

Special thanks are due to Mrs. G.C.M. Mollet and Miss A.A. Douw who were responsible for the typing of the manuscript and to Messrs. G.J. Brouwer, F.A.M. van der Linden and M.G.P. Wessling for their dedication in drawing the figures and graphs.

The author feels indebted to Dr. J.J. Kalker and Mr. A.B.W. de Ruiter of the Department of Applied Mathematics, Delft University of Technology, for supplying the underlying thoughts of the specific application of the ADI method to the present two-phase problem and the development of the corresponding computer program, respectively.

The author is very grateful for the many discussions and valuable suggestions from the members of the laboratory staff. Special mention should be made of the interest and time given by Mr. R. van der Welle, who took a very active part - both before and after his graduation - in the development of the ANALEST procedure, and of the discussions with Mr. B. Vriesema on the physical aspects of two-phase flow.

Last but not least thanks go to Mr. A. Korving, who was responsible for a large part of the design of the instrumentation and automatization of the test loops. The author is very much indebted to him for the dedication he showed in the many aspects of his work for the project ranging from instrument calibration to operation of both loops including the computer data reduction.



## REFERENCES

1. Prins, C.A. Aspects of two-phase, gas-liquid, separation related to nuclear steam supply systems. Ph.D. Thesis. Delft Univ. of Techn. (1971)
2. Martinelli, R.C. and Nelson, D.B. Prediction of pressure drop during forced circulation boiling of water. Trans. ASME, Journ. Heat Transf., 70(1948), pp. 695-702
3. Lockhart, R.W. and Martinelli, R.C. Proposed correlation of data for isothermal two-phase, two-component flow in pipes. Chem. Eng. Progr., 45(1949), pp. 39-48
4. Bankoff, S.G. A variable density single fluid model for two-phase flow with particular reference to steam-water flow. Trans. ASME, Journ. Heat Transf., 82(1960), pp. 265-272
5. Rotta, J.C. Turbulent shear layer prediction on the basis of transport equations for the Reynolds stresses. Conf. on theoretical mechanics. Moscow (1972)
6. Johnsson, J.E., Clift, R. and Grace, J.R. Prediction of bubble distributions in freely bubbling two-dimensional fluidised beds. Symposium multi-phase flow systems, Inst. Chem. Eng. Symposium Series 38, Glasgow (1974)
7. Wallis, G.B. One-dimensional two-phase flow. McGraw-Hill Book Co., New York (1969)
8. Schmidt, E. Properties of water and steam in SI-units. Springer Verlag Berlin (1969)
9. Hinze, J.O. The virtual added mass of a discrete particle in an unsteady flow field. I.U.T.A.M. symposium on flow of fluid-solid mixtures, Cambridge (1969)
10. Prins, C.A. Momentum flow in two-phase flow. Trans. ASME, Journ. Heat Transf., 91 (1969), pp. 454-455
11. Rose, S.G. and Griffith, P. Flow properties of bubbly mixtures. ASME paper no. 65-HT-58 (1965)
12. Wisman, R. Analytical pressure drop correlation for an adiabatic vertical two-phase flow. Appl. Sci. Res., 30 (1975), pp. 367-380
13. Schlichting, H. Boundary layer theory. McGraw-Hill Book Co., New York (1960)

14. Soo, S.L. Fluid dynamics of multiphase systems. Blaisdell Publ. Co., Waltham (1967)
15. Hadamard, J. Compt. Rend. Acad. Sci. Paris, 152 (1911), pp. 1735-1738
16. Rybcynski, W. Bull. Acad. Sci. Cracovic, A (1911), pp. 40-46
17. Levich, V.G. Psysicochemical Hydrodynamics Prentice-Hall, (1962)
18. Moore, D.W. The rise of a gas bubble in a viscous liquid. Journ. of Fluid Mech., 6 (1959), pp. 113-130
19. Chao, B.T. Motion of spherical gas bubbles in a viscous liquid at large Reynolds numbers. Phys. of Fluids, 5 (1962), pp. 69-79
20. Haberman, W.L. and Morton, R.K. An experimental study of bubbles moving in liquids. Trans. ASCE, 121 (1956), pp. 227-252 (First reported in David Taylor Model Basin Report 802 (1953))
21. Rosenberg, B. David Taylor Model Basin Report 727 (1950)
22. Davies, R.M. and Taylor, G.I. The mechanics of large bubbles rising through extended liquid and through liquids in tubes. Proc. Royal. Soc. London, 200 series A(1950), pp. 375-390
23. Peebles, F.N. and Garber, H.J. Studies on the motion of gas bubbles in liquids. Chem. Eng. Progr. 49 (1953), pp. 88-97
24. Aybers, N.M. and Tapucu, A. The motion of gas bubbles rising through stagnant liquid. Wärme- und Stoffübertragung, 2 (1969), pp.118-128
25. Baker, J.L.L. and Chao, B.T. An experimental investigation of air bubble motion in a turbulent water stream. A.I.Ch.E. Journ., 11 (1965), pp. 269-273
26. Reichardt, H. Vollständige Darstellung der turbulenten Geschwindigkeitsverteilung in glatten Leitungen. Zeitschr. für angewandte Mat. und Mech., 31 (1951), p. 208
27. Steam separation technology under the Euratom program, Primary separation by natural separation. Topical report-part I, ACNP-65002 (1965)
28. Moen, R.H. Radial vane steam separator development, Final Report-Phase II. GEAP-5655 (=EURAE C 2060), (1968)

29. Untersuchungen an Zyklonen zur Dampfabscheidung in Siedewasserreaktoren. Abschlussbericht. Teil II. Okt. 1968 bis. Dez. 1969. EURAEC-2144 (=EUR-4033), (1970)
30. Brandes, H. Experimentelle Untersuchungen an Fliehkraftabscheidern. Dissertation Tech. Univ. Hannover (1970)
31. Richardson, J.F. and Zaki, W.N. Sedimentation and fluidisation; part I. Trans. Inst. Chem. Eng., 32 (1954), pp. 35-53
32. Ergun, S. Fluid flow through packed columns. Chem. Eng. Progr., 48 (1952), pp. 89-94
33. Mertes, T.S. and Rhodes, H.B. Liquid-particle behaviour. Chem. Eng. Progr., 51 (1955), pp. 429-432 and pp. 517-522
34. Zuber, N. and Hench, J.E. Steady state and transient void fraction of bubbling systems and their operating limits, part I: Steady state operation. General Electric Report No. 62GL100 (1962)
35. Hench, J.E. and Johnston, J.P. Two-dimensional diffusor performance with subsonic, two-phase, air-water flow. APED-5477 (1968)
36. Smissaert, G.E. Two-component two-phase flow parameters for low circulation rates. Argonne Nat. Lab. Report ANL-6755 (1963)
37. Zuber, N. and Findlay, J.A. Average volumetric concentration in two-phase flow systems. Trans. ASME, Journ. Heat Transf., 85 (1965), pp. 453-468
38. Petrick, M. A study of vapor carry-under and associated problems. Argonne Nat. Lab. Report ANL-6581 (1962)
39. Lamb, H. Hydrodynamics. Dover Publications Inc., New York (1945) (Reprint from Cambridge University Press, Cambridge (1932))
40. Milne-Thomson, L.M. Theoretical hydrodynamics. MacMillan & Co., London (1968)
41. Hinze, J.O. Stromingsleer: voortgezette cursus. (lecture notes on advanced fluid dynamics). Delft Univ. of Techn. (1965)
42. Zuber, N. On the dispersed two-phase flow in the laminar flow regime. Chem. Eng. Sci., 19 (1964), pp. 879-917

43. Wijngaarden, L. van Hydrodynamic interaction between bubbles in a dilute gas bubble/liquid mixture. Journ. Fluid Mech., 77 (1976), pp. 27-44
44. Moody, L.F. Friction factors for pipe flow. Trans. ASME, Journ. Heat Transf., 66 (1944), pp. 671-684
45. Dukler, A.E., Wicks, M. and Cleveland, R.G. Frictional pressure drop in two-phase flow  
Part A: A comparison of existing correlations for pressure loss and holdup.  
Part B: An approach through similarity analysis.  
A.I.Ch.E. Journ., 10 (1964), pp. 38-51
46. Malnes, D. Slipratios and friction factors in the bubble flow regime in vertical tubes. Kjeller report KR-110 (1966)
47. Cravarolo, L. et al A device for measurements of shear stress on the wall of a conduit, its application in two-phase adiabatic vertical flow. CISE, EUREAC 930 (1964)
48. Niese, R.W. Het meten van de wandschuifspanning bij twee-fasenstroming (in Dutch). SWST-20, Lab. for Thermal Power Eng., Delft Univ. of Techn., (1968)
49. Hewitt, G.E. and Roberts, D.N. Studies of two-phase flow patterns by simultaneous x-ray and flash photography. United Kingdom Atomic Energy Authority, AERE-M2159 (1969)
50. Wisman, R. Invloed van interactiekrachten op twee-fasen stromings wandwrijving (in Dutch). KR-memo-74-1 (=SWST-memo-16). Lab. for Thermal Power Eng., Delft Univ. of Techn., (1974)
51. Stoop, P.M. Onderzoek naar het wandwrijvingsdrukverlies bij twee-fasenstroming (in Dutch). KR-440 (=SWST-39), Lab. for Thermal Power Eng., Delft Univ. of Techn., (1975)
52. Muscettola, M. Two-phase pressure drop - comparison of the momentum exchange model and Martinelli and Nelson's correlation with experimental measurements. AEEW-R 284, (1963)
53. Janssen, E. and Kervinen, J.A. Two-phase pressure drop in straight pipes and channels; water-steam mixtures at 600 to 1400 psia. GEAP-4616 (AEC report), (1964)

54. Moore, T.V. and Wilde, H.D. Experimental measurement of slippage in flow through vertical pipes. AIME, Petroleum development and technology, New York Meeting (1931)
55. Hinze, J.O. Fundamentals of the hydrodynamic mechanism of splitting in dispersion processes. A.I.Ch.E. Journ., 1 (1955), pp. 289-295
56. Sevik, M. and Park, S.H. The splitting of drops and bubbles by turbulent fluid flow. Trans. ASME, Journ. of Fluids Eng. 1 (1973), pp. 53-60
57. Batchelor, G.K. Pressure fluctuations in isotropic turbulence. Proc. Cambridge Phil. Soc., 47 (1951), pp. 359-374
58. Hinze, J.O. Momentum and mechanical-energy balance equations for a flowing homogeneous suspension with slip between the two phases. Appl. Sci. Res., A11 (1962), pp. 33-46
59. Clay, P.H. The mechanism of emulsion formation in turbulent flow. Proc. Royal Acad. of Science (Amsterdam), 43 (1940), pp. 852-865
60. Kottler, F. Distribution of particle sizes. Journ. Franklin Inst., 250 (1950), part 1: pp. 339-356, part 2: pp. 419-441
61. Masters, K. Spray drying. Leonard Hill Books, London (1970)
62. Mugele, R.A and Evans, H.D. Droplet size distribution in sprays. Ind. Eng. Chem., 43 (1951), pp. 1317-1324
63. Nikuradse, J. Untersuchungen über die Strömung des Wassers in konvergenten und divergenten Kanälen. Forschungsarbeit Verein. deut. Ing., no. 289 (1929)
64. Olsen, H.O. Theoretical and experimental investigation of impedance void meters. Kjeller report KR-118, (1967)
65. Petrick, M. and Kudirka, A.A. On the relationship between the phase distributions and relative velocities in two-phase flow. Proc. Int. Conf. on Heat Transf., pp. 184-192, Chicago (1966)
66. Hagreis, L.H. Correctiefactoren voor een één-dimensionale impulsbalans voor twee-fasenstroming (in Dutch). Report KR-388 (=SWST-31), Lab. for Thermal Power Eng., Delft Univ. of Techn. (1973)

67. Phillips, G.M. and Taylor, P.J. Theory and applications of numerical analysis. Academic Press, London (1973)
68. Roumy, R. Structure des écoulements diphasés eau-air: étude de la fraction, de la vitesse moyenne et des configurations d'écoulement (in French). Report CEA-R-3892, Centre d'études Nucléaires de Grenoble (1969)
69. Regeln für die Durchflussmessung mit genormten Düsen, Blenden und Venturidüsen. DIN 1952 (1963)
70. Baehr, H.D. Mollier i-x diagramme für Feuchte Luft. Springer Verlag, Berlin (1961)
71. Schrock, V.E. Radiation attenuation techniques in two-phase flow measurements. Two-phase flow instrumentation, 11th, ASME/AIChE, Heat Transfer conference, (1969), Minneapolis, U.S.A.
72. Wisman, R. Metingen aan damp- en drukverdeling van een versneld twee-fasenmengsel (in Dutch). Report SWST-23, Lab. for Thermal Power Eng., Delft Univ. of Techn. (1969)
73. Ferguson, J. and Staley, P.A. Least square piecewise cubic curve fitting. Communications of Association for Computing Machinery ACM, 16 (1973), pp. 280-282
74. Korstanje, H.P. The pressure recovery of a one-component two-phase flow in a two-dimensional diffuser. Argonne Nat. Lab. Report ANL-7504
75. Putte, L.A. van de Stromingsleer. Agon Elsevier, Amsterdam (1975)
76. Jones, A.B. and Dight, D.G. Hydrodynamic stability of a boiling channel. Knolls Atomic Power Laboratory. Part 1: report KAPL-2170 (1961) Part 2: report KAPL-2208 (1962)
77. Safwat, H.H. Digital computation of thermodynamic property values of ordinary water. Lab. for Thermal Power Eng., Delft Univ. of Techn., (1973)
78. Bruggen, P.A. van and Koelmeij, P.A. Experimenten en analyses van stoom + watermengsels aan de Hoge druk Opstelling voor Tweefasenstroming (HOT) (in Dutch). KR-450 (SWST-42), Lab. for Thermal Power Eng., Delft Univ. of Techn., (1975)
79. McAdams, W.H. Heat transmission. McGraw Hill Book Co., New York

80. Harrison, D., Davidson, J.F. and De Kock, J.W. On the nature of aggregative and particulate fluidisation. Trans. Instn. Chem. Engrs., 39 (1961), pp. 202-211
81. Simpson, H.C. and Rodger, B.W. The fluidization of light solids by gases under pressure and heavy solids by water (A study of the transition between aggregative and particulate fluidization). Chem. Eng. Science, 16 (1961), pp. 153-180
82. Stoop, P.M. Analyse van de weerstandscoëfficiënt  $C_D$  voor bellen zwermen (in Dutch). KR-441 (=SWST-40), Lab. for Thermal Power Eng., Delft Univ. of Techn., (1976)
83. Jayaweera, K.O.L.F., Mason, B.J. and Slack, G.W. The behaviour of clusters of spheres falling in a viscous fluid. Part 1: Experiment. Journ. Fluid Mech., 20 (1964), pp. 121-128
84. Streeter, V.L. Handbook of fluid dynamics. McGraw-Hill Book Co., New York, (1961)
85. Landweber, L. and Winzer, A. A comparison of the added mass of streamlined bodies and prolate spheroids. Schiffstechnik, 3 (1956)
86. Nagel, O. and Kürten, H. Untersuchungen zum Dispergieren im turbulenten Scherfeld. Chem. Ing. Tech., 48 (1976), pp. 513-519
87. Rumpf, H. and Herrmann, W. Aufbereit. Tech., 11 (1970), pp. 117-127
88. Sato, Y. and Sekochuchi, K. Liquid velocity distribution in two-phase bubble flow. Int. J. Multiphase Flow, 2 (1975), pp. 79-95
89. van der Welle, R. Uitbreiding van een computerprogramma voor roterende twee-fasen stroming (in Dutch). KR-413(= SWST-36), Lab. for Thermal Power Eng., Delft Univ. of Techn., (1975)
90. Kuipers, L. and Timman, R. Handboek der wiskunde I (in Dutch). Scheltema & Holtema N.V., Amsterdam, (1966)
91. Michlin, S.G. Numerische Realiserung von Variationsmethoden. Akademie Verlag, Berlin, (1969)
92. Taylor, C. and Hood, P. A numerical solution of the Navier-Stokes equation using the finite element technique. Computers and Fluids, 1 (1973), pp. 19-46

93. Peaceman, D.W. and Rachford, H.H. The numerical solution of parabolic and elliptic differential equations. Journal of Soc. for Ind. and Applied Math., 3 (1955), pp. 28-41
94. Frankel, S.P. Convergence rates of iterative treatment of partial differential equations. Math. tables and other aids to computation, 4 (1950), pp. 65-76
95. van der Welle, R. Ontwikkeling van de startwaarden procedure van een computerprogramma voor roterende twee-fasenstroming (in Dutch). KR-414(= SWST-37), Lab. for Thermal Power Eng., Delft Univ. of Techn., (1975)
96. van der Welle, R. Nadere analyse van de procedure INIGUES (in Dutch). KR-415(= SWST-38), Lab. for Thermal Power Eng., Delft Univ. of Techn., (1975).
97. Stuhmiller, J.H. The influences of interfacial pressure forces on the character of two-phase flow model equations. Int. Journ. Multiphase Flow, 3 (1977), pp. 551-560
98. Ishii, M. Thermo-fluid dynamic theory of two-phase flow. Eyrolles, Paris (1975)
99. Wisman, R. and de Ruiter, A.B.W. The description of rotating adiabatic two-phase flow by numerical methods: problem description and - analysis. KR-memo-73-2(= SWST-memo-15), Lab. for Thermal Power Eng., Delft Univ. of Techn., (1973)
100. de Ruiter, A.B.W. Het oplossen van een stelsel eerste orde partiële differentiaal vergelijkingen m.b.v. de ADI methode (berekening van een stoom water scheider) (in Dutch). Dep. of Applied Math., Delft Univ. of Techn., (1974)
101. Isaacson, E. and Keller, H.B. Analysis of numerical methods. John Williamson Inc., New York
102. van Beckum, F.P.H. (from lectures by Zandbergen, P.J.) Partiele differentiaal vergelijkingen: numerieke oplossingsmethoden (elliptische vergelijkingen) (in Dutch). Dep. of Applied Math., Twente Univ. of Techn., (1972)
103. van der Houwen. P.J. Finite difference methods for solving partial differential equations. Math. Centre Tracts, 20, Amsterdam, (1968)

104. Christiaan, A.R. Berekeningen aan roterende twee-fasen stroming (in Dutch). KR-456(= SWST-47), Lab. for Thermal Power Eng., Delft Univ. of Techn., (1976)
105. Wolf, S. and Moen, R.H. Advantages in steam-water separators for boiling water reactors. ASME-paper 73-WA/Pwr-4, (1973)
106. Vollradt, J. Steam-water separators for boiling water reactors. Kerntechnik, 12 (1970), pp. 283-290
107. Würgassen reactor. Nucleonics week, March 29 (1973)
108. Löhr, E., Pollak, G. and Simon, U. Dampf-Wasser-Separation im Siedewasserreaktor.  
Teil A: Die Dampf-Wasser-Separation als Teil des Kühlkreislaufs.  
Teil B: Konstruktion von Dampf-Wasser-Abscheider und Dampftrockner.  
Teil C: Theoretische und experimentelle Ermittlung des Betriebsverhaltens von Zyklonen zur Dampf-Wasser-Separation. Konstruktion, 23 (1971), pp. 439-448.
109. Simon, U. Design and off-design performance of down-flow cyclones for steam-water separation. Meeting of the European two-phase flow group, June 1972, Rome (Italy).
110. Brandes, H. Determination of the performance of steam separators with the aid of the laws of similitude. Kerntechnik, 14 (1972), pp. 210-219
111. Moen, R.H., Kudirka, A.A., Fitzsimmons, G.W. and Burley, E.L. Advances in boiling-water reactor steam separation systems. ASME-paper 69-WA/NE-5 (1969)
112. Cochran, J.T. Axial flow vapour-liquid separator. British patent, 1,157,877 (1966)
113. Moen, R.H. and Wolf, S. Gas-liquid vortex separator. United States Patent, 3,902,876 (1975)
114. Burley, E.L. Performance of internal steam separation system in boiling water reactor. ASME-paper 69-WA/NE-24 (1969)
115. Moen, R.H., Burley, E.L. and Kudirka, A.A. Performance of internal steam separation systems in large boiling water reactor plants. ASME-paper 72-Pwr-5 (1972)

116. Janssen, J.B. Rendementen van gas/vloeistof cycloon-scheiders (in Dutch). KR-462(= SWST-51), Lab. for Thermal Power Eng., Delft Univ. of Techn., (1977)
117. Rossum, J.J. van Separation of emulsions in a cyclone. De Ingenieur, no. 40, Sept. (1953)
118. Ebbenhorst Tengbergen, H.J. van and Rietema, K. Efficiency of phase separations. Cyclones in industry. Elsevier, Amsterdam (1961)
119. Koke, L.C., Roy, G.M. and Brandon, R.E. Optimizing the design of BWR power plants. Paper presented at Amsterdam Power Conf. (1972)
120. Stoop, P.M. Onderzoek naar de toepasbaarheid van een nieuw type stoom-water scheiderv (in Dutch). KR-442(= SWST-40), Lab. for Thermal Power Eng., Delft Univ. of Techn., (1976)
121. Schröder, H.J. Die Arbeitsgrößen der Strahlpumpe und des Strahlgebläses in Uebersichtdiagrammen (in German). VDI-Forschungsheft 517, pp. 26-40, (1966)
122. Vyas, B.D. and Subir Kar Standardisation of water jet pumps. Symposium on jet pumps and ejectors, (1972), London
123. Herfkens, A.H. Beproevingprogramma voor venturi scheiderv in 70-bar installatie (in Dutch). KR-384, Lab. for Thermal Power Eng., Delft Univ. of Techn., (1974)
124. BWR Dynamic System/Plant Operation GE report, MPL A42-4040, (1975)
125. Bekkum, A.J. van, and Siteur, H.W. Deel 1: Beschrijving en analyse experimenten met roterende gaskernstromingen. Deel 2: Analyses scheidings- en hermengings-proces in venturi scheidervs. Deel 3: Computeruitvoer metingen aan rechte testsectie. Deel 4: Computeruitvoer metingen aan enkelconische testsectie. Deel 5: Computeruitvoer metingen aan dubbelconische testsectie (in Dutch). KR-406, Lab. for Thermal Power Eng., Delft Univ. of Techn., (1974)
126. Binnie, A.M. Annular hydraulic jump. Proc. Royal Soc., (London), A282 (1964), pp. 155-165
127. Kedl, R.J. Molten salt reactor experiment (MSRE) progress report ONRL-4344. Oak Ridge Nat. Lab., (1969).

128. Binnie, A.M. and Shaw, A.W. The flow of swirling water down a vertical and an inclined tube. Proc. Royal Soc., (London), A304 (1968), pp. 387-406
129. Bekkum, A.J. van Hydraulic jump in roterende gaskernstromingen. KR-73-36, Lab. for Thermal Power Eng., Delft Univ. of Techn., (1973)
130. Long, R.R. Solitary waves in the one- and two-fluid systems. Tellus, 8 (1956), pp. 460-471
131. Hogenes, J.H.A. Onderzoek naar de leidschoepen voor een axiaal aangestroomde twee-fasen venturi scheidder (in Dutch). Lab. for Aero- and Hydrodynamics, Delft Univ. of Techn., (1975)
132. Christiaan, A.R. Analyse van de metingen aan een lucht-water scheidder (in Dutch). KR-457(=SWST-48), Lab. for Thermal Power Eng., Delft Univ. of Techn., (1977)
133. Bekkum, A.J. van Gasafvoersystemen voor de venturi scheidder (in Dutch). KR-410(=SWST-33), Lab. for Thermal Power Eng., Delft Univ. of Techn., (1975)
134. Siteur, H.W. Onderzoek naar meest optimale geometrie venturi scheidder (in Dutch). KR-411(=SWST-34), Lab. for Thermal Power Eng., Delft Univ. of Techn., (1975)



## SAMENVATTING

Het onderzoek heeft betrekking op gas-vloeistof stromingen en kent twee zwaartepunten, te weten enerzijds de theoretische en experimentele bepaling van de interactie krachten tussen de fasen voor zwermen bellen en anderzijds de numerieke beschrijving van roterende gas-vloeistof stromingen. De toepassing van de zo verkregen kennis en inzichten is gericht op het ontwikkelen en bestuderen van axiale gas-vloeistof cyclonen, o.a. in gebruik als primaire scheidings in kokend water kernreactoren.

Het onderzoek naar interactiekrachten in bellenzwermen heeft geleid tot correlaties voor de vormweerstandskoefficient  $C_D$  en de virtuele massa koefficient  $B$ , welke voorkomen in de gas- en vloeistof-impulsbalansen. Experimentele verifikatie vond plaats zowel met atmosferische lucht-water mengsels als met stoom-water mengsels bij drukken van 5 en 7 MN/m<sup>2</sup>. In beide gevallen zijn testsekties met konstante en variabele doortocht gebruikt zodat stationaire en versnelde twee fasenmengsels bestudeerd konden worden. In alle testsekties is de superficiële watersnelheid gevarieerd van 0,9 tot 2,5 m/s, en de gasvolume-fractie van 0,2 tot 0,75.

Bij de atmosferische lucht-water experimenten is naast het axiale drukprofiel in tien kanaaldoorsneden de gasvolume-fractie gemeten met behulp van fotonen-absorptie, waardoor de twee koefficienten direkt uit de één-dimensionale impulsbalansen konden worden berekend. Voor de hoge druk stoom-water mengsels moesten wegens het ontbreken van gasvolume-fractie metingen speciale procedures worden ontwikkeld voor de berekening van de vormweerstand- en virtuele massa koefficient uit de drukmetingen van respectievelijk de rechte en konvergerende testsektie.

Om de berekening van deze koefficienten uit de impulsbalansen mogelijk te maken zijn ondersteunende correlaties ontwikkeld voor het twee fasen wrijvingsdrukverlies en de bel diameter in gas-vloeistof mengsels. Tevens is de - geringe - invloed van twee-dimensionale effecten op de een-dimensionale impulsbalansen van deze pijpstromingen in rekening gebracht op basis van de resultaten van een numerieke analyse van deze effecten.

De vormweerstandskoefficient is gekorreleerd aan de gasvolume fractie en een kwalitatieve analyse is gemaakt ter verklaring van het aanzienlijke verschil met vaste deeltjes-vloeistof stroming. Deze analyse is gebaseerd op beschouwingen van de interactie van bellen c.q. deeltjes met het zog van een ander bel/deeltje. Voor het korreleren van de virtuele massa koefficient is naast de gasvolume fractie de pieksnelheidsverhouding van de relatieve snelheden in de buurt van de bel als nieuwe parameter geïntroduceerd. Het experimenteel gevonden verband met de pieksnelheidsverhouding is bevestigd door een op potentiaalstroming gebaseerde analyse. De afhankelijkheid van de gasvolume fractie komt overeen met analytisch afgeleide correlaties uit bestaande literatuur.

Bovengenoemde correlaties zijn vervolgens toegepast bij de numerieke beschrijving van de twee-dimensionale (rotatie-symmetrische) stroming. Hiertoe zijn twee numerieke oplossingsmethoden onderzocht voor het stelsel van acht gekoppelde partiële differentiaalvergelijkingen: massabalansen en axiale, radiale en tangentiële impulsbalansen voor de beide fasen.

Bij de "alternating direction implicit" (ADI) methode worden een hoofdstelsel van zes vergelijkingen en het sekondaire stelsel van twee tangentiële impulsbalansen elk simultaan opgelost. Deze ontkoppeling in twee stelsels is gewenst ter besparing van rekentijd en is toelaatbaar wegens de zwakke koppeling van de tangentiële impulsbalansen met de overige balansen. Bij de verwezenlijking van deze oplossingsmethode is grote aandacht besteed aan de stabiliteit van het rekenproces. De benodigde rekentijd bleek evenwel extreem lang te zijn.

Nadat de oorzaken hiervan als inherent aan de combinatie van deze methode en het stromingsprobleem zelf waren onderkend is een tweede oplossingsmethode ontwikkeld, resulterend in het computerprogramma ANALEST. Bij deze oplossingsmethode worden alle balansen ontkoppeld en sequentieel opgelost, waarbij iedere afzonderlijke balans de oplossing van één van de onbekenden geeft. Deze sequentiële oplossingsprocedure wordt iteratief herhaald totdat geen veranderingen in de oplossing van de acht stromingsgrootheden meer optreden. De in hoofdstuk 3 besproken versie van het programma ANALEST berekent evenwel nog slechts zeven van de stromingsgrootheden, te weten de druk en zes snelheden, terwijl de ruimtelijke verdeling van de gasvolume fractie als gegeven wordt ingevoerd. Dit is gedaan om de eerste poging tot berekening van het stromingspatroon zo eenvoudig mogelijk te houden. De noodzakelijke veranderingen voor het berekenen van alle acht stromingsgrootheden worden aansluitend eveneens besproken in hoofdstuk 3.

De resultaten van het voorgaand beschreven werk zijn vervolgens toegepast op de ontwikkeling van een venturi scheider voor kokend water kernreactoren. Mede op basis van inleidende experimenten is hiertoe een venturi scheider ontworpen en getest met lucht-water mengsels waarvan de superficiële watersnelheden en de volumetrische kwaliteiten zijn afgeleid van het deellast regelgedrag van een kokend water kernreaktor. De scheidingsrendementen en drukval van deze scheider zijn vergeleken met de eisen gesteld door reaktorfabrikanten, waarbij ook de economische aspecten in beschouwing zijn genomen. Tot slot wordt aangegeven hoe deze venturi scheider verder ontwikkeld moet worden, waarbij ook de overgang van lucht-water naar stoom-water mengsels en de regels voor het opschalen van de diameter in beschouwing zijn genomen.

## APPENDIX 2-A

### ERROR IN MOMENTUM BALANCE DUE TO CHANGE OF PHASE

Introduction of the error  $\epsilon$  into the momentum balance of the gas phase as given in equation (2-17) yields:

$$\alpha A \rho_g u_g \frac{du_g}{dz} + \varphi_{lg} u_g + \epsilon + F_A A = -\alpha A \frac{dp}{dz} - \alpha A \rho_g g - F_D A \quad (2-A-1)$$

WALLIS [7] writes this equation as:

$$\alpha A \rho_g u_g \frac{du_g}{dz} + \eta \varphi_{lg} (u_g - u_l) + F_A A = -\alpha A \frac{dp}{dz} - \alpha A \rho_g g - F_D A \quad (2-A-2)$$

Subtraction of (2-A-2) from (2-A-1) yields:

$$\epsilon = \{\eta(u_g - u_l) - u_g\} \varphi_{lg} = -\{u_l + (1-\eta)(u_g - u_l)\} \varphi_{lg} \quad (2-A-3)$$

For the present estimation the attention is focussed on the maximum error, which occurs as  $\eta = 0$ , so:

$$|\epsilon| \leq |\varphi_{lg} u_g| \quad (2-A-4)$$

The mass flow changing phase per unit length,  $\varphi_{lg}$ , is obtained from the heat balance for the liquid phase, assuming adiabatic flow between control cross sections 1 and 2:

$$\phi_{l1} h_{l1} = \phi_{l2} h_{l2} + \varphi_{lg} \Delta z h_{g2} \quad (2-A-5)$$

This integral mass balance for this liquid yields:

$$\phi_{l2} = \phi_{l1} - \varphi_{lg} \Delta z \quad (2-A-6)$$

Substitution of (2-A-6) in (2-A-5) gives:

$$\phi_{l1} h_{l1} = (\phi_{l1} - \varphi_{lg} \Delta z) h_{l2} + \varphi_{lg} \Delta z h_{g2}$$

or:

$$\phi_{l1} (h_{l1} - h_{l2}) = \varphi_{lg} \Delta z (h_{g2} - h_{l2}) = \varphi_{lg} \Delta z r_2 \quad (2-A-7)$$

Substitution of

$$h_{l2} = h_{l1} + \frac{dh_{l\text{sat}}}{dp} \frac{dp}{dz} \Delta z \quad (2-A-8)$$

in equation (2-A-7) yields:

$$\phi_{l1} \left( -\frac{dh_{l\text{sat}}}{dp} \frac{dp}{dz} \Delta z \right) = \varphi_{lg} \Delta z r_2 \quad (2-A-9)$$

or:

$$\varphi_{lg} = -\frac{\frac{dh_{l\text{sat}}}{dp}}{r} \phi_{l1} \frac{dp}{dz} \quad (2-A-10)$$

At 7 MN/m<sup>2</sup>, the pressure most relevant for the present investigations the steam tables [8] give:

$$\frac{dh_{l\text{sat}}}{dp} = 5.15 \times 10^{-2}$$

and

$$r = 1504.3 \times 10^3$$

thus

$$\varphi_{1g} = - 3.4 \times 10^{-8} \phi_{11} \frac{dp}{dz} \quad (2-A-11)$$

The error  $\epsilon$  should be compared with the term  $-\alpha A \frac{dp}{dz}$  being the most significant term of equation (2-A-1).

Substitution of equation (2-A-11) in (2-A-4) and rewriting in a suitable form yields:

$$|\epsilon| \leq \left| 3.4 \times 10^{-8} \frac{\phi_{11} u_g}{\alpha A} (-\alpha A \frac{dp}{dz}) \right| \quad (2-A-12)$$

For the present investigation the maximum mass flow is 14 kg/s and the minimum cross sectional area  $\frac{\pi}{4} 0.07^2 = 38.5 \times 10^{-4} \text{ m}^2$ , while the gas velocity depends on the void fraction. The highest value of the ratio  $u_g/\alpha$  - reached in the present investigation - is about 80.

Substitution of these values in (2-A-12) yields:

$$|\epsilon| \leq \left| 0.99 \times 10^{-2} (-\alpha A \frac{dp}{dz}) \right| \quad (2-A-13)$$

Thus the maximum error is less than 1% of the term  $\alpha A \frac{dp}{dz}$ .

## APPENDIX 2-B

### EFFECT OF RADIALLY NONUNIFORM FLOW IN THE DRIFT FLUX MODEL

In subsection 2.2.2.1.4. SMISSAERT's [36] data for the relative velocity were analyzed to vary with a factor  $(1-\alpha)^{-1.8}$  up to  $(1-\alpha)^{-2.5}$  for superficial water velocities from zero up to 0.244 m/s respectively.

No account was taken of local velocity variation over a cross-section, known to exist in channel flow. These two-dimensional effects are mostly (see e.g. WALLIS [7]) analyzed on basis of the model of ZUBER and FINDLAY [37] starting from the so-called drift flux model. This simple model and its consequences for the local relative velocity will be discussed in the present appendix.

The drift flux model makes use of volumetric fluxes defined as follows:

$$j_g = \alpha u_g \quad (2-B-1)$$

$$j_l = (1-\alpha)u_l \quad (2-B-2)$$

and

$$j = j_g + j_l \quad (2-B-3)$$

all values referring to local conditions, as distinct from the superficial velocities defined as average values over a cross section.

In addition the drift fluxes, representing the differences between the volumetric fluxes of constituent phases and the average volumetric flux, are defined by:

$$j_{gl} = \alpha(u_g - j) \quad (2-B-4)$$

and

$$j_{lg} = (1-\alpha)(u_l - j) \quad (2-B-5)$$

from which it can be derived that

$$j_{gl} = -j_{lg} = \alpha(1-\alpha)(u_g - u_l) \quad (2-B-6)$$

The cross-sectional average of a flow variable, here to be denoted by brackets  $\langle \rangle$ , is defined by:

$$\langle x \rangle = \frac{1}{A} \int_A x dA \quad (2-B-7)$$

the outcome of integration of equation (2-B-4) is:

$$\langle j_{gl} \rangle = \langle j_g \rangle - \langle \alpha j \rangle \quad (2-B-8)$$

In order to take into account the effects of nonuniform flow and concentration profiles Zuber and Findlay write the last term as:

$$\langle \alpha j \rangle = C_0 \langle \alpha \rangle \langle j \rangle \quad (2-B-9)$$

where  $C_0$  differs from one for nonuniform channel flow. Substitution of  $C_0$  in equation (2-B-8) yields:

$$\star) \bar{u}_g = \frac{\langle j_g \rangle}{\langle \alpha \rangle} = C_0 \langle j \rangle + \frac{\langle j_{gl} \rangle}{\langle \alpha \rangle} \quad (2-B-10)$$

*\star) The bar for  $\bar{u}_g$  is introduced to distinguish  $\bar{u}_g = \frac{\langle j_g \rangle}{\langle \alpha \rangle}$  from  $\langle u_g \rangle = \frac{j_g}{\alpha}$ .*

Zuber and Findlay established a range of possible values for  $C_0$  by assuming the same radial distribution for the total volumetric flux as for the velocity of single-phase turbulent flow<sup>\*</sup>):

$$\frac{j}{j_{\underline{c}}} = 1 - \left(\frac{r}{R}\right)^m \quad (2-B-11)$$

A similar assumption is made for the void fraction:

$$\frac{\alpha}{\alpha_{\underline{c}}} = 1 - \left(\frac{r}{R}\right)^n \quad (2-B-12)$$

from which Zuber and Findlay finally derived:

$$C_0 = 1 + \frac{2}{m+n+2} \quad (2-B-13)$$

Variation of  $m$  and  $n$  from 1 up to 7 yields:

$$1.125 < C_0 < 1.5 \quad (2-B-14)$$

It should be noticed here that a more accurate value for  $C_0$  might be obtained by using separate distribution functions for  $j_g$  and  $j_l$  rather than one single function for  $j$ .

Verification of correlation (2-B-10) by Zuber and Findlay with experimental data of i.a. PETRICK [38] and SMISSAERT [36] shows a good approximation of  $\bar{u}_g$  by a straight line in the  $\bar{u}_g - \langle j \rangle$  plane intersecting the ordinate at the velocity of a single bubble in an infinite fluidum, i.e.  $\bar{u}_g = u_r^\infty$  as indicated in figure (2-B-1) for the data of Smissaert. Without further motivation Zuber and Findlay concluded that the slope of this straight line is equal to the two-dimensional effect constant  $C_0$ . This conclusion - borne out by the fact that the  $C_0$  values fell within the range predicted by (2-B-14) - implies (cf. equation (2-B-10)):

$$\frac{\langle j_g \rangle}{\langle \alpha \rangle} = u_r^\infty = \text{constant} \quad (2-B-15)$$

which yields, for the local relative velocity:

$$u_r = u_g - u_l = \frac{u_r^\infty}{(1-\alpha)} \quad (2-B-16)$$

This result differs markedly from the analysis of Smissaert's data in subsection 2.2.2.1.4., where the two-dimensional effects are not taken into account and the relative velocity is predicted as varying between  $0.27 (1-\alpha)^{-1.8}$  and  $0.27 (1-\alpha)^{-2.5}$ , depending on the superficial water velocity.

Rather than to the omission of two-dimensional effects from the analysis of subsection 2.2.2.1.4. this discrepancy should in the author's opinion be attributed to Zuber and Findlay's assumption that  $C_0$  is equal to the slope of the straight line plotted in figure (2-B-1).

A first point to be made in support of this opinion concerns the approximation of the experimental data by a straight line. Although the experiments seem to justify this assumption it may be argued that the line of experimental data

<sup>\*</sup>) In single phase cylindrical channel flow the distribution function  $\frac{u}{u_{\underline{c}}} = \left(1 - \frac{r}{R}\right)^{1/m}$  is well known. For use in approximation the difference between  $\left(1 - \frac{r}{R}\right)^{1/m}$  and  $1 - \left(\frac{r}{R}\right)^m$  appears sufficiently small.

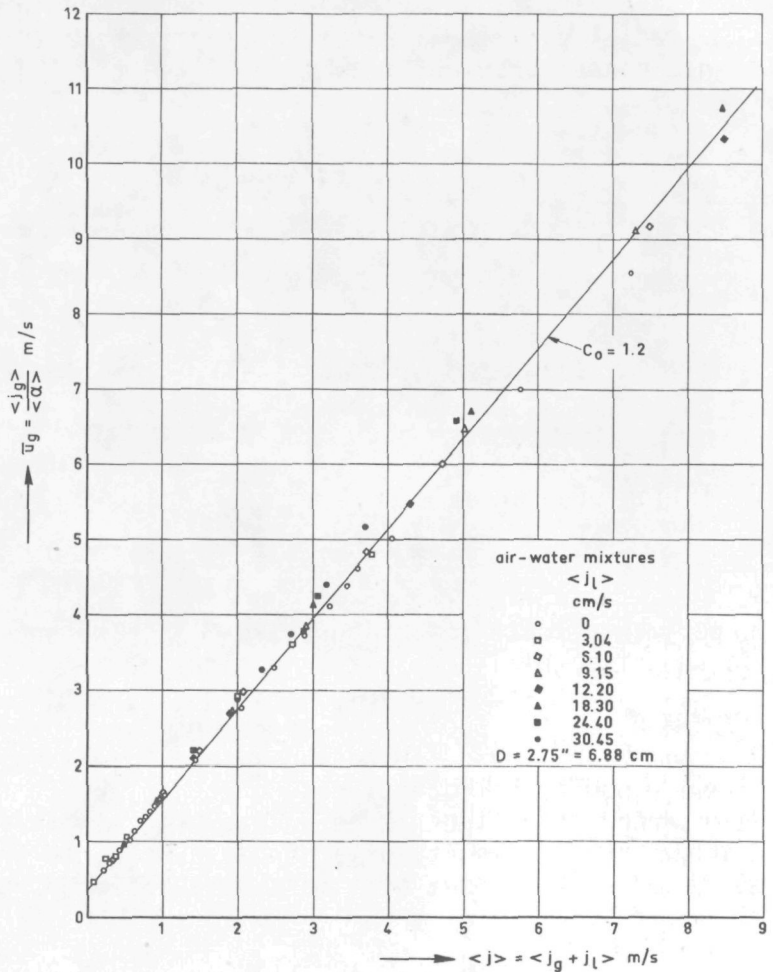


FIGURE 2-B-1  
Data of SMISSAERT [ 36 ]  
for air-water mixtures

should turn downward in the upper part of the plot, as schematically indicated in figure (2-B-2). The ratio  $\frac{\bar{u}_g}{\langle j \rangle}$  may be written as:

$$\frac{\bar{u}_g}{\langle j \rangle} = \frac{\langle j_g \rangle}{\langle j_g + j_l \rangle} = \frac{\beta}{\langle \alpha \rangle} \quad (2-B-17)$$

where  $\beta$  is the volumetric quality.  
The formula for slip

$$\frac{\bar{u}_g}{\bar{u}_l} = s = \frac{\beta}{1-\beta} \frac{1-\langle \alpha \rangle}{\langle \alpha \rangle} = \frac{\beta}{\langle \alpha \rangle} \frac{1-\langle \alpha \rangle}{1 - \frac{\beta}{\langle \alpha \rangle} \langle \alpha \rangle} \quad (2-B-18)$$

indicates that in case of high void fractions - equivalent to high volumetric gas flux  $j_g$  and volumetric quality  $\beta$  - the quotient  $\frac{\beta}{\langle \alpha \rangle}$  (\*) has to tend to one in order to keep the slip finite, which implies a downward trend of the line of

\*) The quotient  $\frac{\beta}{\langle \alpha \rangle}$  has to be greater than one for vertical upward flow.

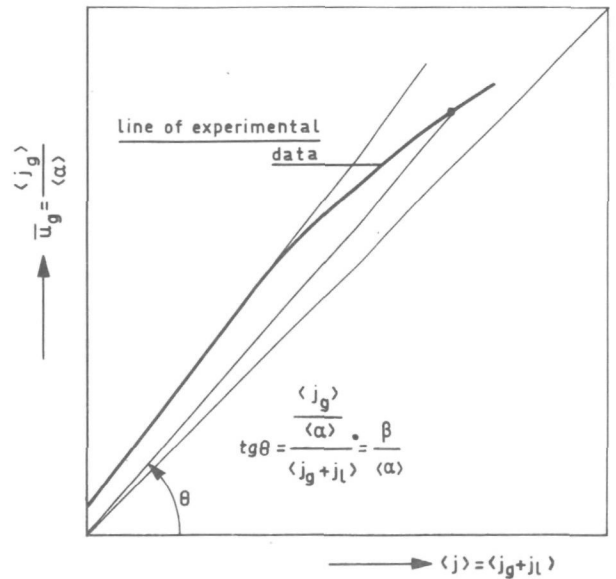


FIGURE 2-B-2

Schematic plot for experimental data at high volumetric fluxes

experimental data (cf. figure 2-B-2)\*). The second and more serious criticism on the straight line plotted in figure 2-B-1 concerns the lower part of the  $\bar{u}_g - \langle j \rangle$  plot where the volumetric gas flux  $\langle j_g \rangle$  approaches zero. In figure 2-B-3 this part of the plot is enlarged and two flow series are distinguished having a volumetric liquid flux of  $\langle j_{l1} \rangle$  and  $\langle j_{l2} \rangle$  respectively. It is obvious that these experimental data lines do not intersect the  $\bar{u}_g$  axis at all, the starting point for these lines is defined by  $\langle j \rangle = \langle j_l \rangle$  and  $\bar{u}_g = \langle j_l \rangle + u_r^\infty$ , where  $u_r^\infty$  is the terminal velocity of a single bubble. In order to obtain a general representation of this set of lines suitable for further analysis, three assumptions are made, viz.

- for low void fractions the curvature of the experimental data lines may be neglected
- the slopes of the resultant straight lines are equal for all volumetric liquid fluxes
- the terminal velocity of a single bubble is independent of the superficial liquid velocity, which appears a reasonable approximation for bubbles in the Newton region in view of the experiments of BAKER and CHAO [25] as discussed in subsection 2.2.2.1.2..

These assumptions lead to the general formula:

$$\bar{u}_{gP} = \langle j_l \rangle + K_0 \langle j_g \rangle + K_1 \quad (2-B-19)$$

Comparison with the general formulation of Zuber and Findlay's model:

$$\bar{u}_{gZF} = C_0 \langle j_g + j_l \rangle + C_1 \quad (2-B-20)$$

shows the following difference between the two predicted values for  $\bar{u}_g$ :

\*) Zuber and Findlay's model - represented by equation (2-B-10) - does not permit a judgement as to whether this expected deviation will be due to variation of the constant  $C_0$  alone or to variation in both  $C_0$  and  $\frac{\langle j_{gl} \rangle}{\langle \alpha \rangle}$ . In the present author's opinion the latter seems more likely, because the assumption that  $\frac{\langle j_{gl} \rangle}{\langle \alpha \rangle}$  remains constant implies a direct and only dependency of  $C_0$  on the volumetric quality, which appears as a gross oversimplification of the two-dimensional effect.

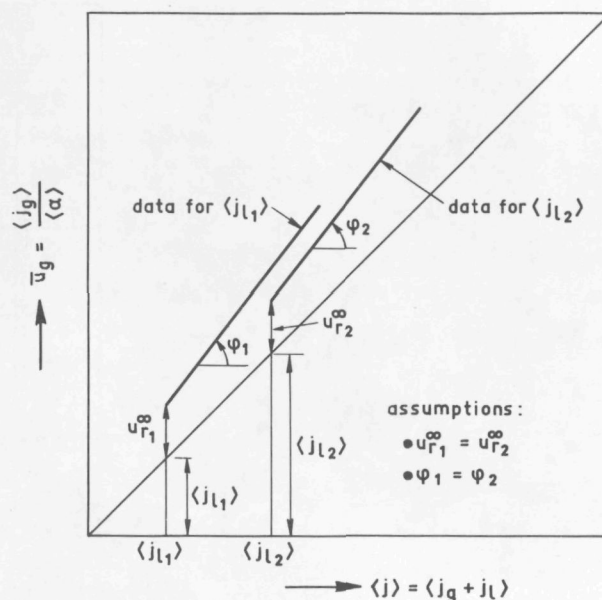


FIGURE 2-B-3

Schematic plot for experimental data at low volumetric gas fluxes

$$\epsilon = \bar{u}_{gZF} - \bar{u}_{gP} = (C_0 - 1)\langle j_1 \rangle + (C_0 - K_0)\langle j_g \rangle + (C_1 - K_1) \quad (2-B-21)$$

For verification of the above assumptions in the present model and comparison to Zuber and Findlay's model twelve of SMISSAERT's [36] air-water measurements having a void fraction less than 0.5 were selected.

The results of the least square fits are:

- for the present model:

$K_1 = 0.346$ ,  $K_0 = 1.372$  and a standard deviation  $\sigma_p = 0.039$

- for the model of Zuber and Findlay:

$C_1 = 0.345$ ,  $C_0 = 1.300$  and a standard deviation  $\sigma_{ZF} = 0.035$ .

The difference between  $K_1$  and  $C_1$  and between  $K_0$  and  $C_0$  is seen to be so small that expression (2-B-21) will only yield values for  $\epsilon$  significantly different from zero for fairly large values of the first right hand term, i.e. for fairly large volumetric water fluxes  $\langle j_1 \rangle$ .

Considering that all of the experiments used by Zuber and Findlay for the verification of their model had low volumetric liquid fluxes it is by no means surprising that they found their model to be in good agreement. In order to obtain a verification with relevant volumetric liquid fluxes, a set of values has been selected from the experiments of the present investigation (see subsection 2.3.1.). From these air-water experiments - having volumetric water fluxes from 0.9 up to 2.5 m/s - ten tests with a void fraction less than 0.4 have been selected from which later on one was eliminated because of having a deviation more than twice the standard deviation. The least square fit made for the remaining nine experiments is presented in table 2-B-4. It appears that the standard deviation for Zuber and Findlay's model  $\sigma_{ZF} = 0.062$  exceeds the standard deviation of the present model ( $\sigma_p = 0.038$ ) by a factor 1.6, indicating that the present model gives a significantly better approximation.

A second indication of the improvement offered by the present model is obtained by taking a close look at the deviation  $\delta$  between the value predicted for  $\bar{u}_g$  by the model and the measured value. A correct model should result in a random distribution for the deviation  $\delta$ . This is seen to be the case for the present model in figure 2-B-5B where the slope of the least square fit tends to zero indicating independency of  $\delta$  from  $\epsilon$ , whereas figure 2-B-5A clearly indicated a correlation between  $\delta$  and  $\epsilon$  for Zuber and Findlay's model.

Having thus established the present model as the correct representation of ex-

present investigation				model of [37] eq. (2-B-20)		present model eq. (2-B-19)		$\epsilon$
$\alpha$	$u_{s1}$	$u_{sg}$	$u_g$	$u_g$	$\delta_{ZF}$	$u_g$	$\delta_p$	
0.239	0.850	0.418	1.753	1.736	0.017	1.729	0.024	-0.007
0.353	0.864	0.786	2.227	2.149	0.078	2.179	0.048	0.030
0.257	1.305	0.600	2.335	2.424	-0.089	2.399	-0.064	-0.025
0.392	1.300	1.216	3.103	3.085	0.018	3.124	-0.021	0.039
0.248	1.711	0.741	2.989	3.015	-0.026	2.972	0.017	-0.043
0.383	1.710	1.471	3.841	3.803	0.038	3.836	0.005	0.033
0.251	2.142	0.896	3.568	3.648	-0.080	3.587	-0.019	-0.062
✓ 0.376	2.102	1.709	4.544	4.484	0.060	4.509	0.035	0.025
* 0.253	2.532	1.009	3.987	4.192	-0.205	4.111	-0.124	-0.081
0.368	2.522	1.874	5.100	5.116	-0.016	5.125	-0.025	0.009

\*) This measurement is not used in the computation for the constants and standard deviation.

$C_1 = 0.366$	$K_1 = 0.384$
$C_0 = 1.080$	$K_0 = 1.184$
$\sigma = 0.062$	$\sigma = 0.038$

TABLE 2-B-4

Approximation of experimental data

perimental data for low void fractions, it can be compared to the analytical derivation of the two-dimensional effect as represented in equation (2-B-10), leading to:

$$C_0 \langle j \rangle + \frac{\langle j_g \rangle}{\langle \alpha \rangle} = \langle j_1 \rangle + K_0 \langle j_g \rangle + u_r^\infty \quad (2-B-22)$$

This equation confirms the earlier statement that it is impossible to satisfy both  $C_0 = \text{constant}$  and  $\frac{\langle j_g \rangle}{\langle \alpha \rangle} = \text{constant} = u_r^\infty$  as results from the model of Zuber and Findlay. It also appears from this equation that a better approximation of the experimental results may be obtained by splitting the two-dimensional effect constant  $C_0$  in two constants  $C_{0g}$  for the gas flux and  $C_{0l}$  for the liquid flux. This can be done by splitting the term  $\langle \alpha j \rangle$  from equation (2-B-9) as follows:

$$\langle \alpha j \rangle = \langle \alpha j_g \rangle + \langle \alpha j_l \rangle = C_{0g} \langle \alpha \rangle \langle j_g \rangle + C_{0l} \langle \alpha \rangle \langle j_l \rangle \quad (2-B-23)$$

and thus

$$C_{0g} = \frac{\langle \alpha j_g \rangle}{\langle \alpha \rangle \langle j_g \rangle} \quad (2-B-24)$$

and

$$C_{0l} = \frac{\langle \alpha j_l \rangle}{\langle \alpha \rangle \langle j_g \rangle} \quad (2-B-25)$$

implying of course the assumption of two separate distribution functions for  $j_g$  and  $j_l$ .

Thus two final conclusions result from this appendix, viz.

- the model of Zuber and Findlay, determining the two-dimensional effect constant  $C_0$  from the  $\bar{u}_g - \langle j \rangle$  plot is incorrect

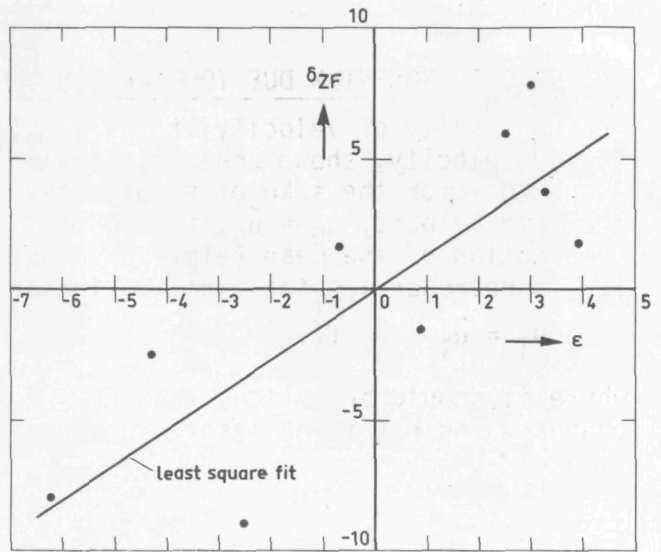


FIGURE 2-B-5A

*Deviations for the model of Zuber and Findlay*

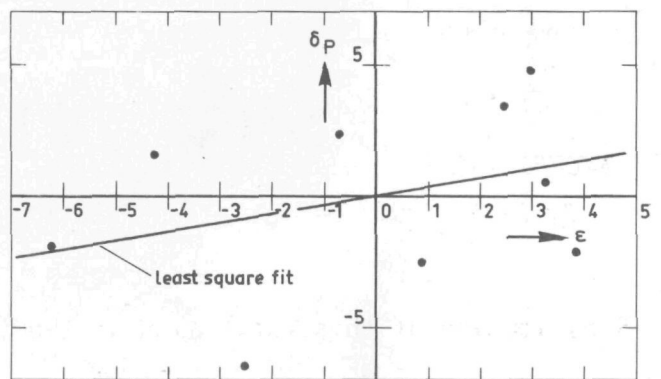


FIGURE 2-B-5B

*Deviations for the present model*

- in order to approximate the local relative velocities as closely as possible it is necessary to distinguish two separate distribution functions for the gas flux  $j_g$  and the liquid flux  $j_l$  respectively.

APPENDIX 2-C

INCREASE OF MOMENTUM DUE TO PEAKS IN THE LIQUID VELOCITY

The continuity of velocity at the bubble/particle boundary causes a peak in the liquid velocity, shown schematically in figure 2-C-1. Assuming - for the sake of simplicity - a bubbly flow with all bubbles having the same velocity  $u_g = \bar{u}_g$ , the local liquid velocity  $u_l$  can be described by a combination of the mean relative velocity  $\bar{u}_r = \bar{u}_g - \bar{u}_l$  and a distribution function  $f(x)$  - representing the local variation of the liquid velocity - as:

$$u_l = \bar{u}_l + \bar{u}_r f(x) \tag{2-C-1}$$

where it should be noticed that  $f(x)$  reaches its maximum value 1 at the bubble boundary and has to be less than zero in part of the flow field, as shown in figure 2-C-1.

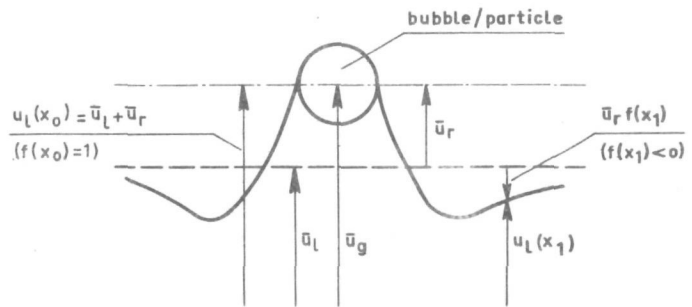


FIGURE 2-C-1

*Typical liquid velocity distribution around a bubble/particle*

Substitution of this expression in the integral for the liquid momentum yields:

$$M = \int_{A_1} \rho_l u_l^2 dA = \int_{A_1} \rho_l (\bar{u}_l + \bar{u}_r f(x))^2 dA \tag{2-C-2}$$

where  $A_1$  stands for the liquid flow area (i.e.  $A_1 = (1-\alpha)A$ ). Further computation yields:

$$M = \rho_l \bar{u}_l^2 \int_{A_1} dA + 2\rho_l \bar{u}_l \bar{u}_r \int_{A_1} f(x) dA + \rho_l \bar{u}_r^2 \int_{A_1} f^2(x) dA \tag{2-C-3}$$

Integration of expression (2-C-1) yields:

$$\frac{1}{A_1} \int_{A_1} u_l dA = \frac{1}{A_1} \int_{A_1} \bar{u}_l dA + \frac{1}{A_1} \int_{A_1} \bar{u}_r f(x) dA \tag{2-C-4}$$

Using the definition of average values the result yields:

$$\bar{u}_l = \bar{u}_l + \frac{1}{A_1} \bar{u}_r \int_{A_1} f(x) dA \tag{2-C-5}$$

and thus:

$$\bar{u}_r \int_{A_1} f(x) dA = 0 \tag{2-C-6}$$

Substitution of this result (2-C-6) in expression (2-C-4) yields:

$$M = \rho_1 \bar{u}_1^2 A_1 + \rho_1 \bar{u}_r^2 \int_{A_1} f^2(x) dA \quad (2-C-7)$$

which clearly indicates that the momentum is increased by an amount proportional to the square of the mean relative velocity  $\bar{u}_r$ .

## APPENDIX 2-D

### DISSIPATION OF MECHANICAL ENERGY IN TWO-PHASE FLOW

The energy dissipation per unit mass and time  $\epsilon$  [ $\text{m}^2/\text{s}^3$ ] will be derived from the mechanical energy balance, which in turn may be derived from the momentum balances for the separate phases (2-16) and (2-19). For the sake of simplicity only non-accelerating flows will be considered in this derivation, yielding

for the gas phase:

$$0 = -\alpha A \frac{dp}{dz} - \alpha A \rho_g g - \frac{3}{4} \alpha A \frac{C_D}{d} \rho_l u_r |u_r| \quad (2-D-1)$$

and for the liquid phase:

$$0 = - (1-\alpha) A \frac{dp}{dz} - (1-\alpha) A \rho_l g + \frac{3}{4} \alpha A \frac{C_D}{d} \rho_l u_r |u_r| - A \left( \frac{dp}{dz} \right)_{fr} \quad (2-D-2)$$

The frictional pressure drop of expression (2-75) is rewritten\* as:

$$\left( \frac{dp}{dz} \right)_{fr} = \frac{\lambda_m}{(1-\alpha \lambda_i) D} \frac{1}{2} (1-\alpha) \rho_l u_l |u_l| [1 + \epsilon_p] \quad (2-D-3)$$

where

$$\epsilon_p = \frac{\alpha}{1-\alpha} \frac{\rho_g}{\rho_l} \left( \frac{u_g}{u_l} \right)^2 + 2 \frac{\lambda_i}{\lambda_m} \frac{\rho_l^{-\rho_g}}{\rho_l} \frac{gD}{u_l |u_l|} \quad (2-D-4)$$

which for bubble flow is mostly negligibly small compared to 1.

The mechanical energy balance is obtained by multiplying the gas balance (2-D-1) by the gas velocity  $u_g$ , the liquid balance (2-D-2) by the liquid velocity  $u_l$  and adding the products, yielding:

$$\begin{aligned} \{ (1-\alpha) u_l + \alpha u_g \} A \frac{dp}{dz} + \{ (1-\alpha) \rho_l u_l + \alpha \rho_g u_g \} A g = \\ = - \left\{ \frac{3}{4} \alpha A \frac{C_D}{d} \rho_l u_r^2 |u_r| + \frac{\lambda_m}{(1-\alpha \lambda_i) D} \frac{1}{2} (1-\alpha) A \rho_l u_l^2 |u_l| [1 + \epsilon_p] \right\} \end{aligned} \quad (2-D-5)$$

The first term of this balance stands for the mechanical energy added to the flow (e.g. by means of a pump), while the second term expresses that part of this supplied energy which is transformed into potential energy, leaving the left hand side as the decrease or dissipation of mechanical energy, yielding:

$$\frac{dE}{dz} = - \frac{3}{4} \alpha A \frac{C_D}{d} \rho_l u_r^2 |u_r| [1 + \epsilon_E] \quad (2-D-6)$$

where

$$\epsilon_E = \frac{2}{3} \frac{1-\alpha}{\alpha} \frac{\lambda_m}{C_D} \frac{d}{D} \frac{u_l^2 |u_l|}{u_r^2 |u_r|} \cdot \frac{1 + \epsilon_p}{1 - \alpha \lambda_i} \quad (2-D-7)$$

which is - in general - small compared to 1, indicating that most of the energy

\* )  $u_l |u_l|$  is introduced instead of  $u_l^2$  in order to make the formulae applicable to the downflow experiments of PETRICK [ 38 ], where  $u_l$  and  $\left( \frac{dp}{dz} \right)_{fr}$  are negative.

is dissipated by the relative motion of the bubbles through the liquid; only in case of very small void fractions will the main dissipation be caused by wall friction.

In view of its definition the dissipation per unit mass and time equals:

$$\epsilon = \frac{\Delta E}{m} = \frac{-\frac{dE}{dz} \Delta z}{m} \quad (2-D-8)$$

The mass  $m$  within the control volume with height  $\Delta z$  may be taken equal to the mass of the continuous liquid, the dissipation in the discontinuous phase being negligible. Hence

$$m = (1-\alpha)\rho_l A \Delta z \quad (2-D-9)$$

Substitution of (2-D-6) and (2-D-9) in (2-D-8) yields for the specific energy dissipation:

$$\epsilon = \frac{3}{4} \frac{\alpha}{1-\alpha} \frac{C_D}{d} u_r^2 |u_r| [1 + \xi_E] \quad (2-D-10)$$

where the quotient  $\frac{C_D}{d}$  can be derived from the momentum balances if necessary.

APPENDIX 2-E

INSTRUMENT LISTING FOR THE ATMOSPHERIC AIR-WATER TEST FACILITY

instrument (cf. figure 2-25)	measured quantity	specifications			
		type	manufacturer	range	calibration
CP central processing unit	scanner for differential pressures	TTL logic	own laboratory	3x16 connections	
DL datalogger		input: analog signals output: punched tape	Solatron	100 input signals (0 ± 30 mV)	manufacturer
D1 differential pressure cell	low range differential pressures	electronic (displacement)	Hottinger & Baldwin (type PD 1/0.1)	0 ± 10 kN/m <sup>2</sup>	water column
D2 idem	high range differential pressures		idem (type PD 1/2)	0 ± 200 kN/m <sup>2</sup>	calibrated air pressure (Wallace & Trenan (FA-2356))
DA amplifiers			idem (type KWS/3-5)		manufacturer
F1 air flow meter	low range air flowrate	rotameter	Brooks (type 12-1110)	0.006-0.06 kg/s (130 kN/m <sup>2</sup> & 20°C)	manufacturer
F2 idem	high range air flowrate		idem (type 15-3611)	0.03-0.3 kg/s (130 kN/m <sup>2</sup> & 20°C)	
FA amplifier			idem (type 5520-D)		
F3 water flow meter	water flowrate	venturi tube (DIN-Norm-venturidüse)	own laboratory	3-30 kg/s	
BP barometer	atmospheric pressure	mercuri column (electrical resistance)	own laboratory	90-120 kN/m <sup>2</sup>	calibrated barometer (Wilhelm Lambrechts (604))
BA amplifier			Peekel (type CEL (RU22))		
T1 thermocouple	temperature of air flow	chromel-alumel mineral insulated with stainless steel sheath	Alliage My.		
T2 idem	ambient temperature				
T3 idem	temperature of water				
V1 photon counter	air volume fraction (photon intensities)	scintilation cristal & photo-multiplier tube	Philips (type PW 4313/01)	10-2x10 <sup>5</sup> photons/s	in situ
V2 amplifier, discriminator & rate meter			idem (type PW 4610)		
R x-y recorder	photon intensities		Hewlett & Packard (type 2 FAM)	25x38 cm	
PM potentiometer	displacement		own laboratory	25 cm	

## APPENDIX 2-F

### COMPUTATION OF RADIAL VOID FRACTION DISTRIBUTION

Computation of the radial void distribution in a cross section is based upon a least square approximation of the same set of mean chordal void fractions at the 41 standard chord locations used for computation of the mean cross sectional void fraction discussed in subsection 2.3.1.3.3.2.. The computation yields the coefficients of a general polynomial for the local void fraction, which is chosen as:

$$\alpha(r) = c_0 + c_2 r^2 + \dots + c_{2n} r^{2n} + \dots + c_{12} r^{12} \quad (2-F-1)$$

where  $r$  is the relative radius.

This general formulation is preferred to a prescribed distribution function to avoid restrictions in the computed radial profiles, while the above form appears to be favourable compared to:

- a polynomial also containing odd powers, because the resulting elimination of the assumption of axial symmetry causes a small but significant deterioration of the standard deviation
- polynomials the order of which is selected so to yield minimum standard deviation, because no significant improvement is found if the maximal order is allowed to exceed 12
- Fourier series - being an orthogonal polynomial - because these yield no significant improvement at all.

The computation of the seven coefficients  $c$  starts with the integration of the polynomial for the local void fraction over a chord:

$$\begin{aligned} \langle \alpha \rangle_k &= \frac{1}{L_k} \int_k \alpha(r) dl = \\ &= \int_k \frac{c_0}{L_k} dl + \int_k \frac{c_2}{L_k} r^2 dl + \dots + \int_k \frac{c_{2n}}{L_k} r^{2n} dl + \dots + \int_k \frac{c_{12}}{L_k} r^{12} dl \end{aligned} \quad (2-F-2)$$

Numbering of the chords from  $p=1$  through 41 yields:

$$\langle \alpha \rangle_{kp} = c_0 a_{p1} + c_2 a_{p2} + \dots + c_{2n} a_{p(n+1)} + \dots + c_{12} a_{p7} \quad (2-F-3)$$

where

$$a_{pi} = \frac{1}{L_k} \int_{k_p} r^{2(i-1)} dl \quad (2-F-4)$$

which can be written in the matrix notation<sup>\*)</sup> as:

$$\langle \alpha \rangle = \underline{A} \underline{c} \quad (2-F-5)$$

The deviation between this computed mean chordal void fractions  $\langle \alpha \rangle$  and the measured void fractions  $\langle \alpha_m \rangle$

$$\underline{\delta} = \underline{\langle \alpha_m \rangle} - \underline{\langle \alpha \rangle} \quad (2-F-6)$$

yields a sum of squares

<sup>\*)</sup> The coefficients  $c$  are renumbered from  $c_0, c_2, \dots, c_{2n}, \dots, c_{12}$  to vector elements  $c_i$  for  $i = 1$  through 7.

$$\delta^T \delta = (\underline{\langle \alpha_m \rangle} - \underline{Ac})^T (\underline{\langle \alpha_m \rangle} - \underline{Ac}) \quad (2-F-7)$$

which is minimized if

$$\frac{\partial}{\partial \underline{c}} \delta^T \delta = (\underline{\langle \alpha_m \rangle} - \underline{Ac})^T A = 0 \quad (2-F-8)$$

This latter equation can be rewritten as:

$$A^T \underline{Ac} = A^T \underline{\langle \alpha_m \rangle} \quad (2-F-9)$$

or

$$\underline{c} = (A^T A)^{-1} A^T \underline{\langle \alpha_m \rangle} \quad (2-F-10)$$

When using the set of 41 standard chords - the relative radii of which are equal at each measurement level - the matrix  $(A^T A)^{-1} A^T$  is the same for each measurement level and hence computed only once at the outset of the data reduction computer program. The coefficients  $c$  are computed for each measurement level by multiplication of this 7x41 standard matrix with the vector of 41 mean chordal void fractions.

The local void fractions are computed as:

$$\alpha(r) = \sum_{i=1}^7 c_i r^{2(i-1)} \quad (2-F-11)$$

where  $r$  is the relative radius in the cross section.

APPENDIX 2-G

ERROR ESTIMATION FOR THE DRAG FORCE COEFFICIENT  $C_D$

All measurements for determining the coefficient  $C_D$  refer to local flow conditions. It is hence to be expected that the corresponding errors will also be strongly dependent on these local flow conditions, thus excluding any general error estimation.

In order to provide an insight in the order of magnitude of these errors measurement 144, level 6 will hereafter be used as a typical example for performing a numerical analysis of the error estimation.

Although the bubble diameter  $d$  will be affected by the measurement error in the void fraction, the influence of this effect on the drag force is small enough to be neglected; therefore only the error in the quotient  $\frac{C_D}{d}$  will be estimated.

measurement 144 level 6				
parameter		value	error	error source
void fraction	$\alpha$ [-]	0.6122	0.003	cf. subsection 2.3.1.3.3.2.
gradient	$\frac{d\alpha}{dz}$ [ $m^{-1}$ ]	0.0648	0.03	estimated at 5% of the total variation along the test section: from -0.42 up to 0.27 [ $m^{-1}$ ]
liquid				
velocity	$u_l$ [m/s]	9.110	0.19	2.1% cf. subsection 2.3.1.3.3.1.
gas velocity	$u_g$ [m/s]	19.741	0.63	3.4% cf. subsection 2.3.1.3.3.1.
relative				
velocity	$u_r$ [m/s]	10.631	0.82	$\Delta u_r = \Delta u_g + \Delta u_l$
diameter	$D$ [m]	0.0769	-	
derivative	$\frac{dD}{dz}$ [-]	-0.0769	-	
pressure				
gradient	$\frac{dp}{dz}$ [ $N/m^3$ ]	-102717	822	0.8% cf. subsection 2.3.1.3.3.3.
fractional				
pressure drop	$(\frac{dp}{dz})_{fr}$ [ $N/m^3$ ]	4090	1153	28.2% cf. table 2-13 subsection 2.2.3.1.

TABLE 2-G-1

Actual values for measurement 144 level 6

This quotient  $\frac{C_D}{d}$  is computed from equation (2-113). Taking the two-dimensional correction factors  $K$  equal to unity for the sake of simplicity one obtains:

$$\frac{C_D}{d} = \frac{\frac{d}{dz} (1-\alpha)\rho_l A u_l^2 + (1-\alpha)A \frac{dp}{dz} + (1-\alpha)A\rho_l g + A(\frac{dp}{dz})_{fr}}{\frac{3}{2}\alpha A\rho_l (u_g - u_l)^2} \quad (2-G-1)$$

Substitution of the liquid mass balance

$$\phi_{m1} = (1-\alpha)A\rho_l u_l = \text{constant} \quad (2-G-2)$$

and the definition  $u_l = \frac{\phi_{m1}}{(1-\alpha)\rho_l A}$  in the first term of the numerator yields

$$\frac{C_D}{d} = \frac{(1-\alpha)\rho_1 Au_1^2 \left(-\frac{2}{D} \frac{dD}{dz} + \frac{1}{1-\alpha} \frac{d\alpha}{dz}\right) + (1-\alpha)A \frac{dp}{dz} + (1-\alpha)A\rho_1 g + A\left(\frac{dp}{dz}\right)_{fr}}{\frac{3}{2}\alpha A\rho_1 (u_g - u_1)^2} \quad (2-G-3)$$

The actual values for the parameters and their errors are given in table 2-G-1. The resulting values and errors in equation (2-G-3) are presented in table 2-G-2.

These values yield

$$\frac{C_D}{d} = \frac{166.9 \pm 35.6}{241.2 \pm 37.3} \quad (2-G-4)$$

or

$$0.471 < \frac{C_D}{d} < 0.993 \quad (2-G-5)$$

TABLE 2-G-2

Values and errors for  $\frac{C_D}{d}$  computation

measurement 144 level 6		
term	value	error
$(1-\alpha)\rho_1 Au_1^2 \left(-\frac{2}{D} \frac{dD}{dz} + \frac{1}{1-\alpha} \frac{d\alpha}{dz}\right)$	315.0	27.1
$(1-\alpha)A \frac{dp}{dz}$	-185.1	2.9
$(1-\alpha)A\rho_1 g$	18.0	0.1
$A\left(\frac{dp}{dz}\right)_{fr}$	19.0	5.4
$\frac{3}{2}\alpha A\rho_1 (u_g - u_1)^2$	241.2	37.3

From the last column of table (2-G-2) it appears clearly that there are two major components in the total error viz.

- the error in the relative velocity
- the error in the liquid acceleration term  $\frac{d}{dz} (1-\alpha)A\rho_1 u_1^2$

The latter does not exist in the computations for the straight test section, whereas the errors for the converging and venturi-shaped test sections increase with increasing liquid acceleration, as evidenced by the scatterbands of figures 2-42 through 2-44. The proportionality of this error with the acceleration term  $\frac{d}{dz} (1-\alpha)\rho_1 Au_1^2$  results - in case of measurements in the venturi-shaped test section and for some measurements in the converging test section - in errors far in excess of the  $\frac{27.1}{166.9} \times 100\% = 17\%$  for the present example of measurement 144 level 6. These large deviations result in an a-symmetric scatterband in logarithmic plots: if for example an error of 60% exists the possible value for  $\frac{C_D}{d}$  varies from  $0.4 \frac{C_D}{d}$  up to  $1.6 \frac{C_D}{d}$ , which deviate a factor 2.5 and 1.6 respectively from the most probable value. This explains apparent downward shift of the scatterband in case of such large errors, shown in figures 2-43 and 2-44.

## APPENDIX 2-H

### SECOND TWO-DIMENSIONAL EFFECT ON THE $C_D$ - $\alpha$ CORRELATION

In this appendix the second two-dimensional effect will be introduced and discussed at first, after which a numerical approximation of this effect will be presented which is partly based on measured values and partly on assumed distribution functions. In subsection 2.3.1.6.2.1. this numerical approximation is evaluated by comparing it to some selected measurements where this effect is minimal.

The strong dependency of the drag force coefficient  $C_D$  on the void fraction, viz.  $C_D = 0.44(1-\langle\alpha\rangle)^6$  according to figures 2-42 through 2-44, indicates a large variation of  $C_D$  over a cross section due to the variation of the local void fraction.

The momentum balance for the gas phase: equation (2-16), yields for non-accelerated flow (straight test section):

$$0 = -\langle\alpha\rangle A \frac{dp}{dz} - \langle\alpha\rangle A \rho_g g - F_D A \quad (2-H-1)$$

The same equation is valid locally in the cross section. Thus omission of the weight of the gas phase yields

$$F_D = \frac{3}{4} \alpha \frac{C_D}{d} \rho_l (u_g - u_l)^2 = -\alpha \frac{dp}{dz} \quad (2-H-2)$$

as a reasonable approximation for the local drag force.

Since  $\frac{dp}{dz} = \text{constant}$  over the cross section the local variation of the coefficient  $C_D$  - as a result of the void fraction variation - will in turn cause the relative velocity  $u_r = u_g - u_l$  to vary over the cross section. This leads to the conclusion that - in general - the location where the local

relative velocity  $u_r$  equals the mean relative velocity  $\langle u_r \rangle = \frac{u_{sg}}{\langle\alpha\rangle} - \frac{u_{sl}}{\langle 1-\alpha \rangle}$

- used for computing the cross-sectional value for the coefficient  $C_D$  - will not coincide with the location where the local void fraction equals the mean void fraction  $\langle\alpha\rangle$ . Hence an error is introduced by correlating the coefficient  $C_D$  to the mean void fraction  $\langle\alpha\rangle$  instead of to the local void fraction  $\alpha_{ur}$  at the location of the relative velocity in use.

A numerical approximation will now be carried out to determine these local void fractions  $\alpha_{ur}$ , related to the mean void fraction  $\langle\alpha\rangle$ . The basic assumption for this numerical approximation is that the correlation

$$C_D = 0.44(1-\alpha)^m \quad (2-H-3)$$

will adequately represent the dependency of the coefficient  $C_D$  on the local void fraction. Thus the required local void fraction  $\alpha_{ur}$  can be computed for each mean void fraction  $\langle\alpha\rangle$  on the basis of

$$C_D = 0.44(1-\langle\alpha\rangle)^6 = 0.44(1-\alpha_{ur})^m \quad (2-H-4)$$

after determination of the power  $m$ .

The numerical approximation of the power  $m$  is based on the integral mass balance for the gas phase, which is written in terms of the superficial gas velocity as:

$$u_{sg} = \frac{1}{A} \int_A \alpha u_g dA = \frac{1}{A} \int_A \alpha (u_l + u_r) dA \quad (2-H-5)$$

where:

- the superficial gas velocity is known for each measurement
- the local void fraction in a cross section  $\alpha$  is taken from the measurements, i.e. instead of the 12th order polynomial the general formulation is chosen as  $\alpha = \alpha_c (1 - \frac{r}{R})^{1/n}$  of which the actual value at the centerline  $\alpha_c$  and the reciprocal power  $n$  are determined according to the actual void fraction distribution under consideration
- the distribution of the local liquid velocity is chosen as  $u_l = u_{lc} (1 - \frac{r}{R})^{1/p}$  in accordance with subsection 2.2.4., where the values 6, 7 and 8 were selected for the reciprocal power  $p$  in the case of the straight test section. Preliminary computations indicated that the power  $m$  is almost independent of the value taken for  $p$ , hence  $p=7$  was selected for all computations.

The value at the centerline  $u_{lc}$  was obtained from the integral mass balance for the liquid phase, written in terms of the superficial liquid velocity as

$$u_{sl} = \frac{1}{A} \int_A (1-\alpha) u_l dA \quad (2-H-6)$$

- the local relative velocity is determined after substituting correlation (2-H-3) into equation (2-H-2), yielding

$$u_r = \sqrt{\frac{-\frac{dp}{dz}}{\frac{3}{4} \rho_l \frac{0.44(1-\alpha)^m}{d}}} = \sqrt{\frac{-\frac{dp}{dz} d}{0.33 \rho_l}} (1-\alpha)^{-m/2} \quad (2-H-7)$$

where all parameters except  $m$  are known for each measurement.

TABLE 2-H-1

Values for power  $m$  (correlation (2-H-3)) for the straight test section

nominal superficial water velocity $u_{sl}$	nominal mean void fraction				
	0.25	0.38	0.50	0.63	0.75
0.9	4.5	4.6	4.8	4.5	4.6
1.3	3.1	4.1	5.2	4.7	4.5
1.7	4.75	4.8	5.6	4.95	4.6
2.1	4.5	4.9	5.7	4.75	4.45
2.5	3.0	5.1	5.6	4.75	4.45
all	4.1	4.75	5.45	4.7	4.45

The actual numerical procedure consisted of numerical integration of the right hand side of equation (2-H-5) for different values for  $m$  and computing the resulting value for  $m$  by interpolation in such a way that the right hand side equals the known value of the superficial gas velocity at the left hand side.

This procedure is elaborated for all 25 measurements in the straight test section - for which equation (2-H-1) is valid - of which the resulting powers for  $m$  are presented in table 2-H-1. Considering possible errors in the assumptions and approximations - the latter of which are particularly large for the lowest mean void fraction  $\langle \alpha \rangle$  where the reciprocal power  $n$  for the void fraction shape function is rather inaccurate - the spread in values is such as to justify the conclusion that there is no dependency of the power  $m$  on the superficial water velocity and hence that  $m$  will only depend on the mean void fraction as given by the values at the bottom of table 2-H-1.

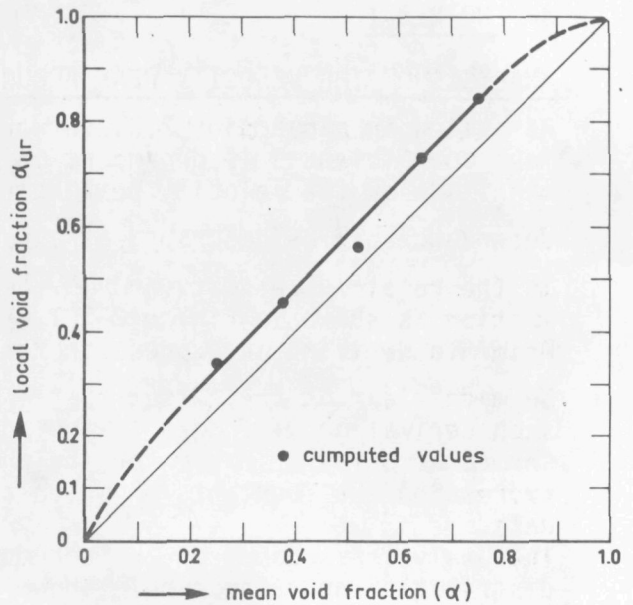


FIGURE 2-H-2

Transformation plot from mean to local void fraction

Substitution of these values in equation (2-H-4) results in the 5 local void fractions - to be inserted in formula (2-H-3) in order to yield the measured  $C_D$  values - belonging to the 5 nominal mean void fractions of the measurements in the straight test section. The results are shown in the 'transformation plot' figure 2-H-2. In view of the great similarity for the results of the three test sections shown in figures 2-42 through 2-44, it may be assumed that the 'transformation plot' is valid for all measurements.

The  $C_D$  correlation for local void fractions obtained from the continuous correlation in figure 2-H-2 is plotted in figure 2-H-3. The result appears to be reasonably well approximated by:  $C_D = 0.44(1-\alpha)^{4.75}$  for void fractions up to 0.8.

Hence it can be concluded that a significant difference exists between the correlation based on local void fractions and that for mean cross-sectional void fractions. This difference is due to the inhomogeneous void fraction profiles and the strong dependency of the drag force coefficient  $C_D$  on the void fraction.

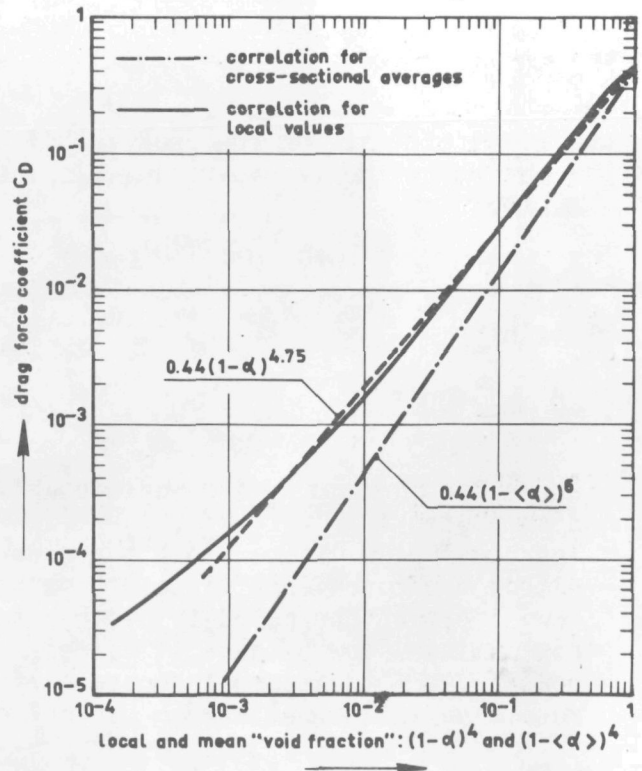


FIGURE 2-H-3

Drag force coefficient correlation for local void fractions

## APPENDIX 2-I

### ANALYSIS OF THE VELOCITY PEAK AROUND A BUBBLE

As stated in subsection 2.3.1.6.2.2. it is highly likely that the virtual mass coefficient  $B$  is dependent on the shape of the velocity distribution and magnitude of the velocity peak near the bubble. It is assumed that this dependence can be described as a function of the velocity ratio  $\frac{u^\oplus}{u_r}$  where  $u_r$  is the relative velocity and  $u^\oplus$  the peak velocity at the maximum bubble cross section as shown in figure 2-I-1.

Prior to deriving an expression for the ratio  $\frac{u^\oplus}{u_r}$  in this appendix it should be made clear at the outset that - at the present stage of knowledge - any such derivation will have to include some unproven assumptions. This is seemed acceptable in view of the present limited aim, viz. to develop an expression the constants of which are to be determined from the experimental data.

The analysis is based on the schematical approximation of the velocity distribution near the bubble shown in figure 2-I-1, where the disturbance of the liquid velocity by the relative velocity of the bubble is restricted to a region - with a width  $b$  - close to the bubble.

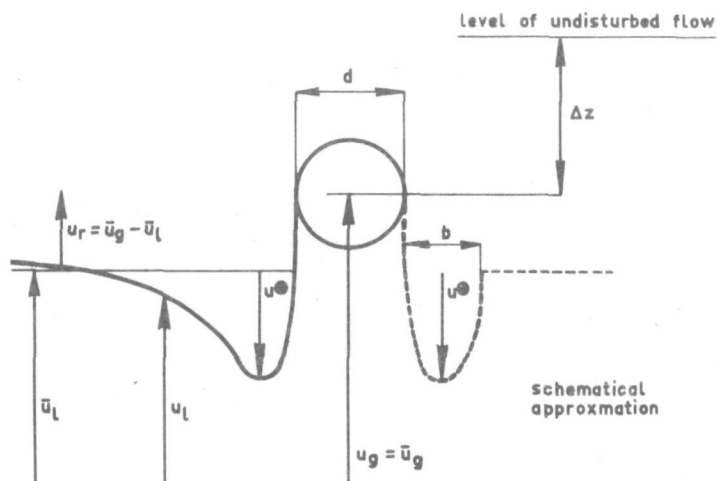


FIGURE 2-I-1

*Liquid velocity distribution near a bubble*

A first estimate of the peak velocity  $u^\oplus$  in this region is given by the equation of the liquid volume displaced due to the relative velocity of the bubble:

$$\frac{\pi}{4} d^2 u_r \approx \pi d b K_1 u^\oplus \quad (2-I-1)$$

yielding

$$\frac{u^\oplus}{u_r} = \frac{1}{4K_1} \frac{d}{b} \quad (2-I-2)$$

where the constant  $K_1$  and width  $b$  are determined by the shape of the velocity distribution.

The peak value  $u^\oplus$  and width  $b$  are dependent on the viscosity of the liquid. Although a turbulence viscosity exists in the churn turbulent flows under investigation the velocity distribution in the peak will be similar to that for laminar flow because it is reasonable - in the absence of solid flow boundaries - to assume a constant viscosity over the full width of the peak, resulting in the well-known parabolic velocity distribution. For laminar

single-phase flow between two plates at a distance  $b$  the velocity distribution is given by (see e.g. [75]):

$$u^{\oplus} = \frac{b^2}{8\eta} \left(-\frac{dp}{dx}\right) \quad (2-I-3)$$

where  $u^{\oplus}$  stands for the maximum velocity at the centerline of the flow channel and  $\frac{dp}{dx}$  is the frictional pressure drop which is constant over the channel cross section.

The difference between this (steady state) laminar channel flow and the flow around a bubble is in the acceleration of the liquid at the center of the peak required to reach the velocity  $u^{\oplus}$ , while it is nevertheless reasonable to assume the pressure gradient  $\frac{dp}{dz}$  constant over the peak width. Hence the equation equivalent to (2-I-3), viz.

$$u^{\oplus} = K_2 \frac{b^2}{8\rho(\epsilon+v)} \left(-\frac{dp}{dz}\right) \quad (2-I-4)$$

is only valid at the outsides of the peak. The constant  $K_2$  is introduced because of the aforementioned differences with channel flow, while the turbulence viscosity  $\epsilon$  will be discussed below.

The magnitude of the pressure gradient may be estimated by analysing the streamline through the center of the peak. On the basis of the unproven assumption that the viscosity forces acting on the liquid along this streamline are negligible compared to the acceleration forces the Bernoulli equation yields

$$\Delta p = \frac{1}{2}\rho u^{\oplus 2} \quad (2-I-5)$$

This pressure difference is generated over the distance  $\Delta z$  (cf. fig. 2-I-1), which is proportional to the diameter of the bubble; thus the mean pressure gradient along this streamline is expressed by:

$$-\frac{\overline{dp}}{dz} = \frac{\Delta p}{K_3 d} = \frac{\rho u^{\oplus 2}}{2K_3 d} \quad (2-I-6)$$

By assuming this mean pressure gradient to be proportional to the local pressure gradient of equation (2-I-4) one obtains

$$u^{\oplus} = K_4 \frac{b^2}{\rho(\epsilon+v)} \frac{\rho u^{\oplus 2}}{d} = \frac{K_4 u^{\oplus 2} d}{\epsilon(1 + \frac{v}{\epsilon})} \frac{b^2}{d^2} \quad (2-I-7)$$

where  $K_4$  stands for the combination of the various proportionality constants. Substitution of equation (2-I-2) yields

$$\frac{u^{\oplus}}{u_r} = \frac{K_4}{16K_1^2} \frac{u_r d}{\epsilon(1 + \frac{v}{\epsilon})} \quad (2-I-8)$$

Despite its poor physical basis formula appears reliable because it indicates that the velocity ratio  $\frac{u^{\oplus}}{u_r}$  depends on the ratio between the inertia and viscosity forces.

In introducing the turbulence viscosity  $\epsilon$  for two-phase flow in subsection 2.2.2.1.3. it was stated that the development of a model for this property appeared beyond the scope of the present investigation. In conformity with this statement the discussion presented below does not pretend to develop

such a model but only serves as a first approximation permitting the use of equation (2-I-8) for determining meaningful values for the virtual mass coefficients.

This approximation is based on the hypothesis of Boussinesq for single-phase flow expressing the Reynolds stresses as a turbulence viscosity, i.e.

$$-\rho \overline{u_i' u_j'} = -\rho R_{ij} \overline{u'^2} = \rho \epsilon \frac{\partial u_i}{\partial x_j} \quad (2-I-9)$$

where  $R_{ij}$  is a coefficient of the second-order velocity-correlation tensor relating the Reynolds stresses  $-\rho \overline{u_i' u_j'}$  to the mean square velocity  $\overline{u'^2}$ . Using the term  $(1-\alpha)\rho_1 \overline{u_i' u_j'}$  derived by HINZE [58] for the Reynolds stresses in two-phase flow, the equivalent expression for two-phase flow becomes

$$(1-\alpha)\rho_1 \overline{u'^2} \sim |(1-\alpha)\rho_1 \epsilon \frac{\partial u_i}{\partial x_j}| \quad (2-I-10)$$

where  $u_i$  refers to the time average velocity in the main flow direction, whereas for the purpose of this appendix the local velocity gradient in the peak near the bubble is of interest. However, both derivatives being affected by the same turbulence viscosity it seems reasonable to assume proportionally between the two of them, yielding

$$(1-\alpha)\rho_1 \overline{u'^2} = K_5 (1-\alpha)\rho_1 \epsilon \frac{u^\oplus}{b} \quad (2-I-11)$$

where the proportionality constant between the main and local velocity gradients  $K_5$  also includes the proportionality between the velocity derivative in the peak and the quotient  $\frac{u^\oplus}{b}$ .

The mean square turbulence velocity  $\overline{u'^2}$  is used in subsection 2.2.3.2. to correlate the bubble diameter. The basic equation (2-84)

$$\frac{(1-\alpha)\rho_1 \overline{u'^2} d}{\sigma} = We_{cr} \quad (2-84)$$

will now be used in the opposite way, viz. to determine the mean square turbulence velocity  $\overline{u'^2}$ .

Subsection of equation (2-84) and (2-I-2) in (2-I-11) yields

$$\epsilon = \frac{2.43}{K_5} \frac{\sigma}{(1-\alpha)\rho_1 u^\oplus} \frac{b}{d} = \frac{2.43}{4K_1 K_5} \frac{\sigma}{(1-\alpha)\rho_1 u_r} \left(\frac{u_r}{u^\oplus}\right)^2 \quad (2-I-12)$$

where the constant 2.43 is the value for the critical Weber number in case of bubble flow (cf. subsection 2.2.3.2.). Subsequent substitution of this result in equation (2-I-8) gives

$$\frac{u^\oplus}{u_r} = \frac{4K_1}{K_4 K_5} \frac{2.43}{(1-\alpha)\rho_1 u_r^2 d} \left\{ 1 + \frac{4K_1 K_5}{2.43} \frac{(1-\alpha)\rho_1 u_r^2 d}{\sigma} \frac{v}{u_r d} \left(\frac{u^\oplus}{u_r}\right)^2 \right\} \quad (2-I-13)$$

where it is the author's opinion that the reciprocal Reynold number  $\frac{v}{u_r d}$  has to be replaced by  $\frac{\eta_1}{(1-\alpha)\rho_1 u_r d}$  pointing towards the probability that the kinematic

viscosity  $\nu$  in case of two-phase flow has to be defined as  $\nu = \frac{\eta_1}{(1-\alpha)\rho_1}$  \*).

Substitution of  $Re = \frac{(1-\alpha)\rho_1 u_r d}{\eta_1}$  and  $We = \frac{(1-\alpha)\rho_1 u_r^2 d}{\sigma}$  gives as solution for the quadratic equation (2-I-13):

$$\frac{u^\oplus}{u_r} = \frac{Re}{K_6} \left( 1 - \sqrt{1 - \frac{K_7}{ReWe}} \right) \quad (2-I-14)$$

where the second root - obtained by adding the square root to unity - is omitted because the term between brackets represents the effect of turbulence viscosity, which has to lower the ratio  $\frac{u^\oplus}{u_r}$  compared to the case of laminar flow represented by the single Reynolds number. The constants  $K_6 = \frac{32K_1^2}{K_4}$  and  $K_7 = \frac{256K_1^3 \cdot 2.43}{K_4^2 K_5}$  have to be determined by fitting the experimental data of the virtual mass coefficient B.

It should be reiterated at this point that the author is well aware of the inadequacies in the "derivation" of expression (2-I-14). The sole purpose of its inclusion in the present investigation is to show that this expression - used for the analysis in subsection 2.3.1.6.2.2. - does at least have some theoretical background.

Further confidence in its use may be derived from the qualitative reasoning given below.

The first analysis considers

$$ReWe \gg K_7 \quad (2-I-15)$$

in which case expression (2-I-14) can be approximated via Taylor series expansion as:

$$\frac{u^\oplus}{u_r} = \frac{Re}{K_6} \left( 1 - \sqrt{\left( 1 - \frac{\frac{1}{2}K_7}{ReWe} \right)^2} \right) \quad (2-I-16)$$

yielding

$$\frac{u^\oplus}{u_r} = \frac{K_7}{2K_6 We} \quad (2-I-17)$$

As was to be expected from condition (2-I-15) this situation corresponds to fully turbulent flow, as appears when the quotient  $\frac{\nu}{\epsilon}$  is taken equal to zero and expression (2-I-12) is substituted in expression (2-I-8). This dependence on the Weber number for fully turbulent flow stems from the fact that the mean square turbulence velocity  $\overline{u'^2}$  - and hence the turbulence viscosity  $\epsilon$  - in two-phase flow are determined by the square of the relative velocity  $u_r^2$  (cf. subsection 2.2.3.2.).

If the product  $ReWe$  decreases the turbulence also decreases until  $ReWe = K_7$ , when expression (2-I-14) changes into

$$\frac{u^\oplus}{u_r} = \frac{Re}{K_6} \quad (2-I-18)$$

\* ) Another possibility is that the missing factor  $(1-\alpha)$  is disappeared on behalf of the abovementioned discrepancy between the present analysis of the liquid velocity peak near the bubble and the use of a turbulence viscosity which has to be defined on the basis of an overall observation of the two-phase mixture.

Substitution of this result in expression (2-I-12) yields

$$\epsilon = \frac{2.43}{4K_1 K_5} \frac{\sigma}{(1-\alpha)\rho_1 u_r} \frac{K_6^2}{Re^2} \quad (2-I-19)$$

Using again the supposition  $\nu = \frac{\eta_1}{(1-\alpha)\rho_1}$  this expression becomes

$$\epsilon = \frac{2.43K_6^2}{4K_1 K_5} \frac{\sigma}{(1-\alpha)\rho_1 u_r} \frac{\nu}{u_r d} \frac{1}{Re}$$

where the constant  $\frac{2.43K_6^2}{4K_1 K_5} = \frac{2.43K_1^4 32^2}{4K_1 K_5 K_4^2} = \frac{256K_1^3 2.43}{K_4^2 K_5} = K_7$

$$\text{so } \frac{\epsilon}{\nu} = \frac{K_7}{ReWe}.$$

Hence in view of the presupposition  $ReWe = K_7$ , it appears that

$$\frac{\epsilon}{\nu} = 1 \quad \text{for } ReWe = K_7 \quad (2-I-20)$$

standing for the Reynolds stresses being equal to the viscosity forces. Any further decrease of the turbulence and the quotient  $\frac{\epsilon}{\nu}$  is impossible because the turbulence will be suppressed abruptly by the viscosity forces, indicating that the physically non-existing region  $0 < \frac{\epsilon}{\nu} < 1$  coincides with the negative determinant - caused by  $ReWe < K_7$  - in expression (2-I-14) which is physically impossible too. The formula for this laminar case  $ReWe < K_7$  is derived by substituting  $\frac{\epsilon}{\nu} = 0$  in expression (2-I-8) yielding

$$\frac{u^\oplus}{u_r} = \frac{K_4}{16K_1^2} Re = \frac{2Re}{K_6} \quad \text{for } ReWe < K_7 \quad (2-I-21)$$

which has to be considered as a completion of expression (2-I-14). This change in formula and flow pattern is analogous to single phase channel flow where at  $Re = 2300$  turbulence is fully suppressed by the viscosity forces making  $\epsilon = 0$  while the correlation for the friction factor  $\lambda$  changes abruptly from a turbulent correlation to the laminar correlation  $\lambda = \frac{64}{Re}$ . The final correlation is thus given by

$$\frac{u^\oplus}{u_r} = \frac{Re}{K_6} \left(1 - \sqrt{1 - \frac{K_7}{ReWe}}\right) \quad \text{for } ReWe \geq K_7 \quad (2-I-14)$$

and

$$\frac{u^\oplus}{u_r} = \frac{2Re}{K_6} \quad \text{for } ReWe < K_7 \quad (2-I-21)$$

where  $Re = \frac{(1-\alpha)\rho_1 u_r d}{\eta_1}$  and  $We = \frac{(1-\alpha)\rho_1 u_r^2 d}{\sigma}$ .

The clear distinction between the turbulent and laminar flow regimes expressed by this correlation fortifies the author's confidence in its validity for the purpose of evaluating the experimental data for the virtual mass coefficients  $B$  in subsection 2.3.1.6.2.2.

APPENDIX 2-J

DERIVATION OF A CORRELATION FOR THE VIRTUAL MASS COEFFICIENT B

The correlation to be developed is based on the general formulation of equation (2-136):

$$B = K_B \times f\left(\frac{u^\oplus}{u_r}\right) \times g(\alpha) \times h(s) \quad (2-136)$$

discussed in subsection 2.3.1.6.2.2. The peak velocity ratio  $\frac{u^\oplus}{u_r}$  is determined in appendix 2-I as:

$$\frac{u^\oplus}{u_r} = \frac{Re}{K_6} \left(1 - \sqrt{1 - \frac{K_7}{ReWe}}\right) \quad \text{for } ReWe \geq K_7 \quad (2-I-14)$$

$$\frac{u^\oplus}{u_r} = 2 \frac{Re}{K_6} \quad \text{for } ReWe < K_7 \quad (2-I-21)$$

For the purpose of determining the function  $f\left(\frac{u^\oplus}{u_r}\right)$  it is assumed that this function can be approximated as:

$$f\left(\frac{u^\oplus}{u_r}\right) = K_f \left(\frac{u^\oplus}{u_r}\right)^n \quad (2-J-1)$$

The constant  $K_f$  in the above formula is not of direct interest because it may subsequently be combined with the constant  $K_6$  from the correlations (2-I-14) and (2-I-21) for the peak velocity ratio  $\frac{u^\oplus}{u_r}$  and factored into the overall constant  $K_B$  from the general correlation (2-136) for the virtual mass coefficient B. This is in contrast with the constant  $K_7$  which affects directly the switch between the correlations (2-I-14) and (2-I-21) and indirect the power  $n$ , therefore  $K_7$  and  $n$  have to be determined simultaneously. This determination is based on two groups of selected data, each having approximately constant void fraction  $\alpha$  and slip  $s$  (cf. table 2-J-1 for the characteristics of these groups). Within each of the two groups the product  $g(\alpha) \times h(s)$  is constant, making the virtual mass coefficients solely proportional to  $\left(K_6 \frac{u^\oplus}{u_r}\right)^n$ . By analyzing the slope only of a number of B versus  $\left(K_6 \frac{u^\oplus}{u_r}\right)$  plots, it was found that a uniform value of  $n = 0.65$  for both groups is obtained by taking the value 35000 for the constant  $K_7$ .

	group 1	group 2
number of measurements	23	23
void fraction	0.34 < $\alpha$ < 0.37	0.51 < $\alpha$ < 0.55
slip	1.43 < $s$ < 1.57	1.67 < $s$ < 1.81
"measured" virtual mass coefficient	0.1 < B < 0.9	0.06 < B < 0.28

TABLE 2-J-1

Characteristics of two groups used for the determination of the function  $f\left(\frac{u^\oplus}{u_r}\right)$

FIGURE 2-J-2

Dependence of the virtual mass coefficients on void fraction (converging test section)

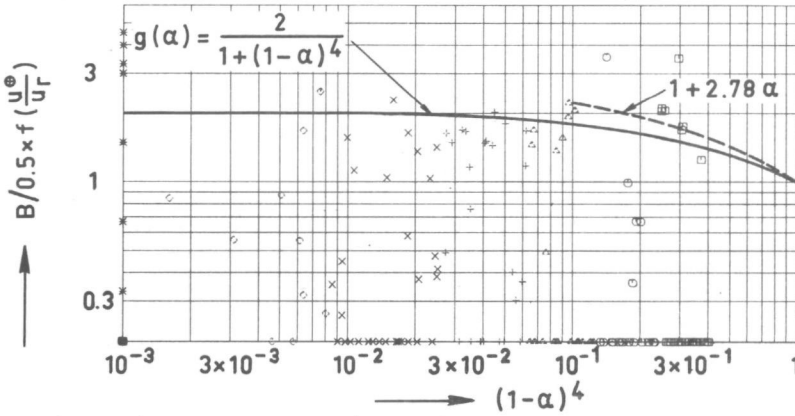
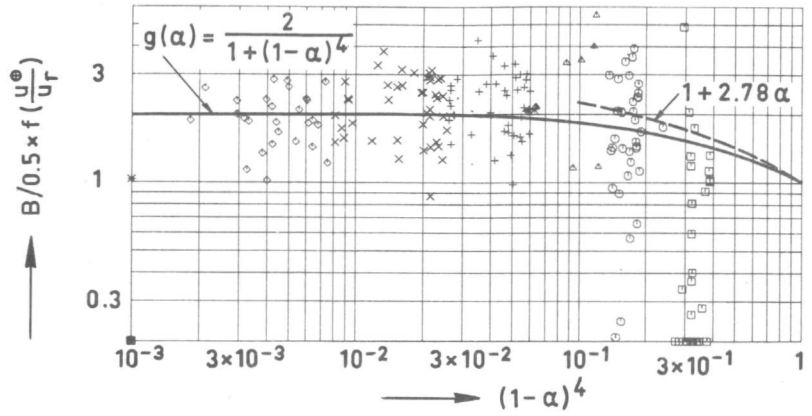


FIGURE 2-J-3

Dependence of the virtual mass coefficients on void fraction (venturi-shaped test section)

FIGURE 2-J-4

Slip dependent virtual mass coefficients as a function of void fraction (converging test section)

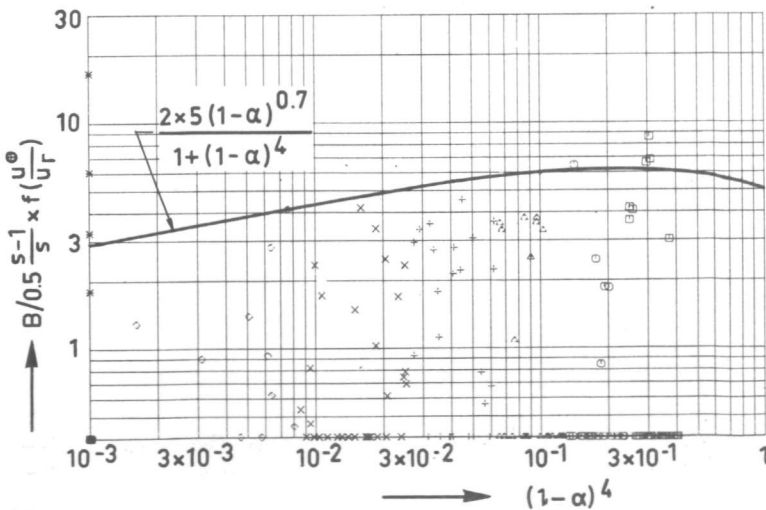
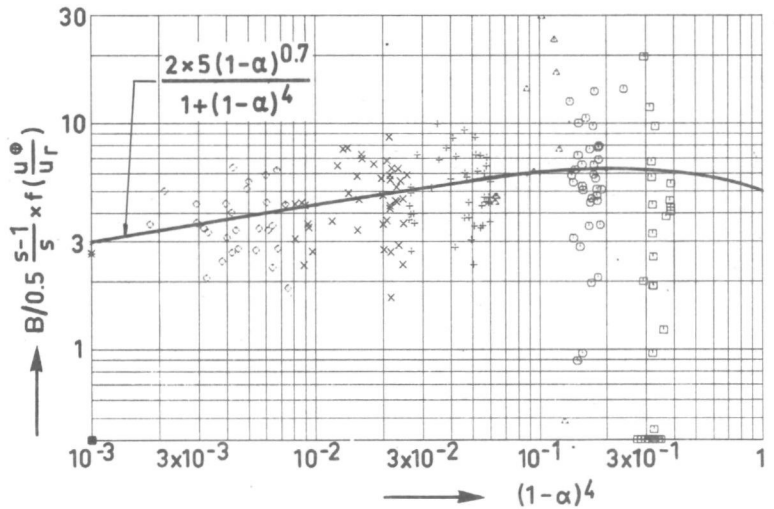


FIGURE 2-J-5

Slip dependent virtual mass coefficients as a function of void fraction (venturi-shaped test section)

FIGURE 2-J-6

Dependence of the virtual mass coefficients on peak velocity ratio (converging test section)

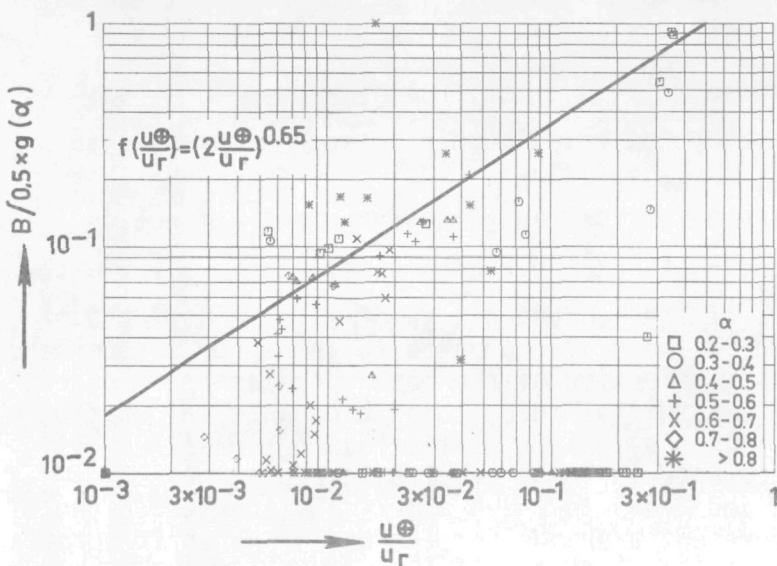
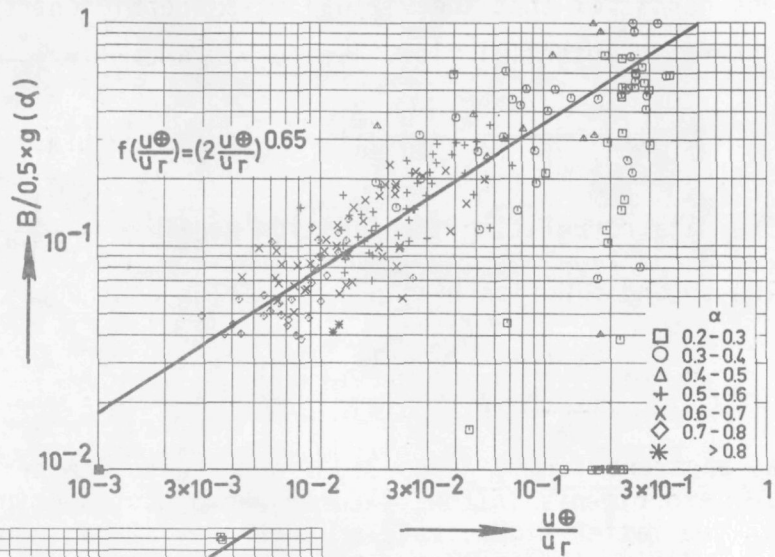


FIGURE 2-J-7

Dependence of the virtual mass coefficients on peak velocity ratio (venturi-shaped test section)

As a next step the product  $g(\alpha) \times h(s)$  was investigated. It was originally intended to separate the effects of void fraction and slip through comparison of the experimental data from the converging and venturi-shaped test sections. The scarcity and inaccuracy of the latter group of data did not, however, permit a proper comparison, leaving only the possibility to assume a function for either the void fraction  $g(\alpha)$  or the slip  $h(s)$  and to determine the remaining the remaining function.

Three functions for the slip were tried viz.:

- $h(s) = 1$ , making the virtual mass coefficient  $B$  independent of the slip
- $h(s) = \frac{s-1}{s}$ , following from the factor  $\frac{u_g - u_1}{u_g}$  discussed in subsection 2.2.2.2.
- $h(s) = (1 + K_s \frac{s-1}{s})$ , resulting from the assumption that the virtual mass term consists of two parts being proportional with  $u_g(u_g - u_1)$  and  $(u_g - u_1)^2$  respectively.

Introduction of the first function,  $h(s) = 1$ , yields, after division of the measured virtual mass coefficients by  $(K_6 \frac{u^oplus}{u_r})^{0.65}$ :

$$B / (K_6 \frac{u^oplus}{u_r})^{0.65} = \frac{0.004}{1 + (1 - \alpha)^4} \quad (2-J-2)$$

The condition that the virtual mass coefficient should equal 0.5 for a single sphere in potential flow, i.e.  $\alpha \rightarrow 0$  and  $\frac{u^\oplus}{u_r} = \frac{1}{2}$ , yields  $K_6 = 10000$  and

$$B = \frac{1}{2} \frac{2}{1+(1-\alpha)^4} \left(2 \frac{u^\oplus}{u_r}\right)^{0.65} \quad (2-J-3)$$

The data correlating the function  $g(\alpha) = \frac{2}{1+(1-\alpha)^4}$  are shown in the figures 2-J-2 and 2-J-3.

The second function  $h(s) = \frac{s-1}{s}$ , yields as the best correlation:

$$B = \frac{1}{2} \frac{2 \times 5 (1-\alpha)^{0.7}}{1+(1-\alpha)^4} \frac{s-1}{s} \left(2 \frac{u^\oplus}{u_r}\right)^{0.65} \quad (2-J-4)$$

as apparent from figures 2-J-4 and 2-J-5. Comparing figures 2-J-3 and 2-J-5 <sup>★)</sup> for experiments in the venturi-shaped test section, it is seen that the data in the latter figure have a larger deviation, hence it is concluded that correlation (2-J-4) does not represent an improvement.

The change of the function for the void fraction from  $g(\alpha) \sim \frac{2}{1+(1-\alpha)^4}$  to  $g(\alpha) \sim \frac{(1-\alpha)^{0.7}}{1+(1-\alpha)^4}$  is necessitated by the relationship between slip and void fraction and of no fundamental significance.

This dependency prevents an adequate investigation of the third function  $h(s) = 1 + K_S \frac{s-1}{s}$ , because ranging  $K_S$  from 0.2 upto 4 results in a variation of less than 30% for the value of the product  $g(\alpha) \times h(s)$  for all of the available data. This variation is too small compared to the error scatterband of about a factor 1.7 to allow a selection of the best correlation, i.e. the best value for the constant  $K_S$ . Notwithstanding this inadequate information it seems likely that the function  $h(s) = 1$  is better than  $h(s) = (1 + K_S \frac{s-1}{s})$ , because increasing  $K_S$  from zero upto infinity results in a continuous transition from figures 2-J-2 and 2-J-3 to 2-J-4 and 2-J-5, the latter two of which were found before to represent a change for the worse. Hence it appears reasonable to assume that this will valid for all intermediate values for  $K_S$  and to consider correlation (2-J-3) as the best fit for this atmospheric air-water data.

It is evident that this conclusion should be considered no more than a likelihood and lacks a firm basis. The remaining uncertainty, however, concerns only the void fraction and slip dependency; the validity of  $f\left(\frac{u^\oplus}{u_r}\right) = \left(2 \frac{u^\oplus}{u_r}\right)^{0.65}$  - including  $K_6 = 10000$  and  $K_7 = 35000$  - represents a fair approximation over a wide range of values for  $\frac{u^\oplus}{u_r}$  as witnessed by figures 2-J-6 and 2-J-7.

★) It should be noticed that the result  $B = 2.5 \frac{s-1}{s}$  for the case of vanishing void fraction and potential flow (i.e.  $\alpha \rightarrow 0$  and  $\frac{u^\oplus}{u_r} = \frac{1}{2}$ ) can only be made consistent with the result of VAN WIJNGAARDEN [43]:  $B' = \frac{1}{5} \frac{s-1}{s}$  by changing the value of constant  $K_6$  from 10000 - used in the correlation for  $\frac{u^\oplus}{u_r}$  - to 205.

APPENDIX 2-K

EXPRESSION FOR THE DERIVATIVE  $\frac{d\alpha}{dz}$  FOR STEAM-WATER MIXTURES IN A STRAIGHT TEST SECTION

The derivation presented here starts from the assumption that the derivative of the quality  $\frac{dx}{dz}$  is known and uses an experimental slip correlation for obtaining the desired relation between void fraction  $\alpha$  and quality  $x$ . For the experimental slip correlation the correlation of BANKOFF [4] is chosen:

$$s = \frac{1-\alpha}{K-\alpha} \quad (2-K-1)$$

using the improved correlation for  $K$  proposed by JONES and DIGHT [76] :

$$K = K_B + (1-K_B)\alpha^r \quad (2-K-2)$$

where Bankoff's constant  $K_B$  and the power  $r$  are functions of the ratio between actual pressure and critical pressure, viz.

$$K_B = 0.71 + 0.29 \left(\frac{p}{p_{cr}}\right) \quad (2-K-3)$$

and

$$r = 3.33 + 0.577 \left(\frac{p}{p_{cr}}\right) + 4.74 \left(\frac{p}{p_{cr}}\right)^2 \quad (2-K-4)$$

The definition for the slip reads:

$$s = \frac{u_g}{u_l} = \frac{\phi_{mg}/\alpha A \rho_g}{\phi_{ml}/(1-\alpha) A \rho_l} = \frac{x \phi_{ml}}{(1-x) \phi_{ml}} \frac{1-\alpha}{\alpha} \frac{\rho_l}{\rho_g} = \frac{x}{1-x} \frac{1-\alpha}{\alpha} \frac{\rho_l}{\rho_g} \quad (2-K-5)$$

Equating (2-K-1) and (2-K-5) yields

$$\frac{1-\alpha}{K-\alpha} = \frac{x}{1-x} \frac{1-\alpha}{\alpha} \frac{\rho_l}{\rho_g} \quad (2-K-6)$$

resulting - after differentiation - in:

$$\begin{aligned} \frac{d\alpha}{dz} = & \frac{K}{\left(1 + \frac{x}{1-x} \frac{\rho_l}{\rho_g}\right)^2} \left\{ \left(\frac{1}{1-x}\right)^2 \frac{\rho_l}{\rho_g} \frac{dx}{dz} + \frac{x}{1-x} \frac{d}{dz} \left(\frac{\rho_l}{\rho_g}\right) \right\} + \\ & + \frac{\frac{x}{1-x} \frac{\rho_l}{\rho_g}}{1 + \frac{x}{1-x} \frac{\rho_l}{\rho_g}} \left\{ \frac{\partial K}{\partial \left(\frac{p}{p_{cr}}\right)} \frac{\partial}{\partial z} \left(\frac{p}{p_{cr}}\right) + \frac{\partial K}{\partial \alpha} \frac{\partial \alpha}{\partial z} \right\} \end{aligned} \quad (2-K-7)$$

For high pressure steam-water mixtures such as used in the experiments of subsection 2.3.2. the terms containing  $\frac{d}{dz} \left(\frac{\rho_l}{\rho_g}\right)$  and  $\frac{d}{dz} \left(\frac{p}{p_{cr}}\right)$  are small compared to the other terms and may hence be omitted, yielding:

$$\frac{d\alpha}{dz} = \frac{\left(\frac{x}{1-x} \frac{\rho_l}{\rho_g}\right)^2}{\left(1 + \frac{x}{1-x} \frac{\rho_l}{\rho_g}\right)^2} \frac{1}{x^2} \frac{\rho_g}{\rho_l} K \frac{dx}{dz} + \frac{\frac{x}{1-x} \frac{\rho_l}{\rho_g}}{1 + \frac{x}{1-x} \frac{\rho_l}{\rho_g}} \frac{\partial K}{\partial \alpha} \frac{\partial \alpha}{\partial z} \quad (2-K-8)$$

Introduction of the volumetric quality  $\beta = \frac{\phi_{vg}}{\phi_{vt}} = \frac{\frac{x}{1-x} \frac{\rho_l}{\rho_g}}{1 + \frac{x}{1-x} \frac{\rho_l}{\rho_g}}$

to obtain a more compact formula, yields

$$\left(1 - \beta \frac{\partial K}{\partial \alpha}\right) \frac{d\alpha}{dz} = \frac{\beta^2}{x^2} \frac{\rho_g}{\rho_l} \frac{dx}{dz} \quad (2-K-9)$$

of which the derivative  $\frac{\partial K}{\partial \alpha}$  is obtained from equation (2-K-2):

$$\frac{\partial K}{\partial \alpha} = r(1 - K_B) \alpha^{r-1} \quad (2-K-10)$$

For the steam-water properties ( $\frac{\rho_l}{\rho_g} \approx 20$ ) and process conditions relevant to the present experiments correlation (2-K-9) varies between  $\frac{d\alpha}{dz} \approx 0.4 \frac{dx}{dz}$  for high qualities and void fractions upto  $\frac{d\alpha}{dz} \approx 6 \frac{dx}{dz}$  for low qualities and void fractions.

APPENDIX 2-L

INSTRUMENT LISTING FOR THE HIGH PRESSURE STEAM-WATER TEST FACILITY

instrument	measured quantity	specifications			
		type	manufacturer	range	calibration
CP central processing unit	scanner for differential pressures	TTL logic	own laboratory	3x16 connections	
DL datalogger		input: analog signals output: punched tape	Solartron	100 input signals (0 ± 30 mV)	manufacturer
D1 differential pressure cell	low range differential pressures	electronic (displacement)	Hottinger & Baldwin (type PD 1/0.1)	0 ± 10 kN/m <sup>2</sup>	water column
D2 idem	high range differential pressures		idem (type PD 1/2)	0 ± 200 kN/m <sup>2</sup>	calibrated air pressure (Wallace & Trenan (FA-2356))
D3 idem	flowmeter differential pressures (venturitubes F1 up to F6)		idem (type PD 1/0.1)	0 ± 10 kN/m <sup>2</sup>	water column
DA amplifiers			idem (type KWS/3-5)		manufacturer
DP differential pressure cell	steamflow from vessel (venturitube F7)	electronic displacement	Foxboro (type 613 D14)	0 - 10 kN/m <sup>2</sup>	water column
DWT dead weight tester	vessel pressure				manufacturer
DP/DWT differential pressure cell		electronic (displacement)	Foxboro (type 613 D14)	0 - 10 kN/m <sup>2</sup>	water column
F1 steam flowmeter	steam to vessel small flowrate (DP 26/27)	venturitube (Normdüse DIN 1952)	Bopp & Reuther	0.05 - 0.56 kg/s (at 7 MN/m <sup>2</sup> & 290°C)	manufacturer
F2 idem	steam to vessel large flowrate (DP 24/25)		Schaeffer & Budenberg	0.22 - 2.22 kg/s (at 7 MN/m <sup>2</sup> & 290°C)	idem
F3 water flowmeter	circulation small flowrate (DP 30/31)		Bopp & Reuther	0.4 - 4.24 kg/s (at 7 MN/m <sup>2</sup> & 280°C)	idem
F4 idem	circulation large flowrate (DP 28/29)		idem	1.4 - 13.46 kg/s (at 7 MN/m <sup>2</sup> & 280°C)	idem
F5 idem	quenching water small flowrate (DP 32/33)		idem	0.05 - 0.57 kg/s (at 7 MN/m <sup>2</sup> & 275°C)	idem
F6 idem	quenching water large flowrate (DP 34/35)		Schaeffer & Budenberg	0.44 - 2.22 kg/s (at 7 MN/m <sup>2</sup> & 275°C)	idem

F7	steam flowmeter	steamflow from vessel	orifice plate (Normblende DIN 1952)	own laboratory	0.22 - 2.22 kg/s (at 0.6 MN/m <sup>2</sup> & 150°C)	
LE	capacitance level gage	two-phase level above test section	electrical capacitance gage	own laboratory (amplifiers: Endress & Hauser silometer SM70)	0 - 1000 mm 0 - 100%	in situ with level testers LT 15 up to LT 20
LT15 up to LT20	level tester		electrical resistance electrode	own laboratory	on/off signal	
LT1 up to LT14	level tester	level in annular cavity	electrical resistance electrode	own laboratory	on/off signal	
LT 21 idem		level in heating vessel of supply water				
P1	manometer	vessel pressure (P22)	straingage manometer	C.E.L. (type RV 22) (strainmeter: Peeke1)	0 - 7 MN/m <sup>2</sup>	dead weight tester
PM1	idem		manometer	Econosto	0 - 10 MN/m <sup>2</sup>	
P2	idem	steam pressure boiler (P25)	straingage manometer	C.E.L. (type RV 22) (strainmeter: Peeke1)	0 - 10.5 MN/m <sup>2</sup>	
PM2	idem		manometer	Econosto	0 - 16 MN/m <sup>2</sup>	
P3	idem	intermediate steam outlet pressure (P26)	straingage manometer	T.N.O. (strainmeter: Peeke1)	0 - 1 MN/m <sup>2</sup>	
PM3	idem		manometer	Econosto	0 - 0.6 MN/m <sup>2</sup>	
T1 up to T4	thermo-couple	temperature in riser/test section	chromel-alumel mineral insulated thermocouple with stainless steel sheat (1.6 mm diameter)			in situ
T5 up to T12	idem	temperature in downcomer				in situ
T13,14 idem	idem	temperature at bottom annular cavity				none
T15,16 idem	idem	steam temperature in steamdome				in situ
T17 up to T24	idem	water temperature in sparger				in situ
T25,26 idem	idem	temperature in annular cavity at sparger level				in situ
T27,28 idem	idem	differential temperature over vessel flange section				none
T29,30 idem	idem	idem over vessel flange bottom section				none

T31,32	thermocouple	steam temperature flowmeters F1 & F2				
T33	idem	steam temperature from boiler				none
T34	idem	steam temperature at vessel inlet				
T35	idem	steam temperature at vessel inlet				
T36,37	idem	water temperature flowmeters F3 & F4				
T38	idem	circulation water temperature at vessel inlet				
T39,40	idem	idem at vessel outlet				in situ
T41	idem	circulation water temperature at pump inlet				
T42	idem	temperature at hydrazine injec- tion system (alarm 100°C)				none
T43	idem	temperature at water supply pump (alarm 100°C)				
T44	idem	temperature in water supply hea- ting vessel (control & alarm 287°C)	chromel-alumel mineral insulated thermocouple with stainless steel sheat (1.6 mm diameter)			in situ
T45	idem	water inlet tempe- rature of supply heating vessel				
T46	idem	idem at outlet				none
T47 up to T49	idem	temperature of drain water at cooler outlet (alarm 80°C)				
T50	idem	water inlet tempe- rature at carry- under quench cooler				in situ
T51	idem	carry-under quench water temperature at vessel inlet				
T52,53	idem	cooling water temperature at drain cooler outlet (alarm 50°C)				
T54	idem	idem at carry- under quench water cooler (alarm 50°C)				none

## APPENDIX 2-M

### COMPUTATION OF THE HEAT LOSS $Q_R$

The heat loss  $Q_R$  from the riser/test section to the downcomer is given by:

$$Q_R = k_R \cdot \pi D_{Ro} \cdot L_R \cdot (\theta_{sat} - \theta_D) \quad (2-M-1)$$

where

- $D_{Ro}$  is the outside diameter of the riser/test section
- $L_R$  is the length of the riser/test section wall corresponding with the control volume
- $\theta_{sat}$  is the saturation temperature inside the riser/test section, obtained as a function of height ( $\theta_{sat} = \theta_{sat}(z)$ ) by a second degree polynomial approximation of the pressures measured at the pressure taps
- $\theta_D$  is the temperature in the downcomer, also approximated by a second degree polynomial based on the measured temperatures  $\theta_6$  through  $\theta_{12}$  in the downcomer ( $\theta_D = \theta_D(z)$ )
- the reciprocal of the overall heat transfer coefficient  $k_R$  is given by:

$$\frac{1}{k_R} = \frac{1}{\alpha_i} \frac{D_{Ro}}{D_{Ri}} + \frac{D_{Ro}}{2\lambda_{ss}} \ln \frac{D_{Ro}}{D_{Ri}} + \frac{1}{\alpha_o} \quad (2-M-2)$$

The film heat transfer coefficients  $\alpha_i$  and  $\alpha_o$  are obtained from the well-known DITTUS-BOELTER [79] correlation for forced convection

$$Nu = 0.023 Re_{tp}^{0.8} Pr^{0.4} \quad (2-M-3)$$

where  $Re_{tp}$  is the Reynolds number for two-phase flow as defined in subsection 2.2.3.1., equation (2-78), i.e.

$$Re = \frac{(1-\alpha)\rho_l u_l D}{\eta_l} (1-\sqrt{\alpha}) \left[ 1 + \frac{\alpha}{1-\alpha} \frac{\rho_g}{\rho_l} \left( \frac{u_g}{u_l} \right)^2 \right]$$

and  $Pr$  is the Prandtl number for the water. Use of the Dittus-Boelter correlation, established for single phase flow, is considered admissible because the Reynolds number for two-phase flow  $Re_{tp}$  has been shown in subsection 2.2.3.1. to give a good representation of the boundary layer for momentum transfer by wall friction and may hence be expected also to properly represent the thermal boundary layer for two-phase flow without boiling at the wall.

As the heat loss  $Q_R$  is only a minor correction in the computation of the steam mass flow and mixture quality, while in addition the film heat transfer resistance  $1/\alpha_i$  at the inner side of the riser/test section represents less than 1/3 of the overall heat transfer resistance  $1/k_R$ , the error caused by invalidity of the above assumption hardly affects the final steam mass flow.

As a matter it should be noted that subsequent computations have shown the relative unimportance of this correction:  $Q_R$ , as computed on the above basis, was found to cause the condensation of less than 1% of the steam flow rate.

## APPENDIX 2-N

### MOMENTUM EXCHANGE IN THE WAKE OF A BUBBLE

The model developed in this appendix is based on the assumption that a bubble enters the wake of a preceding bubble by a stochastic lateral movement as indicated in figure 2-N-1. After determination of the effect of the resulting momentum exchange on the velocity of the second bubble the model is extended to predict the effects on relative velocity and drag force coefficient for a swarm of bubbles.

Notwithstanding the well-known velocity distribution in a wake behind a sphere (see e.g. [13]), the velocity in the wake is taken uniform (cf. figure 2-N-1) in the present model for the sake of simplicity. On entering the wake of the preceding bubble part of the liquid in the wake - equal in volume to the bubble  $V_b$  - is displaced from the wake. The initial momentum of this volume  $\rho_l V_b (u_l + u_w)$  is reduced outside the wake to  $\rho_l V_b u_l$ , while the total amount of momentum is conserved by transforming this decrease in liquid momentum into an increase in momentum of the bubble and its 'added mass', yielding:

$$\rho_l V_b (u_l + u_w) - \rho_l V_b u_l = (\rho_g + B\rho_l) V_b \Delta u_{bw} \quad (2-N-1)$$

where the transfer of momentum due to the drag force is omitted for the sake of simplicity.

Hence the increase in bubble velocity on entering the wake of a preceding bubble is given by:

$$\Delta u_{bw} = \frac{\rho_l}{\rho_g + B\rho_l} u_w \quad (2-N-2)$$

In this way two velocity pairs can be distinguished:  $u_b$  and  $u_l$  for the bubble and liquid respectively outside the wake, and  $u_{bw} = u_b + \Delta u_{bw}$  and  $u_{lw} = u_l + u_w$  in the wake.

The same distinction will be valid for a swarm of bubbles, where a fraction  $\eta$  of the total liquid volume - being the summation of all individual wakes -

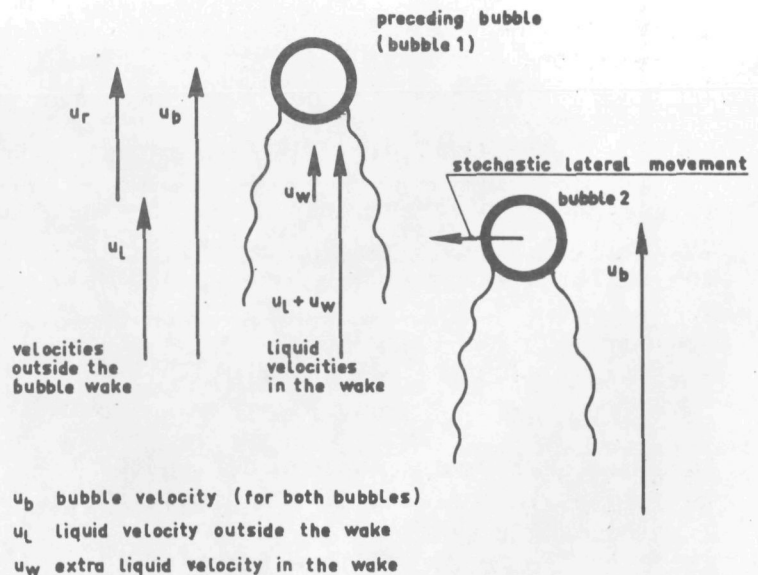


FIGURE 2-N-1

*Bubble entering the wake of a preceding bubble*

will have the velocity  $u_{1W}$ . Because  $\eta$  is a volume fraction it is evident that it will also represent the fraction of bubbles flowing in the wake of an other bubble. Writing the bubble velocity as gas velocity, this yields for the average gas and liquid velocities:

$$\bar{u}_g = (1-\alpha)u_g + \eta u_{gW} \quad (2-N-3)$$

and

$$\bar{u}_l = (1-\alpha)u_l + \eta u_{lW} \quad (2-N-4)$$

These are the average velocities observed for two-phase flow through the test sections and yield the "measured" relative velocity:

$$\bar{u}_r = \bar{u}_g - \bar{u}_l = u_g - u_l + \eta \{(u_{gW} - u_g) - (u_{lW} - u_l)\} \quad (2-N-5)$$

The relative velocity  $u_r = u_g - u_l$  outside the wake can be considered as the "natural" relative velocity, while  $\Delta u_{gW} = u_{gW} - u_g$  and  $u_W = u_{lW} - u_l$  are the extra velocities in the wake. Substitution of these definitions and use of equation (2-N-2) yields:

$$\bar{u}_r = u_r + \eta \left( \frac{\rho_l}{\rho_g + B\rho_l} - 1 \right) u_W = u_r \left\{ 1 + \eta \left( \frac{\rho_l}{\rho_g + B\rho_l} - 1 \right) \frac{u_W}{u_r} \right\} \quad (2-N-6)$$

which is the relation between the relative velocity  $\bar{u}_r$  measured outside the test section and the "natural" relative velocity  $u_r$  outside the wakes of the bubbles.

This measured relative velocity  $\bar{u}_r$  is used for computation of the drag force coefficient  $C_D$  by applying the definition of the drag force  $F_D$ . This drag force, however, acts on the bubble outside the wakes and thus the "natural" drag force coefficient  $C_{Dn}$  and relative velocity  $u_r$  should be used in this definition, yielding a relation between the "measured" and "natural" drag force coefficients:

$$F_D = \frac{3}{4} \alpha \frac{C_D}{d} \rho_l \bar{u}_r^2 = \frac{3}{4} \alpha \frac{C_{Dn}}{d} \rho_l u_r^2 \quad (2-N-7)$$

or with substitution of equation (2-N-6)

$$C_{Dn} = C_D \left\{ 1 + \eta \left( \frac{\rho_l}{\rho_g + B\rho_l} - 1 \right) \frac{u_W}{u_r} \right\}^2 \quad (2-N-8)$$

For gas-liquid flows the gas density  $\rho_g$  can generally be neglected compared to the "added mass"  $B\rho_l$ , yielding  $\frac{\rho_l}{\rho_g + B\rho_l} \approx \frac{1}{B}$ .

This term being larger than unity for the present experiments the term between braces will also exceed unity. For solid-liquid flows - with  $\rho_p > \rho_l$  - the wake and relative velocities  $u_W$  and  $u_r$  are both negative, as is the term

$\left( \frac{\rho_l}{\rho_p + B\rho_l} - 1 \right)$ , hence the term between the braces will be less than unity.

A discussion on the magnitude of this correction term - including an estimation of the values for  $\frac{u_W}{u_r}$  and  $\eta$  - is given in subsection 2.4.1.

An additional remark is in order on the fact that the above model is limited to bubbles in the wake of one preceding bubble only, while the possibility of a third bubble entering in the wake of the second bubble is not taken into account. The model will now be extended to the formation of "chains" of bubbles, which is only meant to indicate the effect of such a "chain" formation, because the existence of these "chains" is not certain at all and in addition the increase in drag force is omitted again. The relative velocity of a second bubble with respect to the liquid velocity in the wake of the preceding bubble

can be written as

$$u_{r,2} = u_{bw} - u_{1w} = (u_b + \Delta u_{bw}) - (u_1 + u_w) \quad (2-N-9)$$

or with substitution of equation (2-N-2)

$$u_{r,2} = u_b - u_1 + \left(\frac{\rho_1}{\rho_g + B\rho_1} - 1\right)u_w \quad (2-N-10)$$

Because  $u_b - u_1$  is the relative velocity of the preceding bubble it can be denoted as  $u_{r,1}$ , while for the same reason  $u_w = u_{w,1}$  leading to the general formulation

$$u_{r,n+1} = u_{r,n} \left\{ 1 + \left(\frac{\rho_1}{\rho_g + B\rho_1} - 1\right) \frac{u_{w,n}}{u_{r,n}} \right\} \quad (2-N-11)$$

The quotient  $\frac{u_{w,n}}{u_{r,n}}$  may be assumed equal for all wakes:  $\frac{u_{w,n}}{u_{r,n}} = \frac{u_w}{u_r}$ .

The average relative velocity  $\bar{u}_r$  can be obtained by summation of distinct groups of bubbles. The first group - having the relative velocity  $u_{r,1}$  - is the fraction  $(1-\eta)$  of all bubbles which does not flow into the wake of any other bubble; thus  $u_{r,1}$  equals the "natural" relative velocity  $u_r$ . The second group - having the relative velocity  $u_{r,2}$  - is part of the remaining bubble fraction which flows into the wake of an other bubble; of this amount a fraction  $(1-\eta)$  flows into the wake of one preceding bubble only, yielding the fraction  $\eta(1-\eta)$  of the total amount of bubbles having the relative velocity  $u_{r,2}$ . Development of the fractions of subsequent groups leads to:

$$\begin{aligned} \bar{u}_r = & (1-\eta)u_{r,1} + \eta(1-\eta)u_{r,2} + \eta^2(1-\eta)u_{r,3} + \dots \\ & \dots + \eta^n(1-\eta)u_{r,n+1} + \dots \end{aligned} \quad (2-N-12)$$

Introduction of

$$p = \left(\frac{\rho_1}{\rho_g + B\rho_1}\right) \frac{u_w}{u_r} \quad (2-N-13)$$

and substitution of equation (2-N-11), yields - after series expansion - for  $\eta p < 1$ :

$$\bar{u}_r = u_r \left\{ 1 + \frac{\eta p}{1 - \eta p} \right\} \quad (2-N-14)$$

This means that the factor for the relative velocity of equation (2-N-6) is amplified by a factor  $\frac{1}{1 - (\eta p)^2}$  through this "chain" formation, hence the correction term between  $C_{Dn}$  and  $C_D$  (cf. expression (2-N-8)) will also be amplified.

It should be stressed that both expressions (2-N-8) and (2-N-14) - apart from the difficulty to derive the fraction  $\eta$  - give no more than an impression of the effects of momentum exchange in the wakes because of the fairly crude simplifications containing the above models, such as omission of the increase in drag force in the wake, uniform velocity distribution in the wake and the postulated existence of infinite 'chains'.

## APPENDIX 2-0

### DROPLET DIAMETERS IN MIST FLOW

The computation of the droplet diameter  $d_d$  in mist flow will be based on the same model and underlying thoughts as used before - in subsection 2.2.3.2. and Appendix 2-D - for the computation of the bubble diameter  $d$ . I.a.v. the model proposed by SEVIK and PARK [56] is assumed to retain its validity for droplets. In view of the application in subsection 2.4.1. the ratio  $\frac{d_d}{d^{\star}}$  will be derived instead of the droplet diameter, where  $d^{\star}$  stands for the bubble diameter resulting from expression (2-97) for the actual flow conditions<sup>★</sup>).

Sevik and Park's model being based on mechanical energy dissipation, it shall be first proved that the numerical value obtained for this energy dissipation is independent of the mathematical description of the flow pattern under consideration be it mist flow or bubble flow<sup>★</sup>.

The momentum balances of non-accelerating mist flow, equivalent to the equations (2-D-1) and (2-D-2) for bubble flow, read

- for the gas phase

$$0 = -\alpha A \frac{dp}{dz} - \alpha A \rho_g g - F_{Dd} A - A \left( \frac{dp}{dz} \right)_{fr} \quad (2-0-1)$$

- and for the liquid phase

$$0 = -(1-\alpha) A \frac{dp}{dz} = (1-\alpha) A \rho_l g + F_{Dd} A \quad (2-0-2)$$

They differ from those for bubble flow by the appearance of the frictional pressure drop in the momentum balance for the gas phase, this being the continuous phase in the case of mist flow.

By adding the product of gas balance and gas velocity to that of liquid balance and liquid velocity the mechanical energy balance is obtained:

$$\begin{aligned} \{(1-\alpha)u_l + \alpha u_g\} A \frac{dp}{dz} + \{(1-\alpha)\rho_l u_l + \alpha \rho_g u_g\} A g = \\ = -\{F_{Dd} A u_r + A \left( \frac{dp}{dz} \right)_{fr} u_g\} \end{aligned} \quad (2-0-3)$$

Hence the mechanical energy dissipation in mist flow is

$$\frac{dE_m}{dz} = -\{F_{Dd} A u_r + A \left( \frac{dp}{dz} \right)_{fr} u_g\} \quad (2-0-4)$$

whereas the corresponding equations (2-D-5) and (2-D-6) for bubble flow yield:

$$\frac{dE^{\star}}{dz} = -\{F_{D^{\star}} A u_r + A \left( \frac{dp}{dz} \right)_{fr} u_l\} \quad (2-0-5)$$

★)  $d^{\star}$  therefore has no physical meaning as there are no bubbles. The superscript  $\star$  will be used throughout this Appendix to indicate parameters referring to bubble flow and therefore having a numerical meaning only.

The apparent difference in the term containing the frictional pressure drop is canceled out by the difference between the expressions for the drag forces  $F_{Dd}$  and  $F_D^*$ . The drag force for mist flow can be derived from the momentum balances (2-0-1) and (2-0-2) by elimination of the pressure gradient, yielding:

$$F_{Dd} = \alpha(1-\alpha)(\rho_l - \rho_g)g - (1-\alpha)\left(\frac{dp}{dz}\right)_{fr} \quad (2-0-6)$$

while the corresponding expression for bubble flow is

$$F_D^* = \alpha(1-\alpha)(\rho_l - \rho_g)g + \alpha\left(\frac{dp}{dz}\right)_{fr} \quad (2-0-7)$$

resulting in

$$F_{Dd} = F_D^* - \left(\frac{dp}{dz}\right)_{fr} \quad (2-0-8)$$

Substitution of this expression in equation (2-0-4) yields

$$\begin{aligned} \frac{dE_m}{dz} &= -\{F_D^* A u_r - A\left(\frac{dp}{dz}\right)_{fr} u_r + A\left(\frac{dp}{dz}\right)_{fr} u_g\} = \\ &= -\{F_D^* A u_r + A\left(\frac{dp}{dz}\right)_{fr} u_l\} = \frac{dE^*}{dz} \end{aligned} \quad (2-0-9)$$

thus confirming that the numerical value for mechanical energy dissipation is independent of the mathematical description of the flow pattern, as stated above. By contrast, the specific energy dissipation  $\epsilon$  per unit mass and time, used for computing the mean square turbulence velocity  $\overline{u'^2} = 2.0(\epsilon d)^{2/3}$  (equation (2-86)), differs for both flow patterns because of the change of continuous phase. The relevant expressions are

$$\epsilon_m = \frac{\Delta E_m}{m_m} = \frac{-\frac{dE_m}{dz} \Delta z}{m_m} = \frac{-\frac{dE_m}{dz} \Delta z}{\alpha \rho_g A \Delta z} \quad (2-0-10)$$

for mist flow, and

$$\epsilon^* = \frac{-\frac{dE^*}{dz} \Delta z}{(1-\alpha)\rho_l A \Delta z} \quad (2-0-11)$$

for bubble flow  $^*$ .

Use of equation (2-0-9) yields

$$\epsilon_m = \epsilon^* \frac{1-\alpha}{\alpha} \frac{\rho_l}{\rho_g} \quad (2-0-12)$$

which expression will be utilized below in the application of Sevik and Park's model for mist flow.

According to the description of this model given in subsection 2.2.3.2. the flow induced frequency

$$f = \frac{\sqrt{u'^2}}{d} \quad (2-0-13)$$

should equal the second natural frequency of the droplet given by

$$(2\pi f_2)^2 = \frac{24}{2\rho_c + 3\rho_d} \frac{\sigma}{\left(\frac{d_d}{2}\right)^3} \quad (2-0-14)$$

For the present case of mist flow the density of the discontinuous phase  $\rho_d = \rho_1$ , while the density of the continuous phase is defined - just as for bubble flow - by the density of the mixture surrounding the droplet:  $\rho_c = \alpha\rho_g + (1-\alpha)\rho_1$ . Equalizing  $f$  to  $f_2$  yields

$$\frac{(2.5-\alpha)\rho_1 \overline{u'^2} d_d}{\sigma} = \frac{2.43}{1 + \frac{\alpha}{2.5-\alpha} \frac{\rho_g}{\rho_1}} \quad (2-0-15)$$

for increasing void fractions:  $\alpha \rightarrow 1$ , the diameter values obtained from this expression will increasingly differ from those resulting from equation (2-94) for bubble flow

$$\frac{(1-\alpha)\rho_1 \overline{u'^2} d}{\sigma} = \frac{2.43}{1 + \frac{1.5+\alpha}{1-\alpha} \frac{\rho_g}{\rho_1}} \quad (2-94)$$

In addition it should be noticed that for large void fractions and high pressures, i.e.  $\frac{\rho_g}{\rho_1} > 0.05$ , the additional term  $\epsilon_W = \frac{1.5+\alpha}{1-\alpha} \frac{\rho_g}{\rho_1}$  omitted from equation (2-94) will not be small compared to unity anymore. Substitution of

$$\overline{u'^2} = 2.0(\epsilon_m d_d)^{2/3} \quad (2-0-16)$$

where  $\epsilon_m$  follows from equation (2-0-12), and of

$$\overline{u'^2} = 2.0(\epsilon^* d^*)^{2/3} \quad (2-0-17)$$

in equations (2-0-15) and (2-94) respectively, yields

$$2.0 \frac{(2.5-\alpha) \left(\frac{1-\alpha}{\alpha}\right)^{2/3} \rho_1 \left(\frac{\rho_1}{\rho_g}\right)^{2/3} \epsilon^{*2/3} d_d^{2/3}}{\sigma} = \frac{2.43}{1 + \frac{\alpha}{2.5-\alpha} \frac{\rho_g}{\rho_1}} \quad (2-0-18)$$

and

$$2.0 \frac{(1-\alpha)\rho_1 \epsilon^{*2/3} d^{*5/3}}{\sigma} = \frac{2.43}{1 + \frac{1.5+\alpha}{1-\alpha} \frac{\rho_g}{\rho_1}} \quad (2-0-19)$$

From these equations it follows that

$$\frac{d_d}{d^*} = \frac{\alpha^2 (1-\alpha)^{1/5}}{(2.5-\alpha)^3} \left(\frac{\rho_g}{\rho_1}\right)^{2/5} \cdot \frac{1 + \frac{1.5+\alpha}{1-\alpha} \left(\frac{\rho_g}{\rho_1}\right)^{3/5}}{1 + \frac{\alpha}{2.5-\alpha} \left(\frac{\rho_g}{\rho_1}\right)} \quad (2-0-20)$$

The numerical difference between the diameters  $d_d$  and  $d^*$  is thus seen to be mostly determined by the density ratio  $\frac{\rho_g}{\rho_1}$ .

## APPENDIX 2-P

### PEAK VELOCITY RATIO OF A RANKINE BODY

A Rankine body is the body of revolution resulting from the superposition of a uniform flow to the flow due to a source and sink of equal strength, the uniform flow having the same direction as the line joining source and sink (cf. [84]). The geometry of such a body and the location of source and sink are shown in figure 2-P-1.

The aim of the present analysis is to derive for such a body the value of the peak velocity  $u^{\oplus}$ , being the increase of velocity from infinity to the boundary at the largest cross section of the body. This peak velocity  $u^{\oplus}$  was been defined in figure 2-46 for viscous flow and is indicated for the present potential flow in figure 2-P-1.

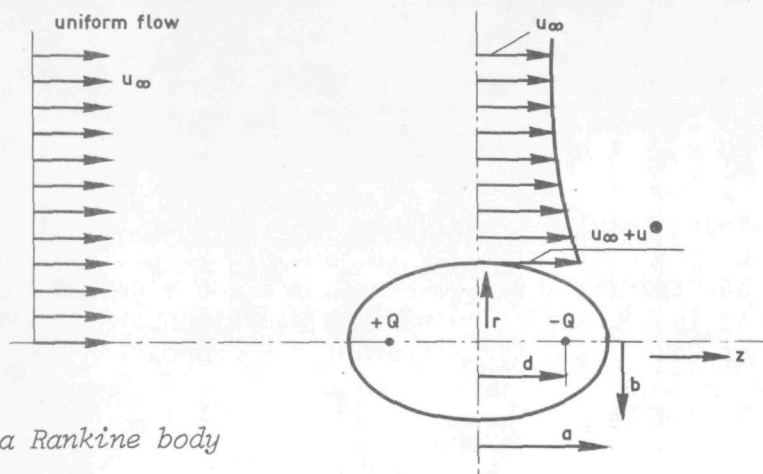


FIGURE 2-P-1

*Flow and body geometry of a Rankine body*

According to potential flow theory (see e.g. [41]) the velocity potential  $\phi$  - expressed in terms of the cylindrical coordinates of figure 2-P-1 - may be obtained from the following superposition:

$$\phi = u_{\infty}z - \frac{Q/4\pi}{\sqrt{(z+d)^2 + r^2}} - \frac{-Q/4\pi}{\sqrt{(z-d)^2 + r^2}} \quad (2-P-1)$$

where  $Q$  is the volumetric flow from and to the source and sink and  $u_{\infty}$  is the

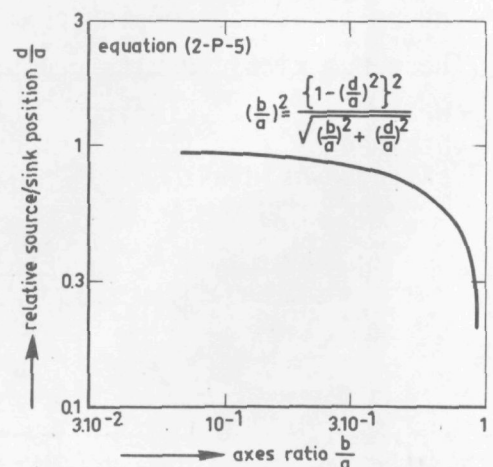


FIGURE 2-P-2

*Source/sink position for a Rankine body*

is the uniform flow at infinity.  
The velocity in the z-direction is given by:

$$u_z = \frac{\partial \phi}{\partial z} = u_\infty + \frac{Q}{4\pi} \left[ \frac{z+d}{\{(z+d)^2 + r^2\}^{3/2}} - \frac{z-d}{\{(z-d)^2 + r^2\}^{3/2}} \right] \quad (2-P-2)$$

The source/sink strength Q can be obtained from the requirement that the axial velocity  $u_z$  must be zero at the boundary of the Rankine body ( $z=a$ ,  $r=0$ ), yielding

$$0 = u_\infty + \frac{Q}{4\pi} \left[ \frac{a+d}{\{(a+d)^2\}^{3/2}} - \frac{a-d}{\{(a-d)^2\}^{3/2}} \right]$$

or equivalent

$$u_\infty = - \frac{Q}{4\pi} \left[ \frac{1}{(a+d)^2} - \frac{1}{(a-d)^2} \right] = - \frac{Q}{4\pi} \left[ \frac{-4ad}{(a^2-d^2)^2} \right]$$

and thus

$$\frac{Q}{4\pi} = \frac{(a^2-d^2)^2}{4ad} u_\infty \quad (2-P-3)$$

These results (2-P-2) and (2-P-3) show that the flow around a Rankine body is determined by the uniform velocity  $u_\infty$ , the longitudinal dimension  $2a$  and the distance between source and sink  $2d$ . For the present purpose, however, it is convenient to use the dimension of the largest cross section  $2b$  instead of  $2d$ . For this replacement the expression for  $b$  given in [84] will be used:

$$b^2 = \frac{Q}{\pi u_\infty} \frac{d}{\sqrt{b^2+d^2}} \quad (2-P-4)$$

Prior to the numerical evaluation of this implicit equation it should be remarked that it is convenient to define the Rankine body by dimensionless variables:  $b \rightarrow \frac{b}{a}$ ,  $d \rightarrow \frac{d}{a}$  and  $a \rightarrow 1$ . Introduction of this scaling and substitution of equation (2-P-3) in correlation (2-P-4), yields

$$\left(\frac{b}{a}\right)^2 = \frac{\{1 - (\frac{d}{a})^2\}^2}{\sqrt{(\frac{b}{a})^2 + (\frac{d}{a})^2}} \quad (2-P-5)$$

The numerical results of this expression are presented in figure 2-P-2, where the relative source/sink position  $\frac{d}{a}$  is related to the axes ratio  $\frac{b}{a}$ .

These numerical results are used to derive the velocity  $(u_z)_{z=0, r=b}$ , needed to obtain the peak velocity  $u^\oplus$ . The expression for the velocity  $(u_z)_{z=0}$  is obtained by substitution of equation (2-P-3) into (2-P-2) and simultaneous scaling, yielding:

$$\begin{aligned} (u_z)_{z=0} &= u_\infty \left[ 1 + \frac{\{1 - (\frac{d}{a})^2\}^2}{4(\frac{d}{a})} \left\{ \frac{d/a}{\{(\frac{d}{a})^2 + (\frac{r}{a})^2\}^{3/2}} - \frac{-d/a}{\{(-\frac{d}{a})^2 + (\frac{r}{a})^2\}^{3/2}} \right\} \right] = \\ &= u_\infty \left[ 1 + \frac{\{1 - (\frac{d}{a})^2\}^2}{2\{(\frac{d}{a})^2 + (\frac{r}{a})^2\}^{3/2}} \right] \end{aligned} \quad (2-P-6)$$

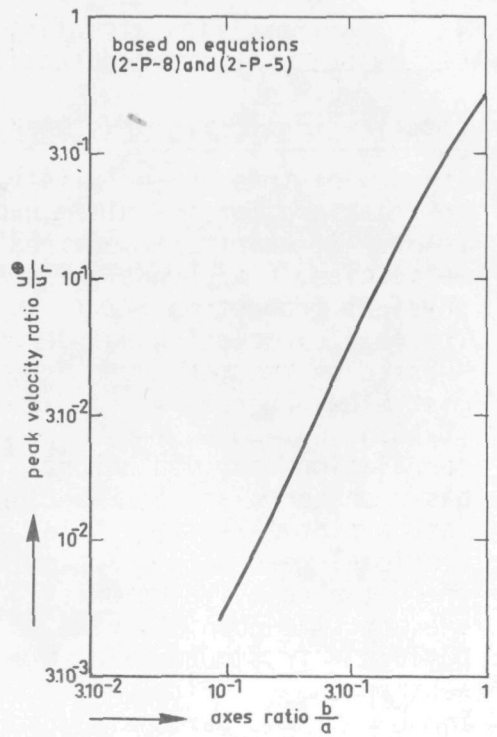


FIGURE 2-P-3  
Peak velocity ratio for a Rankine body

For the peak velocity  $u^{\oplus}$  - defined at the point  $z=0, r=b$  - this results in:

$$u^{\oplus} = \frac{\{1 - (\frac{d}{a})^2\}^2}{2\{(\frac{d}{a})^2 + (\frac{b}{a})^2\}^{3/2}} u_{\infty} \quad (2-P-7)$$

Because the uniform velocity at infinity  $u_{\infty}$  is the relative velocity  $u_r$  with respect to the Rankine body, the peak velocity ratio  $\frac{u^{\oplus}}{u_r}$  for a Rankine body is derived as:

$$\frac{u^{\oplus}}{u_r} = \frac{\{1 - (\frac{d}{a})^2\}^2}{2\{(\frac{d}{a})^2 + (\frac{b}{a})^2\}^{3/2}} \quad (2-P-8)$$

This expression is evaluated by substitution of the numerical effects of equation (2-P-5) for  $\frac{d}{a}$  versus  $\frac{b}{a}$ , and these final results - correlating  $\frac{u^{\oplus}}{u_r}$  to  $\frac{b}{a}$  - are presented in figure 2-P-3.

## APPENDIX 2-Q

### EQUATIONS FOR ONE-DIMENSIONAL VERTICAL UPWARD TWO-PHASE FLOW

The aim of this appendix is to summarize the full set of equations and correlations for one-dimensional two-phase flow, derived and discussed throughout chapter 2, which are required to compute the void fraction, pressure drops and velocities in a channel with arbitrary cross section for given mass flow and physical properties.

The only correlation not derived in chapter 2 is a drag force correlation - based on the mean void fraction - valid for the entire range of bubble and mist flow. Therefore this appendix starts with the extension of correlation (2-135):  $C_D = 0.44(1-\alpha)^6$  into the mist flow region prior to summarizing the correlations derived before. This extension of correlation (2-135) will be based on correlation (2-162) derived for local void fractions and the transformation plot 2-H-2. This plot, used before to "translate" the measured cross-sectional mean void fraction to the local void fraction  $\alpha_{UR}$  at the location where the relative velocity  $u_r$  equals the mean value  $\langle u_r \rangle$ , will now be used for the opposite purpose, viz. to convert the lines - representing correlation (2-162) - in figure 2-78 to a plot of drag force coefficient versus cross-sectional mean void fraction. The resulting curves are shown in figure 2-Q-1 for both atmospheric air-water and steam-water mixtures.

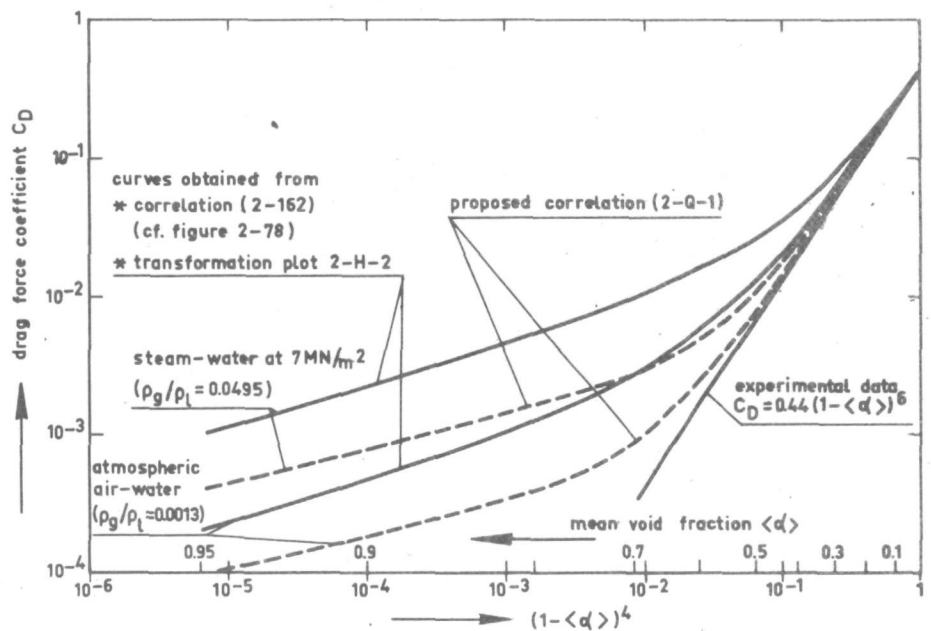


FIGURE 2-Q-1

*Correlations for the drag force coefficient over the entire range of cross-sectional mean void fractions*

The discrepancy between these curves and the measured data for void fractions  $\alpha > 0.5$  is most probably due to the inaccuracy of the plot 2-H-2 resulting from the analyses in appendix 2-H.

Based on the same reasoning as presented in subsection 2.4.1.2. for correlation (2-162) the following correlation based on cross-sectional mean void fractions is proposed:

$$C_D = 0.44(1-\alpha)^6 \left( 1 + 0.06 \frac{(\rho_g/\rho_l)^{0.4}}{(1-\alpha)^5} \right) \quad (2-Q-1)$$

Curves representing this correlation have been included in figure 2-Q-1 and are seen to yield an improved approximation of measured data for void fractions up to 0.65 and 0.55 for atmospheric air-water and steam-water at 7 MN/m<sup>2</sup>, respectively. For higher void fractions no firm conclusion concerning the correlation's validity is warranted due to the dearth of experimental data (and their total absence for void fractions exceeding 0.8). But in view of the analytical basis of the initial correlation (2-162) for void fractions above 0.8, the author expects correlation (2-Q-1) to yield a fair representation for drag force coefficients in the entire range of void fractions up to 0.9.

The summary of equations and correlations will be presented as a basic set of two momentum balances with additional correlations and definitions for the various terms of these balances. For given mass flows and physical properties two unknown parameters of the one-dimensional two-phase flow may be computed directly from the balance equations. Usually these will be the void fraction  $\alpha$  and the pressure gradient  $\frac{dp}{dz}$ . The other flow parameters such as the gas and liquid velocities, frictional component of the pressure gradient, bubble diameter, etc. may be computed simultaneously using the relevant definitions or correlations. It should be noticed that the full set of equations is coupled, thus requiring a simultaneous and iterative solution.

The momentum balances for the gas and liquid phase for vertical upward flow are:

momentum balance (2-156)

$$\frac{d}{dz} \alpha A \rho_g u_g^2 + F_A A = -\alpha A \frac{dp}{dz} - \alpha A \rho_g g - F_D A - \Delta_\alpha \left( \frac{dp}{dz} \right)_{fr}$$

for the gas phase, and (2-157)

$$\frac{d}{dz} (1-\alpha) A \rho_l u_l^2 = -(1-\alpha) A \frac{dp}{dz} - (1-\alpha) A \rho_l g + F_D A - (1-\Delta_\alpha) \left( \frac{dp}{dz} \right)_{fr}$$

for the liquid phase.

The following remarks appear in order:

- they do not incorporate the two-dimensional effects for pseudo-one-dimensional flow as discussed in subsection 2.2.4., because the appropriate constants - defined in equations (2-106) and (2-107) and table 2-21 - only yield significant deviations in some special cases where the slip ratio  $s = \frac{u_g}{u_l}$  is very close to unity.
- the equations are validated for the entire range of bubble and mist flow by introduction of the delta function  $\Delta_\alpha$  and the adjustment of the interaction force correlations (for  $F_D$  and  $F_A$ ) in the mist flow region.
- in accordance with the discussion in subsection 2.2.1.2. no change of phase effects are taken into account
- the gas and liquid velocities are defined as  $u_g = \frac{\phi_{mg}}{\alpha A \rho_g}$  and  $u_l = \frac{\phi_{ml}}{(1-\alpha) A \rho_l}$ , where  $A$  is the cross-sectional area of the channel
- for downward flow the sign of the gravity terms changes to positive.

The frictional pressure drop terms  $(1-\Delta_\alpha) \left( \frac{dp}{dz} \right)_{fr}$  and  $\Delta_\alpha \left( \frac{dp}{dz} \right)_{fr}$  can be computed on the basis of definition (2-155) for the delta function

$$\begin{aligned} \Delta_\alpha &= 0 && \text{for } \alpha \leq 0.75 \\ \Delta_\alpha &= 10(\alpha - 0.75) && \text{for } 0.75 < \alpha < 0.85 \\ \Delta_\alpha &= 1 && \text{for } \alpha \geq 0.85 \end{aligned}$$

and the combinations of equations (2-73) and (2-83) yielding

$$\left(\frac{dp}{dz}\right)_{fr} = \frac{\lambda_m}{D} \frac{1}{2} M_{tp} + \frac{\lambda_m}{2} F_D$$

The friction factor  $\lambda_m$  is computed according to equation (2-79):

$$\lambda_m = 0.00560 + \frac{0.500}{Re_{tp}^{0.32}} \quad (2.10^3 < Re_{tp} < 2.10^5)$$

where the Reynolds number for two-phase flow is defined by expression (2-78)

$$Re_{tp} = \frac{(1-\alpha)\rho_l u_l D}{\eta_l} (1-\sqrt{\alpha}) \left[ 1 + \frac{\alpha}{1-\alpha} \frac{\rho_g}{\rho_l} \left(\frac{u_g}{u_l}\right)^2 \right]$$

The definitions for the two-phase momentum  $M_{tp}$  and the drag force  $F_D$  are given by equations (2-74) and (2-24):

$$M_{tp} = (1-\alpha)\rho_l u_l^2 + \alpha\rho_g u_g^2$$

and

$$F_D = \frac{3}{4} \alpha \frac{C_D}{d} \rho_l u_r |u_r|$$

The drag force coefficient  $C_D$  is given by correlation 2-Q-1.

The "bubble" diameter  $d$  for both bubble and mist flow is obtained from equation (2-98):

$$d = \left\{ \frac{1.22}{1+\xi_W} \left( \frac{\sigma}{(1-\alpha)\rho_l u_r^2} \right)^{1/3} \right\}^{3/5} \left\{ \frac{\sigma}{F_D \frac{u_r}{|u_r|} [1+\xi_E]} \right\}$$

where  $\xi_W$  and  $\xi_E$  are defined by equations (2-95) and (2-99), respectively:

$$\xi_W = \frac{1.5+\alpha}{1-\alpha} \frac{\rho_g}{\rho_l}$$

and

$$\xi_E = \frac{\left(\frac{dp}{dz}\right)_{fr} u_l}{F_D u_r}$$

The acceleration force  $F_A$  is defined in expression (2-66) as:

$$F_A = \rho_l \frac{d}{dz} (\alpha B u_g (u_g - u_l))$$

The virtual mass coefficient  $B$  of this expression follows from equation (2-139):

$$B = \frac{1.569}{1+(1-\alpha)^4} \left(\frac{u^\oplus}{u_r}\right)^{0.65}$$

where the peak velocity  $\frac{u^\oplus}{u_r}$  is given in expression (2-138):

$$\frac{u^\oplus}{u_r} = \frac{Re}{10000} \left( 1 - \sqrt{1 - \frac{35000}{ReWe}} \right) \quad \text{for } ReWe \geq 35000$$

and

$$\frac{u^\oplus}{u_r} = \frac{Re}{5000} \quad \text{for } ReWe < 35000$$

The bubble Reynolds and Weber number in these latter expressions are defined as:

$$Re = \frac{(1-\alpha)\rho_l u_r d}{\eta_l}$$

and

$$We = \frac{(1-\alpha)\rho_l u_r^2 d}{\sigma}$$

## APPENDIX 3-A

### VISCOSITY TERMS IN TURBULENT TWO-PHASE FLOW MOMENTUM BALANCES

The aim of this appendix is to elaborate on and justify the validity of the viscosity terms in formulae (3-9), (3-10) and (3-11) of subsection 3.2.1.2.1.

One of the most detailed descriptions of momentum balances for turbulent two-phase flow is given by HINZE [58]<sup>\*</sup>, who does not, however, enter into the details of the Reynolds stresses nor deal with neglects allowable for practical applications. Both aspects will be discussed in this appendix.

The momentum balance for the liquid phase of turbulent two-phase flow is given in [58] (in Cartesian coordinates) as:

$$\begin{aligned} \frac{\partial}{\partial t} ((1-\alpha)\rho_l u_{li}) + \frac{\partial}{\partial x_k} ((1-\alpha)\rho_l u_{li} u_{lk}) = \\ = - (1-\alpha) \frac{\partial p}{\partial x_i} - (1-\alpha)\rho_l g \frac{\partial x_i}{\partial x_l} + F_{Di} + \\ + \frac{\partial}{\partial x_j} \left( \eta \left( \frac{\partial}{\partial x_j} ((1-\alpha)u_{li} + \alpha u_{gj}) + \frac{\partial}{\partial x_i} ((1-\alpha)u_{lj} + \alpha u_{gj}) \right) \right) + \\ - \frac{2}{3} \frac{\partial}{\partial x_i} \left( \eta ((1-\alpha)u_{lk} + \alpha u_{gk}) - \rho_l \frac{\partial}{\partial x_k} ((1-\alpha)\overline{u'_{li}u'_{lk}}) \right) \end{aligned} \quad (3-A-1)$$

where  $u'$  represents the turbulence velocity and  $u$  the time averaged velocities.

The following remarks concerning this equation appear in order:

- Hinze assumed the two-phase mixture to be a Newtonian fluid, yielding the usual relation between fluid stress and deformation on the basis of the mixture velocity  $u_m = (1-\alpha)u_l + \alpha u_g$  and an appropriate two-phase viscosity, viz. <sup>\*\*</sup>):

$$\begin{aligned} \sigma_{ij} = -p\delta_{ij} + \eta \left( \frac{\partial}{\partial x_j} ((1-\alpha)u_{li} + \alpha u_{gj}) + \frac{\partial}{\partial x_i} ((1-\alpha)u_{lj} + \alpha u_{gj}) \right) + \\ - \frac{2}{3} \eta \frac{\partial}{\partial x_k} ((1-\alpha)u_{lk} + \alpha u_{gk}) \delta_{ij} \end{aligned} \quad (3-A-2)$$

Because of the occurrence of viscosity terms in the liquid momentum balance only, the present author considers it more consistent to relate the stress tensor for these cases to the liquid velocity and liquid viscosity, i.e.

$$\begin{aligned} \sigma_{ij} = -p\delta_{ij} + \eta_l \left( \frac{\partial}{\partial x_j} ((1-\alpha)u_{li}) + \frac{\partial}{\partial x_i} ((1-\alpha)u_{lj}) \right) + \\ - \frac{2}{3} \eta_l \frac{\partial}{\partial x_k} ((1-\alpha)u_{lk}) \delta_{ij} \end{aligned} \quad (3-A-3)$$

<sup>\*</sup>) Hinze derived the equations for a suspension of solid particles, resulting in the absence of viscosity terms in the balances for the dispersed phase. As already stated in subsection 2.2.1.2. this is equally applicable to the gas momentum balances of bubble flows.

<sup>\*\*</sup>)  $\delta_{ij}$  is the Kronecker delta, i.e.  $\delta_{ij}=0$  for  $i \neq j$  and  $\delta_{ij}=1$  for  $i=j$ .

- Hinze arrived at equation (3-A-1) by using the Reynolds procedure for turbulent flows and neglecting the products containing the turbulence fluctuation of the dispersed phase concentration by considering these to be small compared to the other terms in the equation. For the present definition of the void/solid fraction as a time average (cf. definition 2-2), however, these terms do not exist because  $\alpha = \bar{\alpha}$  and  $\alpha' = 0$ .

On the strength of these remarks and considering steady flows with constant liquid density for which

$$\frac{\partial}{\partial t} ((1-\alpha)\rho_l u_{1i}) = 0 \quad (3-A-4)$$

and thus the liquid mass balance reduces to  $\frac{\partial}{\partial x_k} (\rho_l (1-\alpha) u_{1k}) = 0$  it appears that

$$\frac{2}{3} \eta_l \frac{\partial}{\partial x_k} ((1-\alpha) u_{1k}) \delta_{ij} = 0 \quad (3-A-5)$$

yielding the liquid momentum balance for the present flows as

$$\begin{aligned} \rho_l \frac{\partial}{\partial x_k} ((1-\alpha) u_{1i} u_{1k}) = & -(1-\alpha) \frac{\partial p}{\partial x_i} - (1-\alpha) \rho_l g \frac{\partial x_i}{\partial x_1} + F_{Di} + \\ & + \frac{\partial}{\partial x_j} (\eta_l (\frac{\partial}{\partial x_j} ((1-\alpha) u_{1i}) + \frac{\partial}{\partial x_i} ((1-\alpha) u_{1j}))) - \rho_l \frac{\partial}{\partial x_k} ((1-\alpha) \overline{u'_{1i} u'_{1k}}) \end{aligned} \quad (3-A-6)$$

Hinze did not discuss the Reynolds stresses  $-\rho_l (1-\alpha) \overline{u'_{1i} u'_{1k}}$  any further, which in general are replaced by the well-known turbulence viscosity terms, based on the viscosity  $\epsilon$ , as defined by the hypothesis of Boussinesq. In the present case of two-phase flow this turbulence viscosity can be defined in two ways. The first definition adopted e.g. - without any physical or logical reasoning - by SATO and SEKOGUCHI [88] yields:

$$-\rho_l (1-\alpha) \overline{u'_{1i} u'_{1k}} = \rho_l (1-\alpha) \epsilon (\frac{\partial}{\partial x_j} u_{1i} + \frac{\partial}{\partial x_i} u_{1j}) \quad (3-A-7)$$

Since the turbulence viscosity  $\epsilon$  is in fact the turbulence diffusion coefficient for momentum it is obvious that the liquid velocity  $u_1$  is taken as the specific momentum of the liquid. The present author, however, considers it more reasonable to take - in the case of two-phase flow - the product  $(1-\alpha)u_1$  as specific momentum of the liquid phase. This latter assumption leads to the second definition:

$$-\rho_l (1-\alpha) \overline{u'_{1i} u'_{1k}} = \rho_l \epsilon (\frac{\partial}{\partial x_j} ((1-\alpha) u_{1i}) + \frac{\partial}{\partial x_i} ((1-\alpha) u_{1j})) \quad (3-A-8)$$

Defining the kinematic turbulence viscosity as

$$\eta_t = \eta_l (1 + \frac{\epsilon}{\nu}) \quad (3-A-9)$$

The substitution of the latter definition for the Reynolds stresses (3-A-8) in equation (3-A-6), yields the resultant liquid momentum balances for the present flows as

$$\begin{aligned} \rho_l \frac{\partial}{\partial x_k} ((1-\alpha) u_{1i} u_{1k}) = & -(1-\alpha) \frac{\partial p}{\partial x_i} - (1-\alpha) \rho_l g \frac{\partial x_i}{\partial x_1} + F_{Di} + \\ & + \frac{\partial}{\partial x_j} (\eta_t (\frac{\partial}{\partial x_j} ((1-\alpha) u_{1i}) + \frac{\partial}{\partial x_i} ((1-\alpha) u_{1j}))) \end{aligned} \quad (3-A-10)$$

In the following discussion on the allowable neglects for practical applications, only the shear stresses will be written out for the sake of brevity. For the present flows these shear forces are defined as:

$$F_{\tau i} = \frac{\partial}{\partial x_j} \tau_{ij} = \frac{\partial}{\partial x_j} (\eta_t (\frac{\partial}{\partial x_j} ((1-\alpha)u_{1j}) + \frac{\partial}{\partial x_i} ((1-\alpha)u_{1i}))) \quad (3-A-11)$$

Transformation to cylinder coordinates yields:

$$\begin{aligned} F_{\tau r} = & \frac{\partial}{\partial r} \left( \frac{\eta_t}{r} \frac{\partial}{\partial r} (r(1-\alpha)u_{1r}) \right) + \frac{\partial}{r\partial\varphi} \left( \eta_t \frac{\partial}{r\partial\varphi} ((1-\alpha)u_{1r}) \right) + \\ & - 2 \frac{\eta_t}{r} \frac{\partial}{r\partial\varphi} ((1-\alpha)u_{1\varphi}) + \frac{\partial}{\partial z} \left( \eta_t \frac{\partial}{\partial z} (1-\alpha)u_{1r} \right) + \\ & + \frac{\partial\eta_t}{\partial r} \cdot r \frac{\partial}{\partial r} \left( \frac{(1-\alpha)u_{1r}}{r} \right) + \frac{\partial\eta_t}{r\partial\varphi} \cdot r \frac{\partial}{\partial r} \left( \frac{(1-\alpha)u_{1\varphi}}{r} \right) + \frac{\partial\eta_t}{\partial z} \cdot \frac{\partial}{\partial r} ((1-\alpha)u_{1z}) \end{aligned} \quad (3-A-12)$$

$$\begin{aligned} F_{\tau z} = & \frac{1}{r} \frac{\partial}{\partial r} (r\eta_t \frac{\partial}{\partial r} ((1-\alpha)u_{1z})) + \frac{\partial}{r\partial\varphi} \left( \eta_t \frac{\partial}{r\partial\varphi} (1-\alpha)u_{1z} \right) + \\ & + \frac{\partial}{\partial z} \left( \eta_t \frac{\partial}{\partial z} ((1-\alpha)u_{1z}) \right) + \frac{\partial\eta_t}{\partial r} \cdot \frac{\partial}{\partial z} ((1-\alpha)u_{1r}) + \\ & + \frac{\partial\eta_t}{r\partial\varphi} \cdot \frac{\partial}{\partial z} ((1-\alpha)u_{1\varphi}) + \frac{\partial\eta_t}{\partial z} \cdot \frac{\partial}{\partial z} ((1-\alpha)u_{1z}) \end{aligned} \quad (3-A-13)$$

$$\begin{aligned} F_{\tau\varphi} = & \frac{1}{r^2} \frac{\partial}{\partial r} (r^3 \eta_t \frac{\partial}{\partial r} \left( \frac{(1-\alpha)u_{1\varphi}}{r} \right)) + \frac{\partial}{r\partial\varphi} \left( \eta_t \frac{\partial}{r\partial\varphi} ((1-\alpha)u_{1\varphi}) \right) + \\ & + 2 \frac{\partial}{r\partial\varphi} \left( \eta_t \frac{(1-\alpha)u_{1r}}{r} \right) + \frac{\partial}{\partial z} \left( \eta_t \frac{\partial}{\partial z} ((1-\alpha)u_{1\varphi}) \right) + \\ & + \frac{\partial\eta_t}{\partial r} \cdot \frac{\partial}{r\partial\varphi} ((1-\alpha)u_{1r}) + \frac{\partial\eta_t}{r\partial\varphi} \cdot \frac{\partial}{r\partial\varphi} ((1-\alpha)u_{1\varphi}) + \frac{\partial\eta_t}{\partial z} \cdot \frac{\partial}{r\partial\varphi} ((1-\alpha)u_{1z}) \end{aligned} \quad (3-A-14)$$

where the mass balance for steady flow without change of phase for incompressible liquid, i.e.

$$\rho_1 \left\{ \frac{1}{r} \frac{\partial}{\partial r} (r(1-\alpha)u_{1r}) + \frac{\partial}{r\partial\varphi} ((1-\alpha)u_{1\varphi}) + \frac{\partial}{\partial z} ((1-\alpha)u_{1z}) \right\} = 0 \quad (3-A-15)$$

(cf. equations (3-2) and (3-3)) is already taken into account.

The last three terms of each of the shear stress forces - proportional with  $\frac{\partial\eta_t}{\partial r}$ ,  $\frac{\partial\eta_t}{r\partial\varphi}$  and  $\frac{\partial\eta_t}{\partial z}$  - have been neglected in equations (3-9), (3-10) and (3-11). For  $F_{\tau z}$  and  $F_{\tau\varphi}$  this is justified by:

- the assumption that the turbulence is isotropic in the core region, making these terms zero for the core region
- the well-known boundary layer approximation, stating that the variations in the z and  $\varphi$ -direction are much smaller than those in the r-direction, yielding:

$$\frac{\partial \eta_t}{\partial z} \approx \frac{\partial \eta_t}{r \partial \varphi} \ll \frac{\partial \eta_t}{\partial r}$$

and 
$$\frac{\partial u}{\partial z} \approx \frac{\partial u}{r \partial \varphi} \ll \frac{\partial u}{\partial r} \quad (3-A-16)$$

- the fact that for the present type of flows the radial velocity  $u_r$  is much smaller than the axial and tangential velocities,  $u_z$  and  $u_\varphi$ . Hence it is reasonable to assume that

$$\frac{\partial u_r}{\partial x} \ll \frac{\partial u_z}{\partial x} \approx \frac{\partial u_\varphi}{\partial x} \quad (3-A-17)$$

Elaboration of the above remarks, yields that the last three terms of  $F_{tz}$  and  $F_{t\varphi}$  (equations (3-A-13) and (3-A-14)) may be ignored without any significant loss of accuracy, yielding:

$$F_{tz} = \frac{1}{r} \frac{\partial}{\partial r} (r \eta_t \frac{\partial}{\partial r} ((1-\alpha)u_{1z})) + \frac{\partial}{r \partial \varphi} (\eta_t \frac{\partial}{r \partial \varphi} ((1-\alpha)u_{1z})) + \frac{\partial}{\partial z} (\eta_t \frac{\partial}{\partial z} ((1-\alpha)u_{1z})) \quad (3-A-18)$$

and

$$F_{t\varphi} = \frac{1}{r^2} \frac{\partial}{\partial r} (r^3 \eta_t \frac{\partial}{\partial r} (\frac{(1-\alpha)u_{1\varphi}}{r})) + \frac{\partial}{r \partial \varphi} (\eta_t \frac{\partial}{r \partial \varphi} ((1-\alpha)u_{1\varphi})) + 2 \frac{\partial}{r \partial \varphi} (\eta_t \frac{(1-\alpha)u_{1r}}{r}) + \frac{\partial}{\partial z} (\eta_t \frac{\partial}{\partial z} ((1-\alpha)u_{1\varphi})) \quad (3-A-19)$$

These expressions contain the same terms as would be derived for homogeneous viscosity, but now the turbulence viscosity is part of the differential quotients, taking into account the significant contribution to the shear stress forces due to the inhomogeneity of turbulence viscosity.

Strictly speaking the above reasoning is not applicable to  $F_{tr}$  as far as wall region is concerned. However, considering that these last three terms are only non-zero in the wall region, the present author prefers to accept the error in this region introduced by ignoring these last three terms in order to obtain consistency with the above descriptions for  $z$  and  $\varphi$ -directions.

For the present type of rotation-symmetric pipe and separator flows, the derivatives to  $\varphi$  are zero, yielding the actual shear forces

as 
$$F_{tr} = \frac{\partial}{\partial r} (\frac{\eta_t}{r} \frac{\partial}{\partial r} (r(1-\alpha)u_{1r})) + \frac{\partial}{\partial z} (\eta_t \frac{\partial}{\partial z} ((1-\alpha)u_{1r})) \quad (3-A-20)$$

$$F_{tz} = \frac{1}{r} \frac{\partial}{\partial r} (r \eta_t \frac{\partial}{\partial r} ((1-\alpha)u_{1z})) + \frac{\partial}{\partial z} (\eta_t \frac{\partial}{\partial z} ((1-\alpha)u_{1z})) \quad (3-A-21)$$

and

$$F_{t\varphi} = \frac{1}{r^2} \frac{\partial}{\partial r} (r^3 \eta_t \frac{\partial}{\partial r} (\frac{(1-\alpha)u_{1\varphi}}{r})) + \frac{\partial}{\partial z} (\eta_t \frac{\partial}{\partial z} ((1-\alpha)u_{1\varphi})) \quad (3-A-22)$$

## APPENDIX 3-B

### TANGENTIAL VELOCITY COMPONENT BETWEEN BLADES

Subsection 3.2.1.2. contains the assumption - at variance with the true nature of two-phase flow - of ideal flow between the guide vanes at the entrance of the test sections and separators. The resulting absence of secondary circulation implies that the resultant velocity is parallel to the blades. Knowing the direction of the velocity it is possible to express one of the three velocity components - radial, axial and tangential - in the remaining two. The derivation of such an expression for the tangential velocity  $u_\varphi$  in terms of the radial and axial velocities  $u_r$  and  $u_z$ , though published before by VAN DER WELLE [89], is included here for the sake of completeness.

The geometry of vanes of uniform thickness, used in the present experiments, is fully determined by two angles (cf. figure 3-B-1); the curvature in the  $z, \varphi$  plane is given by the angle  $\gamma = \gamma(r, z)$  between the vertical and the tangent in the  $z, \varphi$  plane, while the curvature in the  $r, \varphi$  plane is determined by the angle  $\delta = \delta(r, z)$  between the radius and the tangent in the  $r, \varphi$  plane<sup>\*</sup>.

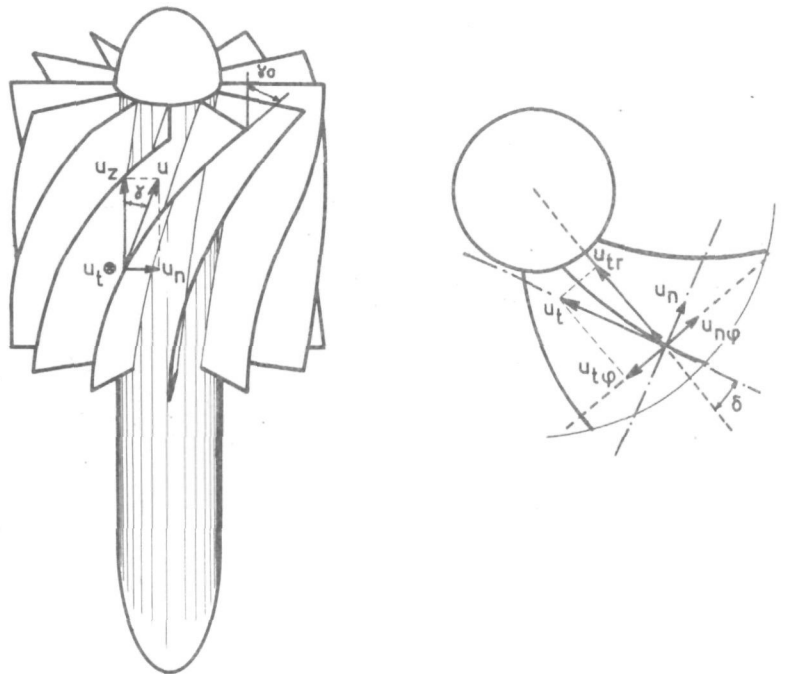


FIGURE 3-B-1

*Velocity components  
between guide vanes*

As can be seen in figure 3-B-1, the total velocity  $u$  is composed of three perpendicular velocity components, viz.:

- the axial velocity  $u_z$
- two velocity components in the  $r, \varphi$  plane, i.e.
  - $u_t$  tangential to the vane
  - $u_n$  normal to the vane

The velocity  $u_\varphi$ , to be derived, consists of two parts:

<sup>\*</sup>) *The actual functions for  $\gamma(r, z)$  and  $\delta(r, z)$  will be given and discussed together with the test section geometries in subsection 4.2.1.2.*

$$u_{\varphi} = u_{n\varphi} - u_{t\varphi} \quad (3-B-1)$$

where  $u_{n\varphi}$  is the component of  $u_n$  in the  $\varphi$ -direction, defined as:

$$u_{n\varphi} = u_n \cos \delta \quad (3-B-2)$$

and in the same way  $u_{t\varphi}$  is defined in relation to the component in the radial direction  $u_{tr}$  as:

$$u_{t\varphi} = u_{tr} \operatorname{tg} \delta \quad (3-B-3)$$

This radial component  $u_{tr}$  is part of the radial velocity  $u_r$ , according to:

$$u_r = -u_{nr} - u_{tr} \quad (3-B-4)$$

where the radial component  $u_{nr}$  of the normal velocity  $u_n$  is defined as:

$$u_{nr} = u_n \sin \delta \quad (3-B-5)$$

Combining equations (3-B-3) up to (3-B-5), yields:

$$u_{t\varphi} = (-u_r - u_n \sin \delta) \operatorname{tg} \delta \quad (3-B-6)$$

and substitution of this expression with equation (2-B-2) in (3-B-1) gives:

$$u_{\varphi} = u_n \cos \delta + (u_r + u_n \sin \delta) \operatorname{tg} \delta \quad (3-B-7)$$

The final step in this derivation is given by the relation between the normal velocity  $u_n$  and the axial velocity  $u_z$  (cf. figure 3-B-1), viz.

$$u_n = u_z \operatorname{tg} \gamma \quad (3-B-8)$$

Substituting this definition in equation (3-B-7) and multiplying both sides with  $\cos \delta$ , yields:

$$u_{\varphi} = \frac{u_z \operatorname{tg} \gamma(r,z) + u_r \sin \delta(r,z)}{\cos \delta(r,z)} \quad (3-B-9)$$

For the assumption of ideal flow this expression is valid for both phases, making it possible to compute  $u_{1\varphi}$  and  $u_{g\varphi}$  from  $u_{1z}$ ,  $u_{1r}$  and  $u_{gz}$ ,  $u_{gr}$ , respectively.

APPENDIX 3-C

SELECTION OF THE PROPER ROOT FROM THE QUADRATIC AXIAL VELOCITY EQUATIONS

The equation to be discussed is (3-55):

$$a_{r,z}^{n-1} [u_z]_{r,z}^n + b_{r,z}^{n-1} [u_z]_{r,z}^n + c_{r,z}^{n-1} = 0$$

For the gas momentum balance the first two coefficients follow from equation (3-53):

$$a_{r,z}^{n-1} = \alpha \rho_g \pm \frac{\Delta z}{2} F_{Dz}^* \tag{3-C-1}$$

$$b_{r,z}^{n-1} = \mp \Delta z F_{Dz}^* u_{1z} \tag{3-C-2}$$

while  $c_{r,z}^{n-1}$  is irrelevant for the present purpose.

As stated in subsection 3.3.2.4.1. the upper sign represents a positive relative velocity, i.e.  $u_{gz} > u_{1z}$  and the lower sign  $u_{gz} < u_{1z}$ .

Defining two determinants  $D = \sqrt{b^2 - 4ac}$ , viz.  $D_1$  for a positive relative velocity and  $D_2$  for a negative velocity, the roots for the two possibilities read:

- for a positive relative velocity  $u_{gz} > u_{1z}$ :

$$[u_{gz}]_{r,z}^n = \frac{\Delta z F_{Dz}^* u_{1z} \pm \sqrt{D_1}}{\Delta z F_{Dz}^* + 2\alpha \rho_g} \tag{3-C-3}$$

- for a negative relative velocity  $u_{gz} < u_{1z}$ :

$$[u_{gz}]_{r,z}^n = \frac{-\Delta z F_{Dz}^* u_{1z} \pm \sqrt{D_2}}{-\Delta z F_{Dz}^* + 2\alpha \rho_g} \tag{3-C-4}$$

Ignoring the possibility of negative determinants, which have no physical meaning, it is seen that for the minus sign root (3-C-3) yields  $u_{gz} < u_{1z}$  and root (3-C-4)  $u_{gz} > u_{1z}$ , being both in contradiction with the particular basic assumption, hence it can be concluded that the minus sign does not represent a valid solution.

The plus sign yields valid solutions for both roots as long as  $\sqrt{D_1}, \sqrt{D_2} > 2\alpha \rho_g u_{1z}$ , and thus the plus sign is prescribed in the computer program.

Similar considerations are applied to the liquid velocity in [95]. The logical outcome is that only the plus sign roots fulfill the initial assumptions, with the additional condition that  $\sqrt{D_1}, \sqrt{D_2} > 2(1-\alpha)\rho_l u_{gz}$ .

## APPENDIX 3-D

### DYNAMIC PRESSURE

In a recent publication STUHMILLER [97] derived momentum balances for two-phase flows which differ in several respects from those presented in subsection 3.2.1.2.3. This may be illustrated by applying Stuhmiller's model, for example to the radial momentum balances for rotation-symmetric flow:

gas phase

$$\begin{aligned} \frac{1}{r} \frac{\partial}{\partial r} (r \alpha \rho_g u_{gr}^2) + \frac{\partial}{\partial z} (\alpha \rho_g u_{gr} u_{gz}) + F_{Ar} = \\ = -\alpha \frac{\partial p}{\partial r} - p_d \frac{\partial \alpha}{\partial r} + \alpha \rho_g \frac{u_{g\varphi}^2}{r} - F_{Dr} \end{aligned} \quad (3-D-1)$$

liquid phase

$$\begin{aligned} \rho_l \frac{1}{r} \frac{\partial}{\partial r} (r(1-\alpha) u_{lr}^2) + \rho_l \frac{\partial}{\partial z} ((1-\alpha) u_{lr} u_{lz}) - F_{Ar} = \\ = - (1-\alpha) \frac{\partial p}{\partial r} + p_d \frac{\partial \alpha}{\partial r} + (1-\alpha) \rho_l \frac{u_{l\varphi}^2}{r} + F_{Dr} - F_{\tau r} \end{aligned} \quad (3-D-2)$$

Compared with equations (3-6) and (3-9), respectively, these equations differ in three respects, viz.:

- both balances contain an extra term  $p_d \frac{\partial \alpha}{\partial r}$ , the dynamic pressure term
- the liquid balance (3-D-2) additionally contains the virtual mass term  $- F_{Ar}$ .

Prior to evaluating the consequences of these differences on the ANALEST procedure

- the physical basis for the dynamic pressure term will be discussed in order to supplement the mathematical derivation of STUHMILLER [97]
- some critical comments will be made on the validity of Stuhmiller's model, leading to a modified set of momentum balances.

The physical basis of the dynamic pressure term is Stuhmiller's extension of the inter-phase pressure difference for bubble flow  $p_g - p_l = \frac{\sigma}{d}$  by a dynamic pressure  $p_d$ , yielding:

$$p_g = p_l - p_d + \frac{\sigma}{d} \quad (3-D-3)$$

Stuhmiller approximates the pressure difference by omitting the surface tension term as insignificant, i.e.:

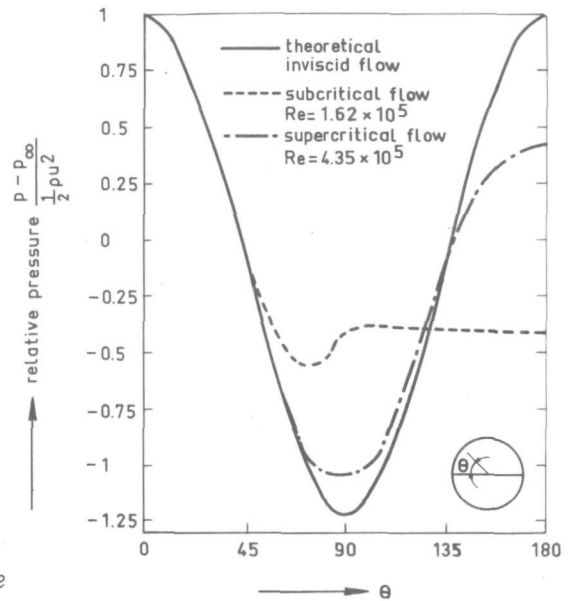
$$p_l - p_g = p_d \quad (3-D-4)$$

The magnitude of this dynamic pressure as well as proof of its existence is obtained from experimental data - presented by SCHLICHTING [13] - on the pressure distribution in the microscopic boundary layer around a sphere, shown in figure 3-D-1. According to STUHMILLER [97] the mean pressure decrease over the surface of the sphere corresponding to this pressure distribution is:

$$p_g - p_l = \frac{1}{S} \int_S (p - p_\infty) dS = - 0.37 C_D \rho u^2 \quad (3-D-5)$$

FIGURE 3-D-1

Pressure distribution at the boundary of a meridian cross section of a sphere



In terms of expression (3-D-4) this means that for bubble flow - having a resultant relative velocity  $u_{rt} = \sqrt{\sum_{i=1}^3 u_{ri}^2}$  - the dynamic pressure

$$p_d = 0.37 C_D \rho_l u_{rt}^2 \quad (3-D-6)$$

It should be emphasized that neither the drag force nor the virtual mass force acting on the bubble surface is affected by this mean pressure decrease. What will be affected, however, is the pressure gradient force derived in subsection 2.2.1.3., which will now be reconsidered for the control volume presented in figure 3-D-2.

In contrast with previous analyses two separate areas will be distinguished at the boundaries of the control volume. For this purpose the liquid boundary layer in which the pressure decreases from the liquid bulk pressure  $p_l$  to the average gas pressure  $p_g$  is assumed thin enough to be neglected.

As apparent from the detail in figure 3-D-2 this approximation yields: the area  $(1-\alpha)dxdy$  formed by the mathematical boundary on which the liquid pressure  $p_l$  acts and the area  $\alpha dxdy$  formed by the projected area of the gas cavities in the boundaries and acted upon by the gas pressure  $p_g = p_l - p_d$ .

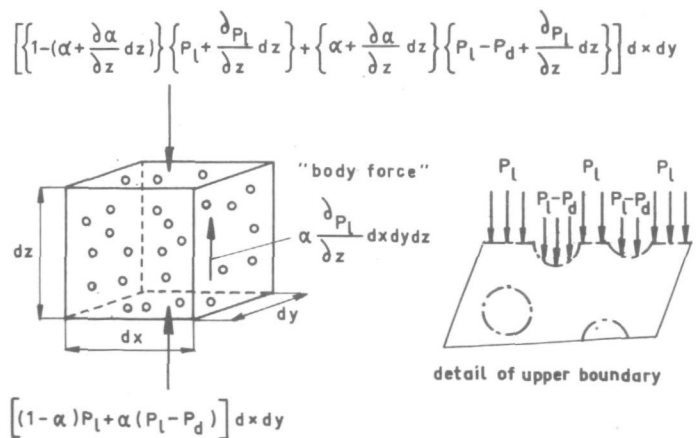


FIGURE 3-D-2

Control volume and pressure forces for the liquid phase of bubble flow

Stuhmiller assumed the dynamic pressure  $p_d$  to be constant over the entire volume, i.e.  $\frac{\partial p_d}{\partial z} = 0$ .

With this assumption elaboration of the pressure forces shown in figure 3-D-2 yields for the resultant pressure force:

$$F_{pz} dx dy dz = \{-(1-\alpha) \frac{\partial p}{\partial z} + p_d \frac{\partial \alpha}{\partial z}\} dx dy dz \quad (3-D-7)$$

which contains the extra dynamic pressure term  $p_d \frac{\partial \alpha}{\partial z}$ . The cause of this term is the difference in gas cavity area between the two boundary surfaces, acted upon by the reduced pressure  $p_g = p_l - p_d$ . Introduction of these extended pressure gradient forces yields Stuhmiller's balance equations containing the extra dynamic pressure terms, typified by equations (3-D-1) and (3-D-2).

While the above confirms the existence of a dynamic pressure difference  $p_d = p_l - p_g$  its occurrence both in the gas and liquid momentum balance appears open to criticism. The introduction by Stuhmiller of the dynamic pressure term  $-p_d \frac{\partial \alpha}{\partial r}$  in the gas momentum balance (3-D-1) violates the generalized equation described by ISHII [98], upon which Stuhmiller's analyses are based. As a discussion covering Ishii's extensive analyses is beyond the scope of this appendix only the nature of Stuhmiller's infringement will be indicated, followed by a more physical justification for elimination of the dynamic pressure term in the gas momentum balances. Neglecting viscous forces, Stuhmiller starts with the generalized equation:

$$\alpha_k \rho_k \left\{ \frac{\partial u_{ki}}{\partial t} + u_{kj} \frac{\partial u_{ki}}{\partial x_j} \right\} = - \frac{\partial}{\partial x_i} (\alpha_k p_k) + M_{ki} \quad (3-D-8)$$

where  $i$  denotes the direction and  $k$  the phases. Although this latter points to a distinction between the phase pressure  $p_k$  in the term  $-\frac{\partial}{\partial x_i} (\alpha_k p_k)$

Stuhmiller replaces these phase pressures - without explanation - by the bulk liquid pressure  $p_l$  in both the gas and liquid balances. According to Stuhmiller the interaction force  $M_{ki}$ , due to the interfacial pressure, has the same value but opposite sign for each of the phase balances, i.e.

$M_{li} = -M_{gi}$ , and contains - additional to the drag and virtual mass force - the term  $p_g \frac{\partial \alpha_g}{\partial x_i}$  representing the averaged decreased interfacial pressure.

Adding this pressure term to  $\frac{\partial}{\partial x_i} (\alpha_k p_l)$  and applying equation (3-D-4) yields as resultant pressure term for the

$$\text{gas balance} \quad : \quad - \frac{\partial}{\partial x_i} (\alpha_g p_l) + p_g \frac{\partial \alpha_g}{\partial x_i} = - \alpha_g \frac{\partial p_l}{\partial x_i} - p_d \frac{\partial \alpha_g}{\partial x_i}$$

$$\text{liquid balance:} \quad - \frac{\partial}{\partial x_i} ((1-\alpha_g) p_l) - p_g \frac{\partial \alpha_g}{\partial x_i} = - (1-\alpha_g) \frac{\partial p_l}{\partial x_i} + p_d \frac{\partial \alpha_g}{\partial x_i}$$

as used in equations (3-D-1) and (3-D-2) where  $p = p_l$  and  $\alpha$  stands for  $\alpha_g$  as used throughout this report.

By contrast consistent elaboration of Ishii's generalized equation (3-D-8), with  $\frac{\partial}{\partial x_i} (\alpha_g p_g)$  as major pressure term in the gas balances, yields  $-\alpha_g \frac{\partial p_g}{\partial x_i}$  as resultant pressure term in these gas momentum balances. Since  $\frac{\partial p_d}{\partial x_i} = 0$

in the control volume as stated above and thus  $-\alpha_g \frac{\partial p_g}{\partial x_i} = -\alpha_g \frac{\partial p_l}{\partial x_i}$  this result will eliminate any possible contribution of the dynamic pressure to the gas momentum balances.

The absence of any effect of the dynamic pressure on the gas momentum balances can also be derived in a more physical manner, by considering a gas control volume constructed in the same way as that of the liquid phase shown in figure 3-D-2. In such a gas control volume only closed gas 'bubbles' exist. Inside the control volume the individual bubbles are completely enclosed by the gas-liquid interface and at the boundaries the 'bubbles' are closed by a combination of the interface and the mathematical boundary of the control volume. Since a change in average pressure level, such as that due to the dynamic pressure, cannot affect the resultant pressure force on a closed contour, it follows that the gas momentum balances are not affected by the dynamic pressure.

The foregoing considerations confirm the validity of the gas momentum balances (3-6) through (3-8) rather than those proposed by Stuhmiller.

For the liquid momentum balances the effect of the dynamic pressure appears too complex for obtaining a quantitative mathematical description for multi-dimensional flows. The differences between Stuhmiller's liquid momentum balances and equations (3-9) through (3-11) caused by the dynamic pressure and virtual mass terms will, however, be elucidated by a qualitative discussion for one-dimensional flow.

For this latter purpose the flow around the discontinuous phase is considered. The flow around these bubbles/particles yields peak velocities in the boundary layers of these bubbles/particles. The resulting pressure distribution at the interface not only includes the dynamic pressure as well as the drag force and the virtual mass force as correctly described by Stuhmiller, but also affects the momentum of the continuous phase.

According to appendix 2-C any peak velocity distribution superimposed upon the mean velocity distribution yields extra momentum, here called the peak momentum  $M_p$ . The effect of this peak momentum is twofold:

- with respect to the virtual mass force it is obvious that acceleration of the bubbles/particles increases the peak momentum, yielding a contribution to the fluid momentum which counteracts the "virtual mass pressure force" at the bubble/particle interfaces. Considering the analysis of HINZE [9], where the virtual mass force does not figure at all in the liquid momentum balance, it may be expected with good reason that this extra liquid peak momentum cancels the resultant "virtual mass pressure force" at the interfaces, an effect not taken into account by Stuhmiller.
- with respect to the dynamic pressure term it should be noticed that this is caused by a void fraction gradient  $\frac{\partial \alpha}{\partial x}$ , i.e. a difference in void fraction across the control volume. This void fraction difference, however, also implies a difference in the amount of bubble/particle boundary layer on both sides, i.e. a variable amount of peak momentum  $M_p$ . Determination of the magnitude of the resultant momentum flux term  $\frac{\partial M_p}{\partial x}$ , if possible at all, would require highly complex analysis of the velocity distribution around random swarms of bubbles/particles, which is beyond the scope of the present investigation. But whatever its magnitude, this extra momentum flux  $\frac{\partial M_p}{\partial x}$  will counteract the dynamic pressure term.

In the author's opinion it is reasonable to expect that this latter effect cancels out the dynamic pressure term, yielding a liquid momentum balance without any contribution of the dynamic pressure.

Notwithstanding the logic of this last conclusion, there exists a possibility that it is invalid for multi-dimensional flows. In such flows the balance or unbalance between the peak momentum flux and dynamic pressure term is much more complex, because this latter term

$$p_d \frac{\partial \alpha}{\partial x_i} = 0.37 C_D \rho_l u_{rt}^2 \frac{\partial \alpha}{\partial x_i} \quad (3-D-9)$$

is not affected by the direction of the resultant relative velocity  $u_{rt}$ , as is the case for the components of the drag force described by expression (3-13):

$$F_{Di} = \frac{3}{4} \alpha \frac{C_D}{d} \rho_l u_{rt} u_{ri}$$

Because the present author considers it reasonable to expect some sort of relation between the drag force and the peak momentum, it seems possible that, for instance, in a direction perpendicular to the resultant relative velocity - where the drag force  $F_{Di} = 0$  because  $u_{ri} = 0$  - there exists no net peak momentum flux. The schematical representation shown in figure 3-D-3 supports the likelihood of such a zero resultant peak momentum perpendicular to the resultant relative velocity. Since the dynamic pressure term remains as long as  $\frac{\partial \alpha}{\partial x_1} \neq 0$  in that direction, it is not cancelled out by the peak momentum flux in this direction.

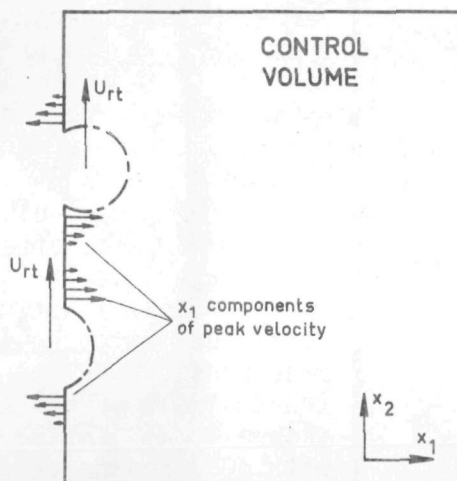


FIGURE 3-D-3

*Perturbation velocities perpendicular to the resultant relative velocity*

Generalizing the above possibilities it is the author's opinion that the dynamic pressure term is cancelled out by the peak momentum flux in the direction of the resultant relative velocity, while contributing by a fraction  $\eta_p$  of its nominal value to the liquid momentum balances for directions other than the relative velocity.

Application of the above analyses to the momentum balances described in subsection 3.2.1.2. leaves the gas momentum balances (3-6), (3-7) and (3-8) unchanged, while in the liquid momentum balances the fraction  $\eta_p$  of the dynamic pressure term not cancelled out by the peak momentum has to be introduced.

The radial and axial liquid balances, (3-9) and (3-10) respectively, thus become:

$$\rho_l \frac{1}{r} \frac{\partial}{\partial r} (r(1-\alpha)u_{lr}^2) + \rho_l \frac{\partial}{\partial z} ((1-\alpha)u_{lr}u_{lz}) =$$

$$= - (1-\alpha) \frac{\partial p}{\partial r} + \eta_{pr} p_d \frac{\partial \alpha}{\partial r} + (1-\alpha) \rho_l \frac{u_{l\varphi}^2}{r} + F_{Dr} - F_{\tau r} \quad (3-D-10)$$

and

$$\rho_l \frac{1}{r} \frac{\partial}{\partial r} (r(1-\alpha)u_{lr}u_{lz}) + \eta_l \frac{\partial}{\partial z} ((1-\alpha)u_{lz}^2) =$$

$$= - (1-\alpha) \frac{\partial p}{\partial z} + \eta_{pz} p_d \frac{\partial \alpha}{\partial z} - (1-\alpha) \rho_l g + F_{Dz} - F_{\tau z} \quad (3-D-11)$$

where for the flows of interest for this investigation  $\eta_{pr}$  is expected to be close to unity and  $\eta_{pz}$  close to zero, because the relative velocity is predominantly axial in direction.

By contrast the tangential liquid momentum balance (3-11), is not affected because  $\frac{\partial \alpha}{\partial \varphi}$  and thus  $\eta_{p\varphi} p_d \frac{\partial \alpha}{\partial \varphi}$  equals zero because of the axial symmetry. The relative importance of the dynamic pressure term  $p_d \frac{\partial \alpha}{\partial x_i} = 0.37 C_D \rho_l u_{rt}^2 \frac{\partial \alpha}{\partial x_i}$  will now be evaluated by comparison with the drag force

$F_{Di} = \frac{3}{4} \alpha \frac{C_D}{d} \rho_l u_{rt} u_{ri}$ . From the expression

$$p_d \frac{\partial \alpha}{\partial x_i} = 0.37 C_D \rho_l u_{rt}^2 \frac{\partial \alpha}{\partial x_i} = \frac{0.37}{0.75} \frac{d}{\alpha} \frac{u_{rt}}{u_{ri}} \frac{\partial \alpha}{\partial x_i} F_{Di} \quad (3-D-12)$$

it follows that the relative importance is determined by the magnitude of the dimensionless number  $\frac{1}{2} \frac{d}{\alpha} \frac{u_{rt}}{u_{ri}} \frac{\partial \alpha}{\partial x_i}$ .

	relative velocity ratio $\frac{u_{rt}}{u_{ri}}$	void fraction gradient $\frac{\partial \alpha}{\partial x_i} [m^{-1}]$	dimensionless number $ \frac{1}{2} \frac{d}{\alpha} \frac{u_{rt}}{u_{ri}} \frac{\partial \alpha}{\partial x_i} $
fixed parameters:  bubble diameter $d = 0.002 [m]$	$\frac{u_{rt}}{u_{rz}} \approx \frac{u_{rz}}{u_{rz}} = 1$	$ \frac{\Delta \alpha}{\Delta z}  = \frac{0.5}{0.05} = 10$	axial: 0.02
void fraction $\alpha = 0.5$	$ \frac{u_{rt}}{u_{rr}}  = \frac{50}{0.5} = 100$	$ \frac{\Delta \alpha}{\Delta r}  = \frac{0.5}{0.015} = 33$	radial: 6.6

TABLE 3-D-4

Components of  $\frac{1}{2} \frac{d}{\alpha} \frac{u_{rt}}{u_{ri}} \frac{\partial \alpha}{\partial x_i}$

The maximum values of this dimensionless number occurring for the air-water experiments discussed in chapter 4 are presented in table (3-D-4), where in addition the various components of this number are tabulated for the axial as well as the radial direction. Even for these maximized components the dimensionless number is only 0.02 for the axial momentum balance, making it irrelevant on the axial liquid balances in use in chapters 3 and 2 whether the term  $p_d \frac{\partial \alpha}{\partial z}$  is fully cancelled out by the extra momentum.

By contrast it will affect computations in which the radial momentum balances are used. For the present state of the subroutine ANALEST, where the radial mixture balance is used to compute the radial pressure gradient, it will affect the computed radial pressure gradient. This gradient, however, is almost completely determined by the centrifugal force field

for the liquid:  $(1-\alpha)\rho_1 \frac{u_{1\varphi}^2}{r}$  and from a preliminary analysis not included here it follows that the maximum value of the dynamic pressure term  $p_d \frac{\partial \alpha}{\partial r}$  does not exceed 10% of the centrifugal force field and this maximum value extends only over a small radial region. Because the expected accuracy of the radial pressure computation of ANALEST is of the same magnitude, the present author accepts the possible inaccuracy introduced by the absence of the dynamic pressure contribution to the radial liquid momentum balance. However, when computing the radial liquid velocity from the radial liquid momentum balance - as proposed in subsection 3.3.2.5. in the extended scheme for subroutine ANALEST - a much larger effect of the dynamic pressure term has to be expected, notably in those regions where the velocities are controlled by the drag force rather than by the acceleration forces. Hence the implementation of this proposed extension will require further investigation of the dynamic pressure term with respect to its compensation by an extra momentum flux in the radial liquid momentum balance as well as to the coefficient 0.37, which most probably also depends on the virtual mass force and perhaps on other flow parameters as well.

In view of this probable significance of the dynamic pressure term for the radial liquid momentum balance it is interesting to note Stuhmiller's conclusion that this term strongly affects the character of numerical computations based on the respective two-phase balances, while PRINS [1] - using the radial liquid momentum balance without this term - reported unstable behaviour of his numerical procedure manifesting itself most strongly in the radial gas velocity.

## APPENDIX 4-A

### COST EFFECTS OF SEPARATOR PERFORMANCE

The costs discussed in this appendix refer to changes in power output and component design of a standard General Electric BWR-6-218/592 due to assumed variations in the performance of primary separators. A full discussion of these cost estimations is given in [120], based on component prices and steam cycle data made available by NUCON B.V., Amsterdam, The Netherlands, as of 1976.

The only change in reactor design caused by variations in carry-over from the primary separators is the adaptation of the impingement dryers required to keep their exit steam quality at the value  $x = 99.90\%$  corresponding to the original General Electric design.

In the absence of operating data the design value for carry-over from the primary separators is assumed to be 10%, i.e.  $x_E = 0.9$ . Considering these in- and outlet qualities and assuming dryer performance is described - with qualities in percent - by:

$$(x_{\text{out}} - x_{\text{ind}}) = (100 - x_{\text{ind}})(1 - e^{-kL}) \quad (4-A-1)$$

it is found that  $k = \frac{\ln 100}{L_d} = \frac{4.61}{L_d}$ , where  $L_d$  is the design length of the dryer.

Based on these expression it follows that:

$$\Delta L_d = \frac{L_d}{4.61} \ln \left( \frac{100 - x_{\text{ind}}}{10} \right) \quad (4-A-2)$$

Roughly half of the total dryer cost of Dfl.  $3.24 \times 10^6$ \*) is for support devices and other accessories, leaving a price per meter of Dfl.  $1.62 \times 10^6/L_d$  for the dryer proper. Thus the extra dryer costs are:

$$\Delta f_{1d} = \frac{1.62 \times 10^6}{4.61} \ln \left( \frac{100 - x_{\text{ind}}}{10} \right) = 0.351 \times 10^6 \ln \left( \frac{100 - x_{\text{ind}}}{10} \right) \quad (4-A-3)$$

To these dryer costs must be added the costs due to the increased pressure vessel containment height.

Based on a price of Dfl.  $18.5 \times 10^6$  for a 26.8 m high pressure vessel, the price per meter is taken as Dfl.  $0.7 \times 10^6$ .

The cost per meter containment for a cross-sectional area of  $204 \text{ m}^2$  of concrete and a concrete price of Dfl. 500 per  $\text{m}^3$  will be Dfl.  $0.1 \times 10^6$ . The resulting extra costs of carry-over for a dryer design height of 2.29 m are:

$$\Delta f_{2d} = \frac{2.29}{4.61} \ln \left( \frac{100 - x_{\text{ind}}}{10} \right) (0.7 + 0.1) \times 10^6 = 0.397 \times 10^6 \ln \left( \frac{100 - x_{\text{ind}}}{10} \right) \quad (4-A-4)$$

The total change in capital costs due to carry-over will thus be:

$$\Delta C_d = \Delta f_{1d} + \Delta f_{2d} = 0.748 \times 10^6 \ln \left( \frac{100 - x_{\text{ind}}}{10} \right) \quad (4-A-5)$$

An assumed increase in primary separator carry-over from the estimated design value of 10% to 20% will thus require an additional investment of

\*) All prices refer to mid 1976.

Dfl.  $0.519 \times 10^6$ .

The consequences of a change in carry-under are much more complex. The first direct effect is the change in live steam flow to the turbine. For a total core flow of 10633 kg/s and a core exit quality of 0.147 the downcomer water flow is  $(1 - 0.147) \times 10633 = 9080$  kg/s. The corresponding decrease in live steam flow resulting from carry-under exceeding the design value of 0.17% [120] will be:

$$\Delta M = 90.8 (x_{cu} - 0.17) \text{ kg/s} \quad (4-A-6)$$

where  $x_{cu}$  is the assumed carry-under percentage.

A second effect is caused by the requirement that the water conditions at the nuclear core inlet remain unchanged. To achieve this the enthalpy of the feed water has to be reduced to quench the extra amount of entrained steam. This enthalpy reduction follows from the heat balance:

$$\Delta h_{fw} (1563 - \Delta M) = 90.8 (x_{cu} - 0.17) 1840 \quad (4-A-7)$$

where

- $\Delta h_{fw}$  is the required reduction in feed water enthalpy [kJ/kg]
- 1563 [kg/s] is the original feed water mass flow
- 1840 [kJ/kg] is the difference in enthalpy between carry-under steam and core inlet water.

The model described in [120] obtains this reduction in feedwater enthalpy by a corresponding decrease in bled steam flow to the last (nr. 6 i.e. highest pressure) feedwater heater. The resulting redistribution of flows through the high pressure turbine and intermediate reheater is shown in figure 4-A-1. This simplified model was selected in order to keep the changes in flow through the turbine as small as possible (because of the highest enthalpy at the first extraction point the amount of steam involved is smallest). The reduction of this extraction flow by P kg/s steam causes:

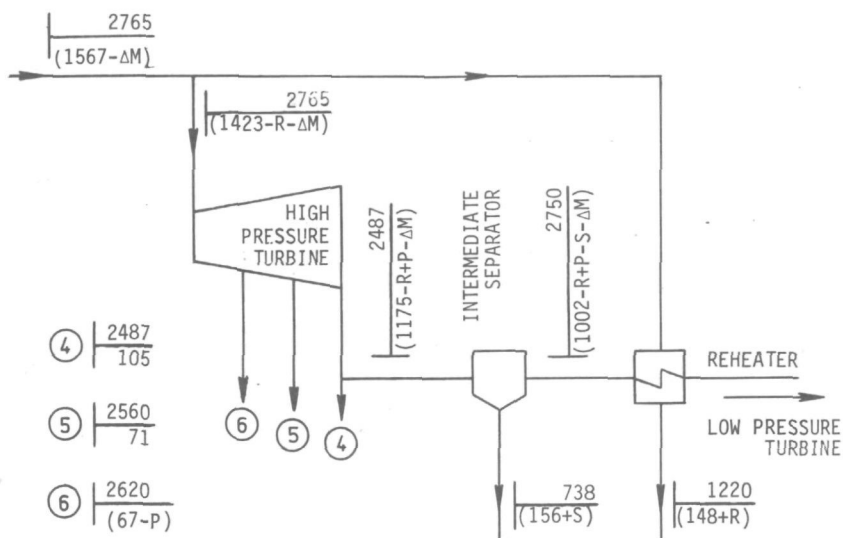
- a decrease in live steam flow to the high pressure turbine by an amount of R kg/s needed for additional reheating in the intermediate steam reheater
- an increase in moisture removal in the intermediate moisture separator by an amount of S kg/s, caused by the increase in flow to the low pressure turbine.

Figure 4-A-1 presents the values for  $\Delta M$ , P, R and S computed in [120] from the original BWR-6-218/592 generating unit heat balance. The combined effect of these flow changes is found in [120] to result in a decrease in nett electric power output by:

$$\Delta P_e = 8.80 (x_{cu} - 0.17) \text{ MW} \quad (4-A-8)$$

This derating may be considered to represent the only cost component due to change in carry-under, as first estimate of the savings through reduced turbine and generator dimensions showed these to be of minor importance. As assumed doubling of the carry-under quality from 0.17% up to 0.34% yields a decrease in nett power by 1.5 MW. On the basis of the 1976 price of Dfl. 45 per MWh (sent out) and 65% capacity factor for the reactor, this results in an annual loss in sales of:

$$\Delta f_{cu} = 0.65 \times 8760 \times 45 \times 1.5 = \text{Dfl. } 0.384 \times 10^6 \quad (4-A-9)$$



NOMENCLATURE

ENTHALPY kJ/kg  
MASS FLOW kg/s

$$\Delta M = 90.8 (x_{cu} - 0.17)$$

$$R = 0.8 (x_{cu} - 0.17)$$

$$P = 98.2 (x_{cu} - 0.17)$$

$$S = 0.9 (x_{cu} - 0.17)$$

FIGURE 4-A-1

Flowsheet of the adapted mass flows for the high pressure turbine

In order to be able to compare this annual income loss with capital costs resulting from the increase of carry-over, it has to be transformed to actualized costs  $\Delta C_{cu}$  over the 35 year life time of the reactor:

$$\Delta C_{cu} = \frac{\Delta f_{cu}}{r_r} \{1 - (1 + r_r)^{-35}\} \quad (4-A-10)$$

where  $r_r$  is the real interest rate, derived from the nominal interest rate  $r$  by correcting it for monetary inflation  $i$ :

$$r_r = \frac{1 + r}{1 + i} - 1 \quad (4-A-11)$$

Assuming a nominal interest rate of 9% p.a. and a monetary inflation of 7% p.a., the real interest rate becomes 1.86% and the total actualized costs due to the above doubling in carry-under will be Dfl.  $9.82 \times 10^6$ .

The cost of separator pressure loss is evaluated in [120] on the basis of power demand variations of the two circulation loops, each having a design value of 4.4 MW (cf. table 3-5). The change in investment costs is ignored, assuming the required variations in pump design to be small enough to be covered by the margin in the original design.

The circulation loops each consist of 10 jet pumps having a discharge head of  $197 \text{ kN/m}^2$ , while the rated pressure loss over the separators equals  $52.6 \text{ kN/m}^2$  (cf. table 4-3). Thus the relative rate of pressure head variation over the jet pump due to the separator pressure loss  $\Delta p_s$  becomes  $\left\{ \frac{197 - 52.6}{197} + \frac{\Delta p_s}{197} - 1 \right\}$  ( $\Delta p_s$  in  $\text{kN/m}^2$ ). On the basis of investigations by SCHROEDER [121] and VYAS and SUBIR KAR [122] it is stated, that

the relative variations of pressure head over the jet pump and of the recirculation flow are equal, as long as the mass flows remain constant. Since this latter condition is fulfilled in the present case, and the relative variation of the recirculation pressure head may be taken equal to that of the power demand, the variation in power demand becomes:

$$\Delta p_C = \frac{\Delta p_S - 52.6}{197} \times 4.4 \text{ MW} \quad (4-A-12)$$

for each of the two circulation loops.

For 65% capacity factor and a price of Dfl. 45 per MWh, the annual loss in sales is:

$$\begin{aligned} f_{\Delta p_S} &= 2 \times \frac{\Delta p_S - 52.6}{197} \times 4.4 \times 0.65 \times 8760 \times 45 = \\ &= \text{Dfl. } 2.25 \times 10^6 \times \frac{\Delta p_S - 52.6}{197} \end{aligned}$$

Assuming a reduction in separation pressure loss to  $40 \text{ kN/m}^2$  the annual savings become  $\text{Dfl. } 0.14 \times 10^6$ , which yields - on the same basis as equations (2-A-10) and (2-A-11) - a total actualized cost of  $\text{Dfl. } 3.68 \times 10^6$  over a 35 year life time.

## APPENDIX 4-B

### MEASUREMENT PROCEDURE FOR SEPARATOR GAS EXIT FLOWS

According to figure 4-B-1 three gas exit flows are to be measured:

- vortex finder exit
- carry-under air
- exhaust vessel vent

The measurement procedure has to satisfy two requirements, viz.

- all three exit flows must have the same pressure. Apart from the small difference between  $p_{15}$  and  $p_{16}$  (cf. figure 4-B-1) mentioned in subsection 4.5.2. this requirement is satisfied by having them discharge to a common exhaust manifold through large diameter piping. For reasons described below the exhaust manifold consists of two separate lines - designated A and B in the figure - with equalized pressures ( $p_{18}$  and  $p_{17}$ )
- these equalized exhaust pressures must not be affected by the flow measurements, which is achieved by readjusting pressures  $p_{17}$  and  $p_{18}$  to their initial value prior to the recording of each individual flow measurement.

Referring to figure 4-B-1 this measurement procedure starts with the discharge valves set in such a way that the air from all three mist separators is discharged to line A, while the pressure reducer in this line is adjusted to supply a small additional flow of air sufficient to maintain a constant pressure of about  $10 \text{ kN/m}^2$  gauge in this exhaust line. The pressure in exhaust line B is then equalized to this value by adjusting the reducer downstream of the flow meter, as the orifices of both lines are identical the exiting gas flows will then also be identical. The pressure reducer upstream of the air flowmeter in the B line is set in a fixed position such as to maintain the reading of this meter in the upper part of its range.

Measurement of each of the three exit air flows takes place by switching the corresponding discharge connection from the A line to the B line. The subsequent decrease of  $p_{18}$  is eliminated by further opening of the A line pressure reducer, while the increase of the B line pressure  $p_{17}$  is eliminated by partial closure of the corresponding B line pressure reducer (downstream the air flow meter). The result of these readjustments is that both outlet pressures  $p_{17}$  and  $p_{18}$  are restored to their original equal value, as are the corresponding exhaust flows. In the case of line B this flowrate, originally obtained from the flowmeter supply alone, now consists of the sum of the exit air flow to be measured and the readjusted flowmeter supply. The difference between the two flowmeter readings thus equals the exit air flow rate to be measured.

The sum of the exit air flows measured in the above way has a standard deviation with respect to the inlet air flow of 4 to 9% depending on the magnitude of the latter value. This relatively large error - corresponding to 5 to 11% and 25 to 50% of the vortex finder exit and downcomer gas flows respectively - is caused by the air flowmeter inaccuracy of 3% (cf. subsection 2.3.1.4.1.) and the summation of four measured flows needed to obtain the difference between the in- and outlet flows. Though the accuracy of the individual flows is improved by taking five readings for each and including a correction to balance the in- and outlet flows, the standard deviation for the resulting downcomer air flow, for example, ranges up to 20%.

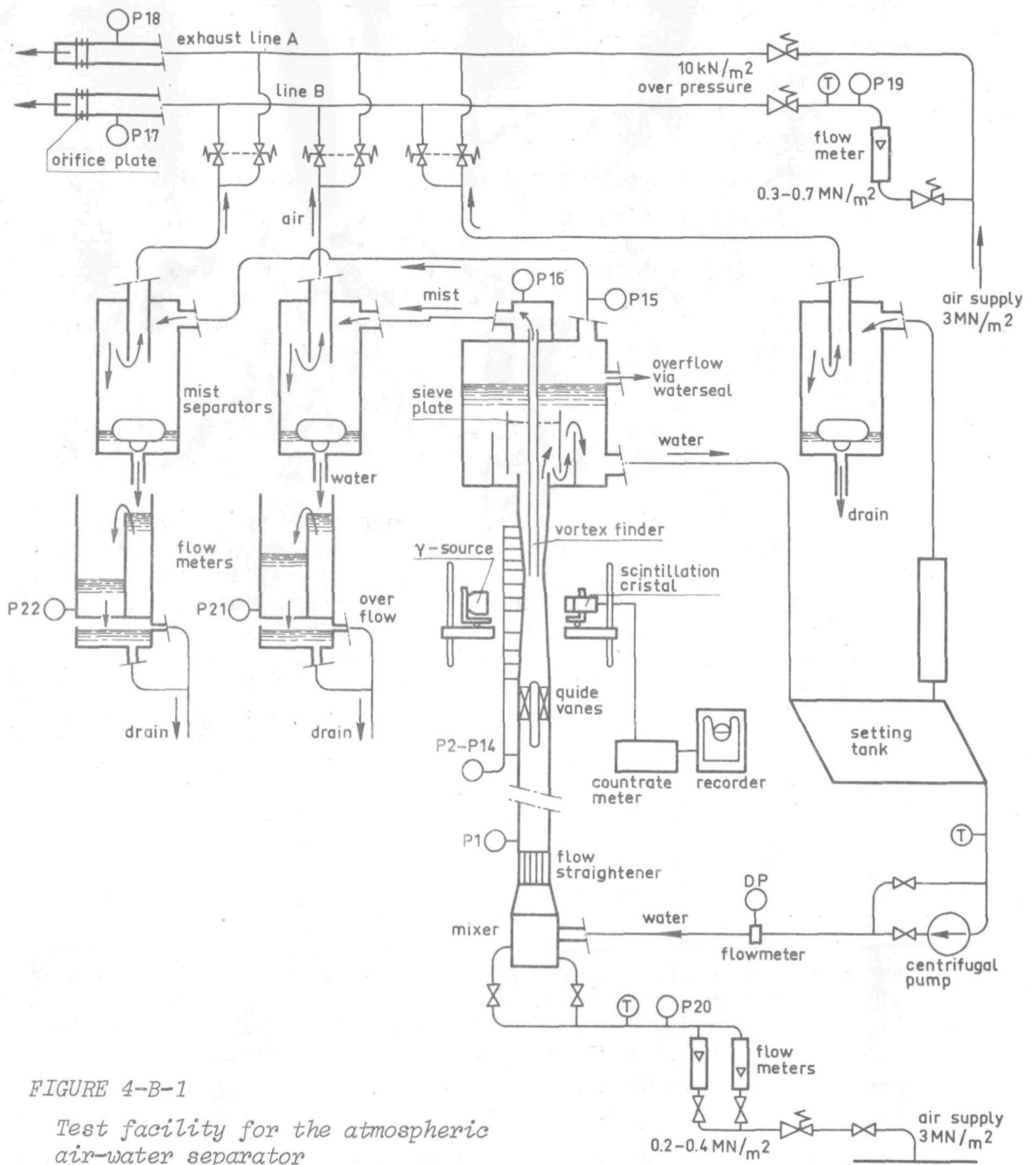


FIGURE 4-B-1

Test facility for the atmospheric air-water separator

## STELLINGEN

1. Gezien de periode der cyclische verschijnselen in de ekonomie gedurende de laatste eeuwen moet worden aangenomen dat de huidige ekonomische teruggang tot omstreeks 1995 zal duren.
2. Het gebruik van prijskompensatie als middel ter verwezenlijking van inkomenspolitiek, door de overheid zowel als de vakbeweging, bemoeilijkt de inflatiebestrijding.
3. Wil het streven naar energiebesparing bij ruimteverwarming door toepassing van betere woningisolatie en zonnewarmte in Nederland leiden tot op landelijke schaal significante resultaten, dan is een aanzienlijke verhoging van de aardgasprijs vereist.
4. Bij de discussie over het al dan niet toepassen van kernsplijtings-energie dient niet zoals tot heden gebruikelijk de grootte van het gevaar van deze energievorm geïsoleerd te worden behandeld, maar dienen de gevolgen van deze toepassing te worden afgewogen tegen die van andere vormen van energievoorziening.
5. Huisartsen en medisch specialisten hebben een hoger inkomen naarmate ze minder aandacht kunnen geven aan hun individuele patiënten.
6. Bij fotokopiëren van tijdschriften en delen van boeken ontstaat veelal aanzienlijke materiaalverspilling doordat het formaat der orginelen niet is aangepast aan het gebruikelijke A4-formaat van de fotokopieer-apparatuur. In het kader van de bestrijding van deze verspilling dient tevens het gebruik van apparatuur met de mogelijkheid tot het maken van tweezijdig bedrukte kopieën te worden gestimuleerd.
7. Het bedrijven van topsport door jonge kinderen is in strijd met de geest van de wet op de kinderarbeid.
8. Het uitbreiden van de wettelijke verplichting tot publikatie in het Staatsblad van wetten, koninklijke besluiten en algemene maatregelen van bestuur, met de verplichting tot een gelijktijdige publikatie van een voor leken begrijpelijke toelichting en waar nodig tot in ruime kring gegeven aansluitende voorlichting hierover, zal in aanzienlijke mate bijdragen tot de rechtszekerheid en tot de spreiding van kennis en macht.
9. Ook in recente literatuur wordt bij het opstellen van modellen en korrelaties voor tweefasenstroming de éénfasestroming veelal als uitgangspunt gekozen. Het verdient echter aanbeveling direkt uit te gaan van een voor tweefasenstroming geldige beschrijvingswijze, waarin éénfasestroming als een bijzondere vorm van tweefasenstroming voorkomt.